

Maximizing Efficiency of Solar Energy Harvesting Systems

Supplying a Microgrid using an Embedded System

by

Haytham Abdelgawad

A thesis submitted to the
School of Graduate and Postdoctoral Studies in partial
fulfillment of the requirements for the degree of

Doctor of Philosophy

in

The Electrical and Computer Engineering

Faculty of Engineering and Applied Science

Ontario Tech University

Oshawa, Ontario, Canada

December 2019

© Haytham Abdelgawad, 2019

THESIS EXAMINATION INFORMATION

Submitted by: **Haytham Abdelgawad**

Ph.D. in Electrical and Computer Engineering

Thesis title: Maximizing Efficiency of Solar Energy Harvesting Systems Supplying a Microgrid using an Embedded System

An oral defense of this thesis took place on November 28th, 2019 in front of the following examining committee:

Examining Committee:

Chair of Examining Committee	Dr. Ying Wang
Research Supervisor	Dr. Vijay Sood
Examining Committee Member	Dr. Sheldon Williamson
Examining Committee Member	Dr. Jing Ren
University Examiner	Dr. Yuping He
External Examiner	Dr. Afshin Rezaei-Zare

The above committee determined that the thesis is acceptable in form and content and that a satisfactory knowledge of the field covered by the thesis was demonstrated by the candidate during an oral examination. A signed copy of the Certificate of Approval is available from the School of Graduate and Postdoctoral Studies.

Abstract

Due to the high initial capital cost of photovoltaic (PV) panels and their low conversion efficiency, it is imperative to operate the PV system at its maximum power point (MPP). In this context, the goal in this thesis is to develop and improve the PV system, by contributing to the optimization of energy withdrawn from the PV panel using an embedded system. For this purpose, the model of the PV panel is first studied in accordance with the real behavior of the PV panel. The single diode model of the PV panel is first developed in Matlab environment to obtain an excellent correspondence to manufacturer's published curves and represent the effects of insolation and temperature on the solar characteristics. Secondly, the small-signal model for DC-DC Boost converter, with/without parasitic elements, operating in continuous conduction mode (CCM)/discontinuous conduction mode (DCM) is developed to understand the basic features of the switching system and investigate the effects of parasitic elements and losses on the model accuracy, the efficiency and the dynamic performance of the system. Next, this work proposes a design of a feedback controller for a DC-DC Boost converter to yield a robust, closed-loop controller structure with stable static and dynamic characteristics over the whole operational range of the converter. Moreover, a study of different numerical integration methods is presented to enable the implementation of real-time models in embedded hardware platforms.

The primary objective of the research proposed is to control the output voltage or current of the PV array to generate maximum possible power at a certain irradiance and temperature. This can be achieved by implementing the maximum power theorem for load matching using the relationship between input and output impedances. To achieve this objective, the popular MPPT Perturb-and-Observe (P&O) technique is used as a test bench. This is followed by the development of a novel intelligent method using a Kalman Filter as an alternative to provide an acceptable performance against both the noises and dynamic environmental changes. Due to the excellent estimation ability of the Kalman Filter in the dynamic system within a noisy environment, an accurate MPP can be predicted without any reduction of system dynamics.

A PV test system with a 100 kW PV array and MPPT controller using the traditional P&O and KF algorithms was used. The PV panel output power was controlled by three methods: (a) without any MPPT (i.e. open loop), (b) with an MPPT using the P&O algorithm, and (c) with an MPPT using the proposed KF algorithm. The obtained results clearly highlight the superiority of the proposed method with a very high level of robustness, reliability and accuracy. Furthermore, a Matlab simulation model yields an efficiency of 99.38 % under the standard test condition (STC), which is almost 5 % higher than the conventional P&O method under the same conditions. Finally, a hardware implementation of the system is tested on an FPGA chip Altera Cyclone II EP2C20F484C7 to verify the efficiencies and tracking speeds in a real-time environment.

Keywords: Kalman Filter; Photovoltaic panel; MPPT; Boost converter; Modelling; Perturb and Observe; Embedded System; Microgrid.

AUTHOR'S DECLARATION

I hereby declare that this thesis consists of original work of which I have authored. This is a true copy of the thesis, including any required final revisions, as accepted by my examiners.

I authorize the University of Ontario Institute of Technology to lend this thesis to other institutions or individuals for the purpose of scholarly research. I further authorize University of Ontario Institute of Technology to reproduce this thesis by photocopying or by other means, in total or in part, at the request of other institutions or individuals for the purpose of scholarly research. I understand that my thesis will be made electronically available to the public.

Haytham Abdelgawad

Acknowledgment

First and foremost, I would like to thank Almighty God, the compassionate, the almighty Merciful, whose guidance kindly lead me to complete my thesis.

The success of this thesis is attributed to the extensive support and assistance from my supervisor, Dr. Vijay Sood. I would like to express my sincere gratitude to him for his guidance, valuable advice, supervision, encouragement and kindness to me throughout this study. My appreciation and deep thanks to all my friends and colleagues in Dr. Sood's Smart Grid and EV research group at Ontario Tech University.

My heartfelt thanks are extended to my father, my mother and my two sisters for giving me the determination to overcome many trying moments to pursue my dreams and to my colleagues who helped me a lot over the course of my Ph.D.

To my wonderful son, Mostafa, thank you for bearing with me and being my greatest supporter. To my incredible wife, my friend, mentor and critic, thank you for not letting me give up and for giving me all the encouragement I needed to continue.

Finally, this dissertation is dedicated to my late father and mother who have been my constant source of inspiration. Their constant love and support have meant more than anything. May their kind souls rest in peace.

My Beloved Dad and Mom, this is for you!!

Table of Contents

ABSTRACT	III
ACKNOWLEDGMENT	VI
TABLE OF CONTENTS	VII
LIST OF FIGURES	XIII
LIST OF TABLES	XX
NOMENCLATURE	XXII
STATEMENT OF CONTRIBUTIONS	XXVII
CHAPTER 1. INTRODUCTION	1
1.1 INTRODUCTION	1
1.2 LITERATURE REVIEW	4
1.3 PROBLEM STATEMENT AND MOTIVATION.....	15
1.3.1 <i>Maximum Power Point Tracking Definition</i>	17
1.4 THESIS OBJECTIVES	19
1.4.1 <i>PV generator model</i>	19
1.4.2 <i>DC-DC Converter model</i>	20
1.4.3 <i>Load model</i>	20
1.4.4 <i>Controller model for the DC-DC Converter</i>	21
1.5 THESIS ORGANIZATION	21
CHAPTER 2. MICROGRIDS ARCHITECTURES	25
2.1 INTRODUCTION	25
2.2 LITERATURE REVIEW OF MG STUDIES.....	28
2.3 MICROGRID MOTIVATION	33
2.4 MICROGRID PROJECTS ACROSS THE GLOBE.....	34
2.4.1 <i>Microgrid Implementation in Ohio, United States</i>	36
2.4.2 <i>Microgrid Implementation in Canada Boston Bar – BC Hydro</i>	37
2.4.3 <i>Microgrid Implementation in Greece</i>	38
2.4.3.1 <i>Microgrid Implementation in Kythnos Island, Greece</i>	38

2.4.3.2	Laboratory-Scale MG Implementation at NTUA – Greece.....	39
2.4.4	<i>Microgrid Implementation in Bronsbergen Holiday Park, Netherlands</i>	40
2.4.5	<i>Microgrid Implementation in DeMoTec – Germany</i>	41
2.4.6	<i>Residential MG Implementation in Am Steinweg, Stutensee - Germany</i>	42
2.4.7	<i>Microgrid Implementation in Cesi Ricerca – Italy</i>	43
2.4.8	<i>Microgrid Implementation in the University of Manchester, UK</i>	44
2.5	DESCRIPTION OF A MG	46
2.5.1	<i>Definition of MG</i>	46
2.5.2	<i>Distributed generators</i>	48
2.5.3	<i>Energy storage devices</i>	49
2.5.4	<i>MG loads</i>	50
2.5.5	<i>MG control</i>	51
2.6	MICROGRIDS ARCHITECTURES	52
2.6.1	<i>AC MG</i>	53
2.6.2	<i>DC MG</i>	54
2.6.3	<i>Hybrid AC/DC MG</i>	56
2.7	CONCLUSION.....	58
CHAPTER 3. PHOTOVOLTAIC ENERGY SYSTEM: AN OVERVIEW.....		62
3.1	INTRODUCTION	62
3.2	COMPONENTS OF PV SYSTEM	62
3.2.1	<i>The light from the sun</i>	63
3.2.2	<i>PV arrays: technology and modeling</i>	64
3.2.3	<i>Power Conditioning Units</i>	74
3.2.4	<i>Energy Storage Devices</i>	77
3.3	CONNECTION TOPOLOGIES OF PV SYSTEMS	77
3.4	STANDARDS AND CODES FOR GRID-CONNECTED PV SYSTEMS	80
3.5	CONCLUSION.....	83
CHAPTER 4. POWER INVERTER TOPOLOGIES AND CONTROL STRUCTURES FOR PHOTOVOLTAIC APPLICATIONS.....		85
4.1	INTRODUCTION	85

4.2	LITERATURE REVIEW	85
4.3	REQUIREMENTS FOR PV CONVERTERS.....	88
4.3.1	<i>Performance Requirements of PV Converters</i>	88
4.3.1.1	Efficiency	88
4.3.1.2	Power Density	89
4.3.1.3	Installation Cost	89
4.3.1.4	Minimization of Leakage Current.....	90
4.3.2	<i>Legal Requirements of PV Systems</i>	90
4.3.2.1	Galvanic Isolation	90
4.3.2.2	Anti-Islanding Detection.....	91
4.3.2.3	Other Codes and Standards	91
4.4	PV SYSTEM CONFIGURATIONS.....	93
4.5	INDUSTRIAL PV INVERTERS	96
4.5.1	<i>String Inverter Topologies</i>	96
4.5.2	<i>Multistring Topologies</i>	98
4.5.3	<i>Central Topologies</i>	99
4.5.4	<i>AC-Module Topologies</i>	99
4.6	IMPACT OF INVERTER CONFIGURATION ON ENERGY COST OF GRID-CONNECTED PV SYSTEMS	100
4.7	RECENT ADVANCES IN GRID-CONNECTED PV INVERTERS	105
4.7.1	<i>Advances in DC–AC Converters for PV Systems</i>	105
4.7.2	<i>Advances in DC–DC Converters for PV Systems</i>	107
4.7.3	<i>Advances in Power Semiconductors for PV Systems</i>	111
4.8	CONTROL TECHNIQUES FOR GRID-CONNECTED SOLAR PV INVERTERS.....	113
4.8.1	<i>Maximum Power Point Tracking Controller</i>	113
4.8.2	<i>Inverter Controller</i>	115
4.8.2.1	Control structure for 3-phase inverter connected to the grid	115
4.8.2.2	1-phase inverters	120
4.8.2.3	Reactive power requirements.....	130
4.9	CONCLUSION.....	131

CHAPTER 5. DC-DC CONVERTER.....	133
5.1 INTRODUCTION	133
5.2 DC-DC BOOST CONVERTER.....	134
5.3 SMALL SIGNAL AVERAGED MODEL OF DC-DC BOOST CONVERTERS OPERATING IN THE CONTINUOUS CONDUCTION MODE (CCM).....	135
5.3.1 <i>Case 1: Ideal Boost Converter</i>	135
5.3.2 <i>Case 2: Parasitic Realization in Boost Converter</i>	140
5.4 SMALL SIGNAL AVERAGED MODEL OF DC-DC BOOST CONVERTERS OPERATING IN THE DISCONTINUOUS CONDUCTION MODE (DCM).....	146
5.4.1 <i>Case 1: Ideal Boost Converter</i>	146
5.4.2 <i>Case 2: Parasitic Realization in Boost Converter</i>	156
5.5 BOOST CONVERTER CONTROLLER DESIGN BASED ON PARTICLE SWARM OPTIMIZATION (PSO).....	165
5.5.1 <i>Overview of Particle Swarm Optimization (PSO)</i>	166
5.5.2 <i>Application of Particle Swarm Optimization (PSO) to Design Boost Converter Controller</i>	172
5.6 PERFORMANCE ANALYSIS OF BOOST CONVERTER BY USING DIFFERENT INTEGRATION ALGORITHMS.....	180
5.7 CONCLUSION.....	192
CHAPTER 6. KALMAN FILTER-BASED MPPT FOR PV ENERGY RESOURCES	195
6.1 INTRODUCTION	195
6.2 PV ARRAY MODEL.....	197
6.3 DC-DC CONVERTER MODEL.....	202
6.4 CONSTANT IMPEDANCE LOAD MODEL	203
6.5 MPPT USING KALMAN FILTER.....	204
6.5.1 <i>Proposal of New Representation</i>	204
6.5.2 <i>Applied Proposed Representation to Kalman Filter</i>	208
6.6 MPPT USING PERTURB AND OBSERVE (P&O) METHOD	210
6.6.1 <i>Principle of P&O Algorithm</i>	210

6.6.2	<i>Advantages and Disadvantages of P&O Algorithm</i>	211
6.7	WITHOUT MPPT OPERATION MODE.....	212
6.8	SIMULATION MODEL AND RESULTS	214
6.9	CONCLUSION.....	222
CHAPTER 7. FPGA-BASED MPPT CONTROLLER FOR PV SYSTEMS		223
7.1	INTRODUCTION	223
7.2	FPGA DESIGN METHODOLOGY	224
7.2.1	<i>FPGAs</i>	224
7.2.2	<i>VHDL Code Implementation</i>	228
7.3	SIMULATION RESULTS USING MODELSIM ENVIRONMENT	230
7.4	CONCLUSION.....	239
CHAPTER 8. SUMMARY, CONTRIBUTIONS, AND FUTURE WORK		240
8.1	SUMMARY	240
8.2	MAIN CONTRIBUTIONS OF THE RESEARCH.....	244
8.3	SCOPE OF FUTURE RESEARCH	247
REFERENCES.....		248
APPENDIX A: THE SPR-305E-WHT-D SOLAR PANEL MANUFACTURERS’ DATA SHEET		288
APPENDIX B: FIELD PROGRAMMABLE GATE ARRAYS.....		290
B.1	INTRODUCTION	290
B.2	EVALUATION OF FPGA.....	293
B.3	FPGA STRUCTURAL CLASSIFICATION	296
B.3.1	<i>Symmetrical arrays</i>	296
B.3.2	<i>Row based architecture</i>	297
B.3.3	<i>Hierarchical PLDs</i>	297
B.4	FPGA CLASSIFICATION ON USER PROGRAMMABLE SWITCH TECHNOLOGIES..	298
B.4.1	<i>SRAM Based</i>	299
B.4.2	<i>Antifuse Based</i>	300
B.4.3	<i>EEPROM Based</i>	301

B.5	LOGIC BLOCK AND ROUTING TECHNIQUES	302
B.5.1	<i>Cross-point FPGA</i>	302
B.5.2	<i>Plessey FPGA</i>	302
B.5.3	<i>Actel Logic Block</i>	303
B.5.4	<i>Xilinx Logic block</i>	303
B.5.5	<i>Altera Logic Block</i>	304
B.6	FPGA DESIGN FLOW	307
APPENDIX C: KALMAN FILTER.....		310
C.1	INTRODUCTION	310
C.2	THE DISCRETE KALMAN FILTER	314
C.2.1	<i>Process to be Estimated</i>	314
C.2.2	<i>Computational Origins of the Filter</i>	315
C.2.3	<i>Discrete Kalman Filter Algorithm</i>	316
C.3	AN INTUITIVE EXAMPLES.....	320
C.3.1	<i>Simple and Intuitive One-Dimensional Tracking Problem Example</i>	320
C.3.1.1	System Model	321
C.3.1.2	Kalman Filter Equations	322
C.3.1.3	Solution and Simulation Results	325
C.3.2	<i>Kalman Filter in Simulink Example</i>	328
C.4	SENSITIVITY ANALYSIS OF THE KALMAN FILTER PARAMETERS	329
C.4.1	<i>Effect of Noise Covariance Assumptions</i>	329
C.4.2	<i>H Matrix as a Linear Transformation</i>	330
C.4.3	<i>An Intuitive Example</i>	331
C.5	CONCLUSION.....	337

List of Figures

FIGURE 1.1: VINE FRESH PRODUCE'S GREENHOUSE PROJECT - THE LARGEST ROOFTOP INSTALLATION IN ONTARIO UNDER THE FIT PROGRAM [9]	3
FIGURE 1.2: FLOWCHART DEPICTING THE PERTURB & OBSERVE ALGORITHM [48]	16
FIGURE 1.3: STAND-ALONE PV SYSTEM WITH INTEGRATED MPPT ALGORITHM	19
FIGURE 2.1: A CONCEPTUAL TOPOLOGY OF FUTURE SMART GRID. [69]	26
FIGURE 2.2: TOTAL MG POWER CAPACITY MARKET SHARE BY SEGMENT, WORLD MARKETS: 1Q 2016 [99].....	35
FIGURE 2.3: CERTS MG TEST-BED [100]	36
FIGURE 2.4: SYSTEM CONFIGURATION FOR THE BOSTON BAR IPP AND BC HYDRO PLANNED ISLANDING SITE [101].....	37
FIGURE 2.5: THE KYTHNOS ISLAND MG – GREECE [104]	39
FIGURE 2.6: THE LABORATORY MG FACILITY AT NTUA [104].....	40
FIGURE 2.7: SCHEMATIC FOR THE BRONSBERGEN HOLIDAY PARK MG – NETHERLANDS [105].....	41
FIGURE 2.8: DEMoTEC MG TEST SYSTEM [107].....	42
FIGURE 2.9: THE RESIDENTIAL MG OF AM STEINWEG IN STUTENSEE – GERMANY [104]	43
FIGURE 2.10: CESI RICERCA, ITALY TEST MG NETWORK CONFIGURATION [104]	45
FIGURE 2.11: UNIVERSITY OF MANCHESTER MG/FLYWHEEL ENERGY STORAGE LABORATORY PROTOTYPE [104]	46
FIGURE 2.12: A TYPICAL MG STRUCTURE INTEGRATING DERs AND LOADS [68].....	47
FIGURE 2.13: AC MG ARCHITECTURE WITH CRITICAL AND NON-CRITICAL LOADS [114] ..	53
FIGURE 2.14: DC MG ARCHITECTURE [3].....	56
FIGURE 2.15: HYBRID AC/DC MG ARCHITECTURE [114]	58
FIGURE 3.1: MAIN COMPONENTS OF PHOTOVOLTAIC ENERGY SYSTEM	62
FIGURE 3.2: PYRANOMETER (LEFT TOP), TWO-AXIS TRACKED PYRHELIOMETER (LEFT BOTTOM), PYRANOMETER WITH SHADING BALL (RIGHT) [119]	63
FIGURE 3.3: I-V CHARACTERISTICS OF A SINGLE PV CELL.....	65
FIGURE 3.4: P-V CHARACTERISTICS OF A SINGLE PV CELL.....	65
FIGURE 3.5: CHARACTERISTICS OF THE PV CELL AT CONSTANT TEMPERATURE AND VARIABLE IRRADIANCE	66

FIGURE 3.6: CHARACTERISTICS OF THE PV CELL AT VARIABLE TEMPERATURE AND CONSTANT IRRADIANCE	66
FIGURE 3.7: LAYOUT OF A PV ARRAY	67
FIGURE 3.8: CIRCUIT DIAGRAM OF THE PV MODEL.....	68
FIGURE 3.9: THE MATLAB MODEL I-V AND P-V CURVES FOR VARIOUS IRRADIATION LEVELS.....	72
FIGURE 3.10: THE MATLAB MODEL I-V AND P-V CURVES FOR VARIOUS TEMPERATURES	73
FIGURE 3.11: P-V CURVE FOR TWO SERIES MODULES IN CASE OF PARTIAL SHADING [154]	75
FIGURE 3.12: CONNECTION TOPOLOGIES OF PV SYSTEMS	78
FIGURE 4.1: THE EVOLUTION OF THE COST DISTRIBUTION OF PV SYSTEMS (IN THE RANGE OF 2-50 kW): (A) THE COSTS IN U.S. DOLLARS AND (B) THE DISTRIBUTION OF EACH COMPONENT COST. [196].....	90
FIGURE 4.2: THE GENERIC STRUCTURE OF A GRID-CONNECTED PV SYSTEM (A LARGE- SCALE CENTRAL INVERTER IS SHOWN AS AN EXAMPLE). [202]	95
FIGURE 4.3: PV SYSTEM CONFIGURATIONS (A) CENTRAL, (B) STRING, (C) MULTISTRING, AND (D) MODULE INTEGRATED.....	95
FIGURE 4.4: INDUSTRIAL PV INVERTER TOPOLOGIES FOR CENTRAL, STRING, MULTISTRING, AND AC-MODULE CONFIGURATIONS. (MV: MEDIUM VOLTAGE; 2L-VSI: 2-LEVEL VOLTAGE SOURCE INVERTER). [222]	102
FIGURE 4.5: GENERALIZED TOPOLOGIES OF THE MOST POPULAR SINGLE-STAGE BUCK- BOOST INVERTERS: (A) 2-LEVEL [227] AND (B) 3-L NPC QUASI-Z-SOURCE INVERTERS [229].....	107
FIGURE 4.6: THE NEW EMERGED TOPOLOGIES OF THE PV MODULE INTEGRATED DC-DC CONVERTERS: (A) A TWO-STAGE TOPOLOGY CONSISTING OF A SYNCHRONOUS BOOST AND A SERIES-RESONANT CONVERTER [246], (B) A QUASI-Z-SOURCE SERIES RESONANT CONVERTER [247], (C) AN LLCC SERIES-PARALLEL RESONANT CONVERTER [250], (D) A SERIES RESONANT CONVERTER WITH A BIDIRECTIONAL AC SWITCH [245], (E) A DUAL-MODE RESONANT CONVERTER [251], (F) A HALF-BRIDGE LLC RESONANT CONVERTER [252], (G) A PARALLEL RESONANT CURRENT-FED PUSH-PULL CONVERTER [253], AND (H) A MULTIRESONANT TWO-INDUCTOR BOOST CONVERTER WITH A NONDISSIPATIVE REGENERATIVE SNUBBER [254].....	111

FIGURE 4.7: GENERAL STRUCTURE FOR dq CONTROL STRATEGY	116
FIGURE 4.8: GENERAL STRUCTURE FOR ab CONTROL STRATEGY	117
FIGURE 4.9: GENERAL STRUCTURE FOR abc CONTROL STRATEGY [283].....	119
FIGURE 4.10: CONTROL STRUCTURE TOPOLOGY FOR 1-PHASE WITH DC–DC CONVERTER	121
FIGURE 4.11: CONTROL STRUCTURE WITH DC–DC CONVERTER AND L FILTER	121
FIGURE 4.12: CONTROL LOOP STRUCTURE OF THE INVERTER OUTPUT CURRENT	122
FIGURE 4.13: CONTROL STRUCTURE WITH DC-DC CONVERTER AND LCL FILTER [279]	124
FIGURE 4.14: CONTROL STRUCTURE FOR SINGLE PHASE WITHOUT DC–DC CONVERTER	126
FIGURE 4.15: INJECTED POWER CONTROL STRUCTURE [279]	126
FIGURE 4.16: CONTROL STRUCTURE OF INPUT POWER (SOLAR PANEL POWER).....	126
FIGURE 4.17: INVERTER CURRENT LOOP WITH PI CONTROLLER.....	127
FIGURE 4.18: INVERTER CURRENT LOOP WITH PR CONTROLLER	127
FIGURE 4.19: CONTROL STRUCTURE BASED ON THE SHIFTING PHASE FOR A 1-PHASE INVERTER CONNECTED TO THE GRID	129
FIGURE 5.1: DC-DC CONVERTER FOR OPERATION AT THE MPP.....	133
FIGURE 5.2: BOOST CONVERTER CIRCUIT	136
FIGURE 5.3: EQUIVALENT CIRCUIT OF BOOST CONVERTER DURING ON-STATE	136
FIGURE 5.4: EQUIVALENT CIRCUIT OF BOOST CONVERTER DURING OFF-STATE	137
FIGURE 5.5: STEADY-STATE WAVEFORMS FOR CCM.....	138
FIGURE 5.6: BOOST CONVERTER CIRCUIT WITH PARASITIC ELEMENTS.....	140
FIGURE 5.7: EQUIVALENT CIRCUIT OF BOOST CONVERTER DURING ON-STATE	141
FIGURE 5.8: EQUIVALENT CIRCUIT OF BOOST CONVERTER DURING OFF-STATE	142
FIGURE 5.9: BODE DIAGRAM FOR IDEAL DC-DC BOOST CONVERTER IN CCM	144
FIGURE 5.10: BODE DIAGRAM FOR NON-IDEAL DC-DC BOOST CONVERTER IN CCM ...	144
FIGURE 5.11: TRANSIENT STEP RESPONSE FOR IDEAL DC-DC BOOST CONVERTER IN CCM	145
FIGURE 5.12: TRANSIENT STEP RESPONSE FOR NON-IDEAL DC-DC BOOST CONVERTER IN CCM.....	146
FIGURE 5.13: INDUCTOR CURRENT WAVEFORM OF DC-DC CONVERTER IN DCM	147
FIGURE 5.14: BOOST CONVERTER CIRCUIT WITH PARASITIC	157

FIGURE 5.15: BODE DIAGRAM FOR IDEAL DC-DC BOOST CONVERTER IN DCM	162
FIGURE 5.16: BODE DIAGRAM FOR NON-IDEAL DC-DC BOOST CONVERTER IN DCM	163
FIGURE 5.17: TRANSIENT STEP RESPONSE FOR IDEAL DC-DC BOOST CONVERTER IN DCM	164
FIGURE 5.18: TRANSIENT STEP RESPONSE FOR NON-IDEAL DC-DC BOOST CONVERTER IN DCM	164
FIGURE 5.19: FLOWCHART OF THE PSO METHOD	169
FIGURE 5.20: CLOSED-LOOP CONTROLLER AND BOOST CONVERTER.....	172
FIGURE 5.21: CLOSED LOOP RESPONSE OF DC-DC BOOST CONVERTER OPERATING IN CCM	175
FIGURE 5.22: CLOSED LOOP RESPONSE OF DC-DC BOOST CONVERTER OPERATING IN CCM WITH $\pm 10\%$ SOURCE VOLTAGE DISTURBANCE	176
FIGURE 5.23: CLOSED LOOP RESPONSE OF DC-DC BOOST CONVERTER OPERATING IN CCM WITH $\pm 13\%$ SUDDEN LOAD DISTURBANCE	176
FIGURE 5.24: CLOSED LOOP RESPONSE OF DC-DC BOOST CONVERTER OPERATING IN CCM WITH $\pm 25\%$ SOURCE VOLTAGE DISTURBANCE	177
FIGURE 5.25: CLOSED LOOP RESPONSE OF DC-DC BOOST CONVERTER OPERATING IN CCM WITH $\pm 35\%$ SUDDEN LOAD DISTURBANCE	177
FIGURE 5.26: THE CONVERGENCE CHARACTERISTIC OF THE PSO ALGORITHM.....	178
FIGURE 5.27: IDEAL DC-DC BOOST CONVERTER OPERATING IN CCM UNDERGOING DIFFERENT NUMERICAL INTEGRATION TECHNIQUES	182
FIGURE 5.28: IDEAL DC-DC BOOST CONVERTER OPERATING IN CCM UNDERGOING BACKWARD EULER TECHNIQUE	183
FIGURE 5.29: IDEAL DC-DC BOOST CONVERTER OPERATING IN CCM UNDERGOING FORWARD EULER TECHNIQUE	183
FIGURE 5.30: IDEAL DC-DC BOOST CONVERTER OPERATING IN CCM UNDERGOING FORWARD EULER TECHNIQUE WITH SMALLER STEP-SIZE	184
FIGURE 5.31: IDEAL DC-DC BOOST CONVERTER OPERATING IN CCM UNDERGOING DIFFERENT NUMERICAL INTEGRATION TECHNIQUES WITH SMALLER STEP-SIZE	185
FIGURE 5.32: NON-IDEAL DC-DC BOOST CONVERTER OPERATING IN CCM UNDERGOING DIFFERENT NUMERICAL INTEGRATION TECHNIQUES	185

FIGURE 5.33: NON-IDEAL DC-DC BOOST CONVERTER OPERATING IN CCM UNDERGOING BACKWARD EULER TECHNIQUE	186
FIGURE 5.34: NON-IDEAL DC-DC BOOST CONVERTER OPERATING IN CCM UNDERGOING FORWARD EULER TECHNIQUE	186
FIGURE 5.35: NON-IDEAL DC-DC BOOST CONVERTER OPERATING IN CCM UNDERGOING DIFFERENT NUMERICAL INTEGRATION TECHNIQUES	187
FIGURE 5.36: NON-IDEAL DC-DC BOOST CONVERTER OPERATING IN CCM UNDERGOING BACKWARD EULER TECHNIQUE	188
FIGURE 5.37: NON-IDEAL DC-DC BOOST CONVERTER OPERATING IN CCM UNDERGOING FORWARD EULER TECHNIQUE	188
FIGURE 5.38: NON-IDEAL DC-DC BOOST CONVERTER OPERATING IN CCM UNDERGOING DIFFERENT NUMERICAL INTEGRATION TECHNIQUES	189
FIGURE 5.39: NON-IDEAL DC-DC BOOST CONVERTER OPERATING IN CCM UNDERGOING BACKWARD EULER TECHNIQUE	190
FIGURE 5.40: NON-IDEAL DC-DC BOOST CONVERTER OPERATING IN CCM UNDERGOING FORWARD EULER TECHNIQUE	190
FIGURE 6.1: STAND-ALONE PV SYSTEM CONTROLLED BY USING DIFFERENT MPPT CONTROL METHODS.....	196
FIGURE 6.2: CIRCUIT DIAGRAM OF THE PV MODEL.....	197
FIGURE 6.3: THE MATLAB MODEL I-V AND P-V CURVES FOR VARIOUS IRRADIATION LEVELS.....	201
FIGURE 6.4: THE MATLAB MODEL I-V AND P-V CURVES FOR VARIOUS TEMPERATURES	202
FIGURE 6.5: KF ITERATION USED TO CALCULATE INPUT FOR THE DC-DC BOOST CONVERTER.....	205
FIGURE 6.6: MEASUREMENT AND TIME UPDATES IN PROPOSED KALMAN FILTER.....	210
FIGURE 6.7: ILLUSTRATION OF THE OSCILLATIONS OF THE P&O ALGORITHM AROUND THE MPP.....	211
FIGURE 6.8: P&O'S TRACKING FAILURE UNDER SUDDEN P-V CHARACTERISTIC CHANGE	212
FIGURE 6.9: STAND-ALONE PV SYSTEM BEHAVIOUR UNDER NON-MPPT OPERATION MODE	213

FIGURE 6.10: PV SYSTEM IMPLEMENTING THE PROPOSED KALMAN FILTER ALGORITHM USING SIMULINK	215
FIGURE 6.11: GENERATED POWER TRAJECTORIES UNDER IRRADIANCE CHANGE: (A) IRRADIANCE CHANGES WITH TIME, (B) PROPOSED METHOD POWER TRAJECTORY, (C) P&O METHOD POWER TRAJECTORY AND (D) WITHOUT MPPT METHOD POWER TRAJECTORY	216
FIGURE 6.12: GENERATED POWER TRAJECTORIES UNDER TEMPERATURE CHANGE: (A) TEMPERATURE CHANGES WITH TIME, (B) PROPOSED METHOD POWER TRAJECTORY, (C) P&O METHOD POWER TRAJECTORY AND (D) WITHOUT MPPT METHOD POWER TRAJECTORY	218
FIGURE 6.13: GENERATED POWER TRAJECTORIES UNDER SIMULTANEOUS CHANGING IN THE IRRADIANCE AND TEMPERATURE: (A) IRRADIANCE CHANGES WITH TIME, (B) TEMPERATURE CHANGES WITH TIME, (C) PROPOSED METHOD POWER TRAJECTORY, (D) P&O METHOD POWER TRAJECTORY AND (E) WITHOUT MPPT METHOD POWER TRAJECTORY	220
FIGURE 6.14: COMPARISON BETWEEN THE MAXIMUM POWER TRAJECTORY AND THE GENERATED POWER TRAJECTORIES FOR ALL METHODS WHEN IRRADIANCE AND TEMPERATURE ARE SIMULTANEOUSLY CHANGED.....	221
FIGURE 7.1: EXAMPLE OF DISTRIBUTION OF CLBs, IOBs, PIs, RAM BLOCKS, AND MULTIPLIERS IN VIRTEX II [373]	226
FIGURE 7.2: A TYPICAL FPGA MAPPING flow [374]	228
FIGURE 7.3: VHDL DESIGN flow [378].....	230
FIGURE 7.4: THE RTL VIEW OF THE PROPOSED MPPT ALGORITHM	231
FIGURE 7.5: THE EVOLUTION OF THE PV POWER, VOLTAGE, CURRENT AND DUTY CYCLE VS. TIME OF THE DESIGNED KF MPPT IN THE STANDARD TEST CONDITIONS (25°C AND 1000W/M ²)	232
FIGURE 7.6: THE EVOLUTION OF THE PV POWER AND DUTY CYCLE VS. TIME OF THE DESIGNED KF MPPT FOR RAPID STEP VARIATION OF SOLAR IRRADIATION.	233
FIGURE 7.7: THE DE2-70 FPGA BOARD USED AND THE DUTY CYCLE D GENERATED BY THE KF MPPT CONTROLLER, DISPLAYED IN PWM FORM UNDER STANDARD TEST CONDITIONS (25°C AND 1000W/M ²).....	233

FIGURE 7.8: THE EVOLUTION OF THE PV POWER AND DUTY CYCLE VS. TIME OF THE DESIGNED KF BASED MPPT CONTROLLER FOR RAPID VARIATION OF SOLAR IRRADIATION AND AIR TEMPERATURE ($G = 700 \text{ W/M}^2$, $T_A=24 \text{ }^\circ\text{C} \rightarrow G = 300 \text{ W/M}^2$, $T_A=19 \text{ }^\circ\text{C} \rightarrow G = 700 \text{ W/M}^2$, $T_A=24 \text{ }^\circ\text{C}$).	234
FIGURE 7.9: SIMULATION OF THE MPP TRACKING BY P&O ALGORITHM FOR ABRUPT CHANGES OF THE WEATHER.....	235
FIGURE 7.10: RESPONSE TIME OF THE DESIGNED P&O ALGORITHM CORRESPONDING TO PERTURBATION STEP (ΔD) = 0.4.....	238
FIGURE 7.11: RESPONSE TIME OF THE DESIGNED P&O ALGORITHM CORRESPONDING TO PERTURBATION STEP (ΔD) = 0.5.....	238

List of Tables

TABLE 1.1: MAJOR CHARACTERISTICS OF DIFFERENT MPPT TECHNIQUES	13
TABLE 2.1: ADVANTAGES AND DISADVANTAGES OF AC AND DC MGS.....	60
TABLE 3.1: PARAMETERS OF THE SPR-305E-WHT-D PV MODULE AT STC	72
TABLE 3.2: COMPARISON BETWEEN DIFFERENT CONNECTION TOPOLOGIES OF PV SYSTEMS.....	81
TABLE 4.1: A SUMMARY OF THE TYPICAL INTERNATIONAL CODES AND STANDARDS FOR PV APPLICATIONS	92
TABLE 4.2: A GRID-CONNECTED PV ENERGY CONVERSION SYSTEMS CONFIGURATIONS OVERVIEW	101
TABLE 4.3: A SUMMARY OF CHARACTERISTICS AND EXAMPLES OF SELECTED INDUSTRIAL PV INVERTER TOPOLOGIES	103
TABLE 4.4: COMMERCIAL POWER SEMICONDUCTOR MODULES FOR GRID- CONNECTED PV INVERTERS.....	113
TABLE 4.5: ADVANTAGES AND DISADVANTAGES OF CONTROL STRUCTURES FOR THREE PHASE INVERTERS.....	119
TABLE 4.6: ADVANTAGE AND DISADVANTAGES OF CONTROL STRUCTURES FOR SINGLE PHASE INVERTERS.....	129
TABLE 5.1: PARAMETERS USED IN THE IMPLEMENTATION OF PSO.....	174
TABLE 5.2: PERFORMANCE EVALUATION OF DC-DC BOOST CONVERTER DYNAMIC RESPONSE OPERATING IN CCM.....	180
TABLE 6.1: PARAMETERS OF THE SPR-305E-WHT-D PV MODULE AT STC ...	200
TABLE 6.2: SUMMARY OF P&O ALGORITHM	211
TABLE 6.3: RESULTS COMPARISON BETWEEN THE KF BASED MPPT METHOD AND P&O ALGORITHM AT TEMPERATURE 25 °C	221
TABLE 6.4: RESULTS COMPARISON BETWEEN THE KF BASED MPPT METHOD AND P&O ALGORITHM AT IRRADIANCE 250 W/M ²	221
TABLE 7.1: FPGA RESOURCES SUMMARY FOR THE DESIGNED KF MPPT CONTROLLER (DEVICE CYCLONE II, EP2C20F484C7).....	234

TABLE 7.2: RESULTS COMPARISON OF THE DESIGNED P&O ALGORITHM
CORRESPONDING TO TWO DIFFERENT PERTURBATION STEPS: $\Delta D = 0.4$
AND $\Delta D = 0.5$ 237

Nomenclature

ACO	Ant Colony Optimization
ADC	Analog-to-Digital Converter
ADS	Active Distribution System
AEP	American Electric Power
AI	Artificial Intelligent
ALMs	Adaptive Logic Modules
ASIC	Application Specific Integrated Circuit
CAD	Computer Aided Design
CCM	Continuous Conduction Mode
CERTs	Consortium for Electric Reliability Technology Solutions
CESS	Composite Energy Storage System
CHP	Combined production of Heat and Power
CLBs	Configurable Logic Blocks
CPLDs	Complex Programmable Logic Devices
CRLB	Cramér-Rao lower bound
CSGs	Conventional Synchronous Generators
CSI	Current Source Inverter
DCM	Discontinuous Conduction Mode
DE	Differential Evolution
DERs	Distributed Energy Resources
DFIG	Doubly Fed Induction Generator
DG	Distributed Generation
DKF	Decentralized Kalman Filter
DSO	Distribution System Operator
DSPs	Digital Signal Processors
DSPWM	Digital Sinusoidal Pulse Width Modulation
DVR	Dynamic Voltage Restorer
EAs	Evolutionary Algorithms
EDIF	Electronic Design Interchange Format
EDPC	Extended Direct Power Control

EEPROM	Electrically Erasable Programmable Read-Only Memory
EKF	Extended Kalman Filter
EMI	Electromagnetic Interference
EMS	Energy Management System
EPS	Electrical Power System
ESR	Equivalent Series Resistance
ESSs	Energy Storage Systems
EV	Electrical Vehicle
FCLs	Fault Current Limiters
FIT	Feed-in Tariff
FLC	Fuzzy Logic Controller
FOCV	Fractional Open Circuit Voltage
FPGA	Field Programmable Gate Array
GA	Genetic Algorithm
GaN	Gallium Nitride
GHG	Green House Gas
GHz	GigaHertz
HC	Harmonic Compensator
HDL	Hardware Description Language
HERIC	Highly Efficient and Reliable Inverter Concept
HF	High-Frequency
HIL	Hardware-In-the-Loop
HVDC	High Voltage Direct Current
Hz	Hertz
INC	Incremental Conductance
IC	Interlinking Converter
ICTs	Information and Communication Technologies
IEC	International Electro technical Commission
IEEE	Institute of Electrical and Electronics Engineers
IGBT	Insulated-Gate Bipolar Transistor
IOBs	Input/Output Blocks

IPP	Independent Power Producer
ISE	Integrated Synthesis Environment
ISET	Institut für Solare Energieversorgungstechnik
ISPR	Inverter System Performance Ratio
JADE	Java Agent Development
KF	Kalman Filter
LABs	Logic Array Blocks
LCOE	Levelized Cost of Energy
LE	Logic Element
LSI	Large Scale Integrated
LUT	Look Up Table
LV	Low-Voltage
MAP	Maximum A Posteriori
MCC	Microgrid Central Controller
MG	Microgrid
MHz	MegaHertz
MICs	Module Integrated Converters
ML	Maximum-Likelihood
MOSFET	Metal–Oxide–Semiconductor Field Effect Transistor
MPOP	Maximum Power Operating Point
MPP	Maximum Power Point
MPPT	Maximum Power Point Tracking
MSI	Medium Scale Integrated
NEC	National Electrical Code
NN	Neural Network
NPC	Neutral-Point-Clamped
NTUA	National Technical University of Athens
OCC	One-Cycle Control
OTP	One-Time Programmable
P&O	Perturb and Observe
PAL	Programmable Array Logic

PCB	Printed Circuit Board
PCBB	Power Converter Building Block
PCC	Point of Common Coupling
PCSP	Power Control Shifting Phase
PCUs	Power Conditioning Units
PE	Power Electronics
PF	Power Factor
PI	Proportional Integral
PIC	Peripheral Interface Controller
PLD	Programmable Logic Device
PLL	Phase-Locked Loop
PMSs	Power Management Strategies
PR	Proportional Resonant
PROM	Programmable Read-Only Memory
PSO	Particle Swarm Optimization
PV	Photovoltaic
PVG	Photovoltaic Generator
PWM	Pulse Width Modulation
qZSI	quasi-Z-Source Inverter
RA	Running Average
RD&D	Research, Development and Demonstration
RTL	Register Transfer Level
SCADA	Supervisory Control and Data Acquisition
SEPRI	Shandong Electric Power Research Institute
SiC	Silicon Carbide
SMES	Superconducting Magnetic Energy Storage
SOC	State of Charge
SPLDs	Simple Programmable Logic Devices
SRAM	Static Random Access Memory
SRC	Series Resonant DC–DC Converter
SS	State Space

SSI	Small Scale Integrated
STATCOM	Static Synchronous Compensator
STC	Standard Test Condition
THD	Total Harmonic Distortion
UAAC	Utility Area Control Centre
UC	Unit Commitment
UKF	Unscented Kalman Filter
VHDL	VHSIC Hardware Description Language
VHSIC	Very-High-Speed Integrated Circuit
VSI	Voltage Source Inverters
WBG	Wide-Band-Gap
ZCD	Zero Crossing Detector
ZCS	Zero Current Switching
ZVS	Zero Voltage Switching

Statement of Contributions

I have the following research publications (3 Journal, 9 conference and 2 book chapters (Published)) to my credit so far:

Journal Papers

- J1.** Haytham Abdelgawad and Vijay Sood, “Kalman Filter-based maximum power point tracking for PV energy resources supplying DC microgrid”, International Journal of Energy Optimization and Engineering (IJEEO) - (submitted, under review)
- J2.** Haytham Abdelgawad and Vijay Sood, “Average Model of Boost Converter, including Parasitics, operating in Discontinuous Conduction Mode (DCM)”, International Journal on Power Engineering and Energy (IJPEE), Vol.7, No.2, April 2016. ISSN Print 2314-7318, And Online 2314-730X, Library of Congress (Control Number: 2009937569)
- J3.** Haytham Abdelgawad and Vijay Sood, “Boost Converter Controller Design based on Particle Swarm Optimization (PSO)”, International Journal on Power Engineering and Energy (IJPEE), Vol.7, No.2, April 2016. ISSN Print 2314-7318, And Online 2314-730X, Library of Congress (Control Number: 2009937569). Ref No. W15-P-0021

Conference Papers

- C1.** Haytham Abdelgawad, and Vijay K Sood, “A Comprehensive Review on Microgrid Architectures for Distributed Generation”, Electrical Power and Energy Conference (EPEC) in Montréal, Québec, Canada, pp. 1-8. IEEE, Oct. 2019.
- C2.** Haytham Abdelgawad, Vijay K Sood, “Kalman Filter-Based Maximum Power Point Tracking for Photovoltaic Energy Resources Supplying DC Microgrid”, International Conference on Energy Engineering and Smart Grids (ESG 2018) Venue: Fitzwilliam College, University of Cambridge, Cambridge City, United Kingdom 25-26 June, 2018
- C3.** Faizan Khan, Ali Sunbul, Mohammad. Y. Ali, Haytham AbdEl-Gawad, Shahryar Rahnamayan, Vijay. K. Sood, “Maximum Power Point Tracking in PV Farms

- Using DE and PSO Algorithms: A Comparative Study”, July 2018-IEEE World Congress on Computational Intelligence (WCCI) 2018, Rio de Janeiro, Brazil.
- C4. Haytham Abdelgawad**, and Vijay K Sood, “Kalman filter-based maximum power point tracking for PV energy resources supplying DC microgrid”, Electrical Power and Energy Conference (EPEC) in Saskatoon, Canada, pp. 1-8. IEEE, Oct. 2017.
- C5. Haytham Abdelgawad** and Vijay K Sood, “Performance analysis of Boost converter by using different integration algorithms”, Electrical and Computer Engineering (CCECE), 2016 IEEE Canadian Conference on Vancouver, Canada, pp. 1-5. IEEE, May 2016.
- C6. Haytham Abdelgawad** and Vijay Sood, “Average Model of Boost Converter, including Parasitics, operating in Discontinuous Conduction Mode (DCM)”, 7th World Congress on Power Engineering and Energy, WCPEE’2015 Dec., 28-31, 2015, Cairo, Egypt.
- C7. Haytham Abdelgawad** and Vijay Sood, “Boost Converter Controller Design based on Particle Swarm Optimization (PSO)”, 7th World Congress on Power Engineering and Energy, WCPEE’2015 Dec., 28-31, 2015, Cairo Egypt.
- C8. H.Abdel-Gawad**, V.K.Sood, “Small-Signal Analysis of Boost Converter, including Parasitics, operating in Continuous Conduction Mode”, 6th IEEE POWER INDIA International Conference 2014, 5-7 December 2014, Le-Meridian, Connaught Place, New Delhi, India.
- C9. H.Abdel-Gawad**, V.K.Sood, “Overview of connection topologies for grid-connected PV systems” Electrical and Computer Engineering (CCECE), 2014 IEEE 27th Canadian Conference on Toronto, pp. 1-8, May 2014.

Book Chapters

- B1.** Vijay K. Sood and **Haytham Abdelgawad**, “Microgrids Architectures”, book chapter (Published), Elsevier S&T Books, 33 pages. Online: https://www.elsevier.com/books/distributed-energy-resources-in-microgrids/chauhan/978-0-12-817774-7?fbclid=IwAR0XkY7zl1mUz2-xxQfNQ2LWSC_y6pqvXK7JmWSa85dq_UvTowZAfmMpyuG_8

- B2.** Vijay K. Sood and **Haytham Abdelgawad**, “Power Converter Solutions and Controls for Green Energy”, book chapter (Published), Elsevier S&T Books, 33 pages. Online: <https://www.elsevier.com/books/distributed-energy-resources-in-icogrids/chauhan/978-0-12-817774-7?fbclid=IwAR0XkY7z11mUz2-xxQfNQ2LWSCy6pqvXK7JmWSa85dqUvTowZAfmMpyuG> 8

Chapter 1. Introduction

This chapter presents the motivation behind the work done in this thesis. The chapter also provides the main objectives of the research as well as the thesis organization.

1.1 Introduction

In recent years, the world's electricity systems are starting to decentralize, decarbonize, and democratize in many cases [1]. These features, known as the “three Ds”, are driven by the need to reduce greenhouse gas (GHG) emissions to alleviate climate change, to provide higher reliability and resilience for critical loads, reduce electricity costs, substitute aging grid infrastructure, and to supply electricity in areas not served by existing grid infrastructure. While the compromise between the technical driving factors and the details of specific solution may differ from one place to another, microgrids came to offer a flexible solution for managing distributed energy resources (DERs) that can meet the different requirements of different communities.

The concept of microgrid is gaining rapid acceptance because of the environmentally friendly energy provision, its cost effectiveness, improvement in power quality and reliability, and reduction in line congestion and losses, reduction in infrastructure investment needs. From the customer point of view, the microgrid is designed to meet their electrical and heat energy demand and avoid load shedding [2].

In order to effectively integrate DERs into a MG, proper architectures should be implemented, based on AC, DC and hybrid AC/DC systems, seeking the highest reliability and efficiency [3]. The existing grid infrastructure, the distributed energy resources to be integrated, as well as specific customer-oriented requirements, will determine the most suitable electrical architecture of the MG. Since the late 19th century, AC has been the standard choice for commercial energy systems, based mainly on the ease to transform AC voltage into different levels, the capability to transmit power over long distances and its inherent characteristic from the fossil energy-driven rotating machines with their synchronous generators. Therefore, AC distribution is the most popular and commonly used structure for MG studies and implementations. By utilizing the existing AC

network infrastructure (distribution, transformers, protections, etc.), AC microgrids are easier to design and implement and are built on proven and thus reliable technology. However, DC distribution has shown a resurgence in recent years due to the development and deployment of RES based on DC power sources, and the rapid growth of DC loads, which constitute today the vast majority of loads in most power systems. DC distribution presents several advantages, such as reduction of the power losses and voltage drops, and an increase of capacity of power lines, mainly due to the lack of reactive power flows, absence of voltage drops in lines reactance and non-existence of skin and proximity effects then reducing ohmic resistance of lines. According to this, its planning, implementation and operation is simpler and less expensive [4].

Conventional power generation schemes are based on the usage of fossil fuels. With the rapid growth of population, the reserve of fossil fuels is on the verge of depletion. Furthermore, this is compounded by the adversities of environmental pollution, threatening all living beings to the very existence. Renewable energy sources on the other hand serve as an alternate source of power generation [5]. Several sources like wind, solar, biogas etc. are important energy sources. Energy from the sun is the best option for renewable energy as it is available almost everywhere and is free to harness. Sunlight is converted to electricity by a physical process known as photovoltaic effect. Sunlight is composed of photons, or particles of solar energy. These photons contain various amounts of energy corresponding to different wavelengths of the solar spectrum. When photons strike a PV cell, they may be reflected or absorbed, or they may pass right through. Only the absorbed photons generate electricity. When this happens, the energy of the photon is transferred to an electron in an atom of the cell (which actually is a semiconductor). With its newfound energy, the electron is able to escape from its normal position associated with that atom to become part of the current in an electrical circuit. By leaving this position, the electron causes a hole to form. Special electrical properties of the PV cell—a built-in electric field—provide the voltage needed to drive the current through an external load. Photovoltaic arrays are used in many applications such as water pumping, battery charging, hybrid vehicles and grid connected systems [6].

With the rapid growth of power electronic (PE) techniques, the use of solar energy in electric power applications is gradually increasing. Solar energy plants can be installed in

places like roofs and deserts, or they can produce electricity for remote locations where there is no electricity network. Due to the equipment required, PV power generation is more expensive than other resources. It suffers from a few drawbacks, including high cost of implementation and low efficiency. Governments are promoting it with subsidies or feed-in tariffs, expecting the development of the technology so that in the near future it will become competitive [7]-[8].

In the province of Ontario, Canada, as of December 2013, the cumulative PV installed capacity stood at 470 MW-AC under the Renewable Energy Standard Offer Program (RESOP), 390 MW-AC under the Feed-in Tariff (FIT) program and 160 MW-AC under the micro FIT program for a total of 1020 MW-AC. The total amount of installed and under development PV capacity in Ontario is approximately 2000 MW-AC [9]. At 2.3 MW-DC, the Vine Fresh Produce Project [9] is the largest rooftop installation in Ontario under the FIT program as shown in Figure 1.1. It is also the largest micro-inverter installation in the world.



Figure 1.1: Vine Fresh Produce's greenhouse project - the largest rooftop installation in Ontario under the FIT program [9]

The principal advantages associated with solar photovoltaic arrays are that it consists of no moving parts. Does not produce any noise and maintenance costs are minimal. Amount of energy from sun is so large that in one hour it can provide more than enough energy for human population in one year [10].

In today's world, renewable energy sources (wind, solar, biogas etc.) play an important role in electricity generation. Solar renewable energy is universally available and is free

to harness. Solar radiation, converted to electrical energy by using photovoltaic (PV) cells, can be used either as standalone or in grid-connected configurations. However, for PV systems the amount of electric power generated changes continuously with daylight hours and weather conditions. In general, the V-I curve for a PV array is non-linear so a specific point on the curve, namely Maximum Power Point (MPP), needs to be tracked so that the whole system operates at maximum efficiency and produces maximum output power. Hence, a Maximum Power Point Tracking (MPPT) algorithm is necessary for extracting maximum power available from a PV module under different conditions [11].

Since, MPPT is an essential part of a PV system, in the literature, many new techniques have been reported. There are many different techniques for maximum power point tracking of photovoltaic PV systems. It is shown that at least 30 methods have been introduced in the literature, with several variations on implementation.

The methods vary in complexity, sensors required, convergence speed, cost, range of effectiveness, implementation hardware, popularity, and in other respects. They range from the almost obvious (but not necessarily ineffective) to the most creative (not necessarily most effective). In fact, so many methods have been developed that it has become difficult to adequately determine which method, newly proposed or existing, is most appropriate for a given PV system.

The effectiveness of MPPT is theoretically defined as a ratio of the practical power output to the true maximum power value. A fair comparison of MPPT methods is difficult because a true MPP is concealed during the real-time operation under natural sunlight. Further, the output difference between solar modules and other non-ideal factors make it impossible to create two identical benches for real-time comparison.

1.2 Literature Review

Solar energy utilization has been studied by many researchers. It is known that solar cell operates at very low efficiency and thus a better control mechanism is required to increase the efficiency. To do that, work at MPP is required where the power produced is a maximum and this point depends on the temperature of the panels and on the irradiance conditions. Both conditions change during the day and are also different depending on the

season of the year. Furthermore, irradiation can change rapidly due to changing atmospheric conditions such as clouds passing by. To this regard, researchers had developed what is called the Maximum Power Point Tracking (MPPT) algorithm. MPPT algorithm keeps the PV systems continuously delivering the maximum power output, regardless of the variation in environment condition. Under the effect of MPPT algorithms, the PV systems are capable of adapting to the environmental change and delivering the maximum power output. Generally, the MPPT controller is embedded in the PE converter systems, so that the corresponding optimal duty cycle is updated to the PV power conversion system to generate the MPP output. There are many algorithms are present which are able to track Maximum Power Point (MPP). Some of these algorithms are simple, such as those based on voltage and current feedback. Some algorithms are more complicated, such as those based on Neural Networks (NN) and Fuzzy Logic (FL). Some MPPT methods have medium complexity such as perturb and observe (P&O) or the incremental conductance (IncCond) methods. Reference [12] has discussed 19 distinct methods in this field. The concluding discussion and table in this reference, containing the major characteristics of all MPPT techniques serves as a useful guide in choosing the right MPPT method for specific PV systems.

Reference [13], proposed a detailed comparison of most popular MPPT algorithms techniques which are P&O and Improved Perturb & Observe algorithm (IP&O). The IP&O method, based on modified fixed algorithm, automatically adjusts the reference step size and hysteresis bandwidth for power conversion. The IP&O method gives high efficiency (about 94.32%) and performs well with changing radiation and temperature conditions. The correctness and validity of MPPT methods is verified through simulation under various weather conditions. No oscillation during tracking and steady state operations were apparent. The results show that the IP&O increases the total PV output power, even at unsettled weather conditions, when compared to traditional P&O method.

Although many MPPT techniques have been developed, most commercial systems still utilize the P&O MPPT technique because of its simple algorithm, low cost and ease of implementation. However, this technique was slow in tracking MPP under rapidly changing irradiance conditions and it also oscillates around the MPP. Reference [14] addressed this problematic behavior of P&O technique and presented a novel MPPT hybrid

technique that was a combination of two basic techniques i.e. P&O and Fractional Open Circuit Voltage (FOCV) technique in order to overcome the inherited deficiencies found in the P&O technique. The proposed MPPT technique was much more robust in tracking the MPP even under the frequently changing irradiance conditions and was less oscillatory around the MPP as compared to the P&O method.

Reference [15] proposed a fast and accurate MPPT algorithm for a PV panel that uses the open circuit voltage and the short circuit current of the PV panel. The mathematical equations describing the nonlinear V-I characteristics of the PV panel were used in developing the algorithm. The MPPT algorithm is valid under different irradiance and temperature conditions. The algorithm is verified using MATLAB simulation and it was found that the results obtained using the algorithm were very close to the theoretical values over a wide range of temperature and illumination levels. The maximum deviation in the maximum power was less than 1.5% for the illumination levels and temperatures normally encountered by a commercial PV panel. The complete derivation of this MPPT algorithm was presented. It is seen that the algorithm is faster than other MPPT algorithms like P&O and more accurate than approximate methods that use the linearity between voltage (current) at maximum power point and open-circuit voltage (short-circuit current).

Reference [16] presented the IncCond MPPT algorithm, which tracks the maximum possible power from a solar array at any instant of time. The tracking algorithm automatically changes the duty cycle of the converter connected to the solar panel. From the result it is found that, under varying irradiation conditions, the system power is found to increase by 25 to 30%. Under varying temperature conditions, the system power increases by almost 8%. Hence, the algorithm provides good tracking of MPP under changing environmental conditions.

Reference [17] mentioned a new Maximum Power Tracking (MPT) algorithm to track Maximum Power Operating Point (MPOP) by comparing the incremental and instantaneous conductance of the PV array. The drawbacks of P&O method were analyzed, and it is shown that the IncCond algorithm has successfully tracked the MPOP even when atmospheric conditions change rapidly.

Reference [18] compared P&O and IncCond methods with DC-DC buck converter by implementing hardware using Arduino Duemilanove as a prototype board. From this it is

found that IncCond method has less oscillation when compared to the P&O method which results in higher efficiency.

A new MPPT algorithm for PV arrays was proposed by [19]. The algorithm detects the MPP of the PV. The computed maximum power was used as a reference value (set point) of the control system. An ON/OFF power controller with hysteresis band was used to control the operation of a Buck chopper such that the PV module always operates at its maximum power computed from the MPPT algorithm. The major difference between the proposed algorithm and other techniques was that the proposed algorithm was used to control directly the power drawn from the PV. The algorithm was tested under various operating conditions. The obtained results have proven that the MPP was tracked even under sudden change of irradiation levels.

In a standalone DC system, a DC-DC converter was used to interconnect solar PV and battery. To utilize solar PV to the fullest, MPPT was incorporated in controller [20]. However, in case when the state of charge (SoC) of battery was high and system was partially loaded, excess power flows into the battery, thereby reducing the life of the battery. It was shown in this paper that output voltage controlled DC-DC converter fed by solar PV may lead to instability. To address these limitations, a charge controller scheme was proposed in this paper. This scheme ensures that the battery voltage remains below its gassing voltage. Salient features of the proposed scheme were optimal utilization of solar PV and battery capacities without effecting life of battery. The effectiveness of the scheme was verified through detailed simulation study. To confirm the viability of the scheme, experimental studies were carried out on a scaled-down laboratory prototype developed for the purpose.

For conventional paralleled PV sources, the current ripple at the load side increases when the ripples were aggregated from each converter, which also reduces the lifetime of the storage batteries. This problem is addressed by [21]. Even though the ripple was able to be reduced by increasing the switching frequency, the extra switching losses must be taken into account. In this paper, a switching technique was proposed based on paralleled multiple-input sources with boost converters. Since the current ripple of the battery charging current can be minimized without the restrictions of source voltages, currents and

duty cycles, the MPPT algorithm was also able to be implemented with the proposed technique for integrating renewables into the smart grid.

A novel cost-effective, more accurate and efficient microcontroller based IncCond MPPT system for a solar voltaic system to ensure fast tracking of Maximum Power Operating Point (MPOP) at all fast changing environmental conditions has been proposed by [22]. It uses a PWM technique to regulate the power output of a boost DC-DC converter at its maximum possible value and simultaneously controls the charging process of battery.

Reference [23] introduced a MPPT algorithm using an artificial neural network for a solar power system. By applying a three-layer neural network and some simple activation functions, the MPP of a solar array can be efficiently tracked. The tracking algorithm integrated with a solar powered battery charging system has been successfully implemented on a low-cost PIC16F876 RISC-microcontroller without external sensor unit requirement. The experimental results with a commercial solar array showed that the proposed algorithm outperforms the conventional controller in terms of tracking speed and mitigation of fluctuation output power in steady state operation. The overall system efficiency was well above 90%. Incremental Conductance algorithm was implemented here.

Reference [24] proposed a MPPT battery charger. In this paper, the P&O algorithm was implemented based on a PIC16F877 microcontroller. According to the experimental results, the proposed charger is capable of charging two 7Ah valve regulated lead-acid (VRLA) batteries to full capacity in less than 3 hours with an efficiency of 84%.

Reference [25] described the way of implementing an adaptive MPPT algorithm for PV applications in a field programmable gate array (FPGA). A dual Kalman filter allows estimating the settling time of the whole system, so that the tracking algorithm self-adapts its parameters to the actual weather conditions. The real-time identification need of this application requires an FPGA platform, so that the intrinsic algorithm parallelism can be exploited, and the execution time is reduced. The tradeoff solutions proposed in this paper, accounting for the algorithm complexity and the limited FPGA hardware, as well as some solutions for optimizing the implementation are described. The proposed adaptive algorithm is implemented in a low-cost Xilinx Spartan-6 FPGA and it is validated through experimental tests.

Reference [26] introduced the use of the Dual Kalman Filter for the identification of PV system parameters. In particular, the proposed approach gives the confidence interval for the system settling time, which is used for the real-time optimization of the perturbation algorithm. The proposed technique is implemented by using a Field-Programmable Gate Array and it is validated by means of both simulation and experimental results.

Reference [27] proposed a comparative study of FPGA implementation of two closely related approaches to track MPP of a solar PV array. This work uses two versions of Kalman filter viz. linear Kalman filter and unscented Kalman filter to track MPP. Using the linear Kalman filter the MPP of a solar PV array has been tracked with an efficiency of 97.11% while using the unscented Kalman filter technique the MPP of the same solar PV array is tracked with a higher efficiency of 98.3%. However, the MPP has been tracked at a much faster rate when using the linear Kalman filter approach as compared to the unscented Kalman filter approach which is in turn faster than existing generic P&O approach. The system has been implemented on an FPGA.

Reference [28] presented a MPPT technique based on the Iterated Unscented Kalman Filter (IUKF). The proposed technique achieves: (i) satisfactory MPPT for PV arrays working under varying environmental conditions, and (ii) PV array modelling with full parameter estimation. Only six operating points on the PV curve are required as inputs to the proposed technique.

To conclude, each method can be categorized based on the type of the control variable it uses: 1) voltage, 2) current, or 3) duty cycle. For the voltage- and current-based techniques, two approaches are used. The first one is the observation of MPP voltage (V_{MP}) or current (I_{MP}) with respect to the open circuit voltage (V_{OC}) [29] and short circuit current (I_{SC}) [30]. Since this method approximates a constant ratio, its accuracy cannot be guaranteed. Consequently, the tracked power would most likely be below the real MPP, resulting in significant power loss [31].

The second approach is to obtain the information on the actual operating point of the PV array (i.e., voltage and current) and these points are updated according to the variation in environmental conditions. The most popular technique is the Perturb and Observe (P&O) method. It is based on the perturbation of voltage (or current) using the present power P and previous operating power P_{old} , respectively. If P is improved, the direction of

perturbation is retained; otherwise, the direction is reversed accordingly. Despite the simplicity of the algorithm, the performance of P&O method is heavily dependent on the trade-off between the tracking speed and the oscillations that occur around the MPP [32]. A smaller perturbation reduces the oscillations but at the expense of tracking speed, or vice versa. Another major drawback of the P&O method is that during rapid fluctuations of irradiation, the algorithm is likely to lose its direction while tracking the true MPP. Several improvements have been proposed to address this issue - mainly by considering adaptive perturbation. However, these techniques are not fully adaptive and hence are not very effective [33]. Moreover, under special conditions such as partial shading and module irregularities, these methods often fail to track the true MPP because the PV curves are characterized by multiple peaks (several local and one global). Since the P&O algorithm could not distinguish the correct peak, its usefulness under such conditions diminishes rapidly [6]. Another method is the Incremental Conductance (IC) method that is based on incrementally comparing the ratio of the derivative of conductance with the instantaneous conductance [34]. Although IC does not suffer from losing the tracking direction, it has the same problems as P&O, namely the unavoidable trade-off between the MPPT speed and oscillation. Several improved IC techniques have been proposed; i.e. it managed to improve the oscillations at MPP but, during rapid fluctuation of environmental conditions, the tracking speed reduced significantly [35].

The third category of MPPT techniques is characterized by duty cycle control, also known as Hill Climbing (HC) or direct control method [6]. In principle, it works on the same concept as P&O, but instead of perturbing the voltage or current, it updates the operating point of the PV array by perturbing the duty cycle. With the absence of the PI and/or hysteresis control loop, the implementation of HC method is greatly simplified. Consequently, this method is extensively used in PV systems [36]. However, it also suffers from the similar drawbacks as in the P&O method.

Obviously, the conventional MPPT algorithms are unable to meet the true MPP point. To overcome the aforementioned drawbacks, several researchers have used Artificial Intelligent (AI) methods such as Fuzzy Logic Controller (FLC) [37] and Neural Network (NN) [38]. Although these methods are effective in dealing with the nonlinear

characteristics of the I–V curves, they require extensive computation. Clearly, a low-cost processor cannot be employed in such a system.

An alternative approach is to use Evolutionary Algorithms (EAs). Due to their ability to handle nonlinear objective functions [39], [40], EAs offer a promising way to deal with the MPPT problem. EAs are popular in many engineering applications but, to date, applications of this method for MPPT purposes have been limited. EAs find the solution by using a set of points (population) instead of a single point used in conventional search and optimization techniques. Hence, it is foreseen to be very efficient in dealing with the MPPT problem [41]. Various EA methods are found in the literature, but the most popular ones are Genetic Algorithm (GA), Differential Evolution (DE) and Particle Swarm Optimization (PSO) [42]–[45].

The main problem solved by the MPPT algorithms is to automatically find the panel operating voltage that allows maximum power output. In a larger system, connecting a single MPPT controller to multiple panels will yield good results, but, in the case of partial shading, the combined power output graph will have multiple peaks and valleys (local maxima). This will confuse most MPPT algorithms and make them track incorrectly. Some techniques to solve problems related to partial shading have been proposed, but they either need to use additional equipment like extra monitoring cells, extra switches and current sensors for sweeping panel current, or complicated models based on the panel characteristics. Ideally, each panel should have their own MPPT controller. This way the risk of partial shading is minimized, each panel is allowed to function at peak efficiency, and the design problems related to converters handling more than 20-30A are eliminated.

Many MPPT techniques have been studied during the literature review; these techniques vary in many aspects as mentioned before, including simplicity, convergence speed, hardware implementation, sensors required, cost range of effectiveness and need for parameterization. The primary challenges for maximum power point tracking of a solar PV array include:

- (i) How to get to the MPP quickly,
- (ii) How to stabilize at the MPP, and
- (iii) How to smoothly transition from one MPP to another for sharply changing weather conditions.

Besides the P&O and the IncCond algorithms, there are many other advanced algorithms, such as fuzzy logic and the neural network-based algorithms. These methods are suitable for solving certain specific problems; however, the realization of the system is complex in the software. Table 1.1 summarizes the major characteristics of 30 MPPT techniques [46].

Overall, P&O and IncCond are superior to all other MPPT algorithms. Though fuzzy and neural networks are being developed, the efficiency remains high in P&O and IncCond methods. The converters such as buck, boost, buck-boost, Cuk etc. converters are being used in MPPT systems. PWM inverters are used for grid connection and standalone AC loads. The selection of converters is based on the load connected to the system. The ripples in DC voltage and current also influence the selection of converters. With the above mentioned converters and MPPT algorithms, solar panels can be configured to feed any kind of load. The vast development in improving efficiency of MPPT algorithms can encourage domestic generation of power using solar panels.

TABLE 1.1: MAJOR CHARACTERISTICS OF DIFFERENT MPPT TECHNIQUES

MPPT technique	PV array dependent ?	True MPPT ?	Analog or Digital?	Periodic tuning?	Convergence speed	Implementation complexity	Sensed parameters
Hill Climbing / P&O	No	Yes	Both	No	Varies	Low	Voltage, Current
Incremental Conductance	No	Yes	Digital	No	Varies	Medium	Voltage, Current
Fractional V_{OC}	Yes	No	Both	Yes	Medium	Low	Voltage
Fractional I_{SC}	Yes	No	Both	Yes	Medium	Medium	Current
Fuzzy Logic Control	Yes	Yes	Digital	Yes	Fast	High	Varies
Neural Network	Yes	Yes	Digital	Yes	Fast	High	Varies
RCC	No	Yes	Analog	No	Fast	Low	Voltage, Current
Current Sweep	Yes	Yes	Digital	Yes	Slow	High	Voltage, Current
DC Link Capacitor Drop Control	No	No	Both	No	Medium	Low	Voltage
Load I or V maximization	No	No	Analog	No	Fast	Low	Voltage, Current
dP/dV or dP/dI Feedback Control	No	Yes	Digital	No	Fast	Medium	Voltage, Current
β Method	No	Yes	Digital	No	Fast	High	Voltage, Current
System Oscillation Method	No	Yes	Analog	No	N/A	Low	Voltage
Constant Voltage Tracker	Yes	No	Digital	Yes	Medium	Low	Voltage
Lookup Table Method	Yes	Yes	Digital	Yes	Fast	Medium	Voltage, Current, Irradiance, Temperature
Online MPP Search Algorithm	No	Yes	Digital	No	Fast	High	Voltage, Current
Array Reconfiguration	Yes	No	Digital	Yes	Slow	High	Voltage, Current
Linear Current Control	Yes	No	Digital	Yes	Fast	Medium	Irradiance
IMPP and VMPP Computation	Yes	Yes	Digital	Yes	N/A	Medium	Irradiance, Temperature
State Based MPPT	Yes	Yes	Both	Yes	Fast	High	Voltage, Current
OCC MPPT	Yes	No	Both	Yes	Fast	Medium	Current

BFV	Yes	No	Both	Yes	N/A	Low	None
LRCM	Yes	No	Digital	No	N/A	High	Voltage, Current
Slide Control	No	Yes	Digital	No	Fast	Medium	Voltage, Current
Temperature Method	No	Yes	Digital	Yes	Medium	High	Voltage, Irradiance, Temperature
Three Point Weight Comparison	No	Yes	Digital	No	Varies	Low	Voltage, Current
POS Control	No	Yes	Digital	No	N/A	Low	Current
Biological Swarm Chasing MPPT	No	Yes	Digital	No	Varies	High	Voltage, Current, Irradiance, Temperature
Variable Inductor MPPT	No	Yes	Digital	No	Varies	Medium	Voltage, Current
INR Method	No	Yes	Digital	No	High	Medium	Voltage, Current

1.3 Problem Statement and Motivation

Photovoltaic solar cells are an evolving technology. The highest commercially available efficiencies of the solar cells in 2019 reached 22.70% [47]. On the other hand, high oil prices, pollution and political pressure to reduce Carbon Dioxide emissions are few of the major reasons that drive governments to consider renewable energy sources. The increasing demand of electric energy drives nations to consider renewable and sustainable energies.

Currently, the usage of energy from PV panels is a reality, and its intensive use will become extremely important in finding solutions to future energy and environmental problems very soon. Unfortunately, solar photovoltaic cells suffer from low efficiency of trapping the solar energy. This efficiency further decreases if there is no load matching between the input side (PV array output) and the output side (load). Currently, solar PV cells can trap solar energy with an efficiency of 22%. These PV solar panels exhibit nonlinear P-V characteristics with a unique point where the power produced is a maximum, and their output supply depends mainly on the changes in the solar irradiance and the temperature which are not known and exhibit multiple maxima in their PV characteristics under partially shaded conditions. In this context, the used MPPT techniques are the most important to extract the maximum power available in PV.

Since, MPPT is an essential part of a PV system, extensive research has occurred in recent years in this field and many new techniques have been reported. There are many different techniques for maximum power point tracking of photovoltaic PV systems. It is shown that at least 30 methods have been introduced in the literature, with several variations on implementation.

The methods vary in complexity, sensors required, convergence speed, cost, range of effectiveness, implementation hardware, popularity, and in other respects. They range from the almost obvious (but not necessarily ineffective) to the most creative (but not necessarily most effective). In fact, so many methods have been developed that it has become difficult to adequately determine which method, newly proposed or existing, is most appropriate for a given PV system.

The effectiveness of MPPT is theoretically defined as a ratio of the practical power output to the true maximum power value. A fair comparison of MPPT methods is difficult because a true MPP is concealed during the real-time operation under natural sunlight. Further, the output difference between solar modules and other non-ideal factors make it impossible to create two identical benches for real-time comparison.

Out of numerous available techniques, the one that is most commonly used is the P&O method. Figure 1.2 shows the flowchart that is depicting the P&O method. P&O is also known as hill climbing method because it checks the rise of the curve until MPP and the fall after that point. Using P&O method, the controller adjusts voltage and measures power and if this measured power is greater than the previous value of power, adjustments are made in the same direction until there is no more increment in power [48]. This method is easy to implement but can cause oscillations in power output and can sometimes show tracking failures in rapid environmental changes i.e. locates operating point away from MPP when there is a sudden change in voltage characteristics.

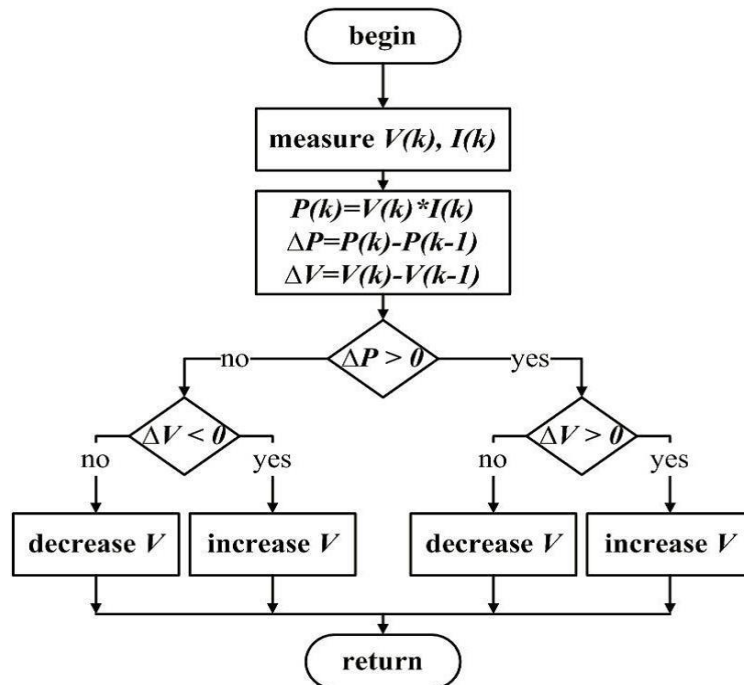


Figure 1.2: Flowchart depicting the Perturb & Observe algorithm [48]

The Perturbation & Observation (P&O) method is widely used due to its easy implementation and simplicity. The P&O usually requires a dithering scheme to reduce

noise effects, but the dithering scheme slows the tracking response time. Tracking speed is the most important factor for improving efficiency under frequent environmental change.

Hence, it is essential to find optimal maximum power point of the panel so as to increase the overall efficiency of the photovoltaic system. Hence, the maximum power point should be tracked efficiently to improve the overall system efficiency.

Kalman Filter (KF), as a dynamic estimation technique, has played an important role in many industrial applications such as sensorless speed estimation in electric drives [49]–[51], non-linear mechanical loads [52], power system protection and harmonics estimation [53], [54], robots/particles localization [55]–[57], and fault diagnostics [58]. In addition, KF-based techniques are widely used in distributed generation and islanding detection applications [59], [60]. The ability to estimate non-measurable signals, fast convergence, and direct implementation encourages wider utilization of KF-based techniques in various industrial applications.

From the previous discussion, it can be seen that the MPP tracking requires a prediction and correction model that can function effectively and economically in real-time. The major reason for using KF here is that it is an efficient, recursive filter that estimates the state of a dynamic system from a series of incomplete and noisy measurements. Kalman Filter is good for tracking MPPT of PV array to ensure that the PV array should work within a certain region of the P-V curve. Kalman Filter exploits the dynamics of the target, which governs its time evolution, to remove the effects of the noise and get a good estimate of the location of the target at the present time (filtering), at a future time (prediction), or at a time in the past (interpolation or smoothing). Kalman Filter provides stochastic estimation in a noisy environment. Kalman Filter operates on estimating states by using recursive time updates and measurement updates over time. Noise effects in the system are decreased due to recursive cycles which finally leads to the true value of the measurement.

1.3.1 Maximum Power Point Tracking Definition

Solar cells have a complex relationship between solar irradiation, temperature and total resistance that produces a nonlinear output efficiency which can be analyzed based on the I-V curve [61]. The power P is given by $P=V*I$. A photovoltaic cell, for the majority of its

useful curve, acts as a constant current source [62]. However, at a photovoltaic cell's MPP region, its curve has an approximately inverse exponential relationship between current and voltage. From basic circuit theory, the power delivered from or to a device is optimized where the derivative (graphically, the slope) dI/dV of the I-V curve is equal and opposite of I/V ratio (where $dP/dV=0$). Hence, a solar photovoltaic array should work at maximum power point to deliver maximum operational efficiency.

MPPT is a technique that inverters, battery chargers and other similar devices use to get maximum possible power from photovoltaic devices [63]. This is known as the maximum power point (MPP) and corresponds to the knee of the curve [64]. A load with resistance $R=V/I$ equals to the reciprocal of this value draws the maximum power from the device. This is sometimes called the characteristic resistance of the cell. This is a dynamic quantity which changes depending on the level of illumination, as well as other factors such as temperature and the age of the cell. If the resistance is lower or higher than this value, the power drawn will be less than the maximum available, and thus the cell will not be used as efficiently as it could be.

The function of a MPPT is analogous to the transmission in a car. When the transmission is in the wrong gear, the wheels do not receive maximum power. That is because the engine is running either slower or faster than its ideal speed range. The purpose of the transmission is to couple the engine to the wheels, in a way that lets the engine run in a favorable speed range in spite of varying acceleration and terrain [65].

Maximum power point trackers utilize different types of control circuit or logic to search for this point and thus to allow the converter circuit to extract the maximum power available from a cell. For any given set of operational conditions, cells have a single operating point where the values of the current (I) and voltage (V) of the cell result in a maximum power output. These values correspond to a particular load resistance, which is equal to V/I as specified by Ohm's law.

In short, the problem considered by Maximum Power Point Tracking techniques is to automatically find the voltage V_{MPP} or current I_{MPP} at which a PV array should operate to obtain the maximum power output P_{MPP} under a given temperature and irradiance. Hence, this research will address an efficient maximum power point tracking scheme of solar photovoltaic array for better power output.

1.4 Thesis Objectives

The main goal of this thesis is to develop and improve the PV system, by contributing to the optimization of energy withdrawn from PV panel using an embedded system; the model of a typical system is shown in Figure 1.3. This figure shows the four main blocks of the stand-alone PV system to be simulated in the Matlab environment:

1. PV generator model
2. DC-DC Converter model - to connect the PV generator model to the load model
3. Load model – energy consumption or storage model
4. Controller model for the DC-DC Converter – various algorithms for generating the PWM pulses for firing the switches in the converter and maximizing the energy transfer between the PV generator and load.

These four blocks are described next.

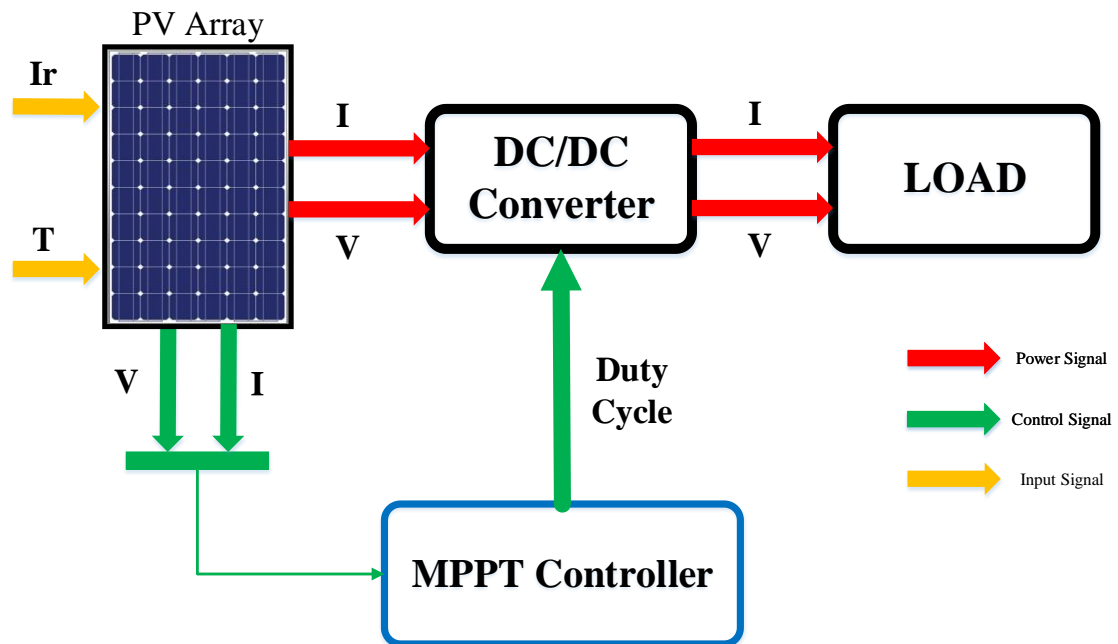


Figure 1.3: Stand-alone PV system with integrated MPPT algorithm

1.4.1 PV array model

An accurate PV array model is required for a practical array (i.e. SunPower SPR-305E-WHT-D). An array consists of various PV cells connected in series and parallel to give the desired voltage and power (current) respectively. The results from the model should show

an excellent correspondence to manufacturer's published curves and show the effect of insolation and temperature on the important solar characteristics. The model of the PV array is simulated in Matlab environment. The Matlab program calculates the current I using typical electrical parameters of the module (I_{SC}, V_{OC}), and the variables Voltage (V), Irradiation (G), and Temperature (T).

1.4.2 DC-DC Converter model

The small-signal model for DC-DC Boost converter, with/without parasitic elements, operating in continuous conduction mode (CCM)/discontinuous conduction mode (DCM) is used to understand the basic features of the switching system and investigate the effects of parasitic elements and losses on the model accuracy, the efficiency and the dynamic performance of the system. The results from the model will help in designing a robust controller for DC-DC Boost converter.

1.4.3 Load model

Load modeling refers to the mathematical representation of the relationship between the power and voltage in a load. Load models can be classified into constant power load, constant impedance load, and constant current load.

As a proof-of-concept, a simple constant impedance load (RC) model is used in this work to investigate the behavior of PV system under the proposed MPPT algorithms. This simplified RC load model consists of a resistor R connected in parallel with two DC link capacitors. DC link capacitors are large enough to eliminate the ripple component induced at the DC side. This aspect is important in order to avoid an unexpected behavior of the MPPT since this ripple is directly perceived in the output voltage of the PV module.

On the other hand, the output power of the PV module can change as a function of the irradiance and hence many disturbances will be produced in this variable. The DC link capacitors play a damping role in this aspect contributing to maintain the stability of the MPPT during these transitory disturbances.

1.4.4 Controller model for the DC-DC Converter

A design of a feedback controller for a DC-DC Boost converter is required to yield a robust, closed-loop controller structure with stable static and dynamic characteristics for operating points over the whole operational range of the converter. Moreover, a study of different numerical integration methods and their stability characteristics is desired to enable the implementation of real-time models in embedded hardware platforms.

One of the main tasks of the DC-DC converter's controller is to control the output voltage or current of the PV array to generate maximum possible power at a certain irradiance and temperature by implementing the maximum power theorem for load matching using the relationship between input and output impedances. There are many techniques that can be used for this purpose with the Perturb-and-Observe (P&O) technique being the most popular one and which will be used as a test bench. Also, Differential Evolution (DE) and Particle Swarm Optimization (PSO) algorithms are two commonly employed techniques in designing maximum power point tracking systems in photovoltaic (PV) farms will be investigated.

Furthermore, the Kalman Filter (KF) technique in designing maximum power point tracking systems in photovoltaic (PV) applications is required to overcome the drawbacks in the test bench technique. The implementation of the KF algorithm and the more traditional P&O algorithm is needed using FPGA chip to test their efficiencies and tracking speeds in a real-time environment.

1.5 Thesis Organization

The work of this dissertation is organized as follows:

Chapter 2 Provides a detailed review regarding microgrids architectures. In the recent years, there has been a growing interest in the concept of microgrids to integrate distributed generation systems like solar photovoltaic (PV) and wind to reduce greenhouse gas (GHG) emissions, to provide higher reliability for critical loads and to supply electricity in areas not served by existing grid infrastructure. A microgrid (MG) is a portion of the electrical system which views generation and associated loads as a subsystem, with the ability to

operate both grid connected or islanded from grid, thus maintaining a high level of service and reliability. The existing grid infrastructure, the distributed energy resources to be integrated, as well as specific customer-oriented requirements will determine the best fitting architecture to constitute a microgrid. Several microgrid demonstration projects have been implemented to investigate further this emerging concept. In this chapter, most common microgrids architectures based on AC, DC and hybrid AC/DC buses are analyzed. Furthermore, comparisons are made between different microgrid architectures. Positive and negative features of different architectures are given as a guide for further microgrid system studies.

Chapter 3 provides a general overview of grid-connected PV systems. This chapter looks at different components of a grid-connected PV system from the solar irradiance received by the PV arrays to the AC power injected into the grid and makes a review of the recent achievements and current research activities in the field.

Chapter 4 presents a detailed survey on the topic of grid-connected PV system used to integrate the solar energy into the utility grid. Topologies of single-phase grid-connected inverters will be analyzed critically, and comparative study of these topologies will be presented. The three-phase grid-connected inverters will be outlined. The control techniques for the single and three-phase grid-connected inverters will be critically reviewed and presented.

Chapter 5 proposes the Small Signal Averaged State-Space modeling technique for DC-DC Boost converters, with and without parasitic elements, operating in continuous conduction mode (CCM). First, the small signal analysis of DC-DC Boost converters with ideal/lossless components operating in CCM will explore in order to develop a simplified model that helps to understand the basic features of the switching system. Then, the small-signal analysis of DC-DC Boost converters with the effects of parasitic elements and losses operating in CCM will investigate in order to improve the model accuracy, study the efficiency and the dynamic performance of the system. Furthermore, the system dynamic behaviour for the DC-DC Boost converter with ideal components and DC-DC Boost

converter with non-ideal components operating in CCM will compare via Bode plots and transient step responses under different values for the load resistance in order to help in designing a robust controller for DC-DC Boost converters operating in continuous conduction mode (CCM).

The various aspects of average modelling of DC-DC Boost converter operating in DCM will be studied. Moreover, the reduced- and full-order average models will derive. In addition, various parasitic components have been taken into consideration and a full-order model will be developed. The system dynamic behavior for the DC-DC Boost converter with ideal components and DC-DC Boost converter with non-ideal components operating in DCM will be compared via Bode plots and transient step responses under different values of the load resistance in order to help in designing a robust controller.

Boost type DC-DC converters are non-linear systems, and output voltage regulation in these converters using a traditionally derived feedback controller does not yield good dynamic responses at different operating points over the complete operating range. Hence, the design of a feedback controller for a DC-DC boost converter operating in CCM will be formulated as an optimization task, and the feedback controller parameters are derived based on a novel PSO technique. This novel optimization method will be designed to yield a robust, closed-loop controller structure with stable static and dynamic characteristics for operating points over the whole operational range of the converter. To evaluate the objective function of the developed PSO algorithm, a small-signal model of a DC-DC boost converter, subjected to various internal and external disturbances, was used.

First, the PID controller parameters for the DC-DC boost converter will be identified based on (a) the traditional Ziegler–Nichol method and (b) the novel PSO algorithm. Then, using the gain parameters obtained by these two methods, the dynamic responses of the DC-DC boost converter operating in CCM will be obtained and compared. Four different performance comparison tests undergoing various input-voltage and load-current step transients will be studied.

The dynamic performance of DC-DC boost converters, with and without parasitic elements, operating in continuous conduction mode (CCM) will be investigated. First, the state-space equations describing DC-DC boost converters were developed. Next, the small signal average models of these converters were derived. Then, the newly developed

average models will be discretized, and simulated in Matlab using nine popular integration techniques for analysis of accuracy and stability.

Chapter 6 introduces the Kalman Filter (KF) as a tool for statistical estimation in the context of linear Gaussian dynamical systems and proposes a novel Kalman Filter (KF) based MPPT technique for PV applications. In this chapter the proposed technique will be designed and implemented. A Matlab simulation model representing a PV panel is constructed. The panel is connected to the load through a DC-DC Boost converter which is controlled by using the KF algorithm.

Chapter 7 defines the field programmable gate array (FPGA). Then, the distinguish between an FPGA and a stored-memory processor will be investigated. The principle of operation of the various functional units within an FPGA will be explained and listed. Furthermore, the architecture and performance specifications of various commercially available FPGA will be compared. Moreover, the steps required in using an FPGA in an embedded system will be described.

The implementation of Kalman filter based MPPT controller and the well-known P&O algorithm will be demonstrated and co-simulated using FPGA chip Altera Cyclone II EP2C20F484C7 to test their efficiencies and tracking speeds in a real-time environment.

Chapter 8 presents the summary and conclusion of the thesis. Moreover, this chapter outlines the contributions of the presented research and suggests future work.

Chapter 2. Microgrids Architectures

2.1 Introduction

Recently, the world's electricity systems are starting to decentralize, decarbonize, and democratize in many cases [1]. These features - known as the “three Ds” - are driven by the need to reduce greenhouse gas (GHG) emissions to alleviate climate change, to provide higher reliability and resilience for critical loads, reduce electricity costs, replace aging grid infrastructure, and to supply electricity in areas not served by existing grid infrastructure. While the compromise between the technical driving factors and the details of specific solution may differ from one place to another, MGs came to the picture as a flexible solution for managing distributed energy resources (DERs) that can meet the different requirements of different communities.

The last decades, the research, development and implementation of renewable energy sources (RESs) have been strongly impelled, mainly as distributed generation (DG). Due to variability and intermittence of RESs (especially wind and solar), their large penetration over traditional energy systems involve operational difficulties that limit their implementation, as variations of supplied voltage magnitudes or unbalances between active and reactive power among generators. Moreover, new power flow patterns may require changes to the distribution grid infrastructure with the application of enhanced distribution automation, adapted protection and control strategies, and improved voltage management techniques [66]. A possible way to conduct the emerging potential of DG is to take a system approach which views generation and associated loads as a subsystem, or a "microgrid" (MG) [67]. The MG can operate either connected to or separated from the distribution system, thereby maintaining a high level of service and reliability. In this sense, distributed energy storage systems (ESSs) become necessary to improve the reliability of the overall system, supporting the distributed generators power capability in the cases when they cannot supply the full power required by the consumers. MGs can also operate isolated in those areas with no access to the utility.

The modularity of emerging generation technologies permits generators to be placed and sized optimally to maximize reliability, security and economic benefits of DG

deployment. As an example, installing microgeneration at the customer side gives the opportunity to locally utilize the waste heat from conversion of primary fuel to electricity (combined production of heat and power - CHP), thus accomplishing a better overall efficiency. In the last few years, there has been a significant progress in developing small, kW-scale CHP applications, which are expected to play a very significant role in upcoming MG implementations [68].

A key feature that distinguishes MGs from active distribution networks with DG is the implementation of the control system. MGs are considered to be the building blocks of the "smart grids", thus integrating the actions of all the DERs including distributed generators and storage devices, plus local loads and the main distribution grid. The target is to efficiently deliver sustainable, economic and secure electricity supply through intelligent monitoring, control, communication and self-healing technologies, with cost-competitive information and communication technologies (ICT) playing a fundamental role.

Microgrids are vital components in the smart grid environment, which is being developed to improve reliability, power quality, and facilitate integration of DERs. MGs are defined as medium or small power systems comprising DERs and controllable and uncontrollable loads; either isolated and meeting their own demand needs or connected to the external grid to supplement their supply requirements. MGs are connected to a distribution grid at a single point known as the Point of Common Coupling (PCC). Figure 2.1 shows a conceptual topology of future smart grid connecting to a small MG [69].

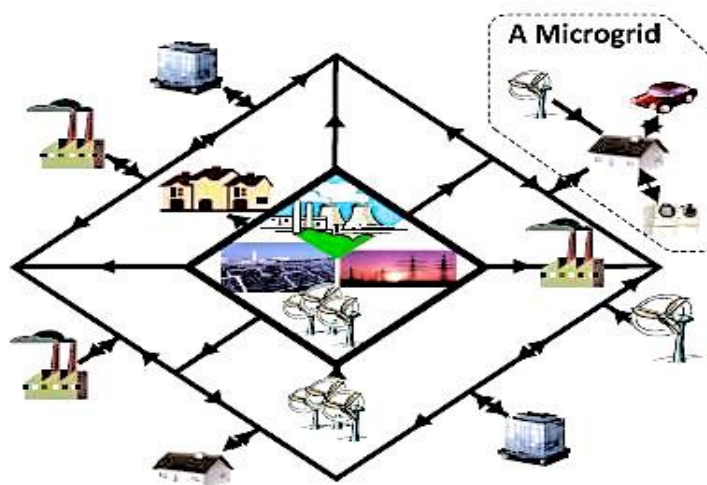


Figure 2.1: A conceptual topology of future smart grid. [69]

MGs are efficient and resilient since they not only allow for a high penetration level of RESs, but also due to their ability to operate in isolated mode when faults occur in the main grid [70]. Consequently, MGs will offer greater reliability, especially when integrated with smart grids, and will continue operation in islanded mode or even put power back into the wider grid during outages. Finally, MGs offer flexibility, because a variety of resources, including CHP and diesel backups can be integrated into the grid, providing reliability, using waste heat for other purposes, and smoothing out supply/demand spikes. However, the implementation of MGs encounters a number of challenges. For instance, maintaining demand supply balance in the presence of RESs is a complex task because of generation intermittencies, load mismatches, and voltage instabilities [71], [72].

The concept of a MG is gaining rapid acceptance because of the environmentally friendly energy provision, its cost effectiveness, improvement in power quality and reliability, and reduction in line congestion and losses, reduction in infrastructure investment needs. From the customer point of view, the MG is designed to meet their electrical and heat energy demand and minimize load shedding [2].

In order to effectively integrate DERs into a MG, proper architectures should be implemented, based on AC, DC and/or hybrid AC/DC systems, seeking the highest reliability and efficiency [3]. The existing grid infrastructure, the distributed energy resources to be integrated, as well as specific customer-oriented requirements, will determine the most suitable electrical architecture of the MG. Since late 19th century, AC has been the standard choice for commercial energy systems, based mainly on the ease to transform AC voltage into different levels, the capability to transmit power over long distances and its inherent characteristic from the fossil energy-driven rotating machines with their synchronous generators. Therefore, AC distribution is the most popular and commonly used structure for MG studies and implementations. By utilizing the existing AC network infrastructure (distribution, transformers, protections, etc.), AC MGs are easier to design and implement and are built on proven and thus reliable technology. However, DC distribution has shown a resurgence in recent years due to the development and deployment of RES based on DC power sources, and the rapid growth of DC loads which constitute today the vast majority of loads. DC distribution presents several advantages, such as reduction of the power losses and voltage drops, and an increase of

capacity of power lines, mainly due to the lack of reactive power flows, absence of voltage drops in reactance of lines and non-existence of skin and proximity effects thence reducing ohmic resistance of lines. According to this, its planning, implementation and operation is simpler and less expensive [4].

This chapter presents different architectures of MGs, such as AC, DC and hybrid AC/DC MGs, including a general definition of the electrical MG, and comparisons are made between different MG architectures. Pros and cons of different architectures are given to guide further MG system studies.

2.2 Literature Review of MG Studies

In reference [73], a 3-phase power-flow algorithm, in the sequence-component frame, for the MG and active distribution system (ADS) applications is presented. This paper also presents steady-state sequence-component frame models of distributed energy resource (DER) units for the developed power-flow approach under balanced/unbalanced conditions and develops sequence component models of directly coupled synchronous machine based and electronically coupled DER units. The validity and accuracy of the power flow algorithm of developed models are verified by comparing power flows of two test systems with those obtained from time-domain simulation results in the PSCAD/EMTDC simulation package.

Reference [74] presented a cost optimization scheme for a MG and also several schemes for sharing power between two generators are compared. The MG considered in this paper consists of two reciprocating gas engines, a combined heat and power plant, a photovoltaic array and a wind generator. A penalty is applied for any heat produced in excess of demand.

Reference [75] discussed the different interconnections of MG and interconnection stability. The evaluation criteria in the MG stability are tie-line power flow and frequency deviation. Two research topics are discussed here:

1. Control method in MG for stability and efficiency.
2. Method of interconnections with MG for stability and efficiency.

Also, this paper discussed the benefits of different architectures regarding mainly frequency quality under limited tie-line power flow capacities. Several operational

architectures of MGs are expected to come into being in the next decade. For a severe fault, the operational mode can be changed in order to maintain system stability; and hence supply reliability could be improved.

Reference [76] proposed the interaction model that has been established between the power system and voltage source inverter based series dynamic voltage restorer (DVR). On the basis of that, the energy exchange between the DVR and the system are discussed and calculated when adopting different compensation strategies. This provides a strong theoretical basis for the design of the DVR system and realization of control unit implementation of compensation strategy.

Reference [77] addressed the timely issues of synchronization and application of 3-phase power converters connected in parallel utilizing the Power-Hardware-in-the-Loop concept. Without proper synchronization, distinguishing the currents circulating between the converters are unclear. The paper centers on control methodology for achieving precise phase synchronization for equal load sharing, with minimum current circulation between the paralleled power converter modules, and robust dynamic system control under different transient conditions. One of the possible applications for the configuration presented in this paper is the conceptual virtual MG, which utilizes the reactive power compensation ability of the Static Synchronous Compensator (STATCOM).

Reference [78] addressed the hierarchical approach to deal with the problem of frequency control in a medium voltage network comprising of several MGs and distributed generation sources operating in islanded mode. Tasks related with coordinated frequency control were successfully fulfilled, either after islanding or for load-following purposes.

Reference [79] proposed an interaction problem that might be induced from various kinds of DGs installed in a MG. One of the most important features of a MG is islanded operation. MG does not include large central generators and all distributed small generators have to share all loads existing in the MG. There is no one inertia large enough to compensate for the quick load changes required in the MG, and all distributed generators must compensate for them accordingly.

Reference [80] proposed a new approach on managing distribution systems based on adaptive agents which are placed at different locations in the grid. For this purpose, a decentralized power flow method is introduced. Depending on available local information,

each agent is able to calculate a system state. Local utilities now face the new challenges by applying decentralized energy management systems which are based on a high degree of automation. Agent-based distributed power flow calculation is applicable in distribution grids, perfectly meets the demands of decentralized energy management systems and leads to correct results.

In reference [81], a MG protection scheme that relies on optimally sizing fault current limiters (FCLs) and optimally setting directional over current relays is proposed. The proposed approach is tested on two medium-voltage networks: a typical radial distribution system and on the IEEE 30 bus looped power distribution system equipped with directly-connected conventional synchronous generators (CSGs). Fault current limiters of the inductive type are located at the main interconnection point of the MG to the main grid. Without the fault current limiters, it was found that it is difficult to set the relays optimally to satisfy both MG modes of operation.

Reference [82] presented a structure of modified DC bus interconnected 1-phase MG, as well as a topology of power converter building block (PCBB) based on the DC bus to perform various functions in a distributed energy network. The main functions of the PCBB are: compensating the current harmonics produced by nonlinear load in the MG, mitigating the voltage sag or swell of the electrical power system (EPS) at the point of common coupling (PCC) and facilitating the islanding and re-closure of MG when a severe fault happens to the EPS. A cascaded PI controller is used to regulate the voltage sag compensation.

Reference [83] proposed a unified control strategy that enables islanded and grid-connected operations of 3-phase electronically interfaced distributed energy resources (DERs), with no need for knowing the prevailing mode of operation or switching between two corresponding control architectures. This paper presents the mathematical model on which the proposed strategy is based. Further, the effectiveness of the proposed strategy is demonstrated through time-domain simulation of a 2-unit test MG in the PSCAD/EMTDC software environment.

Reference [84] shows that the constant-power band offers a solution for this if a large band is included in renewable energy. More controllable units, on the other hand, have a smaller constant power band to exploit their power flexibility. This paper proposed the MG

power is balanced by using a control strategy that modifies the set value of the rms MG voltage at the inverter AC side as a function of the DC-link voltage. In case a certain voltage, which is determined by a constant-power band, is surpassed, this control strategy is combined with (p/v)-droop control. This droop controller changes the output power of the DG unit and its possible storage devices as a function of the grid voltage.

Reference [85] described a major research initiative by British Columbia Institute of Technology for the construction of an Intelligent MG on its campus in Burnaby. The utility companies and researchers are working together to develop architectures, protocols and models of the evolving the intelligent grid.

In reference [86], real and reactive power management strategies of electronically interfaced distributed generation (DG) units in the context of a multiple-DG MG system is addressed in this paper. Based on the reactive power controls adopted, three power management strategies (PMSs) are identified and investigated. These strategies are based on voltage-droop characteristic, voltage regulation, and load reactive power compensation. A systematic approach to develop a small-signal dynamic model of a multiple-DG MG including real and reactive PMSs, is also presented. This paper introduces three PMSs for an autonomous MG system.

Reference [87] proposed that the small grid with high proportions of non-linear and unbalanced loads and it is important to actively control the waveform quality in terms of harmonics, transient disturbances and balance.

Reference [88] introduced the MG planning structure in Shandong Electric Power Research Institute (SEPRI) and discusses the various feasible control approaches used and presents for MG. Then, based on modeling different types of distributed generations and energy storage equipment. MG can maintain stable and voltage and frequency stability by choosing different micro sources reasonably and designing controllers. Storage devices which use power droop control play an important role in MG control.

Reference [89] presented the intermittent nature of renewable energy sources like photovoltaic (PV) demands usage of storage with high energy density. This paper proposed a composite energy storage system (CESS) that contains both high energy density storage battery and high power density storage ultra-capacitor to meet the aforementioned

requirements. The proposed power converter configuration and the energy management scheme can actively distribute the power demand among the different energy storages.

Reference [90] proposed background on various AC motor types, and the control and protection practices. This paper also discussed various electric motor types and different types of motor starting methods. They are as follows: Across the line, Reduced voltage auto transformer, Reduced voltage resistor or reactor, Wye-delta, Part-winding, Solid state soft starter, Rotor resistance. Adjustable speed drive. It proposed motor protection of a motor from abnormal conditions. Various types of motor protection are as follows: Nameplate values, Low voltage motor protection, Medium voltage motor protection.

Reference [91] proposed a system to limit the flow of large line currents and hence, protect the MGs. Also, this paper proposed two current-limiting algorithms, namely, the RL feed forward and flux-charge-model feedback algorithm, for controlling a series inverter connected between the MGs and utility during utility voltage sags. This paper presented the RL algorithm functions by controlling a series inverter, connected between the micro and utility grids, to insert large virtual RL impedance along the distribution feeder to limit the line currents and damp transient oscillation with a finite amount of active power circulating through the series inverter.

Reference [92] presented advanced sensors and measurement techniques which will be used to achieve higher degrees of network automation and better system control, while pervasive communications will allow networks to be reconfigured by intelligent systems. This report has sought to identify the major research challenges facing electrical power networks and the strategic urgency with which the redesign of a key infrastructure must be undertaken. It also serves to create new electricity system for the next century and generate major economic advantages in providing technical solutions and designs for an international market that is currently facing similar electrical networks crossroads.

Reference [93] proposed a novel integration of Doubly Fed Induction Generator (DFIG)-based wind farms within MGs. The voltage and frequency of the MG are controlled by the wind generators through droop characteristics. This paper focused on MG application; however, the method is quite applicable for AC grid and High Voltage Direct Current (HVDC) link connections as well. In a power system with a high wind energy penetration, not tracking maximum wind power is not necessarily a disadvantage.

Reference [94] proposed the concept of a MG village design with the distributed energy resources and its economic feasibility evaluation. The engineering flow is comprised of four parts such as natural environment and demand analysis, selection of applicable distributed energy resources and electrical network design, power network analysis, and its economic evaluation. Furthermore, the effectiveness of the suggested scheme has been demonstrated by case studies on realistic demonstration sites.

Reference [95] proved that storage systems applied in MGs can perform the dual tasks of active power balancing and voltage regulation simultaneously. In grid connected mode of operation, it may ensure load levelling and reducing the power exchange with the network which makes the system operation more efficient and flexible.

Reference [96] presented the results of a research project whose-objective is to extend obtained capabilities of a resilient MG to a conventional distribution network. The presented work is an advanced interface control system for grid connection of this cluster in order to provide the overpower in compliance with the distribution network. As a result, the Distribution System Operator (DSO) considers this locally controlled cluster as a single producer. Also, an advanced interface control system for a MG is presented in this paper. The droop controller for the primary frequency control and power exchange with the distribution network is detailed.

Reference [97] addressed the problem of voltage regulation in MGs that include DFIG-based wind generation. This paper proposed a voltage sensitivity analysis-based scheme to achieve voltage regulation at a target bus in such MGs. The proposed method is local and obviates the need for remote measurements. The proposed methodology can be potentially useful to reactive power management and voltage regulation in MGs.

2.3 Microgrid Motivation

When Hurricane Sandy cut off power to millions of homes and businesses in the Northeast US, a few areas - mostly parts of universities - kept the lights on using their own power generation systems. This ability to sustain electricity service during widespread natural disasters is one reason for the growing interest in MGs. But they offer other important benefits as well. By increasing efficiency, integrating renewables, and helping

manage energy supply and demand, MGs can reduce GHG emissions and save energy. For utilities, MGs can ensure power resiliency and reliability for critical loads such as health care, food and drinking water facilities, transportation and communications facilities. Also, they can provide electricity in remote areas not served by existing grid infrastructure. MGs also appeal to parties looking for self-sufficiency and independence.

The formula is simple: If you can find out what is valuable to someone, then you have the key to motivating them. As a result, energy users that value reliability are the prime candidates for MGs. Hit hard by a string of storms the past five years, states in the east coast of the U.S., including Connecticut and New York, have incentive programs to deploy MGs to improve grid reliability. California recently put in place an energy storage program, which could create financial incentives for MGs. Island nations are also projected to be early customers of large-scale MGs because they typically generate electricity with diesel generators, which is expensive. Navigant Research forecasts that the U.S. will fuel most growth in MGs this decade while Europe, which has a more reliable grid, will lag. It predicts growth from 685 MW last year to five GW by 2020.

2.4 Microgrid Projects Across the Globe

In recent years, MGs - being the core element of the smart grid evolution - have been an area under hot discussion. According to a new report from Navigant Research, as of the fourth quarter of 2017, the research group's Microgrid Deployment Tracker (MDT) had identified 1,869 projects—representing a total capacity of 20.7 GW—operating, under development, or proposed across 123 countries worldwide. That compares to 18 GW of MG capacity identified in the second quarter of 2016.

Across the globe, several MG projects have been productively implemented in advanced countries and few are in progress in developing countries too. The process is expected to take a good pace with more emphasis on the smart grid to be a reality. To mention there are a number of active MG projects around the world namely in North America, European Union and South & East Asia involved in realizing the improved operation of MG, testing and evaluation of MG demonstration systems in a better sense. Looking across the globe it is found that North America remains the foremost region for MG deployments,

representing 69% of total installed capacity. Asia Pacific and Europe are also the promising regions, with 19% and 12% shares of total capacity, respectively [98]. Insistent smart grid deployment, emission reduction, and renewable source targets are fueling the demand for these technologies in both Europe and North America.

Navigant Research noted that the increase in MG capacity was boosted by 60 new projects. These were mostly small installations, with the exception of a 2.2 GW MG installed at the Saudi Aramco gas-oil separation plant in Shaybah, Saudi Arabia, by Schweitzer Engineering Laboratories. That project—which is technically eight interconnected MGs—is the largest single entry in Navigant’s Tracker. Asian Pacific nations led all regions in MG deployments, with 8.4 GW of total capacity, though North America kept pace, with a total 6.97 GW. Navigant Research mentioned that while Asia Pacific and North America still account for more than three-quarters of all MG capacity in the Tracker, a major shift that happened lately is the Middle East and Africa jumping to third place among all regions with more than 3 GW of total capacity. And, recently Europe showed an unusual drop in capacity, with a total of 1.8 GW, due to a number of project updates where totals were adjusted downward to correctly represent their current status.

Consequently, the Navigant Research group mentioned that while it has tracked the MG market since 2009, the MG deployment process is still rapidly taking hold worldwide. Also, the Navigant Research group noted that the MG market breaks into the following segments (with % of total power capacity as of the first quarter of 2016): Remote (54%), Utility Distribution (13%), Community (13%), Institutional/Campus (9%), Military (6%) and Commercial/Industrial (5%) as shown in Figure 2.2 [99].

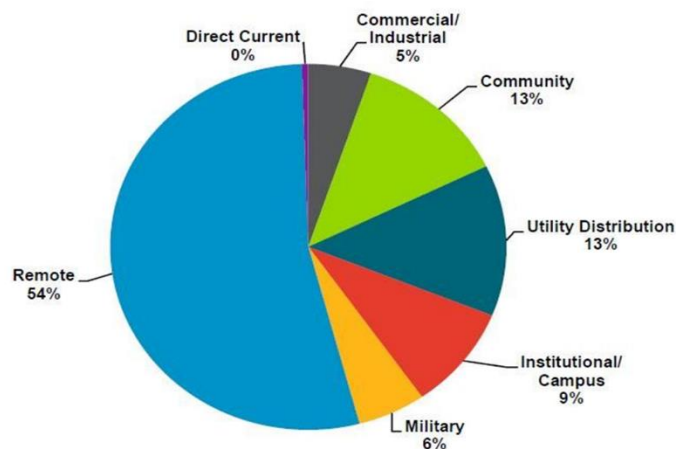


Figure 2.2: Total MG Power Capacity Market Share by Segment, World Markets: 1Q 2016 [99]

2.4.1 Microgrid Implementation in Ohio, United States

The pioneer and most well-known U.S. MG research, development and demonstration (RD&D) effort established in 1999 has been pursued under the Consortium for Electric Reliability Technology Solutions (CERTS). The CERTS MG was constructed at a site owned and operated by American Electric Power (AEP) near Columbus, Ohio. This test-bed, as shown in Figure 2.3, is a 480 V system, connected to the 13.8 kV distribution-voltage system through a transformer at the Point of Common Coupling (PCC). It has two main autonomous components, DG sources and thyristor based static switches [100].

The test-bed has three feeders, two of which have converter based DG units driven by natural gas. One feeder has two 60 kW sources and another feeder has one 60 kW source which can be connected or islanded. The third feeder stays connected to the utility but can receive power from the micro sources when the static switch is closed without injecting power into the utility. Two feeder branch circuits consist of sensitive loads and the third branch circuit has traditional non-sensitive loads. The objective of the test-bed is to demonstrate the system dynamics of each component of the CERTS MG.

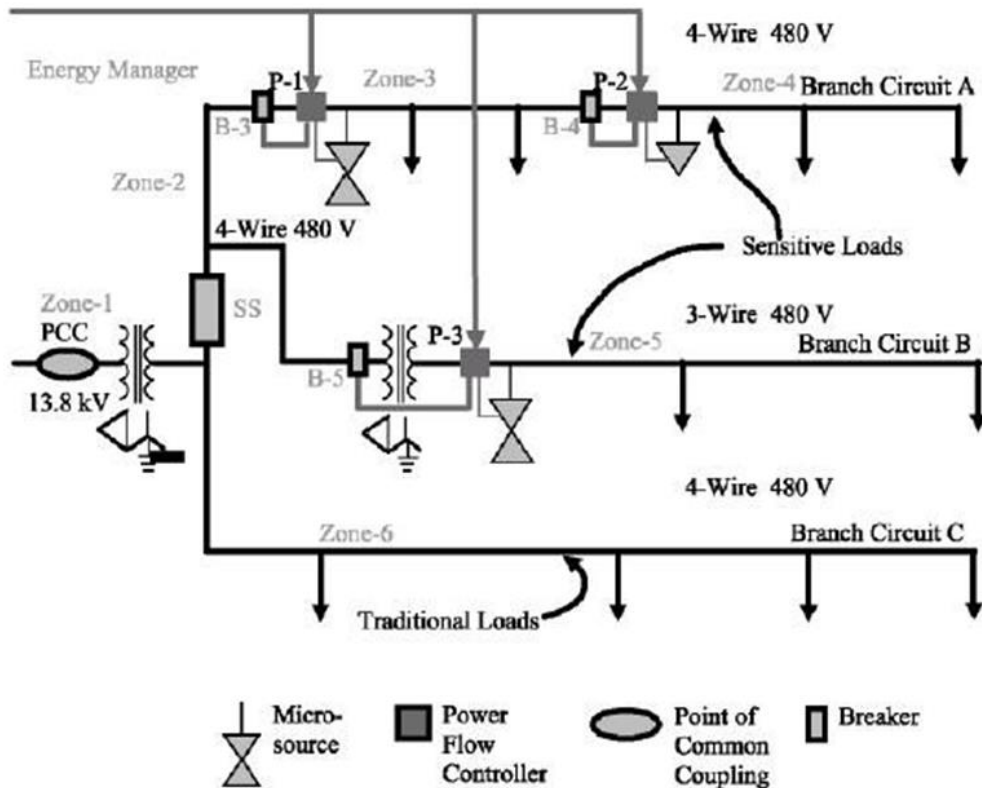


Figure 2.3: CERTS MG Test-Bed [100]

2.4.2 Microgrid Implementation in Canada Boston Bar – BC Hydro

The MG RD&D activities in Canada are focused on development of control and protection strategies for autonomous MG operation at medium voltages. Two of the major utility companies in Canada, BC Hydro and Hydro Quebec, have implemented MG intentional islanding applications. The main objective of planned islanding projects is to reduce sustained power-outage durations and to enhance customer-based power supply reliability on rural feeders by utilizing an appropriately located Independent Power Producer (IPP). Boston Bar town a part of the BC Hydro rural areas is supplied by three 25-kV medium-voltage distribution feeders connected to the BC Hydro high voltage system through 60 km of 69 kV line. The Boston Bar IPP MG comprises of two 4.32 MVA run-of-river hydro power generators and is connected to one of the three feeders with a peak load of 3.0 MW, as shown in Figure 2.4 [101].

Remote auto-synchronization capability was also added at the substation level to synchronize and connect the island area to the 69 kV feeder without causing load interruption. When a sustain power outage event, such as a permanent fault or line breakdown, occurs on the utility side of the substation, the main circuit breaker and feeder reclosers are opened. Then the substation breaker open position is telemetered via leased telephone line used for communication between the generators remote control site and the Utility Area Control Centre (UAAC) to the IPP operator [102].

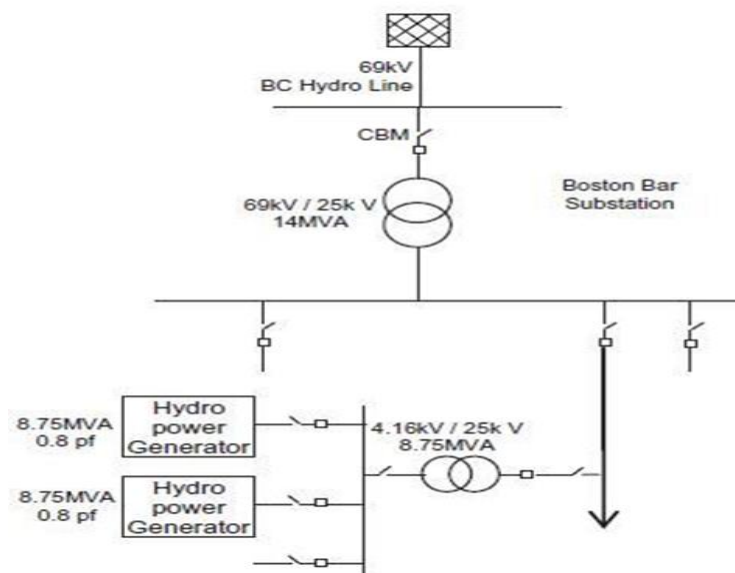


Figure 2.4: System configuration for the Boston Bar IPP and BC Hydro planned islanding site [101]

2.4.3 Microgrid Implementation in Greece

Within the frame of the European MGs projects several set-ups have been installed at different laboratories. The first European Union project funded by the EU was the “Microgrids Project” and it was undertaken by a consortium led by National Technical University of Athens (NTUA). The MGs project investigated a MG Central Controller (MCC) that promotes technical and economical operation, interfaces with loads and micro sources and demand-side management and provides set points or supervises local control to interruptible loads and micro sources [103]. A pilot installation was installed in Kythnos Island, Greece, that evaluated a variety of DER to create a MG. Another project at NTUA is a laboratory-scale MG implementation as detailed below.

2.4.3.1 Microgrid Implementation in Kythnos Island, Greece

There is one field demonstration of stand-alone DG in Greece which possesses some features of MG, and it would be connected to the main grid in the near future. The system provides electricity to 12 houses in a small valley in Kythnos, an island in the cluster of Cyclades situated in the Aegean Sea. Figure 2.5 shows the mini-grid layout for the settlement that is situated about 4 km from the medium voltage grid line of the island [104]. The Kythnos mini-grid consists of 10 kW solar PV capacity distributed in five smaller sub systems, a battery bank of 53 kWh capacity and a diesel generator of 5 kVA nominal output power and three 4.5 kVA each battery inverters to form the grid. Each house has an energy meter with 6A fuse, as per the norms of the local electric utility public power corporation. Specially developed load controllers are installed at every house.

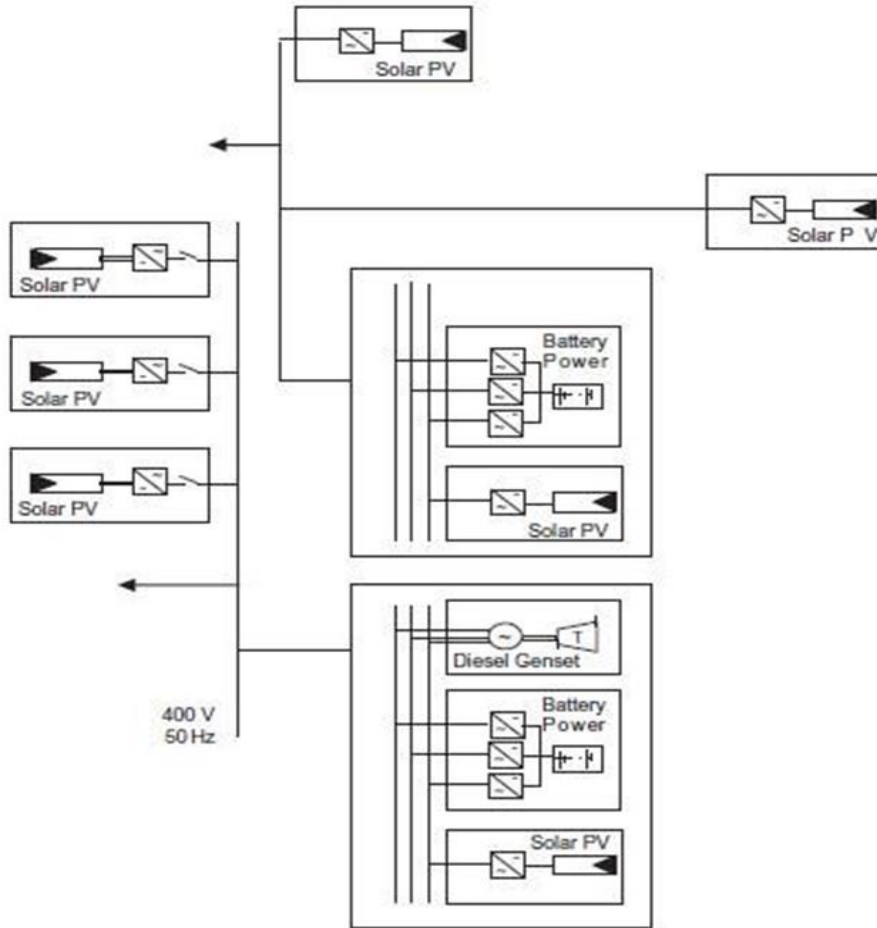


Figure 2.5: The Kythnos Island MG – Greece [104]

2.4.3.2 Laboratory-Scale MG Implementation at NTUA – Greece

At the international level, the European Union has supported second major research efforts devoted exclusively to MGs named “More MG Projects”. This project was executed to study alternative methods, strategies along with universalization and plug-and-play concepts. The demonstration site is an ecological estate in Mannheim–Wallstadt, Germany [103]. Continuing MG projects in Greece include a laboratory facility that has been set up at the National Technical University of Athens (NTUA), a specially designed 1-phase system of the NTUA with agent control software with the objective to test small-scale equipment and control strategies for MG operation. NTUA MG test system (shown in Figure 2.6) consist of one wind turbine, two PV generators, storage in battery energy and controllable loads. The battery is connected via a bi-directional Pulse Width Modulation

(PWM) voltage source converter, which regulates the voltage and frequency when the system operates in the island mode. The battery inverter operates in voltage control mode (regulating the magnitude and phase/frequency of its output voltage) [104]. When the MG operates in parallel to the grid, the inverter follows the grid. Multi-agent technology built on the Java Agent Development Framework (JADE) 3.0 platform has been implemented for the operation and control planning of the sources and the loads. The project has been successfully completed providing several innovative technical solutions.

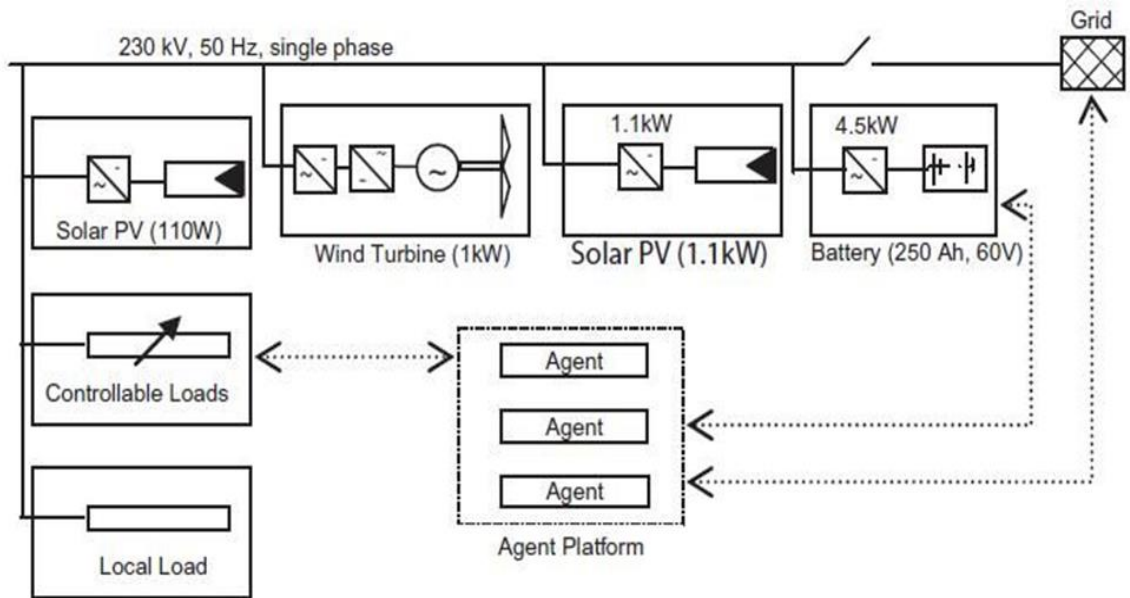


Figure 2.6: The Laboratory MG Facility at NTUA [104]

2.4.4 Microgrid Implementation in Bronsbergen Holiday Park, Netherlands

In the Netherlands one of the “More Microgrids Projects” is located at Bronsbergen Holiday Park, located near Zutphen. The park is electrified by a traditional three-phase 400 V network, which is connected to a 10 kV medium-voltage network via a distribution transformer located on the premises, as shown in Figure 2.7. The distribution transformer does not feed any low-voltage loads outside of the holiday park. Internally in the park, the 400 V supply from the distribution transformer is distributed over four cables, each protected by 200 A fuses on the three phases. It comprises 210 cottages, 108 of which are equipped with grid-connected PV systems of 315 kW catering a peak load of about 90 kW. The objective of this project is experimental validation of islanded MG by means of smart

storage coupled by a flexible AC distribution system including evaluation of islanded operation, automatic isolation and reconnection, fault level of the MG, harmonic voltage distortion, energy management and lifetime optimization of the storage system, and parallel operation of converters [105].

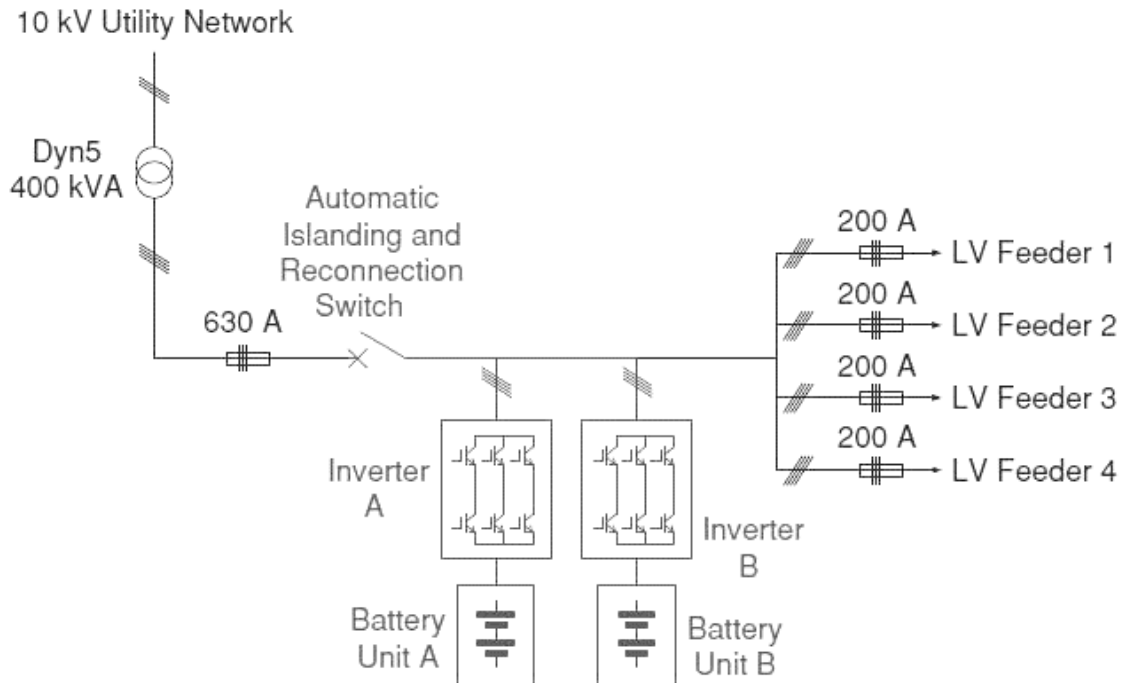


Figure 2.7: Schematic for the Bronsbergen Holiday Park MG – Netherlands [105]

2.4.5 Microgrid Implementation in DeMoTec – Germany

A comprehensive study on MG control methods has been performed in Institut für Solare Energieversorgungstechnik (ISET), Germany. The DeMoTec MG at ISET, which is a general test site for DER has a total available generation capacity of 200 kW comprising of a PV generator, a wind generator, two battery units, and two diesel generators. A number of loads with different priority levels and several automatic switches are there for sectionalizing the MG into up to 3 low voltage island grids. A central crossbar switch cabinet connects all generators and loads to a local grid. Figure 2.8 presents the diagram of the DeMoTec test MG.

To enable a monitoring and control of the generators and of the operating states of the system a Supervisory Control and Data Acquisition System (SCADA) is deployed. The

communication is done via a separate Ethernet communication line and XML-RPC communication protocol is used [106]. The DeMoTec promotes design, development and presentation of systems for the utilization of renewable energies and the rational use of energy. A DeMoTec master display is being used to monitor the operations of a widely dispersed wind power plant system, which comprises about 80 representatively, selected systems throughout Germany. In this master display, moreover, the remote monitoring of remote isolated systems in Greece and Spain as well as the control of active low-voltage grids can also be demonstrated [107].

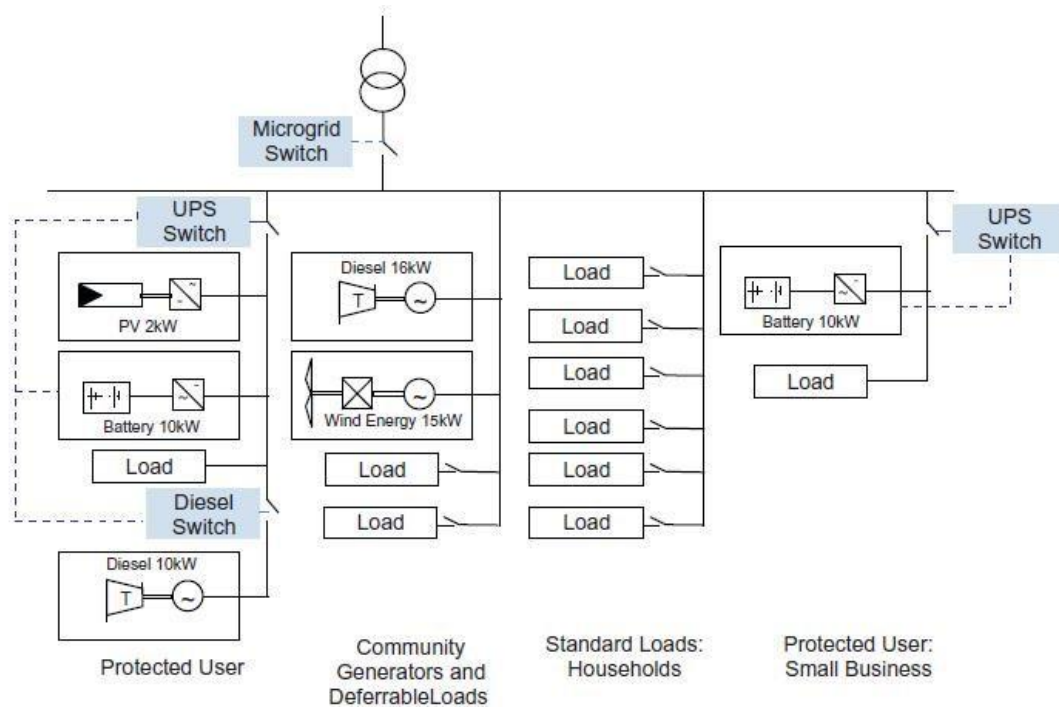


Figure 2.8: DeMoTec MG Test System [107]

2.4.6 Residential MG Implementation in Am Steinweg, Stutensee - Germany

One of the first pilot projects on MG with renewable energy in a residential neighborhood was carried out in the neighborhood Am Steinweg in Stutensee, a German village located about fifteen minutes north of the Karlsruhe.

This is a 3-phase low voltage grid with a neutral conductor, which is linked in one place by a 400 kVA transformer to the medium-voltage grid and has a circular structure. The energy sources in this micro grid are a CHP (with an optional electrical power of 28 kW),

different PV installations (with a nominal power of 35 kWp) and a lead-free battery bank (880 Ah) with a bi-directional inverter. This inverter is designed for a power exchange of 100 kW. The batteries can deliver this power for half an hour. In total, 101 apartments are linked to this grid. The maximum active power through the transformer is determined as 150 kW. Figure 2.9 shows the structure of the MG, with the division of loads and sources [104].

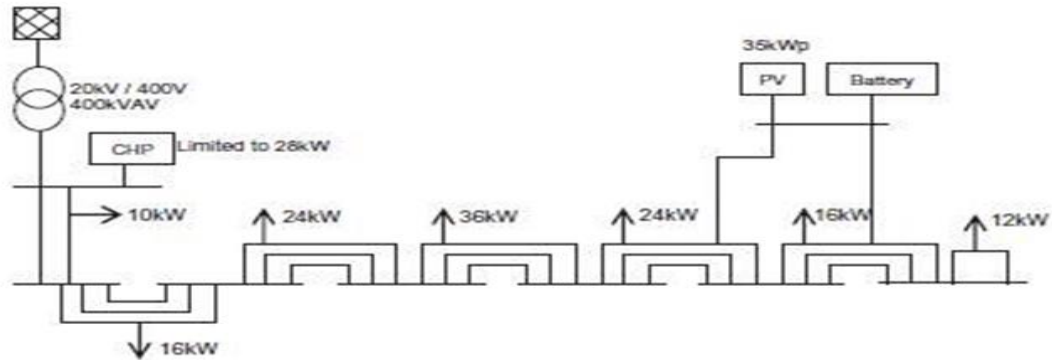


Figure 2.9: The Residential MG of Am Steinweg in Stutensee – Germany [104]

2.4.7 Microgrid Implementation in Cesi Ricerca – Italy

The Cesi Ricerca DER test MG (Italy) is a low voltage (LV) MG, connected to the medium voltage (MV) grid by means of 800 kVA transformer. It is constituted by several generators with different technologies (renewable and conventional), controllable loads and storage systems. This MG can provide electricity to the main grid with a maximum power of 350 kW. Figure 2.10 presents the network configuration of Cesi Ricerca DER test MG [104].

It comprises of the following distributed energy resources and the storage systems:

- A hybrid energy system consisting of a photovoltaic plant (10 kW), a lead-acid storage, a diesel engine coupled with an asynchronous generator (7 kVA), a simulated (8 kVA) asynchronous wind generator
- Five PV fields of different technologies for a total nominal power of 14 kW
- A solar thermal plant with a parabolic dish and a Stirling engine (10 kW)
- An ORC CHP system fuelled by biomass (10 kW, 90 kW)
- A CCHP plant with a gas microturbine (105 kW, 170 kW, 100 kW)

- A Vanadium Redox Battery (42 kW, 2 hours)
- A Lead Acid battery system (100 kW, 1 hour)
- Two high temperature Zebra batteries (64 kW, 30 minutes)
- A high speed flywheel for Power Quality (100 kW, 30 seconds)
- A controllable 3-phase resistive-inductive load (100 kW + 70 kVAR)
- A capacitive load and several RL loads with local control (150 kVAR)

2.4.8 Microgrid Implementation in the University of Manchester, UK

The hardware topology used in the University of Manchester Microgrid/Flywheel energy storage laboratory prototype is shown in Figure 2.11. The overall MG test system is nominally rated at 20 kVA, although the flywheel and power electronics are rated much higher 100 kW connected with 0.4 kV mains supply of the laboratory considered as the main grid. A synchronous generator and an induction motor coupled together acts as the micro-source. A three-phase balanced load of 12 kW is connected at the end of the feeder. Control systems for real-time control of the MG hardware, using the Simulink/dSPACE control environment has been developed in 2005. The test-rig has been designed to allow the investigation of power electronic interfaces for generation, loads or energy storage. The AC/DC inverter labelled ‘flywheel inverter’ can be configured in software to allow the interfacing of the flywheel storage system to the remaining MG unit. The MG may be operated in islanded operation. Breaker 1 is opened to emulate a loss of mains condition as shown in the Figure 1.11. Breaker 2 is under the control of the MG controller system. Thus the onset of islanding, and resynchronization to mains, as well as mains connected operation may be tested [104].

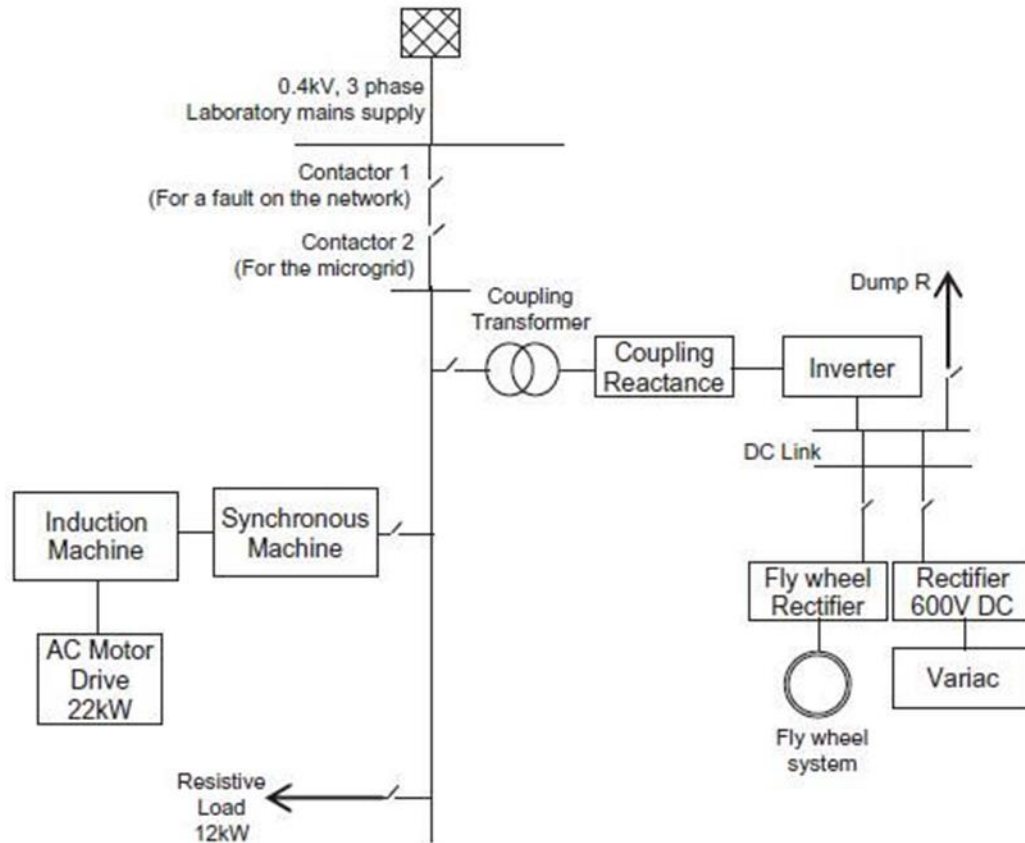


Figure 2.11: University of Manchester MG/flywheel energy storage laboratory prototype [104]

2.5 Description of a MG

Around the world, governments and industries are moving towards use of cleaner energy sources and hence reduce the overall environmental pollution. This has led to an increase in attention towards Distributed Generation (DG) using non-conventional and renewable energy sources, which are connected locally at the distribution system level. However, adverse impact on the grid structure and its operation, with increased penetration of DGs, is unavoidable. To reduce the impact of DGs and make conventional grids more suitable for their large-scale deployment, the concept of MGs is proposed [105].

2.5.1 Definition of MG

A MG is an interconnection of DGs - either a set of dispatchable generating units (such as gas turbines and fuel cells) or non-dispatchable generators (such as wind turbines and

solar PV units), - integrated with electrical and thermal energy storage devices. It operates to meet the customers' local energy needs, operating as a single system and on a small-scale, on low-voltage distribution systems providing both power and heat. To ensure that the MG is operated as a single aggregated system and meets power quality, reliability and security standards, power electronic interfaces and controls need to be applied [108], [2]. This control flexibility allows the MG to present itself to the main utility power system as a single controlled unit.

The MG serves a variety of customers, e.g. residential buildings, commercial entities and industrial parks, with the particularity that some loads (or all of them) may be controllable. A typical MG structure including loads and DER units is depicted in Figure 2.12.

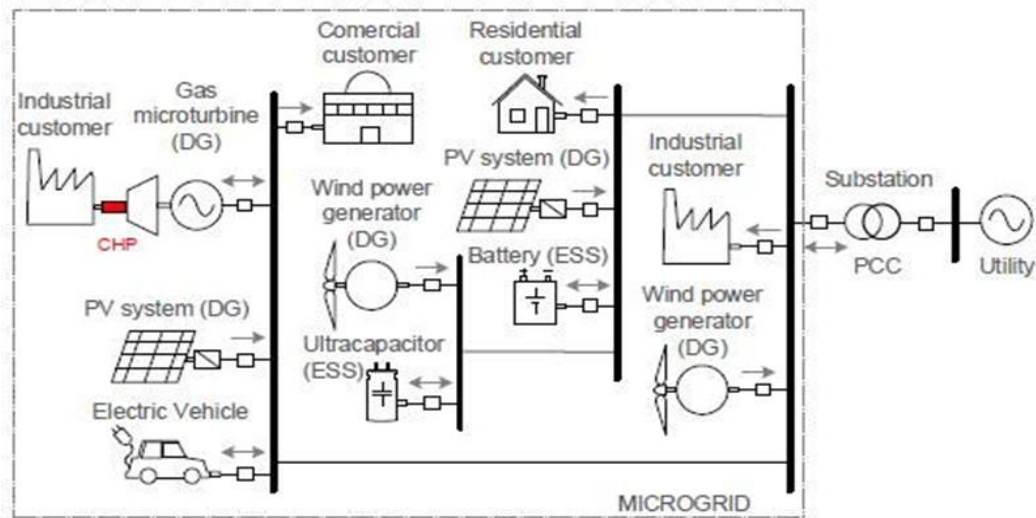


Figure 2.12: A typical MG structure integrating DERs and loads [68]

A MG is generally located downstream of the distribution substation. The electrical connection point of the MG to the utility grid constitutes the point of common coupling (PCC). The internal coordination of groups of final consumers and DERs confined within the MG could be done independently from the distribution grid, so that the distribution system operator (DSO) may only consider the power exchange with the MG at the PCC. This allows to greatly reduce the number of nodes under control by the DSO. This allows simplifying the decision making and the top-level communication infrastructure. The operation of MGs responds to multiple economic, technical and

environmental aims, by implementing smart energy management systems (EMS) and novel operation techniques based on ICTs.

The MG normally operates in a grid-connected mode through the substation transformer. However, it is also expected to provide sufficient generation and storage capacity, controls, and operational strategies to supply at least a portion of the load after being disconnected from the distribution system at the PCC and remain operational (after a smooth transition) as an autonomous (islanded) entity. This islanding capability reduces outages and allows to improve service and power quality, therefore providing high reliability [109].

From the utility point of view, application of micro-sources can potentially reduce the demand for distribution and transmission facilities. Clearly, distributed generation located close to loads within the MGs can reduce power flows in transmission and distribution circuits with the consequent loss reduction, also providing support to the utility network in times of stress by relieving congestion and aiding restoration after fault clearance [68].

To summarize, the basic concept of a MG is to aggregate and integrate DERs ideally near the end-users (loads) in order to provide them with an electric power system characterized by the following functional and operational conditions:

- Efficient power production to meet the consumer's electricity demand.
- Energy management from supply and demand-side to achieve basic operation requirements such as power balance, voltage control, power quality, flexibility and electrical safety, through the implementation of proper control techniques.
- Plug and play functionality, constituting a flexible system where new loads, DERs and other devices can be simply implemented.
- Islanding capability, ensuring a safe, reliable, and prime quality energy supply.

2.5.2 Distributed generators

According to the Institute of Electrical and Electronics Engineers (IEEE), DG is the generation of electricity by facilities sufficiently smaller than central generating plants as to allow interconnection at nearly any point in a power system. Generally, the power of

the generator must be smaller than a few megawatt (10-50 MW) to be considered as a DG [3].

When it comes to MGs, usually smaller scale DG systems are integrated, with installed capacities in the order of tens to hundreds of kW, such as microturbines, photovoltaic arrays, fuel cells and wind turbines, among others. These units have emerged as a promising option to meet growing customer needs for electric power, providing different economic, environmental and technical benefits. The presence of generation close to demand potentially reduces losses and increases reliability. The electronic interfaces used by most DG systems allow to maintain power quality and improve the overall efficiency by the application of control techniques based on energy management systems. However, intermittent DERs such as wind power generators and PV systems may also introduce power quality issues, what requires the implementation of ESS. The economic advantages of DG respond to the lower capital investment for construction of power systems, since distribution of generation units eliminates the extensive transmission systems. Finally, DG power systems provide environmental benefits as a result of offering a more efficient way of generating and distributing electricity, hence emphasizing RES deployment [68].

2.5.3 Energy storage devices

During islanded/isolated operation of MG, power generated from DG units cannot be instantly matched to load demands. A fundamental aspect of MGs island/isolated mode operation is the inclusion of ESS, which allows compensation of unbalances between generation and load to ensure quality of supply. ESS must be able to provide the amount of power required to balance the system disturbances and/or significant load changes. ESS implementation also mitigates the intermittency of RES, such as solar and wind energy, and it allows these distributed generators (together with the ESS) to operate as dispatchable units in order to provide additional power on request. In addition, ESS provides the energy requirements for seamless transition between grid-connected and islanded autonomous operation modes. During grid-connected mode, ESS allows to conveniently establish the optimal periods to interchange power with the distribution grid.

Therefore, power and energy requirements of MGs are supported by ESS, thus raising the overall performance [110].

The storage options include batteries, flywheels, super (or ultra) capacitors, superconducting magnetic energy storage (SMES), compressed air, pumped hydroelectric and thermal energy storage. Electric vehicles (EV) are also seen as an alternative mobile option of energy storage in order to store energy in their batteries when the demand and cost of electricity low, which may be used later during high demand periods [111].

2.5.4 MG loads

A MG can serve electrical and/or thermal loads, although only electrical loads will be treated in this section. Electrical loads can be classified as critical and non-critical (or non-sensitive). Critical loads are those in which the electrical power must be maintained with a high quality and reliability, and thus cannot be interrupted. On the other hand, non-critical loads refer to those loads that can be disconnected from the energy supply for determined periods of time in order to maintain the MG operating conditions. The load management behavior of the MG mainly depends on the mode of operation and system requirements/market incentives, applying different strategies whether the MG operates in grid-connected or islanded modes.

In a grid-connected mode, the utility distribution system can compensate any power discrepancy between demand/generated power within the MG to maintain the net power balance. Any difference could be also mitigated by load or generation shedding, when operational strategies or contractual obligations impose hard limits to the net import/export power. Load shedding is often required to maintain the power balance and consequently stabilize the MG voltage amplitude/angle during an autonomous mode of operation. In this sense, critical loads receive service priority through the implementation of a convenient operation strategy. Load control can also be executed to reduce the peak load and to smoothen load profiles in order to optimize the performance of ESS units and dispatchable DG units [109].

2.5.5 MG control

Advanced control strategies are vital for the realization of MG. In this sense, two different control approaches can be identified: centralized and decentralized. The implementation of a fully centralized control architecture becomes infeasible due to extensive communication and computation needs for the large number of controllable resources and rigorous performance and reliability requirements of MGs. On the other hand, a fully decentralized approach results nonviable due to the strong coupling between units in the MG, what demands a minimum coordination that results impracticable by using only local variables. A compromise solution can be developed by applying a hierarchical control structure, consisting of three levels: primary, secondary, and tertiary [112].

The primary control deals with the inner control of the DG units, in order to keep the system stable using safe and fast control algorithms. Based on local measurements, primary control executes power sharing (and balance), islanding detection, and output control without using any critical communication link, which accomplishes the plug and play capability. In synchronous generators, the voltage regulator, governor and the machine inertia itself perform power sharing and output control. Voltage Source Inverters (VSIs) used in electronic interfaces of DG require controllers to emulate the behavior of synchronous generators, which are composed of two stages: DG power sharing controller and inverter output controller. The latter is generally accomplished by an outer loop for voltage control and an inner loop for current settlement. Power sharing is performed by active power-frequency and reactive power-voltage droop controls simulating droop characteristics of synchronous machines [112].

The existence of line impedances drives load fluctuations to deteriorate the regulation of the MG voltage and frequency under droop control. Secondary control ensures that frequency and voltage deviations are restored towards zero after every change of generation or load inside the MG. Also referred to as the MG EMS, the secondary control is responsible for the secure, reliable and economical operation of MGs in both grid-connected and islanded mode. This control level can be implemented in two different ways: centralized and decentralized. In general, centralized approaches are more suitable for isolated MGs with critical demand-supply balances and a fixed infrastructure, while

decentralized approaches are associated to grid-connected MGs with multiple owners and a variable number of DER units. Secondary control operates on a slower time frame as compared to primary control, determining the optimal (or near optimal) dispatch and unit commitment (UC) of DER units by three main methods: real-time optimization, expert systems, and decentralized hierarchical control [112].

Finally, the tertiary control regulates the power flow between the bulk power system and the MG at the PCC, while defines the long term optimal set points depending on the requirements of the main grid, also coordinating the clusters of MGs. This control level typically operates in the order of several minutes. Tertiary control can also be considered part of the main power grid.

2.6 MICROGRIDS ARCHITECTURES

Thomas Edison built the first DC electricity supply system in September 1882 in New York City. Edison stood up for DC distribution system, while George Westinghouse and Nikola Tesla promoted the AC system. Since late 19th century, AC has been the standard choice for commercial energy systems, based mainly on the ease to transform AC voltage into different levels, the capability to transmit power over long distances and its inherent characteristic from the fossil energy-driven rotating machines with their synchronous generators.

However, DC distribution grids have shown a resurgence in recent years due to the development and deployment of RES based on DC power sources, and the rapid growth of DC loads which constitute today (together with AC loads with power electronic converters) the vast majority of loads in most power systems. DC distribution presents several advantages, such as reduction of the power losses and voltage drops, and an increase of capacity of power lines, mainly due to the lack of reactive power flows, absence of voltage drops in lines reactance and non-existence of skin and proximity effects then reducing ohmic resistance of lines. According to this, its planning, implementation and operation is simpler and less expensive [4].

In this context, MG involve both AC and DC components, and that they can be operated based on the principles of the AC power systems (i.e. AC MG) or DC power systems (i.e.

DC MG), or a combination of both, through different architectures. MG architectures are mainly determined by the nature of the loads, the existing and planned distributed generators, the difficulties to build new electrical lines, the existing communications, the space to place energy storage devices and their specific power and energy requirements, among others. According to the literature, MG architectures can be divided into three main categories, namely: AC MG, DC MG and Hybrid AC/DC MG.

2.6.1 AC MG

Inspired on traditional electric power systems, AC distribution is the most popular and commonly used structure for MG studies and implementations. By utilizing the existing AC network infrastructure (distribution, transformers, protections, etc.), AC MG are easier to design and implement and are built on proven and thus reliable technology. The first MG developed by the Consortium for Electric Reliability Technology Solutions (CERTS) was formulated in 1998 as a cluster of microgenerators and storage with the ability to isolate itself from the utility seamlessly without interruption to the loads [113]. Based on the CERTS MG concept, an example of the AC MG architecture is shown in Figure 2.13.

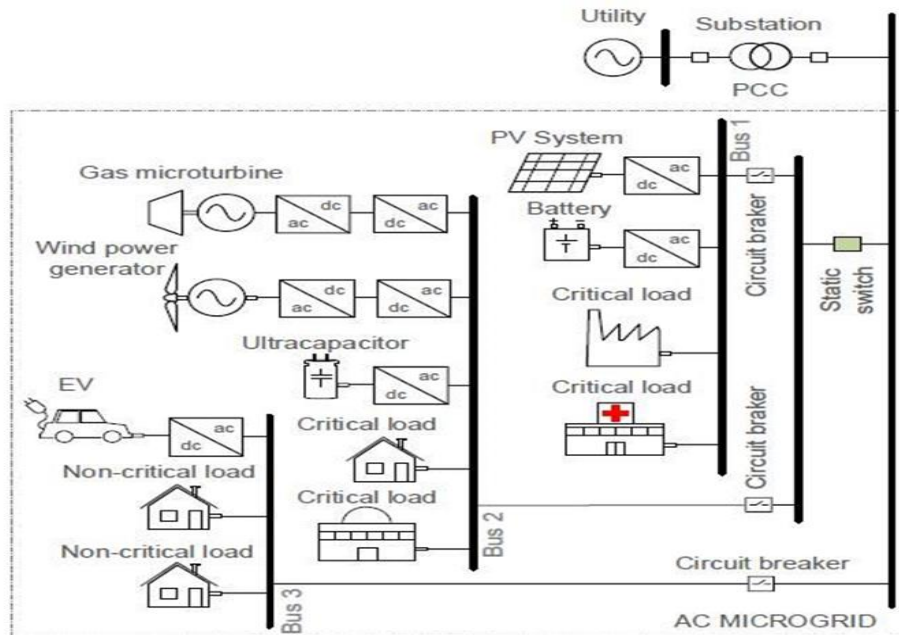


Figure 2.13: AC MG architecture with critical and non-critical loads [114]

In the example, the MG has three AC feeders; two of them containing critical loads, DG and ESS, and the other one grouping non-critical loads. The MG is able to adapt generation and demand to any operating conditions by changing its topology through the circuit breakers. The connection of the MG to the distribution grid is managed by the static switch. This device can be operated to disconnect the MG when the quality of the electrical distribution grid is poor, leaving it in islanded operation mode. This maintains a high quality and reliable supply to the critical loads, which are fed both from the distributed generators and the energy stored in ESS devices. During a grid fault, the static switch is opened, as well as the circuit breaker of the third bus, in order to disconnect the non-critical loads from the grid to avoid their damage or malfunction [3].

In the AC MG architecture operated in grid-connected mode, the power flows directly from/to the grid, avoiding any series-connected converter, what provides high reliability. The feeders have the same voltage and frequency conditions as the grid, so that the loads, generators and energy storage devices must be grid-compliant. In fact, one of the main advantages of AC MG' architecture is their compatibility with the existing electrical grid, which can be reconfigured to an AC MG scheme. One of the main drawbacks is the large amount of complex power electronics interfaces required (inverters and back-to-back converters) to synchronize DERs with the AC utility grid, and to provide high-quality AC currents without harmonics. The efficiency and reliability of the overall MG can be reduced, since complex electronic power converters present lower reliability than those with less components. Generally, an AC distribution system has more conversion steps than a DC system [4].

2.6.2 DC MG

Most DER operate either natively at DC or have an intermediate DC link on their power electronic interface, whereas the end-point connection of ESS such as supercapacitors, batteries, SMES, and fuel cells is exclusively DC. On the other hand, many of today's consumer loads are DC supplied. According to some studies nearly 30% of the generated AC power passes through a power electronic converter before it is utilized, with an amount of lost energy in wasteful conversions within the range of 10-25% [115].

Therefore, integrating these devices into DC MG through DC/DC converters becomes a smart choice not only in terms of increasing efficiency due to the reduction of conversion stages but also for achieving power quality with independence from the distribution grid.

An example of DC MG architecture is illustrated in Figure 2.14 [3]. The main power electronic converter of this architecture is an AC/DC interface usually named as interlinking converter (IC), which connects the DC MG to the AC grid at the PCC, after the voltage shift and galvanic isolation provided by the transformer. This converter must be bidirectional to allow power exchange in both ways. Every DG and ESS device of the MG is linked to a DC bus with a determined voltage, most of them do it through a power electronic interface (DC/DC or AC/DC). The voltage regulation of the DC bus is done by the IC, providing a very high quality to the MG no matter the quality of the main grid.

Compared to AC MGs, DC MGs have a simpler structure, lower system costs and an overall improved efficiency. Grid synchronization of DERs, harmonics and reactive power flows are not the concern of this architecture, what simplify its structure and control requirements. There are lower losses in DC distribution lines as compared to the AC distribution system, due to the absence of a reactive current component. Moreover, DC MGs have fault-ride-through capability and are not affected by blackouts or voltage sags occurred in the utility grid, due to the stored energy of the DC capacitors and the voltage control of the IC. On the other hand, DC MGs have some drawbacks such as the need to build DC distribution lines and the incompatibility with actual power systems. Also, the protection scheme for DC systems faces different challenges, mainly the immaturity of standards and guidelines and a limited practical experience. Special protection devices are needed for DC short-circuit currents interruption since there is no zero point crossing of current wave. Another disadvantage of the DC architecture is that AC loads can't be directly connected to the MG and the voltage of DC loads is not standardized, so additional converters would be required. Nevertheless, the main weakness of this architecture is the series-connected IC handling the whole power flow from/to the distribution grid, since it reduces the reliability [116].

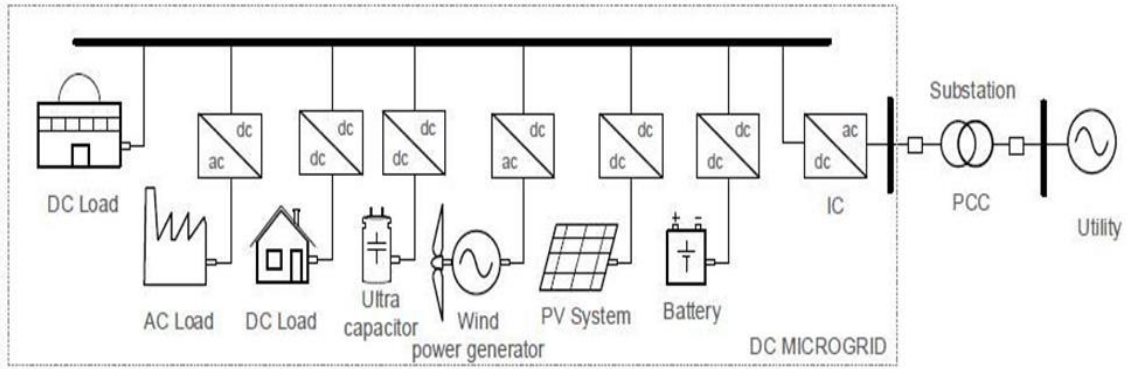


Figure 2.14: DC MG architecture [3]

2.6.3 Hybrid AC/DC MG

Combining the advantages of AC and DC architectures, hybrid AC/DC MGs are gaining interest over the rest of the architectures, mainly because of the integration of two networks together in the same distribution grid, aiding the direct and efficient integration of both AC- and DC-based DERs and loads.

A typical hybrid MG structure is shown in Figure 2.15, where the AC and DC grids can be distinguished, linked through the main AC/DC bidirectional converter [3]. AC loads are connected to the AC bus whereas DC loads are connected to the DC bus, using a power converter to adapt the voltage level when necessary. DG and ESS units can be connected either to the AC or DC buses, always trying to minimize the conversion steps. The AC bus allows using the existing equipment; while the DC bus allows the use of a reduced number of simpler converters. Moreover, this architecture allows the installation of sensible loads in the DC feeder, in combination with more robust loads installed in the AC feeder [3], [117].

When dealing with integration issues, the hybrid AC/DC MG architecture simplifies the electronic interfaces. It also reduces the conversion stages and therefore the energy losses. The inclusion of every DC device on the DC bus, makes it easier to control harmonic injections into the AC side through the main converter, thus guaranteeing high-quality AC in the utility grid. With regard to the transformation of voltage levels, it can be performed in a simple manner in the AC-side by the use of conventional transformers, while in the DC-side this conversion is performed by electronic DC/DC converters.

A hybrid MG can be developed over an existing distribution grid, introducing a main AC/DC converter and a communication network for the connected devices. Although this makes the overall cost higher compared to AC MG due to this main power converter, the investment will be returned faster if the number of attached devices increases, as the number of total interface converters is reduced.

On the other hand, this architecture presents various weaknesses that need to be further investigated. When dealing with protection issues, AC equipment has reliable and widely studied technologies, while DC-side of the MG still needs further research and developments on this aspect. Furthermore, due to the main interface power converter, the reliability of the hybrid architecture is lower than that of the AC MG. Management is also more complex in a hybrid MG than in AC or DC MG, since stable and reliable power supply has to be ensured for both AC and DC buses through the application of appropriate control strategies for the connected devices. The major challenge of this architecture control is related to power balance when power exchange between the two networks (AC and DC) is required, what is still under study.

According to the main interface device and the interconnection to the utility grid, hybrid MGs can be classified in two main groups namely coupled and decoupled AC configurations. At coupled AC topologies the AC bus of the MG is directly connected to the grid via a transformer and an AC/DC converter is used for the DC link. Instead, decoupled AC configurations are composed at least by an AC/DC and DC/AC stage; establishing no direct connection between the utility grid and the AC bus of the MG. By comparing different MG architectures, pros and cons are given in Table 2.1.

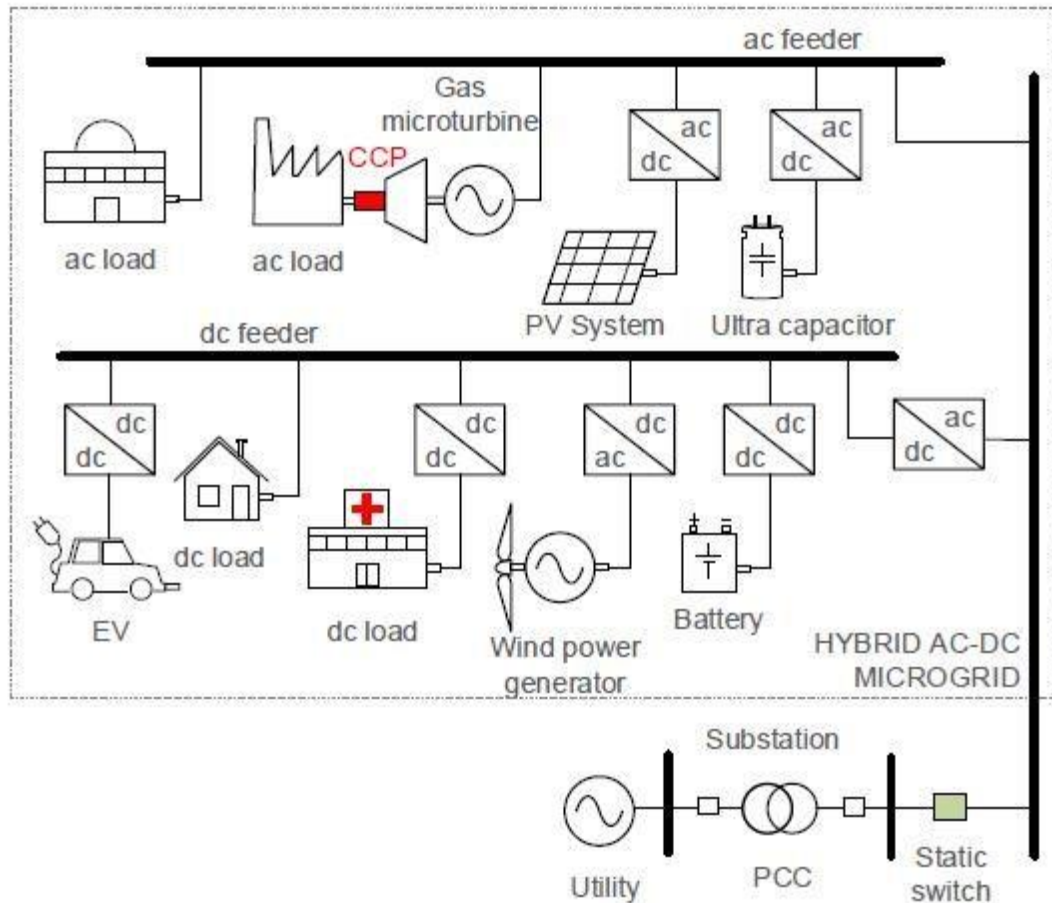


Figure 2.15: Hybrid AC/DC MG architecture [114]

2.7 Conclusion

Microgrids (MGs) are envisioned as an attractive solution towards the integration of DG units in the utility grid, associated to a reduction on fossil fuel dependency, an increment in the efficiency of the overall electric grid and a substantial improvement of the service quality and reliability seen by end customers. In this context, different MG architectures were presented, encompassed into three main categories: AC, DC, and hybrid AC/DC. The AC MG is the most robust architecture due to the direct connection of loads to the utility in a grid-connected mode, and the fact that the whole MG is built on proven and reliable AC elements. In addition, they facilitate the implementation of the MG concept on the existing distribution networks, since they can be adapted to a MG scheme with a

few modifications on their structure and components. This is the main factor that makes AC MGs the most used architecture so far.

Reliability also relies on the energy conversion processes, and complex power electronic converters are more prone to failures than simpler ones. In this sense, hybrid AC/DC MGs present the lowest number of converters (and simpler ones), since DERs and loads can be connected to the AC or DC feeders depending on their characteristics. However, although the conversion processes of DC/AC and AC/DC are reduced compared with an individual AC or DC MG, many practical problems still exist for implementing them.

To obtain high quality power for the MG loads, a DC MG is the most suitable option since voltage of the DC bus is generated electronically, thus being independent from the main grid voltage and frequency, and their possible fluctuations. The main power converter needed to link the MG to the utility grid is nevertheless a weak point of this infrastructure, sacrificing reliability in order to enhance power quality. The integration of DC loads is simpler in this architecture, what makes it a great option to supply energy to modern electronic loads such as computers and servers. Another relevant aspect of the DC architecture is that it provides an easy management of the stored energy in ESS devices.

This new vision of power systems brought forward by the MG concept creates many new challenges that are multidisciplinary in nature. A robust and secure operation of such a complex and distributed system requires novel theoretical approaches regarding sensing, control, computational intelligence, software, and communication. The multiple software layers that the management and control of the distribution grid will require need also to be trustworthy, robust, flexible, user friendly and seamlessly integrated with the enormous databases that will be created. In summary, these issues are at the forefront of the research agenda in many disciplines and will need to be integrated to conceptualize the foundations of what is now called the smart grid.

TABLE 2.1: ADVANTAGES AND DISADVANTAGES OF AC AND DC MGS

Performance	AC MG	DC MG
Conversion efficiency	Less efficient due to more power conversion stages.	Efficient due to fewer power conversion stages.
Topology	Relatively complex, large number of converters used.	Topology is relatively simple.
Controller complicity	Difficult, transient of AC systems are more complex than DC systems.	Easier than AC MG since topology less complicated.
Power quality (PQ) issues	Relatively complex voltage, frequency, phase angle and power factor are necessary to taken care.	Only voltage issue is concerned as PQ issue for DC MG, easier to provide high quality power to customers.
Standardization	Standards for AC MG are mature since existing standards for power systems are applicable for AC MG.	Standards for DC MG are still under construction.
Integration with alternative energy resources	Difficult, more conversion levels needed to integrate with DC DGs, AC current needs synchronized when integrating with high-frequency AC DGs.	Easier to integrate with PV, fuels cells, wind turbine and etc.
Interface with main grid	Can connect to main grid via PCC.	Bidirectional converters are needed to interface with main grid.
Protection	Can utilize existing protection technique from existing AC power system.	Still under research.

Stability	Less stable, frequency need to match when synchronizing, complex controllers, more conversion levels.	More stable, only voltage need to be controlled, less conversion levels increase system robustness.
Reliability	Lower than DC counterpart since more devices are used in AC MG which leads to higher failure rate of the whole System.	High.
Cost	Relatively low cost with the same scale DC counterpart when utilizing existing devices like wires, generators and etc.	Relatively low cost comparing with the same scale AC counterpart when constructing a brand new MG.

Chapter 3. Photovoltaic Energy System: An Overview

3.1 Introduction

This chapter provides an overview of different components of a photovoltaic system and attempts to highlight recent research activities in the field of photovoltaics.

3.2 Components of PV System

The building blocks of a photovoltaic system are shown in Figure 3.1. The system is mainly composed of a matrix of PV arrays, which converts sunlight to DC power, and a power conditioning unit that converts the DC power to AC power. The generated AC power is injected into the grid and/or utilized by the local loads. In some cases, storage devices are used to improve the availability of the power generated by the PV system. In the following sub-sections, more details about different components of the PV system are presented and the recent related research activities are discussed.

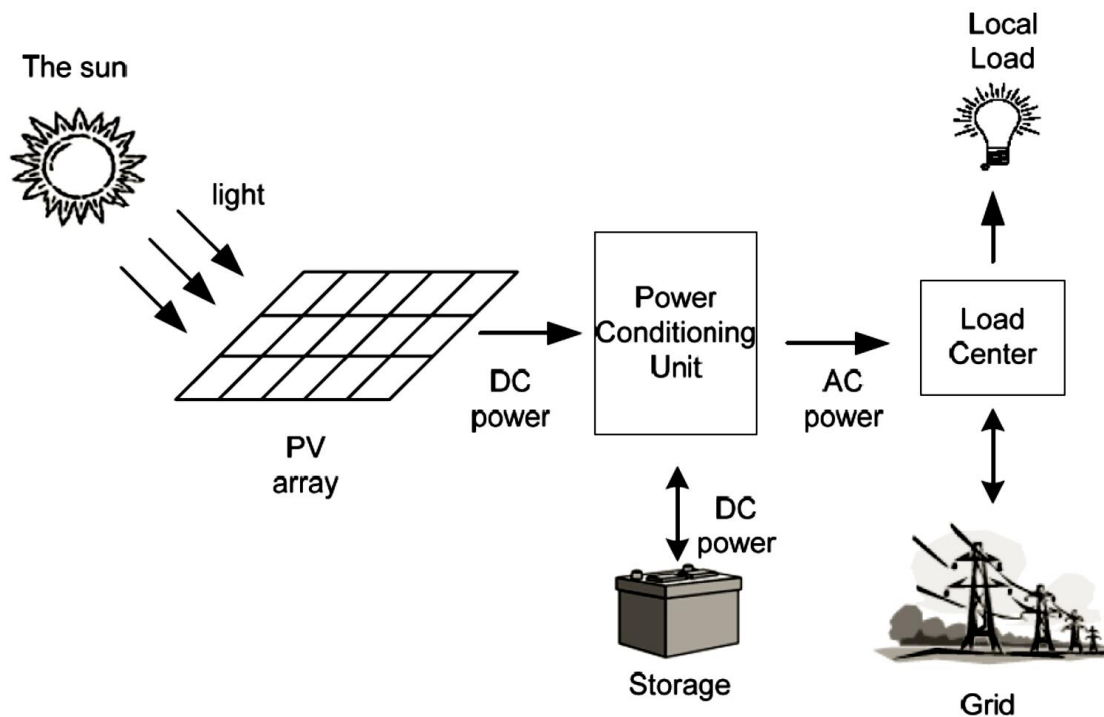


Figure 3.1: Main components of photovoltaic energy system

3.2.1 The light from the sun

Irradiance or insolation is the instantaneous solar power received on a unit surface area and is normally given in W/m^2 . The *global irradiance*, G_g , which reaches a horizontal surface on the earth, is the sum of two components [118]: 1) *direct (beam) irradiance*, G_b , that directly reaches the horizontal surface without being scattered by the atmosphere and; 2) *diffuse irradiance*, G_d , that reaches the horizontal surface after being scattered by clouds. Weather stations usually measure the global horizontal irradiance by a Pyranometer placed horizontally at the required location. On the other hand, a Pyrheliometer is used to measure the direct normal irradiance, which is the irradiance received by a surface that is perpendicular to the sun rays. Accordingly, the direct irradiance on the horizontal surface can be calculated. To measure the diffuse irradiance, a shading ball or ring can be used to permanently shade the Pyranometer. Figure 3.2 shows pictures of the three devices used to measure different irradiance components [119].



Figure 3.2: Pyranometer (left top), Two-axis tracked Pyrheliometer (left bottom), Pyranometer with shading ball (right) [119]

PV arrays are usually tilted to maximize the energy production of the system by maximizing the direct irradiance that can be received. Usually the optimum tilt angle with

respect to the horizontal surface of the earth is calculated for each specific site; however, it can be roughly set within $\pm 15^\circ$ of the site latitude [119]. Thus, the irradiance components received by the tilted surface of the PV array are different from those provided by the weather stations. Accordingly, different models must be used to estimate the different irradiance components on the surface of the PV array from those provided by the weather stations. The accuracy of these models is mainly dependent on the location under study.

Currently, one of the main research activities in this area focuses on analyzing the short-term fluctuations of irradiance due to passage of clouds. Some of these studies use frequency domain analysis to investigate the smoothing effect of extended area of the PV system on the fluctuation of irradiance [120]. Other studies use frequency domain analysis to analyze the amplitude, and persistence of these fluctuations [121].

Another research activity related to this field focuses on developing models for the different irradiance components at a certain location by using either cloud observations obtained from weather stations [122] or images obtained from satellites [123], [124]. These models are important for predicting the output energy produced from PV systems installed at these locations. Short-term prediction of solar irradiance from historical time-series data is very important for short-term planning related to the operation of electric networks in the presence of PV systems, especially in the case of large systems. Different methods, such as auto-regressive moving average (ARMA) models and neural networks have been used for this purpose [125], [126]. However, the research in this field still needs more work to become as mature and well-established as wind speed prediction. In fact, predicting the solar irradiance is a complicated task as it is affected by many factors such as types of clouds, cloud heights, wind speed, and wind direction.

3.2.2 PV arrays: technology and modeling

The first silicon solar cell with an efficiency of 6% was developed at Bell Telephone Laboratories in 1954 by Chapin et al. [127]. Nowadays, a typical efficiency of 22.7% can be reached and different types of materials are used in manufacturing these cells. However, the most widely used cells are polycrystal silicon cells (54.5% of the world's market share) and single crystal silicon cells (29.36% of the world's market share) [128]. Normally, the

electric characteristics of a PV cell are displayed as a relation between the cell voltage and current, and a relation between the cell voltage and power. Accordingly, several electric quantities that are important to the operation of the PV system are identified. These electric quantities include: the cell voltage under open circuit conditions, V_{OC} , the cell current under short circuit conditions, I_{SC} , and the cell voltage, current and power at the maximum power point, V_{MPP} , I_{MPP} , and, P_{MPP} , respectively. Figure 3.3 and Figure 3.4 display the I-V and P-V electric characteristics respectively of a common PV cell.

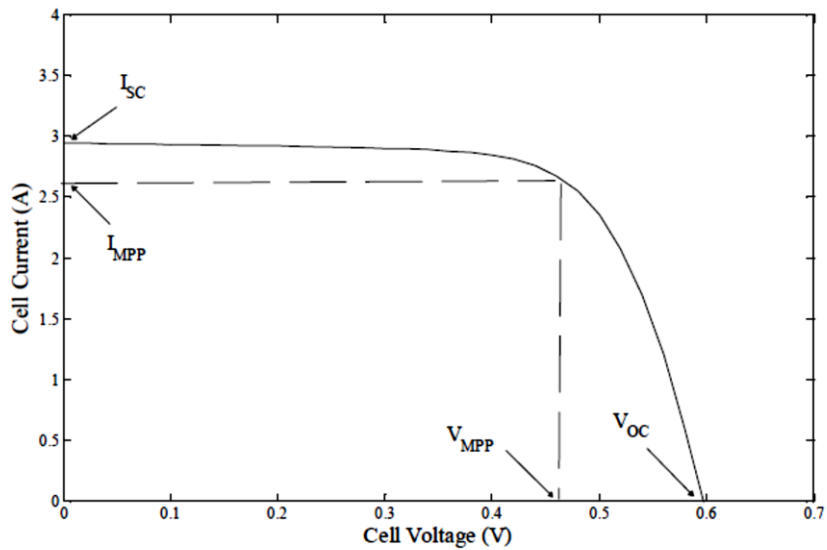


Figure 3.3: I-V characteristics of a single PV cell

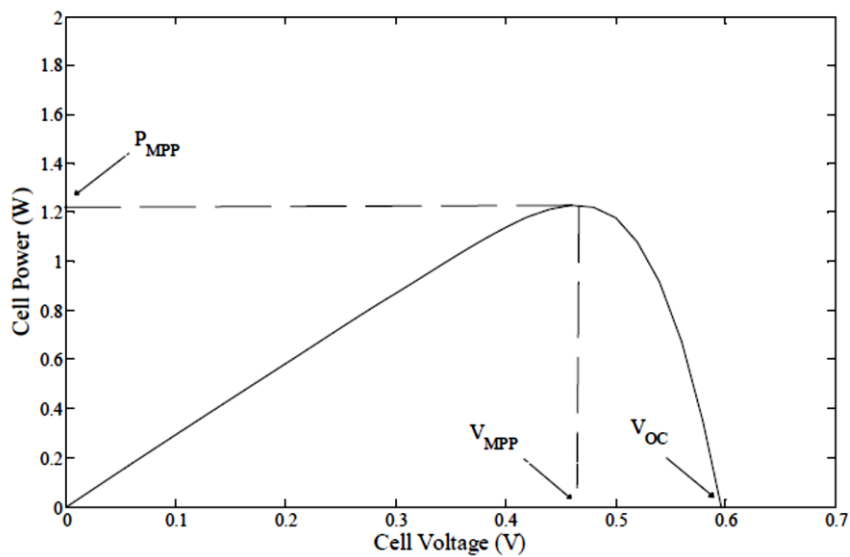


Figure 3.4: P-V characteristics of a single PV cell

The electric characteristics of the PV cell depend mainly on the irradiance received by the cell and the cell temperature. Figure 3.5 displays the electrical characteristics of the cell at different levels of the irradiance and constant temperature. It is clear that the change in irradiance has a strong effect on short-circuit current and output power of the cell, but negligible effect on the open-circuit voltage. On the other hand, Figure 3.6 shows that the change in temperature at constant irradiance has a strong effect on the open-circuit voltage and output power of the cell, but negligible effect on the short-circuit current.

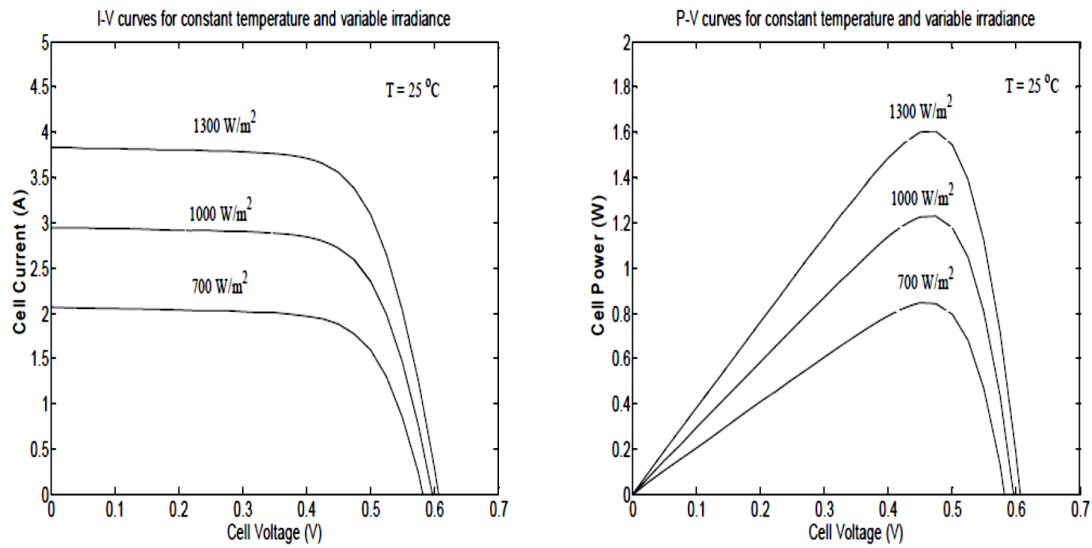


Figure 3.5: Characteristics of the PV cell at constant temperature and variable irradiance

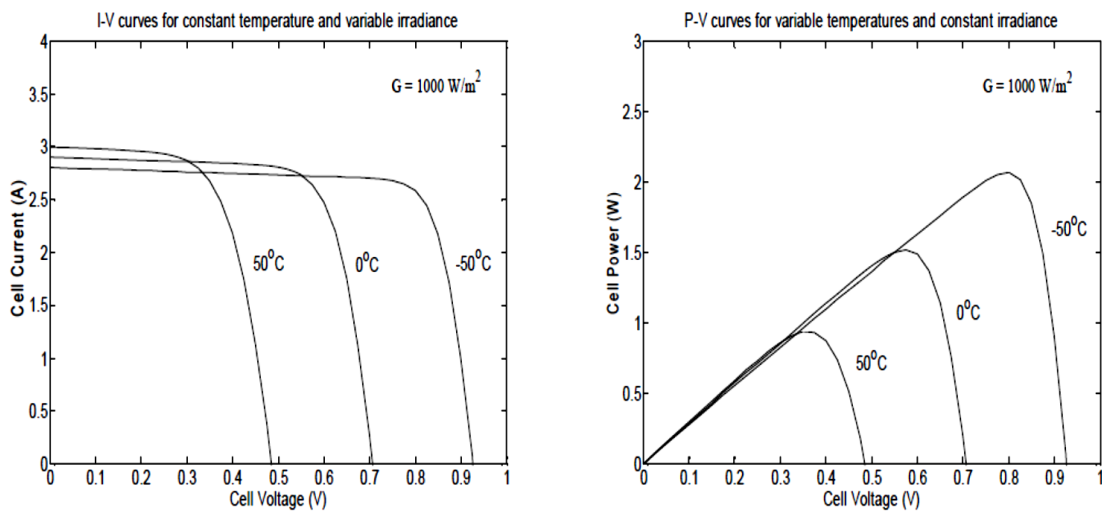


Figure 3.6: Characteristics of the PV cell at variable temperature and constant irradiance

Usually solar cells are connected in series to form a solar module and modules are then connected in series to form a string. Finally, the strings are connected in parallel to form a PV array. The number of modules in each string is specified according to the required voltage level of the array. On the other hand, the number of strings is specified according to the required current rating of the array. Most PV arrays have a power diode, called *bypass diode*, connected in parallel with each individual module or a number of modules. The function of this diode is to conduct the current when one or more of these modules are damaged or shaded. Another diode, called *blocking diode*, is usually connected in series with each string to prevent reverse current flow and protect the modules. The layout of a PV array is illustrated in Figure 3.7.

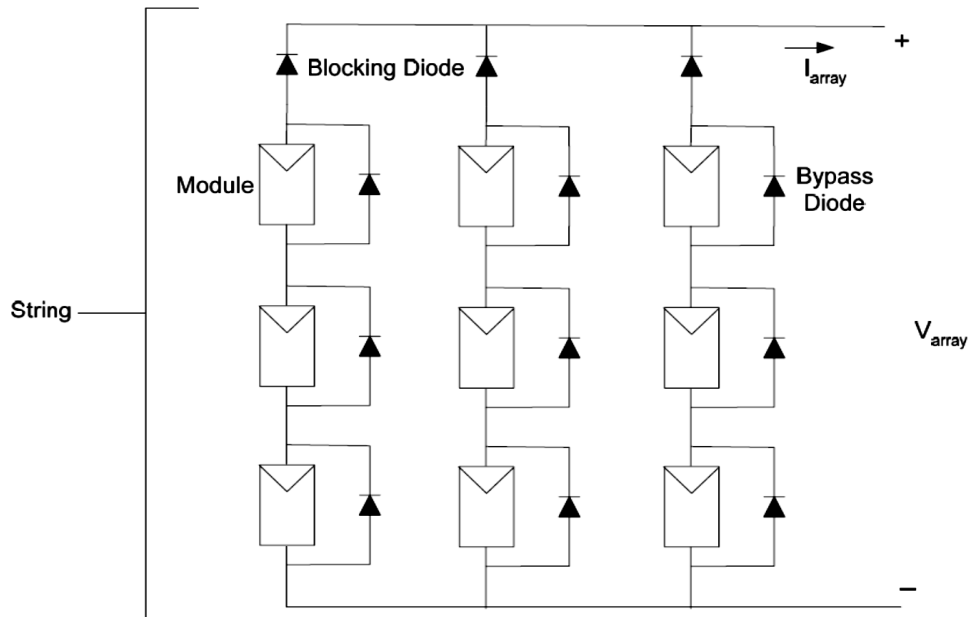


Figure 3.7: Layout of a PV array

The Solar array is the most expensive component in the PV system. The average cost of PV modules is \$4.00–5.00/W; thus, most of the research activities performed in this area are concerned with manufacturing low-cost solar cells with acceptable efficiencies [129], [130]. The advances in this field of research will have a great impact on the large-scale use of PV systems.

Generally, solar cells consist of a p-n junction fabricated in a thin wafer or layer of semiconductor (usually silicon). In the dark, the I-V output characteristic of a solar cell has

an exponential characteristic similar to that of a diode. When solar energy (photons) hits the solar cell with energy greater than band gap energy of the semiconductor, electrons are knocked loose from the atoms in the material which resulting in electron-hole pairs. These carriers are swept apart under the influence of the internal electric fields of the p-n junction and create a current proportional to the incident radiation. When the cell is short circuited, this current flows in the external circuit; when open circuited, this current is shunted internally by the intrinsic p-n junction diode. The characteristics of this diode therefore set the open circuit voltage characteristics of the cell.

Most studies related to the performance of PV systems require the use of a model to convert the irradiance received by the PV array and ambient temperature into the corresponding maximum DC power output of the PV array, P_{MPP} . The models recorded in the literature vary in accuracy and complexity, and thus, appropriateness for different studies. The single-diode model shown in Figure 3.8 is one of the most popular physical models used to represent the electric characteristics of a single PV cell [131]. This simplest equivalent circuit of a solar cell is a current source in parallel with a diode. The output of the current source is directly proportional to the light falling on the cell (photocurrent I_{pv}). During darkness, the solar cell is not an active device; it works as a diode, i.e. a p-n junction. It produces neither a current nor a voltage. However, if it is connected to an external supply (large voltage) it generates a current I_D , called diode current or dark current. The diode determines the I-V characteristics of the cell.

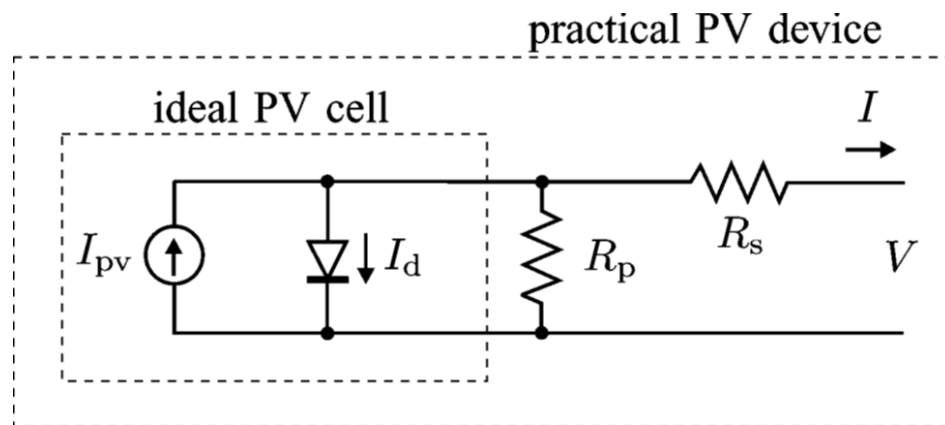


Figure 3.8: Circuit diagram of the PV model

Increasing sophistication, accuracy and complexity can be introduced to the model by adding in turn [132]:

- Temperature dependence of the diode saturation current I_0 .
- Temperature dependence of the photocurrent I_{pv} .
- Series resistance R_s , which gives the relationship between the maximum power point and open circuit voltage and represents internal losses due to current flow.
- Shunt resistance R_p , in parallel with the diode, this corresponds to the leakage current to ground and is commonly neglected.
- Either allowing the diode quality factor n to become a variable parameter (instead of being fixed at either 1 or 2) or introducing two parallel diodes with independently set saturation currents.

In an ideal cell $R_s = R_p = 0$, which is a relatively common assumption. For this work, a model of moderate complexity was used. The net current of the cell is the difference of the photocurrent, I_{pv} and the normal diode current I_0 :

$$I = I_{pv} - I_0 \left[e^{\frac{q(V+IR_s)}{nkT}} - 1 \right] \quad (3.1)$$

The model included temperature dependence of the photocurrent I_{pv} and the saturation current of the diode I_0 .

$$I_{pv} = I_{pv}(T_1) + K_0(T - T_1) \quad (3.2)$$

$$I_{pv}(T_1) = I_{SC}(T_{1,nom}) \frac{G}{G(nom)} \quad (3.3)$$

$$K_0 = \frac{I_{SC}(T_2) - I_{SC}(T_1)}{(T_2 - T_1)} \quad (3.4)$$

$$I_0 = I_0(T_1) \times \left(\frac{T}{T_1} \right)^{\frac{3}{n}} e^{\frac{qV_g(T_1)}{nk \left(\frac{1}{T} - \frac{1}{T_1} \right)}} \quad (3.5)$$

$$I_0(T_1) = \frac{I_{SC}(T_1)}{\left(e^{\frac{qV_{OC}(T_1)}{nkT_1}} - 1\right)} \quad (3.6)$$

A series resistance R_s was included; which represents the resistance inside each cell in the connection between cells.

$$R_s = -\left(\frac{dV}{dI}\right) \Big|_{V_{OC}} - \left(\frac{1}{X_V}\right) \quad (3.7)$$

$$X_V = I_0(T_1) \frac{q}{nkT_1} e^{\frac{qV_{OC}(T_1)}{nkT_1}} \quad (3.8)$$

Where the symbols are defined as follows:

q	is the electron charge ($1.60217646 \times 10^{-19}$ C)
k	is the Boltzmann constant ($1.3806503 \times 10^{-23}$ J/K)
V	is cell output voltage (V)
V_g	is the band gap voltage (V)
n	is the diode quality factor
T_1	is the reference cell operating temperature (25 °C)
T_2	is another cell operating temperature (75 °C)
I_{SC}	is short circuit current at the standard condition (A)
V_{OC}	is open circuit voltage at the standard condition (V)
N_{ser}	is the no. of series-connected modules per string
N_{par}	is the no. of parallel strings

The shunt resistance R_P is neglected. A single shunt diode was used with the diode quality factor set to achieve the best curve match. This model is a simplified version of the two-diode model [133] and shown in Figure 3.8.

All the constants in the above equations can be determined by examining the manufacturers' ratings of the PV array, and then the published or measured I-V curves of

the array. As a typical example, the SunPower SPR-305E-WHT-D ($N_{ser} = 5$, $N_{par} = 66$) array will be used to illustrate the model.

The photo-current I_{pv} (A) is directly proportional to irradiance G (Wm^{-2}). When the cell is short circuited, the current flows in the diode will be negligible. Hence, the proportionality constant in (3.3) is set so the rated short circuit current I_{SC} is delivered under rated irradiation (usually 1 Sun = 1000Wm^{-2}). For the SPR-305E-WHT-D array, $I_{SC} = 5.96$ A at 1 Sun at $T_1 = 25^\circ\text{C}$ (298 K), so $I_{pv}(T_1) = 5.96$ A/Sun.

The relationship between the photo-current and temperature is linear (3.2) and is deduced by noting the change of photo-current with the change of temperature (3.4). For the SPR-305E-WHT-D array, I_{pv} changes from 5.96 A to 6.14 A (3%) as T changes from 25°C to 75°C .

When the cell is not illuminated, the relationship between the cell's terminal voltage and current is given by the Shockley equation. When the cell is open circuited and illuminated, the photo-current flows entirely in the diode. The (I-V) curve is offset from the origin by the photo generated current I_{pv} (3.1). The value of the saturation current I_0 at 25°C is calculated using the open circuit voltage and short circuit current at this temperature (3.6).

An estimate must be made of the unknown "ideality factor" n . Green [134] states that it takes a value between 1 and 2, being near 1 at high currents, and rising towards 2 at low currents. In this study, the ideality factor was estimated to be as 0.95 and it showed great similarity compared to characteristics of an actual PV array.

The relationship of I_0 to temperature is complex, but fortunately contains no variables requiring evaluation (3.5) [133]. Equations (3.7) and (3.8) are found by differentiating (3.1), evaluating at $V = V_{OC}$, and rearranging in terms of R_S [133]. Using the values obtained from the SPR-305E-WHT-D array manufactures' curves, a value of panel series resistance $R_S = 371$ m Ω was calculated.

The SunPower SPR-305E-WHT-D PV module was chosen for modeling. The SPR-305E-WHT-D module provides 305 watts of nominal maximum power and has 96 SunPower all-back contact monocrystalline cells. The key specifications are shown in Table 3.1.

TABLE 3.1: PARAMETERS OF THE SPR-305E-WHT-D PV MODULE AT STC

Peak Power (+/-5%), P_{mmp}	305 W
Peak power voltage, V_{mmp}	54.7 V
Peak power current, I_{mmp}	5.58 A
Open circuit voltage, V_{OC}	64.2 V
Short circuit current, I_{SC}	5.96 A
Temperature coefficient of current, K_i	3.5 mA/°C
Temperature coefficient of voltage, K_v	-176.6 mV/°C

The model of the PV array was implemented using Matlab. The model parameters are evaluated during execution using the equations listed above. The program, calculate the current I , using typical electrical parameter of the module (I_{SC}, V_{OC}), and the variables Voltage (V), Irradiation (G), and Temperature (T). The inclusion of a series resistance in the model makes the solution for the current I as a non-linear problem (3.1), that should be solved by using numerical methods. In this program the Newton-Raphson method was used, because this method converges much more rapidly, and for both positive and negative currents. The Matlab program output is shown for various irradiation levels (Figure 3.9), and for various temperatures (Figure 3.10).

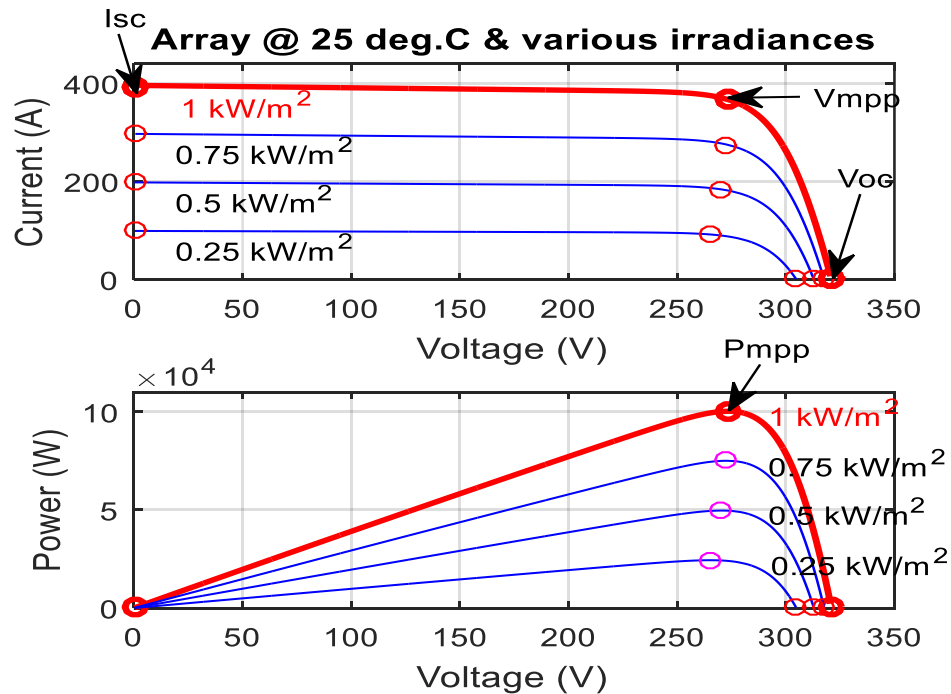


Figure 3.9: The Matlab model I-V and P-V curves for various irradiation levels

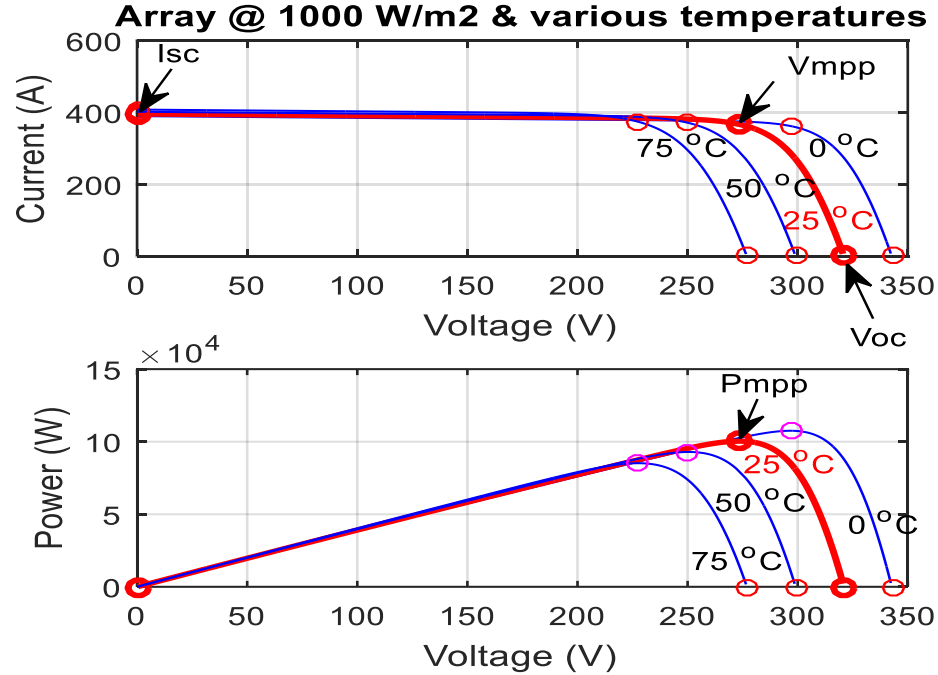


Figure 3.10: The Matlab model I-V and P-V curves for various temperatures

The accuracy of the single-diode model can be further improved by replacing the single diode with two diodes connected in parallel. The first diode represents the diffusion current in the quasi-neutral region of the junction and has an ideality factor of 1. The second diode represents the generation-recombination in the space-charge region of the junction and has an ideality factor of 2 [130]. The main drawback of this model is the increased complexity of the relationship between the output voltage and current of the cell due to the existence of two diode equations.

The identification of the parameters of the single-diode model from the data sheets of PV cells and the effect of irradiance and temperature on these parameters has been the focus of several studies [135]–[138]. Other studies propose the use of new models for the PV cells that can better represent the cell characteristics. Some of these models enhance the performance of the single-diode model by including the detailed physical processes that occur in the PV cell [139]. Other models use soft computing techniques to model the performance of PV cells under different operating conditions by training the PV model using patterns of the I-V curves at specific operating conditions [140]. Recently, a

mathematical model using polynomials has been proposed to represent the performance of the PV cell [141]. This model is useful for the case when real-time identification of the maximum power point is required. However, the model has no physical meaning and its accuracy depends mainly on the available measured data obtained from the cell.

In general, physical PV models provide cell-level information, and thus, are useful for studying the details of the PV system, such as maximum power tracking algorithms and impacts of partial shading. However, these models are not suitable for studying the performance of the electric network in the presence of PV systems. This is mainly because these studies require calculating the power generated from the PV system at different weather conditions over extended periods of time. Thus, simpler models are usually preferred as the amount of calculations is highly reduced. For example, the single-diode model can be simplified by assuming that the shunt resistance is infinitely large or by removing both the shunt and series resistances [136]. Accordingly, the voltage and current are decoupled in the main equation of the model. Other simplified models directly relate the irradiance and temperature at any instant with the maximum power that can be generated from the PV system [142]–[144]. These models are usually used when the performance of the electric network is to be assessed in the presence of a PV system. However, before using such models in the analysis, they should be validated against one of the comprehensive physical models to examine their accuracies.

3.2.3 Power Conditioning Units

Power conditioning units (PCUs) are used to control the DC power produced from the PV arrays and to convert this power to high-quality AC power before injecting it into the electric grid. PV systems can be divided, according to the number of power processing stages, into single-stage and two-stage systems. In single-stage systems, an inverter is used to perform all the required control tasks. But, in the two-stage system, a DC-DC converter precedes the inverter and the control tasks are divided among the two converters. Two-stage systems provide higher flexibility in control as compared to single-stage systems, but at the expense of additional cost and reduction in the reliability of the system [145]. During

the last decade, a large number of inverter and DC-DC converter topologies for PV systems were proposed [145]–[149], almost saturating the research in this area.

In general, PCUs have to perform the following tasks:

1. Maximum power point tracking (MPPT)

One of the main tasks of PCUs is to control the output voltage or current of the PV array to generate maximum possible power at a certain irradiance and temperature. There are many techniques that can be used for this purpose [150]–[152] with the Perturb-and-Observe and Incremental Conductance techniques being the most popular ones. A recent study [153] presented a qualitative comparison between 19 different MPPT techniques to serve as a guideline for choosing a suitable technique.

Partial shading of PV arrays is considered one of the main challenges that face MPPT techniques. In this case, there might exist multiple local maxima, but only one global maximum power point, as illustrated in Figure 3.11. In this case, the task of the PCU is to identify and operate at the global MPP. The research in this field is active and several studies have focused on developing new MPPT techniques and PCU topologies that can perform this task [154]–[156].

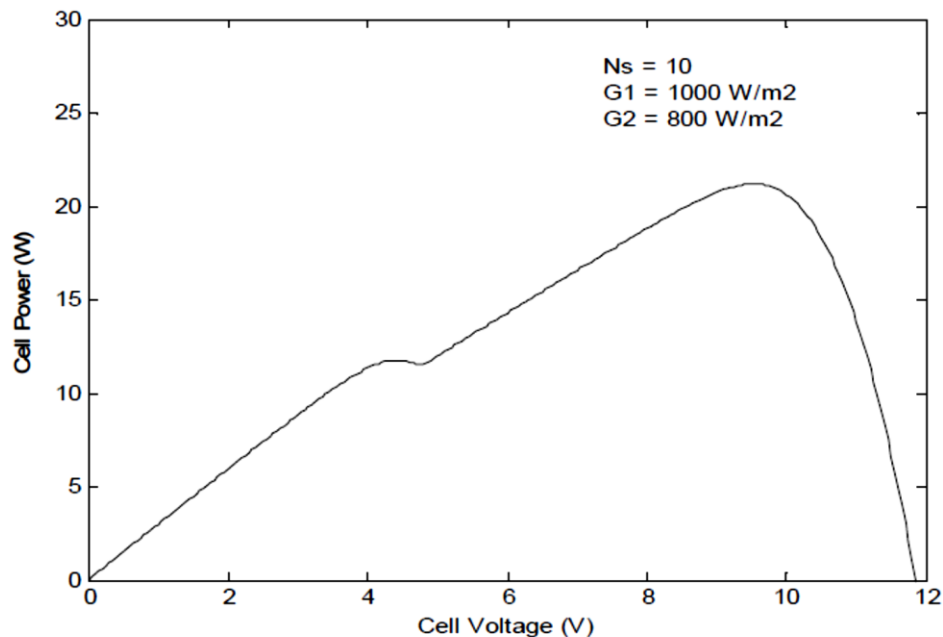


Figure 3.11: P-V curve for two series modules in case of partial shading [154]

2. Control of the injected current

PCUs should control the sinusoidal current injected into the grid to have the same frequency as the grid and a phase shift with the voltage at the point of connection within the permissible limits. Moreover, the harmonic contents of the current should be within the limits specified in the standards. The research in this field is mainly concerned with applying advanced control techniques to control the quality of injected power and the power factor at the grid interface [157]–[159].

3. Islanding detection and protection

Islanding is defined as a condition in which a portion of the utility system containing both loads and distributed resources remains energized while isolated from the rest of the utility system [160]. Most of the standards require that PCUs of PV systems should cease injection of power into the grid under specific abnormal operating conditions of the grid including those leading to islanding [160]. Islanding detection methods can be classified into three categories: 1) Communication based methods that depend on transmitting signals between the PV system and the grid to identify an islanding condition, 2) Passive methods that depend on monitoring a certain parameter and comparing it with a threshold value, and 3) Active methods that depend on imposing an abnormal condition on the grid such as injecting harmonic current with a specific order at the point of connection with the grid. Most of the recent studies have focused on assessing and comparing different islanding techniques as well as developing new methods with minimized non-detection zones [161]–[164].

4. Voltage amplification

Usually, the voltage level of PV systems requires to be boosted to match the grid voltage and to decrease the power losses. This task can be performed using step-up DC-DC converters or multilevel inverters. Three-level inverters can be used for this purpose as they provide a good trade-off between performance and cost in high voltage and high-power systems [165].

5. Additional functions

The control of PCUs can be designed to perform additional tasks such as power factor correction [166], harmonics filtering [167], reactive power control [168], and operating with an energy storage device and/or a dispatchable energy source such as diesel generator as an uninterruptible power supply [169].

3.2.4 Energy Storage Devices

The use of energy storage devices with PV systems is currently receiving a lot of attention, especially due to the fact that the power generated from these systems is intermittent. The installation of storage devices can enhance the performance of PV systems by bridging their power fluctuations, shifting the time of their peak generation, supplying critical loads during power outages, and providing reactive power support.

There are a variety of storage devices such as batteries, super-capacitors, super-inductors, flywheels, and water pumping. These devices vary in their characteristics, method of operation, and accordingly, the tasks that they can perform. Thus, choosing a storage device that can perform the required function efficiently is a preliminary step. Moreover, due to the fact that the majority of storage devices are expensive, it is essential to study the economic value of using these devices.

3.3 Connection Topologies of PV Systems

PV systems have different topologies according to the connection of the PV modules with the PCU. Some of the common topologies are shown in Figure 3-12 and a comparison between these topologies is given in Table 3-2.

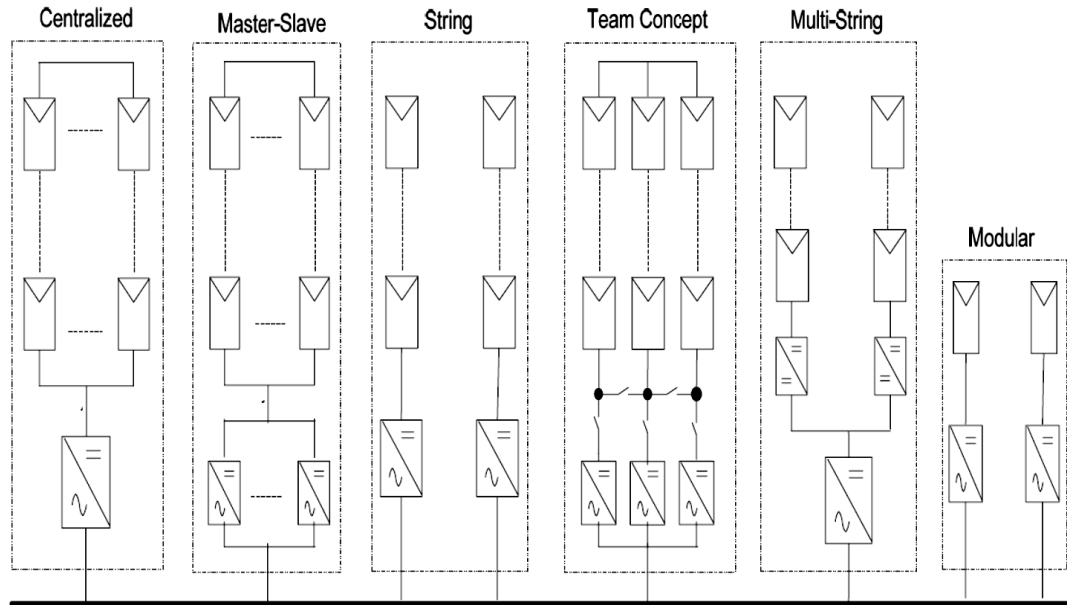


Figure 3.12: Connection topologies of PV systems

A. Centralized topology [170]

This is one of the well-established topologies. It is usually used for large PV systems with high power output of up to several megawatts. In this topology, a single inverter is connected to the PV array. The main advantage of the centralized topology is its low cost as compared to other topologies as well as the ease of maintenance of the inverter. However, this topology has low reliability as the failure of the inverter will stop the PV system from operating. Moreover, there is significant power loss in the cases of mismatch between the modules and partial shading, due to the use of one inverter for tracking the maximum power point.

B. Master-slave topology [171]

This topology aims to improve the reliability of the centralized topology. In this case, a number of parallel inverters are connected to the array and the number of operating inverters is chosen such that if one inverter fails, the other inverters can deliver the whole PV power. The main advantage of this topology is the increase in the reliability of the system. Moreover, the inverters can be designed to operate according to the irradiance level, where for low irradiance level some of the inverters are shut down. This technique of operation extends the lifetime of inverters and overall operating efficiency. However,

the cost of this topology is higher than that of the centralized topology and the power loss due to module mismatch and partial shading is still a problem with this topology.

C. String topology [172]

In the string topology, each string is connected to one inverter; hence, the reliability of the system is enhanced. Moreover, the losses due to partial shading are reduced because each string can operate at its own maximum power point. The string topology increases the flexibility in the design of the PV system as new strings can be easily added to the system to increase its power rating. Usually, each string can have a power rating of up to 2-3 kW. The main disadvantage of this topology is the increased cost due to the increase in the number of inverters.

D. Team Concept topology [173]

This topology is used for large PV systems; it combines the string technology with the master-slave concept. At low irradiance levels, the complete PV array is connected to one inverter only. As the irradiance level increases, the PV array is divided into smaller string units until every string inverter operates at close to its rated power. In this mode, every string operates independently with its own MPP tracking controller.

E. Multi-String topology [172]

In this topology, every string is connected to a DC-DC converter for tracking the maximum power point and voltage amplification. All the DC-DC converters are then connected to a single inverter via a DC bus. This topology combines the advantages of string and centralized topologies as it increases the energy output due to separate tracking of the MPP while using a central inverter for reduced cost. However, the reliability of the system decreases as compared to string topology and the losses due to the DC/DC converters are added to the losses of the system.

F. Modular topology [172]

This is the most recent topology. It is also referred to as "AC modules", because an inverter is embedded in each module. It has many advantages such as reduction of losses

due to partial shading, better monitoring for module failure, and flexibility of array design. However, this topology is suitable only for low power applications (up to 500 W) and its cost is relatively high. Moreover, the lifetime of the inverter is reduced because it is installed in the open air with the PV module, thus increasing its thermal stress.

3.4 Standards and Codes for Grid-Connected PV Systems

There are several standards on the market dealing with the interconnection of distributed resources with the grid. In this context, PV system is of importance where all practice for wiring, design and installation has been standardized. This section is limited to International Electro-technical Commission (IEC), Institute of Electrical and Electronics Engineers (IEEE) and National Electrical Code (NEC).

Standards and codes governing the design of the PV system is based on PV electrical installations practices and interfacing with the grid. The Institute of Electrical and Electronics Engineers (IEEE) 929-2000 Standard: Recommended Practice for Utility Interface of Photovoltaic (PV) Systems which gives the guidance to PV system practices. These practices include power quality and protection functions [174]. The IEEE 929 Standard also contains UL 1741 Standard which has been used as the key to select inverters used in this design.

The International Electro-technical Commission (IEC) Standard gives out the characteristics of PV system and grid interface at the point of common coupling (PCC). The National Electrical Code (NEC), in article 690 on Photovoltaic power systems, shows the necessity and important information for proper installation of PV system. The 690 code explains most of the important information in both design and installation aspects. Some of this important information includes:

- PV system conductors and coding.
- Grounding system and Module connection.
- PV source circuits, PV Inverter output circuits, and circuit routing.
- Identification of equipment used and system circuit requirements i.e. open-circuit voltage and short-circuit current.

TABLE 3.2: COMPARISON BETWEEN DIFFERENT CONNECTION TOPOLOGIES OF PV SYSTEMS

Topology	Advantages	Disadvantages	Power Rating
Centralized	<ul style="list-style-type: none"> ▪ Easy to monitor. ▪ Easy to maintain. ▪ Low cost due to central inverter. 	<ul style="list-style-type: none"> ▪ DC losses in high voltage DC cables. ▪ Power loss due to centralized MPPT, string diodes and mismatch in PV modules. ▪ Low reliability. ▪ Not flexible in design. 	Up to several megawatts.
Master-Slave	<ul style="list-style-type: none"> ▪ Higher reliability as compared to centralized topology. ▪ Improved efficiency for the operating inverters. ▪ Extended lifetime of inverters. 	<ul style="list-style-type: none"> ▪ DC losses in high voltage DC cables. ▪ Power loss due to centralized MPPT, string diodes and mismatch in PV modules. ▪ High cost due to use of multiple inverters. ▪ Not flexible in design. 	Up to several megawatts.
String	<ul style="list-style-type: none"> ▪ Reduction in energy loss that result from partial shading. ▪ Losses in string diodes are eliminated. ▪ Good reliability. ▪ Flexible in the design. 	<ul style="list-style-type: none"> ▪ Higher cost as compared to centralized. ▪ Used for low power ratings. 	3-5 kW/string.
Team Concept	<ul style="list-style-type: none"> ▪ High efficiency due to individual MPPT and increase in the inverters efficiency. 	<ul style="list-style-type: none"> ▪ Losses due to mismatch between PV modules. ▪ High cost due to the use of several inverters. 	Up to several megawatts.

	<ul style="list-style-type: none"> ▪ Higher reliability as compared to centralized topology. 		
Multi-String	<ul style="list-style-type: none"> ▪ Reduction in energy loss that result from partial shading. ▪ Losses in string diodes are eliminated. ▪ MPPT and current control are separated. ▪ Voltage amplification can be achieved by the DC-DC converter 	<ul style="list-style-type: none"> ▪ All strings are connected to a single inverter thus the reliability of the system decreases. ▪ Additional losses inside the DC/DC converter. ▪ The cost is higher as compared to centralized topology. 	5 kW
AC modules	<ul style="list-style-type: none"> ▪ No losses due to partial shading. ▪ No mismatch losses between modules. ▪ Easy in failure detection of the modules. ▪ Flexible & expandable in design. 	<ul style="list-style-type: none"> ▪ High cost. ▪ Replacement of inverter in case of faults is not easy. ▪ Reduced lifetime of the power electronic components due to additional thermal stress. 	up to 500 W

3.5 Conclusion

This chapter presented the main components of PV systems and discussed the recent research activities regarding these components. Starting with the irradiance, weather stations usually measure the global irradiance on a horizontal surface, and thus, models are required to estimate the irradiance on the tilted surface of the PV system. The accuracy of any of these models is usually dependent on the location where the PV system is being installed, thus, it is important to choose a suitable model for the case under consideration. One of the main activities in this area is the development of irradiance models suitable for specific locations. The fluctuations in irradiance due to passage of clouds also received a lot of attention from researchers, where most of the work done in this field relied on the frequency domain analysis. One field that still requires more attention is the prediction of irradiance, which is a complicated task as compared to the prediction of wind speed. This is mainly because of the variety of factors that affect the accuracy of prediction including the wind speed and direction and type, height and thickness of clouds.

Modeling of the PV cells is one of the mature areas in the field. There are a variety of models available in the literature and can be divided into two main categories; detailed and simplified models. Detailed models attempt to represent the physics of the PV cell and are usually suitable for studies that require the detailed cell information such as implementation of maximum power techniques and analysis of the effect of change in irradiance and temperature on the performance of the PV cell. On the other hand, simplified models usually provide a direct estimate of the maximum power generated from the PV cell at certain operating conditions. Thus, simplified models are suitable for system studies that try to identify the impacts of PV systems on the electric network.

In the past few years, developing new topologies for power conditioning units and applying new control techniques were the focus of many studies, almost saturating this field of research. Also, the application of new maximum power point tracking algorithms received a lot of attention. However, most of these algorithms fail to operate properly in the case of partial shadings, which is the case where parts of the PV array are shaded by clouds or nearby buildings.

The use of storage devices with PV systems is currently receiving a lot of attention. These devices can be used to bridge fluctuations in the output power of PV systems, shift the peak generation of the system to match the load peaks, and provide reactive power support. One of the main challenges that still face the use of storage devices is the high cost associated with their installation. Thus, studying the economical aspect of installing these devices is of great importance.

Chapter 4. Power Inverter Topologies and Control Structures for Photovoltaic Applications

4.1 Introduction

The increase in the photovoltaic (PV) installed capacity of recent years has sparked a continuous evolution of the PV power conversion stage [175], [176]. The PV converter industry has evolved rapidly from infancy within the last two decades. One of the drivers behind this progress has been the PV converter market stringent specifications, such as high efficiency (above 98%), long warranty periods (to get closer to PV module warranties of 25 years), high power quality, transformerless operation, leakage current minimization (which imposes restrictions on the topology or modulation), and special control requirements such as the Maximum Power Point Tracking (MPPT). Another driver behind this development was the fact that, for a long time, the power converter represented only a small fraction of the cost of the whole PV system due to high PV module prices, allowing PV inverter manufacturers room for developing higher performance and more sophisticated topologies. The development of new PV converter topologies also motivated manufacturers' to develop proprietary technology to differentiate themselves from their competitors and achieve a competitive advantage in a growing PV converter market [177].

This chapter presented a detailed survey on the topic of grid-connected PV system used to integrate the solar energy into the utility grid. Topologies of single-phase grid-connected inverters are analyzed critically, and a comparative study of these topologies is presented. Moreover, the three-phase grid-connected inverters are outlined. Furthermore, the control techniques for the single- and three-phase grid-connected inverters are critically reviewed and presented.

4.2 Literature Review

Reference [178] presented an overview of grid connected PV systems and then compared their advantages and disadvantages.

Reference [179] introduced a different inverter topology that uses a block of energy storage in a series-connected path with the line interface block. This design facilitated an independent control over the capacitor voltage and soft switching for all semiconductor devices. It increased the converter complexity compared to traditional designs, but it provided control for an energy storage voltage and reduced ripple by using electrolytic or film type capacitors. This topology also provided a facility for reactive power transfer and maintained high efficiency.

Reference [180] discussed different topologies based on cascaded H-bridge multilevel inverters. In one topology, they described a multilevel inverter, with two PV arrays for each phase. In a second topology, they introduced a transformer and decreased the number of PV arrays to one for all three phases. In a third topology, the number of switches was much reduced compared to the other above described topologies and used the same number of PV arrays for all the three phases. They simulated these topologies with a RL load.

Reference [181] presented a grid tied PV inverter with simulation and experimental tests for a reference voltage fixation method for DC-AC inversion, switching techniques by Peripheral Interface Controller (PIC) microcontroller, IGBT gate drive circuit operation with proper filtering and finally power delivery to the grid with proper isolation. The achievements of the practical testing of grid tied inverter lies in successful DC-AC conversion, along with the capability of matching inverter output voltage and frequency with continuous fluctuating grid voltage and frequency.

Reference [182] presented a new current source converter topology for 1-phase PV application. The main principle for this proposed topology is that instantaneous power transfer across the switching bridge is maintained constant. With the help of this topology, the low frequency ripple common to 1-phase inverters was eliminated or reduced enough to reduce the size of passive components to achieve necessary stiffness. With the low current ripple, MPPT performance is readily achieved. They verified modulation and control methods using a detailed SaberTM model.

Reference [183] focused on inverter topologies for 1-phase grid connected PV modules. They described some of the standards for PV and grid application like DC current injection into grid, power quality, islanding operation detection. They classified the inverter topologies based on a number of power processing stages, power decoupling type between

the PV modules and grid, types of grid interfaces, transformers and type of interconnection between stages.

Reference [184] described a novel flyback-type 1-phase inverter circuit, which is suitable for an AC-module system. They removed the problem of low power from PV array due to partial shading on a few modules with the use of an AC module strategy. They described the use of small rating film capacitor instead of electrolytic capacitors, which is necessary for decoupling and with the help of film capacitors, the life of the inverter was increased.

Reference [185] described 1-phase PV transformerless inverter. They proposed a new high efficiency topology that generated no varying common-mode voltage and required very less input voltage as the bipolar PWM full bridge. They verified this topology with a 5-kW hardware prototype.

Reference [186] described a transformerless inverter for grid connected PV system. They designed a very high reliability and efficient inverter. The proposed inverter utilized two different AC coupled inductors for positive and negative half grid cycles, and super junction MOSFETS to achieve high efficiency.

Reference [187] described a transformerless inverter for a grid connected PV system. They proposed two step-down converters where each converter modulated a half wave of output current. They described transformerless topologies like H5 and HERIC which gave very high level of efficiency for low-power grid-tied system.

Reference [188] described a multilevel inverter which offered high power capability with lower harmonic and commutation losses. The proposed multilevel inverter structure consisted of two basic parts. The parts are classified as Level and H-Bridge Modules. They described that multilevel inverter is good for unequal DC sources. They introduced Super Imposed Carrier PWM (SICPWM) technique for harmonic reduction.

Reference [189] presented a 3-phase boost-type grid connected inverter. They proposed a one-cycle control (OCC) method with pulse width modulation (PWM) method. They described a single power stage conversion with the help of Current Source Inverter (CSI) with shorted inductor.

Reference [190] proposed full-bridge series-resonant buck-boost inverter. This inverter included a full-bridge topology and a LC resonant tank without auxiliary switches. The

proposed inverter provided the main switch for turn-on at Zero Current Switching (ZCS) by a resonant tank. This inverter gave a very high efficiency.

Reference [191] presented a 3-phase 2-stage grid connected Module Integrated Converters (MICs). Generally, for MICs single-stage conversion is required but here they proposed Zero Voltage Switching (ZVS) in 2-stage operations for the grid connected PV system. In the first stage, they interfaced a high efficiency full-bridge LLC resonant DC-DC converter which is interfaced to the PV array that produces a DC-link voltage. In the second stage, they considered a 3-phase DC to AC inverter circuit which employed an easy soft switching method without any auxiliary components. This inverter reduced per watt cost and improved reliability.

Reference [192] presented a 1-phase grid connected PV system with power quality conditioner. They used an incremental conductance method for MPPT and shunt controller for voltage support.

4.3 Requirements for PV Converters

In the past, PV modules were very expensive, and the efficiency was very low; PV power integration into the distribution grid was not obvious. In addition, the safety requirements imposed by electric companies and governments were lacking. Today, PV installations are a relatively substantial part of the electrical market, and as PV becomes a more relevant actor in power systems, the corresponding requirements and regulations for the safe and reliable use of PV systems are being standardized.

In general, two groups of requirements have to be met when a PV installation is considered. These two groups are the performance requirements and the legal regulations that the PV installations have to meet.

4.3.1 Performance Requirements of PV Converters

4.3.1.1 Efficiency

The losses of PV inverters have reduced in time, and efficiency figures above 97% (see, for instance, SunnyBoy 5000TL by SMA for domestic applications below 5.25 kW) and

even more for central inverters (see, for instance, SunnyCentral 760CP XT by SMA, a central inverter with nominal power up to 850 kW with 98% of efficiency) are possible [193]. The PV inverter efficiency for state-of-the-art brand products stands around 98%. However, it is notable that the efficiency is expected to improve further when silicon carbide (SiC) and gallium nitride (GaN) devices become the basic power semiconductors of the PV inverters in the next decade [194].

4.3.1.2 Power Density

Since power density is important for domestic and commercial applications (below 20 kW), several such solutions have been recently presented (e.g. ABB PVS300 inverter which is based on a Neutral-Point-Clamped (NPC) topology) [195].

4.3.1.3 Installation Cost

Figure 4.1 shows the evolution of each cost component of a PV system in central Europe [196]. Comparing the figures from the year 2000 to the figures in 2012, there is an important reduction in the total cost (68%), but the most important reduction (78%) is due to the cost of the PV modules. The inverter cost has been reduced by 68%, and the installation-related costs have had the smallest reduction in the entire group (56%). Installation costs may vary greatly from one country or region to another as the land, labor, and other local factors may have a great influence on the total cost.

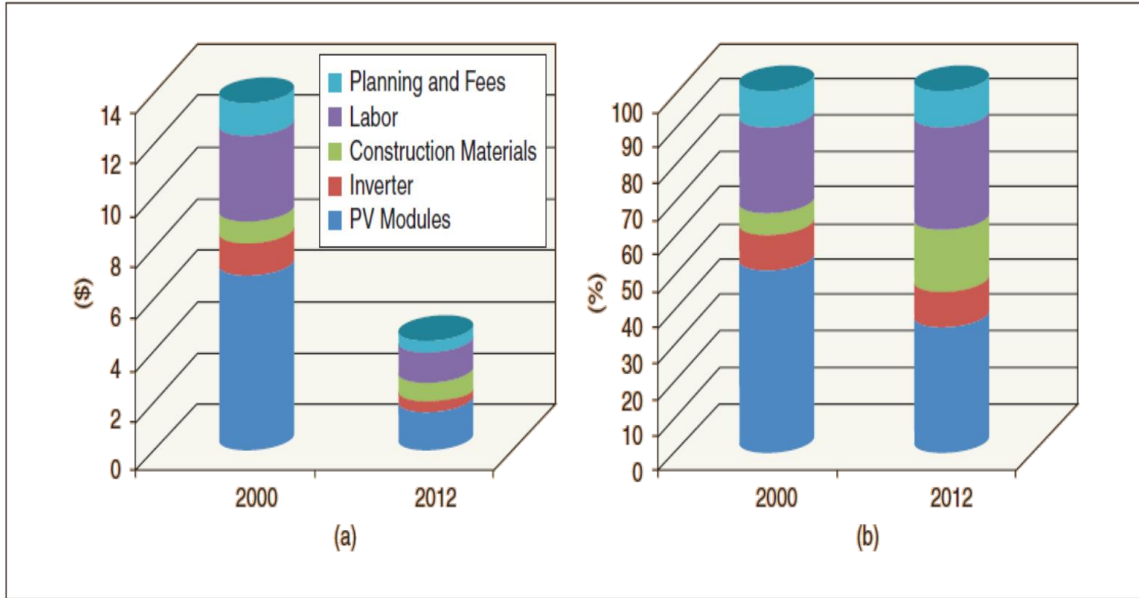


Figure 4.2: The evolution of the cost distribution of PV systems (in the range of 2-50 kW): (a) the costs in U.S. dollars and (b) the distribution of each component cost. [196]

4.3.1.4 Minimization of Leakage Current

The leakage current appears because of the high stray capacitance between the PV cells and the grounded metallic frame of each module and the high-frequency (HF) harmonics caused by the modulation of the power converter. Galvanic isolation can help to interrupt the leakage path, but the use of a transformer presents drawbacks such as higher cost and additional losses, leading in general to a reduction of the efficiency. Nevertheless, the transformer is mandatory in some countries because of local regulations. If the transformer is not mandatory, as a second solution, several power converter topologies have been specifically designed to minimize the effect of the HF harmonics on the leakage currents [197].

4.3.2 Legal Requirements of PV Systems

4.3.2.1 Galvanic Isolation

One important requirement for PV systems is galvanic isolation for safety reasons. This feature is required only by some national codes, such as RD-1699/2011, which applies to

the connection of PV systems at the low-voltage (LV) distribution grid in Spain. This requirement means that the PV topologies are not standardized and that they have to be specifically designed to fulfill this galvanic isolation requirement, which is usually achieved by using a transformer (operating at either high or low frequencies).

4.3.2.2 Islanding Detection

The islanding phenomenon for grid connected PV systems occurs when the PV inverter does not disconnect after the grid has tripped and continues to provide power to the local load [198].

In the conventional case of a residential electrical system, co-supplied by a rooftop PV system, the grid disconnection can appear as a result of a local equipment failure detected by the ground fault protection or of an intentional disconnection of the line for servicing. In both situations, if the PV inverter does not disconnect, some hazardous situations can occur, such as

- Retripping the line with an out-of-phase closure, damaging some equipment.
- A safety hazard for utility line workers who assume that the lines are de-energized.

To avoid these serious situations, safety measures and detection methods called anti-islanding requirements have been required in some standards. In IEEE 1574 Standard, it is defined that after an unintentional islanding where the PV system continues to energize a portion of the power system (island) through the point of common coupling, the PV system shall detect the islanding and stop to energize the area within 2 seconds [199].

4.3.2.3 Other Codes and Standards

Since PV applications are becoming more prevalent, codes and standards are continuously being defined by international and national committees and governments to achieve a safe, high-quality, and normalized operation. Usually, governments define their specific codes based on international standards, but consider local factors such as the geography, grid structure, and ratio between the renewable energy and the total installed power. For instance, VDE-AR-N 4105 is applied in Germany as a local code defining the power curtailment, frequency and voltage support, and dynamic grid support (ride-through

capability). Note that a national code can become an international standard if it is successfully accepted by the international commissions [200]. A summary of the current international standards for PV applications is included in Table 4.1.

TABLE 4.1: A SUMMARY OF THE TYPICAL INTERNATIONAL CODES AND STANDARDS FOR PV APPLICATIONS

	Codes and Standards	Scope and Content of The Standard
Grid connected	IEC 60364-7-712, IEC 61727, IEC 61683, IEC 62093, IEC 62116, IEC 62446, UL 1741	<ul style="list-style-type: none"> ▪ Installations of buildings. ▪ Utility interface and measuring efficiency. ▪ Interconnected PV inverters. ▪ System documentation, commissioning tests, and inspection. ▪ Use in independent power systems.
Off grid	IEC 62509, IEC 61194 IEC 61702, IEC/PAS 62111, IEEE Standard 1526, IEC 62124	<ul style="list-style-type: none"> ▪ Battery charge controllers. ▪ Stand-alone systems. ▪ Rating of direct-coupled pumping systems. ▪ Specifications for rural decentralized electrification.
Rural systems	IEC/TS 62257	<ul style="list-style-type: none"> ▪ Small renewable energy and hybrid systems. ▪ Protection against electrical hazards. ▪ Selection of generator sets and batteries. ▪ Micropower systems and microgrids. ▪ Household lighting equipment.
Monitoring	IEC 61724, IEC 61850-7, IEC 60870	<ul style="list-style-type: none"> ▪ Measurement, data exchange, and analysis. ▪ Communication networks and systems for power utility automation. ▪ Distributed energy resources and logical nodes.
Electromagnetic compatibility (EMC)/ electromagnetic interference emissions	EN 61000, FCC Part 15	<ul style="list-style-type: none"> ▪ European Union EMC directive for residential, commercial, light industrial and industrial facilities. ▪ U.S. EMC directive for residential, commercial, light industrial and industrial facilities.

4.4 PV System Configurations

Grid-connected PV power generation systems can be found in different sizes and power levels for different needs and applications, ranging from a single PV module from around 200 W to more than a million modules for PV plants over 100 MW [201]. Therefore, the generic PV energy conversion systems' structure (Figure 4.2), can vary significantly from one plant to another [202]. For simplicity, grid-connected PV systems are subdivided depending on their power rating: small scale from a few watts to a few tens of kilowatts, medium scale from a few tens of kilowatts to a few hundred kilowatts, and large scale from a few hundreds of kilowatts to several hundreds of megawatts. In addition, PV systems can be further classified depending on the PV module arrangement: a single module, a string of modules, and multiple strings and arrays (parallel connected strings) [203]. The PV module arrangement also gives the inverter configuration its name: AC-module inverter, string inverter, multistring inverter, or central inverter, as shown in Figure 4.3 and Table 4.2.

The AC-module configuration uses a dedicated grid-tied inverter for each PV module of the system [204]. Therefore, this configuration is also known as a module-integrated inverter and micro-inverter because of the small size and low power rating of the converter. The LV rating of PV modules (generally around 30 V) requires voltage elevation for grid connection. Therefore, AC-module inverters are only found with an additional DC-DC stage, usually with a HF transformer to provide galvanic isolation and elevate the voltage. Because of the additional DC-DC stage and HF isolation, this is the configuration with the lowest power converter efficiency, which is compensated somewhat by the highest MPPT accuracy due to the dedicated converter. This configuration is useful for places with lots of partial shading, complex roof structures, small systems, or combinations of different roof orientations. The small size of the converter allows a very compact enclosure design that can be attached to the back of each PV module, hence the name module integrated inverter. Because of their LV operation, metal-oxide-semiconductor field effect transistor (MOSFET) devices are most commonly found in these topologies.

String inverters interface a single PV string to the grid [205]. They can be subdivided into single- and two-stage conversion topologies, depending on the addition (or not) of a

DC-DC stage used to adapt the DC voltage output from the PV string to the DC side voltage of the grid inverter. In addition, the DC-DC stage decouples the MPPT control from the grid side control (active and reactive power) by enabling a fixed voltage at the inverter DC side. Furthermore, grid inverters can be found with or without galvanic isolation. Isolation can be introduced at the grid side with LF transformers or within the DC-DC stage with a HF transformer.

The different combinations between single- or two-stage, with transformer or transformerless string inverters, has led to a wide range of different configurations (Figure 4.4). Compared to AC-module inverters, the string inverter has a less accurate MPPT of the PV systems and, under partial shading, would reduce the energy yield. However, for a PV system of the same power rating, the string inverter has a lower cost per watt and is more efficient. The string inverter is very popular for small-to-medium scale PV systems, particularly for residential rooftop PV plants.

To add more flexibility to the string inverter and improve the MPPT performance of the PV system, the multistring concept was developed [206]. The strings are divided into smaller pieces (fewer modules in series) and connected through independent MPPT DC-DC converters to the grid-tied inverter. The DC-DC stage also boosts the voltage of the smaller strings. The additional DC-DC stages are a cost-effective solution compared to having several string inverters. As can be seen in Figure 4.4, multistring inverters can also be found with or without isolation. Since they reduce partial shading and mismatching, they are suitable not only for rooftop PV systems but also for medium-and large-scale plants.

Finally, the central inverter interfaces a whole PV array to the grid through a single inverter [176]. The array is composed of parallel-connected strings. A blocking diode in series to each string is necessary to prevent them from acting as load when partial shading or mismatch occurs. Because the whole array is connected to a single inverter, this configuration can only provide a single MPPT operation, leading to the lowest MPPT efficiency of all configurations. Nevertheless, it provides a simple-structure, reliable, and efficient converter, making it one of the most common solutions for large-scale PV plants. Since they operate at a LV (11 kV), the limit of insulated-gate bipolar transistor (IGBT) technology enables converters of up to 850 kW. To increase the power rating, some

manufacturers commercialize two central inverters connected through a 12-pulse transformer, with a rating up to 1.6 MW. Nevertheless, very large PV plants can currently reach several hundreds of megawatts. Therefore, several hundreds of dual central inverters are needed in large PV farms.

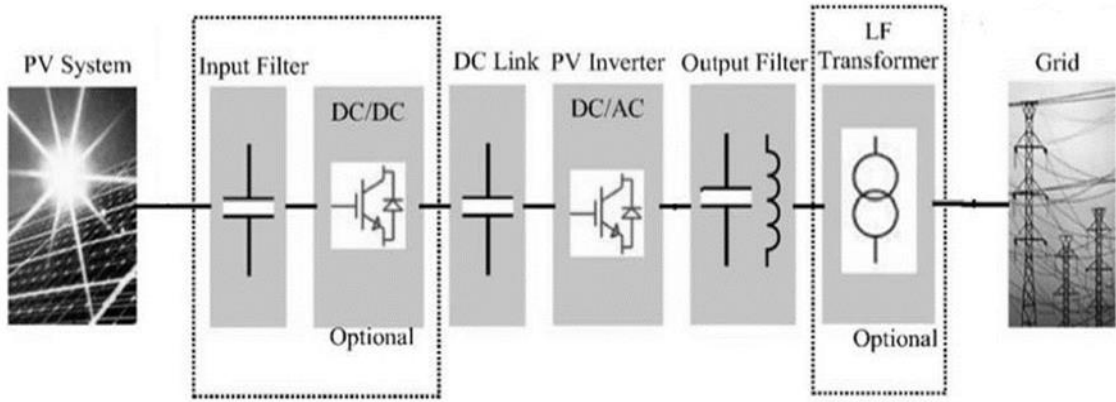


Figure 4.2: The generic structure of a grid-connected PV system (a large-scale central inverter is shown as an example). [202]

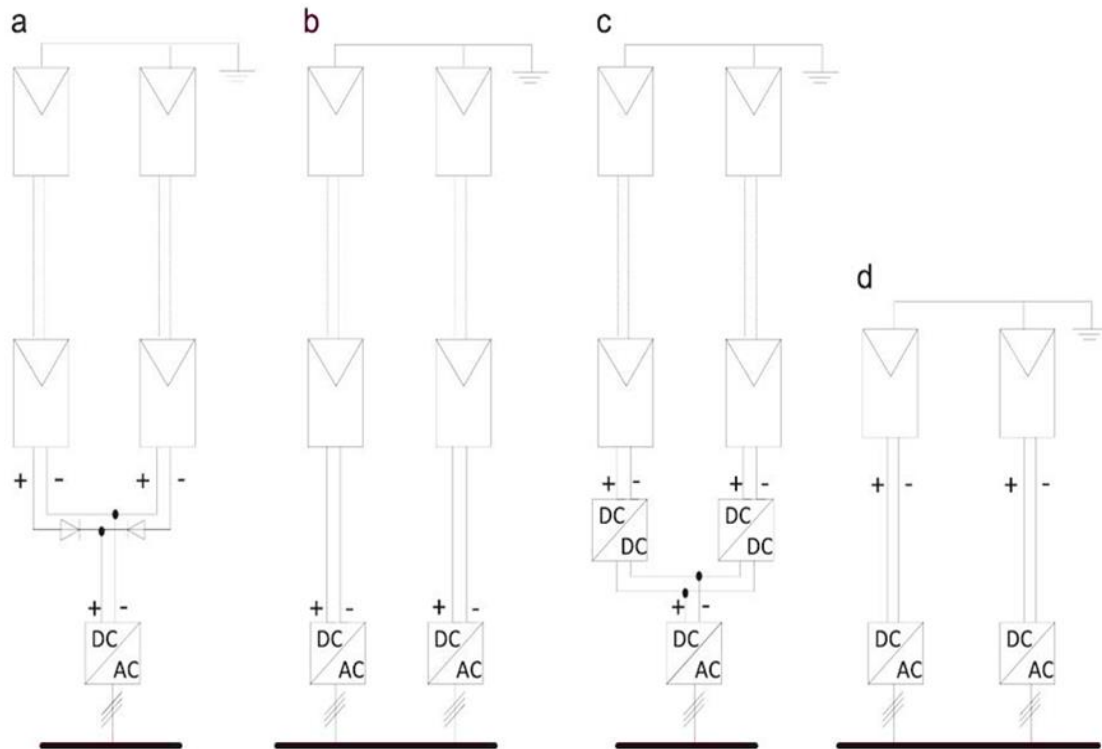


Figure 4.3: PV System Configurations (a) central, (b) string, (c) multistring, and (d) module integrated

4.5 Industrial PV Inverters

The evolution in power converter technology for PV applications, driven by the growth in the PV installed capacity and the search for the ultimate PV inverter, has led to the existence of a wide variety of power converter topologies used in practice. Figure 4.4 shows several industrial PV inverter topologies for central, string, multistring, and AC-module configurations, which will be analyzed in this section. Table 4.3 summarizes some of the characteristics of some commercial power converter topologies for these PV inverter applications.

4.5.1 String Inverter Topologies

The most common string inverter topology is the full- or H-bridge inverter. Several modified and enhanced versions have found their way into the market [207]. The H-bridge with a grid-side LF transformer features a simple power circuit, galvanic isolation, and voltage elevation provided by the transformer, which enables a larger range of input voltages. This converter can be controlled with 3-level carrier-based PWM techniques since the common mode voltages cannot generate a leakage current due to isolation. The bypass switching state (zero voltage level) prevents a reactive current flow between the filter inductor and the DC-link capacitor. Nevertheless, the bulky transformer has several disadvantages making this topology less popular.

The transformerless H-bridge, also known as an H4 inverter (shown in a two-stage configuration with a boost DC-DC stage), gets rid of the LF transformer by splitting the grid inductor into the phase and neutral wires of the systems and using a bipolar PWM (2-level) to solve the issues of the switched common-mode voltage and leakage currents and by using a boost stage for a wider input voltage range. The downside is that the 2-level modulation reduces the power quality at the grid connection and lowers the efficiency since there is a reactive current flow between the passive elements of the circuit at zero voltage through the freewheeling diodes as the DC-link capacitor is not isolated from the grid at any time. To overcome the problem of the reactive current transfer between the grid filter and the DC-link capacitor in transformerless H-bridge string inverters during freewheeling, several proprietary solutions have been introduced by manufacturers [207]–[209].

The H-bridge with the HF isolated DC-DC stage is composed of a MOSFET full bridge inverter, an HF transformer, and a diode full-bridge rectifier. This approach greatly reduces the size of the converter, improving the power density compared to LF transformer-based topologies. However, the additional converter stages introduce higher losses.

The H5 string inverter by SMA adds an additional switch between the DC-link and the H-bridge inverter to open the current path between both passive components, increasing the efficiency and reducing the leakage current.

The Highly Efficient and Reliable Inverter Concept (HERIC), introduced by Sunways, uses instead a bidirectional switch that bypasses the whole H-bridge inverter, separating the grid filter from the converter during freewheeling.

The H6 topology, introduced by Ingeteam [210], adds an additional switch in the negative DC bar to the H5 topology. Two versions were introduced: one with a diode connected in parallel to the DC side of the H-bridge of the H6 topology, called the H6D1, and the H6D2, which adds two auxiliary freewheeling diodes instead of one. Both allow freewheeling without interaction between passive components while enabling a unipolar output compared to the H5. The difference between the H6D1 and the H6D2 is that in the former, the additional switches block the total DC voltage, while in the latter, they only block half.

The 3-level Neutral Point Clamped inverter (3L-NPC) also has several modified and enhanced versions for PV string inverters [211]. The advantage of the 3L-NPC over the H-bridge is that it provides a 3-level output without a switched common-mode voltage since the neutral of the grid is grounded to the same potential as the midpoint of the DC link. This enables transformerless operation without the problem of the leakage currents and modulation methods that do not use the potential of the converter. The main drawback compared to the H-bridge is that it requires a total DC link of double the voltage to connect to the same grid. Hence, more modules need to be connected in series or an additional boost stage is required.

A full-bridge of two 3L-NPC legs was introduced by ABB, resulting in the 5L-NPC inverter [212]. As with the H-bridge, this converter also requires a symmetrical grid filter distributed between the grid phase and neutral wires. A special modulation technique can

achieve a line frequency common-mode voltage; hence, no leakage currents are generated while enabling transformerless operation.

The T-type or 3-level transistor clamped string inverter was introduced by Conergy. The converter can clamp the phase of the grid directly to the neutral to generate the zero-voltage level using a bidirectional power switch. For the same reason as the 3L-NPC, it can operate transformerless. The main difference is that it does not require the two additional diodes of the 3L-NPC. The bidirectional switches block each half of the voltage blocked by the phase-leg switches.

The asymmetric cascaded H-bridge was introduced by Mitsubishi [213] and features three series-connected H-bridge cells operating with unequal DC voltage ratios (1:2:4). The PV system is connected through a boost DC-DC stage to only one of the H-bridge cells, which is the only one processing active power to the grid. The other two cells use floating DC links for power quality improvement through the generation of 13 voltage levels. This enables a reduction of the switching frequency without compromising the power quality. The topology requires a bidirectional bypass switch connected to the large cell to reduce the changing potential between the PV system and the ground to reduce the possibility of leakage currents and enable transformerless operation.

4.5.2 Multistring Topologies

The main difference between the multistring and string configuration is that multistring is exclusively a two-stage system composed by more than one DC-DC stage [206]. Hence, all inverter topologies in the “String Inverter Topologies” section could be used in a multistring configuration. Like with string inverters, the same combinations of isolated and transformerless configurations apply with or without symmetric grid filters.

One of the first multistring inverters introduced in practice was the half bridge inverter with boost converters in the DC-DC stage by SMA [206]. Other topologies that have followed include the H-bridge, the H5, the 3-phase 2-level voltage source inverter (2L-VSI), the 3L-NPC, and the 3-phase 3-level T-type converter (3L-T) [207]. Figure 4.4 shows some examples of practical multistring configurations. The most common DC-DC stages

used for multistring configurations are the boost converter and the HF isolated DC–DC switch mode converter based on an H-bridge, HF transformer, and diode rectifier.

4.5.3 Central Topologies

Central inverter configurations are mainly used to interface large PV systems to the grid. The most common inverter topology found in practice is the 2L-VSI, composed of three half-bridge phase legs connected to a single DC link. The inverter operates below 1,000 V at the DC side (typically between 500 and 800 V), limited by the PV module's insulation, which prevents larger strings. Grid connection is done through a LF transformer to elevate the voltage already within the collector of the power plant to reduce losses. More recently, the 3-phase 3L-NPC and the 3-phase 3L-T converter have been also used for this configuration (Figure 4.4). The characteristics, advantages, and disadvantages analyzed for the 1-phase versions of these topologies for PV string systems also hold for the central inverter version.

4.5.4 AC-Module Topologies

A commercial AC-module topology is the interleaved Flyback converter (Figure 4.4), developed by Enphase Energy [214]. The converter performs MPPT and voltage elevation and provides galvanic isolation while the H-bridge inverter controls the link voltage, grid synchronization, and active/reactive power control. Several Flyback converters are connected in parallel, which enables a higher switching frequency, resulting in a further reduction of the HF transformer and, hence, a very compact inverter. It also allows for a reduction in the current ripple both at the input and output of the DC-DC stage due to the phase-shifted carrier modulation, extending the life span of the capacitors.

Another commercial AC-module integrated converter (Figure 4.4), includes a resonant H-bridge stage with an HF isolation transformer and a diode bridge rectifier as a DC-DC converter instead of the Flyback developed by Enecsys [215]. The H-bridge DC-DC stage has better power conversion properties when compared to the Flyback.

4.6 Impact of Inverter Configuration on Energy Cost of Grid-Connected PV Systems

References [216], [217] present an overview of the state-of-the-art for PV inverters used in low voltage grid-connected PV systems: Different aspects with respect to performance of some PV grid-installation have been analyzed. Reference [218] studied the impact of inverter configuration on energy yield based on a simple efficiency model. Reference [219] optimized the selection and configuration of PV modules and inverters based on a generalized PV system model to maximize the net profit. The efficiency and reliability of inverters were not modeled in detail in such a complicated problem. Reference [220] introduced a reliability model to energy yield estimation to compare central inverters and module integrated inverters. However, they did not take into account environmental conditions and inverter efficiency characteristics. Reference [221] suggested that energy yield and levelized cost of energy (LCOE) should be estimated considering the PV array scale, environmental conditions, system cost, inverter efficiency and reliability. The efficiency characteristic of parallel inverters with a common DC bus is discussed along with the optimal operation strategy. Inverter system performance ratio (ISPR) is proposed as an overall index of lifetime energy conversion efficiency. It shows that the configuration with a common DC bus is a potential solution to reduce the energy cost of PV power generation systems. As a result, it is found that optimizing the PV panel orientation can improve the probability distribution of solar irradiance on the panel, and it is confirmed that an oversized PV array may help reduce the energy cost.

TABLE 4.2: A GRID-CONNECTED PV ENERGY CONVERSION SYSTEMS CONFIGURATIONS OVERVIEW

		Small Scale	Medium Scale		Large Scale
		AC Module	String	Multistring	Central
Power Range		< 350 W	< 10 kW	< 500 kW	< 850 kW (< 1.6 MW for dual)
Devices		MOSFET	MOSFET & IGBT	MOSFET & IGBT	IGBT
MPPT Efficiency		Highest (one module—one MPPT)	Good (one large string—one MPPT)	High (one small string—one MPPT)	Good (one array—one MPPT)
Converter Efficiency		Lowest (up to 96.5%)	High (up to 97.8%)	High (up to 98%)	Highest (up to 98.6%)
Features	Positive	<ul style="list-style-type: none"> ▪ Flexible/modular. ▪ Highest MPPT efficiency. ▪ Easy installation. 	<ul style="list-style-type: none"> ▪ Good MPPT efficiency. ▪ Reduced DC wiring. ▪ Transformerless (very common). 	<ul style="list-style-type: none"> ▪ Flexible/modular. ▪ High MPPT efficiency. ▪ Low cost for multiple string system. 	<ul style="list-style-type: none"> ▪ Simple structure. ▪ Highest converter efficiency. ▪ Reliable.
	Negative	<ul style="list-style-type: none"> ▪ Higher losses. ▪ Higher cost per watt. ▪ Two stage is mandatory. 	<ul style="list-style-type: none"> ▪ High component count. ▪ One string, one inverter. 	<ul style="list-style-type: none"> ▪ Two stage is mandatory. 	<ul style="list-style-type: none"> ▪ Needs blocking diodes (for array). ▪ Poor MPPT performance. ▪ Not flexible.
Examples		Power One Aurora MICRO-0.3-I and Siemens SMIINV215R 60	Danfoss DLX 4.6 and ABB PVS 300	SMA SB5000TL and SATCON Solstice	SMA MV Power Platform and 1.6 Siemens SINVERT PVS630

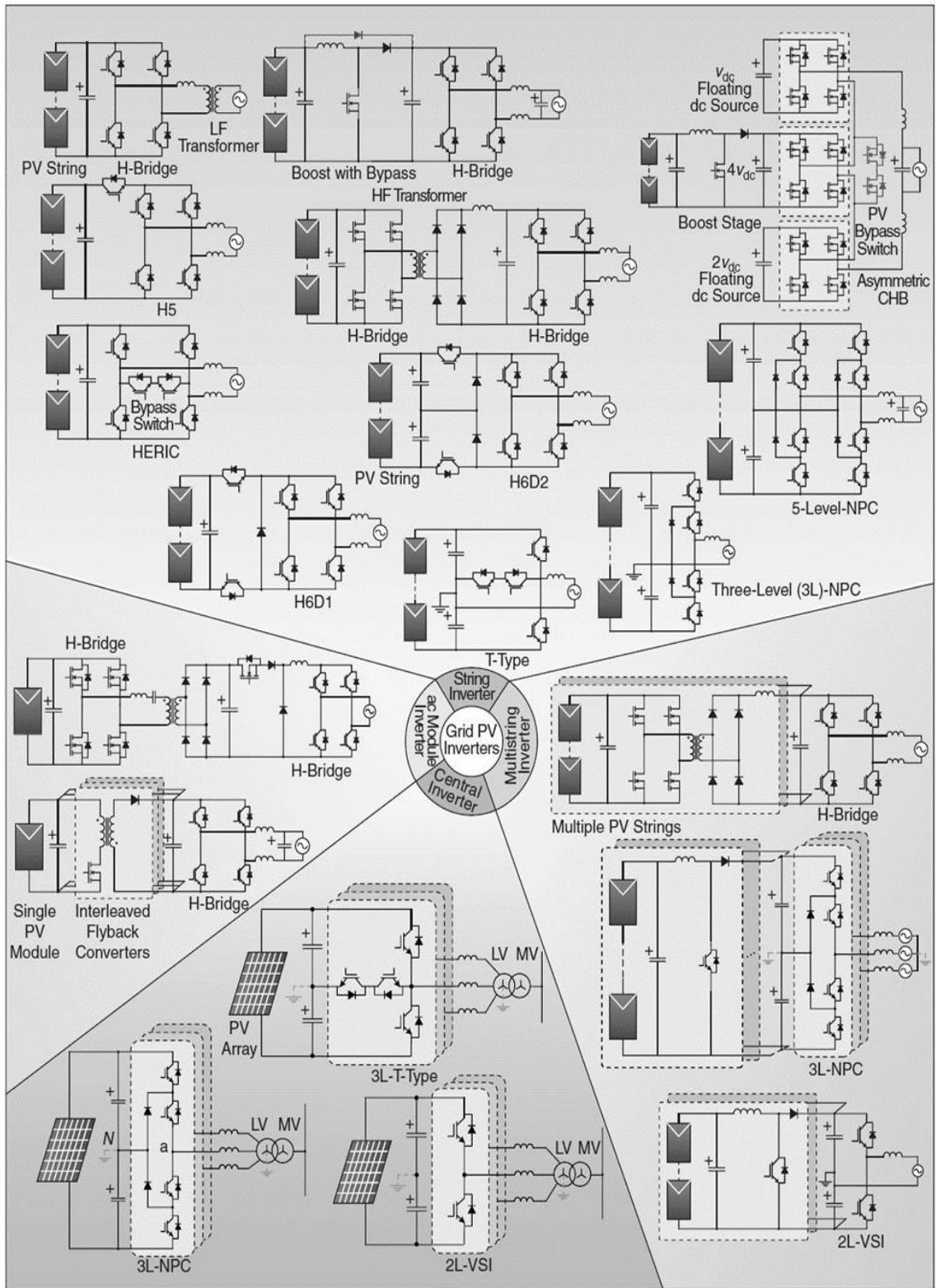


Figure 4.4: Industrial PV inverter topologies for central, string, multistring, and AC-module configurations. (MV: medium voltage; 2L-VSI: 2-level voltage source inverter). [222]

TABLE 4.3: A SUMMARY OF CHARACTERISTICS AND EXAMPLES OF SELECTED INDUSTRIAL PV INVERTER TOPOLOGIES

Topology	2L-VSI	HERIC	3L-NPC	H-NPC	1:2:4-CHB	H5	HF H-BRIDGE DC-DC	HF FLYBACK DC-DC
Pros	<ul style="list-style-type: none"> ▪ Simple ▪ Robust ▪ Large capacity 	<ul style="list-style-type: none"> ▪ No freewheeling current losses ▪ Transformer-less 	<ul style="list-style-type: none"> ▪ Constant CM voltage ▪ Low THD 	<ul style="list-style-type: none"> ▪ Low THD ▪ Transformer-less 	<ul style="list-style-type: none"> ▪ High power quality ▪ Transformer-less 	<ul style="list-style-type: none"> ▪ No freewheeling current losses ▪ Transformer-less 	<ul style="list-style-type: none"> ▪ Small ▪ Compact ▪ Easy installation 	<ul style="list-style-type: none"> ▪ Small ▪ Compact ▪ Easy installation
Cons	<ul style="list-style-type: none"> ▪ Higher THD ▪ Large transformer ▪ Poor MPPT 	<ul style="list-style-type: none"> ▪ Bidirectional bypass switch 	<ul style="list-style-type: none"> ▪ HF isolation ▪ High number of devices 	<ul style="list-style-type: none"> ▪ No 5 level waveform ▪ High number of devices 	<ul style="list-style-type: none"> ▪ Complex module ▪ Complex control 	<ul style="list-style-type: none"> ▪ Special PWM modulation 	<ul style="list-style-type: none"> ▪ High input-output voltage ratio ▪ Soft switching 	<ul style="list-style-type: none"> ▪ High input-output voltage ratio ▪ Less efficient HF transformer concept
Configuration	Central	String	String	String	String	Multistring	AC module	AC module
Input voltage	550-850 V	900 V	600 V	900 V	380 V	750 V	60 V	45 V
Rated AC power	1.5 MW	4.8 kW	4.8 kW	8 kW	4 kW	5,250 W	200 and 300 W	190-260 W
Grid connection	Three phase	Single phase	Single phase	Single phase	Single phase	Single phase	Single phase	Single, three phase
Efficiency	98.5%	97.8%	97.3%	97%	97.5%	97.0%	96.5%	96.3%
Isolation	LF transformer	Transformer-less	HF transformer	Transformer-less	Transformer-less	Transformer-less	HF transformer	HF transformer

Number of independent MPPT	Two arrays	One string	One string	One string	One string	Two string	One module	One module
Brand / model	Satcon Prism Platform Equinox	Sunways NT 5000	Danfoss DLX 4.6	ABB PVS 300 TL 8000	Mitsubishi PV-PN40G	SMA Sunny Boy 5000TL	Power One Aurora MICRO-0.3-I	Siemens Microinverter System

4.7 Recent Advances in Grid-Connected PV Inverters

The last decade has seen marked progress in the research and development of new power converter topologies for PV applications. The research efforts have concentrated on efficiency, power density, and reliability of the converter to further increase the overall performance of the PV installation. In the majority of cases, the new topologies are the full-power converters in which the total PV panel (or PV string) power has to be processed.

4.7.1 Advances in DC–AC Converters for PV Systems

As shown in Figure 4.2, in a typical PV inverter, the two-stage power conversion is currently the most common approach to cope with a wide input DC voltage range produced by the PV panel. In that case, the PV power conditioning system consists of the front-end DC–DC converter for the MPPT and the inverter to feed the power to the AC load or grid [223]–[225]. However, this multiple-stage power conversion system could lower the efficiency and reliability of the PV installation. To overcome these problems, in 2003, a novel family of single-stage buck–boost inverters was introduced [226], with the most promising topology being the quasi-Z-source inverter (qZSI) [227]. This buck–boost inverter is a combination of the two-port passive quasi-impedance network with a 2L-VSI [Figure 4.5(a)]. The distinctive feature of the qZSI is that it can boost the input voltage by using an extra switching state—the shoot-through state. The shoot-through state is the simultaneous conduction of both switches of the same phase leg of the inverter. This operation state is forbidden for traditional VSI because it causes the short circuit of the DC-link capacitors. In the qZSI, the shoot-through state is used to boost the magnetic energy stored in the inductors of the quasi-Z-source network without short-circuiting the DC capacitors. This increase in inductive energy, in turn, provides the boost of the voltage across the inverter during the traditional operating states (active states). The qZSI has the input inductor that buffers the source current, which means that during the continuous conduction mode, the input current never drops to zero, thus featuring the reduced stress of the input voltage source. Moreover, the properties of the qZSI allow the energy storage (typically the battery) to be connected in parallel with one of the capacitors of the quasi-Z-source network [228]. The state of charge of the battery is then controlled by varying the

shoot-through duty cycle of the inverter switches. Therefore, the simple energy storage system for covering the peak power demands could be used in the qZSI without any additional circuits. The two-level qZSI could be easily extended to the multilevel topology, as presented in Figure 4.5(b). The 3-level NPC qZSI has similar advantages as the 2-level topology; moreover, it could be used with single or multiple PV sources [229]. As in the case of 2-level qZSI, the short-term energy storage (battery) can be connected in parallel either with the external or internal capacitors of the quasi-Z-source-network. Thanks to all of these advantages, the qZSI is referred to as one of the most promising power conversion approaches for future PV power conditioners.

Another hot topic regarding recent PV inverters is the use of different multilevel converter topologies to enable medium-voltage (MV) grid connection. Most commercial topologies shown in Figure 4.4 are in fact multilevel converters (e.g., 3-level H-bridge, 3-level NPC, 3-level T-type, and their derivatives). However, all of these converters connect to LV grids since PV strings cannot surpass the 1,000 V limit due to the module insulation standard. Therefore, to be able to connect to MV grids, the multilevel converters must be able to support several individual strings at the DC side and connect them somehow in series through the converter power stages to the output. Several alternative topologies have been introduced to achieve a high number of levels and reach MV operation [230]–[237]. An advantage of using multilevel converters as PV inverters is related to the output waveform's high quality, which reduces the grid connection filter requirements, leading to a compact design for low-power applications (usually domestic rooftops). In addition, the use of multilevel converters can lead to avoidance of the additional boost converter in the input or the step-up transformer in the output, eliminating the additional power conversion stages and improving the efficiency of the system. On the other hand, some multilevel converter topologies, such as the cascaded H-bridge converter or the modular multilevel converter, can take advantage of splitting the PV array system to achieve higher efficiency values using independent MPPT algorithms. This could be interesting for central inverters of PV medium and high-power plants [233]–[237].

Another research focus involves developing PV inverters with additional energy storage capability usually based on batteries. These hybrid systems present the advantages of improving the frequency and voltage regulation, storing the energy if it is not demanded

by local loads, and supplying this energy when required, increasing the overall system operation (usually called peak load shaving). These systems are mainly focused for stand-alone systems, household applications, or weak grid-connected applications of large PV plants [238]–[241]. The use of hybrid PV batteries can already be found as a commercial product for household applications (for instance, the Sunny Boy 3600/5000 Smart Energy by SMA) [242]. This trend emerges as an important field of development for the future.

On the other hand, it is important to note that the high penetration of PV systems has led to the consideration of future regulations following the path already written by the wind energy sector. In this way, future regulations about LV ride-through and reactive power compensation could be also applied to medium and large PV systems [243], [244]. This issue will become particularly important for large PV plants normally using conventional two-level, 3-phase central inverters. Future regulations may force the power conversion stage to upgrade and motivate the introduction of more advanced multilevel converters and include energy storage to meet grid codes and provide system operational flexibility.

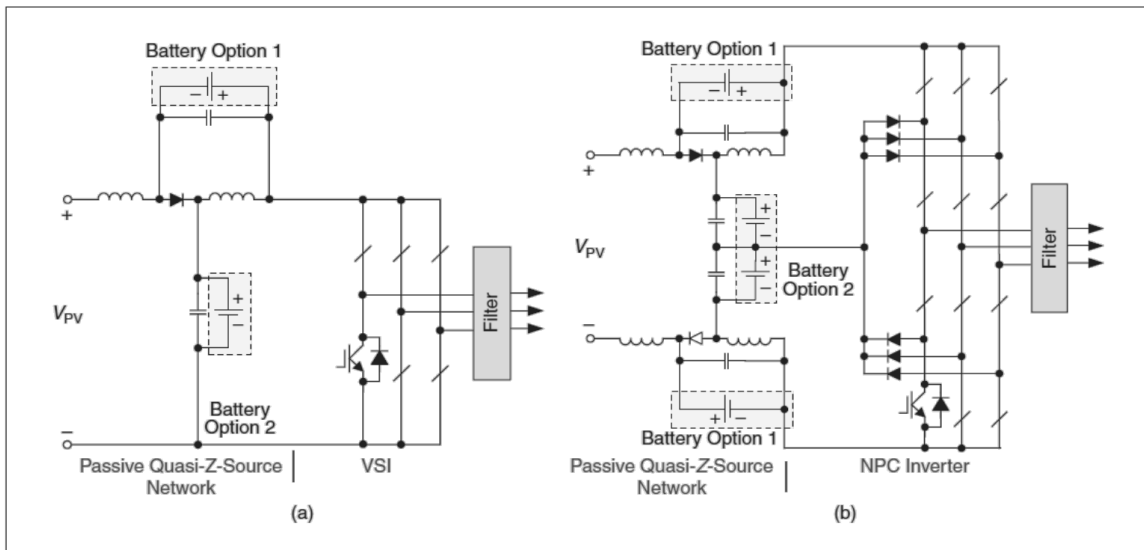


Figure 4.5: Generalized topologies of the most popular single-stage buck-boost inverters: (a) 2-level [227] and (b) 3-L NPC quasi-Z-source inverters [229]

4.7.2 Advances in DC–DC Converters for PV Systems

As indicated in Figure 4.2, the DC–DC conversion stage is usually introduced to adapt the PV array voltage range to the DC bus of the PV inverter, and it simultaneously develops the MPPT control.

Related to this issue, another topic of growing interest in the PV topologies has emerged in the field of module integrated converters (MICs). Generally, a MIC is a self-powered, high-efficiency, step-up DC–DC converter with galvanic isolation that operates with autonomous control and is integrated to the PV panel for tracking the maximum power point locally. The galvanic isolation is essential to reduce ground leakage currents and grid current total harmonic distortion [245]. As in the case of the previously mentioned PV inverters, the research trends here are directed toward the highest possible power conversion efficiency and power density. According to research survey, the resonant power conversion with the maximum possible utilization of the parasitic elements of the circuit and the wide-bandgap semiconductors is the most popular approach for MIC performance improvement.

Generally, MICs can be categorized as topologies either with a double- or single-stage power conversion. In the first case, the auxiliary boost converter steps up the varying voltage of the PV panel to a certain constant voltage level and supplies the input terminals of the isolated DC–DC converter. In that case, the primary inverter within the DC–DC converter operates with a near-constant duty cycle, thus ensuring better utilization of an isolation transformer. In [246], the combination of a synchronous boost converter with a series resonant DC–DC converter (SRC) was presented (Figure 4.6(a)). The SRC offers the advantages of high efficiency as it can operate without switching losses due to zero voltage switching (ZVS) and a high power density because of its bidirectional core excitation. The two stage structure could be simplified by the replacement of a boost converter with a passive impedance network (Figure 4.6(b)) [247]. The impedance network is a 2-port passive circuit that consists of capacitors, inductors, and diodes in a special configuration. A specific feature of the impedance network is that it can be short-circuited, which,

in turn, will lead to the voltage boost across the input terminals of the main converter [248]. Thus, the varying output voltage of the PV panel is first pre-regulated by adjusting the shoot-through duty cycle (simultaneous conduction of both switches of the same phase leg of the inverter); afterwards, the isolation transformer is supplied a voltage of constant amplitude. The impedance source DC–DC converter [249] extended by the series resonant network can minimize the switching frequency range of the traditional SRC and will lead

to a high converter efficiency over a wide input voltage and load variation range. Moreover, because of inherent short-circuit immunity, the reliability can be enhanced substantially.

In a single-stage power converter, the primary inverter operates within the wide input voltage range and the efficiency optimization could become an issue. Here, different approaches were recently studied. For example, in [250], a highly efficient multi-resonant DC–DC converter was proposed (Figure 4.6(c)). Despite its complex structure, the converter has a minimal number of external discrete components in the design of the resonant tank: the series and parallel inductances are realized by using the leakage and magnetizing inductances of the isolation transformer, respectively. The parallel capacitance is mostly formed by the sum of the parasitic capacitances of the rectifying diodes and the isolation transformer. In this converter, the carefully optimized resonant tank leads to high efficiency within a wide specified input voltage range.

Another approach to the high-efficiency resonant converter for PV MIC applications is presented in Figure 4.6(d). With the simple addition of a bidirectional AC switch across the secondary winding of the isolation transformer, the highly efficient series resonant converter is combined with both a phase-shift modulated full-bridge buck converter and a PWM boost converter to provide input voltage regulation over a wide input voltage and output power range [245]. The converter features the ZVS and/or ZCS of the primary side switches and the ZCS of the rectifying diodes, which finally results in a high efficiency within a wide operation range of the converter.

The new resonant converter topology shown in Figure 4.6(e) can operate in two resonant modes adaptively depending on the panel operation conditions, thus maintaining a high efficiency within a wide input range at different output power levels [251]. As in the case of the previous topology, the specific properties of the circuit components, such as parasitic capacitances of MOSFETs, leakage, and the magnetizing inductance of the transformers, were used as snubbers or elements of the resonant network. One of the distinctive features of this novel topology is a half-wave rectifier added to the secondary side of the auxiliary transformer. When the half-wave rectifier is enabled, together with the voltage doubler rectifier of the main circuit, it will provide the output voltage equal to their summed output voltages. The converter features ZVS for primary side switches and ZCS for rectifying diodes for both resonance modes and achieves the maximum efficiency close to 97%. In

all of the previously mentioned DC–DC converter topologies, special attention was paid to the reduction of circulation energy to further increase the power conversion efficiency.

One of the significant advantages of the high-efficiency half-bridge LLC DC–DC converter (Figure 4.6(f)) is a reduced number of primary side switches and, therefore, a simpler structure than the previous MICs. As in the previous cases, the leakage and magnetizing inductances of the isolation transformer together with the external resonant capacitor form the LLC resonant network. As a result, the main power switches can achieve ZVS and the output diodes can realize ZCS in a wide input and load range [252]. Traditionally, with the help of the voltage doubler rectifier, the high voltage gain is realized with the optimal turns-ratio of the isolation transformer.

The soft-switching current-fed push–pull converter (Figure 4.6(g)) is another realization possibility of a simplified-structure MIC. [253]. It has the advantages of a traditional current-fed push–pull converter, such as low input current stress, high voltage gain, and low conduction losses of switches. Moreover, thanks to the parallel resonance between the secondary leakage inductance of the isolation transformer and a resonant capacitor, the transistors are turned on and off at the zero-voltage and zero-current conditions. The diodes of the voltage-doubler rectifier are also turned off at zero current.

An interesting topology of the low-cost MIC was presented in [254]. The classical two-inductor isolated boost converter was further improved by use of a non-dissipative regenerative snubber along with a hysteresis controller and constant duty cycle control (Figure 4.6(h)). Furthermore, a multi-resonant tank formed by the magnetizing inductance of the transformer, its leakage inductance, and the external resonant capacitor was introduced. As a result of all of these modifications, the proposed converter features a low input current ripple, ZCS conditions for the input switches and output rectifying diodes, and improved light-load behavior.

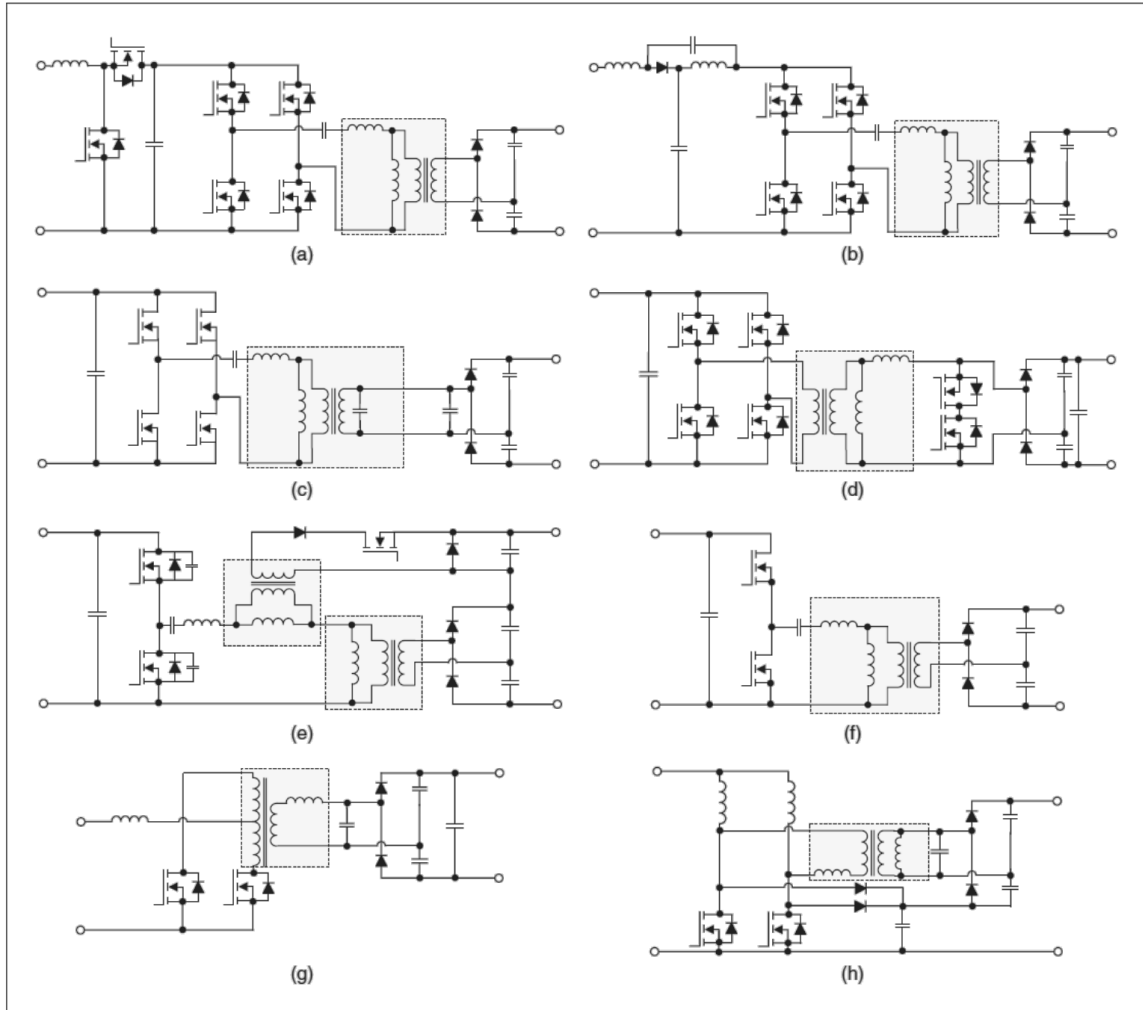


Figure 4.6: The new emerged topologies of the PV module integrated DC–DC converters: (a) a two-stage topology consisting of a synchronous boost and a series-resonant converter [246], (b) a quasi-Z-source series resonant converter [247], (c) an LLC series-parallel resonant converter [250], (d) a series resonant converter with a bidirectional AC switch [245], (e) a dual-mode resonant converter [251], (f) a half-bridge LLC resonant converter [252], (g) a parallel resonant current-fed push-pull converter [253], and (h) a multiresonant two-inductor boost converter with a nondissipative regenerative snubber [254]

4.7.3 Advances in Power Semiconductors for PV Systems

Power converters for PV systems are slowly taking advantage of the good characteristics of wide-band-gap (WBG) devices built using non-silicon materials such as SiC or GaN. The main characteristics that make WBG devices attractive as an alternative to silicon devices are:

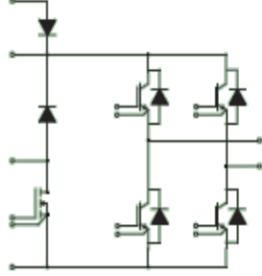
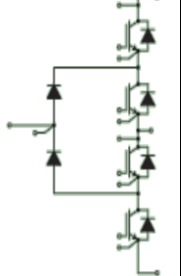
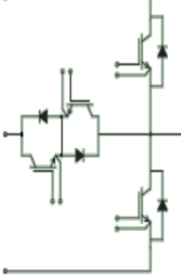
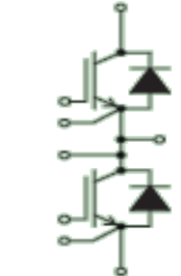
- High voltage ranks that help to build converters with larger nominal power.

- Very fast commutation, enabling high switching frequency and reducing the size, volume, weight, and cost of passive reactive components while reducing switching losses.
- High maximum working temperature, leading to an important reduction of size, volume, weight, and cost of auxiliary thermal management devices.

As an alternative to silicon devices, the cost of the WBG devices must be considered. The silicon industry takes advantage of 60 years of expertise and consequently, the production processes are very mature and well optimized. On the other hand, the new processes are still far from maturity as they are in their first steps; however, they are a very promising technology as, no doubt, the cost reductions will come gradually. It is important to highlight that the extra cost of the devices may be compensated by important reductions in the costs related to the passive reactive components and heat management. For critical applications, the reduction in size and the increase in performance can make these devices very attractive [255]–[257].

Solar power converters benefit greatly from the good characteristics of new WBG devices [245], [255]–[263]. It seems that efficiencies of more than 99.5% can be reached with SiC devices for converters in the range of 10–100 kW. Converters as small as 100 W (suitable for the panel integrated with the inverters) have been demonstrated to reach 1 MHz of switching frequency [260]. A summary of some of the power modules with SiC diodes already on the market is shown in Table 4.4.

TABLE 4.4: COMMERCIAL POWER SEMICONDUCTOR MODULES FOR GRID-CONNECTED PV INVERTERS

TOPOLOGY	H-BRIDGE + BOOST	NPC	T-TYPE	2L-VSI
Ratings	650 V @ 50 A	600 V @ 150 A	1.2 kV @ 75 A	650 V @ 300 A
Configuration	String, Multistring, AC module	Central, String, Multistring	Central, String, Multistring	Central
Circuit				
Commercial example	Infineon F4-75R07W2H3_B51	Semikron SK150MLI066T	Infineon F3L75R12W1H3_B27	Semikron SK300GB063D

4.8 Control Techniques for Grid-Connected Solar PV Inverters

The control of a grid-connected PV system can be divided into two important parts:

- 1) MPPT controller to extract the maximum power from the PV modules, and
- 2) Inverter controller, which ensures the control of active/reactive power fed to the grid; the control of DC-link voltage; high quality of the injected power and grid synchronization.

4.8.1 Maximum Power Point Tracking Controller

The basic principle of maximum power point tracking (MPPT) algorithm depends on the exploitation of voltage and current variations caused by pulsations of instantaneous power. Analyzing these variations allows us to obtain power gradient and evaluate, if the solar PV

system operates close to the maximum power point [264]. The maximum power delivered by the solar PV array is given by the relation

$$P_{max} = V_{mpp} I_{mpp}$$

where V_{mpp} and I_{mpp} are respectively the optimal operating voltage and current of PV array at the condition of maximum power output.

The solar cell exhibits non-linear V-I characteristics; therefore, a MPPT controller must track the maximum power and match the current environmental changes [265]. The MPPT is achieved by using DC-DC converter between PV array and inverter. From the measured voltage and current, the MPPT algorithm generates the optimal duty ratio (D) in order to maintain the electrical quantities at values corresponding to the maximum power point [266]. The most widely used MPPT techniques include perturbation and observation (P&O), incremental conductance, open circuit voltage, short circuit current, Fuzzy logic, and neural network based methods.

Reference [267] proposed a hybrid MPPT method which combines the P&O and particle swarm optimization (PSO) methods with advantage that search space for the PSO is reduced, and hence, the time required for convergence can be greatly improved. In [268], authors proposed a single-stage 3-phase PV system that features an enhanced MPPT capability, and an improved energy yield under partial shading conditions. A MPPT method based on controlling an AC/DC converter connected at the PV array output, such that it behaves as a constant input-power load is proposed in [269]. A one dimensional Newton-Raphson method based calculation for evaluation of MPP of PV array is proposed in [270]. Chaos search theory [271], self-synchronization error dynamics formulation [265], and ripple correlation control [264] based MPPT methods have been reported. A comparison of multiple MPPT techniques is presented in [272]. Performance comparison of various MPPT techniques applied to a 1-phase, single-stage, grid-connected PV system are presented in [273]. A comparative study of MPPT techniques for PV systems available until January 2012, is presented in [274].

A comparative study of commonly used MPPT algorithms is carried out based on critical reviews of publications [264], [265], [274], [266]–[273] cited in this subsection.

4.8.2 Inverter Controller

The control strategy applied to the inverter consists mainly of two cascaded loops. Usually, there is a fast internal current loop, which regulates the grid current, and an external voltage loop, which controls the DC-link voltage. The current loop is responsible for power quality issues and current protection; thus, harmonic compensation and dynamics are the important properties of the current controller. The DC-link voltage controller is designed for balancing the power flow in the system. Usually, the design of this external controller aims the optimal regulation and stability of systems having slow dynamics. This voltage loop is designed for a stability time higher than the internal current loop by 5 to 20 times. The internal and external loops can be considered decoupled; therefore, the transfer function of the current control loop is not considered when the voltage controller is designed [275]–[283].

In some works, the control of the inverter connected to the grid is based on a DC-link voltage loop cascaded with an inner power loop instead of a current one. In this way, the current injected into the grid is indirectly controlled.

4.8.2.1 Control structure for 3-phase inverter connected to the grid

To study stationary and dynamic regimes in 3-phase systems, the application of “vector control” (Park vector) is used for the analysis and control of DC–AC converters, enabling abstraction of differential equations that govern the behavior of the 3-phase system in independent rotating frames.

4.8.2.1.1 *dq*–control

The concept of decoupled active/reactive power control of 3-phase inverter is realized in the synchronous reference frame by using the *abc-dq* transformation for converting the grid current and voltages. In this way, the AC current is decoupled into active and reactive power components, I_d and I_q , respectively. These current components are then regulated in order to eliminate the error between the reference and measured values of the active and reactive powers. In most cases, the active power current component, I_d , is regulated

through a DC-link voltage control aiming at balancing the active power flow in the system [284]–[286]. As shown in Figure 4.7, the power control loop is followed by a current control system. By comparing the reference and measured currents, the current controller should generate the proper switching states for the inverter to eliminate the current error and produce the desired AC current waveform [287], [288]. In the case that the reactive power has to be controlled, a reactive power reference must be imposed to the system. Linear PI controller is an established reference tracking technique associated with the dq control structure due their satisfactory combinational performance. Eq. (4.1) states the transfer function on the dq coordinate structure.

$$G_{PI}^{dq}(s) = \begin{pmatrix} K_P + \frac{K_I}{s} & 0 \\ 0 & K_P + \frac{K_I}{s} \end{pmatrix} \quad (4.1)$$

where K_P is the proportional gain and K_I is the integral gain of the controller.

For improving the performance of PI controller in such a structure (Figure 4.7), cross-coupling terms and voltage feed forward are usually used [281]–[283]. In any case, with all these improvements, the compensation capability of the low-order harmonics in the case of PI controllers is very poor. References [289]–[292] propose the use of PR+HC controller to improve the system dynamic response, harmonic distortion, eliminate steady state error and prevent the use of the feed-forward. The phase-locked loop (PLL) technique [279], [280] is usually used in extracting the phase angle of the grid voltages in the case of PV systems.

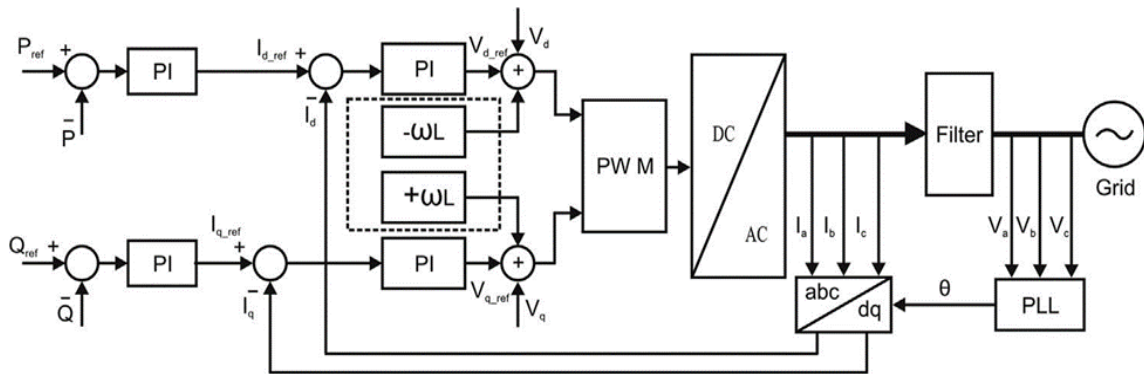


Figure 4.7: General structure for dq control strategy

4.8.2.1.2 $\alpha\beta$ -control

In this case, the grid currents are transformed into a stationary reference frame using the $abc \rightarrow \alpha\beta$ module [283], [284], [293], [285]–[292], as shown in Figure 4.8. The abc control is to have an individual controller for each grid current; characteristic to this controller is the fact that it achieves a very high gain around the resonance frequency, thus being capable of eliminating the steady-state error between the controlled signal and its reference. High dynamic characteristics of the Proportional Resonant (PR) controller have been reported in different works, and which is gaining common popularity in the current control for networked systems, is an alternative solution for performance under the proportional integral (PI) controller. The basic operation of the controller (PR) is based on the introduction of an infinite gain at the resonant frequency to eliminate the steady state error at this frequency between the control signal and the reference. It does not require the use of feed forward [291]–[294]. The transfer matrix of the PR controller in the stationary reference frame is given by:

$$G_{PR}^{\alpha\beta}(s) = \begin{pmatrix} K_P + \frac{K_I}{s^2 + \omega^2} & 0 \\ 0 & K_P + \frac{K_I}{s^2 + \omega^2} \end{pmatrix} \quad (4.2)$$

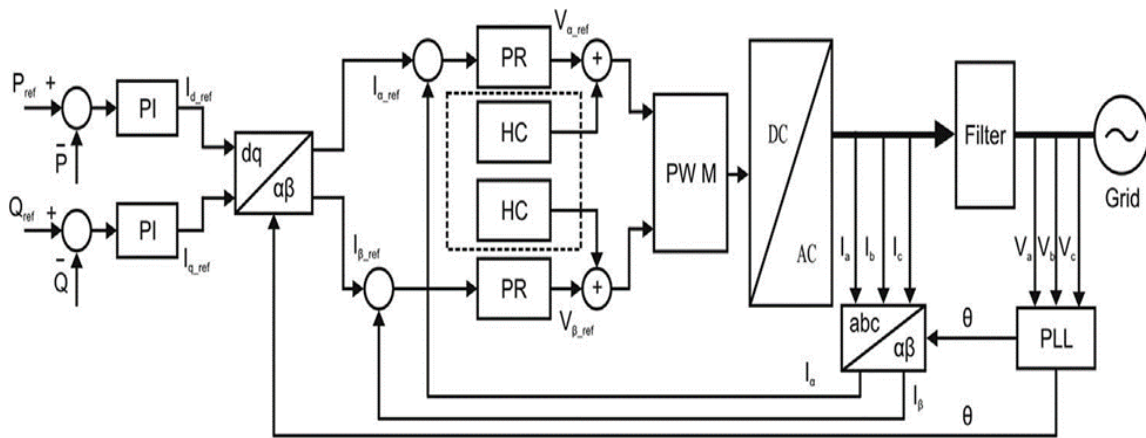


Figure 4.8: General structure for $\alpha\beta$ control strategy

4.8.2.1.3 *abc*-control

As mentioned in [283], in *abc* control an individual controller for each grid current is used. However, in any case, having three independent controllers is possible by having extra considerations in the controller design. *abc* control is a structure where nonlinear controllers like hysteresis or dead-beat are preferred due to their high dynamics. The performance of these controllers is proportional to the sampling frequency; hence, the employment of digital signal processors (DSPs) or field-programmable gate array (FPGA) is an advantage for such an implementation. A possible implementation of *abc* control is depicted in Figure 4.9 [283], where the output of DC-link voltage controller sets the active current reference. Using the phase angle of the grid voltages provided by a PLL system, the three current references are created. Each of them is compared with the corresponding measured current, and the error goes into the controller. If hysteresis or dead-beat controllers are employed in the current loop, the modulator is not necessary. The output of these controllers are the switching states for the switches in the power converter. In the case that three PI or PR controllers are used, the modulator is necessary to create the duty cycles for the PWM pattern.

The PI controller is widely used in conjunction with the *dq* control, but its implementation in the *abc* frame is also possible, as described in [282]. The implementation of PR controller in *abc* is simple since the controller is already in a stationary frame and the implementation of three controllers is possible as expressed in Eq. (4.3). Table 4.5 summarizes the pros and cons of control structures in 3-phase inverters.

$$G_{PR}^{abc}(s) = \begin{pmatrix} K_P + \frac{K_I}{s^2 + \omega^2} & 0 & 0 \\ 0 & K_P + \frac{K_I}{s^2 + \omega^2} & 0 \\ 0 & 0 & K_P + \frac{K_I}{s^2 + \omega^2} \end{pmatrix} \quad (4.3)$$

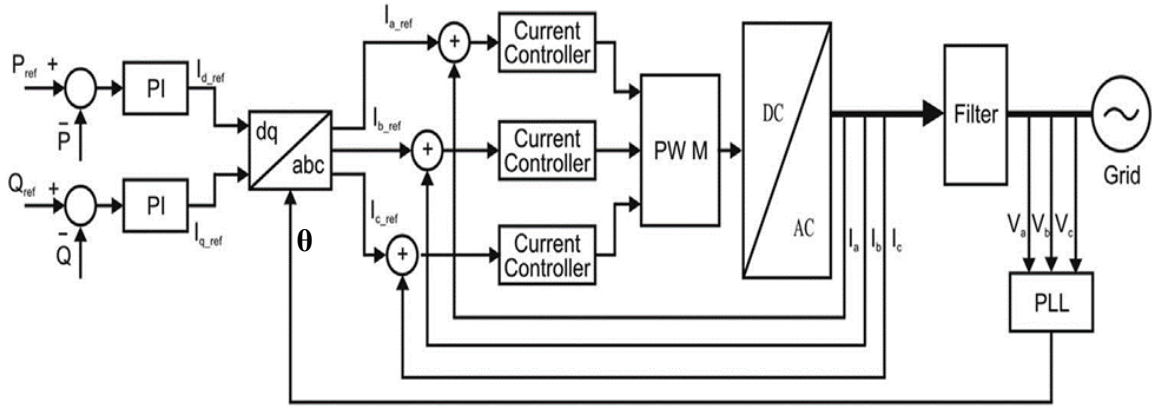


Figure 4.9: General structure for *abc* control strategy [283]

TABLE 4.5: ADVANTAGES AND DISADVANTAGES OF CONTROL STRUCTURES FOR THREE PHASE INVERTERS

Control strategies	Associated controller type	Advantages	Disadvantages
<i>dq</i> -control	PI	<ul style="list-style-type: none"> Filtering and controlling can be easier achieved Simplicity 	<ul style="list-style-type: none"> Very poor compensation capability of the low-order harmonics The steady-state error is not eliminated
<i>αβ</i> -control	PR	<ul style="list-style-type: none"> Very high gain around the resonance frequency is achieved The steady-state error is eliminated High dynamic 	<ul style="list-style-type: none"> No full control of PF Complex Hardware circuit
<i>abc</i> -control	PI	<ul style="list-style-type: none"> 	<ul style="list-style-type: none"> The transfer function is complex
	PR	<ul style="list-style-type: none"> The transfer function is simple 	<ul style="list-style-type: none"> More complex than hysteresis and Dead beat
	Hysteresis	<ul style="list-style-type: none"> High dynamic Rapid development 	<ul style="list-style-type: none"> High complexity of the control for current regulation
	Dead-Beat	<ul style="list-style-type: none"> Simple control for current regulation High dynamic Rapid development 	<ul style="list-style-type: none"> Implementation in high frequency micro controller

4.8.2.2 1-phase inverters

The control structures for 1-phase grid-connected inverters fall into three categories:

- 1) Control structure for 1-phase inverter with DC-DC converter,
- 2) Control structure for 1-phase inverter without DC-DC converter, and
- 3) Control structure based on power control shifting phase (PCSP).

4.8.2.2.1 Control structure for 1-phase with DC–DC converter

The control structure for the 1-phase with DC–DC converter, proposed in [279], [280], [289], [281]–[288], is shown in Figure 4.10. The most common control structure for the DC–AC grid converter is a current-controlled H-bridge PWM inverter having low-pass output filters. Typically, L filters are used but the new trend is to use LCL filters that have a higher order, which leads to more compact designs:

- Control of instantaneous current values
- Current is injected in phase with the grid voltage (i.e. PF=1)
- Use PLL for synchronization of the current I_{grid} and V_{grid} .

In order to control the output DC-voltage to a desired value, an inverter control system which can automatically adjust the duty cycle is needed (Figure 4.10). This controller has two control loops: the internal current control loop and the external DC-bus voltage control loop.

- The internal control loop is used to control the instantaneous values of AC current in order to generate a sinusoidal current in phase with the grid voltage. The reference current I_{ref} , is generated from a PLL sinusoidal signal reference which synchronizes the output inverter current with grid voltage [279]. The current amplitude is regulated from the external voltage loop.
- The external loop ensures the regulation of DC-bus voltage V_{DC} . It is necessary to limit the V_{DC} voltage, however, the control of V_{DC} guarantees the regulation of power injected into the grid.

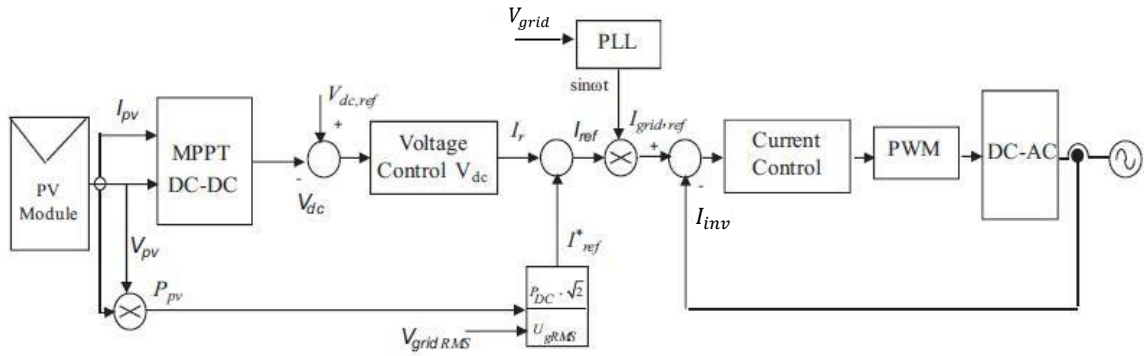


Figure 4.10: Control structure topology for 1-phase with DC-DC converter

In Figure 4.11 [275], a control structure for topology with DC-DC converter and L filter is presented. In this case, the reference current I_{ref} , is generated from the sinusoidal signal reference determined from a grid voltage sample. This structure is associated with PI controllers. To improve the performance of the PI controller in such a current control structure and to cancel the voltage ripples of the PV generator, due to variations in the instantaneous power flow through the PV system which depend on the change of atmospheric conditions (mainly the irradiance and temperature), the faster response of the boost control loop, the inverter and the DC bus capacitor is required. On the other hand, the output voltage (the main voltage) represents an external disturbance of considerable magnitude at 60 Hz for the system. There exists a compensation of these effects at the output of the PI controller so as to calculate directly the reference voltage for the inductance [275]. Figure 4.12 shows the control loop of the inverter output current.

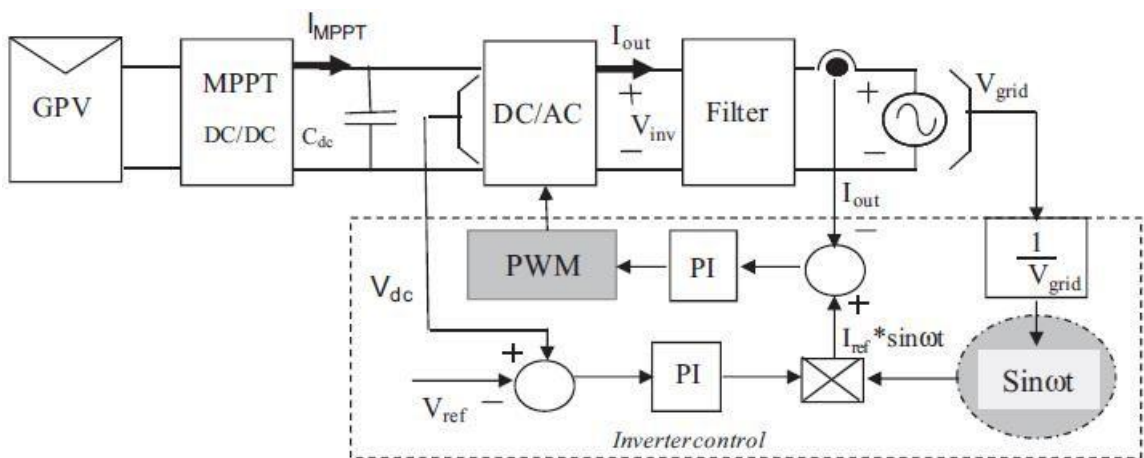


Figure 4.11: Control structure with DC-DC converter and L filter

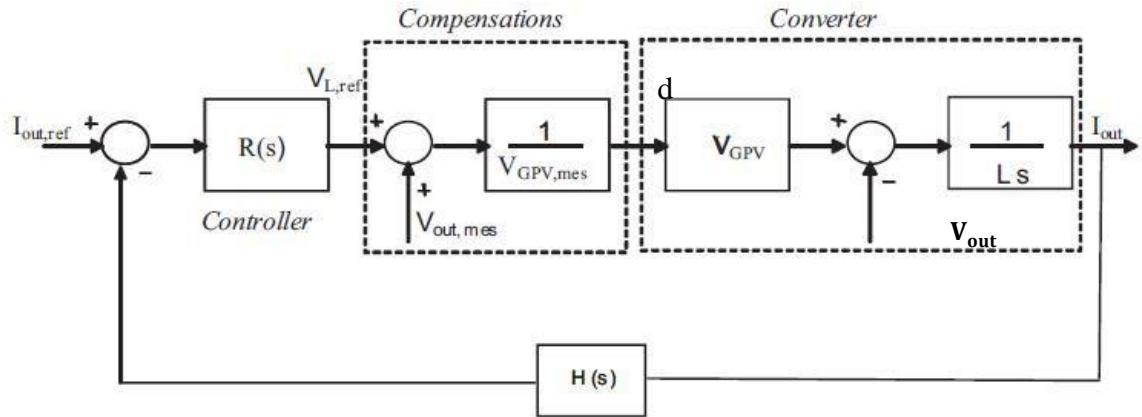


Figure 4.12: Control loop structure of the inverter output current

The inverter output current expression is given by:

$$I_{out}(s) = \frac{d \times V_{GPV}(s) - V_{out}(s)}{Ls} \quad (4.4)$$

The feed-forward technique [275] is based on including new terms to control variables, in this case the duty cycle (d), in order to eliminate the dependence related to the perturbations of control system.

To compensate the effect of output voltage, the average and filtered output voltage values, called $V_{out,mes}$, are used in Figure 4.12. However, to compensate the voltage V_{GPV} , it is necessary to use, the measured value before filtering. In this case, it is necessary to calculate the duty cycle (d) as following:

$$d = \frac{V_{L,ref} + V_{out,mes}}{V_{GPV,mes}} \quad (4.5)$$

as K_{sv} is the same step of the measured circuits. So,

$$d = \frac{V_{L,ref} + K_{sv}V_{out}}{K_{sv}V_{GPV}} \quad (4.6)$$

Hence, the inductance voltage V_L can be deduced as:

$$V_L = dV_{\text{GPV}} - V_{\text{out}} = \frac{V_{L,\text{ref}}}{K_{\text{sv}}} \quad (4.7)$$

The advantage of this control structure is the control of the instantaneous power injected into the grid from the solar module and the synchronization of the current signal with the grid voltage (i.e. to keep the voltage and current in phase) which guarantees unity PF and improves the MPPT dynamic. The disadvantage is the noise in the inverter output current signal due to the use of the grid signal sample for generating and synchronizing the reference current with the grid signal.

References [279], [280] propose a control structure for topologies with DC–DC converter and LCL filter as shown in Figure 4.13. This structure has the following characteristics:

- Typical structure for powers up to 5 kW max.
- PI controller (Proportional Integral) or PR (Proportional Resonant) for current control.
- PWM control, hysteresis or predictive.
- PI controller for voltage control.
- Optional transformer.

The principal elements of this control structure are the control algorithm based on the PLL, the MPPT and the control of the provided power and the injected current into the grid.

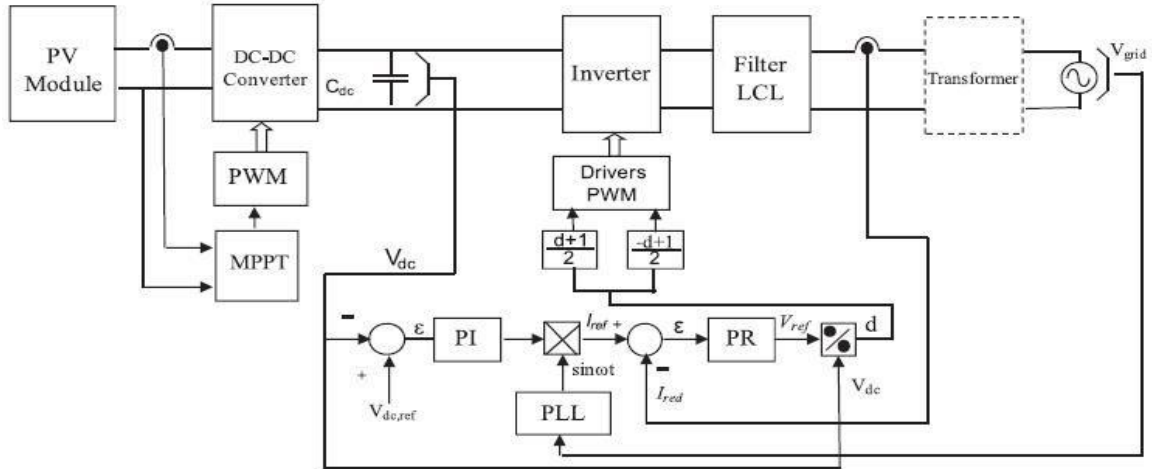


Figure 4.13: Control structure with DC-DC converter and LCL filter [279]

4.8.2.2.2 Control structure for 1-phase system without DC-DC converter

In Figure 4.14 shows the control structure for 1-phase system without DC-DC converter [289]. The same control loops are used: the internal current one and the external voltage loop [291]. The difference with respect to the control structure for topologies with DC-DC converter, the DC-AC inverter determines the maximum power point.

Another control structure is proposed in [279]; here the power control is based on the current control injected into the grid. The power control structure for the PV system connected to the grid is in the range of 1–5 kW. The full bridge inverter connected to the grid across the LCL filter is shown in Figure 4.15. This power control structure is divided principally on the synchronize algorithm based on the PLL, a MPPT, the input power control of the continuous side and the injected current control into the grid.

- *PLL*: used for the synchronization of the inverter output current with the grid voltage, the PF equal to the unity, also allowing for the generation of the sinusoidal and clean reference signal [280], [295]–[297].
- *Input power control*: In this case, the control strategy for power configuration of PV system uses a feed-forward and does not include the DC-DC converter is presented in Figure 4.16. The amplitude value of the reference current is calculated from the solar modules power P_{pv} and the RMS voltage grid ($V_{grid, RMS}$), adding the controller value (I_r) of the output continued DC bus (V_{dc}). The result is

expressed with the amplitude reference (I_{ref}) as shown in Figure 16 [279]. The use of the feed-forward improves the dynamic response of the PV system. The DC bus voltage controller ensures a fast PV system response to the input power change [275], [279].

- *Current control*: the PI controller is used with the feed-forward technique of the grid voltage as shown in Figure 4.17. The transfer function of the PI controller, $G_{PI}(s)$ is defined as:

$$G_{PI}(s) = K_P + \frac{K_I}{s} \quad (4.8)$$

As mentioned previously, the feed-forward technique improves the dynamic response. This guarantees the stability of perturbations in the system introduced by the feedback voltage [279], [280], [289], [290] and proposes an alternative solution for the poor performances of the PI controller, which includes the use of the proportional resonant controller PR.

The current loop of the PV inverter with the PR controller is presented in Figure 4.18. The transfer function of the PR current controller is defined in [281], [282], [290], [298] as:

$$G_c(s) = K_p + K_I \frac{s}{s^2 + \omega_0^2} \quad (4.9)$$

and the transfer function $G_h(s)$ of the harmonic compensator (HC) is defined in [289] as:

$$G_h(s) = \sum_{h=3,5,7} K_{Ih} \frac{s}{s^2 + (\omega_0 h)^2} \quad (4.10)$$

The HC is designed to compensate for the 3rd, 5th and 7th harmonics as they are the most predominant ones in the current spectrum.

In this case, it is shown that the use of the PR+HC controller gives a better dynamic response of the system, very low harmonic distortion (0.5%) and eliminates the error in the

steady state without using the feed-forward technique. Adding the HC to the proportional resonant (PR) controller makes the system more reliable with better elimination of harmonics.

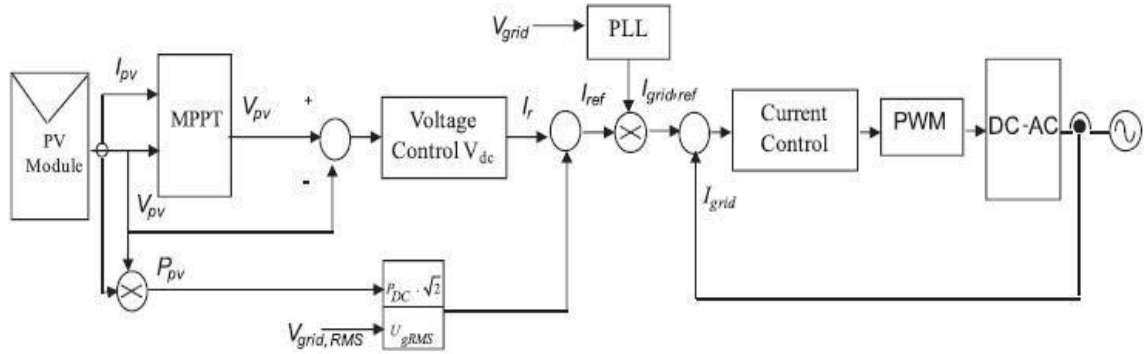


Figure 4.14: Control structure for single phase without DC-DC converter

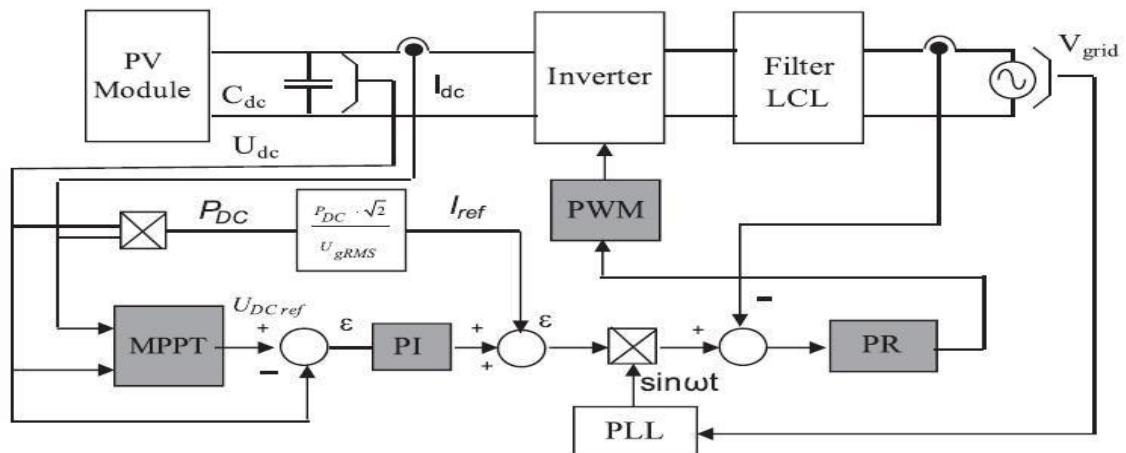


Figure 4.15: Injected power control structure [279]

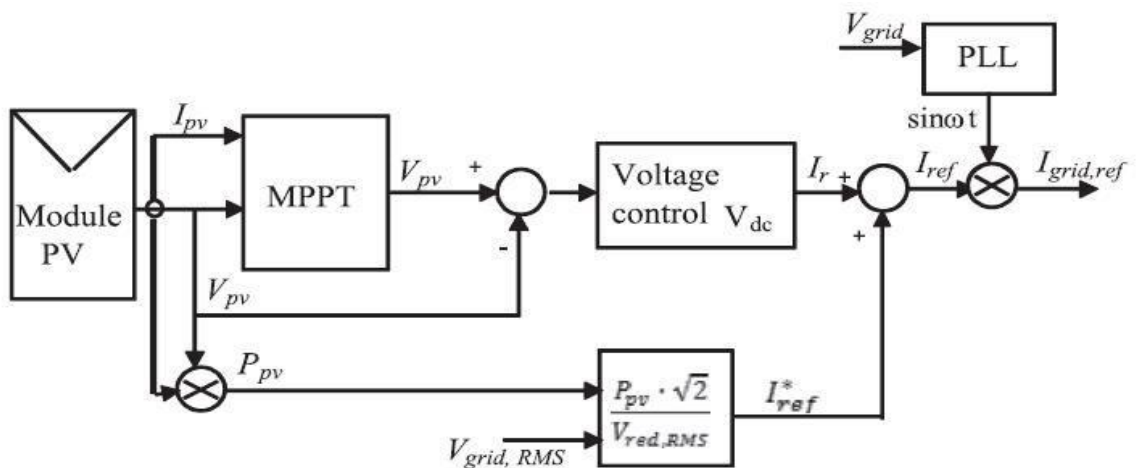


Figure 4.16: Control structure of input power (Solar panel power)

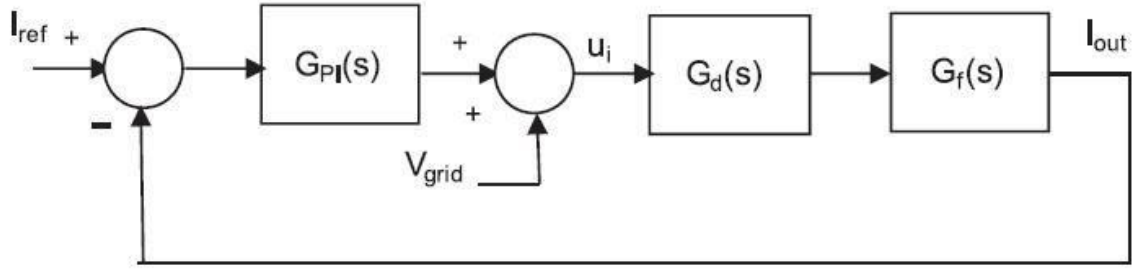


Figure 4.17: Inverter current loop with PI controller

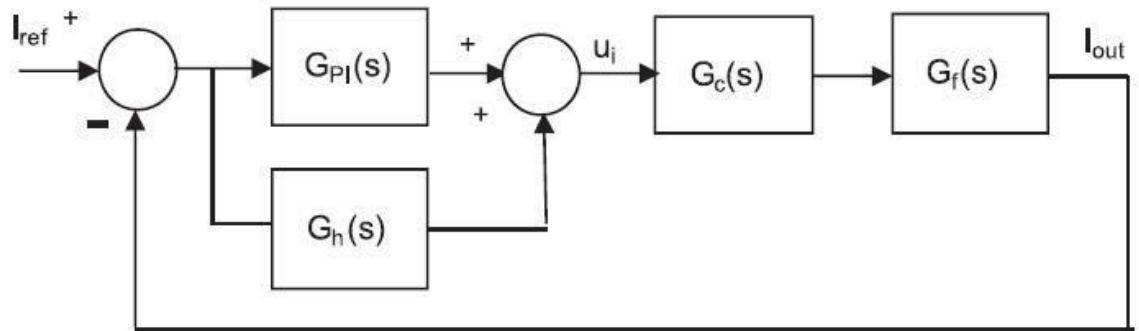


Figure 4.18: Inverter current loop with PR controller

4.8.2.2.3 Control structure based on power control shifting phase (PCSP)

Figure 4.19 shows the control structure for a PWM 1-phase inverter connected to the grid as proposed in [299], [300]. The PV system consists of a photovoltaic generator (PVG), a MPPT block and a PWM 1-phase inverter (DC-AC).

The DC-DC converter is employed to boost the PV array voltage to an appropriate level based on the magnitude of utility voltage, while the controller of the DC-DC converter is designed to operate at the maximum power point (MPP) to increase the economic feasibility of the PV system. Several algorithms can be used in order to implement the MPPT [301], [302]: perturb and observe, incremental conductance, parasitic capacitance, constant voltage etc.. For the MPPT controller, the perturb and observe method is adopted owing to its simple structure and the fact that it requires fewer measured parameters. This strategy is implemented to operate under rapidly changing solar radiation in a power PV grid connected system, using only one variable: PV output current.

The control loop for the PWM inverter is assured by the output current control, the DC bus control and synchronizing to the grid, to inject power into the grid at all time. In this

case the voltage at the Point of Common Coupling (PCC); the point where the load would be connected in parallel to the two sources), is not considering. The inverter is decoupled of the grid. The output voltage of the PWM inverter is already set by the utility PV modules. Therefore, the inverter is current controlled to ensure only power injection into the grid.

The power control is obtained by means of the inverter output voltage shifting phase, PCSP (Power Control Shifting Phase). Figure 4.19 represents a controller with two control loops: an inner one, that allows controlling the inverter output current and an outer one to control the DC bus voltage (V_{dc}).

The reference of the output current (I_{ref}) depends on the DC bus voltage (V_{dc}) and its reference (V_{ref}). A low pass filter is incorporate in order to ensure that high frequency switching noise present in the measured inverter output current signal does not pass through to the PI controller.

The control structure is associated with proportional integral (PI) controllers since they have a satisfactory behavior when regulating DC variables.

In this case the output current I_{out} is not controlled by varying the amplitude modulation index m_a , since it is considered constant, but by the phase shifting of the inverter output voltage with respect to the grid voltage. The adequate value of the phase shifting is obtained by taking into the account the zero crossing detector (ZCD) of the reference grid voltage ($V_{grid,ref}$). The digital sinusoidal pulse width modulation (DSPWM) block generates the driving signals for the PWM inverter according to the switching pattern, with the corresponding phase shifting, in order to satisfy the current reference, I_{ref} . So, the PF is indirectly controlled. As a result, a certain amount of reactive power can be generated.

The main advantage of this control strategy is its simplicity with respect to the computational requirements of the control circuit and hardware implementation. On the other hand, it allows reconfiguring the control in a fast and simple way in case that not only an active power needs to be injected but also a reactive one.

Table 4.6 resume the advantage and inconvenient of each control structures for single phase topologies.

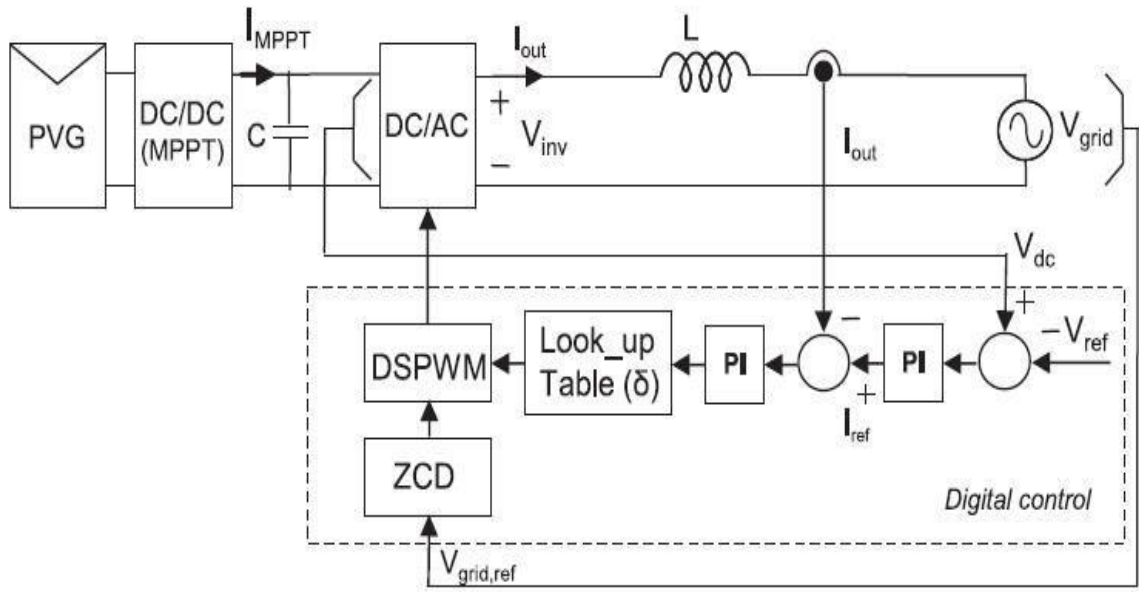


Figure 4.19: Control structure based on the shifting phase for a 1-phase inverter connected to the grid

TABLE 4.6: ADVANTAGE AND DISADVANTAGES OF CONTROL STRUCTURES FOR SINGLE PHASE INVERTERS

Topologies	Advantage	Disadvantages
Single phase inverter with DC-DC converter	<ul style="list-style-type: none"> ▪ Instantaneous current control ▪ Fast Dynamic 	<ul style="list-style-type: none"> ▪ No full control of PF ▪ Complex Hardware circuit
Single phase inverter without DC-DC converter	<ul style="list-style-type: none"> ▪ Instantaneous current control ▪ Simplicity of the conversion system ▪ Fast dynamic 	<ul style="list-style-type: none"> ▪ No full control of PF ▪ Complex Hardware circuit
Single phase inverter with PCSP	<ul style="list-style-type: none"> ▪ Simplicity ▪ Less circuitry ▪ Few resources ▪ Reactive power controlled 	<ul style="list-style-type: none"> ▪ No full control of current ▪ No fast dynamics

4.8.2.3 Reactive power requirements

PF control and reactive power regulation is the most important issue in connecting PV arrays to the grid. The grid connected inverter must be controlled in such a way that not only does it inject a current with low THD, but it also allows controlling the injected reactive power into the grid selecting a proper PF according to the grid demands. Thus, the most efficient systems are those that allow varying the power injected into the grid, both active and reactive, depending on the power grid needs [303]–[305].

Some solutions are proposed in [306]–[309] to obtain the high reliability inverter and many control techniques of grid connected PV inverter. Multiple closed loop control structure for grid current and DC link voltage are described in [310]–[314]. Other control structures consist of using a classical PI and/or bang-bang controllers are given in [315], [316]. Other authors propose the use of PLL control of the grid current in [317]–[319]. An Extended Direct Power Control (EDPC), based on geometrical considerations about inverter voltage vectors and their influences on active and reactive power change, is proposed in [320]. The input/output Feedback Linearization Control (FLC) technique widely applied on electrical motors control [321] and PWM rectifier's control [322] has been applied on PV inverters by Ref. [323], but it gives a complex model of the inverter, including switching functions.

In [324], the PF of a grid connected PV inverter is controlled using the input/output Feedback Linearization Control (FLC) technique. This technique transforms the nonlinear state model of the inverter in the dq reference frame into two equivalent linear subsystems, in order to separately control the grid PF and the DC link voltage of the inverter. This method allows control of both PF and DC link voltage using the same control algorithm. Also, in this control method, the MPP control is moved towards the DC–AC converter, hence, there is no need to use a DC–DC converter, which increases the simplicity of the conversion system. Compared to other control methods, in [299], [300], the grid PF is controlled using a previously calculated and tabulated PWM and acting on the phase shift between grid voltage and inverter output voltage as a control parameter. The proposed control strategy is capable to control, not only the current injected into the grid, but also the PF, with a minimum number of DSPWM (Digital Sinusoidal Pulse Width Modulation)

patterns. Varying the PF, within a certain range, the injected reactive power (inductive or capacitive) can be dynamically changed and controlled, in order to obtain the high reliability of the inverter. This method breaks the limitations of existing grid connected system where the inverter topology is designed to supply only active power to the grid without injecting a reactive power.

4.9 Conclusion

A comprehensive literature review of the grid-connected photovoltaic systems is carried out. This chapter presents a detailed survey on the topic of grid-connected PV system used to integrate the solar energy into the utility grid. Topologies of single-phase grid-connected inverters have been analyzed critically and comparative study of these topologies is presented. The three-phase grid-connected inverters have also been outlined. The control techniques for the single and three-phase grid-connected inverters are critically reviewed and presented.

According to the developed review, it can be concluded that the PV market has experienced exponential growth in the last decade, becoming an important alternative and a clean energy source in many countries. Along with the decrease in price and the increase in efficiency of the PV modules, the PV converter topologies have been continuously changing, following more demanding requirements and standards. These regulations are being adapted to a new power system scenario where renewable energy sources are an important part of the energy mix. Today, and meeting these legal requirements, PV converter topologies deal with issues such as high efficiency, high power density, grid code compliance, reliability, long warranties, and economic costs.

The efficiency characteristic of parallel inverters with a common DC bus is deliberated along with the optimal operation strategy. Inverter system performance ratio (ISPR) is proposed as an overall index of lifetime energy conversion efficiency. It shows that the configuration with a common DC bus is a potential solution to reduce the energy cost of PV power generation systems.

A good number of PV converter topologies can be found on the market for string, multistring, central, and AC-module PV applications. Among all of these converter

topologies, it can be affirmed that one of the most important appearances has been the multilevel converters, mainly the NPC, the T-type, and the H-bridge, not only for high-power applications but also for residential applications in the kilowatt and LV range.

In the near future, it is expected that a completely new family of PV converters will be developed based on SiC power semiconductors. (There are some commercial PV converters but only with SiC diodes.) These new SiC-based PV converters and the next-generation GaN PV converters will reduce the compromise between performance and efficiency, enabling the next generation of grid-connected PV systems.

Some implementation structures for three phase inverters, like dq , $\alpha\beta$ and abc control were reported. The PI controller is widely used in conjunction with the dq control. The implementation of PR controller in $\alpha\beta$ is commonly used. In the abc control, nonlinear controllers like hysteresis or dead beat are preferred due to their high dynamics.

A discussion of the different 1-phase inverters controllers and their ability to compensate for low-order harmonics presented in the grid was given. The PR+HC controller gives a better dynamic response of the system, very low harmonic distortion and eliminates the error in the steady state without using the feed-forward voltage. Adding the harmonic compensator to the resonant proportional controller (PR) makes the system more reliable with better elimination of harmonics.

Power factor control and reactive power regulation is known as the most important issue in connecting PV array to the grid, the control based on the Shifting Phase for Grid Connected Photo-voltaic inverter allows the control in a fast and simple way in case that not only an active power needs to be injected but also a reactive one.

Chapter 5. DC-DC Converter

5.1 Introduction

A DC-DC converter consists of a number of storage elements and switches that are connected in a topology such that the periodic switching controls the dynamic transfer of power from the input to the output, in order to produce the desired DC conversion. The basic block diagram is shown in Figure 5.1. It consists of a solar panel, DC-DC power converter, MPPT controller, and load. Initially, voltage and current from the solar panel are sensed by using sensors. These voltage and current values can be inputted to the MPPT controller. Later these values can be processed according to the MPPT algorithm used to track the maximum power point of the solar panel. The output of MPPT block is used as input to DC-DC converter as the duty cycle. DC-DC converter helps in maintaining the operating voltage at the maximum power point of the solar panel by varying the duty cycle of DC-DC converter irrespective of solar irradiance and temperature .

Usually either a Buck, Boost, or Buck-Boost configuration is used according to requirement. In this work, Boost converter is used to step-up the operating voltage to the maximum power point.

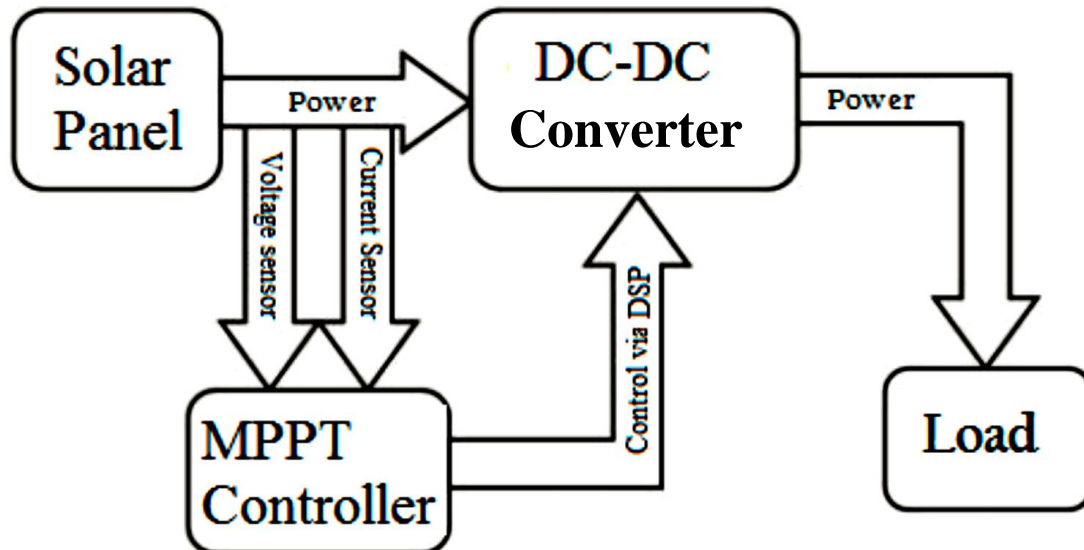


Figure 5.1: DC-DC converter for operation at the MPP

5.2 DC-DC Boost Converter

Amongst the different topologies of DC-DC converters [325], the Boost converter - with typical efficiencies of 70-95% - is the one where the output voltage is always greater than its input voltage. By comparing the Boost converter with the Buck or Buck-Boost converters, it will be found that the design of the Boost converter is more difficult where the Boost converter is considered as a non-minimum phase system and also has a zero root in the right half of the s -plane. In other words, as a result of the duty cycle which is the control input for this converter and appears in the current and voltage equations, the solution of the state-space equations of this converter are more difficult [326].

The structure of DC-DC converters consists of linear (i.e. resistor R , inductor L and capacitor C) and nonlinear (i.e. switch) components. Since these converters can be characterized as nonlinear and time-variant system, then the small-signal model of the state-space average model is required to design a linear controller. References [327]–[329] show examples of the small-signal analysis and design of a linear controller in the frequency domain for DC-DC converters.

Consideration of all of the system parameters (such as conduction resistances, switch conduction voltages, switching times, and inductor and capacitor resistances) in the modelling procedure is an essential step towards the designing of a robust controller for Boost converters. In [330] Basso, Tomescue and Towati considered the inductor and capacitor resistances and the output current in the modelling procedure of the Boost converter. In [331], Benyakov considered the capacitor resistance and the output current in the modelling procedure of the Boost converter. In [332], the Pulse Width Modulator (PWM) converter with ideal system parameters, operating in both continuous and discontinuous conduction modes, is modelled. The effect of conduction resistances are included in [333] for the same model. In [334], the average model of the PWM converter is demonstrated by considering the conduction resistances and their voltage drops in discontinuous conduction mode (DCM).

5.3 Small Signal Averaged Model of DC-DC Boost converters operating in the Continuous Conduction Mode (CCM).

The small signal averaged state-space technique is a general analysis tool which can be applied to simple or complex circuits [335], [336]. The linear averaged time-invariant models created by using this technique are relatively simple but need a lot of mathematical computational effort to determine the final results. To get such models, the detailed generalized procedure explained in [335], [336] is applied to our case.

For modeling with the state-space technique, the desired state variables for any electric circuit are the energy storing elements (i.e. inductor current and capacitance voltage). To start applying the state-space technique in any complicated circuit, it must be converted first into a simplified circuit in which the basic circuit laws can be applied.

5.3.1 Case 1: Ideal Boost Converter

The Boost converter is a non-isolated power converter topology, also known as a step-up power converter. Power electronics engineers choose the Boost converter when the required output voltage must be greater than the input voltage. The output current for Boost converter is continuous because the output diode becomes forward biased only during a portion of the switching cycle and the output capacitor gives the whole load current during the other portion of the switching cycle.

In the Boost switching converter (Figure 5.2), there are two modes of operation; the ON-mode and OFF-mode. The ON-time (t_{on}) is defined by dT_s , and the OFF-time (t_{off}) is defined by $(1-d)T_s$, where T_s is the total time period for one cycle and d is the duty cycle which is defined as the ratio of the ON-time period to the total switching time period for one cycle i.e. $d = t_{on} / T_s$.

The main switch S is turned ON and OFF by a pulse with a duty cycle equal to d . Therefore, the piece-wise linearized equivalent circuit of the system in ON and OFF modes with dT_s and $(1-d)T_s$ seconds is represented by Figure 5.3 and Figure 5.4 respectively.

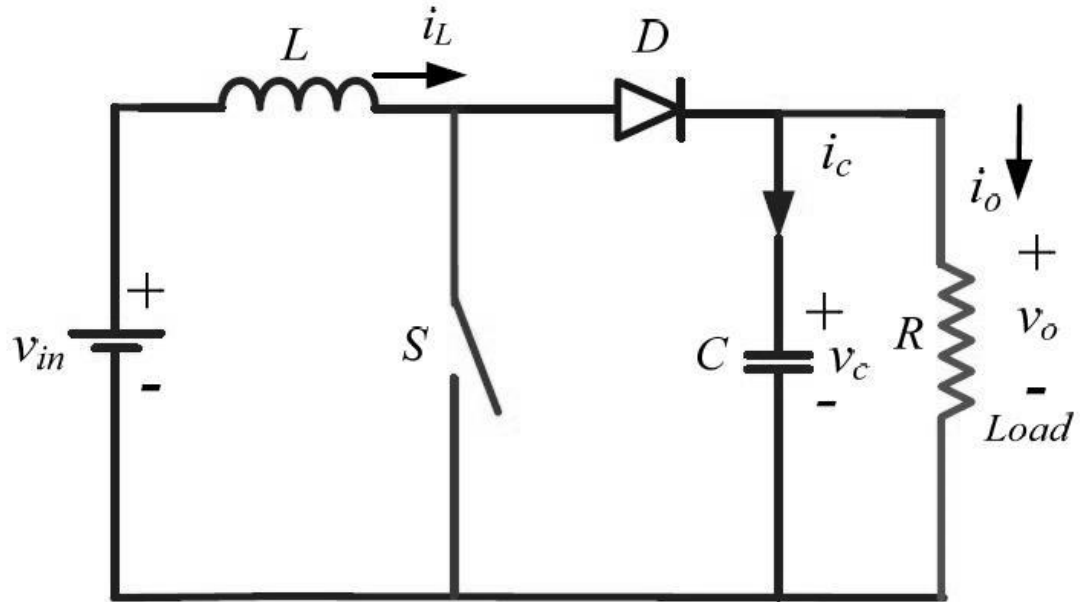


Figure 5.2: Boost converter circuit

Using i_L and v_C as the two state variables ($x = [i_L \ v_C]^T$), and by writing the KVL and KCL for the loops of Figure 5.3 and Figure 5.4, the state-space equations can be derived:

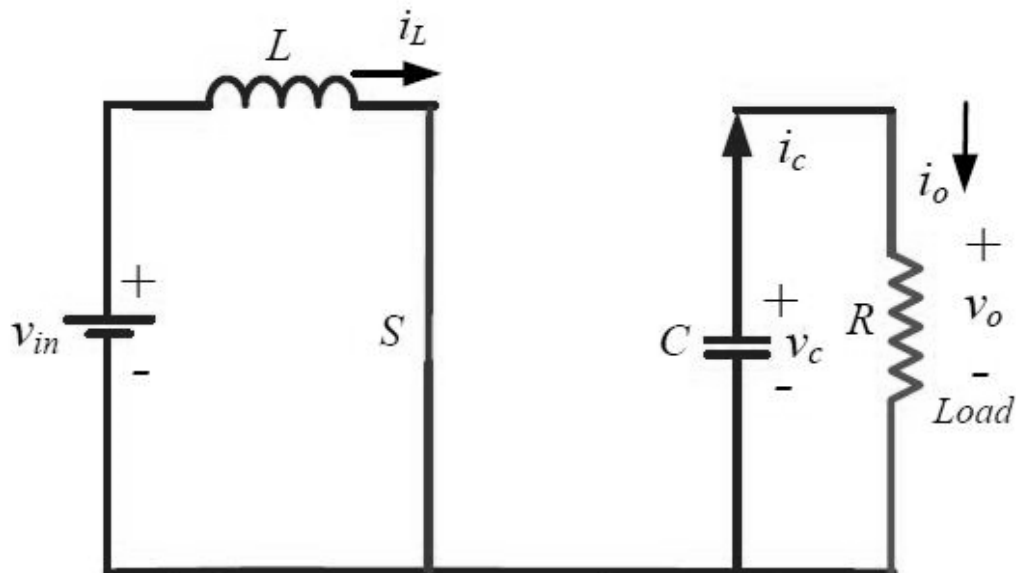


Figure 5.3: Equivalent circuit of Boost converter during on-state

During the on-state, the state space (ss) form will be:-

$$\begin{bmatrix} \frac{di_L}{dt} \\ \frac{dv_C}{dt} \end{bmatrix} = \begin{bmatrix} 0 & 0 \\ 0 & \frac{-1}{RC} \end{bmatrix} \begin{bmatrix} i_L \\ v_C \end{bmatrix} + \begin{bmatrix} 1 \\ 0 \end{bmatrix} v_{in} \quad (5.1)$$

$$v_o = [0 \quad 1] \begin{bmatrix} i_L \\ v_C \end{bmatrix} \quad (5.2)$$

During the off-state, in ss form:-

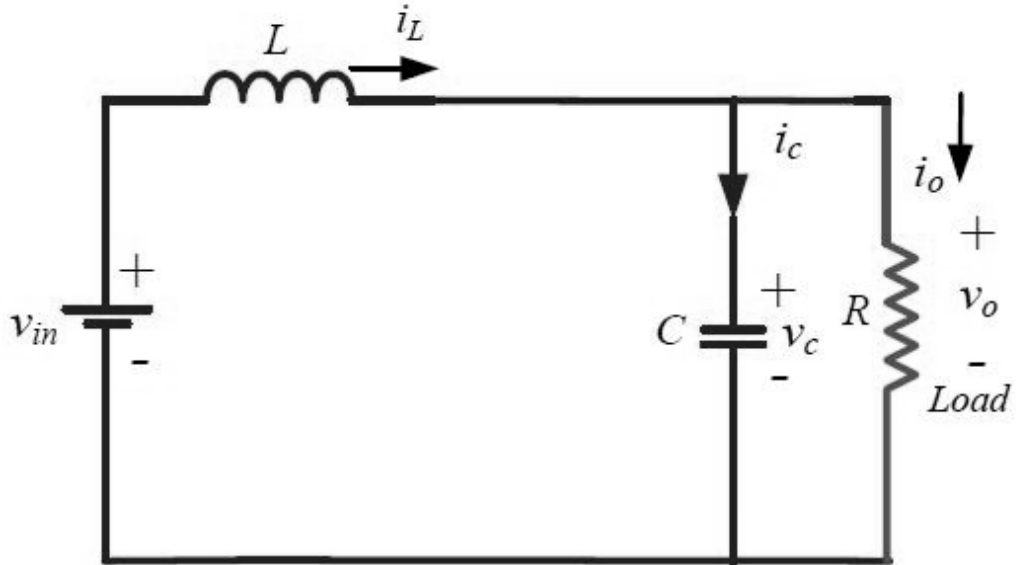


Figure 5.4: Equivalent circuit of Boost converter during off-state

$$\begin{bmatrix} \frac{di_L}{dt} \\ \frac{dv_C}{dt} \end{bmatrix} = \begin{bmatrix} 0 & \frac{-1}{L} \\ \frac{1}{C} & \frac{-1}{RC} \end{bmatrix} \begin{bmatrix} i_L \\ v_C \end{bmatrix} + \begin{bmatrix} 1 \\ 0 \end{bmatrix} v_{in} \quad (5.3)$$

$$v_o = [0 \quad 1] \begin{bmatrix} i_L \\ v_C \end{bmatrix} \quad (5.4)$$

Figure 5.5 shows the steady-state waveforms for the CCM where the inductor current flows continuously [$i_L(t) > 0$].

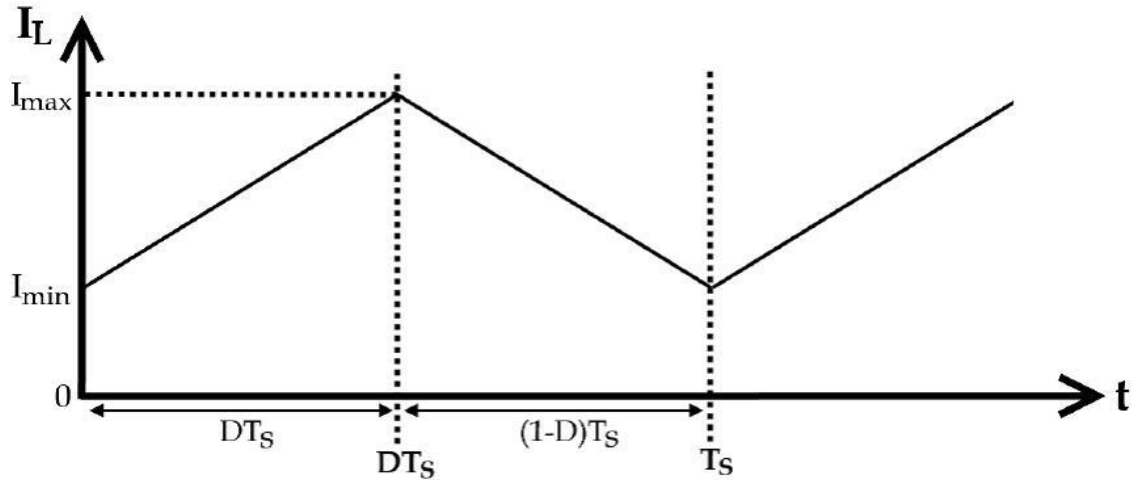


Figure 5.5: Steady-state waveforms for CCM

Thus,

‘ON’ Mode

$$\dot{x} = A_1 x + B_1 v_{in} \quad \text{For } t \in [0, dT_s] \quad (5.5)$$

‘OFF’ Mode

$$\dot{x} = A_2 x + B_2 v_{in} \quad \text{For } t \in [dT_s, T_s] \quad (5.6)$$

where,

dT_s = ON Period time

$(1-d)T_s$ = OFF Period time

T_s = Total time period for one cycle

V_{in} = Input voltage

State space averaging techniques are employed to get a set of equations that describe the system over one switching cycle. After applying averaging technique to (5.5) and (5.6), the following expression can be found:

$$\dot{\bar{x}} = [A_1 * d + A_2 * (1 - d)]\bar{x} + [B_1 * d + B_2 * (1 - d)]v_{in} \quad (5.7)$$

Thus, with the help of state space equations, values of matrices A_1, B_1, C_1, D_1 parameters of ON-state and A_2, B_2, C_2, D_2 parameters of OFF-state are extracted and A, B, C, D parameters can be obtained as follows: $A = [A_1 * d + A_2 * (1 - d)]$. Similarly, B, C and D parameters are also obtained. Thus, state-space average model for DC-DC Boost converter in CCM would be like below:

$$\begin{bmatrix} \frac{di_L}{dt} \\ \frac{dv_C}{dt} \end{bmatrix} = \begin{bmatrix} 0 & \frac{-(1-d)}{L} \\ \frac{(1-d)}{C} & \frac{-1}{RC} \end{bmatrix} \begin{bmatrix} i_L \\ v_C \end{bmatrix} + \begin{bmatrix} 1 \\ 0 \end{bmatrix} v_{in} \quad (5.8)$$

$$v_o = [0 \quad 1] \begin{bmatrix} i_L \\ v_C \end{bmatrix} \quad (5.9)$$

Now applying standard linearization techniques and applying perturbations as follows:

$$\begin{aligned} i_L &= I_L + \tilde{i}_L \\ v_C &= V_C + \tilde{v}_C \\ v_{in} &= V_{in} + \tilde{v}_{in} \\ d &= D + \tilde{d} \end{aligned} \quad (5.10)$$

$$L \frac{d(I_L + \tilde{i}_L)}{dt} = (V_{in} + \tilde{v}_{in}) - (1 - D - \tilde{d})(V_C + \tilde{v}_C) \quad (5.11)$$

$$C \frac{d(V_C + \tilde{v}_C)}{dt} = -(1 - D - \tilde{d})(I_L + \tilde{i}_L) - \frac{(V_C + \tilde{v}_C)}{R} \quad (5.12)$$

Separating terms of $\tilde{i}_L, \tilde{v}_C, \tilde{v}_{in}$, and \tilde{d} . Hence, the small-signal model for DC-DC Boost converter in CCM would be like below:

$$\begin{bmatrix} \frac{d\tilde{i}_L}{dt} \\ \frac{d\tilde{v}_C}{dt} \end{bmatrix} = \begin{bmatrix} 0 & \frac{-(1-D)}{L} \\ \frac{(1-D)}{C} & \frac{-1}{RC} \end{bmatrix} \begin{bmatrix} \tilde{i}_L \\ \tilde{v}_C \end{bmatrix} + \begin{bmatrix} 1 & \frac{V_C}{L} \\ 0 & \frac{-I_L}{C} \end{bmatrix} \begin{bmatrix} \tilde{v}_{in} \\ \tilde{d} \end{bmatrix} \quad (5.13)$$

$$v_o = [0 \quad 1] \begin{bmatrix} \tilde{i}_L \\ \tilde{v}_C \end{bmatrix} \quad (5.14)$$

5.3.2 Case 2: Parasitic Realization in Boost Converter

Due to the different difficulties found during the modeling procedure of the Boost converter systems, parasitic elements such as conduction voltages, conduction resistances, inductor DC resistance and equivalent series resistance's (ESR) of capacitors are ignored. The idea of considering ideal/lossless components and leaving parasitic elements like we have done earlier is to simplify model development procedure and to understand the basic features of the switching system. However, the effects of parasitic elements and losses are important for improving model accuracy, studying efficiency and dynamic performance of the system. The problem with including the parasitic elements is that they lead to nonlinear current and voltage waveforms and hence result in complications in the modelling development procedure.

Figure 5.6 shows a simplified equivalent circuit of the DC-DC Boost converter with parasitic elements. Inductor L and capacitor C can be considered as an output filter. The capacitor equivalent series resistance (ESR), R_c , and the inductor DC resistance, R_L , are included in the analysis. Resistor R represents the load seen by the power supply.

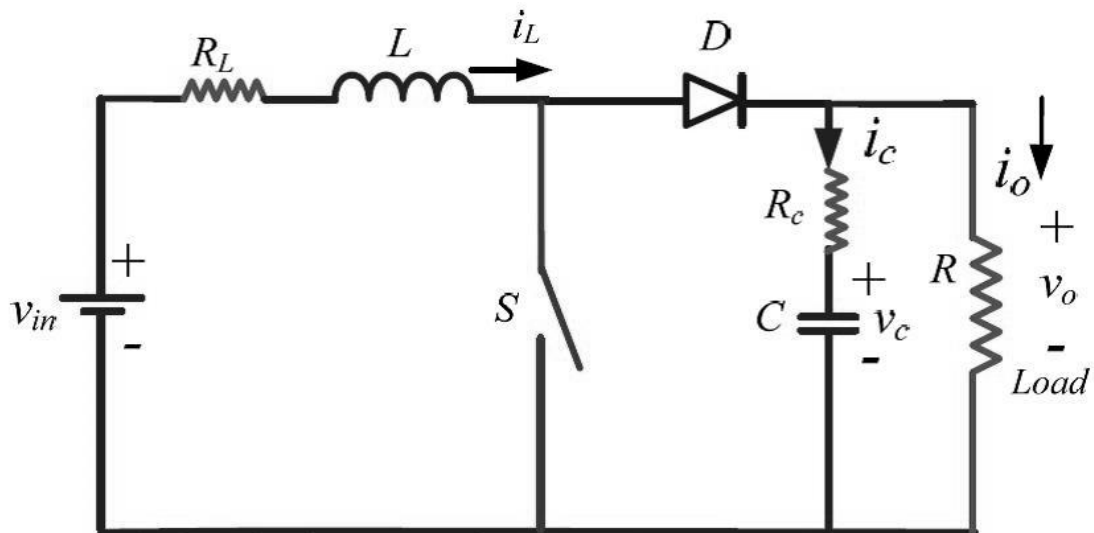


Figure 5.6: Boost Converter Circuit with parasitic elements

In continuous conduction mode (CCM), the Boost converter has two modes per switching cycle. In the ON-mode, S is ON and D is OFF. In the OFF-mode, S is OFF and D is ON. Therefore, the piece-wise linearized equivalent circuit of the Boost converter in ON and OFF modes with dT_s and $(1-d)T_s$ seconds is represented by Fig. 5.7 and Fig. 5.8 respectively.

Using i_L and v_C as the two state variables ($x = [i_L \ v_C]^T$), and by writing the KVL and KCL for the loops of Figure 5.7 and Figure 5.8, the state-space equations can be derived:

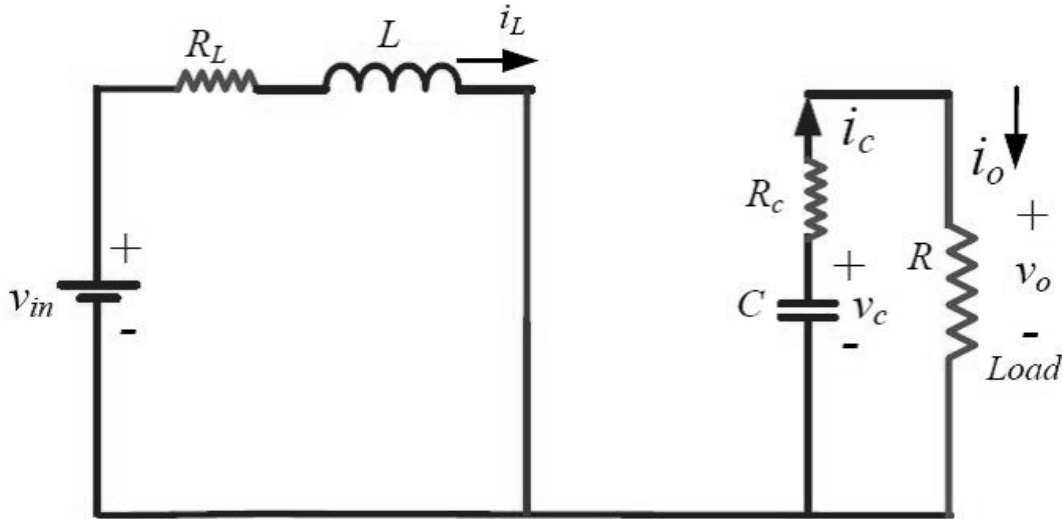


Figure 5.7: Equivalent circuit of Boost converter during ON-state

During the ON-state, the state space (ss) form will be:-

$$\begin{bmatrix} \frac{di_L}{dt} \\ \frac{dv_C}{dt} \end{bmatrix} = \begin{bmatrix} \frac{-R_L}{L} & 0 \\ 0 & \frac{-1}{C(R + R_C)} \end{bmatrix} \begin{bmatrix} i_L \\ v_C \end{bmatrix} + \begin{bmatrix} \frac{1}{L} \\ 0 \end{bmatrix} v_{in} \quad (5.15)$$

$$v_o = \begin{bmatrix} 0 & \frac{R}{(R + R_C)} \end{bmatrix} \begin{bmatrix} i_L \\ v_C \end{bmatrix} \quad (5.16)$$

During the OFF-state, in ss form:-

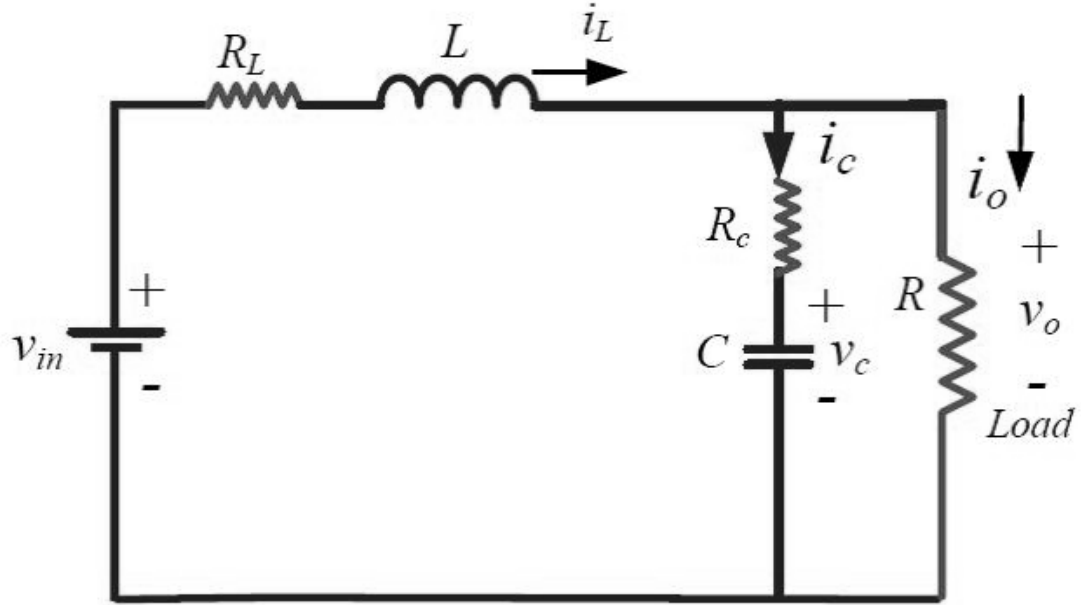


Figure 5.8: Equivalent circuit of Boost converter during OFF-state

$$\begin{bmatrix} \frac{di_L}{dt} \\ \frac{dv_c}{dt} \end{bmatrix} = \begin{bmatrix} \left[\left(\frac{-R_L}{L} \right) - \left(\frac{RR_c}{L(R+R_c)} \right) \right] & \left(\frac{-R}{L(R+R_c)} \right) \\ \frac{R}{C(R+R_c)} & \frac{-1}{C(R+R_c)} \end{bmatrix} \begin{bmatrix} i_L \\ v_c \end{bmatrix} + \begin{bmatrix} \frac{1}{L} \\ 0 \end{bmatrix} v_{in} \quad (5.17)$$

$$v_o = \begin{bmatrix} \left(\frac{RR_c}{R+R_c} \right) & \frac{R}{(R+R_c)} \end{bmatrix} \begin{bmatrix} i_L \\ v_c \end{bmatrix} \quad (5.18)$$

Thus with the help of state space equations, values of matrices A_1, B_1, C_1, D_1 parameters of on-state and A_2, B_2, C_2, D_2 parameters of off-state are extracted and A, B, C, D parameters are obtained as follows: $A = [A_1 * d + A_2 * (1 - d)]$. Similarly B, C and D parameters are also obtained. Thus state-space average model for DC-DC Boost converter with parasitic elements in CCM is shown below:

$$\begin{bmatrix} \frac{di_L}{dt} \\ \frac{dv_C}{dt} \end{bmatrix} = \begin{bmatrix} \left[\left(\frac{-R_L}{L} \right) - \left(\frac{(1-d)^2(RR_C)}{L(R+R_C)} \right) \right] & \left(\frac{-(1-d)R}{L(R+R_C)} \right) \\ \frac{R}{C(R+R_C)} & \frac{-1}{C(R+R_C)} \end{bmatrix} \begin{bmatrix} i_L \\ v_C \end{bmatrix} + \begin{bmatrix} 1 \\ 0 \end{bmatrix} v_{in} \quad (5.19)$$

$$v_o = \left[\left(\frac{(1-d)RR_C}{R+R_C} \right) \quad \frac{R}{(R+R_C)} \right] \begin{bmatrix} i_L \\ v_C \end{bmatrix} \quad (5.20)$$

Now, apply perturbations, this will result in the small signal model as:-

$$\begin{bmatrix} \frac{d\tilde{i}_L}{dt} \\ \frac{d\tilde{v}_C}{dt} \end{bmatrix} = \begin{bmatrix} \left[\left(\frac{-R_L}{L} \right) - \left(\frac{(1-D)^2(RR_C)}{L(R+R_C)} \right) \right] & \left(\frac{-(1-D)R}{L(R+R_C)} \right) \\ \frac{(1-D)R}{C(R+R_C)} & \frac{-1}{C(R+R_C)} \end{bmatrix} \begin{bmatrix} \tilde{i}_L \\ \tilde{v}_C \end{bmatrix} + \begin{bmatrix} \frac{1}{L} & \left[\left(\frac{V_o}{L} \right) + \left(\frac{(1-D)RR_C I_L}{L(R+R_C)} \right) \right] \\ 0 & \frac{-RI_L}{C(R+R_C)} \end{bmatrix} \begin{bmatrix} \tilde{v}_{in} \\ \tilde{d} \end{bmatrix} \quad (5.21)$$

$$v_o = \left[\left(\frac{(1-D)RR_C}{R+R_C} \right) \quad \frac{R}{(R+R_C)} \right] \begin{bmatrix} \tilde{i}_L \\ \tilde{v}_C \end{bmatrix} + \left[0 \quad \frac{-RR_C I_L}{(R+R_C)} \right] \begin{bmatrix} \tilde{v}_{in} \\ \tilde{d} \end{bmatrix} \quad (5.22)$$

Now simulations will be done by using the following model parameters: $L= 180 \mu\text{H}$, $C= 4.7 \mu\text{F}$, $V_{in}= 5 \text{ V}$, $D= 0.7$, $R_C= 0.1 \Omega$, $R_L= 0.8 \Omega$, and $F_S= 350 \text{ kHz}$. The simulations were performed for two different cases. Figure 5.9 and Figure 5.10 show the Bode diagrams for the transfer function represented the relation between the output voltage and duty ratio (d) (i.e. Control transfer function) for ideal and non-ideal DC-DC Boost converters in CCM, respectively.

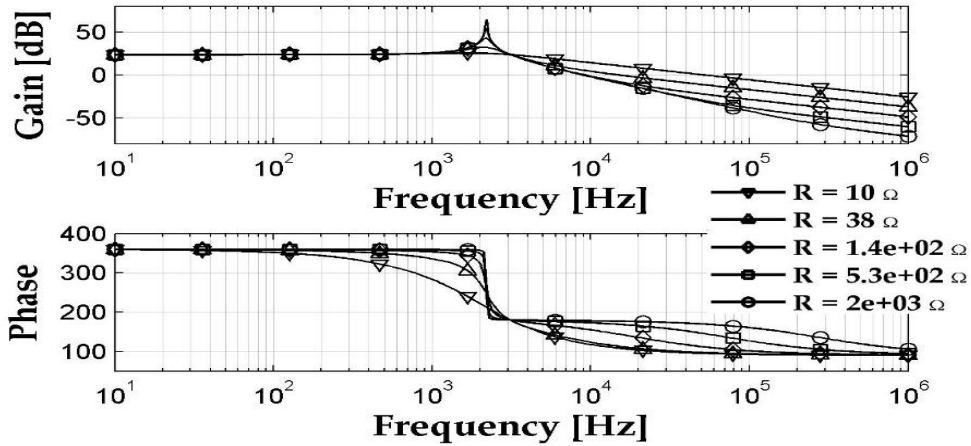


Figure 5.9: Bode diagram for ideal DC-DC Boost converter in CCM

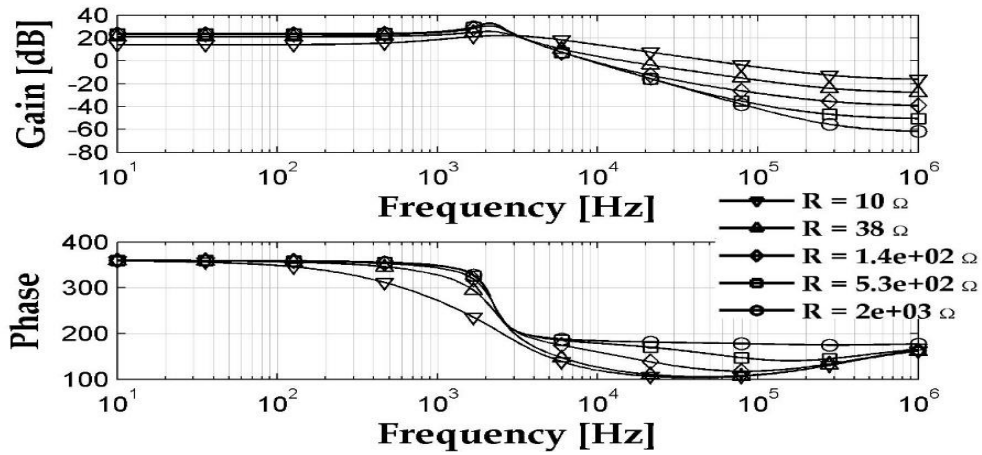


Figure 5.10: Bode diagram for non-ideal DC-DC Boost converter in CCM

In Figure 5.9, a resonant peak occurs when the load resistance value becomes large. To explain this phenomenon, when the diode becomes reverse biased during the ON-mode, the output capacitor becomes responsible to supply the load current. Since the value of the load resistance is large, then the value of the load current must be small which results in increasing the discharging time for the energy stored in the capacitor. Then, when the switch becomes open during the OFF-mode and the diode becomes forward biased, the load current starts to flow through the inductor which results in energy stored in the inductor and there is still an amount of energy stored in the capacitor which results in the resonance at a certain switching frequency. As seen from Figure 5.9, the switching frequency results in the resonance point for the ideal DC-DC Boost converter at 2.2 kHz. Also, as seen from Figure 5.10, the switching frequency results in the resonance point for

the non-ideal DC-DC Boost converter at less than the switching frequency in the ideal case. This is due to the losses in the inductor and capacitor resistances.

Figures 5.11 and 5.12 show the transient step responses for ideal and non-ideal DC-DC Boost converters in CCM, respectively. As seen from Figure 5.11 and Figure 5.12, the non-ideal DC-DC Boost converter is faster to reach the steady state condition than the ideal DC-DC Boost converter at any value of the load resistance. Also, as seen from Figure 5.11 and Figure 5.12, since the value of the load resistance is small, the value of the load current is high; it results in decreasing the discharging time of the energy stored in the capacitor and hence it makes the system reach the steady state condition faster. Moreover, by comparing Figures 5.11 and 5.12 for the same value of the load resistance, it is easy to note that the steady state value for the non-ideal DC-DC Boost converter is less than the steady state value for the ideal DC-DC Boost converter and the reason behind that is the result of the inductor and capacitor resistance losses in the non-ideal DC-DC Boost converter case. Furthermore, as seen from Figure 5.11 and Figure 5.12, the negative output voltage appears at the start of the converter's operation with a small load. This is due to the initial resonance behaviour between the boost inductor (L) and output capacitor (C), at which, the inductor initially starts to charge the capacitor till all of its stored energy is transferred. In return, the capacitor starts to charge back the inductor, and hence, a negative voltage appears at the output terminals. Such resonance behaviour is continuously damped with time and the system reaches steady state operation as seen in Figure 5.11 and Figure 5.12.

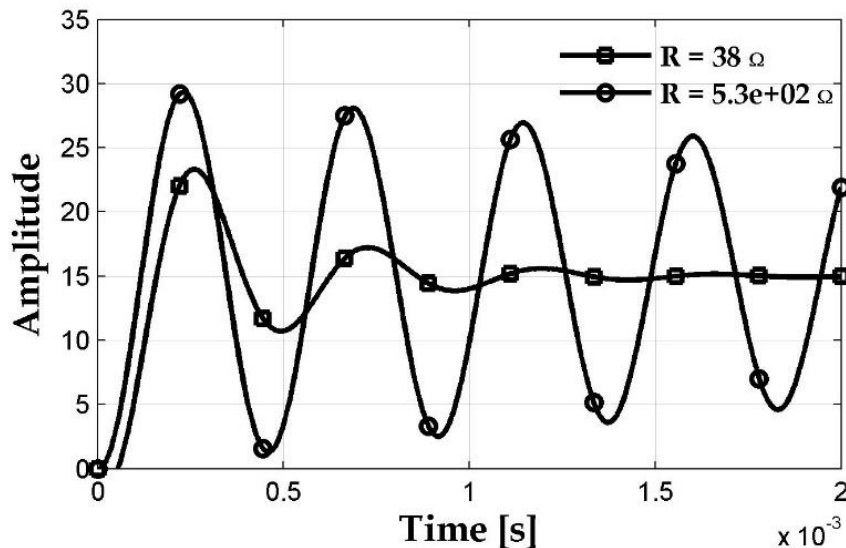


Figure 5.11: Transient step response for ideal DC-DC Boost converter in CCM

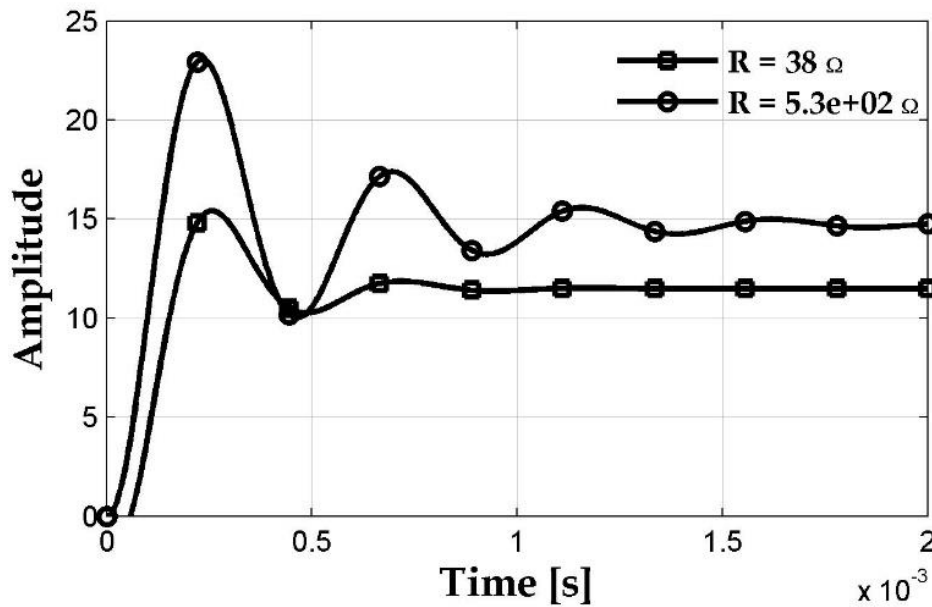


Figure 5.12: Transient step response for non-ideal DC-DC Boost converter in CCM

5.4 Small Signal Averaged Model of DC-DC Boost converters operating in the Discontinuous Conduction Mode (DCM).

The modelling method for DCM operation comprises of three steps:

- a) Averaging;
- b) Inductor current analysis;
- c) Duty-ratio constraint.

Generally, state-space averaging techniques are employed to get a set of equations that describe the system dynamics over one switching period.

5.4.1 Case 1: Ideal Boost Converter

In Discontinuous Conduction Mode (DCM), in addition to two modes in Continuous Conduction Mode (CCM), there is a third mode of operation in which capacitor voltage or inductor current is zero. For DCM operation, during first interval (i.e. ON-period) the switch is turned ON and inductor current rises and reaches a peak when the switch is about to turn OFF, and resets to zero at the end of the OFF-period as shown in Figure 5.13.

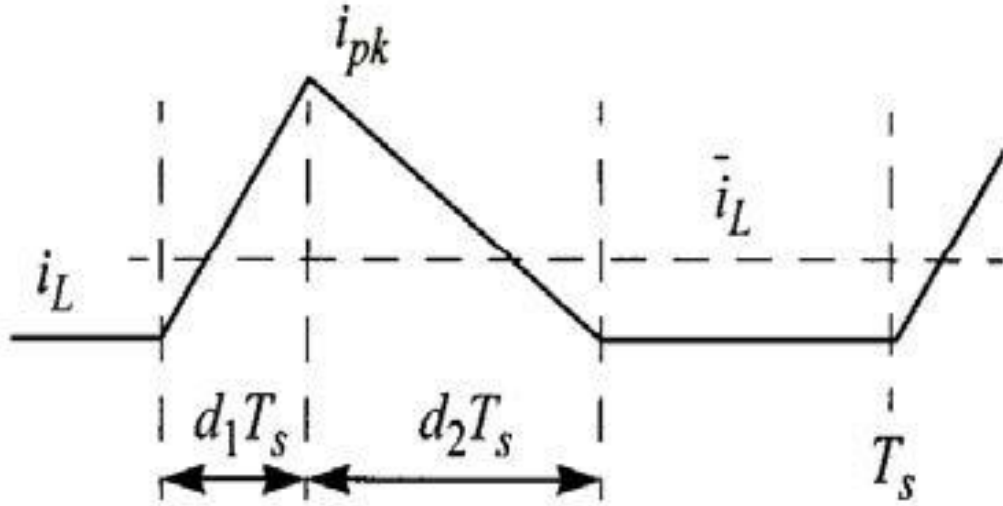


Figure 5.13: Inductor current waveform of DC-DC Converter in DCM

During DCM, in ss form:

$$\begin{bmatrix} \frac{di_L}{dt} \\ \frac{dv_C}{dt} \end{bmatrix} = \begin{bmatrix} 0 & 0 \\ 0 & \frac{-1}{RC} \end{bmatrix} \begin{bmatrix} i_L \\ v_C \end{bmatrix} + \begin{bmatrix} 0 \\ 0 \end{bmatrix} v_{in} \quad (5.23)$$

$$v_o = \begin{bmatrix} 0 & 0 \end{bmatrix} \begin{bmatrix} i_L \\ v_C \end{bmatrix} \quad (5.24)$$

Thus,

$$\text{'ON' Mode } \dot{x} = A_1 x + B_1 v_{in} \quad \text{For } t \in [0, d_1 T_s] \quad (5.25)$$

$$\text{'OFF' Mode } \dot{x} = A_2 x + B_2 v_{in} \quad \text{For } t \in [d_1 T_s, (d_1 + d_2) T_s] \quad (5.26)$$

$$\text{'DC' Mode } \dot{x} = A_3 x + B_3 v_{in} \quad \text{For } t \in [(d_1 + d_2) T_s, T_s] \quad (5.27)$$

where,

$d_1 T_s$ = ON-period time

$d_2 T_s$ = OFF-period time

T_s = Total time period for one cycle

i_{pk} = Peak value of inductor current

\bar{i}_L = Average value of inductor current

v_{in} = Input voltage

After applying an averaging technique to equations (5.25)-(5.27), the following expression can be found:

$$\dot{x} = [A_1d_1 + A_2d_2 + A_3(1 - d_1 - d_2)]x + [B_1d_1 + B_2d_2 + B_3(1 - d_1 - d_2)]u \quad (5.28)$$

The above equation can be written as $\dot{x} = Ax + Bu$, where, $A = [A_1d_1 + A_2d_2 + A_3(1 - d_1 - d_2)]$ & $B = [B_1d_1 + B_2d_2 + B_3(1 - d_1 - d_2)]$. For state-space averaging technique in DCM, only the matrix parameters are averaged and not the state variables. Equation (5.28) will hold when true average of every state variable is used.

From Figure 5.13, it can be deduced that the average value of inductor current is:

$$\bar{i}_L = \frac{i_{pk}}{2}(d_1 + d_2) \quad (5.29)$$

Consider the circuit behavior when the switch is ‘OFF’; the current which is delivered to the capacitor does not necessarily have the same value as the average inductor current. Since the inductor current changes slowly with time, the capacitor equation can be solved employing the ‘conservation of energy’ principle, and after that the averaging step is performed. The total amount of charge which the capacitor obtains from the inductor during switching cycle is:

$$Q_C = \frac{i_{pk}d_1T_s}{2} \quad (5.30)$$

Thus, average charging current would be of value:

$$\frac{Q_C}{T_s} = \frac{i_{pk}d_1}{2} \quad (5.31)$$

When a capacitor is connected to a resistive load, then the net average charging current which is delivered to the capacitor is given by:

$$\left(\frac{i_{pk}d_1}{2}\right) - \left(\frac{v_C}{R}\right) \quad (5.32)$$

Hence, the average capacitor current will be given by:

$$C \frac{dv_C}{dt} = \left(\frac{i_{pk}d_1}{2}\right) - \left(\frac{v_C}{R}\right) \quad (5.33)$$

Note here that the above expression differs from the KCL expression of capacitor which is obtained through state-space averaging. From (5.28), we can define the state-space-average (SSA) charging current as the inductor current's average multiplied by the duty ratio for which the inductor is charging the capacitor. From (5.29), the SSA charging current can be expressed as:

$$\bar{i}_L d_1 = \frac{i_{pk}d_1}{2}(d_1 + d_2) \quad (5.34)$$

This expression is different from the actual charging current in (5.31). It can be implied that a 'charge conservation' law is violated in unmodified SSA as the averaging step is done on a complete model thus leading to mismatching of responses with averaged response of DC-DC converters. Thus (5.28) is modified by dividing the inductor current by the factor (d_1+d_2) . The basic method is to rearrange the x , thus $x = [i_L, v_C]^T$, where sub-vector i_L contains all (n_L) inductor currents of the converter and defined by a matrix K , as below:

$$K = \text{diag} \left[\underbrace{\frac{1}{d_1 + d_2}, \dots, \frac{1}{d_1 + d_2}}_{n_L}, 1, 1, 1, \dots, 1 \right] \quad (5.35)$$

With this correction matrix, the average modified model becomes

$$\dot{x} = [A_1 d_1 + A_2 d_2 + A_3(1 - d_1 - d_2)]Kx + [B_1 d_1 + B_2 d_2 + B_3(1 - d_1 - d_2)]u \quad (5.36)$$

where,

$$A_1 = \begin{bmatrix} 0 & 0 \\ 0 & \frac{-1}{RC} \end{bmatrix}, A_2 = \begin{bmatrix} 0 & \frac{-1}{L} \\ \frac{1}{C} & \frac{-1}{RC} \end{bmatrix} \text{ and } A_3 = \begin{bmatrix} 0 & 0 \\ 0 & \frac{-1}{RC} \end{bmatrix}$$

$$B_1 = \begin{bmatrix} \frac{1}{L} \\ 0 \end{bmatrix}, B_2 = \begin{bmatrix} \frac{1}{L} \\ 0 \end{bmatrix} \text{ and } B_3 = \begin{bmatrix} 0 \\ 0 \end{bmatrix}$$

The SSA model for the above equation is

$$\frac{d}{dt} \begin{bmatrix} i_L \\ v_C \end{bmatrix} = \begin{bmatrix} 0 & \frac{-d_2}{L} \\ \frac{d_2}{C} & \frac{-1}{RC} \end{bmatrix} \begin{bmatrix} i_L \\ v_C \end{bmatrix} + \begin{bmatrix} d_1 + d_2 \\ L \\ 0 \end{bmatrix} v_{in} \quad (5.37)$$

Since there is only one inductor, the x is of dimension two, the correction matrix K is simply given by

$$K = \begin{bmatrix} \frac{1}{d_1 + d_2} & 0 \\ 0 & 1 \end{bmatrix} \quad (5.38)$$

Thus, the modified average model of Boost converter in DCM is given below:

$$\begin{aligned} \frac{d}{dt} \begin{bmatrix} i_L \\ v_C \end{bmatrix} &= \begin{bmatrix} 0 & \frac{-d_2}{L} \\ \frac{d_2}{C} & \frac{-1}{RC} \end{bmatrix} K \begin{bmatrix} i_L \\ v_C \end{bmatrix} + \begin{bmatrix} d_1 + d_2 \\ L \\ 0 \end{bmatrix} v_{in} \\ &= \begin{bmatrix} 0 & \frac{-d_2}{L} \\ \frac{d_2}{C(d_1 + d_2)} & \frac{-1}{RC} \end{bmatrix} \begin{bmatrix} i_L \\ v_C \end{bmatrix} + \begin{bmatrix} d_1 + d_2 \\ L \\ 0 \end{bmatrix} v_{in} \end{aligned} \quad (5.39)$$

To complete the average model represented in (5.36), a duty ratio constraint is defined showing the dependency of d_2 on other variables. Usually, in conventional SSA techniques, the inductor voltage balance equation is used in defining the duty-ratio constraint.

For the Boost converter topology, utilizing the volt-second balance over the switching cycle,

$$v_L = L \frac{di}{dt}$$

$$\therefore di = \frac{v_L dt}{L}$$

For time $T_1 = d_1 T_s$,

$$I_{max} - 0 = \frac{v_{in}}{L} T_1$$

For time $T_2 = d_2 T_s$,

$$0 - I_{max} = \frac{v_{in} - v_C}{L} T_2$$

By removing I_{max} from above equations,

$$I_{max} = \frac{v_{in}}{L} d_1 T_s = \frac{v_C - v_{in}}{L} d_2 T_s$$

$$\therefore v_{in} d_1 = (v_C - v_{in}) d_2$$

$$\therefore d_2 = \frac{v_{in}}{v_C - v_{in}} d_1 \tag{5.40}$$

Substituting d_2 in (5.39), this will result in

$$\frac{di_L}{dt} = 0 \tag{5.41}$$

$$\frac{dv_C}{dt} = \frac{v_{in}}{v_C} \frac{i_L}{C} - \frac{v_C}{RC} \tag{5.42}$$

From these calculations for a Boost converter, it can be seen that inductor current dynamics disappear, thus resulting in a degenerate model. Since inductor current is not present in the state variable in this reduced-order model, it must be replaced by expressing it as an algebraic function of other variables, so that inductor dynamics are removed.

For a Boost converter, the peak of the inductor current is given by:

$$i_{pk} = \frac{v_{in}}{L} d_1 T_s \quad (5.43)$$

The average value of inductor current is given by:

$$\bar{i}_L = \frac{i_{pk}}{2} (d_1 + d_2) = \frac{v_{in}}{2L} d_1 (d_1 + d_2) T_s \quad (5.44)$$

Substituting by (5.40), the above relationship can be written as

$$\bar{i}_L = \frac{v_{in}}{2L} \left(\frac{d_1^2 T_s v_C}{v_C - v_{in}} \right) \quad (5.45)$$

Substituting (5.45) in (5.42), this will result in the conventional average model for a Boost converter in DCM. In this model, the dependency on the average inductor current is removed.

$$\frac{dv_C}{dt} = \left(\frac{v_{in}^2}{2LC} \right) \left(\frac{d^2 T_s}{v_C - v_{in}} \right) - \left(\frac{v_C}{RC} \right) \quad (5.46)$$

Now, applying standard linearization techniques and applying small perturbations as follows to (5.46):

$$\begin{aligned} i_L &= I_L + \tilde{i}_L; \\ v_C &= V_C + \tilde{v}_C; \\ v_{in} &= V_{in} + \tilde{v}_{in}; \\ d &= D + \tilde{d}; \end{aligned}$$

$$\therefore \frac{d(V_C + \widetilde{v}_C)}{dt} = \left(\frac{(V_{in} + \widetilde{v}_{in})^2}{2LC} \right) \left(\frac{(D + \check{d})^2 T_s}{(V_C + \widetilde{v}_C) - (V_{in} + \widetilde{v}_{in})} \right) - \left(\frac{(V_C + \widetilde{v}_C)}{RC} \right) \quad (5.47)$$

Separating terms of \widetilde{i}_L , \widetilde{v}_C , \widetilde{v}_{in} and \check{d} and then converting it to state-space form,

$$\begin{aligned} \begin{bmatrix} \dot{\widetilde{i}}_L \\ \dot{\widetilde{v}}_C \end{bmatrix} &= \begin{bmatrix} 0 & 0 \\ 0 & \left(\frac{-1}{RC} \right) \left(\frac{2M-1}{M-1} \right) \end{bmatrix} \begin{bmatrix} \widetilde{i}_L \\ \widetilde{v}_C \end{bmatrix} \\ &+ \begin{bmatrix} 0 & 0 \\ \left(\frac{D^2 T_s}{LC(M-1)} + \frac{M}{RC(M-1)} \right) & \left(\frac{DT_s V_{in}}{LC(M-1)} \right) \end{bmatrix} \begin{bmatrix} \widetilde{v}_{in} \\ \check{d} \end{bmatrix} \end{aligned} \quad (5.48)$$

which is in the form of:

$$\frac{d}{dt} \begin{bmatrix} \widetilde{i}_L \\ \widetilde{v}_C \end{bmatrix} = A \begin{bmatrix} \widetilde{i}_L \\ \widetilde{v}_C \end{bmatrix} + B \begin{bmatrix} \widetilde{v}_{in} \\ \check{d} \end{bmatrix}$$

Since,

$$\begin{bmatrix} \widetilde{i}_L(s) \\ \widetilde{v}_C(s) \end{bmatrix} = \tilde{x}(s) = (sI - A)^{-1} B U(s)$$

$$\therefore \begin{bmatrix} \widetilde{i}_L(s) \\ \widetilde{v}_C(s) \end{bmatrix} = \frac{1}{\Delta} \cdot \begin{bmatrix} 0 & 0 \\ s \left(\frac{D^2 T_s}{LC(M-1)} + \frac{M}{RC(M-1)} \right) & s \left(\frac{DT_s V_{in}}{LC(M-1)} \right) \end{bmatrix} \cdot \begin{bmatrix} \widetilde{v}_{in}(s) \\ \check{d}(s) \end{bmatrix} \quad (5.49)$$

where,

$$\Delta = s^2 + s \left[\frac{1}{RC} \left(\frac{2M-1}{M-1} \right) \right]$$

Hence, two transfer functions can be found as follows:

$$\frac{\widetilde{v}_C(s)}{\widetilde{v}_{in}(s)} = \frac{s \left(\frac{D^2 T_s}{LC(M-1)} + \frac{M}{RC(M-1)} \right)}{\Delta} \quad (5.50)$$

and

$$\frac{\widetilde{v}_C(s)}{\widetilde{d}(s)} = \frac{s \left(\frac{DT_s V_{in}}{LC(M-1)} \right)}{\Delta} \quad (5.51)$$

The reduced-order model (5.48) can correctly only predict DC and low frequency behavior of PWM converters. However, at high frequencies, it is unable to capture the dynamics of the converter. Hence, a full-order model is also desired.

The full-order derivation starts from a modified averaged model represented by (5.36). This model differs from the reduced-order one in terms of duty ratio constraint. From (5.43), the following relationship is obtained:

$$i_{pk} = \frac{v_{in}}{L} d_1 T_s$$

Substituting this into (5.29), this will result in a duty constraint

$$d_2 = \frac{2Li_L}{d_1 T_s v_{in}} - d_1 \quad (5.52)$$

This constraint is different from the earlier one which is derived for a reduced-order model showing that it enforces correct average charging of output capacitor. Putting d_2 into (5.39), the following relations are derived:

$$\frac{di_L}{dt} = \frac{2i_L}{d_1 T_s} \left(1 - \frac{v_C}{v_{in}} \right) + \frac{d_1 v_C}{L} \quad (5.53)$$

$$\frac{dv_C}{dt} = \frac{i_L}{C} - \frac{d_1^2 T_s v_{in}}{2LC} - \frac{v_C}{RC} \quad (5.54)$$

Equating (5.53) and (5.54) to zero and finding the solutions for i_L and v_C , the DC-operating point can be obtained. Let the scalar value of M be the output to input voltage ratio. Thus,

$$M = \frac{v_C}{v_{in}} = \frac{1}{2} + \frac{1}{2} \sqrt{1 + \frac{2D^2R}{LF_s}} \quad (5.55)$$

Now applying standard linearization techniques and applying small perturbations as follows to (5.53) and (5.54):

$$\begin{aligned} i_L &= I_L + \tilde{i}_L; \\ v_C &= V_C + \tilde{v}_C; \\ v_{in} &= V_{in} + \tilde{v}_{in}; \\ d_1 &= d = D + \tilde{d}; \end{aligned}$$

Then,

$$\frac{d(I_L + \tilde{i}_L)}{dt} = \frac{2(I_L + \tilde{i}_L)}{(D + \tilde{d})T_s} \left(1 - \frac{(V_C + \tilde{v}_C)}{(V_{in} + \tilde{v}_{in})}\right) + \frac{(D + \tilde{d})(V_C + \tilde{v}_C)}{L} \quad (5.56)$$

And

$$\frac{d(V_C + \tilde{v}_C)}{dt} = \frac{(I_L + \tilde{i}_L)}{C} - \frac{(D + \tilde{d})^2 T_s (V_{in} + \tilde{v}_{in})}{2LC} - \frac{(V_C + \tilde{v}_C)}{RC} \quad (5.57)$$

Now, the small signal model can be derived with the following equation:

$$\frac{d}{dt} \begin{bmatrix} \tilde{i}_L \\ \tilde{v}_C \end{bmatrix} = A \begin{bmatrix} \tilde{i}_L \\ \tilde{v}_C \end{bmatrix} + B \begin{bmatrix} \tilde{v}_{in} \\ \tilde{d} \end{bmatrix}$$

Where,

$$A = \begin{bmatrix} \frac{2(1-M)}{DT_s} & \frac{-D}{L(M-1)} \\ \frac{1}{C} & \frac{-1}{RC} \end{bmatrix} \text{ and } B = \begin{bmatrix} \frac{DM^2}{L(M-1)} & \frac{2MV_{in}}{L} \\ \frac{-D^2T_s}{2LC} & \frac{-DT_sV_{in}}{LC} \end{bmatrix}$$

Since,

$$\begin{bmatrix} \tilde{i}_L(s) \\ \tilde{v}_C(s) \end{bmatrix} = \tilde{x}(s) = (sI - A)^{-1}BU(s)$$

$$\begin{aligned}
& \therefore \begin{bmatrix} \tilde{i}_L(s) \\ \tilde{v}_C(s) \end{bmatrix} \\
& = \frac{1}{\Delta} \cdot \begin{bmatrix} \left(\frac{sM^2}{L(M-1)} + \frac{M^2}{RLC(M-1)} + \frac{MD}{RLC} \right) & \left(\frac{2sMV_{in}}{L} + \frac{4MV_{in}}{RLC} \right) \\ \left(\frac{M^2}{LC(M-1)} + \frac{D(1-M)}{LC} + \frac{-sD^2T_s}{2LC} \right) & \left(\frac{-sDT_sV_{in}}{LC} + \frac{2V_{in}}{LC} \right) \end{bmatrix} \cdot \begin{bmatrix} \tilde{v}_{in}(s) \\ \tilde{d}(s) \end{bmatrix} \quad (5.58)
\end{aligned}$$

Where,

$$\Delta = s^2 + s \left(\frac{1}{RC} - \frac{2(1-M)}{DT_s} \right) + \frac{2(2M-1)}{DT_sRC}$$

Hence, the following transfer functions can be formulated from the small signal model:

$$\frac{\tilde{i}_L(s)}{\tilde{v}_{in}(s)} = \frac{1}{\Delta} \cdot \left(\frac{sM^2}{L(M-1)} + \frac{M^2}{RLC(M-1)} + \frac{MD}{RLC} \right) \quad (5.59)$$

$$\frac{\tilde{i}_L(s)}{\tilde{d}(s)} = \frac{1}{\Delta} \cdot \left(\frac{2sMV_{in}}{L} + \frac{4MV_{in}}{RLC} \right) \quad (5.60)$$

$$\frac{\tilde{v}_C(s)}{\tilde{v}_{in}(s)} = \frac{1}{\Delta} \cdot \left(\frac{M^2}{LC(M-1)} + \frac{D(1-M)}{LC} + \frac{-sD^2T_s}{2LC} \right) \quad (5.61)$$

$$\frac{\tilde{v}_C(s)}{\tilde{d}(s)} = \frac{1}{\Delta} \cdot \left(\frac{-sDT_sV_{in}}{LC} + \frac{2V_{in}}{LC} \right) \quad (5.62)$$

5.4.2 Case 2: Parasitic Realization in Boost Converter

Due to the difficulties faced during the modelling procedure of the Boost converter, parasitic elements such as conduction voltages, conduction resistances, inductor resistances and equivalent series resistances (ESR) of capacitors have been ignored. The idea of simply considering ideal/lossless components and leaving out parasitic elements simplifies the model development procedure and allows us to understand the fundamental behaviour of the switching converter system. However, the effects of parasitic elements and losses are important for improving model accuracy, studying efficiency and dynamic performance of the system. The problem with including the parasitic elements is that they lead to nonlinear

current and voltage waveforms and hence result in complications in the modelling procedure.

A Boost converter circuit, with parasitics included, will look like as shown in Figure 5.14.

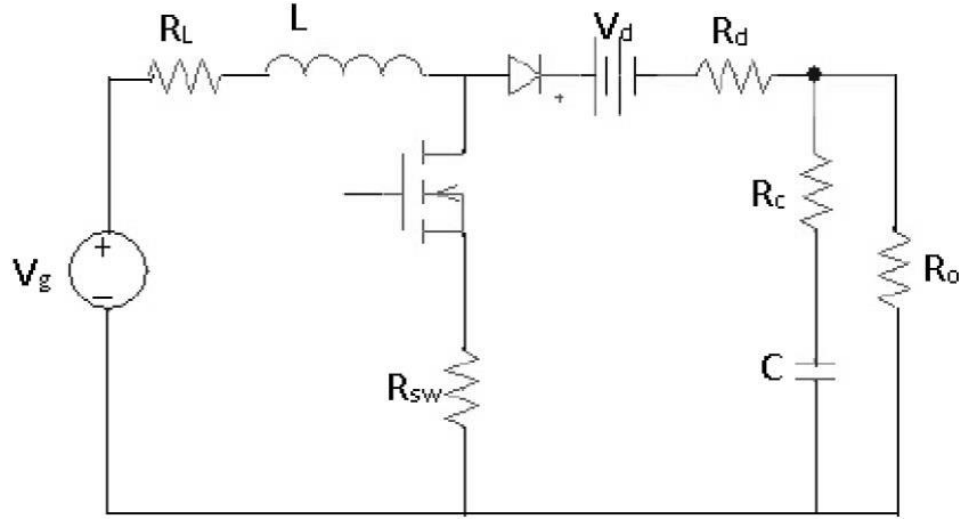


Figure 5.14: Boost Converter Circuit with parasitic

During the ON-state:

$$\begin{bmatrix} \frac{di_L}{dt} \\ \frac{dv_C}{dt} \end{bmatrix} = \underbrace{\begin{bmatrix} \frac{(R_L + R_{sw})}{L} & 0 \\ 0 & \frac{-1}{C(R_o + R_c)} \end{bmatrix}}_{A_1} \begin{bmatrix} i_L \\ v_C \end{bmatrix} + \underbrace{\begin{bmatrix} 1 \\ 0 \end{bmatrix}}_{B_1} v_{in} \quad (5.63)$$

During the OFF-state:

$$\begin{bmatrix} \frac{di_L}{dt} \\ \frac{dv_C}{dt} \end{bmatrix} = \underbrace{\begin{bmatrix} \frac{-(R_c + R_d)}{L} - \frac{R_c}{L \left(1 + \frac{R_c}{R_o}\right)} & \frac{-1}{\left(1 + \frac{R_c}{R_o}\right)} \\ \left(1 - \frac{R_c}{R_o \left(1 + \frac{R_c}{R_o}\right)}\right) & -1 \\ \frac{C}{C R_o \left(1 + \frac{R_c}{R_o}\right)} & \end{bmatrix}}_{A_2} \begin{bmatrix} i_L \\ v_C \end{bmatrix} + \underbrace{\begin{bmatrix} 1 \\ 0 \end{bmatrix}}_{B_2} v_{in} \quad (5.64)$$

During DCM period:

$$\begin{bmatrix} \frac{di_L}{dt} \\ \frac{dv_C}{dt} \end{bmatrix} = \underbrace{\begin{bmatrix} 0 & 0 \\ 0 & -1 \\ 0 & \frac{1}{C(R_o + R_C)} \end{bmatrix}}_{A_3} \begin{bmatrix} i_L \\ v_C \end{bmatrix} + \underbrace{\begin{bmatrix} 0 \\ 0 \end{bmatrix}}_{B_3} v_{in} \quad (5.65)$$

Now, applying the averaging technique, this will result in:

$$\dot{x} = [A_1 d_1 + A_2 d_2 + A_3(1 - d_1 - d_2)]x + [B_1 d_1 + B_2 d_2 + B_3(1 - d_1 - d_2)]u$$

So, the SSA model for the above equation is

$$\begin{aligned} \frac{d}{dt} \begin{bmatrix} i_L \\ v_C \end{bmatrix} = & \underbrace{\begin{bmatrix} \frac{-d_1(R_L + R_{sw})}{L} & \frac{d_2 R_L}{L} & \frac{d_2 R_d R_C}{L(1 + \frac{R_C}{R_o})} & \frac{-d_2}{(1 + \frac{R_C}{R_o})} \\ \frac{d_2 R_o}{C(R_o + R_C)} & & & \frac{-1}{C(R_C + R_o)} \end{bmatrix}}_A \begin{bmatrix} i_L \\ v_C \end{bmatrix} \\ & + \underbrace{\begin{bmatrix} d_1 + d_2 \\ L \\ 0 \end{bmatrix}}_B v_{in} \end{aligned} \quad (5.66)$$

Since there is only one inductor, the x is of dimension two, the correction matrix K is simply given by

$$K = \begin{bmatrix} \frac{1}{d_1 + d_2} & 0 \\ 0 & 1 \end{bmatrix} \quad (5.67)$$

With this correction matrix, the average modified model becomes

$$\dot{x} = [A_1 d_1 + A_2 d_2 + A_3(1 - d_1 - d_2)]Kx + [B_1 d_1 + B_2 d_2 + B_3(1 - d_1 - d_2)]u$$

Hence, the modified average model of Boost converter in DCM will look like:

$$\frac{d}{dt} \begin{bmatrix} i_L \\ v_C \end{bmatrix} = \underbrace{\begin{bmatrix} \frac{-d_1(R_L + R_{sw})}{L} - \frac{d_2 R_L}{L} - \frac{d_2 R_d R_C}{L \left(1 + \frac{R_C}{R_o}\right)} & \frac{-d_2}{\left(1 + \frac{R_C}{R_o}\right)} \\ \frac{d_2 R_o}{C(R_o + R_C)} & \frac{-1}{C(R_C + R_o)} \end{bmatrix}}_A \cdot \underbrace{\begin{bmatrix} 1 & 0 \\ d_1 + d_2 & 0 \\ 0 & 1 \end{bmatrix}}_K \begin{bmatrix} i_L \\ v_C \end{bmatrix} + \underbrace{\begin{bmatrix} d_1 + d_2 \\ L \\ 0 \end{bmatrix}}_B v_{in} \quad (5.68)$$

In the above state-space equation, replacing d_2 by the duty constraint (5.52), this will result in

$$\frac{di_L}{dt} = \frac{-d_1(R_L + R_{sw})i_L}{\left(\frac{2Li_L}{d_1 T_s v_{in}}\right)} - \frac{\left(\frac{2Li_L}{d_1 T_s v_{in}} - d_1\right) \left(R_L + R_d + \frac{R_C R_o}{R_C + R_o}\right) i_L}{\left(\frac{2Li_L}{d_1 T_s v_{in}}\right)} - \frac{\left(\frac{2Li_L}{d_1 T_s v_{in}} - d_1\right) R_o v_C}{(R_C + R_o)} + \frac{2i_L}{d_1 T_s} - \frac{\left(\frac{2Li_L}{d_1 T_s v_{in}} - d_1\right) v_{in}}{L} \quad (5.69)$$

And

$$\frac{dv_C}{dt} = \frac{\left(\frac{2Li_L}{d_1 T_s v_{in}} - d_1\right) R_o i_L}{\left(\frac{2Li_L}{d_1 T_s v_{in}}\right) C(R_C + R_o)} - \frac{v_C}{C(R_C + R_o)} \quad (5.70)$$

Now applying standard linearization techniques and applying small perturbations to (5.69) and (5.70), this will result in the small-signal model as:

$$\frac{d}{dt} \begin{bmatrix} \tilde{i}_L \\ \tilde{v}_C \end{bmatrix} = A \begin{bmatrix} \tilde{i}_L \\ \tilde{v}_C \end{bmatrix} + B \begin{bmatrix} \tilde{v}_{in} \\ \tilde{d} \end{bmatrix}$$

Where,

$$A = \begin{bmatrix} \frac{A_1}{DV_{in}} & \frac{A_2}{DV_{in}} \\ \frac{R_o}{C(R_C + R_o)} & -1 \end{bmatrix} \text{ and } B = \begin{bmatrix} \frac{A_3}{DV_{in}} & \frac{A_4}{DV_{in}} \\ \frac{-D^2 T_s R_o}{2LC(R_C + R_o)} & \frac{-DT_s V_{in} R_o}{LC(R_C + R_o)} \end{bmatrix} \quad (5.71)$$

Where,

$$A_1 = \frac{DV_{in}}{L} \left(R_L + R_d + \frac{R_C R_o}{R_C + R_o} \right) - \frac{2LV_C}{T_s} \left(\frac{R_o}{R_C + R_o} \right) + \frac{2V_{in}}{T_s};$$

$$A_2 = -\frac{2LV_C}{T_s} \left(\frac{R_o}{R_C + R_o} \right) I_L + D^2 V_{in} \left(\frac{R_o}{R_C + R_o} \right);$$

$$A_3 = \frac{D^3 T_s V_{in}}{L^2} \left(R_d - R_{sw} + \frac{R_C R_o}{R_C + R_o} \right) + D^2 V_C \left(\frac{R_o}{R_C + R_o} \right) + \frac{2I_L}{T_s} \\ - \frac{DI_L}{L} \left(R_C + R_d + \frac{R_C R_o}{R_C + R_o} \right);$$

$$A_4 = \frac{3D^2 T_s V_{in}^2}{2L^2} \left(R_d - R_{sw} + \frac{R_C R_o}{R_C + R_o} \right) - \frac{DI_L}{L} \left(R_C + R_d + \frac{R_C R_o}{R_C + R_o} \right).$$

Since,

$$\begin{bmatrix} \tilde{v}_L(s) \\ \tilde{v}_C(s) \end{bmatrix} = \tilde{x}(s) = (sI - A)^{-1} B U(s)$$

$$\therefore \begin{bmatrix} \tilde{v}_L(s) \\ \tilde{v}_C(s) \end{bmatrix} = \frac{1}{\Delta} \cdot \begin{bmatrix} \left(s + \frac{1}{C(R_C + R_o)} \right) & \frac{-A_2}{DV_{in}} \\ \frac{-R_o}{C(R_C + R_o)} & \left(s - \frac{A_1}{DV_{in}} \right) \end{bmatrix} \\ * \begin{bmatrix} \frac{A_3}{DV_{in}} & \frac{A_4}{DV_{in}} \\ \frac{-D^2 T_s R_o}{2LC(R_C + R_o)} & \frac{-DT_s V_{in} R_o}{LC(R_C + R_o)} \end{bmatrix} \cdot \begin{bmatrix} \tilde{v}_{in}(s) \\ \tilde{d}(s) \end{bmatrix} \quad (5.72)$$

Where,

$$\Delta = s^2 + s \left(\frac{1}{C(R_C + R_o)} - \frac{A_1}{DV_{in}} \right) - \frac{A_1}{CDV_{in}(R_C + R_o)} + \frac{A_2 R_o}{CDV_{in}(R_C + R_o)}$$

Hence, the following transfer functions can be formulated from the small signal model:

$$\frac{\tilde{i}_L(s)}{\tilde{v}_{in}(s)} = \frac{1}{\Delta} \cdot \left[\left(s + \frac{1}{C(R_C + R_o)} \right) \left(\frac{A_3}{DV_{in}} \right) + \frac{D^2 T_s R_o A_2}{2LCDV_{in}(R_C + R_o)} \right] \quad (5.73)$$

$$\frac{\tilde{i}_C(s)}{\tilde{d}(s)} = \frac{1}{\Delta} \cdot \left[\left(s + \frac{1}{C(R_C + R_o)} \right) \left(\frac{A_4}{DV_{in}} \right) + \frac{-DT_s V_{in} R_o A_2}{LCDV_{in}(R_C + R_o)} \right] \quad (5.74)$$

$$\frac{\tilde{v}_C(s)}{\tilde{v}_{in}(s)} = \frac{1}{\Delta} \cdot \left[\frac{-R_o A_3}{CDV_{in}(R_C + R_o)} - \frac{-sD^2 T_s R_o}{2LC(R_C + R_o)} + \frac{DA_1 T_s R_o}{2LCV_{in}(R_C + R_o)} \right] \quad (5.75)$$

$$\frac{\tilde{v}_C(s)}{\tilde{d}(s)} = \frac{1}{\Delta} \cdot \left[\frac{-DT_s V_{in} R_o}{LC(R_C + R_o)} - \frac{sDT_s V_{in} R_o}{LC(R_C + R_o)} - \frac{R_o A_4}{CDV_{in}(R_C + R_o)} \right] \quad (5.76)$$

Since,

$$v_o = \frac{v_C + R_C i_L}{\left(1 + \frac{R_C}{R_o}\right)} = \frac{v_C}{\left(1 + \frac{R_C}{R_o}\right)} + \frac{R_C i_L}{\left(1 + \frac{R_C}{R_o}\right)} \quad (5.77)$$

$$\therefore v_o = \begin{bmatrix} \frac{R_C}{\left(1 + \frac{R_C}{R_o}\right)} & \frac{1}{\left(1 + \frac{R_C}{R_o}\right)} \end{bmatrix} \begin{bmatrix} i_L \\ v_C \end{bmatrix} \quad (5.78)$$

This is in the form of:

$$Y(s) = C(s)x(s)$$

Since,

$$x(s) = (sI - A)^{-1}BU(s)$$

$$\therefore Y(s) = C(s)(sI - A)^{-1}BU(s)$$

$$\begin{aligned} \therefore Y(s) = \frac{1}{\Delta} \cdot \begin{bmatrix} \frac{R_C}{\left(1 + \frac{R_C}{R_o}\right)} & \frac{1}{\left(1 + \frac{R_C}{R_o}\right)} \end{bmatrix} * \begin{bmatrix} \left(s + \frac{1}{C(R_C + R_o)} \right) & \frac{-A_2}{DV_{in}} \\ \frac{-R_o}{C(R_C + R_o)} & \left(s - \frac{A_1}{DV_{in}} \right) \end{bmatrix} \\ * \begin{bmatrix} \frac{A_3}{DV_{in}} & \frac{A_4}{DV_{in}} \\ \frac{-D^2 T_s R_o}{2LC(R_C + R_o)} & \frac{-DT_s V_{in} R_o}{LC(R_C + R_o)} \end{bmatrix} \cdot \begin{bmatrix} \tilde{v}_{in}(s) \\ \tilde{d}(s) \end{bmatrix} \end{aligned} \quad (5.79)$$

Hence, two transfer functions can be found as follows:

$$\frac{v_o(s)}{\widehat{v}_{in}(s)} = \frac{1}{\Delta} \cdot \left(\frac{1}{\left(1 + \frac{R_C}{R_o}\right)} \right) \left\{ \left[\left(s + \frac{1}{C(R_C + R_o)} \right) \left(\frac{A_3}{DV_{in}} \right) + \frac{D^2 T_s R_o A_2}{2LCDV_{in}(R_C + R_o)} \right] \cdot R_C \right. \\ \left. + \left[\frac{-R_o A_3}{CDV_{in}(R_C + R_o)} - \frac{-sD^2 T_s R_o}{2LC(R_C + R_o)} + \frac{DA_1 T_s R_o}{2LCV_{in}(R_C + R_o)} \right] \right\} \quad (5.80)$$

$$\frac{v_o(s)}{\widehat{d}(s)} = \frac{1}{\Delta} \cdot \left(\frac{1}{\left(1 + \frac{R_C}{R_o}\right)} \right) \left\{ \left[\left(s + \frac{1}{C(R_C + R_o)} \right) \left(\frac{A_4}{DV_{in}} \right) + \frac{-DT_s V_{in} R_o A_2}{LCDV_{in}(R_C + R_o)} \right] \cdot R_C \right. \\ \left. + \left[\frac{-DT_s V_{in} R_o}{LC(R_C + R_o)} - \frac{sDT_s V_{in} R_o}{LC(R_C + R_o)} - \frac{R_o A_4}{CDV_{in}(R_C + R_o)} \right] \right\} \quad (5.81)$$

Now simulations will be done by using the following model parameters: $L= 18 \mu\text{H}$, $C= 4.7 \mu\text{F}$, $V_{in}= 5\text{V}$, $D = 0.7$, $R_C = 0.1 \Omega$, $R_d = 0.15 \Omega$, $R_L = 0.8 \Omega$, $R_{sw} = 0.17 \Omega$ and $F_S = 350 \text{ kHz}$. The simulations were performed for two different cases.

Figures 5.15 and 5.16 show the Bode diagrams for the transfer function representing the relation between the output voltage and duty ratio (d) (i.e. Control transfer function) for ideal and non-ideal DC-DC Boost converters in DCM, respectively.

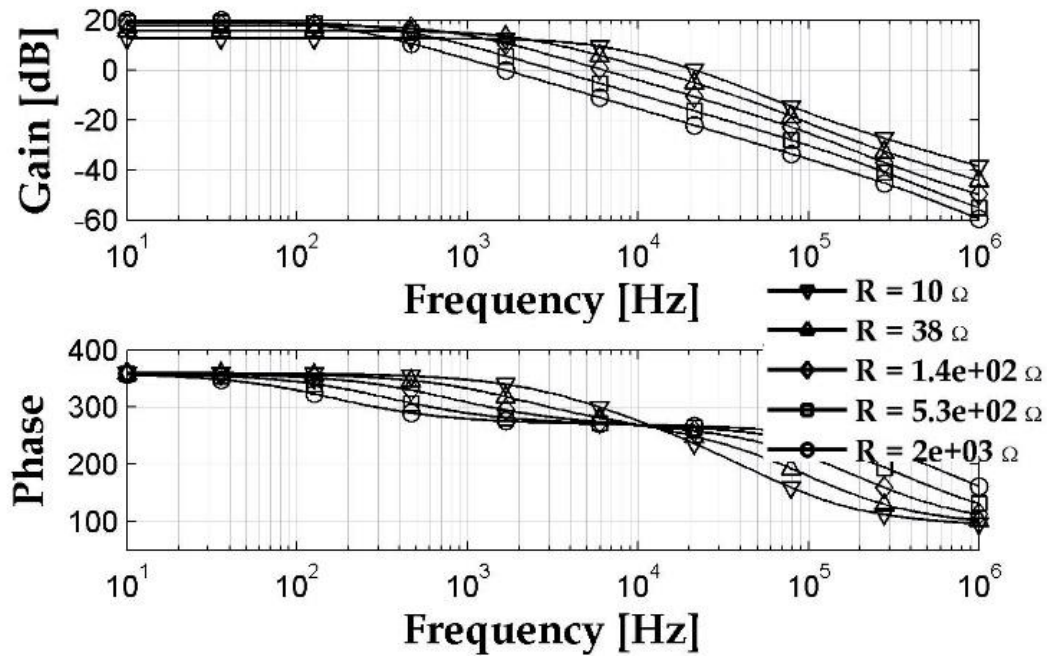


Figure 5.15: Bode diagram for ideal DC-DC Boost converter in DCM

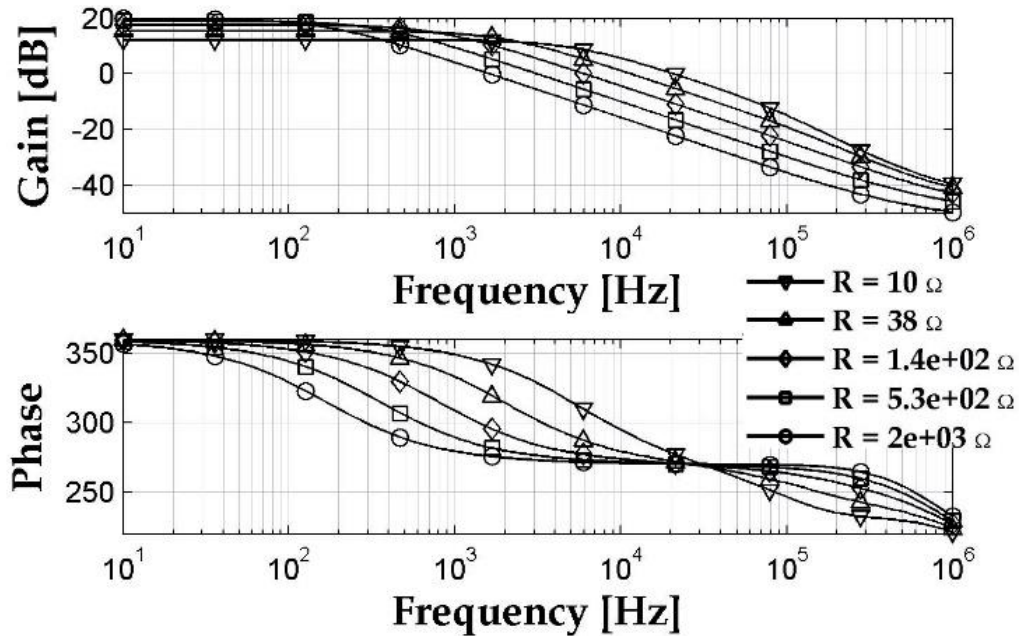


Figure 5.16: Bode diagram for non-ideal DC-DC Boost converter in DCM

As seen from Figure 5.15 and Figure 5.16, there is a remarkable decrease in the open loop gain as the load resistance decreases. When the load resistance goes below a certain range, the open loop gain goes under 0 dB which makes the converter ineffective without an external feedback controller.

Figures 5.17 and 5.18 show the transient step responses for ideal and non-ideal DC-DC Boost converters in DCM respectively. As indicated in Figure 5.17 and Figure 5.18, these figures were plotted by using two different load values to see the transient behavior as a function of the load value. As seen from Figure 5.17 and Figure 5.18, the steady-state behavior is a function of the load value. This is the important reason behind why the closed-loop control is essential, where the duty cycle (the only controllable parameter in the circuit) must be controlled and adapted in order to preserve the required steady-state DC voltage for different load values. Moreover, by comparing Figure 5.17 and Figure 5.18 for the same values of the load resistance, it is easy to observe that the step response for the ideal DC-DC Boost converter is looking identical to the step response for the non-ideal DC-DC Boost converter. This indicates that the ideal and non-ideal transfer functions should be approximately equal; which, in turn, reveals that the loss elements found in the non-ideal DC-DC Boost converter circuit have little effect on the dynamic response of the DC-DC Boost converter operating in DCM.

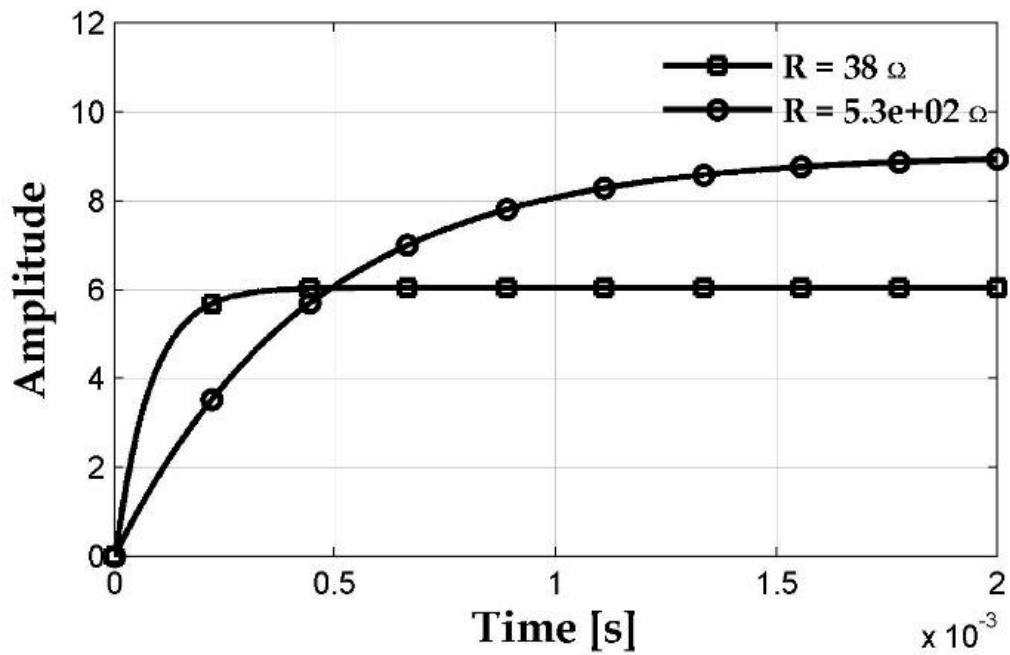


Figure 5.17: Transient step response for ideal DC-DC Boost converter in DCM

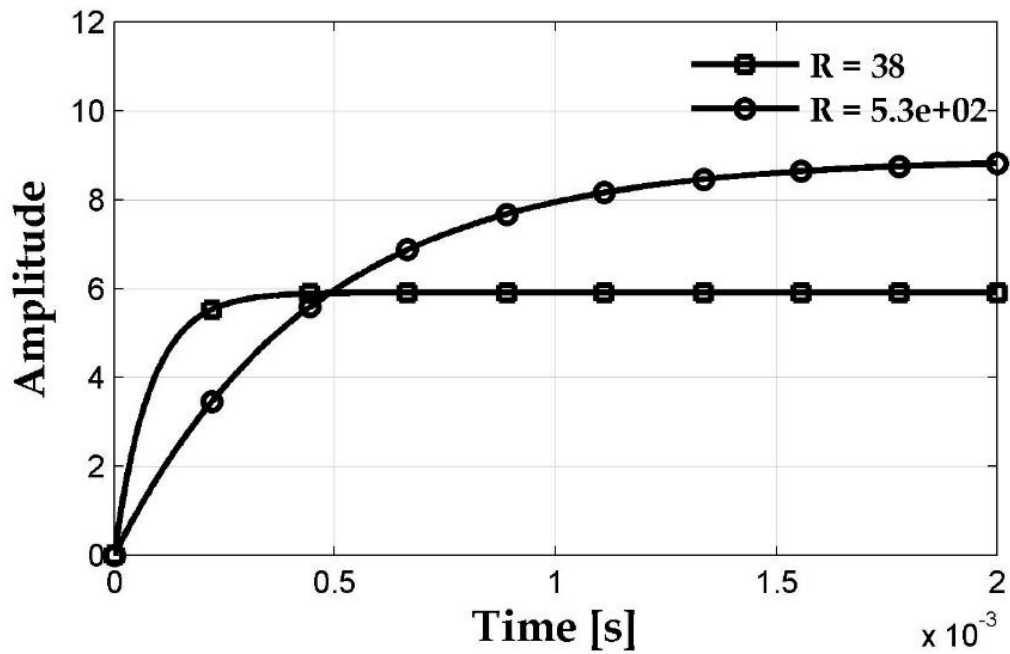


Figure 5.18: Transient step response for non-ideal DC-DC Boost converter in DCM

5.5 Boost Converter Controller Design Based on Particle Swarm Optimization (PSO)

Boost converters are employed when the required output voltage must be greater than its input voltage. Such converters are largely used in battery charging, solar power applications, fuel cell power converting systems, and battery driven vehicles [337], [338]. These converters, when operated in the open-loop mode, exhibit poor voltage regulation and unsatisfactory dynamic response. Hence, these converters are generally provided with a closed-loop controller to achieve good transient response and output voltage regulation. The mode of operation of the converter varies from ON- to OFF-state of the main power switch and, traditionally, small-signal linearization techniques have been employed for controller design.

Several conventional methods of closed-loop controller design for boost type DC-DC converters have been proposed to obtain the desired output voltage in the literature [339], [340]. In all of these works, the linearized transfer function model of a boost type DC-DC converter is employed for the closed-loop controller design. Linear PID and PI controllers are usually employed with boost type DC-DC converters, where these controllers are designed using standard frequency response techniques based on the small-signal model of the converter. The design is based on linear control theory such as Ziegler-Nichol method [341], Root Locus technique [342], Circle Based criterion [343], Hysteresis method [344], Bode plot, etc. These control strategies that are based on the linearized small-signal model of the converter generally have good performance around the operating point. However, a boost converter's small-signal model changes when its operating point changes. The poles and the right-half-plane zero, as well as the magnitude of the frequency response, are all dependent on the operating point. Thus, when the operating point changes, the fixed gain controller designed at one typical operating point through conventional techniques does not guarantee a satisfactory dynamic response at other operating points. Furthermore, DC-DC converters are switched mode circuits; hence, the mode of operation of these converters varies from the ON- to the OFF-state of the power switch, and therefore, it is difficult for the PID controller to respond well to changes in the operating point, and it often exhibits a poor performance when the system is subjected to large load variations.

Thus, the control of a boost type DC-DC converter has been a challenging task. The underlying fact of all of the above works is that the boost converter dynamics are strongly non-linear, and the controller designed at a specific operating point often fails to perform satisfactorily over a wide range of operating points. The past few decades have witnessed a number of contributions for the controller design of the DC-DC converters. The improved methods of controller design reported in the literature are Predictive Control [345], Sliding Mode Control [346], Adaptive Control [347], Passivity Based Control [348], H^∞ Control [331], Robust Control [349], Nominal and Tolerance Design [350], etc.

Recently the Genetic Algorithm (GA) [343], Ant Colony Optimization (ACO) [351] and Particle Swarm Optimization (PSO) [352] based approaches were also explored for the closed-loop controller design of boost type DC-DC converters. Controllers designed through such techniques have been shown to guarantee high dynamic and static performance over a wide range of operating points.

In this section, a novel optimization model based on the Particle Swarm Optimization (PSO) algorithm for the closed-loop controller design of a converter is designed to obtain the static and dynamic characteristics at all operating points. To test the methodology, the small-signal model of a boost type DC-DC converter which derived in previous sections is used to evaluate the objective function to yield a robust closed-loop controller structure that is subjected to internal and external disturbances. Design equations are derived, and the system is modeled in MATLAB. Extensive simulation tests are carried out with linear controller parameters and the results are presented.

5.5.1 Overview of Particle Swarm Optimization (PSO)

Particle swarm optimization (PSO) is a population-based, robust, stochastic optimization technique developed in 1995 by Eberhart and Kennedy [352], and is inspired by social behavior of fish schooling or bird flocking. PSO is initialized with a number of random agents (particles) that constitute a swarm moving in the search space looking for optima by updating the particles positions during the generations. Each particle represents a candidate solution to the problem at hand. In a PSO system, particles change their positions by flying around in a multi-dimensional search space until a relatively unchanging position has been

encountered, or until computational limitations are exceeded. In a social science context, a PSO system combines a social-only model and a cognition-only model [353]. The social-only component suggests that individuals ignore their own experience and adjust their behavior according to the successful beliefs of individuals in the neighborhood. On the other hand, the cognition-only component treats individuals as isolated beings. A particle changes its position using these models.

The basic elements of PSO technique are briefly stated and defined as follows:

- **Particle position, $X(t)$:** It is a candidate solution represented by an m -dimensional vector, where m is the number of optimized parameters. At time t , the j th particle $X_j(t)$ can be described as $X_j(t) = [x_{j,1}(t), \dots, x_{j,m}(t)]$, where x 's are the optimized parameters and $x_{j,k}(t)$ is the position of the j th particle with respect to the k th dimension, i.e. the value of the k th optimized parameter in the j th candidate solution.
- **Population, $pop(t)$:** It is a set of n particles at time t , i.e. $pop(t) = [X_1(t), \dots, X_n(t)]^T$.
- **Swarm:** It is an apparently disorganized population of moving particles that tend to cluster together while each particle seems to be moving in a random direction.
- **Particle velocity, $V(t)$:** It is the velocity of the moving particles represented by an m -dimensional vector. At time t , the j th particle velocity $V_j(t)$ can be described as $V_j(t) = [v_{j,1}(t), \dots, v_{j,m}(t)]$, where $v_{j,k}(t)$ is the velocity component of the j th particle with respect to the k th dimension.
- **Inertia weight, $w(t)$:** It is a control parameter that is used to control the impact of the previous velocities on the current velocity. Hence, it influences the trade-off between the global and local exploration abilities of the particles. For initial stages of the search process, large inertia weight to enhance the global exploration is recommended while, for last stages, the inertia weight is reduced for better local exploration.
- **Individual best position, $X^*(t)$:** As a particle moves through the search space, it compares its fitness value at the current position to the best fitness value it has ever attained at any time up to the current time. The best position that is associated with the best fitness encountered so far is called the individual best position, $X^*(t)$. For each particle in the swarm, $X^*(t)$ can be determined and updated during the search. In a minimization problem with objective function J , the individual best of the j th particle $X_j^*(t)$ is determined such

that $J(X_j^*(t)) \leq J(X_j(\tau))$, $\tau \leq t$. For simplicity, assume that $J_j^* = J(X_j^*(t))$. For the j th particle, individual best can be expressed as $X_j^*(t) = [x_{j,1}^*(t), \dots, x_{j,m}^*(t)]$.

- **Global best position, $X^{**}(t)$:** It is the best position among all individual best positions achieved so far. Hence, the global best can be determined such that $J(X^{**}(t)) \leq J(X_j^*(t))$, $j = 1, \dots, n$. For simplicity, assume that $J^{**} = J(X^{**}(t))$.

- **Stopping criteria:** these are the conditions under which the search process will terminate. In this study, the search will terminate if one of the following criteria is satisfied:

- a) The number of iterations since the last change of the best solution is greater than a pre-specified number or
- b) The number of iterations reaches the maximum allowable number.

Figure 5.19 illustrates the flowchart of the PSO method.

In this work, the PSO algorithm has been developed as follows:

- An annealing procedure has been incorporated in order to make uniform search in the initial stages and very local search in the later stages. A decrement function for decreasing the inertia weight given as $w(t) = \alpha w(t - 1)$, where α is a decrement constant smaller than but close to 1, is proposed in this work.
- Feasibility checks procedure of the particle positions has been imposed after the position updating to prevent the particles from flying outside the feasible search space.
- The particle velocity in the k th dimension is limited by some maximum value, v_k^{max} . This limit enhances the local exploration of the problem space and it realistically simulates the incremental changes of human learning [353].

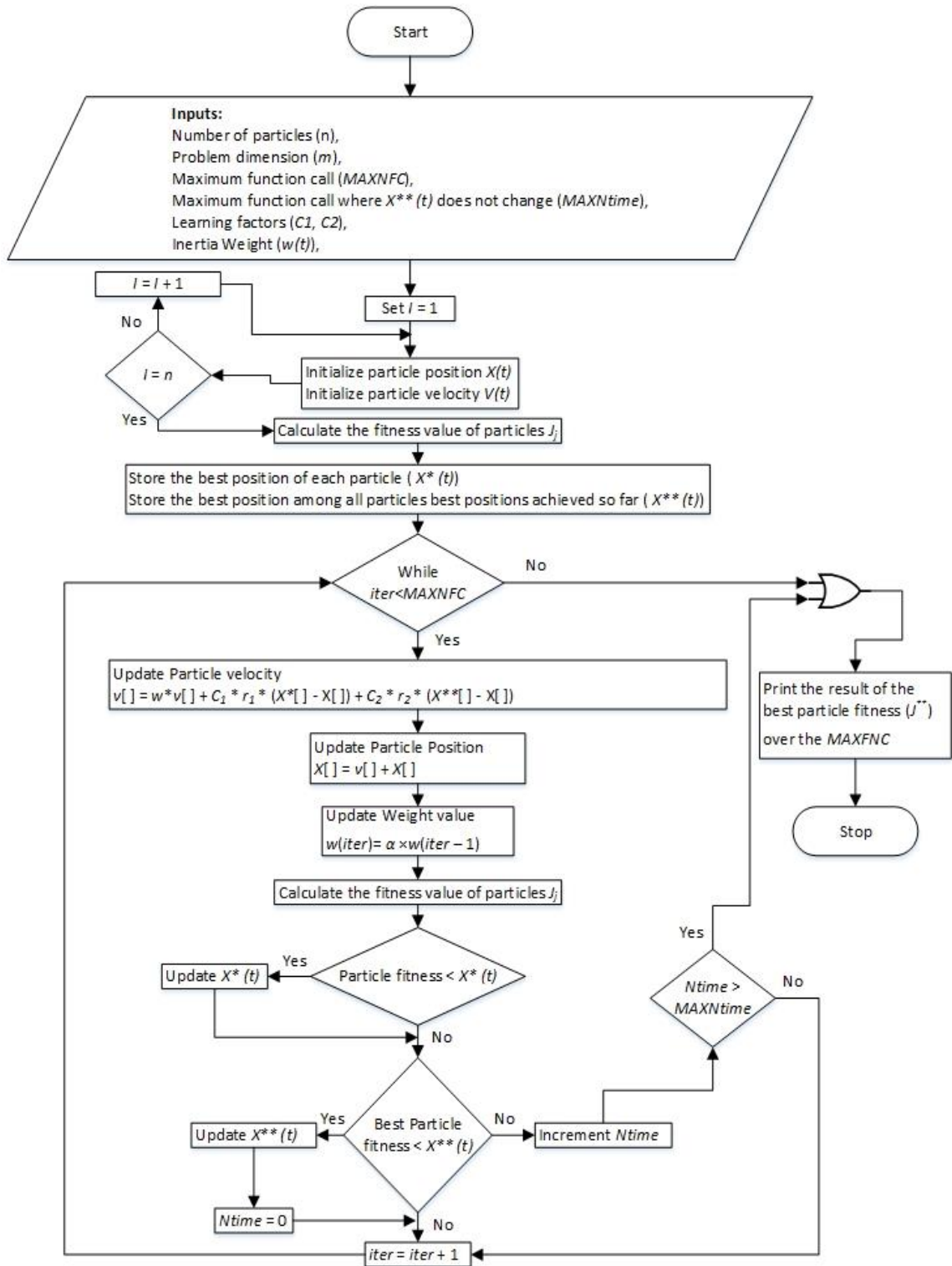


Figure 5.19: Flowchart of the PSO method

In the PSO algorithm, the population has n particles and each particle is an m -dimensional vector, where m is the number of optimized parameters. Incorporating the above modifications, the computational flow of PSO technique can be described in the following steps:

Step 1 (Initialization):

- Set the time counter $t = 0$ and generate randomly n particles, $\{X_j(0), j = 1, \dots, n\}$, where $X_j(0) = [x_{j,1}(0), \dots, x_{j,m}(0)]$. $x_{j,k}(0)$ is generated by randomly selecting a value with uniform probability over the k th optimized parameter search space $[x_k^{min}, x_k^{max}]$.
- Similarly, generate randomly initial velocities of all particles, $\{V_j(0), j = 1, \dots, n\}$, where $V_j(0) = [v_{j,1}(0), \dots, v_{j,m}(0)]$. $v_{j,k}(0)$ is generated by randomly selecting a value with uniform probability over the k th dimension $[-v_k^{max}, v_k^{max}]$.
- Each particle in the initial population is evaluated using the objective function, J .
- For each particle, set $X_j^*(0) = X_j(0)$ and $J_j^* = J_j, j = 1, \dots, n$.
- Search for the best value of the objective function J_{best} .
- Set the particle associated with J_{best} as the global best, $X^{**}(0)$, with an objective function of J^{**} .
- Set the initial value of the inertia weight $w(0)$.

Step 2 (Time updating):

- Update the time counter $t = t + 1$.

Step 3 (Weight updating):

- Update the inertia weight $w(t) = \alpha w(t - 1)$, where alpha is a decrement constant which is smaller than but close to 1, to encourage the global exploration (i.e., diversify the search in the whole search space) in the initial stages and encourage local exploitation (i.e., intensify the search in the current region) in the later stages.

Step 4 (Velocity updating):

- Using the global best and individual best of each particle, the j th particle velocity in the k th dimension is updated, according to the following equation:

$$v_{j,k}(t) = w(t)v_{j,k}(t-1) + C_1r_1(x_{j,k}^*(t-1) - x_{j,k}(t-1)) + C_2r_2(x_{j,k}^{**}(t-1) - x_{j,k}(t-1)) \quad (5.82)$$

where C_1 and C_2 are positive constants and r_1 and r_2 are uniformly distributed random numbers between 0 to 1.

- It is worth mentioning that the second term in the previous equation represents the cognitive part of PSO where the particle changes its velocity based on its own thinking and memory.
- The third term in the previous equation represents the social part of PSO where the particle changes its velocity based on the socio-psychological adaptation of knowledge. If a particle violates the velocity limits, its velocity is set equal to the limit.

Step 5 (Position updating):

- Based on the updated velocities, each particle changes its position according to the following equation:

$$x_{j,k}(t) = v_{j,k}(t) + x_{j,k}(t-1) \quad (5.83)$$

If a particle violates its position limits in any m -dimensional space, set its position at the proper limits (i.e. set the value to the limit it exceeds) to prevent the particles from flying outside the feasible search space.

Step 6 (Individual best updating):

- Each particle is evaluated according to its updated position. If $J_j < J_j^*$, $j = 1, \dots, n$, then update individual best as $X_j^*(t) = X_j(t)$ and $J_j^* = J_j$ and go to step 7; else go to step 7.

Step 7 (Global best updating):

- Search for the minimum value J_{min} among J_j^* , where min is the index of the particle with minimum objective function, i.e. $min \in \{j; j = 1, \dots, n\}$. If $J_{min} < J^{**}$, then update global best as $X^{**}(t) = X_{min}(t)$ and $J^{**} = J_{min}$ and go to step 8; else go to step 8.

Step 8 (Stopping criteria):

- If one of the stopping criteria is satisfied, then terminate the program; else go to step 2. In this study, the search will terminate the program if one of the following criteria is satisfied:
 - (a) The number of iterations since the last change of the best solution (N_{time}) is greater than a pre-specified number ($MAXN_{time}$), or
 - (b) The number of iterations reaches the maximum allowable number ($MAXNFC$).

5.5.2 Application of Particle Swarm Optimization (PSO) to Design Boost Converter Controller

A closed-loop boost converter using a MOSFET, as a switching element, is shown in Figure 5.20. The parameters of the converter are: input voltage, $V_{in} = 20$ V; switching frequency, $f_s = 1.5$ kHz; inductance, $L = 33$ mH; equivalent resistance of the inductor, $R_L = 1.5$ Ω ; capacitance, $C = 220$ μ F; equivalent resistance of the capacitor, $R_C = 0.3$ Ω ; and load resistance, $R = 230$ Ω .

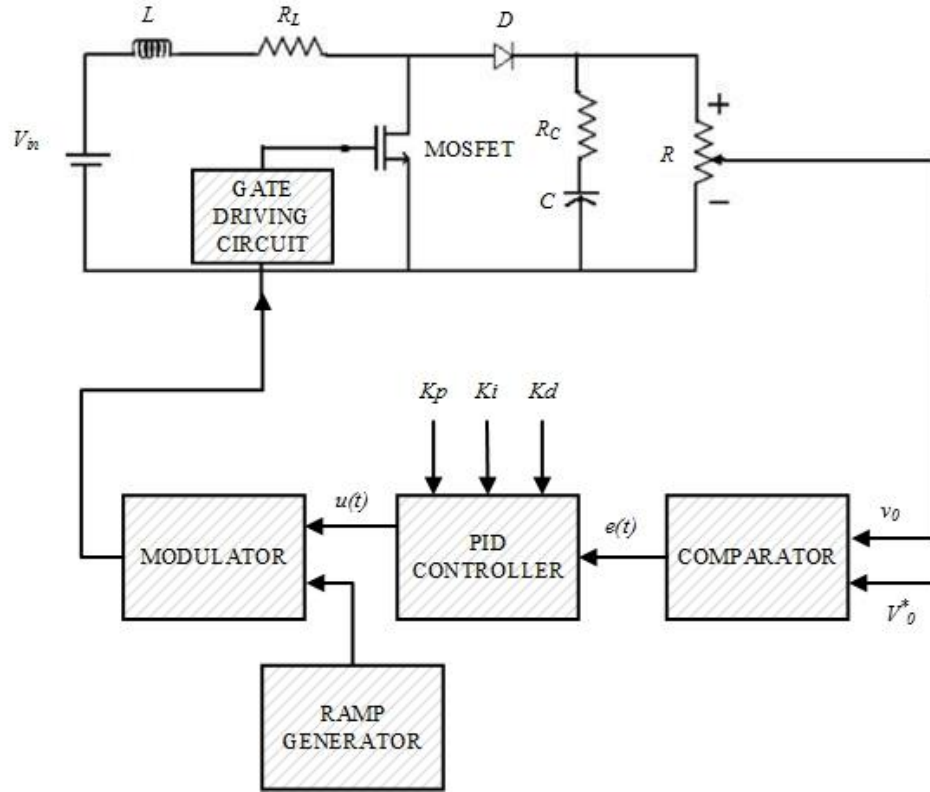


Figure 5.20: Closed-loop controller and boost converter

In the closed-loop control system, first, the actual output voltage v_0 is compared with its reference voltage V_0^* using a comparator and the error voltage $e(t)$, so obtained, is processed by the PID controller. The output voltage of the PID controller $u(t)$ is an analog signal which must be converted into a gating pulse for the MOSFET with an adjustable duty cycle. This task is performed by the modulator, which compares the PID controller output voltage with a ramp signal so that the output of the modulator is a gating pulse with its duty cycle varying in accordance with PID controller output voltage.

In this work, more emphasis is given to improving the dynamic response of the boost converter by identifying the best values for the controller parameters. The following dynamic parameters are considered in this work:

- i) Rise Time (t_r).
- ii) Settling Time (t_s).
- iii) Peak Overshoot (P_o).
- iv) Steady State Error (E_{ss}).

The DC-DC Boost converter, when it works in a closed-loop mode with PID controller, the error voltage is

$$e(t) = V_0^* - v_0 \quad (5.84)$$

The error voltage is processed by the PID controller, and the output of the PID controller is

$$u(t) = [K_p e(t) + K_i \int e(t) dt + K_d \frac{d}{dt} e(t)] \quad (5.85)$$

Equations (5.1) to (5.22) completely describe the dynamics of the output voltage of the closed-loop DC-DC Boost converter operating in CCM.

The objective here is to identify the optimal controller parameters values to achieve the best dynamic response of DC-DC Boost converter. This problem is solved as an optimization problem formulated as:

$$\text{Minimize } J = ((1 + t_r)(1 + t_s)(1 + P_o)(1 + E_{ss})) \quad (5.86)$$

Subject to constraints:

$$K_p^{min} < K_p < K_p^{max}$$

$$K_i^{min} < K_i < K_i^{max}$$

$$K_d^{min} < K_d < K_d^{max}$$

The initial values of K_p , K_i , and K_d must be judiciously chosen to speed up the process of optimum parameter identification. For this, one might use methods such as Routh–Hurwitz, Symmetrical Optimum [354], etc., with averaged state-space model of DC-DC Boost converter operating in CCM.

Now the performance of the DC-DC Boost converter in terms of its dynamic response is analyzed. A dedicated program is developed in MATLAB for controller identification using PSO. The parameters of the proposed PSO, such as C_1 , C_2 , inertia weight factor, population size, and number of iterations, are usually selected by means of trial and error method to achieve the best solution set. The parameters used in the implementation of the PSO are listed in Table 5.1.

TABLE 5.1: PARAMETERS USED IN THE IMPLEMENTATION OF PSO

C_1	1.4
C_2	1.4
w_{max}	0.9
w_{min}	0.4
Population size (n)	50
Number of iterations ($iter$)	300

The controller constants obtained through a traditional method (i.e. Ziegler–Nichol) are listed below:

$$K_p = 1.8788, \quad K_i = 18.8046, \quad K_d = 0.000608$$

For comparison, the controller design is also carried out using standard PSO. The controller constants obtained through standard PSO are listed below:

$$K_P = 1.325, \quad K_i = 15.8851, \quad K_d = 0.000489$$

The computed closed loop response of the DC-DC Boost converter operating in CCM obtained by using traditional method of designing a PID controller and PSO algorithm with small signal model is given in Figure 5.21.

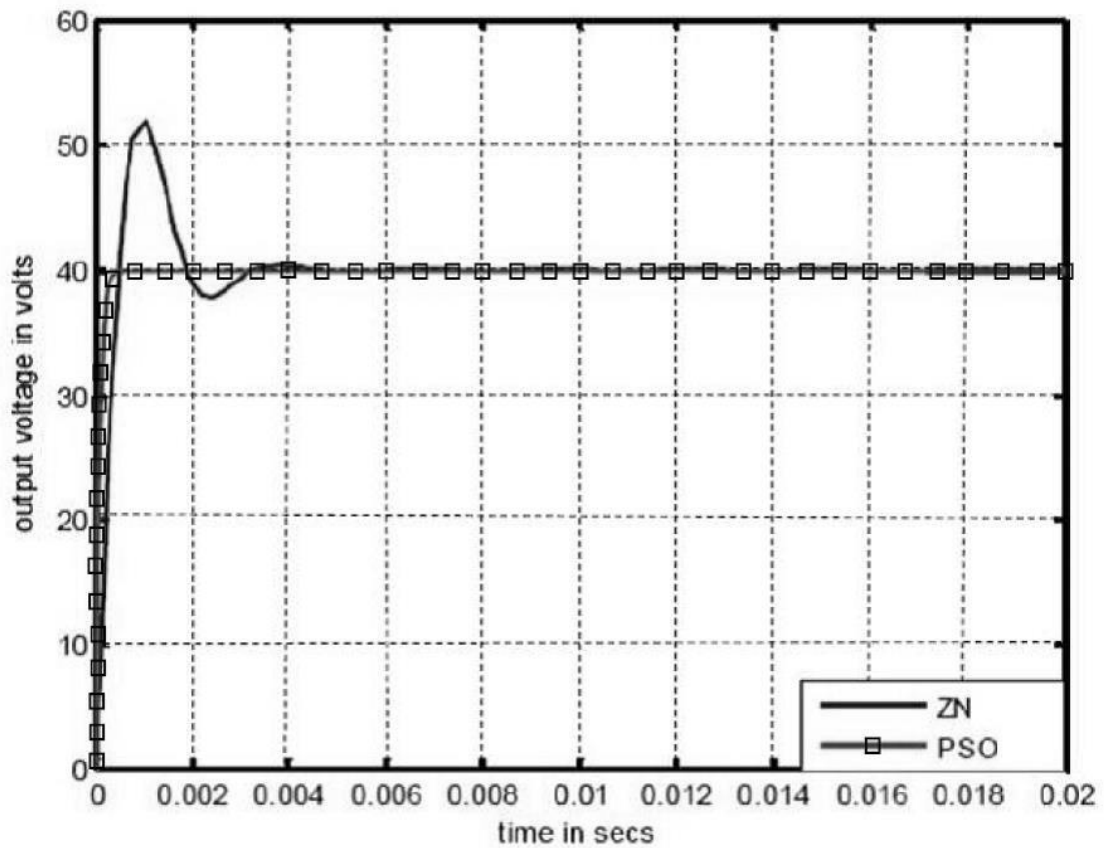


Figure 5.21: Closed loop response of DC-DC Boost converter operating in CCM

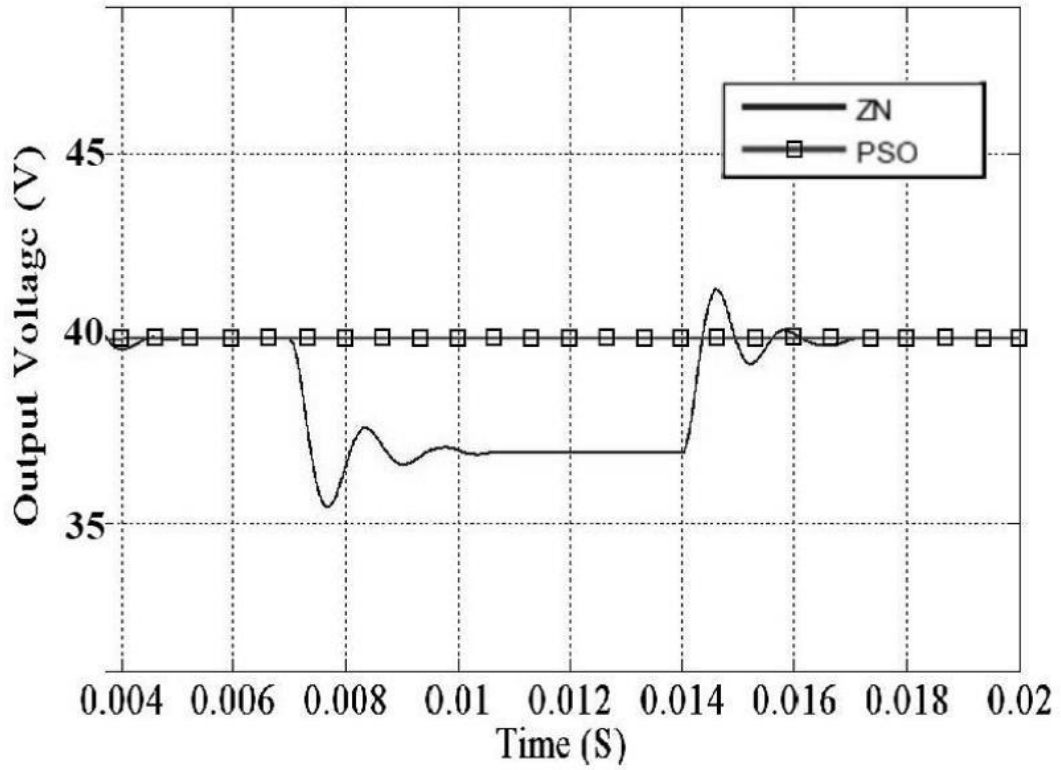


Figure 5.22: Closed loop response of DC-DC Boost converter operating in CCM with $\pm 10\%$ source voltage disturbance

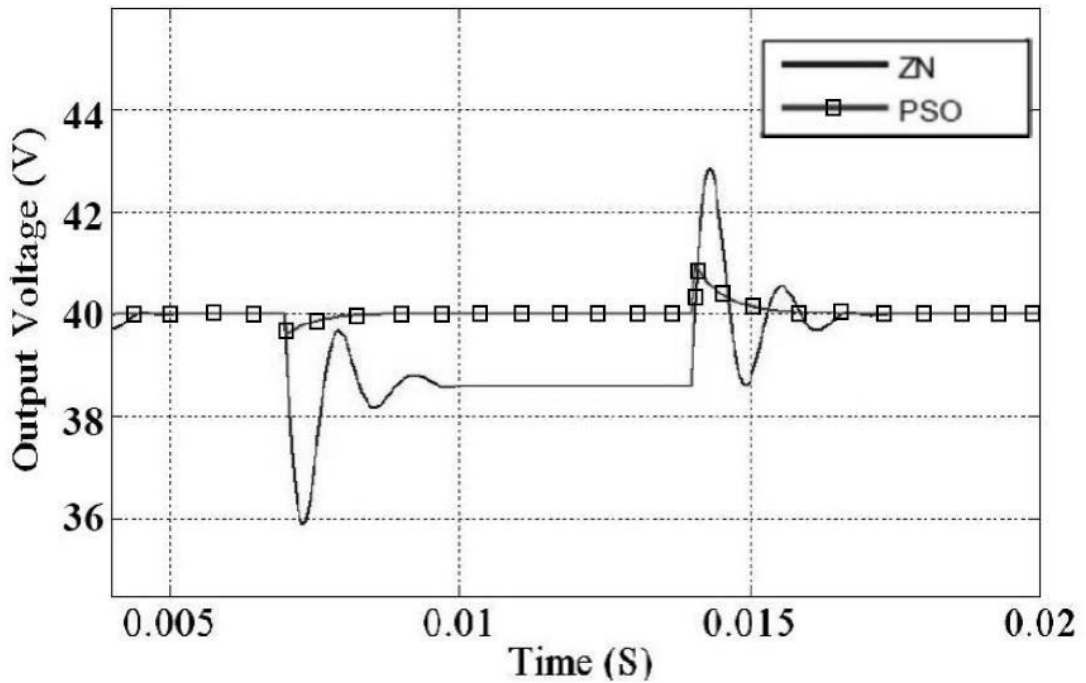


Figure 5.23: Closed loop response of DC-DC Boost converter operating in CCM with $\pm 13\%$ sudden load disturbance

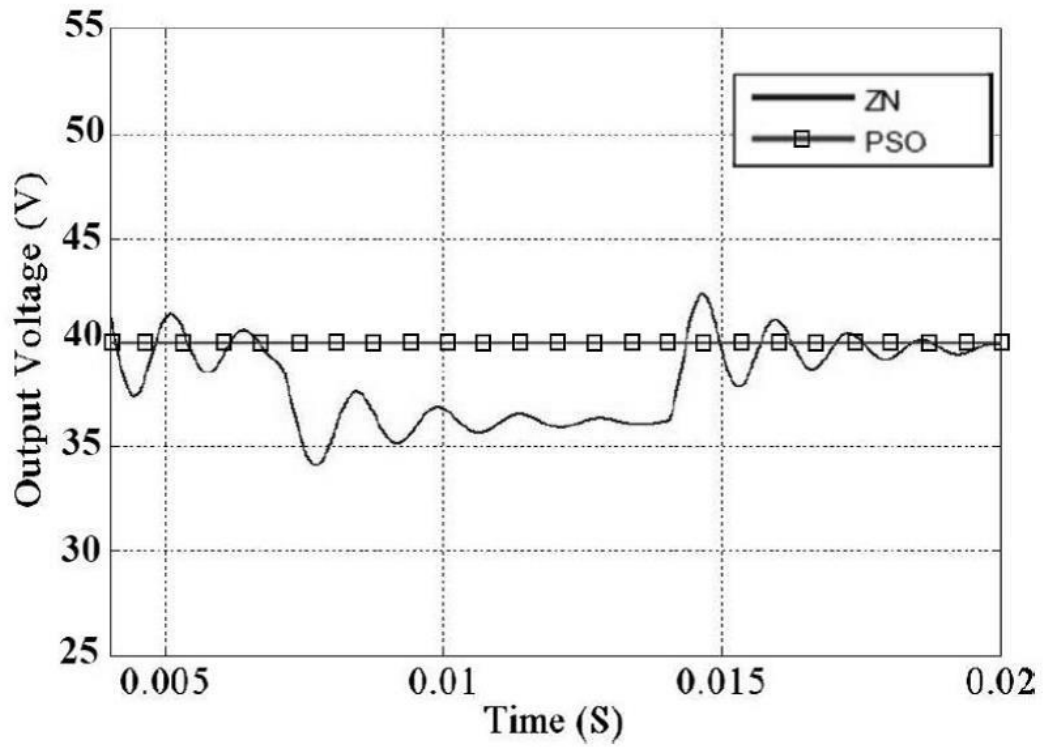


Figure 5.24: Closed loop response of DC-DC Boost converter operating in CCM with $\pm 25\%$ source voltage disturbance

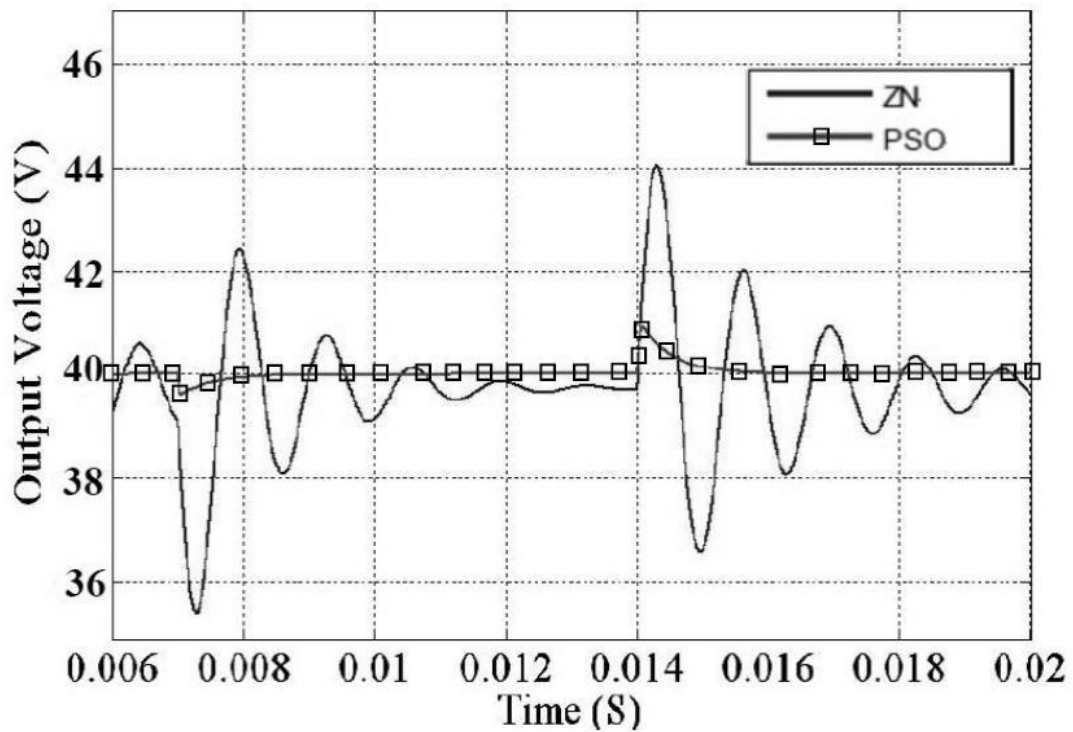


Figure 5.25: Closed loop response of DC-DC Boost converter operating in CCM with $\pm 35\%$ sudden load disturbance

In this section, simulation results are presented for comparison between the dynamic responses of the DC-DC Boost converter operating in CCM obtained by using either a traditional method of designing a PID controller or a PSO algorithm undergoing input-voltage and load-current step transients. Four different scenarios of performance comparison tests are presented:

1. $\pm 10\%$ source voltage disturbance.
2. $\pm 13\%$ sudden load disturbance.
3. $\pm 25\%$ source voltage disturbance.
4. $\pm 35\%$ sudden load disturbance.

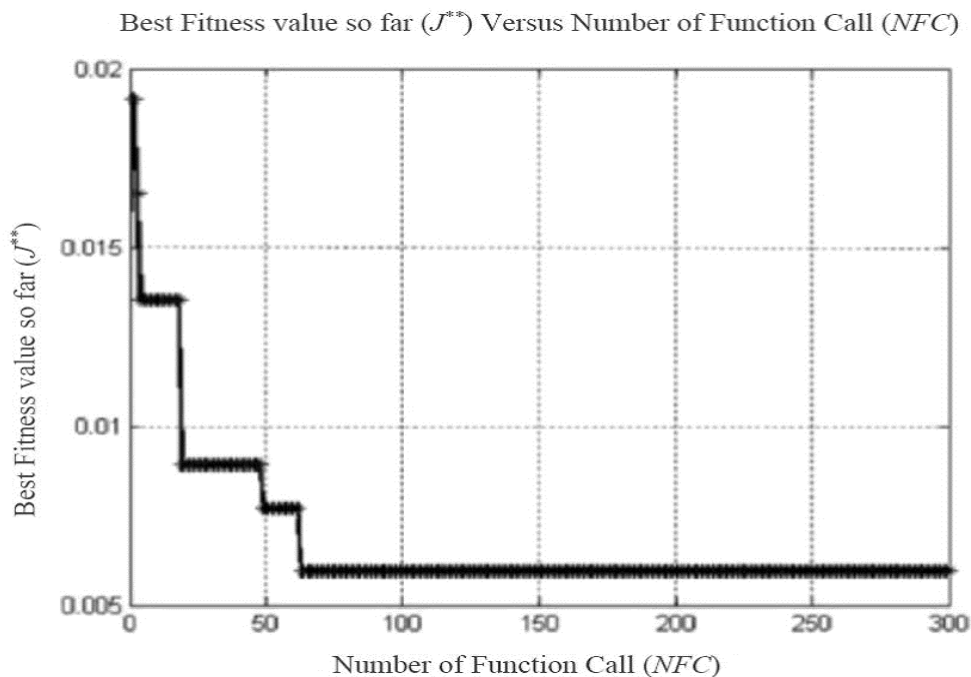


Figure 5.26: The convergence characteristic of the PSO algorithm

Figure 5.22 shows the dynamic behavior of the DC-DC Boost converter output voltage with a $\pm 10\%$ step-change in input voltage. The simulation results show that the output voltage remains virtually constant at the set value, regardless of change in input voltage especially with the PSO tuned controller whereas the performance of the DC-DC Boost converter with traditional method tuned controller degrades having an overshoot of 12%, 3.5 ms settling time and 6.9% E_{ss} .

Figure 5.23 shows the dynamic behavior of the converter system with a $\pm 13\%$ step-change in load resistance. In the case of the PSO tuned controller, the output voltage of the

converter has an overshoot of 2.5% at the set value for the load resistance disturbance, 2 ms settling time and zero steady-state error. However, in the case of the converter with traditional method tuned controller, it has an overshoot of 7.5%, 4 ms settling time and 3.7% E_{ss} .

Figure 5.24 shows the DC-DC Boost converter output voltage response for a $\pm 25\%$ step-change in input voltage for both traditional method tuned controller and PSO tuned controller. It is seen that the output voltage of the DC-DC Boost converter is not affected by the input voltage variation in case of PSO tuned controller whereas the performance of the DC-DC Boost converter with traditional method tuned controller degrades having an overshoot of 15%, 6.8 ms settling time and 9.3% E_{ss} .

Figure 5.25 shows the DC-DC Boost converter output voltage response for a $\pm 35\%$ step-change in load resistance for both traditional method tuned controller and PSO tuned controller. The PSO tuned controller scheme takes 1.6 ms settling time with an overshoot of 2.2% as compared to 7 ms and 12.5% in case of the traditional method tuned controller. Hence, PSO tuned controller has a smaller overshoot and zero steady state error than the traditionally tuned controller.

Table 5.2 shows the performance evaluation of DC-DC Boost converter dynamic response obtained by using traditional method of designing a PID controller and PSO algorithm in terms of percent overshoot, rise time and setting time under the starting case, the changing of command input and load. In addition, the convergence characteristic of the proposed optimization algorithm is depicted in Figure 5.26.

The simulation results in Figures 5.22, 5.23, 5.24 and 5.25 clearly indicate the robustness and effectiveness of the controller tuned by the PSO algorithm over the traditional method tuned controller by providing a faster transient response for a wide operating range.

TABLE 5.2: PERFORMANCE EVALUATION OF DC-DC BOOST CONVERTER DYNAMIC RESPONSE
OPERATING IN CCM

Test Cases		Transient Parameters	ZN-PID Controller	PSO-PID Controller
Starting case	100% Step Change	Rising time (ms)	0.50	0.45
		Settling time (ms)	4.71	1.22
		Peak Overshoot (%)	28.75	0.00
SMALL Source Voltage Disturbance	-10% Step Change	Settling time (ms)	3.34	0.25
		Peak Overshoot (%)	12.15	0.00
	+10% Step Change	Settling time (ms)	3.53	0.23
		Peak Overshoot (%)	12.15	0.00
SMALL Load Resistance Disturbance	-13% Step Change	Settling time (ms)	3.84	1.22
		Peak Overshoot (%)	7.51	1.53
	+13% Step Change	Settling time (ms)	4.03	2.14
		Peak Overshoot (%)	7.51	2.52
LARGE Source Voltage Disturbance	-25% Step Change	Settling time (ms)	6.55	0.25
		Peak Overshoot (%)	15.02	0.00
	+25% Step Change	Settling time (ms)	6.75	0.24
		Peak Overshoot (%)	15.02	0.00
LARGE Load Resistance Disturbance	-35% Step Change	Settling time (ms)	7.24	1.25
		Peak Overshoot (%)	12.53	1.38
	+35% Step Change	Settling time (ms)	7.22	1.65
		Peak Overshoot (%)	12.53	2.23

5.6 Performance Analysis of Boost Converter by Using Different Integration Algorithms

It is currently accepted that online real-time, or Hardware-In-the-Loop (HIL), simulation paradigm is an indispensable tool in the design and testing of advanced complex systems. A HIL control and test platform is of vital importance to verify the proper operation of these systems before its installation and to guide its commissioning and trial phases.

Real-time simulation [355] places severe demands on the simulation time-step that can be used, stipulating that such a time-step be much smaller than the natural frequency of the fastest dynamics in the simulated system. This demand becomes problematic since the computations performed at each time-step can only be carried out in a finite time period, which may be longer than the minimum time-step necessitated by the real-time simulation. Unfortunately, this is typically the case for many multi-level power converters and their controllers, where their complexity coupled with the latency barrier in the conventional computing platforms makes real-time simulation unfeasible. To address this problem, a new trend is to use re-configurable platforms with Field Programmable Gate Arrays (FPGAs), instead of the conventional microprocessor-based platforms to enable real-time models with very small time-step and very low latency.

The numerical integration methods used in the circuit transient analysis packages are not necessarily the most accurate approximations to obtain the actual transient response of a circuit. The study of different numerical integration methods and their stability characteristics is the focus of this section to enable HIL testing.

The structure of DC-DC converters consists of linear (i.e. resistor R, inductor L and capacitor C) and nonlinear (i.e. switch) components. Since these converters can be characterized as nonlinear and time-variant system, then the small-signal model of the state-space average model is required to design a linear controller. References [329], [327], [328] show examples of the small-signal analysis and design of a linear controller in the frequency domain for DC-DC converters.

The developed average models in the previous sections were discretized and simulated in Matlab platform using nine popular integration techniques/algorithms. This permitted further analysis in terms of accuracy, stability as well as algorithm complexity involved with implementing the integration methodologies.

Dedicated programs are developed in Matlab for simulation of DC-DC Boost converter. The dynamic performance of ideal and Non-ideal DC-DC Boost converter operating in CCM models were evaluated after solving the small-signal models for DC-DC Boost converter in CCM which described the system dynamics by nine different numerical integration techniques, namely:

1. Laplace Transform.

2. Ode45 Matlab solver.
3. Ode23t Matlab solver.
4. Forward Euler.
5. Improved Euler.
6. Backward Euler.
7. Runge-Kutta 4th order.
8. Trapezoidal Rule.
9. Simpson Rule.

The simulations were done by using the following model parameters: $L= 180 \mu\text{H}$, $C = 4.7 \mu\text{F}$, $V_{in} = 5\text{V}$, $D= 0.7$, $R_C = 0.1 \Omega$, $R_L = 0.8 \Omega$, and $F_S = 350 \text{ kHz}$.

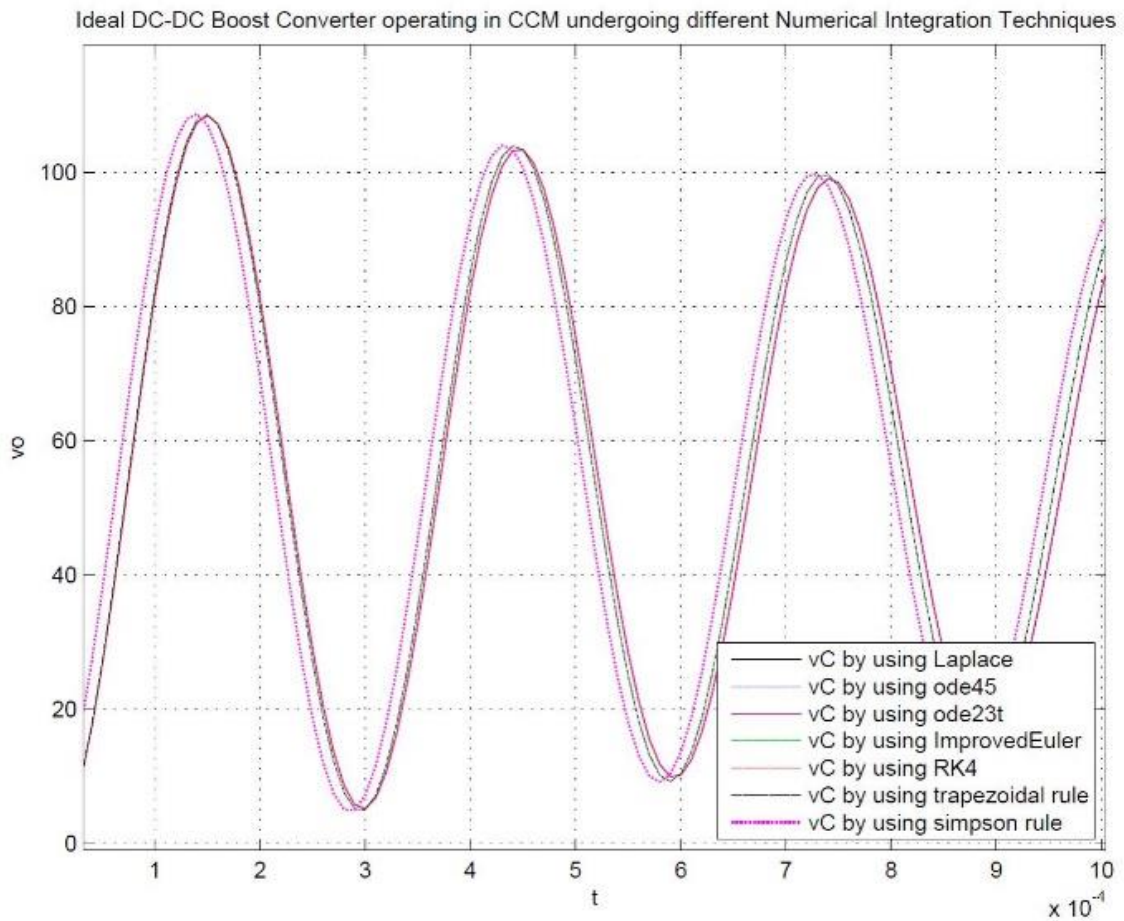


Figure 5.27: Ideal DC-DC Boost converter operating in CCM undergoing different numerical integration techniques

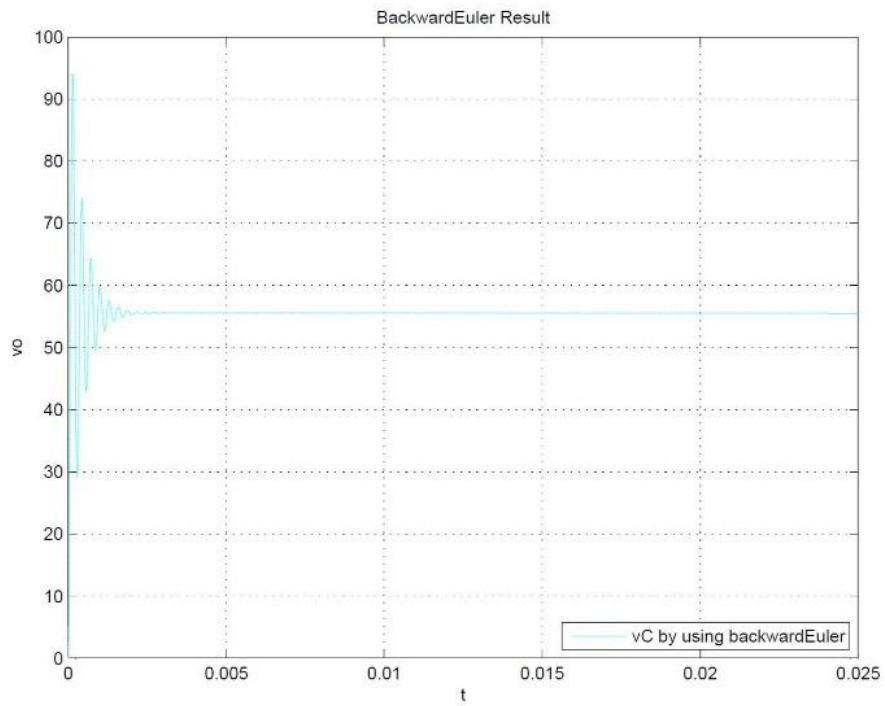


Figure 5.28: Ideal DC-DC Boost converter operating in CCM undergoing Backward Euler technique

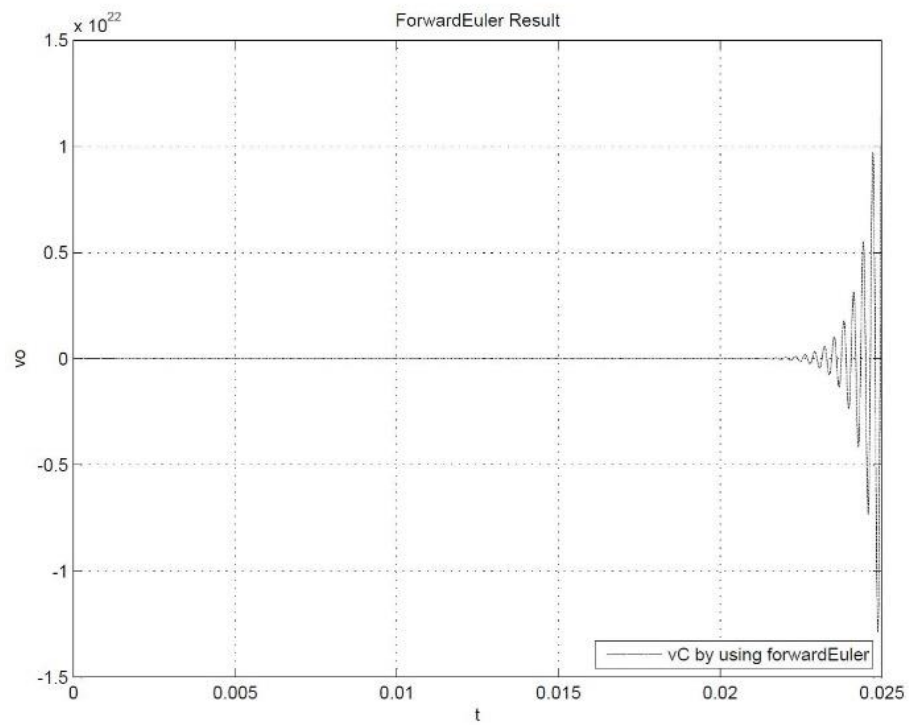


Figure 5.29: Ideal DC-DC Boost converter operating in CCM undergoing Forward Euler technique

From the simulation results, it is clear that, there are four different groups of simulation results:

1. Simulation results for Laplace Transform, Ode45 Matlab solver, Ode23t Matlab solver and Runge-Kutta 4th order are all virtually identical (Figure 5.27). These results are considered as accurate.
2. The simulation results for Improved Euler and Trapezoidal Rule are virtually identical and have a little bit difference from the previous group. (Figure 5.27)
3. Simulation result for Simpson Rule have some differences from the first group, which are considered as accurate. (Figure 5.27)
4. Simulation result (Figure 5.28) for Backward Euler method have a big difference from the first group results (which are considered as accurate) and the simulation result (Figure 5.29) for Forward Euler is unstable.

Now, if the time-step used for simulation is decreased by 10 times, the simulation result for the Ideal DC-DC Boost converter using the Forward Euler technique is changes from unstable behavior to stable behavior, but with a larger settling time as shown in Figure 5.30. Also, decreasing the time-step made the simulation results for the other numerical integration techniques also became closer to each other as shown in Figure 5.31.

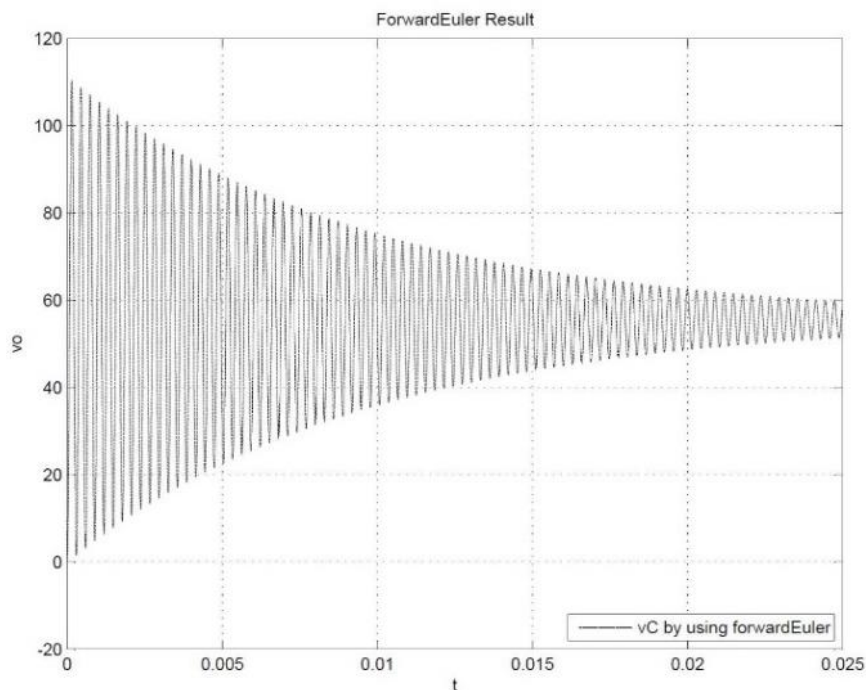


Figure 5.30: Ideal DC-DC Boost converter operating in CCM undergoing Forward Euler technique with smaller step-size

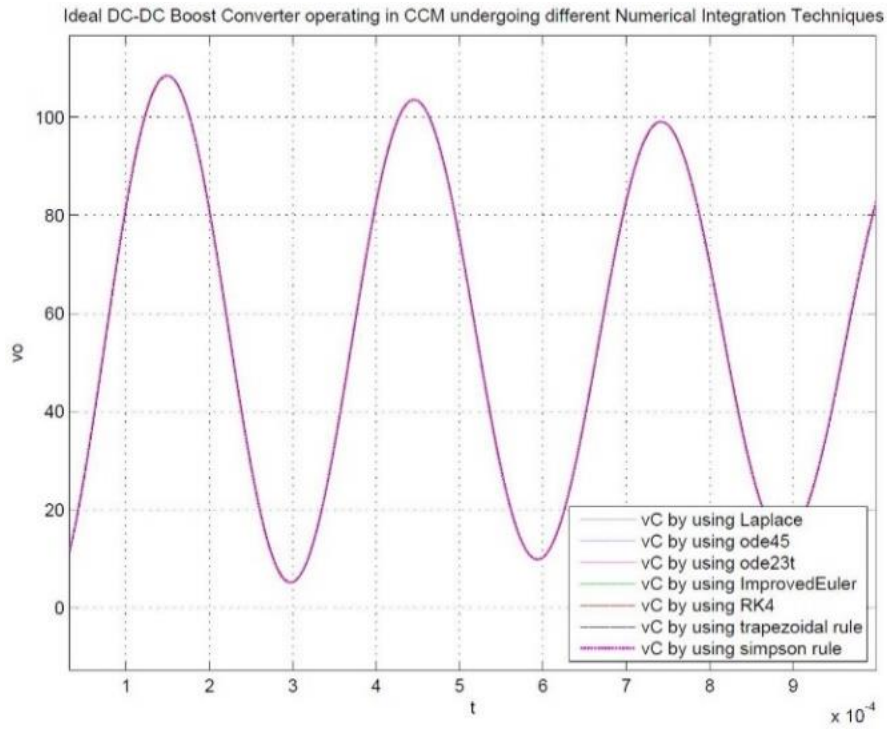


Figure 5.31: Ideal DC-DC Boost converter operating in CCM undergoing different numerical integration techniques with smaller step-size

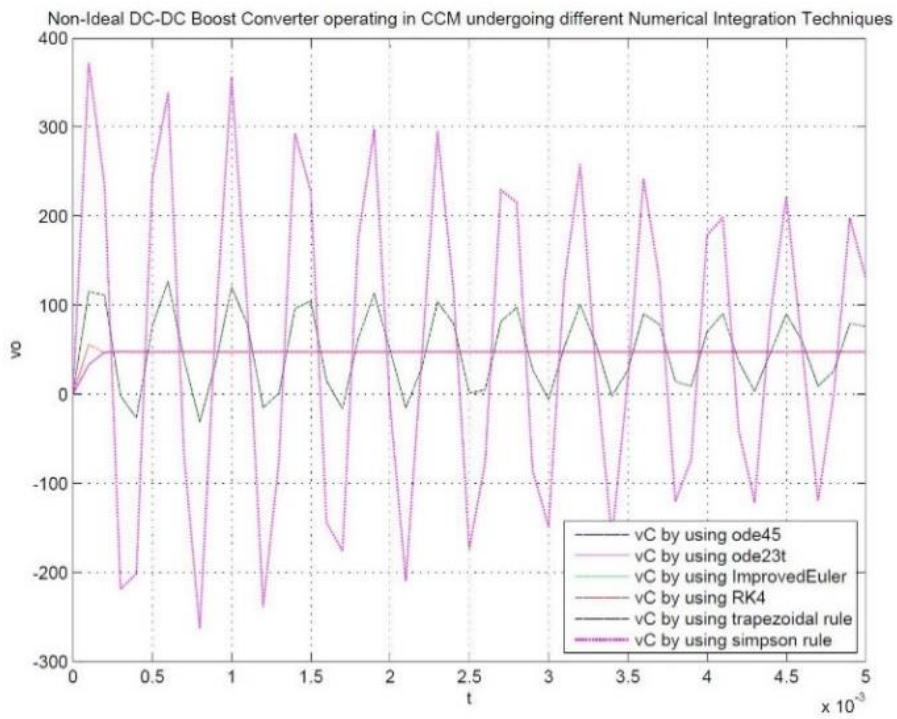


Figure 5.32: Non-ideal DC-DC Boost converter operating in CCM undergoing different numerical integration techniques

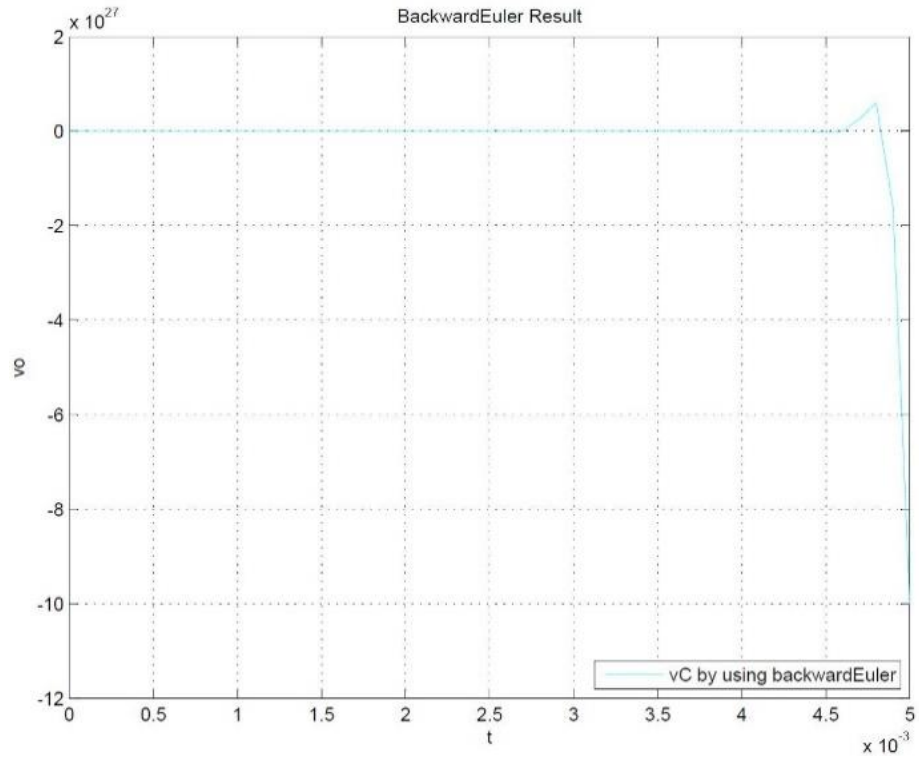


Figure 5.33: Non-ideal DC-DC Boost converter operating in CCM undergoing Backward Euler technique

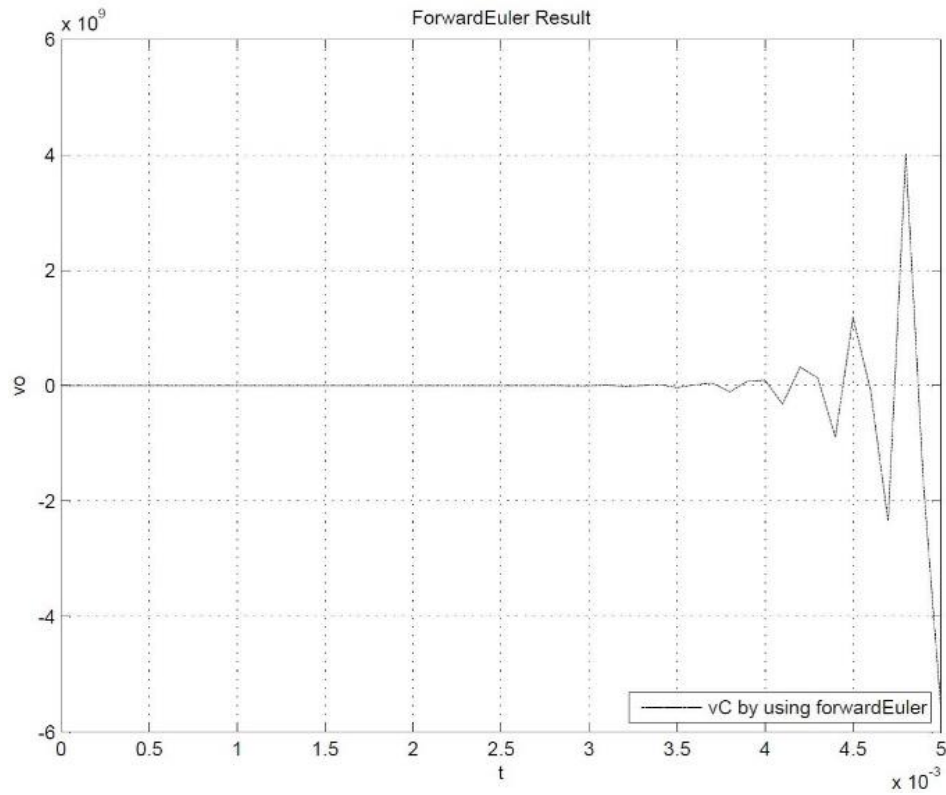


Figure 5.34: Non-ideal DC-DC Boost converter operating in CCM undergoing Forward Euler technique

From the simulation results, it is clear that, there are now five different groups of simulation results:

1. Simulation results for Laplace Transform, Ode45 and Ode23t Matlab solvers are all identical (Figure 5.32). This group results are considered as accurate.
2. Simulation results for Runge-Kutta 4th order have a little bit difference from previous group. (Figure 5.32)
3. The simulation results for Improved Euler and Trapezoidal Rule are identical and have some difference from first group. (Figure 5.32)
4. Simulation result for Simpson Rule have a big difference from first group (which are considered as accurate) (Figure 5.32).
5. Simulation results (Figure 5.33 & Figure 5.34) using Backward Euler and Forward Euler methods are unstable.

Now, if the time-step used for simulation is decreased by 1.5 times the previous value, the simulation results for Non-ideal DC-DC Boost converter using different numerical integration techniques will be changed.

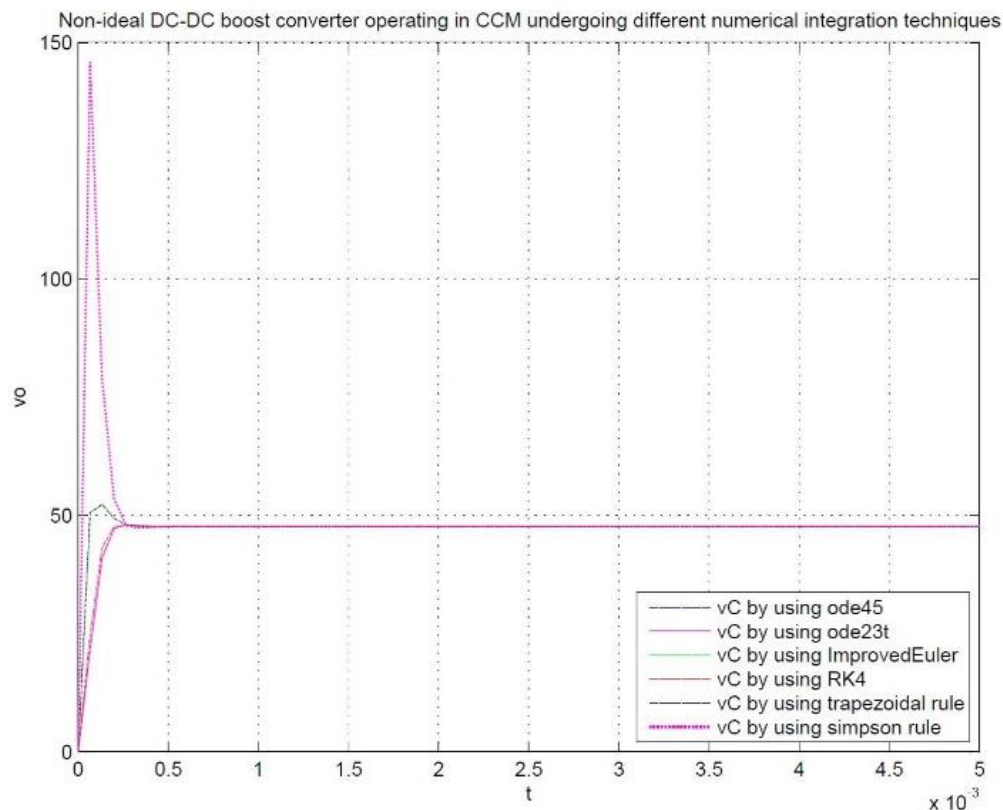


Figure 5.35: Non-ideal DC-DC Boost converter operating in CCM undergoing different numerical integration techniques

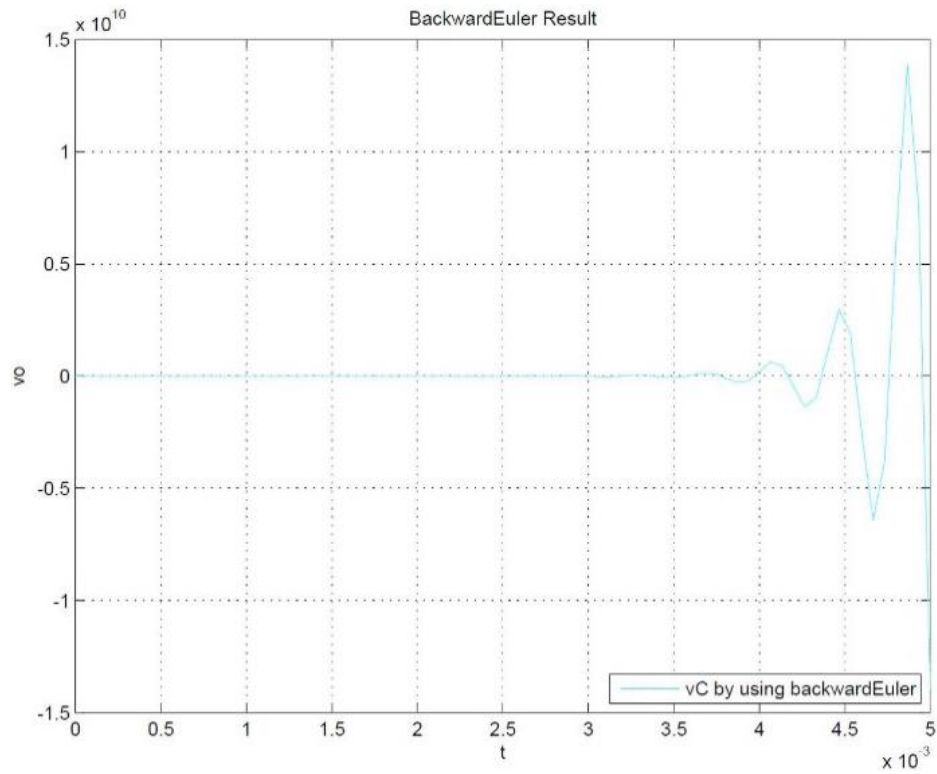


Figure 5.36: Non-ideal DC-DC Boost converter operating in CCM undergoing Backward Euler technique

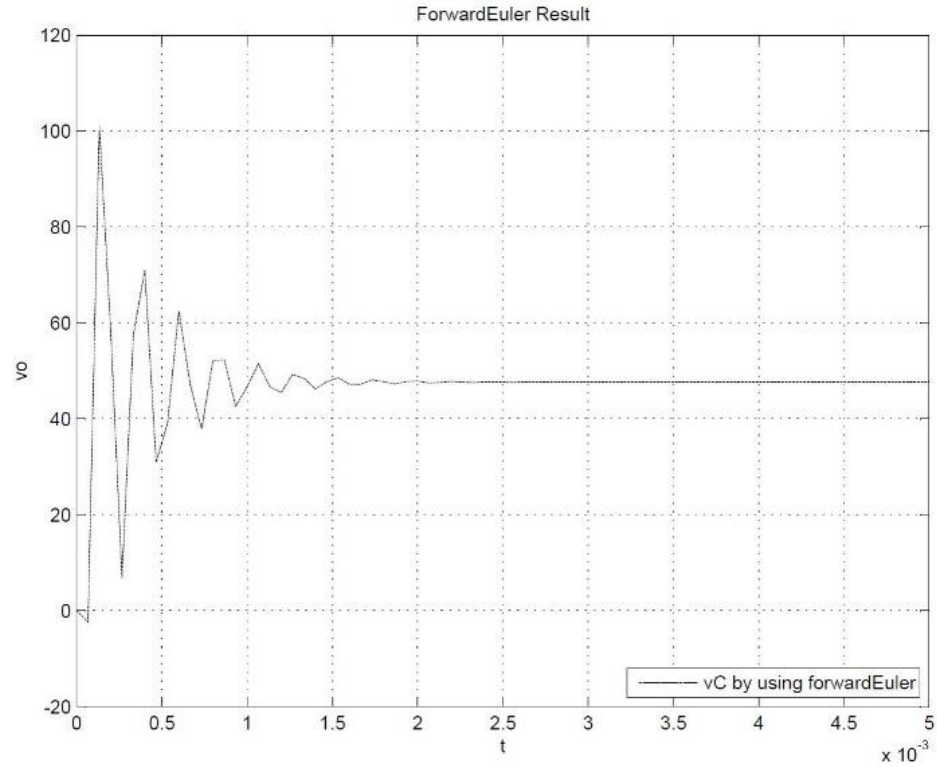


Figure 5.37: Non-ideal DC-DC Boost converter operating in CCM undergoing Forward Euler technique

From the simulation results, it's clear that, there are five different groups of simulation results:

1. Simulation results for Laplace Transform, Ode45 and Ode23t Matlab solvers are all identical (Figure 5.35).
2. Simulation results for Runge-Kutta 4th order have a little bit difference from previous group (Figure 5.35).
3. The simulation results for Improved Euler and Trapezoidal Rule are identical and have some difference from the first group (Figure 5.35).
4. Simulation result for Simpson Rule show a big difference from the first group which are considered as accurate (Figure 5.35).
5. Simulation result (Figure 5.36) for Backward Euler is still unstable but the simulation result (Figure 5.37) for Forward Euler is changing from unstable behavior to stable behavior with more settling time.

Now, if the time-step used for simulation decreased by 1.33 times the previous value, the simulation results for Non-ideal DC-DC Boost converter undergoing different numerical integration techniques will be changed.

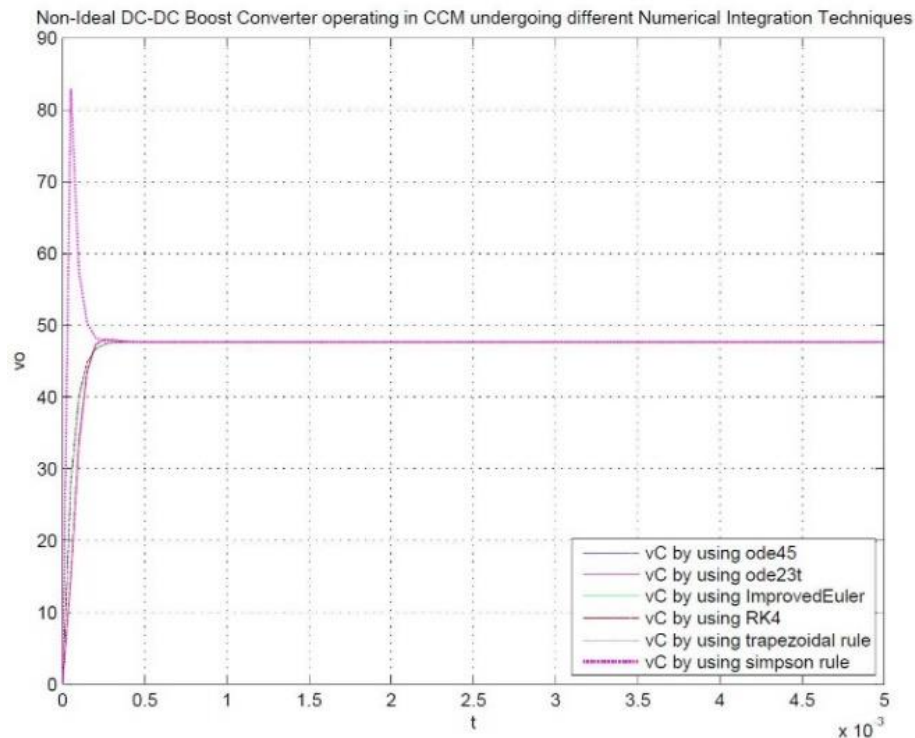


Figure 5.38: Non-ideal DC-DC Boost converter operating in CCM undergoing different numerical integration techniques

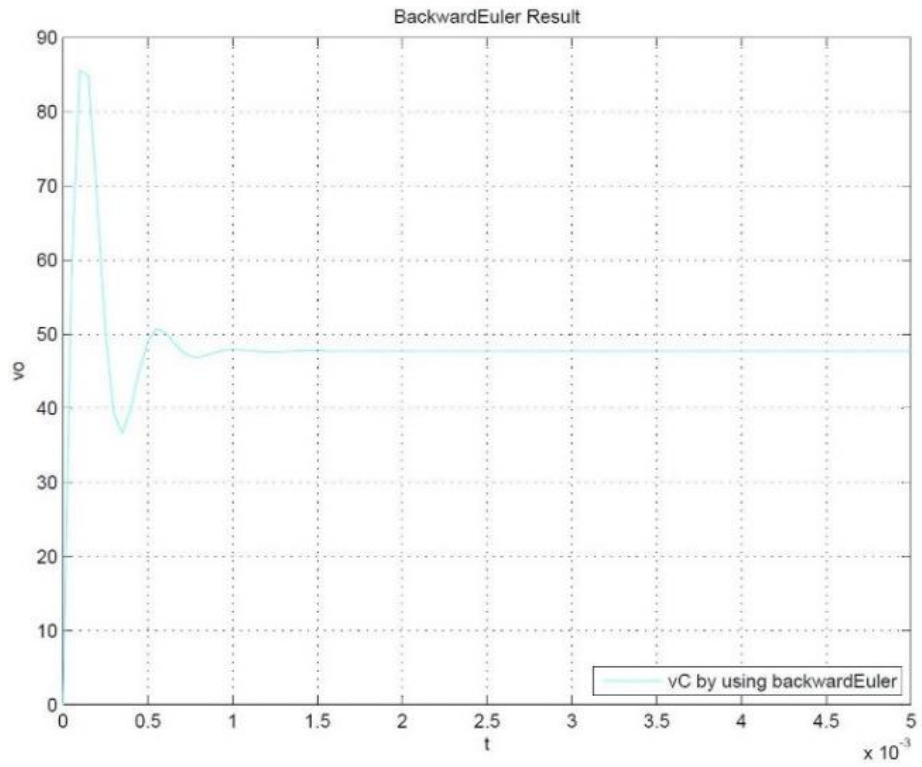


Figure 5.39: Non-ideal DC-DC Boost converter operating in CCM undergoing Backward Euler technique

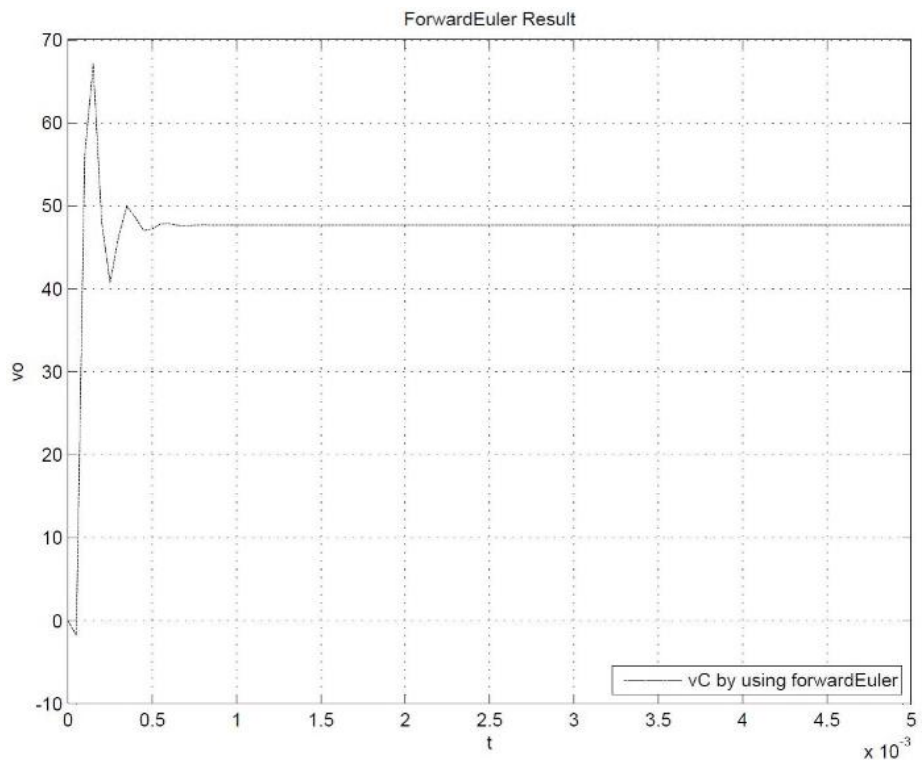


Figure 5.40: Non-ideal DC-DC Boost converter operating in CCM undergoing Forward Euler technique

From the simulation results, it's clear that, there are five different groups of simulation results:

1. Simulation results for Laplace Transform, Ode45 and Ode23t Matlab solvers are still identical. (Figure 5.38)
2. Simulation results for Runge-Kutta 4th order have a very little bit difference from previous group. (Figure 5.38)
3. The simulation results for Improved Euler and Trapezoidal Rule are identical and have small difference from first group. (Figure 5.38)
4. Simulation result for Simpson Rule have some difference from first group which are considered as accurate. (Figure 5.38)
5. Simulation results (Figure 5.39 & Figure 5.40) for Backward Euler and Forward Euler are changing from unstable behavior to stable behavior but with some settling time.

Now, it became obvious that the choice of the time-step used for simulation is an important consideration and the results from the nine pre-selected algorithms were narrowed to those either in Group 1 or 2:

- Group 1: Simulation results for Laplace Transform, Ode45 Matlab solver, Ode23t Matlab solver and Runge-Kutta 4th order are all close. This group was considered to be accurate.
- Group 2: The simulation results for Improved Euler and Trapezoidal Rule methods were identical and had a small, but noticeable, difference from the previous Group 1.

Closer examination of these methods revealed the following choices for further evaluation:

- The Laplace transform method was discarded as it was deemed unsuitable for solving more complex circuits.
- The Ode45 and Ode23t Matlab solvers, although efficient, were proprietary solvers and details of the coding were unavailable. So, they were discarded.
- Only the Runge-Kutta 4th order method was feasible from Group 1.
- From Group 2, the Improved Euler or the Trapezoidal methods were both feasible.

The Trapezoidal method is already used by EMTP, EMTDC-PSCAD and other well-known circuit solving programs; hence, it is the preferred choice going forward for circuit analysis.

5.7 Conclusion

The Small Signal Averaged State-Space modeling technique for DC-DC Boost converters, with and without parasitic elements, operating in continuous conduction mode (CCM) was presented. First, the small signal analysis of DC-DC Boost converters with ideal/lossless components operating in CCM was explored in order to develop a simplified model that helps to understand the basic features of the switching system. Then, the small-signal analysis of DC-DC Boost converters with the effects of parasitic elements and losses operating in CCM was investigated in order to improve the model accuracy, study the efficiency and the dynamic performance of the system. Furthermore, the system dynamic behaviour for the DC-DC Boost converter with ideal components and DC-DC Boost converter with non-ideal components operating in CCM are compared via Bode plots and transient step responses under different values for the load resistance in order to help in designing a robust controller for DC-DC Boost converters operating in continuous conduction mode (CCM).

The various aspects of average modelling of DC-DC Boost converter operating in DCM are studied. Basically, the modelling procedure consists of three steps:

1. Averaging the matrix parameters and selection of the correction matrix (K) depending on the number of inductor currents of the converter.
2. Conversion of state-space equations into differential equations for inductor current and capacitor voltage.
3. Defining a duty ratio constraint so that the expression consists of only one duty ratio.

Moreover, the reduced- and full-order average models have been derived. It was found that the reduced-order model can estimate the behavior in the low frequency range but the full-order model, since dynamics of inductor are present, is more precise.

In addition, various parasitic components have been taken into consideration and a full-order model is developed. The system dynamic behavior for the DC-DC Boost converter with ideal components and DC-DC Boost converter with non-ideal components operating in DCM are compared via Bode plots and transient step responses under different values of the load resistance in order to help in designing a robust controller.

Boost type DC-DC converters are non-linear systems, and output voltage regulation in these converters using a traditionally derived feedback controller does not yield good dynamic responses at different operating points over the complete operating range. Hence, the design of a feedback controller for a DC-DC Boost converter operating in CCM is formulated as an optimization task, and the feedback controller parameters are derived based on a novel PSO technique. This novel optimization method was designed to yield a robust, closed-loop controller structure with stable static and dynamic characteristics for operating points over the whole operational range of the converter. To evaluate the objective function of the developed PSO algorithm, a small-signal model of a DC-DC Boost converter, subjected to various internal and external disturbances, was used.

First, the PID controller parameters for the DC-DC Boost converter were identified based on (a) the traditional Ziegler–Nichol method and (b) the novel PSO algorithm. Then, using the gain parameters obtained by these two methods, the dynamic responses of the DC-DC Boost converter operating in CCM were obtained and compared. Four different performance comparison tests undergoing various input-voltage and load-current step transients were studied. By comparing the qualitative criteria (comprised of rise time, settling time, peak overshoot from the step response curves which are obtained under the variations in both command input and load resistance), it can be concluded that the robustness and effectiveness of the controller tuned by PSO algorithm (compared to the traditional method) is much more superior over a wide range of operating conditions.

A Matlab based simulation shows that the PSO algorithm and converter system is not computationally demanding and present day micro-processor based embedded controllers will be able to handle the duty requirements.

The dynamic performance of DC-DC Boost converters, with and without parasitic elements, operating in continuous conduction mode (CCM) was investigated. First, the state-space equations describing DC-DC Boost converters were developed. Next, the small

signal average models of these converters were derived. Then, the newly developed average models were discretized, and simulated in Matlab using nine popular integration techniques for analysis of accuracy and stability.

It became obvious that the choice of the time-step used for simulation is an important consideration and the choices of the nine pre-selected algorithms were narrowed to those either in Group 1 or 2.

Chapter 6. Kalman Filter-Based MPPT for PV Energy Resources

6.1 Introduction

The traditional P&O method is widely used due to its easy implementation and simplicity. It is an adaptive MPPT algorithm based on an instantaneous power slope, but process and sensor noises disturb its estimations. The P&O method usually requires a dithering scheme to reduce noise effects, but the dithering scheme slows the tracking response time. Tracking speed is the most important factor for improving efficiency under frequent environmental changes.

This chapter proposes implementation of a novel MPPT technique based on the Kalman Filter (KF) algorithm to track the MPP. By applying the proposed KF algorithm to track the MPP, the tracking failures caused by the process and sensor noises were reduced. Also, since the KF also maintains fast tracking of the MPP, it transfers more power during rapid weather changes.

The Kalman Filter (KF) is among the most notable innovations of the 20th century. This algorithm recursively estimates the state variables in a noisy linear dynamical system as new observations are measured and as the system evolves in time. It optimally updates the estimates of the system variables, by minimizing the mean-squared estimation error of the current state as noisy measurements are received. Each update provides the latest unbiased estimate of the system variables together with a measure on the uncertainty of those estimates in the form of a covariance matrix. Since the updating process is fairly general and relatively easy to compute, the KF can often be implemented in real time. The KF is used widely in virtually every technical or quantitative field. The ability to estimate non-measurable signals, fast convergence, and direct implementation encourages wider utilization of KF-based techniques in various industrial applications.

Further details about Kalman Filter and a glimpse into some of its features, mathematical and statistical formulations, overview of its history, and applications are provided in the Appendix C.

For system modelling purposes, a PV test system with a 100 kW PV array and MPPT controller using the traditional P&O and KF algorithms was used. Figure 6.1 shows the PV

panel output power controlled by three methods: (a) without any MPPT (i.e. open loop), (b) MPPT using P&O algorithm, and (c) MPPT using the proposed KF algorithm. The model for the PV panel has as inputs the weather variables: temperature and solar irradiance and, as outputs: voltage, current and power. This PV panel feeds into a DC-DC boost converter that is used to match between its input impedance and output (constant load) impedance and calculate the operating duty cycle based on the algorithm to get the correct MPP.

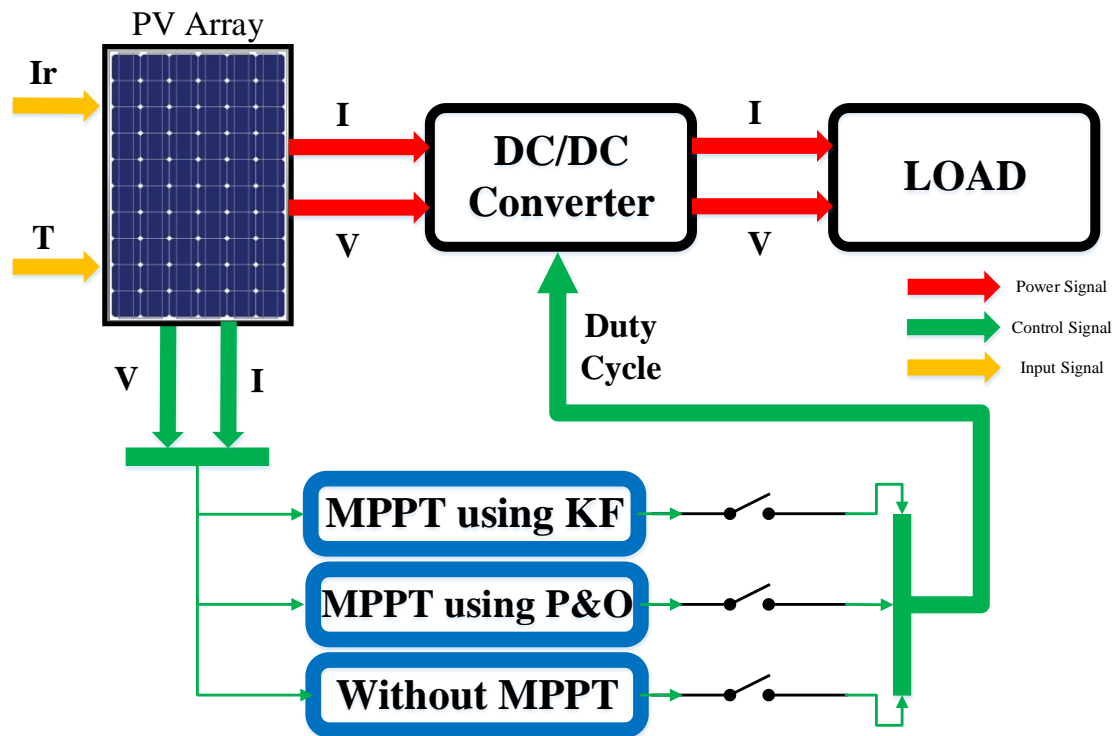


Figure 6.1: Stand-alone PV system controlled by using different MPPT control methods

This chapter is organized as follows: Section 6.2 describes the characteristics of the PV panel. Section 6.3 describes the DC-DC converter and section 6.4 discusses the constant impedance load. Section 6.5 explains the KF approach for tracking the maximum power point. Section 6.6 explains the P&O technique for tracking the MPP, then section 6.7 demonstrates the non-MPPT operation mode for a stand-alone PV system. Section 6.8 discusses the comparative results of the MPPT using KF algorithm and finally the last section presents the conclusions.

6.2 PV Array model

The simplest equivalent circuit of a solar cell is a current source in parallel with a diode (Figure 6.2). This model is a simplified version of the more detailed two-diode model [133]. The output of the current source (photocurrent I_{pv}) is directly proportional to the light falling on the cell. During darkness, the solar cell is not an active device; it works as a diode, i.e. a p-n junction. However, if it is connected to an external supply (large voltage), it generates a current I_d , called diode current or dark current. The diode determines the I-V characteristics of the cell.

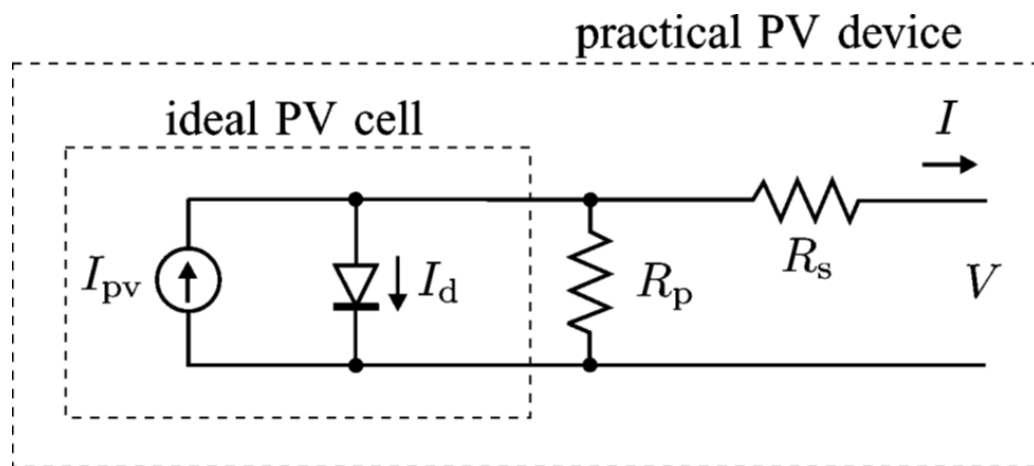


Figure 6.2: Circuit diagram of the PV model

Increasing sophistication, accuracy and complexity can be introduced to the model by adding, in turn [132]:

- Temperature dependence of the diode saturation current I_0 .
- Temperature dependence of the photocurrent I_{pv} .
- Series resistance R_s , which gives the relationship between the maximum power point and open circuit voltage and represents internal losses due to current flow.
- Shunt resistance R_p , in parallel with the diode; this corresponds to the leakage current to ground and is commonly neglected.
- Either allowing the diode quality factor n to become a variable parameter (instead of being fixed at either 1 or 2) or introducing two parallel diodes with independently set saturation currents.

For this work, a model of moderate complexity was used; this model is widely accepted within the industry and gives good results for most transient and load flow cases. The net current of the cell is the difference of the photocurrent, I_{pv} and the normal diode current I_0 :

$$I = I_{pv} - I_0 \left[e^{\frac{q(V+IR_S)}{nkT}} - 1 \right] \quad (6.1)$$

The model included temperature dependence of the photocurrent I_{pv} and the saturation current of the diode I_0 .

$$I_{pv} = I_{pv}(T_1) + K_0(T - T_1) \quad (6.2)$$

$$I_{pv}(T_1) = I_{SC}(T_1) \frac{G}{G(nom)} \quad (6.3)$$

$$K_0 = \frac{I_{SC}(T_2) - I_{SC}(T_1)}{(T_2 - T_1)} \quad (6.4)$$

$$I_0 = I_0(T_1) \times \left(\frac{T}{T_1} \right)^{\frac{3}{n}} e^{\frac{qV_g(T_1)}{nk \left(\frac{1}{T} - \frac{1}{T_1} \right)}} \quad (6.5)$$

$$I_0(T_1) = \frac{I_{SC}(T_1)}{\left(e^{\frac{qV_{OC}(T_1)}{nkT_1}} - 1 \right)} \quad (6.6)$$

A series resistance R_S was included; which represents the resistance inside each cell in the connection between cells.

$$R_S = - \left(\frac{dV}{dI} \right) |_{V_{OC}} - \left(\frac{1}{X_V} \right) \quad (6.7)$$

$$X_V = I_0(T_1) \frac{q}{nkT_1} e^{\frac{qV_{OC}(T_1)}{nkT_1}} \quad (6.8)$$

Where the symbols are defined as follows:

Q	is the electron charge ($1.60217646 \times 10^{-19}$ C)
K	is the Boltzmann constant ($1.3806503 \times 10^{-23}$ J/K)
V	is cell output voltage (V)
V_g	is the band gap voltage (V)
N	is the diode quality factor
T_1	is the reference cell operating temperature (25 °C)
T_2	is another cell operating temperature (75 °C)

The shunt resistance R_P is neglected. A single shunt diode was used with the diode quality factor set to achieve the best curve match.

All of the constants in the above equations can be determined by examining the manufacturers' ratings of the PV array, and then the published or measured I-V curves of the array. As a typical example, the SunPower SPR-305E-WHT-D ($N_{ser}=5$, $N_{par}=66$) array will be used to illustrate the model.

The photo-current I_{pv} (A) is directly proportional to irradiance G (Wm^{-2}). When the cell is short-circuited, the current in the diode will be negligible. Hence, the proportionality constant in (6.3) is set so that the rated short circuit current I_{SC} is delivered under rated irradiation (usually 1 Sun = $1000Wm^{-2}$). For the SPR-305E-WHT-D, $I_{SC} = 5.96$ A at 1 Sun at $T_1 = 25$ °C (298 K), so $I_{pv}(T_1) = 5.96$ A/Sun.

The relationship between the photo-current and temperature is linear (6.2) and is deduced by noting the change of photo-current with the change of temperature (6.4). For the SPR-305E-WHT-D, I_{pv} changes from 5.96 A to 6.14 A (3%) as T changes from 25°C to 75°C.

When the cell is not illuminated, the relationship between the cell's terminal voltage and current is given by the Shockley equation. When the cell is open circuited and illuminated, the photo-current flows entirely in the diode. The I-V curve is offset from the origin by the photo generated current I_{pv} (6.1). The value of the saturation current I_0 at 25°C is calculated using the open circuit voltage and short circuit current at this temperature (6.6).

An estimate must be made of the unknown “ideality factor” n . Green [134] states that it takes a value between 1 and 2, being near 1 at high currents, rising towards 2 at low currents. In our study, the ideality factor was estimated to be as 0.95 and it showed great similarity compared to characteristics of an actual PV array.

The relationship of I_0 to temperature is complex, but fortunately contains no variables requiring evaluation (6.5) [133]. Equations (6.7) and (6.8) are found by differentiating (6.1), evaluating at $V = V_{OC}$, and rearranging in terms of R_S [133]. Using the values obtained from the SPR-305E-WHT-D manufactures’ curves, a value of panel series resistance $R_S = 371 \text{ m}\Omega$ was calculated.

The SunPower SPR-305E-WHT-D PV module was chosen for modeling. The SPR-305E-WHT-D module provides 305 watts of nominal maximum power and has 96 SunPower all-back contact monocrystalline cells. The key specifications are shown in Table 6.1.

TABLE 6.1: PARAMETERS OF THE SPR-305E-WHT-D PV MODULE AT STC

Peak Power (+/-5%), P_{mmp}	305 W
Peak power voltage, V_{mmp}	54.7 V
Peak power current, I_{mmp}	5.58 A
Open circuit voltage, V_{OC}	64.2 V
Short circuit current, I_{SC}	5.96 A
Temperature coefficient of current, K_i	3.5 mA/°C
Temperature coefficient of voltage, K_v	-176.6 mV/°C

The model of the PV array was implemented using Matlab. The model parameters are evaluated during execution using the equations listed above. The program calculates the current I , using typical electrical parameters of the module (I_{SC}, V_{OC}), and the variables Voltage (V), Irradiation (G), and Temperature (T). The inclusion of a series resistance in the model makes the solution for the current I as a non-linear problem (6.1), that should be solved by using numerical methods. In this model, the Newton-Raphson method (discussed earlier in chapter 3) was used, because this method converges much more rapidly, and for both positive and negative currents. The Matlab program output is shown for various irradiation levels (Figure 6.3), and for various temperatures (Figure 6.4).

Temperature and irradiance are dominant factors for deciding the relationship between the output current and voltage of the cell. Figure 6.3 and Figure 6.4 include the I-V characteristics of a certain PV panel - SunPower SPR-305E-WHT-D - under various irradiances and temperatures. Figure 6.3 shows the irradiance dependence of the I-V characteristic of SunPower SPR-305E-WHT-D. Under higher irradiance, the PV cell produces higher output currents because the current is proportionally generated by the flux of photons. This feature also explains that the current of the MPP decreases with decreasing irradiance. Figure 6.4 shows the temperature dependence of the I-V characteristic of SunPower SPR-305E-WHT-D. As temperature increases, the overall voltage range of the cell is decreasing. This feature indicates that the voltage of the MPP decreases with increasing temperature. Since decreasing either current or voltage reduces output power, lower temperature and higher irradiance are required to get more power under the same panel.

In addition, the irradiance has a much greater effect on changing the panel characteristics than does the temperature. When the temperature drops 50% from 50°C to 25°C, the panel voltage is increased by about 10%. However, a 50% change of the irradiance from 1 kW/m² to 0.5 kW/m² causes a reduction of the panel current by 50%.

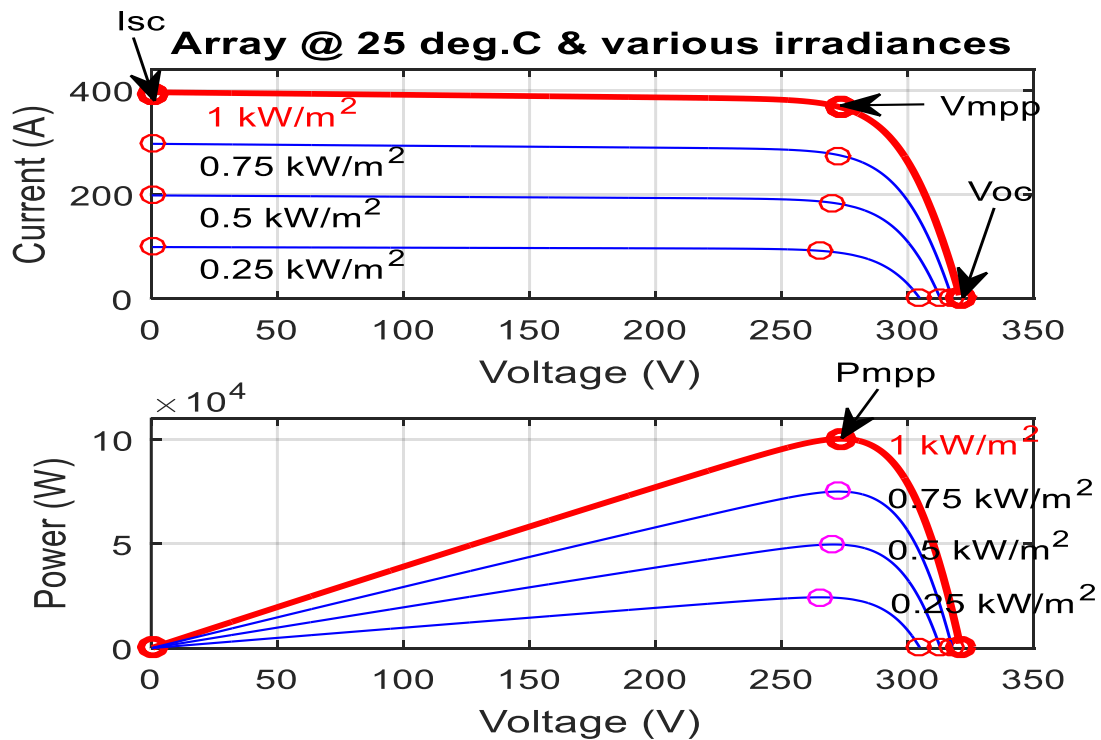


Figure 6.3: The Matlab model I-V and P-V curves for various irradiation levels

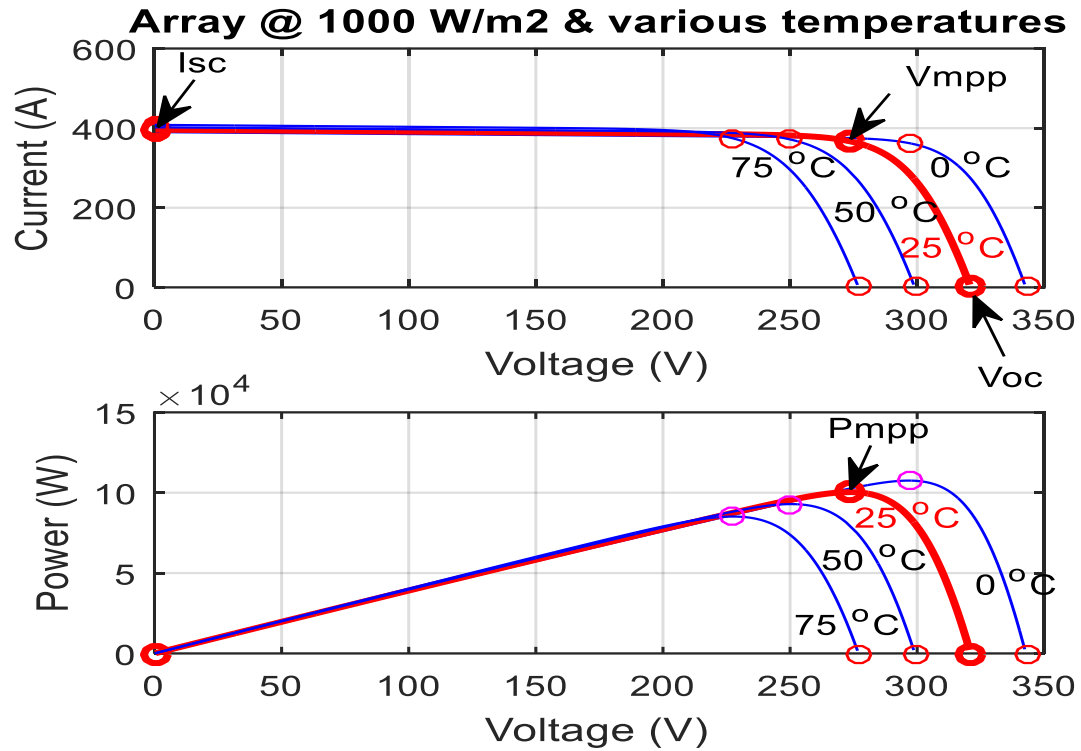


Figure 6.4: The Matlab model I-V and P-V curves for various temperatures

6.3 DC-DC Converter model

A DC-DC converter consists of a number of storage elements and switches that are connected together in a topology such that the periodic switching controls the dynamic transfer of power from the input to the output, in order to produce the desired DC conversion. Usually either a Buck, Boost, Buck-Boost configuration is used according to requirement. In this work, Boost converter is used to step up the operating voltage at the maximum power point. The DC-DC power converter is connected between the solar panel and load.

As mentioned in chapter 5, the small-signal model for the DC-DC Boost converter, with parasitic elements, was utilized. Moreover, the output voltage regulation using a PSO technique as a feedback controller to yield a good dynamic response at different operating points over the complete operating range was exploited. Furthermore, different numerical integration methods were tried in the transient circuit analysis packages to evaluate the

impact on the dynamic simulation. Finally, as explained earlier, the Runge-Kutta 4th order method was the preferred choice to use.

6.4 Constant Impedance Load model

Stand-alone PV systems are designed to operate independently of the electric utility grid and are generally designed and sized to supply certain DC and/or AC electrical loads. These types of systems may be powered by a PV array only or may use wind generator, a diesel engine-generator or utility power as an auxiliary power source in what is called a PV-hybrid system.

There are two types of stand-alone PV power systems: direct-coupled system without batteries and stand-alone system with batteries.

Direct-coupled system

The simplest type of stand-alone PV system is a direct-coupled system, where the output of a PV array is directly connected to a DC load. Matching the impedance of the electrical load to the maximum power output of the PV array is a critical part of designing a well-performing direct-coupled system. For certain loads, a type of electronic DC–DC converter, called a maximum power point tracker (MPPT) is used between the array and load to help better utilize the available array maximum power output. This simple type is used later in this work.

Stand-alone system with batteries

In stand-alone photovoltaic power systems, the electrical energy produced by the PV panels cannot always be used directly. As the demand from the load does not always equal the solar panel capacity, battery banks are generally used. The primary functions of a storage battery in a stand-alone PV system are:

- **Energy Storage Capacity and Autonomy:** To store energy when there is an excess available and to provide it when required.
- **Voltage and Current Stabilization:** To provide stable current and voltage by eradicating transients.
- **Supply Surge Currents:** to provide surge currents to loads like motors when required.

As a proof-of-concept, a simple constant impedance load (RC) model is used in this work to investigate the behavior of PV system under the new proposed MPPT algorithm. This simplified RC load model consists of a resistor R connected in parallel with two DC link capacitors. DC link capacitors C1 and C2 (Figure 6.10) are large enough to eliminate the ripple component induced at the DC side. This aspect is important in order to avoid an unexpected behavior of the MPPT because this ripple is directly perceived in the output voltage of the PV module.

On the other hand, the output power of the PV module can change as a function of the irradiance and hence many disturbances will be produced in this variable. The DC link capacitors play a damping role in this aspect contributing to maintain the stability of the MPPT during these transitory disturbances.

6.5 MPPT Using Kalman Filter

This section describes the design procedure of the KF approach for tracking the MPP.

6.5.1 Proposal of New Representation

Present day power electronic devices use a Field Programmable Gate Array (FPGA) or digital signal processor (DSP) as a hardware controller. Due to the large capacity of FPGAs and DSPs, the MPPT function can be incorporated in the same controller. However, the power electronic devices suffer from various noises e.g., switching noise, thermal noise, etc. In addition, voltage and current sensors are used to monitor data from the array, but the sensors also have errors from an accuracy specification and analog-to-digital converter (ADC) quantization point of view. As the above noises and errors degrade the tracking performance, the MPPT controller is required to be robust against such noises and errors.

Consequently, the MPPT using by the Kalman Filter is an alternative to expect an acceptable performance against both the noises and dynamic environmental changes. Due to the excellent estimation ability of the Kalman Filter in the dynamic system within the noisy environment, an accurate MPP can be predicted by the Kalman Filter without any reduction of system dynamics. Other MPPT methods sometimes degrade their system dynamics partially to eliminate the noise effects. High computing requirements of the

Kalman Filter may be considered to be a disadvantage. However, present day commercial FPGAs or DSPs are capable of performing their calculations at hundreds of megahertz (MHz) to a gigahertz (GHz). Those speeds are adequate to overcome the Kalman Filter’s computations with several hundreds of hertz (Hz) speed of the MPPT controller.

Figure 6.5 shows the flowchart depicting the KF MPPT implementation algorithm. In order to use the KF to track the Maximum Power Point (MPP), the first step is to measure both the PV array voltage and current, and then compute the power. After that, start to use the Kalman Filters’ two sets of equations to calculate the right duty cycle (d) of the DC-DC Boost converter to work on the MPP.

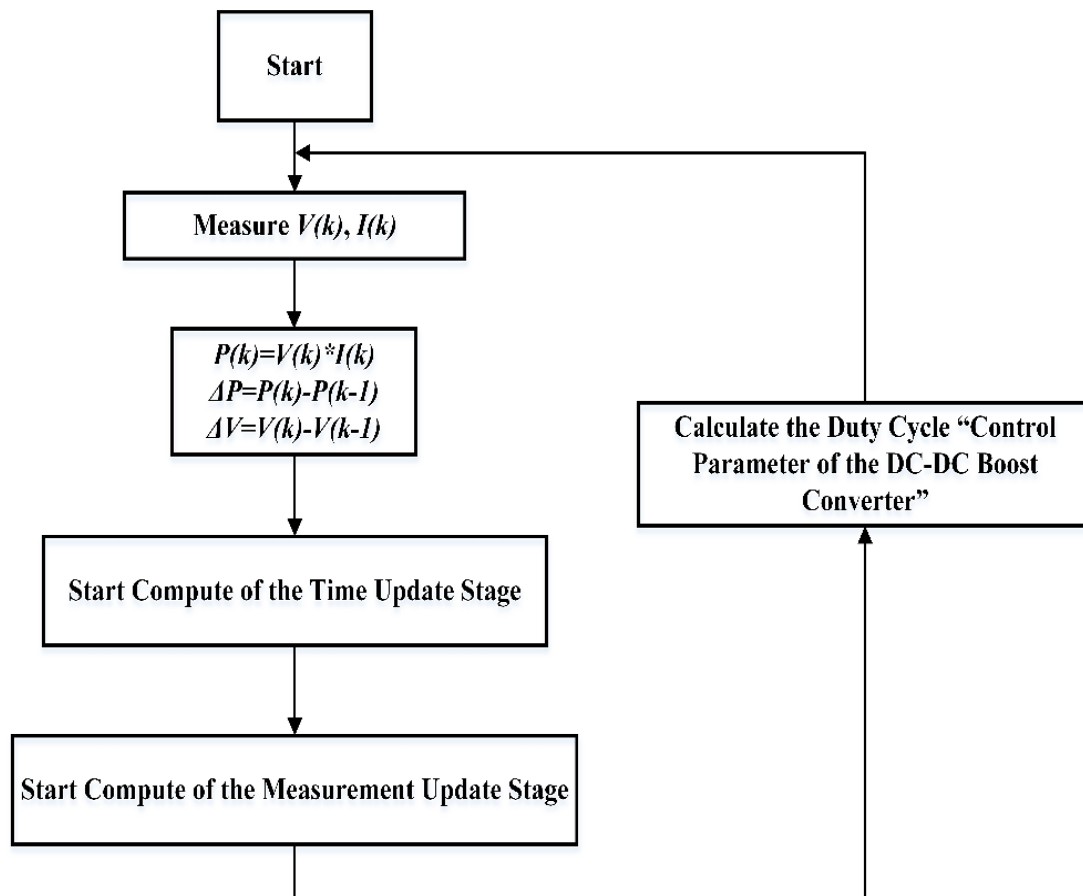


Figure 6.5: KF iteration used to calculate input for the DC-DC Boost converter

According to the P-V curve of a PV array, power increases with a gradual positive slope until it reaches an optimal point and decreases steeply after that. Based on that feature, the MPPT algorithm is governed by the given state equation [356] where V_{actual}^{k+1} is the value of voltage updated by the MPPT controller at iteration $k + 1$.

$$V_{actual}^{k+1} = V_{actual}^k + M \frac{\Delta P^k}{\Delta V^k} \quad (6.9)$$

From the previous equation (6.9), we can note that $A = 1$ and $B = M$. Where M is a step-size corrector and $\frac{\Delta P^k}{\Delta V^k}$ denotes the instantaneous power slope of the P-V curve at step k of the solar array. The instantaneous power slope can be approximated by

$$\frac{\Delta P^k}{\Delta V^k} \approx \frac{P^k - P^{k-1}}{V^k - V^{k-1}}$$

The MPPT controller samples voltages (V) and currents (I) of the array at every sampling time, then it updates the instantaneous power slope. Consequently, the estimated voltage V_{actual}^{k+1} is derived from the updated slope at every sampling time.

For realistic conditions, it is required to analyze noises in a PV system. First, there are a mixture of system disturbances which are capable of interfering with the MPPT operations. The disturbances may be caused by thermal noise, switching noise, electromagnetic interference (EMI) etc. The switching noise is mostly generated by switching devices such as insulated gate bipolar transistors (IGBTs), metal-oxide-semiconductor field-effect transistors (MOSFETs) etc. and it depends on the switching speed and size of the device. The thermal noise and EMI are also considerable disturbances in the device. Consequently, the estimation results of the controller may contain errors influenced by this disturbance. Since it is hard to determine those disturbances, it is assumed that there exist three different percentage errors (1%, 0.1% and 0.01%) that interfere with the controller's estimation in the system. From the signal viewpoint, 0.1% error means that a signal-to-noise ratio (SNR) is 1000 or 60 decibels (dB). Accordingly, 0.01% and 1% process errors are 80dB and 40dB respectively.

Next, it is expected that errors caused by voltage and current sensors exist in the system. The voltage sensors for electronic measurements have a quantization error from resolution of an ADC. The resolution is calculated in the following way:

$$Resolution = \frac{V_{Hi} - V_{Lo}}{2^N}$$

where N is the number of bits. The common current sensors (or transducers), usually have $\pm 1\%$ accuracy at 25°C . The $\pm 1\%$ error is 100 (40dB) in SNR.

Hence, in the real PV system, equation (6.9) must consider the effects caused by the mix of the disturbances and sensor errors. When the errors resulted by the mix of the disturbances and sensors' accuracies is added as a process noise w^k , equation (6.9) can be changed to:

$$V_{actual}^{k+1} = V_{actual}^k + M \frac{\Delta P^k}{\Delta V^k} + w^k \quad (6.10)$$

This thesis proposes to consider the instantaneous power slope $\frac{\Delta P^k}{\Delta V^k}$ is same as control input signal u_k of the system. Therefore, equation (6.10) can be assumed as a one-dimension difference equation in the linear state-space representation.

The MPPT algorithm used by equation (6.10) is adapted to the FPGA- or DSP-based designs due to its easy application to a digital design. The algorithm is also capable of predicting the next voltage adaptively by the instantaneous power slope while the conventional methods move to the next voltage with the fixed value.

The measurement equation dependent on V_{actual}^k and measurement noise v^k will be as follows

$$z_k = V_{actual}^k + v^k$$

From the above equation, we can note that $H = 1$. Considering z_k as the reference voltage at any given instant, we can get the updated measurement equation [357] as

$$V_{ref}^k - V_{actual}^k = v^k \quad (6.11)$$

Based on two known values, V_{ref}^k and $\frac{\Delta P^k}{\Delta V^k}$, equations (6.10) and (6.11) are applicable for the Kalman Filter to estimate the state in a noisy environment.

6.5.2 Applied Proposed Representation to Kalman Filter

From the above derived linear state-space representation (6.10) and (6.11), the Kalman Filter can be applied to track the MPP. The recursive computation of the filter is divided by the time update and measurement update steps.

I. Time Update

Based on voltage estimate V_{actual}^{k-1} and state error covariance P_{k-1} of the previous state, we can predict the new estimate

$$V_{actual}^{k-} = V_{actual}^{k-1} + M \frac{\Delta P^{k-1}}{\Delta V^{k-1}} \quad (6.12)$$

with a specific step size M and note that, V_{actual}^{k-} is analogous to \hat{x}_k^- .

The *a priori* estimate state error covariance P_k^- is also projected in the following way

$$P_k^- = P_{k-1} + Q \quad (6.13)$$

where Q is the process noise covariance of a plant.

II. Measurement Update

From the state error covariance P_k^- update in prediction (time update) stage, we initially can calculate the Kalman gain K_k in the following way

$$K_k = P_k^- (P_k^- + R)^{-1} \quad (6.14)$$

where R is the measurement noise covariance. The measurement noise is assumed as a disturbance which interferes in the operation of both voltage and current sensors.

Now, the corrected gain K_k updates the estimate of V_{actual}^k given by the sensor measurement V_{ref}^k and the estimate from last time update V_{actual}^{k-} in the following way

$$V_{actual}^k = V_{actual}^{k-} + K_k(V_{ref}^k - V_{actual}^{k-}) \quad (6.15)$$

In addition, the gain K_k also updates the error covariance P_k by using P_k^- from the prediction state and K_k from equation (6.14) in the following way

$$P_k = (1 - K_k)P_k^- \quad (6.16)$$

As the above steps occur in turn, the estimated result becomes to exclude the noises since the error covariance P_k gets smaller and tends to approach to zero. Hence, the final estimation is expected to be closer to the Maximum Power Point (MPP).

III. Operating Summary of Proposed Method

Figure 6.6 shows the summary of the time and measurement updates in the proposed method. In the time update, based on voltage estimate V_{actual}^{k-1} and state error covariance P_{k-1} of the previous state we can predict the new estimate V_{actual}^{k-} and *a priori* estimate state error covariance P_k^- . In the measurement update, from the state error covariance P_k^- update in prediction (time update) stage, we initially can calculate the Kalman gain K_k . Then, the corrected gain K_k updates the estimate of V_{actual}^k given by the sensor measurement V_{ref}^k and the estimate from last time update V_{actual}^{k-} . In addition, the Kalman gain K_k also updates the error covariance P_k by using P_k^- from the prediction state. Consequently, the estimation result V_{actual}^k is expected to be closer to a MPP than V_{actual}^{k-} as a result of the filter's recursive nature.

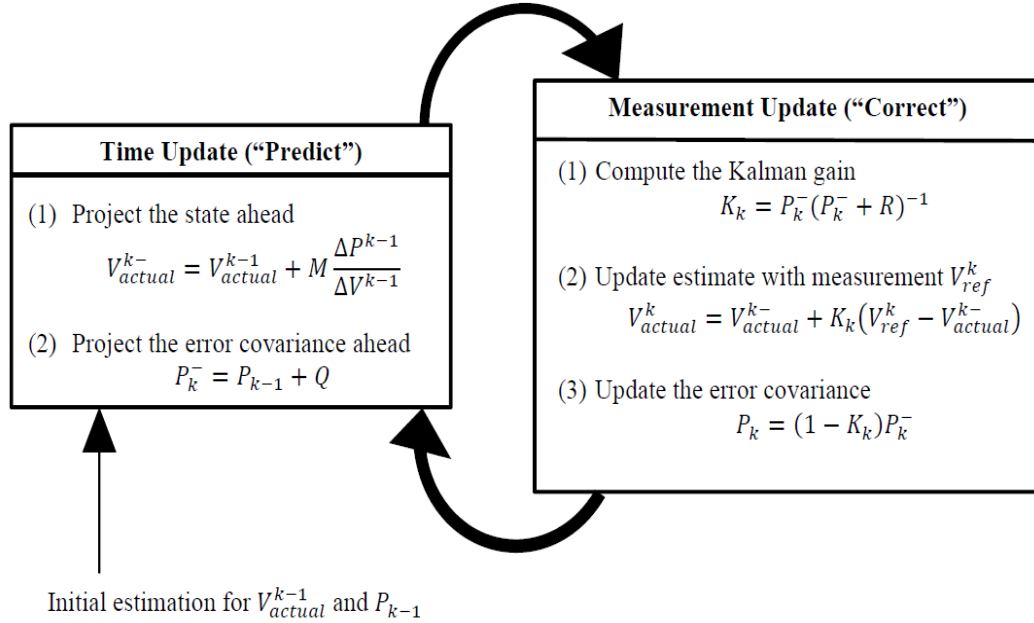


Figure 6.6: Measurement and time updates in proposed Kalman Filter

6.6 MPPT Using Perturb and Observe (P&O) Method

6.6.1 Principle of P&O Algorithm

The P&O algorithm is based on a comparison of perturbation voltage and changed power. As shown in Figure 1.2, the P&O controller first measures voltage $V(k)$ and current $I(k)$ of a PV array at time k via voltage and current sensors. It also calculates power $P(k)$ by the product of $V(k)$ and $I(k)$. And then, the controller compares the present power $P(k)$ with the previous power $P(k-1)$, and between the present voltage $V(k)$ and previous voltage $V(k-1)$. If both voltage perturbation ΔV and changed power ΔP are positive or negative together, next voltage perturbation must be positive because the present point is located on the left side of the MPP. If one is positive and the other is negative, next perturbation must be negative because the point is on the right of the MPP. When the MPP is reached, the system then oscillates around the MPP. In order to minimize the oscillation, the perturbation step size should be reduced such that when the operating is away from the MPP, the step change should be large, when it nears the MPP, the step change should reduce. This algorithm is summarized in Table 6.2.

TABLE 6.2: SUMMARY OF P&O ALGORITHM

Voltage Perturbation	Change in Power	Next Perturbation
Positive	Positive	Positive
Positive	Negative	Negative
Negative	Negative	Positive
Negative	Positive	Negative

6.6.2 Advantages and Disadvantages of P&O Algorithm

The P&O algorithm is popular mostly due to its simplicity and easy implementation [12], [358]. It can be applied to both analog and digital designs. It is also compatible with any kind of PV arrays [359]. Therefore, the P&O is frequently applied to digital designs although it was initially developed for analog designs.

In [34], the authors state that the P&O method has a problem at steady state as shown in Figure 6.7; namely that it continually oscillates around the maximum power point, since the voltage is always being changed. However, they acknowledge that this can easily be remedied by decreasing the perturbation step size.

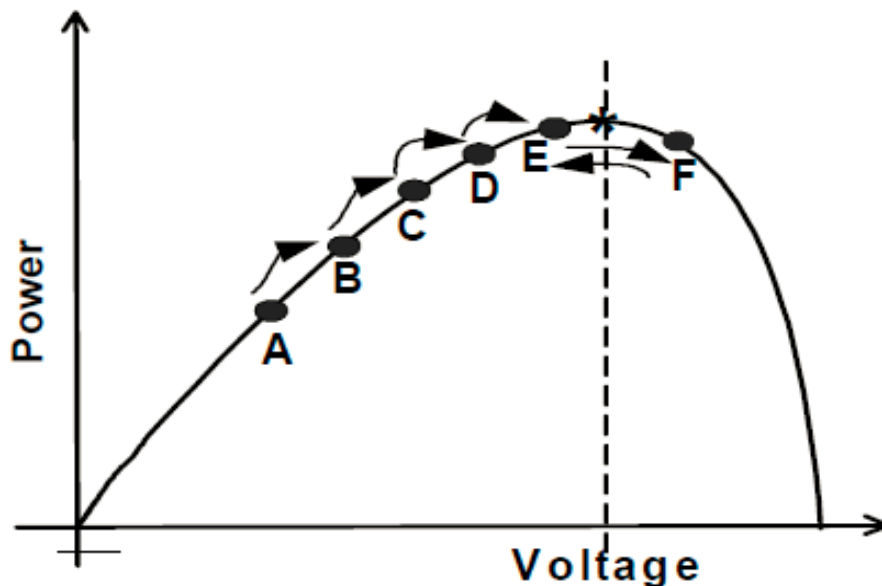


Figure 6.7: Illustration of the oscillations of the P&O Algorithm around the MPP

Also, the P&O sometimes shows tracking failure under rapid environmental changes [12], [358]. As illustrated in Figure 6.8, let us suppose that the P-V characteristic C1 is suddenly shifted to C2 because of an environmental change. Under the constant C1, the MPP point M1 must move to P1 by a positive perturbation step $+\Delta V$, and then it would come back to M1 by a negative perturbation step $-\Delta V$ as a result of comparing powers at between M1 and P1. However, the point M1 will move to P2 due to the changed characteristic C2. In this case, the next perturbation must be negative for moving from P2 to M2, but P2 will jump oppositely to P3 due to the positive perturbation $+\Delta V$. The P&O controller orders the positive perturbation as the result that the power at P2 is still higher than the power at M1. This phenomenon disturbs the controller to track toward the new MPP immediately when the environmental condition is changed.

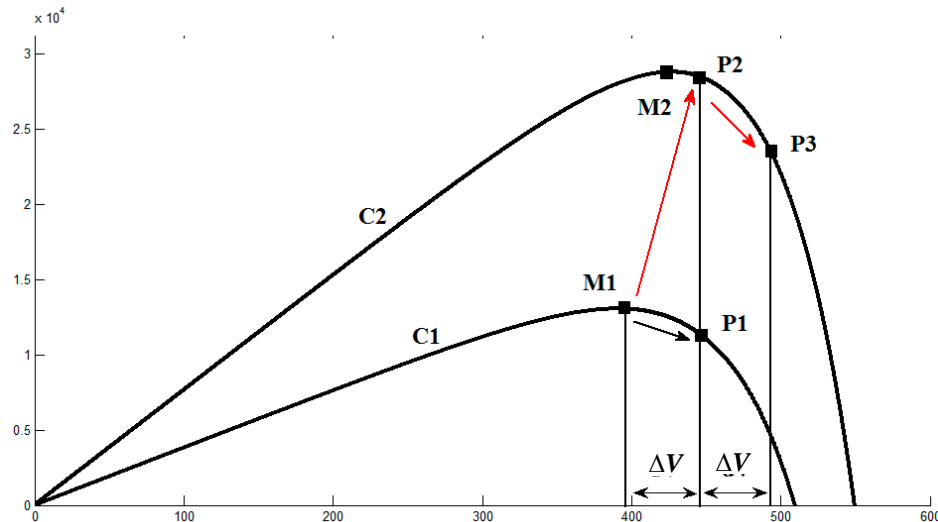


Figure 6.8: P&O's tracking failure under sudden P-V characteristic change

6.7 Without MPPT Operation Mode

The maximum power of the PV module changes with climatic conditions, and there is only one value for the current (I_{mpp}) and the voltage (V_{mpp}), which defines the maximum power point (MPP). The PV current changes with the solar irradiation level, whereas the PV output voltage changes with the temperature of the PV module. Therefore, an important challenge in a PV system is to ensure the maximum energy generation from the PV array with a dynamic variation of its output characteristic and with the connection of a variable load. A solution for this problem is the insertion of a power converter between the PV array

and load, which could dynamically change the impedance of the circuit by using a MPPT control algorithm. Thus, MPP operation can be obtained under any operational condition.

The non-MPPT operation mode for the stand-alone PV system is proposed to investigate the stand-alone PV system behavior as moving operation point from the MPP to the open circuit voltage point.

As illustrated in Figure 6.9, when irradiance and temperature are simultaneously changed, the power-voltage characteristic of the array and its MPP are also changed. However, in the non-MPPT operation mode where the duty cycle is kept constant at its initial condition with the simultaneously changing in the irradiance and temperature, the generated power trajectory will fail to follow up this changing and track the correct steady-state value of MPP even with a bad transient characteristics. As a consequence, when the stand-alone PV system is working under non-MPPT operation mode, the maximum utilization of the solar panel power available can't be done.

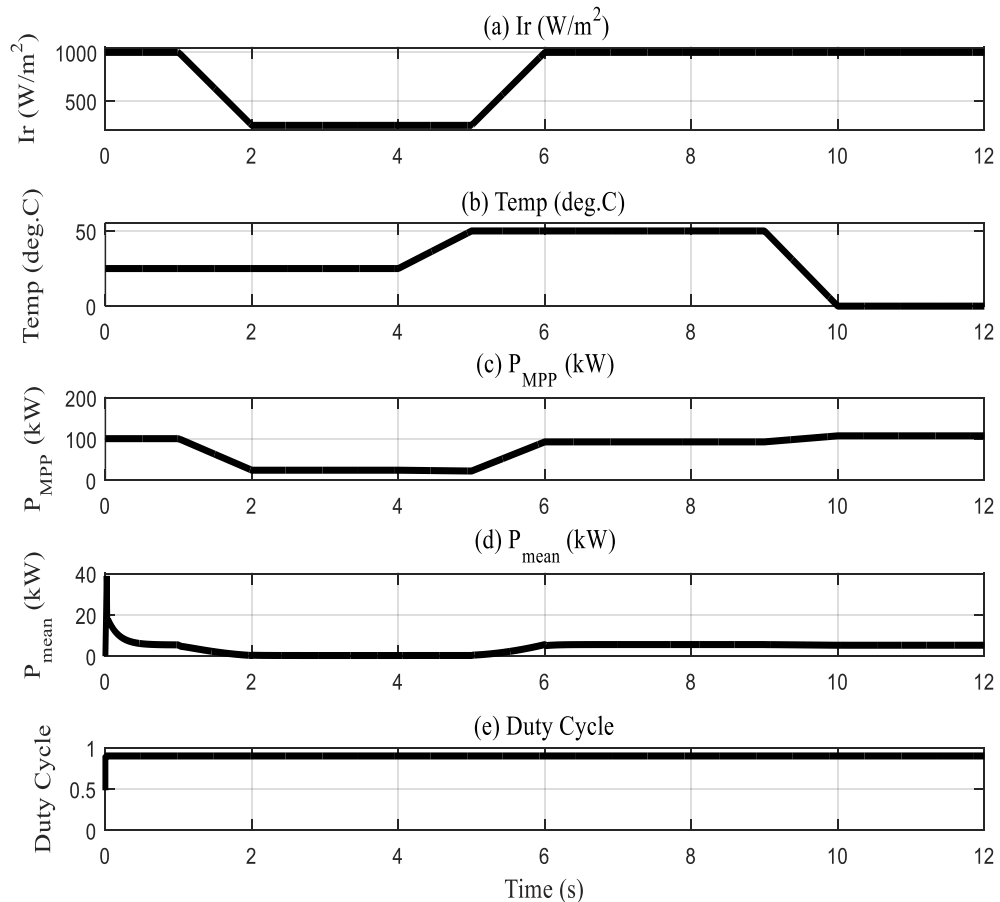


Figure 6.9: Stand-alone PV system behaviour under non-MPPT operation mode

6.8 Simulation Model and Results

MODEL DESCRIPTION:

A 100 kW PV test system is designed in Matlab/Simulink environment for case studies, as shown in Figure 6.10.

For the 100 kW solar array block [360], we used 330 SunPower SPR-305E-WHT-D modules, connected in a combination of 66 cells in-parallel by 5 cells in-series. A series connection of cells results in higher voltages, while parallel connection results in higher current. This array generates 100.7 kW at an irradiance of 1 kW/m^2 at a temperature of 25°C . Its MPP voltage varies approximately from 250.2 V to 296.6 V up to given environmental conditions.

The DC-DC Converter block operates at a switching frequency of 5 kHz and provides an output at 500 V DC. The DC link capacitors C1 and C2 play a damping role in this aspect contributing to maintain the stability of the MPPT during these transitory disturbances. DC link capacitors are large enough to eliminate the ripple component induced at the DC side. This aspect is important because this ripple is directly perceived in the output voltage of the PV module.

The MPPT controller block samples array voltages and currents at 10 kHz. Calculations for all methods are considered to be done within the sampling rates of present day power electronics devices.

An RC load (constant impedance) model is used to investigate the behavior of PV system under the new proposed MPPT algorithm. The simplified RC load model consists of a resistor R connected in parallel with the two DC link capacitors.

On the other hand, the output power of the PV module can change as a function of the irradiance and hence many disturbances will be produced in this variable.

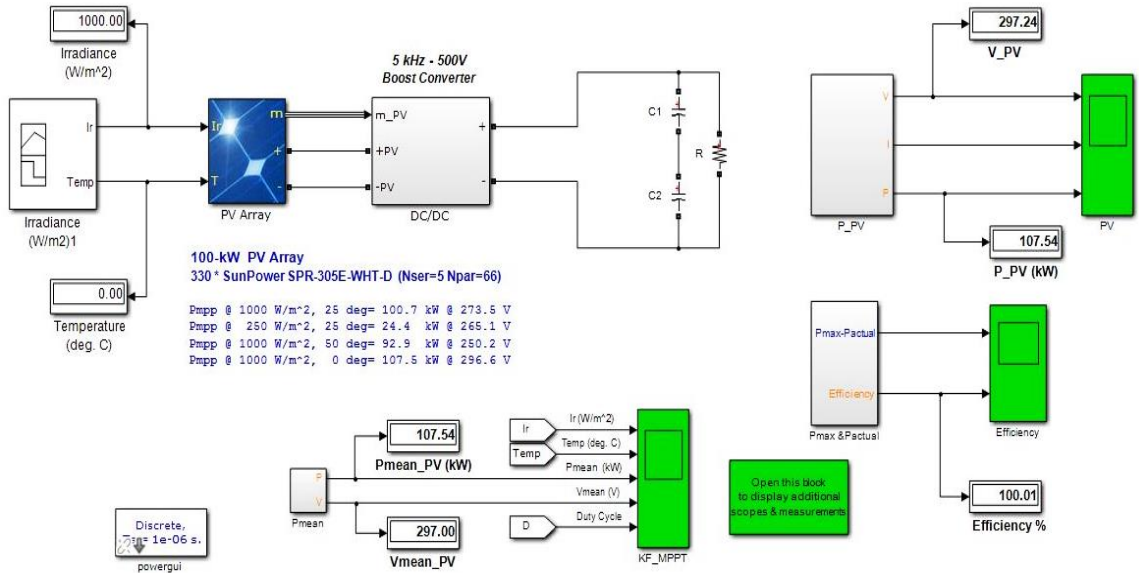


Figure 6.10 : PV system implementing the proposed Kalman Filter algorithm using Simulink

All simulations are based on comparisons between (a) the proposed method, (b) conventional P&O method and (c) without any MPPT method.

RESULTS:

To study the tracking performance of (a) the proposed method, (b) conventional P&O method and (c) without any MPPT method under different environmental changes, three test scenarios are checked.

First test scenario deals with the effect of the irradiance change on the tracking performance of (a) the proposed method, (b) conventional P&O method and (c) without any MPPT method.

PV arrays are sensitive to rapid environmental changes and, it is well known that an irradiance change has a much greater effect on array characteristics than does the temperature change. When the irradiance is changed, the power-voltage characteristic of the array and its MPP are simultaneously reformulated. Therefore, the MPPT is required to track the changed MPP rapidly.

Figures 6.11 (a), (b), (c) and (d) show the generated power trajectories for all three methods when the irradiance is first ramped down 1000 - 250 kW/m² at 1 s and then ramped up from 5 s. The temperature is held steady at 25 °C. This phenomenon is commonly known as “shadowing”.

The generated power trajectories for the proposed method and the P&O method are compared with three different transient criteria:

- Settling time: this is the time needed by the method to achieve maximum power.
- Efficiency: this factor defines how close the obtained results are to the ideal maximum power.
- Oscillations: this factor defines how much the power oscillates when the MPP is reached.

The results are tabulated in Table 6.3. It is clear from the results that the proposed method shows the best and fastest tracking response to follow up these changes in the irradiance.

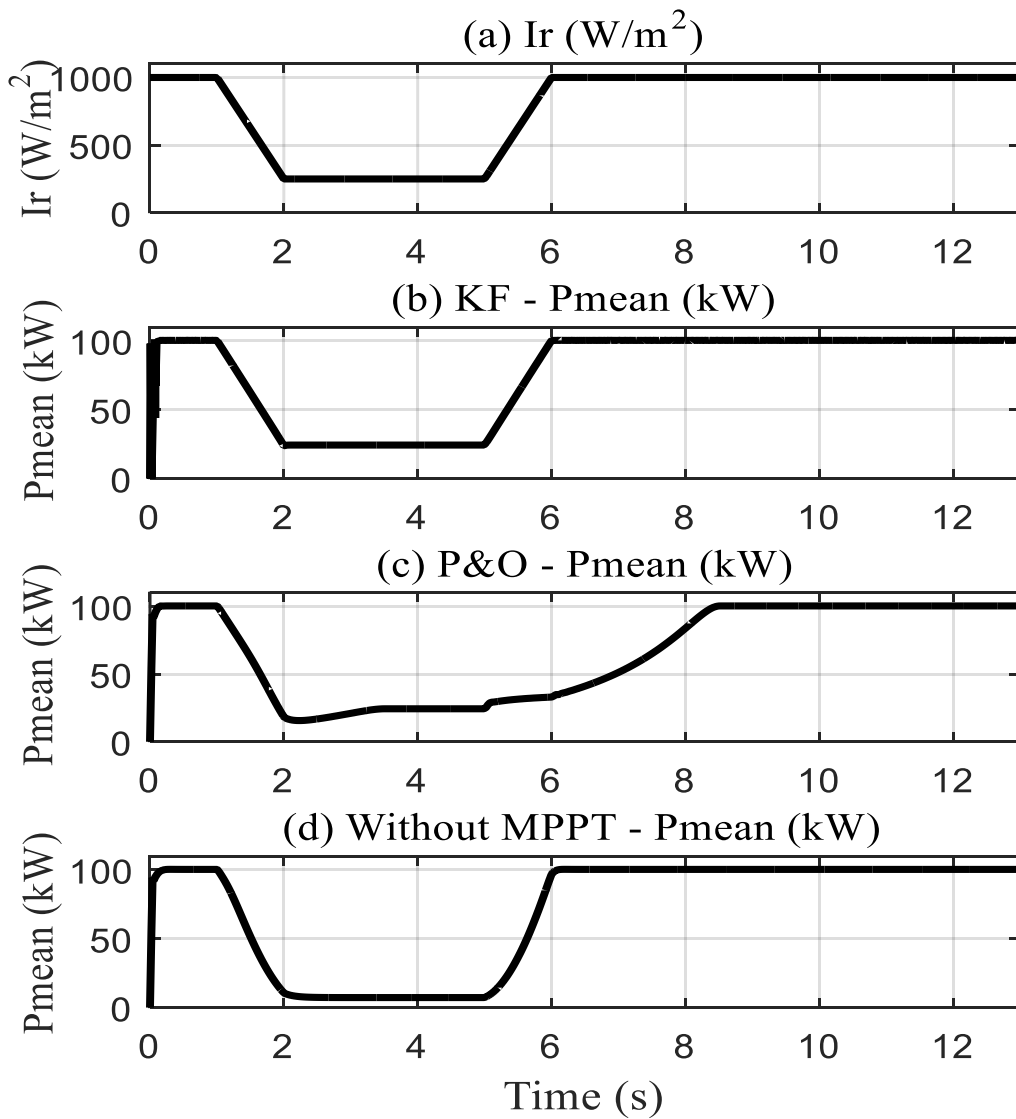


Figure 6.11: Generated power trajectories under irradiance change: (a) irradiance changes with time, (b) proposed method power trajectory, (c) P&O method power trajectory and (d) without MPPT method power trajectory

Second scenario deals with the effect of the temperature change on the tracking performance of (a) the proposed method, (b) conventional P&O method and (c) without any MPPT method. When temperature is changed, the power-voltage characteristic of the array and its MPP are simultaneously affected. Therefore, the MPPT is required to track the changed MPP rapidly. Figures 6.12 (a), (b), (c) and (d) show the generated power trajectories for all methods when the temperature is changed from 25 °C to 50 °C at a certain time, then remains at 50 °C for 4 seconds, and thereafter goes back to 0 °C. The irradiance is held constant at 1 kW/m².

The temperature change has a smaller effect on PV array characteristics than does the irradiance change, as shown through the generated power trajectories in Figures 6.12 (b), (c) and (d). When the temperature is changed from 25 °C to 50 °C and the irradiance holds steady at 1 kW/m², the generated power trajectories for all three methods are changed down with different transient characteristics. The generated power trajectories for all three methods are compared with three different transient specifications (Settling time, Efficiency, and Oscillations). The results are tabulated in Table 6.4. It is clear from the results that the proposed method shows the best and fastest tracking response to follow up these changes in the temperature.

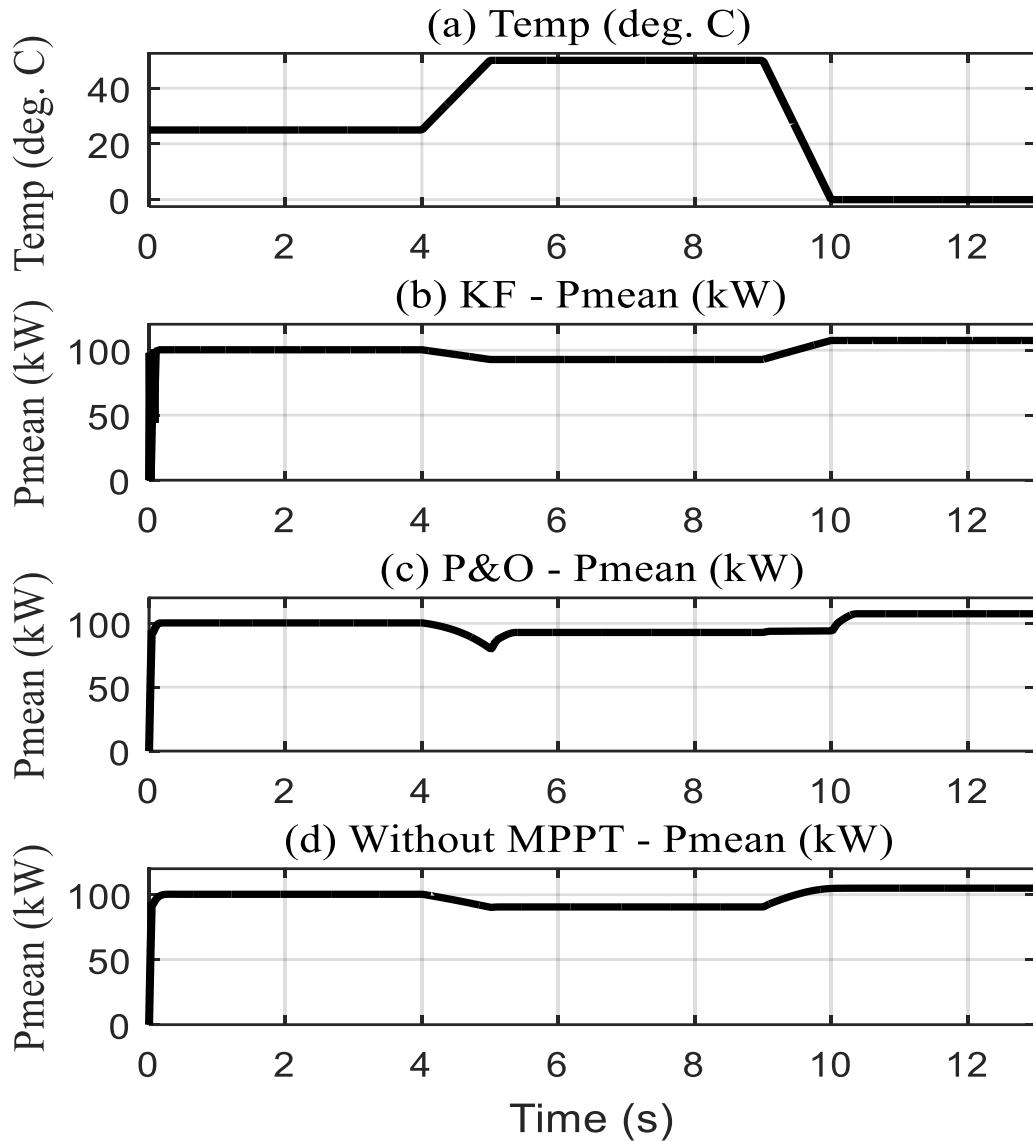


Figure 6.12: Generated power trajectories under temperature change: (a) temperature changes with time, (b) proposed method power trajectory, (c) P&O method power trajectory and (d) without MPPT method power trajectory

Last scenario deals with the effect of a simultaneous change in irradiance and temperature on the tracking performance of (a) the proposed method, (b) conventional P&O method and (c) without any MPPT method. When irradiance and temperature are simultaneously changed, the power-voltage characteristic of the array and its MPP are also changed. Therefore, the MPPT is required to track the changed MPP rapidly. Figure 6.13 (a), (b), (c), (d) and (e) show the generated power trajectories for all three methods when

irradiance and temperature are simultaneously changed. The result shows the promising performance and accurate tracking of the proposed method.

The plots of results show that the tracking performance of the “without MPPT method” is better than the tracking performance of the conventional P&O MPPT algorithm in all scenarios; this is due to the effect of the selection of the initial duty cycle (d) value. The selection of the initial duty cycle value has a higher effect on the tracking performance of the “without MPPT method” than on the tracking performance of the other “with MPPT” algorithms.

Furthermore, Figure 6.14 shows a comparison between the maximum power trajectory and the generated power trajectories for all three methods when irradiance and temperature are simultaneously changed. The result illustrates the promising performance and accurate tracking of the proposed method. After presenting the results obtained by the conventional P&O algorithm and Kalman Filter based MPPT, these results are summarized in Tables 6.3 and 6.4.

Based on the results obtained in this work and the criteria cited before, we can see that the proposed KF method presents better results than the conventional P&O algorithm. From the tables, we notice that the response time of the proposed KF method is about 6 times lower than the conventional P&O algorithm settling time. KF based MPPT presents better efficiency around 99.38%, and the oscillations are 8 times lower. These results show that KF based MPPT presents superior performances than conventional P&O algorithm.

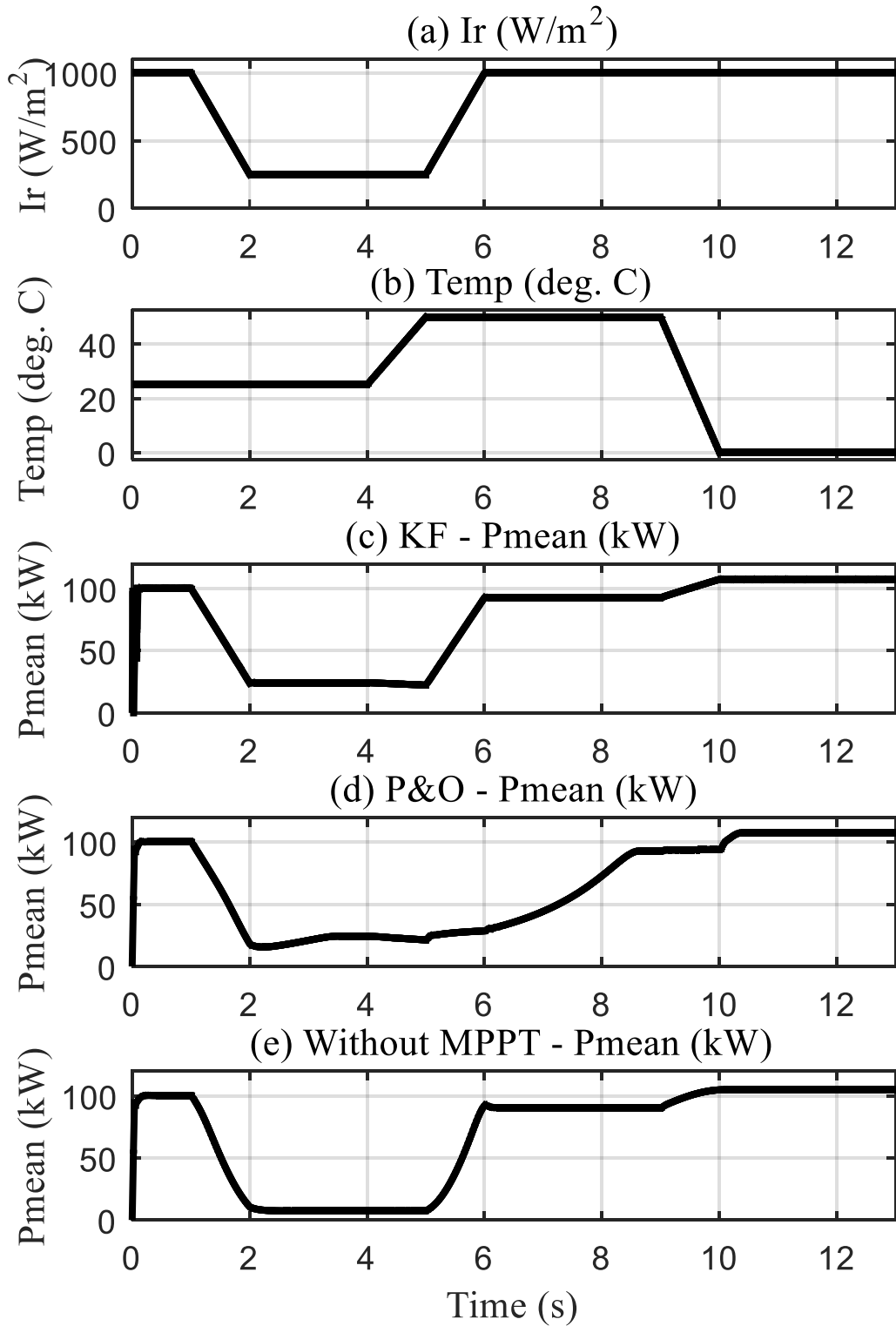


Figure 6.13: Generated power trajectories under simultaneous changing in the irradiance and temperature: (a) irradiance changes with time, (b) temperature changes with time, (c) proposed method power trajectory, (d) P&O method power trajectory and (e) without MPPT method power trajectory

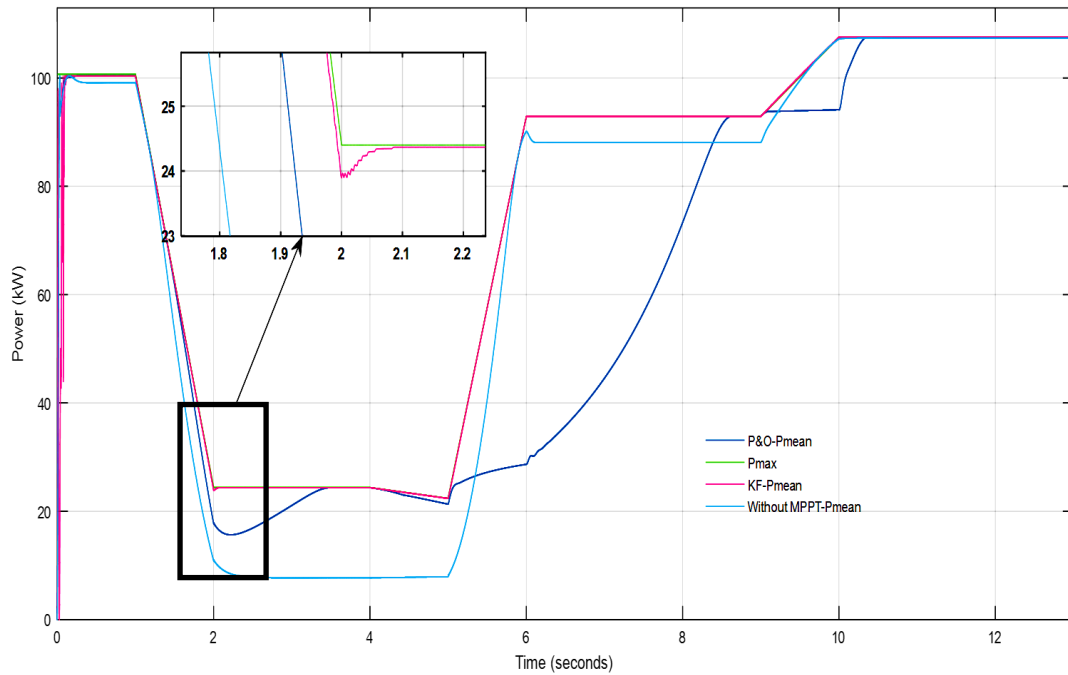


Figure 6.14: Comparison between the maximum power trajectory and the generated power trajectories for all methods when irradiance and temperature are simultaneously changed

TABLE 6.3: RESULTS COMPARISON BETWEEN THE KF BASED MPPT METHOD AND P&O ALGORITHM AT TEMPERATURE 25 °C

Irradiance (W/m ²)	Kalman filter based MPPT			P&O algorithm		
	Settling time (ms)	Efficiency (%)	Oscillations (W)	Settling time (ms)	Efficiency (%)	Oscillations (W)
1000	5.0	99.38	0.8	30	94.64	6.0
250	4.0	99.25	0.2	24	94.72	1.6

TABLE 6.4: RESULTS COMPARISON BETWEEN THE KF BASED MPPT METHOD AND P&O ALGORITHM AT IRRADIANCE 250 W/M²

Temperature (°C)	Kalman filter based MPPT			P&O algorithm		
	Settling time (ms)	Efficiency (%)	Oscillations (W)	Settling time (ms)	Efficiency (%)	Oscillations (W)
25	4.0	99.49	0.40	28	94.92	1.6
50	4.0	99.42	0.45	28	94.96	1.8

6.9 Conclusion

In this chapter, a novel Kalman Filter (KF) based MPPT technique for PV applications has been designed and implemented in a Matlab simulation model. The PV panel is connected to the load through a DC-DC Boost converter which is controlled by using the KF algorithm.

The Matlab simulation results show good performance for the KF algorithm as it is able to maintain the tracking speed in the face of frequent environmental changes conditions affecting both temperature and irradiance. Comparisons between the KF algorithm and the more traditional P&O algorithm show the superior performance of the KF algorithm. The fast tracking speed is the most dominant factor for the MPPT in the face of frequent environmental changes.

The expected outcome of the Kalman Filter (KF) based MPPT technique is an efficient MPPT method which presents a very high level of robustness, reliability and accuracy. The obtained results clearly highlight the superiority of the proposed method; it yields an efficiency of 99.38 % under the standard test condition (STC), which is almost 5 % higher than the conventional P&O method under the same conditions. The oscillations generated by the conventional P&O algorithm are higher when compared to KF. We can conclude that KF is better when used as an MPPT than the conventional P&O algorithm.

The next step is to implement these techniques on FPGA chip Altera Cyclone II EP2C20F484C7 to test their efficiencies and tracking speeds in a real-time environment. This stage of research is required an advanced technical knowledge and skills, especially in FPGA design and VHDL code.

Chapter 7. FPGA-Based MPPT Controller for PV Systems

7.1 Introduction

In PV applications, software solutions are commonly used to implement MPPT algorithms [361], [362]. However, with high-speed high density performance demands, the hardware solutions using FPGAs are more frequently employed [363]. Some recent power processing system for PV applications, including those ones dedicated to single modules, e.g. power optimizers and micro inverters, employ FPGAs in order to embed many advanced control functions or real-time PV emulators [364]. In addition, an FPGA platform can be adopted in order to carry out real-time identification of the PV system.

Concerning the speed performance, FPGAs takes advantage of the inherent algorithm parallelism, reducing drastically the execution time. This characteristic makes the FPGA the most suitable platform for real-time MPPT implementation.

As far as the high integration density is concerned, more complex algorithms and distributed control can be implemented within the same device. Moreover, the same hardware block implemented in the FPGA can be re-used and the whole architecture is quite easily scalable and portable in a dedicated Application Specific Integrated Circuit (ASIC) device.

Advances in intelligent techniques, embedded into a FPGA, allowed the application of such technologies into real engineering problems; however, the application of such technologies in the solar energy field is still relatively limited. The embedded intelligent algorithm into programmable devices such as FPGAs may play a very important role in PV systems. For example in [364], [365], intelligent PV emulators for stand-alone PV systems have been developed.

Conventional MPPT methods such as perturb and observe (P&O), variable step-size P&O, incremental conductance (IncCond) and new improved P&O have been implemented into FPGA due to the simplicity of implementation [366], [367]. However, these algorithms are not as efficient as the MPPT methods based on artificial intelligence techniques such as fuzzy logic, neural network, etc. [368], [369].

In this work, we are implementing the MPPT system using reconfigurable FPGAs. This chip offer lower cost implementation since the functions of various components can be integrated onto the same FPGA chip as opposed to digital signal processor (DSPs), which can perform only DSP-related computations. In addition, FPGAs can provide equivalent or higher performance with the customization potential of ASICs. Because FPGAs can be reprogrammed at any time, repairs can be performed in situ while the system is running, thus providing a high degree of robustness [370]. In some cases, (e.g. in simple applications) the use of a microcontroller is very suitable. However, some critical mathematic processing, such as DSP, would need real-time processing that is time critical. In these situations, FPGAs would be a good solution. FPGAs have a key impact on hardware or software co-design, and they are used as devices for rapid prototyping, and for final products.

7.2 FPGA Design Methodology

Initially, Matlab/Simulink is used to simulate and verify the designed proposed MPPT controller. Secondly, a hardware description language HDL (VHSIC: very-high-speed integrated circuits) is employed to design the different parts of the overall system. Finally, the Quartus II software tool of Altera and ModelSim software are used to simulate and implement the designed proposed MPPT into an FPGA chip (Altera Cyclone II EP2C20F484C7 FPGA).

7.2.1 FPGAs

FPGAs are programmable semiconductor devices that are based around a matrix of configurable logic blocks (CLBs) connected through programmable interconnections. As opposed to ASICs, where the device is custom built for the particular design, FPGAs can be programmed to the desired application or functionality requirements [371].

The fundamental FPGA structures are as follows [372]: logic blocks, routing matrix & global signals, I/O blocks (IOBs), clock resources, multiplier, memory and advanced

features. Generally, all FPGAs contain the same basic resources as shown in Figure 7.1 [373].

Although one-time programmable (OTP) FPGAs are available, the dominant types are SRAM-based which can be reprogrammed as the design evolves. The logic and routing elements in an FPGA are controlled by programming points, which may be based on antifuse, Flash, or SRAM technology. For reconfigurable computing, SRAM-based FPGAs are the preferred option, and in fact are the primary style of FPGA devices in the electronics industry as a whole. In these devices, every routing choice and every logic function are controlled by a simple memory bit. With all of its memory bits programmed, by way of a configuration file or bit stream, an FPGA can be configured to implement the user's desired function. Thus, the configuration can be carried out quickly and without permanent fabrication steps, allowing customization at the user's electronics bench, or even in the final end product. This is why FPGAs are field programmable, and why they differ from mask programmable devices, which have their functionality fixed by masks during fabrication [374].

FPGAs allow designers to change their designs very late in the design cycle; even after the end product has been manufactured and deployed in the field. In addition, most of FPGAs allow for field upgrades to be completed remotely, eliminating the costs associated with re-design or manually updating electronic systems [371]. ASIC and FPGAs have different value to designers, and they must be carefully evaluated before choosing any one over the other. While FPGAs used to be selected for lower speed/complexity/volume designs in the past, today's FPGAs easily push the 500 MHz performance barrier. With unprecedented logic density increase and a host of other features, such as embedded processors, DSP blocks, clocking, and high-speed serial at ever-lower price points, FPGAs are a compelling proposition for almost any type of design [371].

FPGAs based hardware solutions, using the device's inherent parallelism, have been recently received increased attention, as they allow engineers/designers to develop efficient hardware architectures based on flexible software. Additional FPGA advantages include the fact that their hardware logic is extremely fast, much faster than software-based logic. They are easier to interface to the outside world, either through custom peripherals or via glue logic to custom co-processors. They are also better suited for bit-level operations than

a microprocessor. Other advantages are: ability to control part obsolescence through design ownership and viable technology roadmap, improved design update and enhancement options, higher system performance, lower tool costs and verification costs than ASIC implementation, lower implementation costs, and allows consolidation of multiple components into a single component. More potential FPGA advantages are listed in [372]. Furthermore, FPGAs are especially suited to control applications requiring custom hardware, such as digital communication protocols, rapid control prototyping, hardware-in-the-loop simulation, in-vehicle data acquisition, machine control and machine condition monitoring [375]. As reported in [376] ASIC and FPGA developments can be done in parallel to get the benefits of both technologies. The FPGA devices are used as prototypes and in initial shipments to cut the manufacturing lead-time. When the ASIC devices become available later, they are used for volume production to reduce cost. Actually, modern FPGAs embed dedicated multipliers to increase the speed of multiply-accumulate operations that are essential for many DSP designs. However, the best system performance relies on more than raw multiplier speed [377]. It is critical to couple these multipliers with a complementary logic structure and routing fabrics of the same performance. For example, The Stratix II family seamlessly integrates DSP blocks that operate at up to 450 MHz with high performance Adaptive Logic Modules (ALMs) and routing fabric to offer the highest system performance for the DSP designs [377].

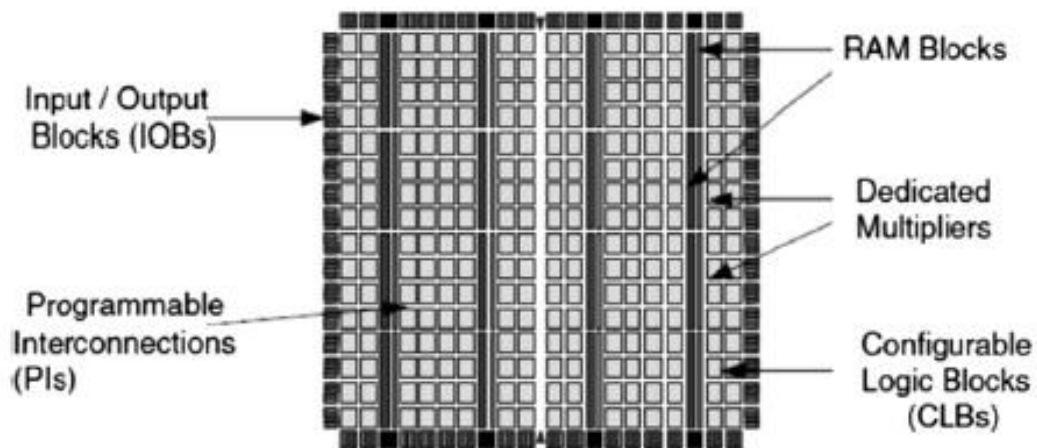


Figure 7.1: Example of distribution of CLBs, IOBs, PIs, RAM blocks, and multipliers in Virtex II [373]

The following are some of the most important advantages of FPGAs, which motivated us to implement proposed MPPT controllers:

- Programmed and reprogrammed many times and consolidation of multiple components into a single component.
- Eliminating the costs associated with re-design or manually updating electronic systems and higher speed compared with Microcontroller or DSP.
- Much faster than software-based logic and improved design update and enhancement options.
- Relatively lower implementation costs; however, microcontrollers are low-cost and power consumption.
- Flexible, it means that you can add subtract the functionality as required, this cannot be done in microcontroller.
- Concurrent, its means that you can take sequential functionality like adding soft processor core. While the microcontroller as always sequential. This makes FPGAs better suited for real-time applications such as executing DSP algorithms.
- FPGA is used mainly for programmable logic, but microcontroller is mainly for hard-core processing.

The different steps to realize and simulate a project into FPGA are summarized as follows:

- Write a program in HDL (VHDL, Verilog, schematics) or use System Generator (Matlab/Simulink).
- Simulate (using ModelSim, or co-simulation with Matlab/Simulink).
- Synthesis (Develop the RTL schematic and technology, etc.).
- Place and route (place and route of the designed project, estimate the consumption power, pins, etc.)
- Timing, maximum clock rate is determined by tools.
- Generating the bit-stream into the FPGA.
- Configure the target device and download it into a FPGA.

ModelSim, Matlab/Simulink and Quartus II software are used for this subject. A typical FPGA mapping flow is shown in Figure 7.2.

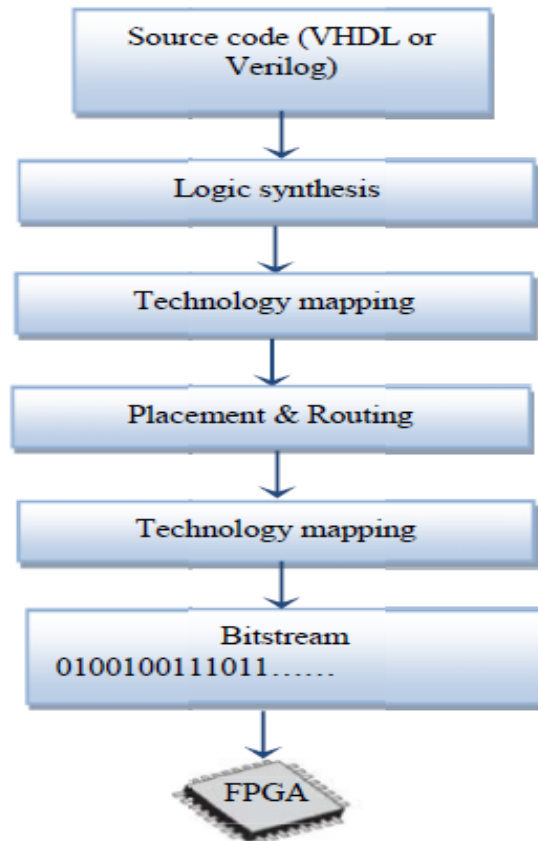


Figure 7.2: A typical FPGA mapping flow [374]

7.2.2 VHDL Code Implementation

Generally, implementation of any algorithm into FPGA can be done by using a hardware description language, such as VHDL. VHDL is a hardware description language; it describes the behaviour of an electronic circuit or system, from which the physical circuit or system can then be implemented. VHDL stands for VHSIC Hardware Description Language. VHSIC is itself an abbreviation for Very High Speed Integrated Circuits, an initiative funded by the United States Department of Defense in the 1980s that led to the creation of VHDL [378]. Its first version VHDL 87 was later upgraded to the so-called VHDL 93. VHDL was the original and first hardware description language to be standardized by the Institute of Electrical and Electronics Engineers, though the IEEE 1076 standard. As reported in [378] a fundamental motivation to use VHDL is that VHDL is a standard. The two main immediate applications of VHDL are in the FPGA and in the field

of ASICs. Once the VHDL code is written, it can be used either to implement the circuit in a programmable device (from Altera, Xilinx, Atmel, etc.) or can be submitted to foundry for fabrication of an ASIC chip. Currently many complex commercial chips (for example, microcontrollers) are designed using such an approach. Figure 7.3 depicts a summary of VHDL design flow. Implanting a VHDL code is principally a two-step process, i.e., synthesis and placement-and-routing [379] as described below:

I. Synthesis

Synthesis involves “compiling” the VHDL code with tools (e.g. Quartus II software) which is a commercially available tool. The result of this compilation is a flip-flop and logic function transcription of the high-level functionalities. Some functions can be resolved in different ways, depending on the target component. VHDL codes can be simulated using ModelSim or other tools.

II. Placement-and-Routing

The result of the “Placement-and-Routing” is the final code to be implanted on the FPGA. An auxiliary result is the VHDL file giving the operation of the implanted code and taking the propagation times of the target device into account. This file can be used in co-simulation and this results in a representation of a virtual prototype. This allows checking that the “Placement-and-Routing” has not altered the performance and that the synchronization of all signals is compatible with the propagation times.

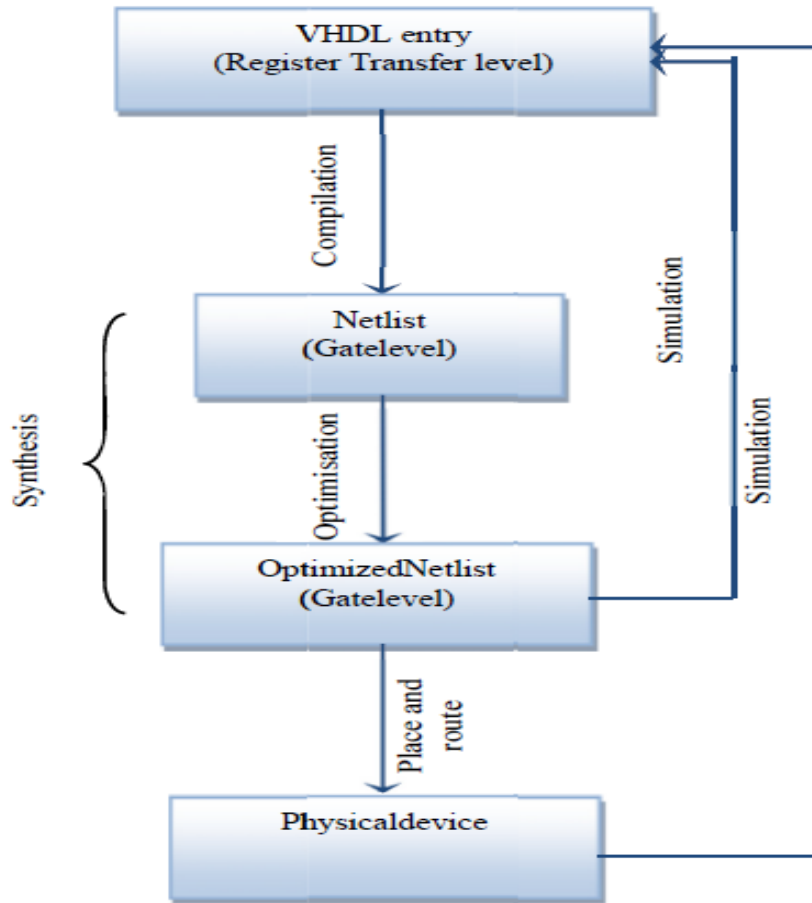


Figure 7.3: VHDL design flow [378]

Further details about FPGAs and their implementation are provided in the Appendix B.

7.3 Simulation Results Using ModelSim Environment

The ModelSim software is a Hardware Description Language (HDL) simulator, manufactured by Mentor Graphics Corporation, and can run independently without an Integrated Synthesis Environment (ISE). The simulation results are based on a ModelSim Altera version 6.6d (Altera, Inc.). The ModelSim software as a real-time test tool provides a simulation of developed VHDL codes which executes the function of MPPT controller adopted in this work. This gives faster and better approach for verification of the control algorithms and confirms the possibility of practical realization of the designed digital controller for stand-alone PV system.

The KF MPPT technique is designed using VHDL hardware description language integrated in the ModelSim environment. Figure 7.4 depicts the overall RTL (Register Transfer Level) of the proposed MPPT algorithm using Quartus II software. The 8 bit S_{out} from the output of the controller is connected to the Pulse Width Modulation (PWM) generator that is used to change the output of the DC-DC Converter. The PWM modulation can be achieved using three basic components, which are a register, to hold the duty cycle value, a counter which value will be compared with the duty cycle value, and the comparator block. The PWM structure is designed on FPGA using the VHDL language. The PWM frequency is equal to the 200 kHz. This value is obtained by dividing the frequency of the FPGA (50 MHz) by 250.

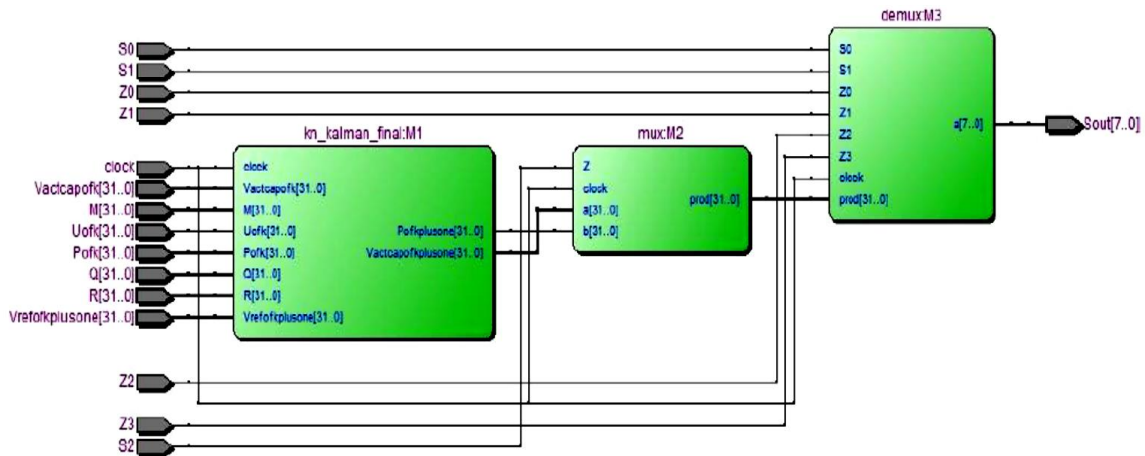


Figure 7.4: The RTL view of the proposed MPPT algorithm

Initially, the selected MPP-controller (i.e., the Kalman filter based MPPT method), starts to work with a low value of duty cycle, e.g. $D = 10\%$, and subsequently the controller behavior is observed and then the required time to reach the maximum power point is calculated automatically (in the screen of ModelSim software).

The simulated output power, voltage, current and duty cycle of the designed KF MPPT controller in the case of the standard test conditions (25°C and $1000\text{W}/\text{m}^2$) are shown in Figure 7.5. As can be seen, the designed controller reaches the MPP very fast, which confirms the accuracy of the developed code under VHDL as well as the implementation of this controller. The designed KF MPPT controller is also tested in the case of rapid step variation of solar irradiance as illustrated in Figure 7.6. From this figure, it is clear that the implemented KF MPPT controller converges quickly to the maximum power point even

under sudden changes in irradiance level. The Duty cycle (D) value is always sent to PWM generator that is used to pilot the DC-DC converter. Table 7.1 reports the FPGA resources summary for the designed MPPT controller. The selected implementation platform was Cyclone II (Device EP2C20F484C7) Altera FPGA family included in the DE2-70 development board (Figure 7.7). This chip was sufficient to implement all the requirements of the MPPT controller addressed in this work. Figure 7.7 shows the duty cycle generated by the designed KF MPPT controller, which is displayed in PWM form under standard test conditions (25°C and 1000W/m²). This result proves that the designed system extracts successfully the MPP for the photovoltaic system.

Furthermore, the simulated output power P and the duty cycle D of the designed KF MPPT controller for rapid variation of solar irradiation and air temperature are shown in Figure 7.8. From this figure, it is obvious that the implemented KF MPPT controller is able to converge quickly and accurately to the maximum power point even under frequent environmental changes conditions affecting both temperature and irradiance, which confirms the accuracy of the developed code under VHDL as well as the implementation of this controller.

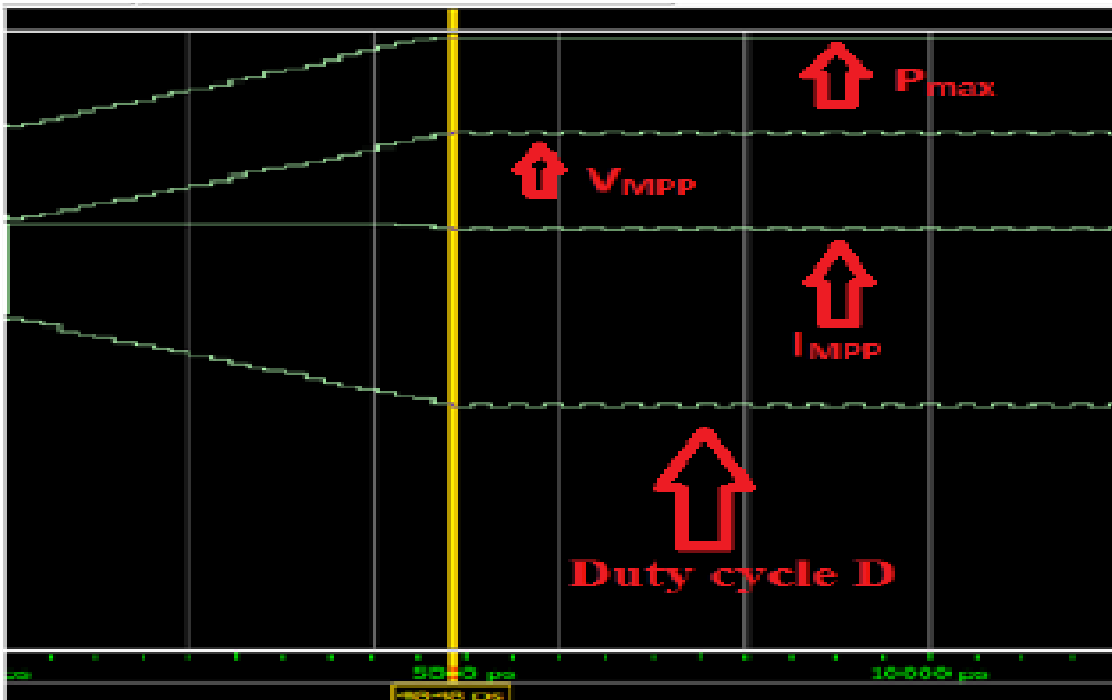


Figure 7.5: The evolution of the PV power, voltage, current and duty cycle vs. time of the designed KF MPPT in the standard test conditions (25°C and 1000W/m²)

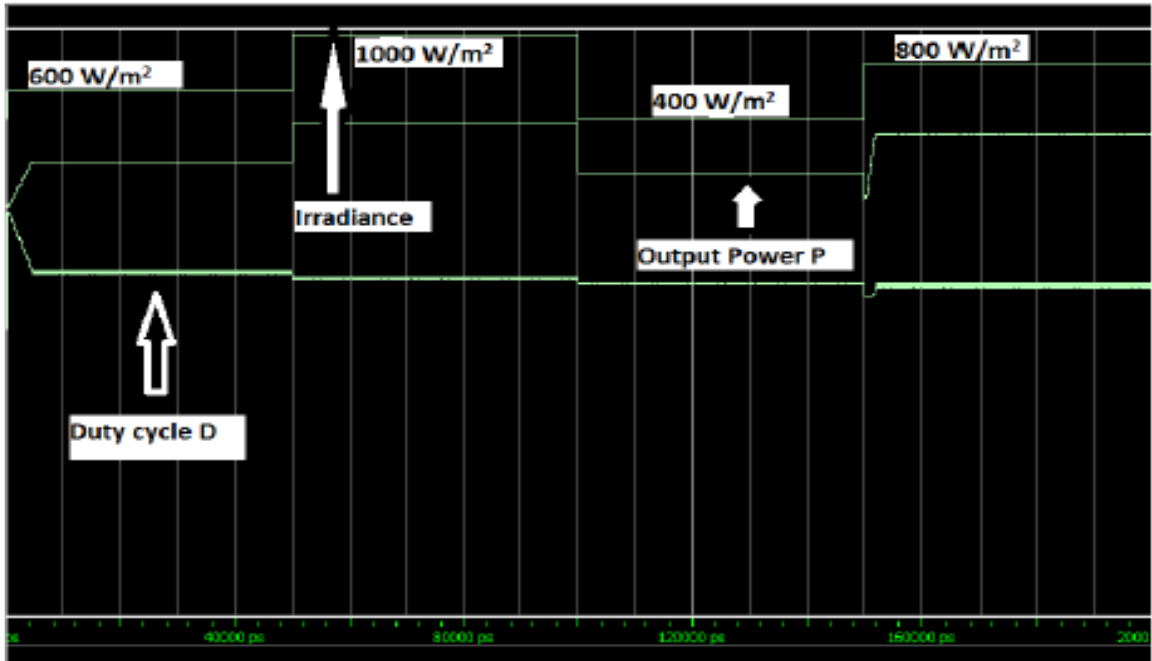


Figure 7.6: The evolution of the PV power and duty cycle vs. time of the designed KF MPPT for rapid step variation of solar irradiation.

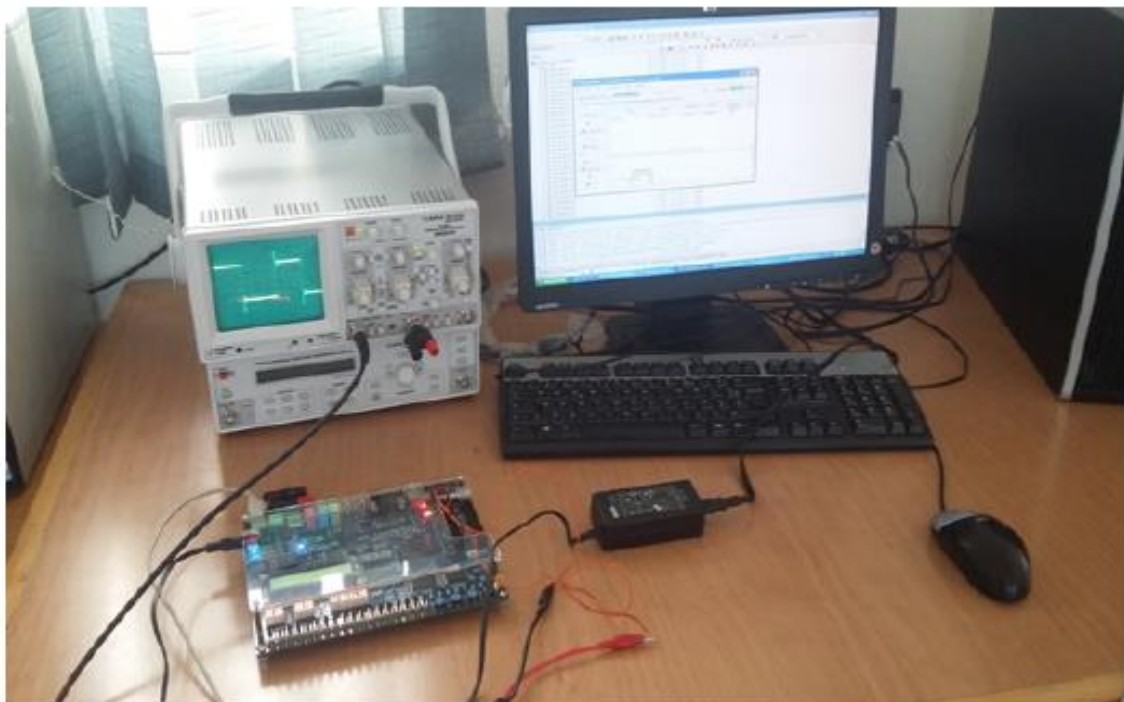


Figure 7.7: The DE2-70 FPGA Board used and the duty cycle D generated by the KF MPPT controller, displayed in PWM form under standard test conditions (25°C and 1000W/m²).

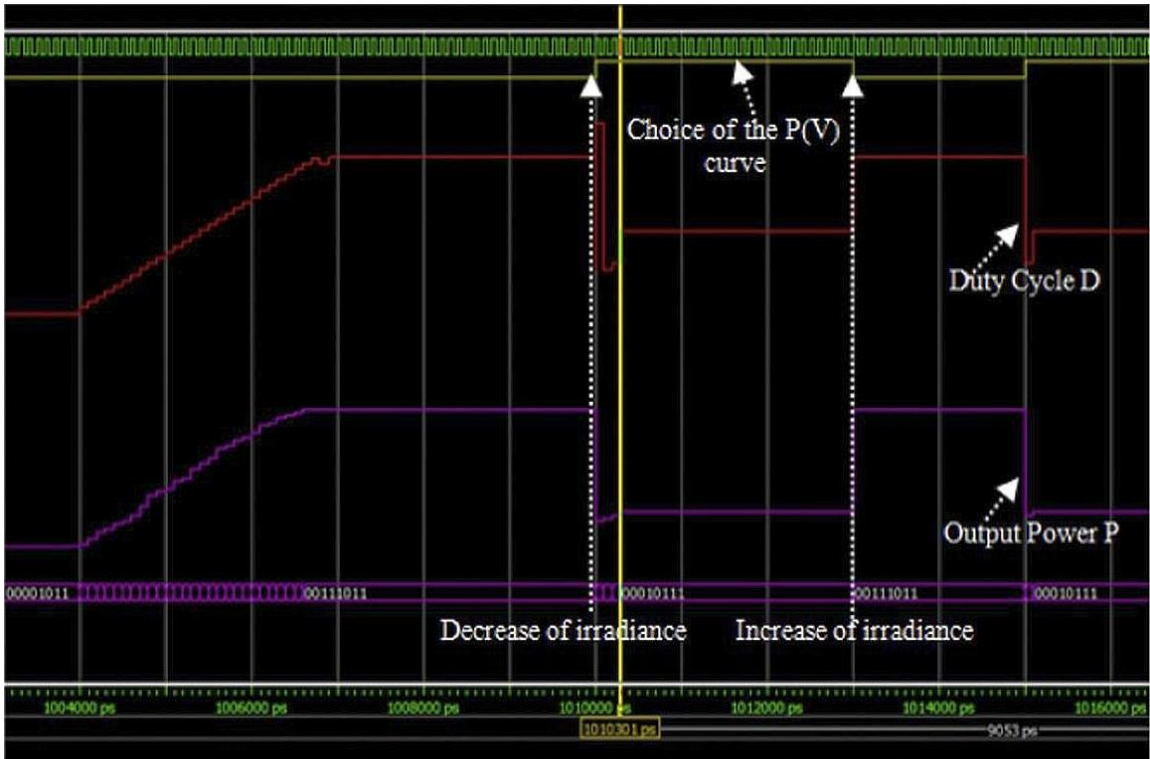


Figure 7.8: The evolution of the PV power and duty cycle vs. time of the designed KF based MPPT controller for rapid variation of solar irradiation and air temperature ($G = 700 \text{ W/m}^2$, $T_a=24 \text{ }^\circ\text{C} \rightarrow G = 300 \text{ W/m}^2$, $T_a=19 \text{ }^\circ\text{C} \rightarrow G = 700 \text{ W/m}^2$, $T_a=24 \text{ }^\circ\text{C}$).

TABLE 7.1: FPGA RESOURCES SUMMARY FOR THE DESIGNED KF MPPT CONTROLLER (DEVICE CYCLONE II, EP2C20F484C7)

Resources	Used
Total Logic Elements (<i>LEs</i>)	12,6/50,53 (25%)
Total Registers	149
Total Pins	34/450 (8%)
Embedded Multiplier Elements	16/172 (9%)
Maximum Frequency	50 MHz

Next, the well-known P&O algorithm has been implemented on a FPGA for real-time tracking of the MPP of a PV system. The P&O algorithm has been designed using the very high-speed description language (VHDL) and implemented on Altera Cyclone II EP2C20F484C7 FPGA. The algorithm has been simulated and tested by conditioning the power produced by the PV-modules. The main advantages of the developed MPPT are low

cost, good velocity, acceptable reliability, and easy implementation. However, its main disadvantage is related to the fact that for fast changes in irradiance it may fail to track the MPP. The efficiency of the implemented P&O controller is about 94%. Figure 7.9 depicts the simulation of the MPP tracking by P&O algorithm for abrupt changes of the weather. Indeed, in an abrupt decrease of solar irradiance, the controller finds the new MPP after 3 clock cycles, and during a sudden increase of solar irradiance, the controller response is estimated by 4 clock cycles before stabilizing at the MPP.

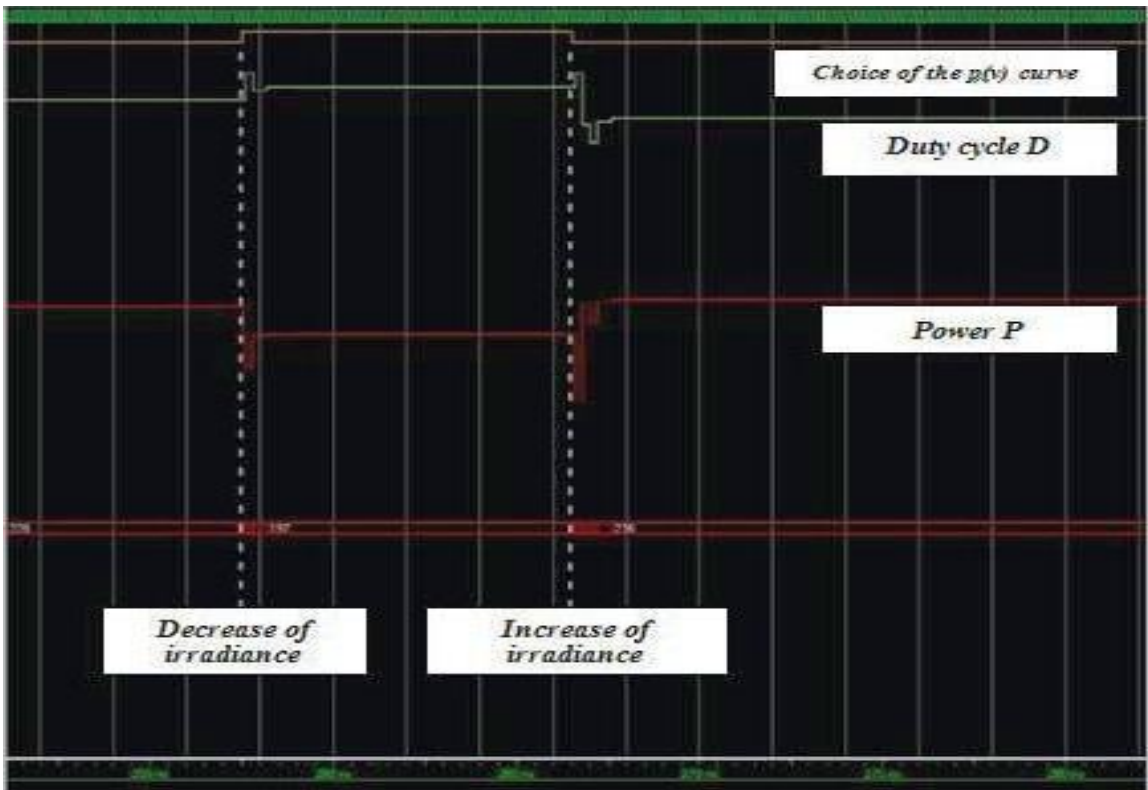


Figure 7.9: Simulation of the MPP tracking by P&O algorithm for abrupt changes of the weather

The use of a fixed increment size leads to follow slowly the MPP. The size of the perturbation step influences the convergence speed of the MPPT control system and leads to less oscillations near the MPP. Large step sizes intrinsically lead to fast convergence to the MPPT; however, the oscillations near the MPP are in this case large, while small step sizes give smaller oscillations.

Figure 7.10 and Figure 7.11 show the results of the implemented P&O controller for two different perturbations step (ΔD) 0.4 and 0.5. In order to evaluate the performances of the implemented digital controller (P&O) the following parameters have been calculated:

- The maximum power tracked by the controller $P_{max} (system)$;
- The power losses caused by the fluctuations near the MPP, ΔP_T .

This latter can be written as:

$$\Delta P_T = \Delta P_{max1} + \Delta P_{max2} \quad (7.1)$$

Where

$$\Delta P_{max1} = P_{max} - P_1 \text{ and } P_1 = I_1 V_1;$$

$$\Delta P_{max2} = P_{max} - P_2 \text{ and } P_2 = I_2 V_2;$$

Other important performance parameters are:

- The produced power under the MPPT control (P_{sim}), can be written as

$$1) P_{sim} = P_{max}(system) - \Delta P_T$$

- The efficiency (η), can be given by

$$2) \eta = P_{sim} / P_{max} (system)$$

The obtained results are summarized in Table 7.2.

Table 7.2 and Figures 7.10 and 7.11 clearly show that the implemented P&O controller converges quickly to the MPP: the response times are 0.2198 ms and 0.1736 ms for perturbation steps set to 0.4 and 0.5, respectively. It can also be noticed that, once the MPP is reached, the PWM signal is zero and the system starts to oscillate around the MPP between two extreme values P_1 and P_2 . This oscillation causes a power loss that depends on the step width of a single perturbation; these oscillations are acceptable if they do not exceed 3.86% for a perturbation step of $\Delta D = 0.4$, and 4.76% for a perturbation step of $\Delta D = 0.5$.

It can be concluded that for a perturbation step of $\Delta D = 0.5$ the system converges more rapidly to the MPP (0.1736 ms) with respect to the perturbation step of $\Delta D = 0.4$ (0.2198 ms). Moreover, the power fluctuations are bigger, and the efficiency of the P&O controller

decreases. The efficiency of the system is 94.13% and 93.23% for perturbation steps of $\Delta D = 0.4$ and $\Delta D = 0.5$, respectively.

The size of the ideal step-width is system dependent and, in order to pursue the trade-off between increased losses and tracking speed, has to be determined experimentally. The magnitude of oscillation depends on the duty step size ΔD . In order to reduce the power loss caused by the oscillation, the duty step size has to be adjusted dynamically according to different weather conditions. Longer sampling period can be used if weather condition is constant.

TABLE 7.2: RESULTS COMPARISON OF THE DESIGNED P&O ALGORITHM CORRESPONDING TO TWO DIFFERENT PERTURBATION STEPS: $\Delta D = 0.4$ AND $\Delta D = 0.5$

Variables and parameters		Perturbation step (ΔD)	
		$\Delta D = 0.4$	$\Delta D = 0.5$
P_{max} (system)	(W)	317.7538	317.7538
I_{opt} (controller)	(A)	11.83	11.59
V_{opt} (controller)	(V)	26.86	27.29
P_{opt} (controller)	(W)	317.7538	316.2911
I_1 (oscillation)	(A)	12.72	12.72
V_1 (oscillation)	(V)	24.24	24.24
P_1 (oscillation)	(W)	308.3328	308.3328
ΔP_{max1}	(W)	9.421	9.421
I_2 (oscillation)	(A)	11.48	11.22
V_2 (oscillation)	(V)	27.43	27.81
P_2 (oscillation)	(W)	314.8964	312.0282
ΔP_{max2}	(W)	9.8574	11.7256
$\Delta P_T = \Delta P_{max1} + \Delta P_{max2}$	(W)	18.6521	21.5119
$P_{sim} = P_{max}(system) - \Delta P_T$	(W)	299.102	296.2419
Efficiency (η)	(%)	94.13	93.23
Response time	(ms)	0.2198	0.1736
Duty cycle (D)	(%)	59.21	58.82

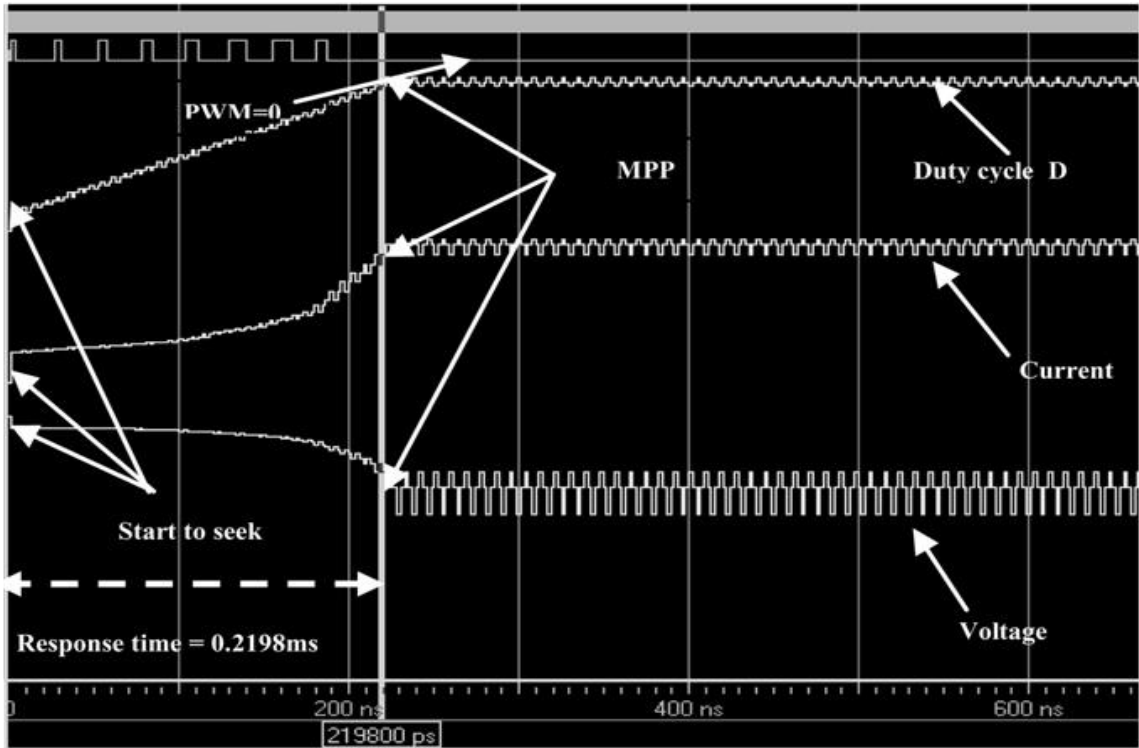


Figure 7.10: Response time of the designed P&O algorithm corresponding to perturbation step (ΔD) = 0.4

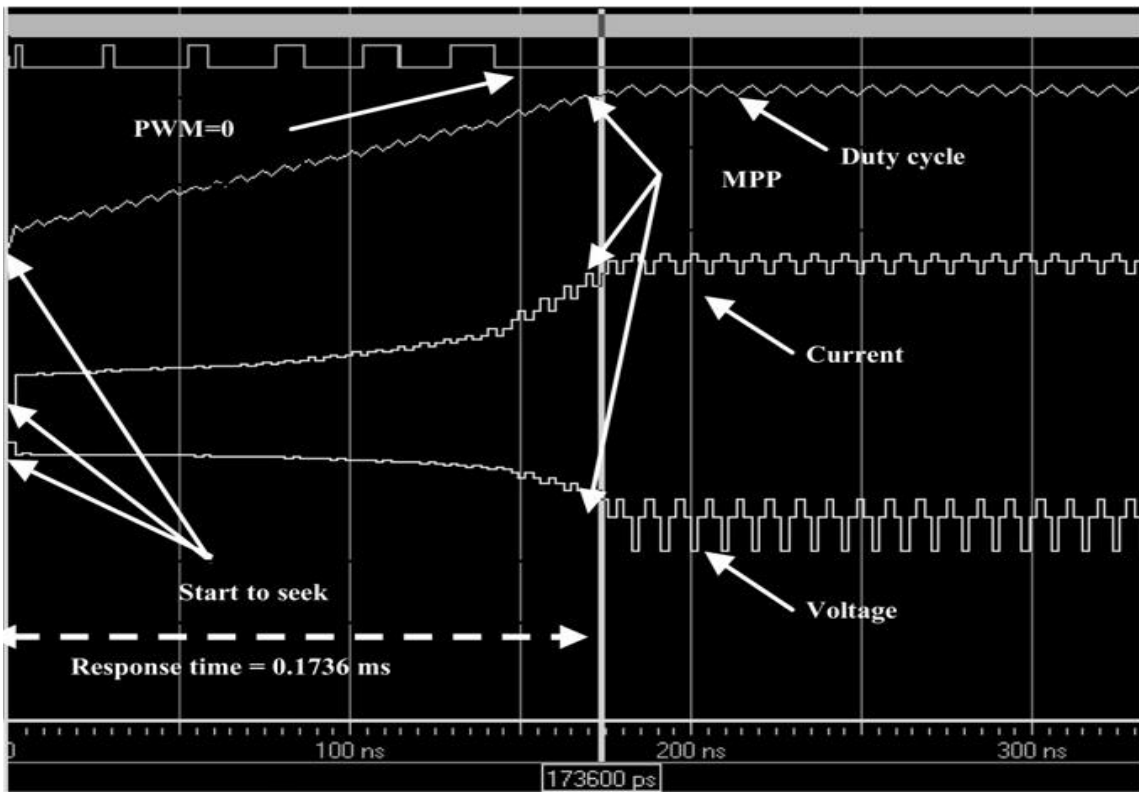


Figure 7.11: Response time of the designed P&O algorithm corresponding to perturbation step (ΔD) = 0.5

7.4 Conclusion

In this chapter, the FPGA module was defined. Then, the difference between an FPGA and a stored-memory processor was investigated. The principle of operation of the various functional units within an FPGA were explained and listed. Furthermore, the architecture and performance specifications of various commercially available FPGA were compared. Moreover, the steps required in implementing an FPGA in an embedded system were described.

The implementation of Kalman filter based MPPT controller and the well-known P&O algorithm has been demonstrated and co-simulated using FPGA chip Altera Cyclone II EP2C20F484C7 to test their efficiencies and tracking speeds in a real-time environment. Finally, KF MPPT implementation on FPGA, Altera DE2-70 board, proves that the designed system extracts successfully the MPP for photovoltaic system.

The main observation of this stage of research is that advanced technical knowledge and skills are required, especially in FPGA design and VHDL code.

Chapter 8. Summary, Contributions, and Future Work

8.1 Summary

The main objective of this thesis is to develop and improve the PV system, by contributing to the optimization of energy withdrawn from PV panel using an embedded system. To achieve this objective, the thesis proposed the implementation of a novel MPPT technique based on the Kalman Filter (KF) algorithm to track the MPP. By applying the proposed KF algorithm to track the MPP, the tracking failures caused by the process and sensor noises were reduced. Also, since the KF also maintains fast tracking of the MPP, it transfers more power during rapid weather changes. The results were first obtained by a Matlab simulation model. Then these results were verified with the hardware implementation of KF based MPPT controller and the well-known P&O algorithm using an FPGA chip Altera Cyclone II EP2C20F484C7 to test their efficiencies and tracking speeds in a real-time environment.

In Chapter 2, a detailed review regarding microgrid architectures was presented. In this chapter, most common microgrids architectures based on AC, DC and hybrid AC/DC buses are analyzed. Furthermore, comparisons are made between different microgrid architectures. Positive and negative features of different architectures are given as a guide for further microgrid system studies.

In Chapter 3, a general overview of the main components of a photovoltaic energy system was provided. This chapter looks at different components of a grid-connected PV system from the solar irradiance received by the PV arrays to the AC power injected into the grid and makes a review of the recent achievements and current research activities regarding these components. Moreover, an accurate PV array electrical model for a practical array (i.e. SunPower SPR-305E-WHT-D) was developed in Matlab environment. An array consists of various PV cells connected in series and parallel ($N_{ser} = 5$, $N_{par} = 66$) to give the desired voltage and power (current) respectively. The results from the model showed an excellent correspondence to manufacturer's published curves and illustrated the effect of insolation and temperature on the important solar characteristics.

In Chapter 4, a comprehensive literature review of the grid-connected photovoltaic systems was carried out. Topologies of single-phase grid-connected inverters were analyzed critically, and a comparative study of these topologies was presented. The three-phase grid-connected inverters were also outlined. The control techniques for the single- and three-phase grid-connected inverters were also critically reviewed and presented.

The main purpose of Chapter 5 was to discuss, in detail, the Small Signal Averaged State Space modeling technique for DC-DC Boost converters, with and without parasitic elements, operating in continuous conduction mode (CCM)/discontinuous conduction mode (DCM). First, the small signal analysis of DC-DC Boost converters with ideal/lossless components operating in CCM was explored in order to develop a simplified model that helps to understand the basic features of the switching system. Then, the small-signal analysis of DC-DC Boost converters with the effects of parasitic elements and losses operating in CCM was investigated in order to improve the model accuracy, study the efficiency and the dynamic performance of the system. Furthermore, the system dynamic behaviour for the DC-DC Boost converter with ideal components and DC-DC Boost converter with non-ideal components operating in CCM was compared via Bode plots and transient step responses under different values for the load resistance in order to help in designing a robust controller for DC-DC Boost converters.

The various aspects of average modelling of DC-DC Boost converter operating in DCM was studied. Basically, the modelling procedure consists of three steps: 1) Averaging the matrix parameters and selection of the correction matrix (K) depending on the number of inductors of the converter, 2) Conversion of state-space equations into differential equations for inductor current and capacitor voltage, and 3) Defining a duty ratio constraint so that the expression consists of only one duty ratio. Moreover, the reduced- and full-order average models were derived. It was found that the reduced-order model can estimate the behavior in the low frequency range but the full-order model, since dynamics of inductor are present, is more precise.

In addition, various parasitic components were taken into consideration and a full-order model was developed. The system dynamic behavior for the DC-DC Boost converter with ideal components and DC-DC Boost converter with non-ideal components operating in

DCM were compared via Bode plots and transient step responses under different values of the load resistance in order to help in designing a robust controller.

Chapter 5 also highlighted that, boost type DC-DC converters are non-linear systems, and output voltage regulation in these converters using a traditionally derived feedback controller does not yield good dynamic responses at different operating points over the complete operating range. Hence, the design of a feedback controller for a DC-DC Boost converter operating in CCM was formulated as an optimization task, and the feedback controller parameters were derived based on a novel PSO technique. This novel optimization method was designed to yield a robust, closed-loop controller structure with stable static and dynamic characteristics for operating points over the whole operational range of the converter. To evaluate the objective function of the developed PSO algorithm, a small-signal model of a DC-DC Boost converter, subjected to various internal and external disturbances, was used. First, the PID controller parameters for the DC-DC Boost converter were identified based on (a) the traditional Ziegler–Nichol method and (b) the novel PSO algorithm. Then, using the gain parameters obtained by these two methods, the dynamic responses of the DC-DC Boost converter operating in CCM were obtained and compared. Four different performance comparison tests undergoing various input-voltage and load-current step transients were studied. By comparing the qualitative criteria (comprised of rise time, settling time, peak overshoot from the step response curves which are obtained under the variations in both command input and load resistance), it was concluded that the robustness and effectiveness of the controller tuned by PSO algorithm (compared to the traditional method) was more superior over a wide range of operating conditions.

Finally, the dynamic performance of DC-DC Boost converters, with and without parasitic elements, operating in CCM was investigated. Different numerical integration methods were tried in the transient circuit analysis packages to evaluate the impact on the dynamic simulation. Eventually, it became obvious that the Runge-Kutta 4th order method was the preferred choice to use.

Based on the discussions presented in previous chapters, the layout of a new method, the KF MPPT based method, was introduced in Chapter 6. The main advantage of the applying the proposed KF algorithm to track the MPP, the tracking failures caused by the process

and sensor noises were reduced. Also, since the KF also maintains fast tracking of the MPP, it transfers more power during rapid weather changes. The main idea of the proposed method is the MPPT using a KF as an alternative to expect an acceptable performance against both the noises and dynamic environmental changes. Due to the excellent estimation ability of the KF in the dynamic system within the noisy environment, an accurate MPP can be predicted by the KF without any reduction of system dynamics. Other MPPT methods sometimes degrade their system dynamics partially to eliminate the noise effects.

After presenting the layout of the proposed method, Chapter 6 also introduced the details of different stages of the method. Firstly, the KF was introduced as a tool for statistical estimation in the context of linear Gaussian dynamical systems. An overview of its history, its mathematical and statistical formulations, and its use in applications was mentioned. Moreover, the effects of the selection of the assumed covariance matrices Q and R and how significantly they affected the overall estimation performance of a KF was investigated.

Secondly, for system modelling purposes, a PV test system with a 100 kW PV array and MPPT controller using the traditional P&O and KF algorithms was used. The PV panel output power controlled by three methods: (a) without any MPPT (i.e. open loop), (b) MPPT using P&O algorithm, and (c) MPPT using the proposed KF algorithm. The model for the PV panel has as inputs the weather variables: temperature and solar irradiance and, as outputs: voltage, current and power. This PV panel feeds into a DC-DC boost converter that is used to match between its input impedance and output (constant load) impedance and calculate the operating duty cycle based on the algorithm to get the correct MPP.

Finally, the Matlab simulation results showed a good performance for the KF algorithm as it is able to maintain the tracking speed in the face of frequent environmental changes conditions affecting both temperature and irradiance. Comparisons between the KF algorithm and the more traditional P&O algorithm showed the superior performance of the KF algorithm. The obtained results clearly highlight the superiority of the proposed method; it yields an efficiency of 99.38 % under the STC, which is almost 5 % higher than the conventional P&O method under the same conditions. The oscillations generated by the conventional P&O algorithm are higher when compared to KF. We can conclude that KF is better when used as an MPPT than the conventional P&O algorithm.

After introducing, designing and implementing the KF based MPPT technique in Matlab environment, and comparing it with the well-known P&O algorithm, Chapter 7 demonstrated and co-simulated these algorithms using an FPGA chip Altera Cyclone II EP2C20F484C7 to test their efficiencies and tracking speeds in a real-time environment. Moreover, in this chapter the FPGA was defined. Then, the distinction between an FPGA and a stored-memory processor was investigated. The principle of operation of the various functional units within an FPGA were explained and listed. Furthermore, the architecture and performance specifications of various commercially available FPGA were compared. Also, the steps required in using an FPGA in an embedded system were described.

8.2 Main Contributions of the Research

The main contributions of the research presented in this thesis are summarized below:

- The thesis proposed an accurate PV array electrical model for a practical array (i.e. SunPower SPR-305E-WHT-D) in Matlab environment. An array consists of various PV cells connected in series and parallel ($N_{ser} = 5$, $N_{par} = 66$) to give the desired voltage and power (current) respectively. The Newton-Raphson method was selected to solve this non-linear set of equations describing the dynamics of the PV array, because this method converges much more rapidly, and for both positive and negative currents. The results from this model showed an excellent correspondence to manufacturer's published curves and illustrated the effect of insolation and temperature on the important solar characteristics.
- The thesis discussed in detail the Small Signal Averaged State-Space modeling technique for DC-DC Boost converters, with and without parasitic elements, operating in CCM/DCM. First, the small signal analysis of DC-DC Boost converters with ideal/lossless components operating in CCM was explored in order to develop a simplified model that helps to understand the basic features of the switching system. Then, the small-signal analysis of DC-DC Boost converters with the effects of parasitic elements and losses operating in CCM was investigated in order to improve the model accuracy, study the efficiency and the dynamic performance of the system. Furthermore, the system dynamic behaviour for the DC-

DC Boost converter with ideal components and DC-DC Boost converter with non-ideal components operating in CCM was compared via Bode plots and transient step responses under different values for the load resistance in order to help in designing a robust controller for DC-DC Boost converters.

- The thesis also mentioned the various aspects of average modelling of DC-DC Boost converter operating in DCM. Basically, the modelling procedure consists of three steps: 1) Averaging the matrix parameters and selection of the correction matrix (K) depending on the number of inductors of the converter, 2) Conversion of state-space equations into differential equations for inductor current and capacitor voltage, and 3) Defining a duty ratio constraint so that the expression consists of only one duty ratio. Moreover, the reduced- and full-order average models were derived. It was found that the reduced-order model can estimate the behavior in the low frequency range but the full-order model, since dynamics of inductor are present, is more precise. In addition, various parasitic components were taken into consideration and a full-order model was developed. The system dynamic behavior for the DC-DC Boost converter with ideal components and DC-DC Boost converter with non-ideal components operating in DCM were compared via Bode plots and transient step responses under different values of the load resistance in order to help in designing a robust controller.
- The thesis proposed the design of a feedback controller for a DC-DC boost converter operating in CCM as an optimization task, and the feedback controller parameters are derived based on a novel PSO technique. This novel optimization method was designed to yield a robust, closed-loop controller structure with stable static and dynamic characteristics for operating points over the whole operational range of the converter.
- The thesis investigated nine popular integration algorithms and simulated the DC-DC boost converters, with and without parasitic elements, operating in CCM. The off-line simulations were performed under the Matlab environment. The results from the nine different integration techniques were then compared to validate their accuracy and efficiency. It soon became obvious that the Runge-Kutta 4th order and Trapezoidal techniques could be considered as potential candidates for further work

due to their speed, accuracy and stability in the implementation of real-time models in embedded hardware platforms.

- The research highlighted two commonly employed techniques in designing MPPT systems in PV farms, Differential Evolution (DE) and Particle Swarm Optimization (PSO) algorithms. A comprehensive comparative study is conducted on DE and PSO algorithms in terms of control parameters, search components, and population initialization methods to determine the best algorithm with its corresponding optimal parameters settings and population initialization to solve a MPPT problem associated with PV systems.
- The Center-based Latin Hypercube (CLHS) initialization scheme for population-based algorithms proposed in this research is a novel method; it is shown that for population initialization, the newly proposed initialization technique (CLHS) gives better results with a small population size.
- The thesis proposed design and implementation of a novel MPPT technique based on the Kalman Filter (KF) algorithm to track the MPP. By applying the proposed KF algorithm to track the MPP, the tracking failures caused by the process and sensor noises were reduced. Also, since the KF also maintains fast tracking of the MPP, it transfers more power during rapid weather changes.
- The thesis also investigated the effects of the selection of the assumed covariance matrices Q and R and how significantly they affected the overall estimation performance of the Kalman Filter.
- The thesis demonstrated and co-simulated the Kalman Filter (KF) based MPPT technique and the well-known P&O algorithm using an FPGA chip Altera Cyclone II EP2C20F484C7 to test their efficiencies and tracking speeds in a real-time environment.

8.3 Scope of Future Research

This thesis establishes a new direction for research related to PV systems and other intermittent renewable energy sources. Based on the research presented in this thesis, some of the studies that can be carried out in the future are summarized in the following:

- Investigate the use of another type of Kalman Filter such as Unscented Kalman Filter (UKF) which can handle better the nonlinearity of the PV characteristics.
- Evaluate the impact of both aging and presence of dust on the PV panel surface on the energy production and MPPT controller performance.
- Create a detailed sensitivity analysis of different process and measurement noises in a PV system and their effect on the MPPT controller performance.
- Investigate the effect of the non-Gaussian noises on the Kalman Filter performance and how to optimize the Kalman filter under such processes.
- Examine the use of different power electronic converter types such as resonant converter with the proposed control algorithm.
- Investigate the effect of integrating a battery storage system with stand-alone PV systems on the proposed MPPT controller performance.
- Investigate in more details the effect of partial shading on the proposed MPPT controller performance.
- Evaluate the impact of different type of electric faults in PV system on the power converter devices and MPPT controller performance.

References

- [1] M. Green, "Community power," *Nat. Energy*, vol. 1, no. 3, p. 16014, Feb. 2016.
- [2] R. Lasseter *et al.*, "Integration of distributed energy resources: the CERTS MicroGrid concept," *Lawrence Berkeley Natl. Lab.*, pp. 1–24, 2002.
- [3] I. Patrao, E. Figueres, G. Garcerá, and R. González-Medina, "Microgrid architectures for low voltage distributed generation," *Renew. Sustain. Energy Rev.*, vol. 43, pp. 415–424, Mar. 2015.
- [4] J. J. Justo, F. Mwasilu, J. Lee, and J.-W. Jung, "AC-microgrids versus DC-microgrids with distributed energy resources: A review," *Renew. Sustain. Energy Rev.*, vol. 24, pp. 387–405, Aug. 2013.
- [5] E. Koutroulis, K. Kalaitzakis, and N. C. Voulgaris, "Development of a microcontroller-based, photovoltaic maximum power point tracking control system," *IEEE Trans. Power Electron.*, vol. 16, no. 1, pp. 46–54, 2001.
- [6] N. Femia, G. Petrone, G. Spagnuolo, and M. Vitelli, "Optimization of Perturb and Observe Maximum Power Point Tracking Method," *IEEE Trans. Power Electron.*, vol. 20, no. 4, pp. 963–973, Jul. 2005.
- [7] S. Gomathy, S. Saravanan, and D. S. Thangavel, "Design and implementation of Maximum Power Point Tracking (MPPT) algorithm for a standalone PV system," *Int. J. Sci. Eng. Res.*, vol. 3, no. 3, 2012.
- [8] C. Liu, B. Wu, and R. Cheung, "Advanced algorithm for MPPT control of photovoltaic systems," in *Canadian Solar Buildings Conference, Montreal, 2004*, vol. 8.
- [9] "Solar Panels and Home Energy Efficiency - Energy Informative." [Online]. Available: <https://energyinformative.org/>. [Accessed: 02-Apr-2019].
- [10] J. J. Nedumgatt, K. B. Jayakrishnan, S. Umashankar, D. Vijayakumar, and D. P. Kothari, "Perturb and observe MPPT algorithm for solar PV systems-modeling and simulation," in *2011 Annual IEEE India Conference*, 2011, pp. 1–6.
- [11] R. Faranda and S. Leva, "Energy Comparison of MPPT techniques for PV systems," *WSEAS Trans. Power Syst.*, vol. 3, no. 6, pp. 446–455, 2008.
- [12] T. Esum and P. L. Chapman, "Comparison of photovoltaic array maximum power point tracking techniques," *IEEE Trans. Energy Convers.*, vol. 22, no. 2, pp. 439–

449, Jun. 2007.

- [13] J. S. Kumari and C. Saibabu, "Maximum Power Point Tracking Algorithms for Grid-Connected Photovoltaic Energy Conversion System," *Int. J. Power Electron. Drive Syst.*, vol. 3, no. 4, Dec. 2013.
- [14] A. F. Murtaza, H. A. Sher, M. Chiaberge, D. Boero, M. D. Giuseppe, and K. E. Addoweesh, "A Novel Hybrid MPPT Technique for Solar PV Applications using Perturb & Observe and Fractional Open Circuit Voltage Techniques," in *Proceedings of 15th International Conference MECHATRONIKA, Prague*, 2012, pp. 1–8.
- [15] S. Yuvarajan and J. Shoeb, "A fast and accurate maximum power point tracker for PV systems," in *2008 Twenty-Third Annual IEEE Applied Power Electronics Conference and Exposition*, 2008, pp. 167–172.
- [16] A. Chitra, R. M. S. Palackal, and K. Viswanathan, "A Incremental Conductance Based Maximum Power Point Tracking Algorithm for a Solar Photovoltaic System," *Int. J. Appl. Eng. Res. [IJAER]*, vol. 8, no. 19, pp. 2299–2302, 2013.
- [17] K. H. Hussein, I. Muta, T. Hoshino, and M. Osakada, "Maximum photovoltaic power tracking: an algorithm for rapidly changing atmospheric conditions," *IEE Proc. - Gener. Transm. Distrib.*, vol. 142, no. 1, pp. 59–64, 1995.
- [18] R. Kini, G. Narayanan, and A. Dalvi, "Comparative Study And Implementation Of Incremental Conductance Method And Perturb And Observe Method With Buck Converter By Using Arduino," *Int. J. Res. Eng. Technol.*, vol. 03, no. 01, pp. 461–469, Jan. 2014.
- [19] M. Azab, "A New Maximum Power Point Tracking for Photovoltaic Systems," *World Acad. Sci. Eng. Technol.*, vol. 2, no. 8, pp. 1600–1603, 2008.
- [20] S. Anand, R. S. Farswan, B. Mangu, and B. G. Fernandes, "Optimal charging of battery using solar PV in standalone DC system," in *6th IET International Conference on Power Electronics, Machines and Drives (PEMD 2012)*, 2012, pp. 1–6.
- [21] Boyang Hu and S. Sathiakumar, "Current ripple cancellation of multiple paralleled boost converters for PV/battery charging system with MPPT," in *2011 IEEE PES Innovative Smart Grid Technologies*, 2011, pp. 1–6.

- [22] S. Yam Prasad, B. Bimal Chhetri, B. Adhikary, and D. Bista, "Microcontroller based intelligent DC/DC converter to track Maximum Power Point for solar photovoltaic module," in *2010 IEEE Conference on Innovative Technologies for an Efficient and Reliable Electricity Supply*, 2010, pp. 94–101.
- [23] P. Petchjaturporn, W. Ngamkham, N. Khaehintung, P. Sirisuk, W. Kiranon, and A. Kunakorn, "A Solar-powered Battery Charger with Neural Network Maximum Power Point Tracking Implemented on a Low-Cost PIC-microcontroller," in *TENCON 2005 - 2005 IEEE Region 10 Conference*, 2005, pp. 1–4.
- [24] Yi-Hwa Liu, Rong-Ceng Leou, and Jeng-Shiung Cheng, "Design and implementation of a maximum power point tracking battery charging system for photovoltaic applications," in *2005 IEEE Russia Power Tech*, 2005, pp. 1–5.
- [25] M. Ricco, P. Manganiello, E. Monmasson, G. Petrone, and G. Spagnuolo, "FPGA-Based Implementation of Dual Kalman Filter for PV MPPT Applications," *IEEE Trans. Ind. Informatics*, vol. 13, no. 1, pp. 176–185, Feb. 2017.
- [26] P. Manganiello, M. Ricco, G. Petrone, E. Monmasson, and G. Spagnuolo, "Dual-Kalman-Filter-Based Identification and Real-Time Optimization of PV Systems," *IEEE Trans. Ind. Electron.*, vol. 62, no. 11, pp. 7266–7275, Nov. 2015.
- [27] V. Ramchandani, K. Pamarthi, and S. R. Chowdhury, "Comparative Study Of Maximum Power Point Tracking Using Linear Kalman Filter & Unscented Kalman Filter For Solar Photovoltaic Array On Field Programmable Gate Array," *Int. J. Smart Sens. Intell. Syst.*, vol. 5, no. 3, pp. 701–716, Sep. 2012.
- [28] A. K. Abdelsalam, S. Goh, O. Abdelkhalik, S. Ahmed, and A. Massoud, "Iterated unscented Kalman filter-based maximum power point tracking for photovoltaic applications," in *IECON 2013 - 39th Annual Conference of the IEEE Industrial Electronics Society*, 2013, pp. 1685–1693.
- [29] M. A. S. Masoum, H. Dehbonei, and E. F. Fuchs, "Theoretical and experimental analyses of photovoltaic systems with voltage and current-based maximum power-point tracking," *IEEE Trans. Energy Convers.*, vol. 17, no. 4, pp. 514–522, Dec. 2002.
- [30] T. Noguchi, S. Togashi, and R. Nakamoto, "Short-current pulse-based maximum-power-point tracking method for multiple photovoltaic-and-converter module

- system,” *IEEE Trans. Ind. Electron.*, vol. 49, no. 1, pp. 217–223, 2002.
- [31] H. Patel and V. Agarwal, “Maximum Power Point Tracking Scheme for PV Systems Operating Under Partially Shaded Conditions,” *IEEE Trans. Ind. Electron.*, vol. 55, no. 4, pp. 1689–1698, Apr. 2008.
- [32] S. L. Brunton, C. W. Rowley, S. R. Kulkarni, and C. Clarkson, “Maximum Power Point Tracking for Photovoltaic Optimization Using Ripple-Based Extremum Seeking Control,” *IEEE Trans. Power Electron.*, vol. 25, no. 10, pp. 2531–2540, Oct. 2010.
- [33] S. Jain and V. Agarwal, “A Single-Stage Grid Connected Inverter Topology for Solar PV Systems With Maximum Power Point Tracking,” *IEEE Trans. Power Electron.*, vol. 22, no. 5, pp. 1928–1940, Sep. 2007.
- [34] K. H. Hussein, I. Muta, T. Hoshino, and M. Osakada, “Maximum photovoltaic power tracking: an algorithm for rapidly changing atmospheric conditions,” *IEE Proc. - Gener. Transm. Distrib.*, vol. 142, no. 1, pp. 59–64, 1995.
- [35] Y.-H. Ji, D.-Y. Jung, J.-G. Kim, J.-H. Kim, T.-W. Lee, and C.-Y. Won, “A Real Maximum Power Point Tracking Method for Mismatching Compensation in PV Array Under Partially Shaded Conditions,” *IEEE Trans. Power Electron.*, vol. 26, no. 4, pp. 1001–1009, Apr. 2011.
- [36] A. Safari and S. Mekhilef, “Simulation and Hardware Implementation of Incremental Conductance MPPT With Direct Control Method Using Cuk Converter,” *IEEE Trans. Ind. Electron.*, vol. 58, no. 4, pp. 1154–1161, Apr. 2011.
- [37] B. N. Alajmi, K. H. Ahmed, S. J. Finney, and B. W. Williams, “Fuzzy-Logic-Control Approach of a Modified Hill-Climbing Method for Maximum Power Point in Microgrid Standalone Photovoltaic System,” *IEEE Trans. Power Electron.*, vol. 26, no. 4, pp. 1022–1030, Apr. 2011.
- [38] A. K. Rai, N. D. Kaushika, B. Singh, and N. Agarwal, “Simulation model of ANN based maximum power point tracking controller for solar PV system,” *Sol. Energy Mater. Sol. Cells*, vol. 95, no. 2, pp. 773–778, Feb. 2011.
- [39] K. Ishaque and Z. Salam, “An improved modeling method to determine the model parameters of photovoltaic (PV) modules using differential evolution (DE),” *Sol. Energy*, vol. 85, no. 9, pp. 2349–2359, Sep. 2011.

- [40] K. Ishaque, Z. Salam, H. Taheri, and A. Shamsudin, "A critical evaluation of EA computational methods for Photovoltaic cell parameter extraction based on two diode model," *Sol. Energy*, vol. 85, no. 9, pp. 1768–1779, Sep. 2011.
- [41] M. Miyatake, M. Veerachary, F. Toriumi, N. Fujii, and H. Ko, "Maximum Power Point Tracking of Multiple Photovoltaic Arrays: A PSO Approach," *IEEE Trans. Aerosp. Electron. Syst.*, vol. 47, no. 1, pp. 367–380, Jan. 2011.
- [42] V. Phimmasone, Y. Kondo, T. Kamejima, and M. Miyatake, "Evaluation of extracted energy from PV with PSO-based MPPT against various types of solar irradiation changes," in *International Conference on Electrical Machines and Systems*, 2010, pp. 487–492.
- [43] V. Phimmasone, T. Endo, Y. Kondo, and M. Miyatake, "Improvement of the Maximum Power Point Tracker for photovoltaic generators with Particle Swarm Optimization technique by adding repulsive force among agents," in *2009 International Conference on Electrical Machines and Systems*, 2009, pp. 1–6.
- [44] Y. Liu, D. Xia, and Z. He, "MPPT of a PV system based on the particle swarm optimization," in *2011 4th International Conference on Electric Utility Deregulation and Restructuring and Power Technologies (DRPT)*, 2011, pp. 1094–1096.
- [45] M. A. Hassan and M. A. Abido, "Optimal Design of Microgrids in Autonomous and Grid-Connected Modes Using Particle Swarm Optimization," *IEEE Trans. Power Electron.*, vol. 26, no. 3, pp. 755–769, Mar. 2011.
- [46] A. N. A. Ali, M. H. Saied, M. Z. Mostafa, and T. M. Abdel- Moneim, "A survey of maximum PPT techniques of PV systems," in *2012 IEEE Energytech*, 2012, pp. 1–17.
- [47] "19 Most Efficient Solar Panels of 2019 - Updated 03/06/19." [Online]. Available: <https://ecotality.com/most-efficient-solar-panels/>. [Accessed: 05-Apr-2019].
- [48] N. Khaehintung, T. Wiangtong, and P. Sirisuk, "FPGA Implementation of MPPT Using Variable Step-Size P&O Algorithm for PV Applications," in *2006 International Symposium on Communications and Information Technologies*, 2006, pp. 212–215.
- [49] N. Salvatore, A. Caponio, F. Neri, S. Stasi, and G. L. Cascella, "Optimization of

- Delayed-State Kalman-Filter-Based Algorithm via Differential Evolution for Sensorless Control of Induction Motors,” *IEEE Trans. Ind. Electron.*, vol. 57, no. 1, pp. 385–394, Jan. 2010.
- [50] M. Barut, S. Bogosyan, and M. Gokasan, “Experimental Evaluation of Braided EKF for Sensorless Control of Induction Motors,” *IEEE Trans. Ind. Electron.*, vol. 55, no. 2, pp. 620–632, 2008.
- [51] E. S. de Santana, E. Bim, and W. C. do Amaral, “A Predictive Algorithm for Controlling Speed and Rotor Flux of Induction Motor,” *IEEE Trans. Ind. Electron.*, vol. 55, no. 12, pp. 4398–4407, Dec. 2008.
- [52] K. Szabat and T. Orłowska-Kowalska, “Performance improvement of industrial drives with mechanical elasticity using nonlinear adaptive Kalman filter,” *IEEE Trans. Ind. Electron.*, vol. 55, no. 3, pp. 1075–1084, Mar. 2008.
- [53] R. Agha Zadeh, A. Ghosh, and G. Ledwich, “Combination of Kalman filter and least-error square techniques in power system,” *IEEE Trans. Power Deliv.*, vol. 25, no. 4, pp. 2868–2880, Oct. 2010.
- [54] C. I. Chen, G. W. Chang, R. C. Hong, and H. M. Li, “Extended Real Model of Kalman Filter for Time-Varying Harmonics Estimation,” *IEEE Trans. Power Deliv.*, vol. 25, no. 1, pp. 17–26, Jan. 2010.
- [55] S. P. Won, W. W. Melek, and F. Golnaraghi, “A Kalman/Particle Filter-Based Position and Orientation Estimation Method Using a Position Sensor/Inertial Measurement Unit Hybrid System,” *IEEE Trans. Ind. Electron.*, vol. 57, no. 5, pp. 1787–1798, May 2010.
- [56] S.-H. P. Won, F. Golnaraghi, and W. W. Melek, “A Fastening Tool Tracking System Using an IMU and a Position Sensor With Kalman Filters and a Fuzzy Expert System,” *IEEE Trans. Ind. Electron.*, vol. 56, no. 5, pp. 1782–1792, May 2009.
- [57] C. Mitsantisuk, S. Katsura, and K. Ohishi, “Kalman-Filter-Based Sensor Integration of Variable Power Assist Control Based on Human Stiffness Estimation,” *IEEE Trans. Ind. Electron.*, vol. 56, no. 10, pp. 3897–3905, Oct. 2009.
- [58] Pinjia Zhang, Yi Du, Jing Dai, T. G. Habetler, and Bin Lu, “Impaired-Cooling-Condition Detection Using DC-Signal Injection for Soft-Starter-Connected Induction Motors,” *IEEE Trans. Ind. Electron.*, vol. 56, no. 11, pp. 4642–4650, Nov.

2009.

- [59] A. G. Beccuti, S. Mariethoz, S. Cliquennois, Shu Wang, and M. Morari, “Explicit Model Predictive Control of DC–DC Switched-Mode Power Supplies With Extended Kalman Filtering,” *IEEE Trans. Ind. Electron.*, vol. 56, no. 6, pp. 1864–1874, Jun. 2009.
- [60] M. Liserre, A. Pigazo, A. Dell’Aquila, and V. M. Moreno, “An Anti-Islanding Method for Single-Phase Inverters Based on a Grid Voltage Sensorless Control,” *IEEE Trans. Ind. Electron.*, vol. 53, no. 5, pp. 1418–1426, Oct. 2006.
- [61] “Invert your thinking: Squeezing more power out of your solar panels - Scientific American Blog Network,” 2009. [Online]. Available: <https://blogs.scientificamerican.com/solar-at-home/invert-your-thinking-squeezing-more-power-out-of-your-solar-panels/>. [Accessed: 11-Apr-2019].
- [62] B. Tull, “Photovoltaic Cells: Science and Materials,” *Columbia Univ.*, vol. 20, no. 11, 2011.
- [63] S. Surawdhaniwar and R. Diwan, “Study of Maximum Power Point Tracking Using Perturb and Observe Method,” *Int. J. Adv. Res. Comput. Eng. Technol.*, vol. 1, no. 5, pp. 106–110, 2012.
- [64] S. M. Sze and K. K. Ng, *Physics of Semiconductor Devices*. Hoboken, NJ, USA: John Wiley & Sons, Inc., 2006.
- [65] “Increase Solar Charging With An MPPT Power Tracking Charge Controller.” [Online]. Available: <https://www.wholesalesolar.com/solar-information/mppt-article>. [Accessed: 11-Apr-2019].
- [66] A. Ipakchi and F. Albuyeh, “Grid of the future,” *IEEE Power Energy Mag.*, vol. 7, no. 2, pp. 52–62, Mar. 2009.
- [67] R. H. Lasseter, “MicroGrids,” in *2002 IEEE Power Engineering Society Winter Meeting. Conference Proceedings (Cat. No.02CH37309)*, vol. 1, pp. 305–308.
- [68] N. Hatziargyriou, *Microgrid : architectures and control*. John Wiley and Sons Ltd. IEEE Press, 2014.
- [69] A. Timbus, A. Oudalov, and C. N. M. Ho, “Islanding detection in smart grids,” in *2010 IEEE Energy Conversion Congress and Exposition*, 2010, pp. 3631–3637.
- [70] G. Platt, A. Berry, and D. Cornforth, “What role for microgrid?,” in *Smart grid :*

integrating renewable, distributed & efficient energy, Elsevier/Academic Press, 2012, pp. 185–207.

- [71] M. Q. Wang and H. B. Gooi, “Spinning Reserve Estimation in Microgrids,” *IEEE Trans. Power Syst.*, vol. 26, no. 3, pp. 1164–1174, Aug. 2011.
- [72] S. X. Chen, H. B. Gooi, and M. Q. Wang, “Sizing of Energy Storage for Microgrids,” *IEEE Trans. Smart Grid*, vol. 3, no. 1, pp. 142–151, Mar. 2012.
- [73] M. Z. Kamh and R. Iravani, “Unbalanced Model and Power-Flow Analysis of Microgrids and Active Distribution Systems,” *IEEE Trans. Power Deliv.*, vol. 25, no. 4, pp. 2851–2858, Oct. 2010.
- [74] C. A. Hernandez-Aramburo, T. C. Green, and N. Mugniot, “Fuel Consumption Minimization of a Microgrid,” *IEEE Trans. Ind. Appl.*, vol. 41, no. 3, pp. 673–681, May 2005.
- [75] Y. Uno, G. Fujita, R. Yokoyama, M. Matubara, T. Toyoshima, and T. Tsukui, “Evaluation of Micro-grid Supply and Demand Stability for Different Interconnections,” in *2006 IEEE International Power and Energy Conference*, 2006, pp. 612–617.
- [76] J. Zhou, Z. Qi, Y. Zhao, and W. Ye, “Study of the active power exchanging between dynamic voltage restorer and the distribution power system,” in *2009 International Conference on Applied Superconductivity and Electromagnetic Devices*, 2009, pp. 171–175.
- [77] O. Vodyakho, C. S. Edrington, M. Steurer, S. Azongha, and F. Fleming, “Synchronization of three-phase converters and virtual microgrid implementation utilizing the Power-Hardware-in-the-Loop concept,” in *2010 Twenty-Fifth Annual IEEE Applied Power Electronics Conference and Exposition (APEC)*, 2010, pp. 216–222.
- [78] N. J. Gil and J. a. P. Lopez, “Exploiting Automated Demand Response, Generation and Storage Capabilities for Hierarchical Frequency Control in Islanded Multi-Microgrids,” *Proc. PSCC2008, 16th Power Syst. Comput. Conf.*, pp. 1–7, 2008.
- [79] Y. Zoka, H. Sasaki, N. Yorino, K. Kawahara, and C. C. Liu, “An interaction problem of distributed generators installed in a MicroGrid,” in *2004 IEEE International Conference on Electric Utility Deregulation, Restructuring and Power*

Technologies, 2004, pp. 795–799.

- [80] M. Wolter, H. Guercke, T. Isermann, and L. Hofmann, “Multi-agent based distributed power flow calculation,” in *IEEE PES General Meeting*, 2010, pp. 1–6.
- [81] W. K. A. Najy, H. H. Zeineldin, and W. L. Woon, “Optimal Protection Coordination for Microgrids With Grid-Connected and Islanded Capability,” *IEEE Trans. Ind. Electron.*, vol. 60, no. 4, pp. 1668–1677, Apr. 2013.
- [82] Xiaoxiao Yu and A. M. Khambadkone, “Multi-functional power converter building block to facilitate the connection of micro-grid,” in *2008 11th Workshop on Control and Modeling for Power Electronics*, 2008, pp. 1–6.
- [83] M. B. Delghavi and A. Yazdani, “A Unified Control Strategy for Electronically Interfaced Distributed Energy Resources,” *IEEE Trans. Power Deliv.*, vol. 27, no. 2, pp. 803–812, Apr. 2012.
- [84] T. L. Vandoorn, B. Meersman, L. Degroote, B. Renders, and L. Vandeveldel, “A Control Strategy for Islanded Microgrids With DC-Link Voltage Control,” *IEEE Trans. Power Deliv.*, vol. 26, no. 2, pp. 703–713, Apr. 2011.
- [85] H. Farhangi, “Intelligent Micro Grid research at BCIT,” *2008 IEEE Electr. Power Energy Conf. - Energy Innov.*, 2008.
- [86] F. Katiraei and M. R. Iravani, “Power Management Strategies for a Microgrid With Multiple Distributed Generation Units,” *IEEE Trans. Power Syst.*, vol. 21, no. 4, pp. 1821–1831, Nov. 2006.
- [87] M. Prodanovic and T. C. Green, “High-Quality Power Generation Through Distributed Control of a Power Park Microgrid,” *IEEE Trans. Ind. Electron.*, vol. 53, no. 5, pp. 1471–1482, Oct. 2006.
- [88] Y. Zhao and L. Guo, “Dynamical Simulation of Laboratory MicroGrid,” in *2009 Asia-Pacific Power and Energy Engineering Conference*, 2009, pp. 1–5.
- [89] H. Zhou, T. Bhattacharya, D. Tran, T. S. T. Siew, and A. M. Khambadkone, “Composite Energy Storage System Involving Battery and Ultracapacitor With Dynamic Energy Management in Microgrid Applications,” *IEEE Trans. Power Electron.*, vol. 26, no. 3, pp. 923–930, Mar. 2011.
- [90] B. Brown, P.E., and S. D. E. Services, “AC Motors, motor control and motor protection,” pp. 1–25.

- [91] D. M. Vilathgamuwa, P. C. Loh, and Y. Li, "Protection of Microgrids During Utility Voltage Sags," *IEEE Trans. Ind. Electron.*, vol. 53, no. 5, pp. 1427–1436, Oct. 2006.
- [92] J. McDonald, "Adaptive intelligent power systems: Active distribution networks," *Energy Policy*, vol. 36, no. 12, pp. 4346–4351, Dec. 2008.
- [93] M. Fazeli, G. M. Asher, C. Klumpner, and L. Yao, "Novel Integration of DFIG-Based Wind Generators Within Microgrids," *IEEE Trans. Energy Convers.*, vol. 26, no. 3, pp. 840–850, Sep. 2011.
- [94] D. Lee, J. Park, H. Shin, Y. Choi, H. Lee, and J. Choi, "Microgrid village design with renewable energy resources and its economic feasibility evaluation," in *2009 Transmission & Distribution Conference & Exposition: Asia and Pacific*, 2009, pp. 1–4.
- [95] R. Pawelek, I. Wasiak, P. Gburczyk, and R. Mienski, "Study on operation of energy storage in electrical power microgrid - Modeling and simulation," in *Proceedings of 14th International Conference on Harmonics and Quality of Power - ICHQP 2010*, 2010, pp. 1–5.
- [96] Peng Li, P. Degobert, B. Robyns, and B. Francois, "Implementation of interactivity across a resilient microgrid for power supply and exchange with an active distribution network," in *CIREN Seminar 2008: SmartGrids for Distribution*, 2008, pp. 81–81.
- [97] R. Aghatehrani and R. Kavasseri, "Reactive Power Management of a DFIG Wind System in Microgrids Based on Voltage Sensitivity Analysis," *IEEE Trans. Sustain. Energy*, vol. 2, no. 4, pp. 451–458, Oct. 2011.
- [98] N. Research, "Microgrid Deployment Tracker 2Q11," 2014. [Online]. Available: <https://www.navigantresearch.com/>. [Accessed: 23-Oct-2018].
- [99] P. Asmus and M. Lawrence, "Emerging Microgrid Business Models," *Navigant*, p. 14, 2016.
- [100] D. K. Nichols, J. Stevens, R. H. Lasseter, J. H. Eto, and H. T. Vollkommer, "Validation of the CERTS microgrid concept the CEC/CERTS microgrid testbed," *2006 IEEE Power Eng. Soc. Gen. Meet.*, pp. 1–3, 2006.
- [101] B. Kroposki, R. Lasseter, T. Ise, S. Morozumi, S. Papathanassiou, and N. Hatziargyriou, "Making microgrids work," *IEEE Power Energy Mag.*, vol. 6, no. 3,

pp. 40–53, May 2008.

- [102] I. Mitra, T. Degner, and M. Braun, “Distributed Generation and Microgrids for Small Island Electrification in Developing Countries : A Review,” *Sol. Energy Soc. India*, vol. 18, no. 1, pp. 6–20, 2008.
- [103] M. Barnes *et al.*, “Microgrid laboratory facilities,” in *2005 International Conference on Future Power Systems*, 2005, pp. 1–6.
- [104] N. W. A. Lidula and A. D. Rajapakse, “Microgrids research: A review of experimental microgrids and test systems,” *Renew. Sustain. Energy Rev.*, vol. 15, no. 1, pp. 186–202, Jan. 2011.
- [105] T. S. Ustun, C. Ozansoy, and A. Zayegh, “Recent developments in microgrids and example cases around the world—A review,” *Renew. Sustain. Energy Rev.*, vol. 15, no. 8, pp. 4030–4041, Oct. 2011.
- [106] N. Hatziargyriou, H. Asanob, R. Iravanic, and C. Marnayd, “An Overview of Ongoing Research, Development, and Demonstration Projects Microgrids,” *IEEE Power and Energy Magazine*, pp. 78–94, 2007.
- [107] D. Georgakis, S. Papathanassiou, N. Hatziargyriou, A. Engler, and C. Hardt, “Operation of a prototype microgrid system based on micro-sources equipped with fast-acting power electronics interfaces,” in *2004 IEEE 35th Annual Power Electronics Specialists Conference (IEEE Cat. No.04CH37551)*, pp. 2521–2526.
- [108] N. D. Hatziargyriou *et al.*, “Microgrids - Large scale integration of microgeneration to low voltage grids,” *CIGRE*, 2006.
- [109] F. Katiraei, R. Iravani, N. Hatziargyriou, and A. Dimeas, “Microgrids management,” *IEEE Power Energy Mag.*, vol. 6, no. 3, pp. 54–65, May 2008.
- [110] M. Soshinskaya, W. H. J. Crijns-Graus, J. M. Guerrero, and J. C. Vasquez, “Microgrids: Experiences, barriers and success factors,” *Renew. Sustain. Energy Rev.*, vol. 40, pp. 659–672, Dec. 2014.
- [111] M. G. Molina, “Emerging advanced energy storage systems: dynamic modeling, control and simulation,” in *1st Ed., Nova Science Pub., Hauppauge , New York , USA*, 2013.
- [112] D. E. Olivares *et al.*, “Trends in Microgrid Control,” *IEEE Trans. Smart Grid*, vol. 5, no. 4, pp. 1905–1919, Jul. 2014.

- [113] “Consultant report: Integration of distributed energy resources. The CERTS MicroGrid concept,” in *California Energy Commission*, 2013.
- [114] C. Wang, *Theoretical analysis and simulation Microgrid*. 2013.
- [115] H. Gabbar, *Smart Energy Grid Engineering*. Elsevier Inc., 2016.
- [116] E. Planas, J. Andreu, J. I. Gárate, I. Martínez de Alegría, and E. Ibarra, “AC and DC technology in microgrids: A review,” *Renew. Sustain. Energy Rev.*, vol. 43, pp. 726–749, Mar. 2015.
- [117] E. Unamuno and J. A. Barrena, “Hybrid ac/dc microgrids—Part I: Review and classification of topologies,” *Renew. Sustain. Energy Rev.*, vol. 52, pp. 1251–1259, Dec. 2015.
- [118] E. Vartiainen, “A new approach to estimating the diffuse irradiance on inclined surfaces,” *Renew. Energy*, vol. 20, no. 1, pp. 45–64, May 2000.
- [119] S. Roy, “Optimal Planning for Utility Generation by Photovoltaic Sources Spread Across Multiple Sites,” *IEEE Trans. Energy Convers.*, vol. 21, no. 1, pp. 181–186, Mar. 2006.
- [120] N. Kawasaki, T. Oozeki, K. Otani, and K. Kurokawa, “An evaluation method of the fluctuation characteristics of photovoltaic systems by using frequency analysis,” *Sol. Energy Mater. Sol. Cells*, vol. 90, no. 18–19, pp. 3356–3363, Nov. 2006.
- [121] A. Woyte, R. Belmans, and J. Nijs, “Fluctuations in instantaneous clearness index: Analysis and statistics,” *Sol. Energy*, vol. 81, no. 2, pp. 195–206, Feb. 2007.
- [122] J. S. G. Ehnberg and M. H. J. Bollen, “Simulation of global solar radiation based on cloud observations,” *Sol. Energy*, vol. 78, no. 2, pp. 157–162, Feb. 2005.
- [123] F. Vignola, P. Harlan, R. Perez, and M. Kmiecik, “Analysis of satellite derived beam and global solar radiation data,” *Sol. Energy*, vol. 81, no. 6, pp. 768–772, Jun. 2007.
- [124] J. Polo, L. F. Zarzalejo, L. Ramirez, and B. Espinar, “Iterative filtering of ground data for qualifying statistical models for solar irradiance estimation from satellite data,” *Sol. Energy*, vol. 80, no. 3, pp. 240–247, Mar. 2006.
- [125] A. Mellit, M. Benghanem, and M. Bendekhis, “Artificial neural network model for prediction solar radiation data: application for sizing stand-alone photovoltaic power system,” in *IEEE Power Engineering Society General Meeting, 2005*, pp. 2187–2191.

- [126] A. Moreno-Munoz, J. J. G. de la Rosa, R. Posadillo, and V. Pallares, "Short term forecasting of solar radiation," in *2008 IEEE International Symposium on Industrial Electronics*, 2008, pp. 1537–1541.
- [127] D. M. Chapin, C. S. Fuller, and G. L. Pearson, "A New Silicon p - n Junction Photocell for Converting Solar Radiation into Electrical Power," *J. Appl. Phys.*, vol. 25, no. 5, pp. 676–677, May 1954.
- [128] W. T. Rhodes *et al.*, Eds., *Photovoltaic Solar Energy Generation*, vol. 112. Berlin/Heidelberg: Springer-Verlag, 2005.
- [129] A. J. Breeze, "Next generation thin-film solar cells," in *2008 IEEE International Reliability Physics Symposium*, 2008, pp. 168–171.
- [130] J. Szlufcik, S. Sivoththaman, J. F. Nlis, R. P. Mertens, and R. Van Overstraeten, "Low-cost industrial technologies of crystalline silicon solar cells," *Proc. IEEE*, vol. 85, no. 5, pp. 711–730, May 1997.
- [131] J. W. Bishop, "Computer simulation of the effects of electrical mismatches in photovoltaic cell interconnection circuits," *Sol. Cells*, vol. 25, no. 1, pp. 73–89, Oct. 1988.
- [132] G. Walker, "Evaluating MPPT converter topologies using a MATLAB PV model," *J. Electr. Electron. Eng. Aust.*, vol. 21, no. 1, pp. 49–56, 2001.
- [133] J. A. Gow and C. D. Manning, "Development of a photovoltaic array model for use in power-electronics simulation studies," *IEE Proc. - Electr. Power Appl.*, vol. 146, no. 2, pp. 193–200, 1999.
- [134] M. A. Green, *Solar cells : operating principles, technology, and system applications*. University of New South Wales, 1992.
- [135] W. De Soto, S. A. Klein, and W. A. Beckman, "Improvement and validation of a model for photovoltaic array performance," *Sol. Energy*, vol. 80, no. 1, pp. 78–88, Jan. 2006.
- [136] Weidong Xiao, W. G. Dunford, and A. Capel, "A novel modeling method for photovoltaic cells," in *2004 IEEE 35th Annual Power Electronics Specialists Conference (IEEE Cat. No.04CH37551)*, pp. 1950–1956.
- [137] E. E. van Dyk and E. L. Meyer, "Analysis of the effect of parasitic resistances on the performance of photovoltaic modules," *Renew. Energy*, vol. 29, no. 3, pp. 333–

344, Mar. 2004.

- [138] J. A. Gow and C. D. Manning, "Development of a photovoltaic array model for use in power-electronics simulation studies," *IEE Proc. - Electr. Power Appl.*, vol. 146, no. 2, p. 193, 1999.
- [139] Shengyi Liu and R. A. Dougal, "Dynamic multiphysics model for solar array," *IEEE Trans. Energy Convers.*, vol. 17, no. 2, pp. 285–294, Jun. 2002.
- [140] M. AbdulHadi, A. M. Al-Ibrahim, and G. S. Virk, "Neuro-Fuzzy-Based Solar Cell Model," *IEEE Trans. Energy Convers.*, vol. 19, no. 3, pp. 619–624, Sep. 2004.
- [141] W. Xiao, M. G. J. Lind, W. G. Dunford, and A. Capel, "Real-Time Identification of Optimal Operating Points in Photovoltaic Power Systems," *IEEE Trans. Ind. Electron.*, vol. 53, no. 4, pp. 1017–1026, Jun. 2006.
- [142] M. E. Ropp, M. Begovic, and A. Rohatgi, "Determination of the curvature derating factor for the Georgia Tech Aquatic Center photovoltaic array," in *Conference Record of the Twenty Sixth IEEE Photovoltaic Specialists Conference - 1997*, pp. 1297–1300.
- [143] M. Veerachary and H. Khas, "PSIM circuit-oriented simulator model for the nonlinear photovoltaic sources," *IEEE Trans. Aerosp. Electron. Syst.*, vol. 42, no. 2, pp. 735–740, Apr. 2006.
- [144] J. V. Paatero and P. D. Lund, "Effects of large-scale photovoltaic power integration on electricity distribution networks," *Renew. Energy*, vol. 32, no. 2, pp. 216–234, Feb. 2007.
- [145] S. B. Kjaer, J. K. Pedersen, and F. Blaabjerg, "A Review of Single-Phase Grid-Connected Inverters for Photovoltaic Modules," *IEEE Trans. Ind. Appl.*, vol. 41, no. 5, pp. 1292–1306, Sep. 2005.
- [146] B. M. T. Ho, H. S. H. Chung, and S. Y. R. Hui, "An integrated inverter with maximum power tracking for grid-connected PV systems," in *Nineteenth Annual IEEE Applied Power Electronics Conference and Exposition, 2004. APEC '04.*, vol. 3, pp. 1559–1565.
- [147] C. Cecati, A. Dell'Aquila, and M. Liserre, "A Novel Three-Phase Single-Stage Distributed Power Inverter," *IEEE Trans. Power Electron.*, vol. 19, no. 5, pp. 1226–1233, Sep. 2004.

- [148] G. R. Walker and P. C. Sernia, "Cascaded DC–DC Converter Connection of Photovoltaic Modules," *IEEE Trans. Power Electron.*, vol. 19, no. 4, pp. 1130–1139, Jul. 2004.
- [149] Y. Xue, L. Chang, S. B. Kjaer, J. Bordonau, and T. Shimizu, "Topologies of Single-Phase Inverters for Small Distributed Power Generators: An Overview," *IEEE Trans. Power Electron.*, vol. 19, no. 5, pp. 1305–1314, Sep. 2004.
- [150] N. Mutoh, M. Ohno, and T. Inoue, "A Method for MPPT Control While Searching for Parameters Corresponding to Weather Conditions for PV Generation Systems," *IEEE Trans. Ind. Electron.*, vol. 53, no. 4, pp. 1055–1065, Jun. 2006.
- [151] J.-H. Park, J.-Y. Ahn, B.-H. Cho, and G.-J. Yu, "Dual-Module-Based Maximum Power Point Tracking Control of Photovoltaic Systems," *IEEE Trans. Ind. Electron.*, vol. 53, no. 4, pp. 1036–1047, Jun. 2006.
- [152] N. Femia, G. Petrone, G. Spagnuolo, and M. Vitelli, "Optimization of Perturb and Observe Maximum Power Point Tracking Method," *IEEE Trans. Power Electron.*, vol. 20, no. 4, pp. 963–973, Jul. 2005.
- [153] T. Esmam and P. L. Chapman, "Comparison of Photovoltaic Array Maximum Power Point Tracking Techniques," *IEEE Trans. Energy Convers.*, vol. 22, no. 2, pp. 439–449, Jun. 2007.
- [154] S. Busquets-Monge, J. Rocabert, P. Rodriguez, S. Alepuz, and J. Bordonau, "Multilevel Diode-Clamped Converter for Photovoltaic Generators With Independent Voltage Control of Each Solar Array," *IEEE Trans. Ind. Electron.*, vol. 55, no. 7, pp. 2713–2723, Jul. 2008.
- [155] K. Kobayashi, I. Takano, and Y. Sawada, "A study on a two stage maximum power point tracking control of a photovoltaic system under partially shaded insolation conditions," in *2003 IEEE Power Engineering Society General Meeting (IEEE Cat. No.03CH37491)*, pp. 2612–2617.
- [156] T. Shimizu, M. Hirakata, T. Kamezawa, and H. Watanabe, "Generation control circuit for photovoltaic modules," *IEEE Trans. Power Electron.*, vol. 16, no. 3, pp. 293–300, May 2001.
- [157] B. Blazic and I. Papic, "Advanced control of a converter used for connection of photovoltaic modules," in *2006 IEEE Power Engineering Society General Meeting*,

2006, p. 6 pp.

- [158] J.-M. Kwon, K.-H. Nam, and B.-H. Kwon, "Photovoltaic Power Conditioning System With Line Connection," *IEEE Trans. Ind. Electron.*, vol. 53, no. 4, pp. 1048–1054, Jun. 2006.
- [159] F. Blaabjerg, R. Teodorescu, M. Liserre, and A. V. Timbus, "Overview of Control and Grid Synchronization for Distributed Power Generation Systems," *IEEE Trans. Ind. Electron.*, vol. 53, no. 5, pp. 1398–1409, Oct. 2006.
- [160] on F. C. IEEE Standards Coordinating Committee 21, Institute of Electrical and Electronics Engineers., and IEEE-SA Standards Board., *IEEE recommended practice for utility interface of photovoltaic (PV) systems*. Institute of Electrical and Electronics Engineers, 2000.
- [161] L. A. C. Lopes and Y. Zhang, "Islanding Detection Assessment of Multi-Inverter Systems With Active Frequency Drifting Methods," *IEEE Trans. Power Deliv.*, vol. 23, no. 1, pp. 480–486, Jan. 2008.
- [162] A. Woyte, R. Belmans, and J. Nijs, "Testing the islanding protection function of photovoltaic inverters," *IEEE Trans. Energy Convers.*, vol. 18, no. 1, pp. 157–162, Mar. 2003.
- [163] L. A. C. Lopes and H. Sun, "Performance Assessment of Active Frequency Drifting Islanding Detection Methods," *IEEE Trans. Energy Convers.*, vol. 21, no. 1, pp. 171–180, Mar. 2006.
- [164] M. E. Ropp, M. Begovic, A. Rohatgi, G. A. Kern, R. H. Bonn, and S. Gonzalez, "Determining the relative effectiveness of islanding detection methods using phase criteria and nondetection zones," *IEEE Trans. Energy Convers.*, vol. 15, no. 3, pp. 290–296, 2000.
- [165] S. Alepuz, S. Busquets-Monge, J. Bordonau, J. Gago, D. Gonzalez, and J. Balcells, "Interfacing Renewable Energy Sources to the Utility Grid Using a Three-Level Inverter," *IEEE Trans. Ind. Electron.*, vol. 53, no. 5, pp. 1504–1511, Oct. 2006.
- [166] T.-F. Wu, C.-H. Chang, and Y.-K. Chen, "A multi-function photovoltaic power supply system with grid-connection and power factor correction features," in *2000 IEEE 31st Annual Power Electronics Specialists Conference. Conference Proceedings (Cat. No.00CH37018)*, vol. 3, pp. 1185–1190.

- [167] M. I. Marei, E. F. El-Saadany, and M. M. A. Salama, "A Novel Control Algorithm for the DG Interface to Mitigate Power Quality Problems," *IEEE Trans. Power Deliv.*, vol. 19, no. 3, pp. 1384–1392, Jul. 2004.
- [168] Wu Libo, Zhao Zhengming, and Liu Jianzheng, "A Single-Stage Three-Phase Grid-Connected Photovoltaic System With Modified MPPT Method and Reactive Power Compensation," *IEEE Trans. Energy Convers.*, vol. 22, no. 4, pp. 881–886, Dec. 2007.
- [169] C. V. Nayar, M. Ashari, and W. W. L. Keerthipala, "A grid-interactive photovoltaic uninterruptible power supply system using battery storage and a back up diesel generator," *IEEE Trans. Energy Convers.*, vol. 15, no. 3, pp. 348–353, 2000.
- [170] J. M. Carrasco *et al.*, "Power-Electronic Systems for the Grid Integration of Renewable Energy Sources: A Survey," *IEEE Trans. Ind. Electron.*, vol. 53, no. 4, pp. 1002–1016, Jun. 2006.
- [171] A. Pregelj, M. Begovic, and A. Rohatgi, "Impact of inverter configuration on PV system reliability and energy production," in *Conference Record of the Twenty-Ninth IEEE Photovoltaic Specialists Conference, 2002.*, pp. 1388–1391.
- [172] M. Calais, J. Myrzik, T. Spooner, and V. G. Agelidis, "Inverters for single-phase grid connected photovoltaic systems-an overview," in *2002 IEEE 33rd Annual IEEE Power Electronics Specialists Conference. Proceedings (Cat. No.02CH37289)*, vol. 4, pp. 1995–2000.
- [173] J. M. A. Myrzik and M. Calais, "String and module integrated inverters for single-phase grid connected photovoltaic systems - a review," in *2003 IEEE Bologna Power Tech Conference Proceedings*, vol. 2, pp. 430–437.
- [174] Hui Zhang, Hongwei Zhou, Jing Ren, Weizeng Liu, Shaohua Ruan, and Yongjun Gao, "Three-phase grid-connected photovoltaic system with SVPWM current controller," in *2009 IEEE 6th International Power Electronics and Motion Control Conference, 2009*, pp. 2161–2164.
- [175] R. Teodorescu, M. Liserre, and P. Rodríguez, *Grid Converters for Photovoltaic and Wind Power Systems*. Piscataway, NJ: IEEE Press/Wiley, 2011.
- [176] J. M. Carrasco *et al.*, "Power-Electronic Systems for the Grid Integration of Renewable Energy Sources: A Survey," *IEEE Trans. Ind. Electron.*, vol. 53, no. 4,

- pp. 1002–1016, Jun. 2006.
- [177] I. E. Agency, “PVPS Report Snapshot of Global PV 1992-2013,” pp. 1–16, 2014.
- [178] H. AbdEl-Gawad and V. K. Sood, “Overview of connection topologies for grid-connected PV systems,” in *2014 IEEE 27th Canadian Conference on Electrical and Computer Engineering (CCECE)*, 2014, pp. 1–8.
- [179] B. J. Pierquet and D. J. Perreault, “A Single-Phase Photovoltaic Inverter Topology With a Series-Connected Energy Buffer,” *IEEE Trans. Power Electron.*, vol. 28, no. 10, pp. 4603–4611, Oct. 2013.
- [180] K. N. V. Prasad, N. Chellamma, S. S. Dash, A. M. Krishna, and Y. S. A. Kumar, “Comparison of photo voltaic array based different topologies of cascaded H-bridge multilevel inverter,” in *International Conference on Sustainable Energy and Intelligent Systems (SEISCON 2011)*, 2011, pp. 110–115.
- [181] F. B. Zia, K. M. Salim, N. B. Yousuf, R. Haider, and M. R. Alam, “Design and Implementation of a Single Phase Grid Tie Photo Voltaic Inverter,” in *2nd International Conference on the Developments in Renewable Energy Technology (ICDRET 2012)*, 2012, pp. 1–4.
- [182] C. R. Bush and B. Wang, “A Single-Phase Current Source Solar Inverter with Reduced-Size DC Link,” in *IEEE Energy Conversion Congress and Exposition*, 2009, pp. 54–59.
- [183] S. B. Kjaer, J. K. Pedersen, and F. Blaabjerg, “Power inverter topologies for photovoltaic modules-a review,” in *Conference Record of the 2002 IEEE Industry Applications Conference. 37th IAS Annual Meeting (Cat. No.02CH37344)*, 2002, vol. 2, pp. 782–788.
- [184] T. Shimizu, K. Wada, and N. Nakamura, “Flyback-Type Single-Phase Utility Interactive Inverter With Power Pulsation Decoupling on the DC Input for an AC Photovoltaic Module System,” *IEEE Trans. Power Electron.*, vol. 21, no. 5, pp. 1264–1272, Sep. 2006.
- [185] R. Gonzalez, J. Lopez, P. Sanchis, and L. Marroyo, “Transformerless Inverter for Single-Phase Photovoltaic Systems,” *IEEE Trans. Power Electron.*, vol. 22, no. 2, pp. 693–697, Mar. 2007.
- [186] B. Gu, J. Dominic, J.-S. Lai, C.-L. Chen, T. LaBella, and B. Chen, “High Reliability

- and Efficiency Single-Phase Transformerless Inverter for Grid-Connected Photovoltaic Systems,” *IEEE Trans. Power Electron.*, vol. 28, no. 5, pp. 2235–2245, May 2013.
- [187] S. V. Araujo, P. Zacharias, and R. Mallwitz, “Highly Efficient Single-Phase Transformerless Inverters for Grid-Connected Photovoltaic Systems,” *IEEE Trans. Ind. Electron.*, vol. 57, no. 9, pp. 3118–3128, Sep. 2010.
- [188] J. Lakwal and M. Dubey, “Modeling and simulation of a novel multilevel inverter for PV systems using unequal DC sources,” in *2014 IEEE International Conference on Advanced Communications, Control and Computing Technologies*, 2014, pp. 296–300.
- [189] Y. Chen and K. Smedley, “Three-Phase Boost-Type Grid-Connected Inverter,” *IEEE Trans. Power Electron.*, vol. 23, no. 5, pp. 2301–2309, Sep. 2008.
- [190] C.-M. Wang, “A Novel Single-Stage Full-Bridge Buck-Boost Inverter,” *IEEE Trans. Power Electron.*, vol. 19, no. 1, pp. 150–159, Jan. 2004.
- [191] L. Chen, A. Amirahmadi, Q. Zhang, N. Kutkut, and I. Batarseh, “Design and Implementation of Three-Phase Two-Stage Grid-Connected Module Integrated Converter,” *IEEE Trans. Power Electron.*, vol. 29, no. 8, pp. 3881–3892, Aug. 2014.
- [192] R. A. Mastromauro, M. Liserre, T. Kerekes, and A. Dell’Aquila, “A Single-Phase Voltage-Controlled Grid-Connected Photovoltaic System With Power Quality Conditioner Functionality,” *IEEE Trans. Ind. Electron.*, vol. 56, no. 11, pp. 4436–4444, Nov. 2009.
- [193] “Products - Overview | SMA Solar.” [Online]. Available: <https://www.sma.de/en/products/overview.html>. [Accessed: 09-Oct-2018].
- [194] “ABB,” 2013. [Online]. Available: <http://www.abb.com/product/seitp322/df4308429896b1a3c1257c8a0054355c.aspx>.
- [195] L. Feitknecht, *100-days electricity from the sun*. 2013.
- [196] M. Liserre, T. Sauter, and J. Hung, “Future Energy Systems: Integrating Renewable Energy Sources into the Smart Power Grid Through Industrial Electronics,” *IEEE Ind. Electron. Mag.*, vol. 4, no. 1, pp. 18–37, Mar. 2010.
- [197] T. Kerekes, R. Teodorescu, and M. Liserre, “Common mode voltage in case of transformerless PV inverters connected to the grid,” in *2008 IEEE International*

Symposium on Industrial Electronics, 2008, pp. 2390–2395.

- [198] A. Yafaoui, B. Wu, and S. Kouro, “Improved Active Frequency Drift Anti-islanding Detection Method for Grid Connected Photovoltaic Systems,” *IEEE Trans. Power Electron.*, vol. 27, no. 5, pp. 2367–2375, May 2012.
- [199] “IEEE 1547-2003 - IEEE Standard for Interconnecting Distributed Resources with Electric Power Systems.” [Online]. Available: <https://standards.ieee.org/standard/1547-2003.html>. [Accessed: 09-Oct-2018].
- [200] A. for E. E. & I. T. (VDE), “Power generation systems connected to the low-voltage distribution network: Technical minimum requirements for the connection to and parallel operation with low-voltage distribution networks,” 2011.
- [201] “First solar Sarnia PV power plant, Ontario, Canada.” [Online]. Available: http://www.solaripedia.com/13/303/3431/sarnia_solar_farm_photovoltaics.html. [Accessed: 19-Dec-2013].
- [202] S. Kouro, B. Wu, H. Abu-Rub, and F. Blaabjerg, “Photovoltaic Energy Conversion Systems,” in *Power Electronics for Renewable Energy Systems, Transportation and Industrial Applications*, Chichester, UK: John Wiley & Sons, Ltd, 2014, pp. 160–198.
- [203] F. Blaabjerg, Z. Chen, and S. B. Kjaer, “Power Electronics as Efficient Interface in Dispersed Power Generation Systems,” *IEEE Trans. Power Electron.*, vol. 19, no. 5, pp. 1184–1194, Sep. 2004.
- [204] R. Carbone and A. Tomaselli, “Recent advances on AC PV-modules for grid-connected PV plants,” in *Proc. Int. Conf. Clean Electrical Power (ICCEP 2011)*, 2011, pp. 124–129.
- [205] M. Meinhardt and G. Cramer, “Multi-string-converter: The next step in evolution of string converter technology,” in *9th European Power Electronics and Applications Conf. (EPE 2001)*, 2001, pp. 1–9.
- [206] A. M. Pavan, S. Castellan, S. Quaia, S. Roitti, and G. Sulligoi, “Power Electronic Conditioning Systems for Industrial Photovoltaic Fields: Centralized or String Inverters?,” in *2007 International Conference on Clean Electrical Power*, 2007, pp. 208–214.
- [207] B. Burger and D. Kranzer, ““Extreme high efficiency PV-power converters,”” in

- 2009 *13th European Conference on Power Electronics and Applications*, 2009, pp. 1–13.
- [208] J. R. Dreher, F. Marangoni, L. Schuch, M. L. da S. Martins, and L. Della Flora, “Comparison of H-bridge single-phase transformerless PV string inverters,” in *2012 10th IEEE/IAS International Conference on Industry Applications*, 2012, pp. 1–8.
- [209] S. B. Kjaer, J. K. Pedersen, and F. Blaabjerg, “A Review of Single-Phase Grid-Connected Inverters for Photovoltaic Modules,” *IEEE Trans. Ind. Appl.*, vol. 41, no. 5, pp. 1292–1306, Sep. 2005.
- [210] R. Gonzalez, J. Coloma, L. Marroyo, J. Lopez, and P. Sanchis, “Single-phase inverter circuit for conditioning and converting DC electrical energy into AC electrical energy,” Eur. Patent EP 2 053 730 A1, 2009.
- [211] S. Saridakis, E. Koutroulis, and F. Blaabjerg, “Optimal Design of Modern Transformerless PV Inverter Topologies,” *IEEE Trans. Energy Convers.*, vol. 28, no. 2, pp. 394–404, Jun. 2013.
- [212] D. W. Karraker, K. P. Gokhale, and M. T. Jussila, “Inverter for solar cell array,” U.S. patent 2011/0299312 A1, 2011.
- [213] T. Urakabe, K. Fujiwara, T. Kawakami, and N. Nishio, “High efficiency power conditioner for photovoltaic power generation system,” in *The 2010 International Power Electronics Conference - ECCE ASIA -*, 2010, pp. 3236–3240.
- [214] M. Fornage, “Method and apparatus for converting direct current to alternating current,” U.S. patent 7,796,412B2, 2010.
- [215] P. Garrity, “Solar photovoltaic power conditioning unit,” U.S. patent 8,391,031B2, 2013.
- [216] V. Salas and E. Olías, “Overview of the state of technique for PV inverters used in low voltage grid-connected PV systems: Inverters below 10 kW,” *Renew. Sustain. Energy Rev.*, vol. 13, no. 6–7, pp. 1541–1550, Aug. 2009.
- [217] V. Salas and E. Olías, “Overview of the state of technique for PV inverters used in low voltage grid-connected PV systems: Inverters above 10 kW,” *Renew. Sustain. Energy Rev.*, vol. 15, no. 2, pp. 1250–1257, Feb. 2011.
- [218] A. Pregelj, M. Begovic, and A. Rohatgi, “Impact of inverter configuration on PV system reliability and energy production,” in *Conference Record of the Twenty-*

- Ninth IEEE Photovoltaic Specialists Conference, 2002.*, pp. 1388–1391.
- [219] A. Kornelakis and E. Koutroulis, “Methodology for the design optimisation and the economic analysis of grid-connected photovoltaic systems,” *IET Renew. Power Gener.*, vol. 3, no. 4, pp. 476–492, 2009.
- [220] S. V. Dhople, A. Davoudi, P. L. Chapman, and A. D. Dominguez-Garcia, “Integrating photovoltaic inverter reliability into energy yield estimation with Markov models,” in *2010 IEEE 12th Workshop on Control and Modeling for Power Electronics (COMPEL)*, 2010, pp. 1–5.
- [221] F. He, Z. Zhao, and L. Yuan, “Impact of inverter configuration on energy cost of grid-connected photovoltaic systems,” *Renew. Energy*, vol. 41, pp. 328–335, May 2012.
- [222] S. Kouro, J. I. Leon, D. Vinnikov, and L. G. Franquelo, “Grid-Connected Photovoltaic Systems: An Overview of Recent Research and Emerging PV Converter Technology,” *IEEE Ind. Electron. Mag.*, vol. 9, no. 1, pp. 47–61, Mar. 2015.
- [223] J.-S. Lai, “Power conditioning circuit topologies,” *IEEE Ind. Electron. Mag.*, vol. 3, no. 2, pp. 24–34, Jun. 2009.
- [224] G. Spagnuolo *et al.*, “Renewable Energy Operation and Conversion Schemes: A Summary of Discussions During the Seminar on Renewable Energy Systems,” *IEEE Ind. Electron. Mag.*, vol. 4, no. 1, pp. 38–51, Mar. 2010.
- [225] E. Romero-Cadaval, G. Spagnuolo, L. G. Franquelo, C. A. Ramos-Paja, T. Suntio, and W. M. Xiao, “Grid-Connected Photovoltaic Generation Plants: Components and Operation,” *IEEE Ind. Electron. Mag.*, vol. 7, no. 3, pp. 6–20, Sep. 2013.
- [226] Fang Zheng Peng, “Z-source inverter,” *IEEE Trans. Ind. Appl.*, vol. 39, no. 2, pp. 504–510, Mar. 2003.
- [227] Y. Li, J. Anderson, F. Z. Peng, and D. Liu, “Quasi-Z-Source Inverter for Photovoltaic Power Generation Systems,” in *2009 Twenty-Fourth Annual IEEE Applied Power Electronics Conference and Exposition*, 2009, pp. 918–924.
- [228] B. Ge *et al.*, “An Energy-Stored Quasi-Z-Source Inverter for Application to Photovoltaic Power System,” *IEEE Trans. Ind. Electron.*, vol. 60, no. 10, pp. 4468–4481, Oct. 2013.

- [229] O. Husev, S. Stepenko, C. Roncero-Clemente, E. Romero-Cadaval, and D. Vinnikov, "Single phase three-level quasi-z-source inverter with a new boost modulation technique," in *IECON 2012 - 38th Annual Conference on IEEE Industrial Electronics Society*, 2012, pp. 5852–5857.
- [230] N. A. Rahim and J. Selvaraj, "Multistring Five-Level Inverter With Novel PWM Control Scheme for PV Application," *IEEE Trans. Ind. Electron.*, vol. 57, no. 6, pp. 2111–2123, Jun. 2010.
- [231] N. A. Rahim, K. Chaniago, and J. Selvaraj, "Single-Phase Seven-Level Grid-Connected Inverter for Photovoltaic System," *IEEE Trans. Ind. Electron.*, vol. 58, no. 6, pp. 2435–2443, Jun. 2011.
- [232] L. Zhang, K. Sun, L. Feng, H. Wu, and Y. Xing, "A Family of Neutral Point Clamped Full-Bridge Topologies for Transformerless Photovoltaic Grid-Tied Inverters," *IEEE Trans. Power Electron.*, vol. 28, no. 2, pp. 730–739, Feb. 2013.
- [233] S. Rivera, S. Kouro, B. Wu, J. I. Leon, J. Rodriguez, and L. G. Franquelo, "Cascaded H-bridge multilevel converter multistring topology for large scale photovoltaic systems," in *2011 IEEE International Symposium on Industrial Electronics*, 2011, pp. 1837–1844.
- [234] S. Kouro, C. Fuentes, M. Perez, and J. Rodriguez, "Single DC-link cascaded H-bridge multilevel multistring photovoltaic energy conversion system with inherent balanced operation," in *IECON 2012 - 38th Annual Conference on IEEE Industrial Electronics Society*, 2012, pp. 4998–5005.
- [235] S. Rivera, B. Wu, R. Lizana, S. Kouro, M. Perez, and J. Rodriguez, "Modular multilevel converter for large-scale multistring photovoltaic energy conversion system," in *2013 IEEE Energy Conversion Congress and Exposition*, 2013, pp. 1941–1946.
- [236] J. Echeverria, S. Kouro, M. Perez, and H. Abu-rub, "Multi-modular cascaded DC-DC converter for HVDC grid connection of large-scale photovoltaic power systems," in *IECON 2013 - 39th Annual Conference of the IEEE Industrial Electronics Society*, 2013, pp. 6999–7005.
- [237] Liming Liu, Hui Li, Yaosuo Xue, and Wenxin Liu, "Decoupled Active and Reactive Power Control for Large-Scale Grid-Connected Photovoltaic Systems Using

- Cascaded Modular Multilevel Converters,” *IEEE Trans. Power Electron.*, vol. 30, no. 1, pp. 176–187, Jan. 2015.
- [238] Y. Yang, H. Li, A. Aichhorn, J. Zheng, and M. Greenleaf, “Sizing Strategy of Distributed Battery Storage System With High Penetration of Photovoltaic for Voltage Regulation and Peak Load Shaving,” *IEEE Trans. Smart Grid*, vol. 5, no. 2, pp. 982–991, Mar. 2014.
- [239] G. Wang, M. Ciobotaru, and V. G. Agelidis, “Power Smoothing of Large Solar PV Plant Using Hybrid Energy Storage,” *IEEE Trans. Sustain. Energy*, vol. 5, no. 3, pp. 834–842, Jul. 2014.
- [240] M. N. Kabir, Y. Mishra, G. Ledwich, Z. Y. Dong, and K. P. Wong, “Coordinated Control of Grid-Connected Photovoltaic Reactive Power and Battery Energy Storage Systems to Improve the Voltage Profile of a Residential Distribution Feeder,” *IEEE Trans. Ind. Informatics*, vol. 10, no. 2, pp. 967–977, May 2014.
- [241] S. Hashemi, J. Ostergaard, and G. Yang, “A Scenario-Based Approach for Energy Storage Capacity Determination in LV Grids With High PV Penetration,” *IEEE Trans. Smart Grid*, vol. 5, no. 3, pp. 1514–1522, May 2014.
- [242] “Solar Inverters | SMA Solar.” [Online]. Available: <https://www.sma.de/en/products/solarinverters.html>.
- [243] B.-I. Craciun, T. Kerekes, D. Sera, and R. Teodorescu, “Overview of recent Grid Codes for PV power integration,” in *2012 13th International Conference on Optimization of Electrical and Electronic Equipment (OPTIM)*, 2012, pp. 959–965.
- [244] Y. Yang, P. Enjeti, F. Blaabjerg, and H. Wang, “Suggested grid code modifications to ensure wide-scale adoption of photovoltaic energy in distributed power generation systems,” in *2013 IEEE Industry Applications Society Annual Meeting*, 2013, pp. 1–8.
- [245] T. LaBella and J.-S. Lai, “A hybrid resonant converter utilizing a bidirectional GaN AC switch for high-efficiency PV applications,” in *2014 IEEE Applied Power Electronics Conference and Exposition - APEC 2014*, 2014, pp. 1–8.
- [246] D. B. and J. W. K. M. Kasper, M. Ritz, “‘PV Panel-Integrated High Step-up High Efficiency Isolated GaN DC-DC Boost Converter,’ Intelec 2013; 35th International Telecommunications Energy Conference, SMART POWER AND EFFICIENCY,

- Hamburg, Germany,” 2013, pp. 1–7.
- [247] D. Vinnikov and I. Roasto, “Quasi-Z-Source-Based Isolated DC/DC Converters for Distributed Power Generation,” *IEEE Trans. Ind. Electron.*, vol. 58, no. 1, pp. 192–201, Jan. 2011.
- [248] F. Z. Peng, “Z-source networks for power conversion,” in *2008 Twenty-Third Annual IEEE Applied Power Electronics Conference and Exposition*, 2008, pp. 1258–1265.
- [249] H. Cha, F. Z. Peng, and D. Yoo, “Z-source resonant DC-DC converter for wide input voltage and load variation,” in *The 2010 International Power Electronics Conference - ECCE ASIA -*, 2010, pp. 995–1000.
- [250] C. P. Dick, F. K. Titz, and R. W. De Doncker, “A high-efficient LLC series-parallel resonant converter,” in *2010 Twenty-Fifth Annual IEEE Applied Power Electronics Conference and Exposition (APEC)*, 2010, pp. 696–701.
- [251] Z. Liang, R. Guo, J. Li, and A. Q. Huang, “A High-Efficiency PV Module-Integrated DC/DC Converter for PV Energy Harvest in FREEDM Systems,” *IEEE Trans. Power Electron.*, vol. 26, no. 3, pp. 897–909, Mar. 2011.
- [252] H.-D. Gui, Z. Zhang, X.-F. He, and Y.-F. Liu, “A high voltage-gain LLC micro-converter with high efficiency in wide input range for PV applications,” in *2014 IEEE Applied Power Electronics Conference and Exposition - APEC 2014*, 2014, pp. 637–642.
- [253] Young-Ho Kim, Soo-Cheol Shin, Jung-Hyo Lee, Yong-Chae Jung, and Chung-Yuen Won, “Soft-Switching Current-Fed Push–Pull Converter for 250-W AC Module Applications,” *IEEE Trans. Power Electron.*, vol. 29, no. 2, pp. 863–872, Feb. 2014.
- [254] J. V. Mapurunga Caracas, G. De Carvalho Farias, L. F. Moreira Teixeira, and L. A. De Souza Ribeiro, “Implementation of a High-Efficiency, High-Lifetime, and Low-Cost Converter for an Autonomous Photovoltaic Water Pumping System,” *IEEE Trans. Ind. Appl.*, vol. 50, no. 1, pp. 631–641, Jan. 2014.
- [255] J. Rabkowski, D. Pefitsis, and H. Nee, “Silicon Carbide Power Transistors: A New Era in Power Electronics Is Initiated,” *IEEE Ind. Electron. Mag.*, vol. 6, no. 2, pp. 17–26, Jun. 2012.

- [256] S. R. and B. B. O. Stalter, D. Kranzer, “Advanced solar power electronics,” *2010 22nd International Symposium on Power Semiconductor Devices & IC’s (ISPSD), Hiroshima, Japan*. Institute of Electrical and Electronics Engineers, 2010.
- [257] R. Singh and M. Pecht, “Commercial impact of silicon carbide,” *IEEE Ind. Electron. Mag.*, vol. 2, no. 3, pp. 19–31, Sep. 2008.
- [258] C. Sintamarean, F. Blaabjerg, and H. Wang, “Comprehensive evaluation on efficiency and thermal loading of associated Si and SiC based PV inverter applications,” in *IECON 2013 - 39th Annual Conference of the IEEE Industrial Electronics Society*, 2013, pp. 555–560.
- [259] M. Acanski, J. Popovic-Gerber, and J. A. Ferreira, “Comparison of Si and GaN power devices used in PV module integrated converters,” in *2011 IEEE Energy Conversion Congress and Exposition*, 2011, pp. 1217–1223.
- [260] T. Stubbe et al., “GaN Power Semiconductors for PV Inverter Applications - Opportunities and Risks,” *CIPS 2014; 8th Int. Conf. Integr. Power Electron. Syst. Nuremberg, Ger.*, pp. 1–6, 2014.
- [261] M. Kasper, D. Bortis, and J. W. Kolar, “Classification and Comparative Evaluation of PV Panel-Integrated DC–DC Converter Concepts,” *IEEE Trans. Power Electron.*, vol. 29, no. 5, pp. 2511–2526, May 2014.
- [262] P. Parikh, Y. Wu, and L. Shen, “Commercialization of high 600V GaN-on-silicon power HEMTs and diodes,” in *2013 IEEE Energytech*, 2013, pp. 1–5.
- [263] A. Guerra and J. Zhang, “GaN Power Devices for Micro Inverters,” *Power Electron. Eur.*, no. 4, pp. 28–31, 2010.
- [264] D. Casadei, G. Grandi, and C. Rossi, “Single-Phase Single-Stage Photovoltaic Generation System Based on a Ripple Correlation Control Maximum Power Point Tracking,” *IEEE Trans. Energy Convers.*, vol. 21, no. 2, pp. 562–568, Jun. 2006.
- [265] C.-L. Kuo, C.-H. Lin, H.-T. Yau, and J.-L. Chen, “Using Self-Synchronization Error Dynamics Formulation Based Controller for Maximum Photovoltaic Power Tracking in Micro-Grid Systems,” *IEEE J. Emerg. Sel. Top. Circuits Syst.*, vol. 3, no. 3, pp. 459–467, Sep. 2013.
- [266] B. Bendib, H. Belmili, and F. Krim, “A survey of the most used MPPT methods: Conventional and advanced algorithms applied for photovoltaic systems,” *Renew.*

- Sustain. Energy Rev.*, vol. 45, pp. 637–648, May 2015.
- [267] K. L. Lian, J. H. Jhang, and I. S. Tian, “A Maximum Power Point Tracking Method Based on Perturb-and-Observe Combined With Particle Swarm Optimization,” *IEEE J. Photovoltaics*, vol. 4, no. 2, pp. 626–633, Mar. 2014.
- [268] H. Ghoddami and A. Yazdani, “A Single-Stage Three-Phase Photovoltaic System With Enhanced Maximum Power Point Tracking Capability and Increased Power Rating,” *IEEE Trans. Power Deliv.*, vol. 26, no. 2, pp. 1017–1029, Apr. 2011.
- [269] E. Koutroulis and F. Blaabjerg, “A New Technique for Tracking the Global Maximum Power Point of PV Arrays Operating Under Partial-Shading Conditions,” *IEEE J. Photovoltaics*, vol. 2, no. 2, pp. 184–190, Apr. 2012.
- [270] M. Uoya and H. Koizumi, “A Calculation Method of Photovoltaic Array’s Operating Point for MPPT Evaluation Based on One-Dimensional Newton–Raphson Method,” *IEEE Trans. Ind. Appl.*, vol. 51, no. 1, pp. 567–575, Jan. 2015.
- [271] L. Zhou, Y. Chen, K. Guo, and F. Jia, “New Approach for MPPT Control of Photovoltaic System With Mutative-Scale Dual-Carrier Chaotic Search,” *IEEE Trans. Power Electron.*, vol. 26, no. 4, pp. 1038–1048, Apr. 2011.
- [272] E. Romero-Cadaval, G. Spagnuolo, L. G. Franquelo, C. A. Ramos-Paja, T. Suntio, and W. M. Xiao, “Grid-Connected Photovoltaic Generation Plants: Components and Operation,” *IEEE Ind. Electron. Mag.*, vol. 7, no. 3, pp. 6–20, Sep. 2013.
- [273] S. Jain and V. Agarwal, “Comparison of the performance of maximum power point tracking schemes applied to single-stage grid-connected photovoltaic systems,” *IET Electr. Power Appl.*, vol. 1, no. 5, p. 753, 2007.
- [274] B. Subudhi and R. Pradhan, “A Comparative Study on Maximum Power Point Tracking Techniques for Photovoltaic Power Systems,” *IEEE Trans. Sustain. Energy*, vol. 4, no. 1, pp. 89–98, Jan. 2013.
- [275] A. Barrado Bautista and A. Lázaro Blanco, *Power Electronics Problems*. Pearson Prentice Hall, 2007.
- [276] E. J. Bueno Peña, “Optimization of the behavior of a three-level NPC converter connected to the electricity grid,” University of Alcalá, 2005.
- [277] S. Buso, L. Malesani, P. Mattavelli, and A. Member, “Comparison of Current Control Techniques for Active Filter Applications,” *IEEE Trans. Ind. Electron.*, vol.

- 45, no. 5, pp. 722–729, 1998.
- [278] M. Ciobotaru, R. Teodorescu, and F. Blaabjerg, “Improved PLL structures for single-phase grid inverters,” *Proc. Power Electron. Intell. Control Energy Conserv. Conf.*, no. February, pp. 1–6, 2005.
- [279] M. P. Kazmierkowski and L. Malesani, “Current control techniques for three-phase voltage-source PWM converters: a survey,” *IEEE Trans. Ind. Electron.*, vol. 45, no. 5, pp. 691–703, 1998.
- [280] M. Ciobotaru, R. Teodorescu, and F. Blaabjerg, “Control of single-stage single-phase PV inverter,” in *2005 European Conference on Power Electronics and Applications*, 2005, pp. 10 pp.-P.10.
- [281] S. Fukuda and T. Yoda, “A novel current-tracking method for active filters based on a sinusoidal internal model [for PWM invertors],” *IEEE Trans. Ind. Appl.*, vol. 37, no. 3, pp. 888–895, 2001.
- [282] D. N. Zmood and D. G. Holmes, “Stationary frame current regulation of PWM inverters with zero steady-state error,” *IEEE Trans. Power Electron.*, vol. 18, no. 3, pp. 814–822, May 2003.
- [283] F. Blaabjerg, R. Teodorescu, M. Liserre, and A. V. Timbus, “Overview of Control and Grid Synchronization for Distributed Power Generation Systems,” *IEEE Trans. Ind. Electron.*, vol. 53, no. 5, pp. 1398–1409, Oct. 2006.
- [284] I. Agirman and V. Blasko, “A novel control method of a VCS without AC line voltage sensors,” *IEEE Trans. Ind. Appl.*, vol. 39, no. 2, pp. 519–524, Mar. 2003.
- [285] Huibin Zhu, B. Arnet, L. Haines, E. Shaffer, and Jih-Sheng Lai, “Grid synchronization control without AC voltage sensors,” in *Eighteenth Annual IEEE Applied Power Electronics Conference and Exposition, 2003. APEC '03.*, vol. 1, pp. 172–178.
- [286] L. Zhang, K. Sun, Y. Xing, L. Feng, and H. Ge, “A Modular Grid-Connected Photovoltaic Generation System Based on DC Bus,” *IEEE Trans. Power Electron.*, vol. 26, no. 2, pp. 523–531, Feb. 2011.
- [287] Z. Zeng, H. Yang, R. Zhao, and C. Cheng, “Topologies and control strategies of multi-functional grid-connected inverters for power quality enhancement: A comprehensive review,” *Renew. Sustain. Energy Rev.*, vol. 24, pp. 223–270, Aug.

2013.

- [288] M. Monfared and S. Golestan, "Control strategies for single-phase grid integration of small-scale renewable energy sources: A review," *Renew. Sustain. Energy Rev.*, vol. 16, no. 7, pp. 4982–4993, Sep. 2012.
- [289] R. Teodorescu and F. Blaabjerg, "Overview of renewable energy system, ECPE seminar renewable energy," *ISET, Kassel, Ger.*, 2006.
- [290] R. Teodorescu, F. Blaabjerg, U. Borup, and M. Liserre, "A new control structure for grid-connected LCL PV inverters with zero steady-state error and selective harmonic compensation," in *Nineteenth Annual IEEE Applied Power Electronics Conference and Exposition, 2004. APEC '04.*, vol. 1, pp. 580–586.
- [291] R. Teodorescu, F. Blaabjerg, M. Liserre, and P. C. Loh, "Proportional-resonant controllers and filters for grid-connected voltage-source converters," *IEE Proc. - Electr. Power Appl.*, vol. 153, no. 5, p. 750, 2006.
- [292] J.-Y. Chen, C.-H. Hung, J. Gilmore, J. Roesch, and W. Zhu, "LCOE reduction for megawatts PV system using efficient 500 kW transformerless inverter," in *2010 IEEE Energy Conversion Congress and Exposition*, 2010, pp. 392–397.
- [293] J. Svensson, "Synchronisation methods for grid-connected voltage source converters," *IEE Proc. - Gener. Transm. Distrib.*, vol. 148, no. 3, p. 229, 2001.
- [294] Y. C. Qin, N. Mohan, R. West, and R. Bonn, "Status and Needs of Power Electronics for Photovoltaic Inverters," 2002.
- [295] L. Hassaine, "Implementation of a Digital Control of Active and Reactive Power for Investors. Application to Photovoltaic Systems Connected to the Network," UNIVERSITY OF MADRID, 2010.
- [296] A. Pregelj, M. Begovic, and A. Rohatgi, "Impact of inverter configuration on PV system reliability and energy production," in *Conference Record of the Twenty-Ninth IEEE Photovoltaic Specialists Conference, 2002.*, pp. 1388–1391.
- [297] S.-J. Lee, H. Kim, S.-K. Sul, and F. Blaabjerg, "A Novel Control Algorithm for Static Series Compensators by Use of PQR Instantaneous Power Theory," *IEEE Trans. Power Electron.*, vol. 19, no. 3, pp. 814–827, May 2004.
- [298] Guan-Chyun Hsieh and J. C. Hung, "Phase-locked loop techniques. A survey," *IEEE Trans. Ind. Electron.*, vol. 43, no. 6, pp. 609–615, Dec. 1996.

- [299] A. Timbus, M. Liserre, R. Teodorescu, and F. Blaabjerg, “Synchronization Methods for Three Phase Distributed Power Generation Systems. An Overview and Evaluation,” in *IEEE 36th Conference on Power Electronics Specialists, 2005.*, pp. 2474–2481.
- [300] L. Hassaine, E. Olias, J. Quintero, and M. Haddadi, “Digital power factor control and reactive power regulation for grid-connected photovoltaic inverter,” *Renew. Energy*, vol. 34, no. 1, pp. 315–321, Jan. 2009.
- [301] V. Salas, E. Olías, A. Lázaro, and A. Barrado, “New algorithm using only one variable measurement applied to a maximum power point tracker,” *Sol. Energy Mater. Sol. Cells*, vol. 87, no. 1–4, pp. 675–684, May 2005.
- [302] M. A. Eltawil and Z. Zhao, “MPPT techniques for photovoltaic applications,” *Renew. Sustain. Energy Rev.*, vol. 25, pp. 793–813, Sep. 2013.
- [303] G. Tsengenes and G. Adamidis, “Investigation of the behavior of a three phase grid-connected photovoltaic system to control active and reactive power,” *Electr. Power Syst. Res.*, vol. 81, no. 1, pp. 177–184, Jan. 2011.
- [304] K. Turitsyn, P. Sulc, S. Backhaus, and M. Chertkov, “Options for Control of Reactive Power by Distributed Photovoltaic Generators,” *Proc. IEEE*, vol. 99, no. 6, pp. 1063–1073, Jun. 2011.
- [305] M. Oshiro *et al.*, “Optimal voltage control in distribution systems using PV generators,” *Int. J. Electr. Power Energy Syst.*, vol. 33, no. 3, pp. 485–492, Mar. 2011.
- [306] European Photovoltaic Industry Association (EPIA), “Annual Report 2008,” 2008.
- [307] S. B. Kjær and F. Blaabjerg, “A Novel Single-Stage Inverter for the AC-Module with Reduced Low-Frequency Ripple Penetration,” in *Proceed. of EPE’2003, Toulouse, France, 2-4 September, 2003*, p. 10.
- [308] M. S. ElNozahy and M. M. A. Salama, “Technical impacts of grid-connected photovoltaic systems on electrical networks—A review,” *J. Renew. Sustain. Energy*, vol. 5, no. 3, p. 032702, May 2013.
- [309] A. Cagnano, F. Torelli, F. Alfonzetti, and E. De Tuglie, “Can PV plants provide a reactive power ancillary service? A treat offered by an on-line controller,” *Renew. Energy*, vol. 36, no. 3, pp. 1047–1052, Mar. 2011.

- [310] R. Teodorescu and F. Blaabjerg, "Flexible Control of Small Wind Turbines With Grid Failure Detection Operating in Stand-Alone and Grid-Connected Mode," *IEEE Trans. Power Electron.*, vol. 19, no. 5, pp. 1323–1332, Sep. 2004.
- [311] E. Twining and D. G. Holmes, "Grid current regulation of a three-phase voltage source inverter with an LCL input filter," *IEEE Trans. Power Electron.*, vol. 18, no. 3, pp. 888–895, May 2003.
- [312] M. P. Kaźmierkowski, R. (Ramu) Krishnan, and F. Blaabjerg, *Control in power electronics : selected problems*. Academic Press, 2002.
- [313] M. G. Molina and P. E. Mercado, "Modeling and control of grid-connected photovoltaic energy conversion system used as a dispersed generator," in *2008 IEEE/PES Transmission and Distribution Conference and Exposition: Latin America*, 2008, pp. 1–8.
- [314] R. Gonzalez, E. Gubia, J. Lopez, and L. Marroyo, "Transformerless Single-Phase Multilevel-Based Photovoltaic Inverter," *IEEE Trans. Ind. Electron.*, vol. 55, no. 7, pp. 2694–2702, Jul. 2008.
- [315] N. A. Rahim, J. Selvaraj, and C. Krismadinata, "Five-level inverter with dual reference modulation technique for grid-connected PV system," *Renew. Energy*, vol. 35, no. 3, pp. 712–720, Mar. 2010.
- [316] S. Jain and V. Agarwal, "New current control based MPPT technique for single stage grid connected PV systems," *Energy Convers. Manag.*, vol. 48, no. 2, pp. 625–644, Feb. 2007.
- [317] N. Hamrouni, M. Jraidi, and A. Chérif, "New control strategy for 2-stage grid-connected photovoltaic power system," *Renew. Energy*, vol. 33, no. 10, pp. 2212–2221, Oct. 2008.
- [318] T. Kerekes, R. Teodorescu, M. Liserre, C. Klumpner, and M. Sumner, "Evaluation of Three-Phase Transformerless Photovoltaic Inverter Topologies," *IEEE Trans. Power Electron.*, vol. 24, no. 9, pp. 2202–2211, Sep. 2009.
- [319] J.-M. Kwon, K.-H. Nam, and B.-H. Kwon, "Photovoltaic Power Conditioning System With Line Connection," *IEEE Trans. Ind. Electron.*, vol. 53, no. 4, pp. 1048–1054, Jun. 2006.
- [320] J. Alonso-Martínez, J. Eloy-García, and S. Arnaltes, "Direct power control of grid

- connected PV systems with three level NPC inverter,” *Sol. Energy*, vol. 84, no. 7, pp. 1175–1186, Jul. 2010.
- [321] S. Mehta and J. Chiasson, “Nonlinear control of a series DC motor: theory and experiment,” *IEEE Trans. Ind. Electron.*, vol. 45, no. 1, pp. 134–141, 1998.
- [322] L. Yacoubi, K. Al-Haddad, F. Fnaiech, and L.-A. Dessaint, “A DSP-Based Implementation of a New Nonlinear Control for a Three-Phase Neutral Point Clamped Boost Rectifier Prototype,” *IEEE Trans. Ind. Electron.*, vol. 52, no. 1, pp. 197–205, Feb. 2005.
- [323] A. Ovono Zue and A. Chandra, “State feedback linearization control of a grid connected photovoltaic interface with MPPT,” in *2009 IEEE Electrical Power & Energy Conference (EPEC)*, 2009, pp. 1–6.
- [324] D. Lalili, A. Mellit, N. Lourci, B. Medjahed, and E. M. Berkouk, “Input output feedback linearization control and variable step size MPPT algorithm of a grid-connected photovoltaic inverter,” *Renew. Energy*, vol. 36, no. 12, pp. 3282–3291, Dec. 2011.
- [325] N. Mohan, T. M. Undeland, and W. P. Robbins, *Power electronics : converters, applications, and design*. John Wiley & Sons, 2003.
- [326] V. I. Utkin, “Sliding mode control design principles and applications to electric drives,” *IEEE Trans. Ind. Electron.*, vol. 40, no. 1, pp. 23–36, Feb. 1993.
- [327] P. Li and B. Lehman, “A Design Method for Paralleling Current Mode Controlled DC–DC Converters,” *IEEE Trans. Power Electron.*, vol. 19, no. 3, pp. 748–756, May 2004.
- [328] R. B. Ridley, “A new, continuous-time model for current-mode control (power convertors),” *IEEE Trans. Power Electron.*, vol. 6, no. 2, pp. 271–280, Apr. 1991.
- [329] Huing-Huei Su, Jiann-Jong Chen, and Dong-Shiuh Wu, “Learning feedback controller design of switching converters via MATLAB/SIMULINK,” *IEEE Trans. Educ.*, vol. 45, no. 4, pp. 307–315, Nov. 2002.
- [330] F. Alonge, F. D’Ippolito, and T. Cangemi, “Identification and Robust Control of DC/DC Converter Hammerstein Model,” *IEEE Trans. Power Electron.*, vol. 23, no. 6, pp. 2990–3003, Nov. 2008.
- [331] R. Naim, G. Weiss, and S. Ben-Yaakov, “ H^∞ Control Applied to Boost Power

- Converters,” *IEEE Trans. Power Electron.*, vol. 12, no. 4, pp. 677–683, Jul. 1997.
- [332] V. Vorperian, “Simplified analysis of PWM converters using model of PWM switch. II. Discontinuous conduction mode,” *IEEE Trans. Aerosp. Electron. Syst.*, vol. 26, no. 3, pp. 497–505, May 1990.
- [333] V. Vorperian, *Fast analytical techniques for electrical and electronic circuits*. Cambridge: Cambridge University Press, 2002.
- [334] M. Corina, D. Lascu, and V. Popescu, “A new averaged switch model including conduction losses for PWM converters operating in discontinuous inductor current mode,” *Facta Univ. - Ser. Electron. Energ.*, vol. 19, no. 2, pp. 219–230, 2006.
- [335] R. W. Erickson, *Fundamentals of power electronics*. Chapman & Hall, 1997.
- [336] J. G. Kassakian, M. F. Schlecht, and G. C. Verghese, *Principles of power electronics*. Addison-Wesley, 1991.
- [337] C. Sreekumar and V. Agarwal, “A Hybrid Control Algorithm for Voltage Regulation in DC–DC Boost Converter,” *IEEE Trans. Ind. Electron.*, vol. 55, no. 6, pp. 2530–2538, Jun. 2008.
- [338] K. Sundareswaran and V. T. Sreedevi, “Boost Converter Controller Design Using Queen-Bee-Assisted GA,” *IEEE Trans. Ind. Electron.*, vol. 56, no. 3, pp. 778–783, Mar. 2009.
- [339] A. J. Forsyth and S. V. Mollov, “Modelling and control of DC-DC converters,” *Power Eng. J.*, vol. 12, no. 5, pp. 229–236, Oct. 1998.
- [340] D. M. Mitchell, *DC-DC switching regulator analysis*. New York : McGraw-Hill, 1988.
- [341] A. G. Perry, Guang Feng, Yan-Fei Liu, and P. C. Sen, “A Design Method for PI-like Fuzzy Logic Controllers for DC–DC Converter,” *IEEE Trans. Ind. Electron.*, vol. 54, no. 5, pp. 2688–2696, Oct. 2007.
- [342] A. Balestrino, D. Corsanini, A. Landi, and L. Sani, “Circle-Based Criteria for Performance Evaluation of Controlled DC–DC Switching Converters,” *IEEE Trans. Ind. Electron.*, vol. 53, no. 6, pp. 1862–1869, Dec. 2006.
- [343] Jun Zhang, H. S. H. Chung, Wai-Lun Lo, S. Y. Hui, and A. K.-M. Wu, “Implementation of a decoupled optimization technique for design of switching regulators using genetic algorithms,” *IEEE Trans. Power Electron.*, vol. 16, no. 6,

pp. 752–763, 2001.

- [344] J. Y. Hung, W. Gao, and J. C. Hung, “Variable structure control: a survey,” *IEEE Trans. Ind. Electron.*, vol. 40, no. 1, pp. 2–22, 1993.
- [345] A. G. Beccuti, S. Mariethoz, S. Cliquennois, Shu Wang, and M. Morari, “Explicit Model Predictive Control of DC–DC Switched-Mode Power Supplies With Extended Kalman Filtering,” *IEEE Trans. Ind. Electron.*, vol. 56, no. 6, pp. 1864–1874, Jun. 2009.
- [346] Siew-Chong Tan, Y. M. Lai, and C. K. Tse, “General Design Issues of Sliding-Mode Controllers in DC–DC Converters,” *IEEE Trans. Ind. Electron.*, vol. 55, no. 3, pp. 1160–1174, Mar. 2008.
- [347] A. J. Forsyth, I. K. Ellis, and M. Möller, “Adaptive control of a high-frequency DC–DC converter by parameter scheduling,” *IEE Proc. - Electr. Power Appl.*, vol. 146, no. 4, p. 447, 1999.
- [348] H. Sira-Ramirez and R. Ortega, “Passivity-based controllers for the stabilization of DC-to-DC power converters,” in *Proceedings of 1995 34th IEEE Conference on Decision and Control*, vol. 4, pp. 3471–3476.
- [349] S. Hiti and D. Borojevic, “Robust nonlinear control for boost converter,” *IEEE Trans. Power Electron.*, vol. 10, no. 6, pp. 651–658, 1995.
- [350] M. DiLorenzodelCasale, N. Femia, P. Lamberti, and V. Mainardi, “Selection of Optimal Closed-Loop Controllers for DC–DC Voltage Regulators Based on Nominal and Tolerance Design,” *IEEE Trans. Ind. Electron.*, vol. 51, no. 4, pp. 840–849, Aug. 2004.
- [351] Jun Zhang, H. S.-H. Chung, A. W.-L. Lo, and Tao Huang, “Extended Ant Colony Optimization Algorithm for Power Electronic Circuit Design,” *IEEE Trans. Power Electron.*, vol. 24, no. 1, pp. 147–162, Jan. 2009.
- [352] J. Kennedy and R. Eberhart, “Particle swarm optimization,” in *Proceedings of ICNN’95 - International Conference on Neural Networks*, vol. 4, pp. 1942–1948.
- [353] J. Kennedy, “The particle swarm: social adaptation of knowledge,” in *Proceedings of 1997 IEEE International Conference on Evolutionary Computation (ICEC ’97)*, pp. 303–308.
- [354] V. Nicolau, “On PID Controller Design by Combining Pole Placement Technique

- with Symmetrical Optimum Criterion,” *Math. Probl. Eng.*, vol. 2013, pp. 1–8, 2013.
- [355] J. G. Proakis and D. G. Manolakis, *Digital signal processing*. Pearson Prentice Hall, 2007.
- [356] P. Huynh and B. H. Cho, “Design and analysis of a microprocessor-controlled peak-power-tracking system [for solar cell arrays],” *IEEE Trans. Aerosp. Electron. Syst.*, vol. 32, no. 1, pp. 182–190, Jan. 1996.
- [357] B. O. Kang and J. H. Park, “Kalman filter MPPT method for a solar inverter,” in *2011 IEEE Power and Energy Conference at Illinois*, 2011, pp. 1–5.
- [358] Fangrui Liu, Yong Kang, Yu Zhang, and Shanxu Duan, “Comparison of P&O and hill climbing MPPT methods for grid-connected PV converter,” in *2008 3rd IEEE Conference on Industrial Electronics and Applications*, 2008, pp. 804–807.
- [359] Youngseok Jung, Junghun So, Gwonjong Yu, and Jaeho Choi, “Improved perturbation and observation method (IP&O) of MPPT control for photovoltaic power systems,” in *Conference Record of the Thirty-first IEEE Photovoltaic Specialists Conference, 2005.*, 2005, pp. 1788–1791.
- [360] R. A. Messenger and J. Ventre, *Photovoltaic systems engineering*. CRC Press, 2004.
- [361] E. Koutroulis, K. Kalaitzakis, and N. C. Voulgaris, “Development of a microcontroller-based, photovoltaic maximum power point tracking control system,” *IEEE Trans. Power Electron.*, vol. 16, no. 1, pp. 46–54, 2001.
- [362] O. Lopez-Lapena, M. T. Penella, and M. Gasulla, “A Closed-Loop Maximum Power Point Tracker for Subwatt Photovoltaic Panels,” *IEEE Trans. Ind. Electron.*, vol. 59, no. 3, pp. 1588–1596, Mar. 2012.
- [363] A. Mellit, H. Rezzouk, A. Messai, and B. Medjahed, “FPGA-based real time implementation of MPPT-controller for photovoltaic systems,” *Renew. Energy*, vol. 36, no. 5, pp. 1652–1661, May 2011.
- [364] E. Koutroulis, K. Kalaitzakis, and V. Tzitzilouis, “Development of an FPGA-based system for real-time simulation of photovoltaic modules,” *Microelectronics J.*, vol. 40, no. 7, pp. 1094–1102, Jul. 2009.
- [365] H. Mekki, A. Mellit, S. A. Kalogirou, A. Messai, and G. Furlan, “FPGA-based implementation of a real time photovoltaic module simulator,” *Prog. Photovoltaics Res. Appl.*, vol. 18, no. 2, pp. 115–127, Mar. 2010.

- [366] N. Khaehintung, T. Wiangtong, and P. Sirisuk, "FPGA Implementation of MPPT Using Variable Step-Size P&O Algorithm for PV Applications," in *2006 International Symposium on Communications and Information Technologies*, 2006, pp. 212–215.
- [367] N. Chettibi, A. Mellit, and M. Drif, "FPGA-Based implementation of IncCond algorithm for photovoltaic applications," in *2012 24th International Conference on Microelectronics (ICM)*, 2012, pp. 1–4.
- [368] A. Mellit and S. A. Kalogirou, "Artificial intelligence techniques for photovoltaic applications: A review," *Prog. Energy Combust. Sci.*, vol. 34, no. 5, pp. 574–632, Oct. 2008.
- [369] Y.-H. Liu, C.-L. Liu, J.-W. Huang, and J.-H. Chen, "Neural-network-based maximum power point tracking methods for photovoltaic systems operating under fast changing environments," *Sol. Energy*, vol. 89, pp. 42–53, Mar. 2013.
- [370] T. E. PERSEN, "FPGA-based design of a maximum-power-point tracking system for space applications," University of Central Florida, 2004.
- [371] "Xilinx - Adaptable. Intelligent." [Online]. Available: <https://www.xilinx.com/>. [Accessed: 19-Mar-2019].
- [372] R. C. Cofer and B. F. Harding, *Rapid system prototyping with FPGAs*. Elsevier/Newnes, 2006.
- [373] J.-P. Deschamps, G. J. A. Bioul, and G. D. Sutter, *Synthesis of arithmetic circuits : FPGA, ASIC and embedded systems*. John Wiley, 2006.
- [374] S. Hauck and A. DeHon, *Reconfigurable computing : the theory and practice of FPGA-based computation*. Morgan Kaufmann, 2008.
- [375] "Real World Embedded Systems Magazine | produced by Intelligent Systems Source." [Online]. Available: <http://www.rtcmagazine.com/>. [Accessed: 19-Mar-2019].
- [376] P. P. Chu, *RTL hardware design using VHDL : coding for efficiency, portability, and scalability*. Wiley-Interscience, 2006.
- [377] Altera Corporation, "FPGAs for High-Performance DSP Applications," no. May 2005, pp. 1–10.
- [378] V. A. Pedroni, *Circuit design with VHDL*. MIT Press, 2004.

- [379] R. Ruelland, G. Gateau, T. A. Meynard, and J.-C. Hapiot, "Design of FPGA-based emulator for series multicell converters using co-simulation tools," *IEEE Trans. Power Electron.*, vol. 18, no. 1, pp. 455–463, Jan. 2003.
- [380] A. Papoulis and S. U. Pillai, *Probability, random variables, and stochastic processes*. McGraw-Hill, 2002.
- [381] H. L. Van Trees, *Detection, Estimation, and Modulation Theory, Part I*. New York, USA: John Wiley & Sons, Inc., 2001.
- [382] R. E. Kalman and R. S. Bucy, "New Results in Linear Filtering and Prediction Theory," *J. Basic Eng.*, vol. 83, no. 1, p. 95, Mar. 1961.
- [383] R. E. Kalman, "A New Approach to Linear Filtering and Prediction Problems," *J. Basic Eng.*, vol. 82, no. 1, p. 35, Mar. 1960.
- [384] B. Ristic and S. Arulampalam, *Beyond the Kalman filter : particle filters for tracking applications*. Artech House, 2004.
- [385] E. D. Kaplan and C. (Christopher J. . Hegarty, *Understanding GPS : principles and applications*. Artech House, 2006.
- [386] G. Strang and K. (Kai) Borre, *Linear algebra, geodesy, and GPS*. Wellesley MA: Wellesley-Cambridge Press, 1997.
- [387] A. J. Lipton, H. Fujiyoshi, and R. S. Patil, "Moving target classification and tracking from real-time video," in *Proceedings Fourth IEEE Workshop on Applications of Computer Vision. WACV'98 (Cat. No.98EX201)*, pp. 8–14.
- [388] P. Zarchan, *Tactical and Strategic Missile Guidance, Sixth Edition*. Washington, DC: American Institute of Aeronautics and Astronautics, Inc., 2012.
- [389] S. I. Roumeliotis and G. A. Bekey, "Bayesian estimation and Kalman filtering: a unified framework for mobile robot localization," in *Proceedings 2000 ICRA. Millennium Conference. IEEE International Conference on Robotics and Automation. Symposia Proceedings (Cat. No.00CH37065)*, vol. 3, pp. 2985–2992.
- [390] J. Pearson and E. Stear, "Kalman Filter Applications in Airborne Radar Tracking," *IEEE Trans. Aerosp. Electron. Syst.*, vol. AES-10, no. 3, pp. 319–329, May 1974.
- [391] R. Isermann, "Process fault detection based on modeling and estimation methods—A survey," *Automatica*, vol. 20, no. 4, pp. 387–404, Jul. 1984.
- [392] C. Ridder, O. Munkelt, and H. Kirchner, "Adaptive Background Estimation and

- Foreground Detection using Kalman-Filtering,” pp. 193--199, 1995.
- [393] L. L. Scharf and C. Demeure, *Statistical signal processing : detection, estimation, and time series analysis*. Addison-Wesley Pub. Co, 1991.
- [394] S. Gannot, D. Burshtein, and E. Weinstein, “Iterative and sequential Kalman filter-based speech enhancement algorithms,” *IEEE Trans. Speech Audio Process.*, vol. 6, no. 4, pp. 373–385, Jul. 1998.
- [395] S. Ertürk, “Real-Time Digital Image Stabilization Using Kalman Filters,” *Real-Time Imaging*, vol. 8, no. 4, pp. 317–328, Aug. 2002.
- [396] U. Kiencke and L. Nielsen, *Automotive control systems : for engine, driveline, and vehicle*. Springer, 2005.
- [397] A. C. Harvey, *Forecasting, structural time series models and the Kalman filter*. Cambridge: Cambridge University Press, 1990.
- [398] Bomhoff and E.J., “Four econometric fashions and the Kalman filter alternative : A simulation study,” *Discuss. Pap.*, 1992.
- [399] M. Manoliu and S. Tompaidis, “Energy futures prices: term structure models with Kalman filter estimation,” *Appl. Math. Financ.*, vol. 9, no. 1, pp. 21–43, Mar. 2002.
- [400] L. Ljung, *System identification : theory for the user*. Prentice Hall PTR, 1999.
- [401] S. S. Haykin, *Kalman filtering and neural networks*. Wiley, 2001.
- [402] N. Salvatore, A. Caponio, F. Neri, S. Stasi, and G. L. Cascella, “Optimization of Delayed-State Kalman-Filter-Based Algorithm via Differential Evolution for Sensorless Control of Induction Motors,” *IEEE Trans. Ind. Electron.*, vol. 57, no. 1, pp. 385–394, Jan. 2010.
- [403] K. Szabat and T. Orłowska-Kowalska, “Performance Improvement of Industrial Drives With Mechanical Elasticity Using Nonlinear Adaptive Kalman Filter,” *IEEE Trans. Ind. Electron.*, vol. 55, no. 3, pp. 1075–1084, Mar. 2008.
- [404] C. I. Chen, G. W. Chang, R. C. Hong, and H. M. Li, “Extended Real Model of Kalman Filter for Time-Varying Harmonics Estimation,” *IEEE Trans. Power Deliv.*, vol. 25, no. 1, pp. 17–26, Jan. 2010.
- [405] R. Agha Zadeh, A. Ghosh, and G. Ledwich, “Combination of Kalman Filter and Least-Error Square Techniques in Power System,” *IEEE Trans. Power Deliv.*, vol. 25, no. 4, pp. 2868–2880, Oct. 2010.

- [406] S. P. Won, W. W. Melek, and F. Golnaraghi, "A Kalman/Particle Filter-Based Position and Orientation Estimation Method Using a Position Sensor/Inertial Measurement Unit Hybrid System," *IEEE Trans. Ind. Electron.*, vol. 57, no. 5, pp. 1787–1798, May 2010.
- [407] Pinjia Zhang, Yi Du, Jing Dai, T. G. Habetler, and Bin Lu, "Impaired-Cooling-Condition Detection Using DC-Signal Injection for Soft-Starter-Connected Induction Motors," *IEEE Trans. Ind. Electron.*, vol. 56, no. 11, pp. 4642–4650, Nov. 2009.
- [408] A. G. Beccuti, S. Mariethoz, S. Cliquennois, Shu Wang, and M. Morari, "Explicit Model Predictive Control of DC–DC Switched-Mode Power Supplies With Extended Kalman Filtering," *IEEE Trans. Ind. Electron.*, vol. 56, no. 6, pp. 1864–1874, Jun. 2009.
- [409] R. E. Kalman, "A New Approach to Linear Filtering and Prediction Problems," *J. Basic Eng.*, vol. 82, no. 1, p. 35, Mar. 1960.
- [410] R. E. Kalman, "Mathematical Description of Linear Dynamical Systems," *J. Soc. Ind. Appl. Math. Ser. A Control*, vol. 1, no. 2, pp. 152–192, Jan. 1963.
- [411] M. S. Grewal and A. P. Andrews, *Kalman filtering: theory and practice using MATLAB*. Wiley, 2008.
- [412] L. A. McGee, *Discovery of the Kalman filter as a practical tool for aerospace and industry*. Moffett Field, Calif.: National Aeronautics and Space Administration, Ames Research Center, 1985.
- [413] R. Azuma and G. Bishop, "Improving static and dynamic registration in an optical see-through HMD," in *Proceedings of the 21st annual conference on Computer graphics and interactive techniques - SIGGRAPH '94*, 1994, pp. 197–204.
- [414] R. E. Kalman, "A New Approach to Linear Filtering and Prediction Problems," *J. Basic Eng.*, vol. 82, no. 1, pp. 35–45, Mar. 1960.
- [415] V. Ramchandani, K. Pamarthi, and S. R. Chowdhury, "Comparative Study Of Maximum Power Point Tracking Using Linear Kalman Filter & Unscented Kalman Filter For Solar Photovoltaic Array On Field Programmable Gate Array," *Int. J. Smart Sens. Intell. Syst.*, vol. 5, no. 3, pp. 701–716, Sep. 2012.
- [416] Chao Zhang, Dean Zhao, Jinjing Wang, and Guichang Chen, "A modified MPPT

method with variable perturbation step for photovoltaic system,” in *2009 IEEE 6th International Power Electronics and Motion Control Conference*, 2009, pp. 2096–2099.

- [417] R. G. Brown and P. Y. C. Hwang, *Introduction to random signals and applied Kalman filtering : with MATLAB exercises*. J. Wiley & Sons, 2012.

Appendix A: The SPR-305E-WHT-D Solar Panel Manufacturers' Data Sheet

SUNPOWER™

E18 / 305 SOLAR PANEL

EXCEPTIONAL EFFICIENCY AND PERFORMANCE

BENEFITS

Highest Efficiency

SunPower™ Solar Panels are the most efficient photovoltaic panels on the market today.

More Power

Our panels produce more power in the same amount of space—up to 50% more than conventional designs and 100% more than thin film solar panels.

Reduced Installation Cost

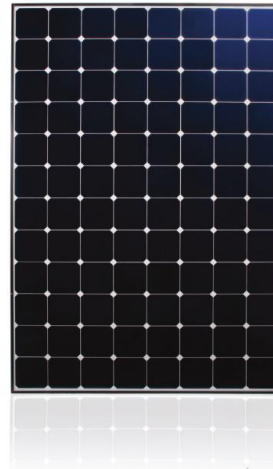
More power per panel means fewer panels per install. This saves both time and money.

Reliable and Robust Design

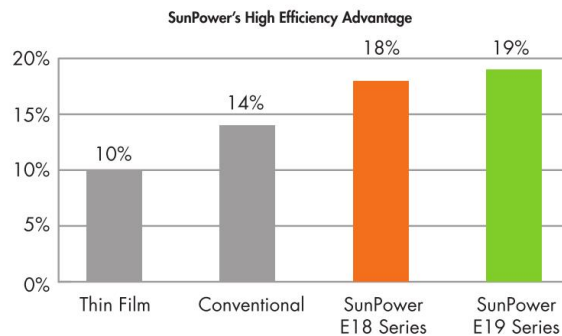
Proven materials, tempered front glass, and a sturdy anodised frame allow panel to operate reliably in multiple mounting configurations.



SPR-305E-WHT-D



The SunPower™ 305 Solar Panel provides today's highest efficiency and performance. Utilising 96 SunPower all back-contact solar cells, the SunPower 305 delivers a total panel conversion efficiency of 18,7%. The 305 panel's reduced voltage-temperature coefficient, anti-reflective glass and exceptional low-light performance attributes provide outstanding energy delivery per peak power watt.



SUNPOWER™

E18 / 305 SOLAR PANEL

EXCEPTIONAL EFFICIENCY AND PERFORMANCE

Electrical Data

Measured at Standard Test Conditions (STC): Irradiance 1000W/m², AM 1.5, and cell temperature 25° C

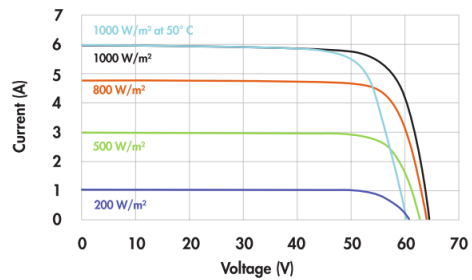
Nominal Power (+5/-3%)	P _{nom}	305 W
Efficiency	η	18,7 %
Rated Voltage	V _{mpp}	54,7 V
Rated Current	I _{mpp}	5,58 A
Open Circuit Voltage	V _{oc}	64,2 V
Short Circuit Current	I _{sc}	5,96 A
Maximum System Voltage	IEC	1000 V
Temperature Coefficients	Power [P]	-0,38% / K
	Voltage [V _{oc}]	-176,6mV / K
	Current [I _{sc}]	3,5mA / K
NOCT		45° C +/-2° C
Series Fuse Rating		15 A
Limiting Reverse Current (3-strings)	I _r	14,9 A

Electrical Data

Measured at Nominal Operating Cell Temperature (NOCT): Irradiance 800W/m², 20° C, wind 1 m/s

Nominal Power	P _{nom}	227 W
Rated Voltage	V _{mpp}	50,4 V
Rated Current	I _{mpp}	4,49 A
Open Circuit Voltage	V _{oc}	60,1 V
Short Circuit Current	I _{sc}	4,82 A

I-V Curve



Current/voltage characteristics with dependence on irradiance and module temperature.

Tested Operating Conditions

Temperature	-40° C to +85° C
Max load	550 kg / m ² (5400 Pa), front (e.g. snow) w / specified mounting configurations 245 kg / m ² (2400 Pa) front and back - e.g. wind
Impact Resistance	Hail - 25 mm at 23 m/s

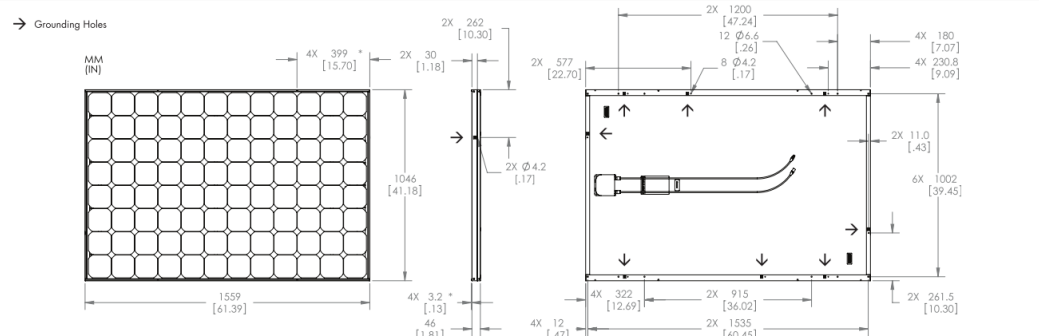
Warranties and Certifications

Warranties	25 year limited power warranty 10 year limited product warranty
Certifications	IEC 61215 Ed. 2, IEC 61730 (SCII)

Mechanical Data

Solar Cells	96 SunPower all-back contact monocrystalline	Output Cables	1000mm length cables / MultiContact (MC4) connectors
Front Glass	high transmission tempered glass with anti-reflective (AR) coating	Frame	Anodised aluminium alloy type 6063 (black)
Junction Box	IP-65 rated with 3 bypass diodes 32 x 155 x 128 (mm)	Weight	18,6 kg

Dimensions



CAUTION: READ SAFETY AND INSTALLATION INSTRUCTIONS BEFORE USING THE PRODUCT.

Visit sunpowercorp.com for details

SUNPOWER and the SUNPOWER logo are trademarks or registered trademarks of SunPower Corporation.
© September 2010 SunPower Corporation. All rights reserved. Specifications included in this datasheet are subject to change without notice.

sunpowercorp.com
Australia: sunpowercorp.com.au
Document #001-64025 Rev** / A4_EN

Appendix B: Field Programmable Gate Arrays

B.1 Introduction

A Field Programmable Gate Array (FPGA) is a device that contains a matrix of reconfigurable gate array logic circuitry. When a FPGA is configured, the internal circuitry is connected in a way that creates a hardware implementation of the software application. Unlike processors, FPGAs use dedicated hardware for processing logic and do not have an operating system. FPGAs are truly parallel in nature so different processing operations do not have to compete for the same resources. As a result, the performance of one part of the application is not affected when additional processing is added. Also, multiple control loops can run on a single FPGA device at different rates. FPGA-based control systems can enforce critical interlock logic and can be designed to prevent I/O forcing by an operator. However, unlike hard-wired printed circuit board (PCB) designs which have fixed hardware resources, FPGA-based systems can literally rewire their internal circuitry to allow reconfiguration after the control system is deployed to the field. FPGA devices deliver the performance and reliability of dedicated hardware circuitry.

A single FPGA can replace thousands of discrete components by incorporating millions of logic gates in a single integrated circuit (IC) chip. The internal resources of an FPGA chip consist of a matrix of configurable logic blocks (CLBs) surrounded by a periphery of I/O blocks shown in Figure B.1. Signals are routed within the FPGA matrix by programmable interconnect switches and wire routes.

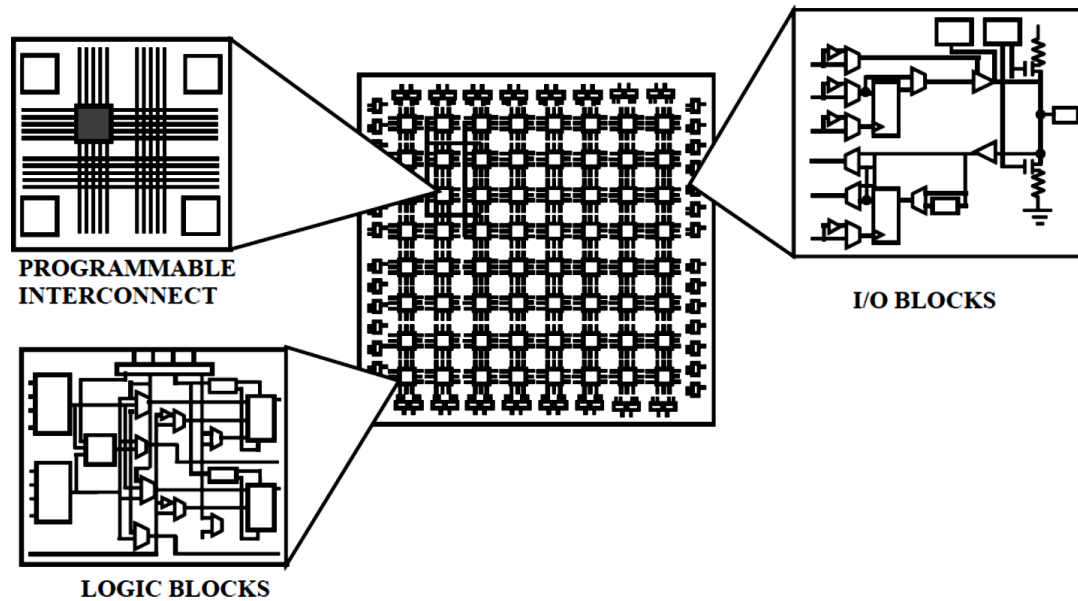


Figure B.1: Internal Structure of FPGA

In an FPGA logic blocks are implemented using multiple level low fan-in gates, which gives it a more compact design compared to an implementation with two-level AND-OR logic. FPGA provides its user a way to configure:

1. The intersection between the logic blocks and
2. The function of each logic block.

Logic block of an FPGA can be configured in such a way that it can provide functionality as simple as that of transistor or as complex as that of a microprocessor. It can be used to implement different combinations of combinational and sequential logic functions. Logic blocks of an FPGA can be implemented by any of the following:

1. Transistor pairs
2. Combinational gates like basic NAND gates or XOR gates
3. n-input Lookup tables
4. Multiplexers
5. Wide fan-in And-OR structure.

Routing in FPGAs consists of wire segments of varying lengths which can be interconnected via electrically programmable switches. Density of logic block used in an FPGA depends on length and number of wire segments used for routing. Number of segments used for interconnection typically is a tradeoff between density of logic blocks

used and amount of area used up for routing. Simplified version of FPGA internal architecture with routing is shown in Figure B.2.

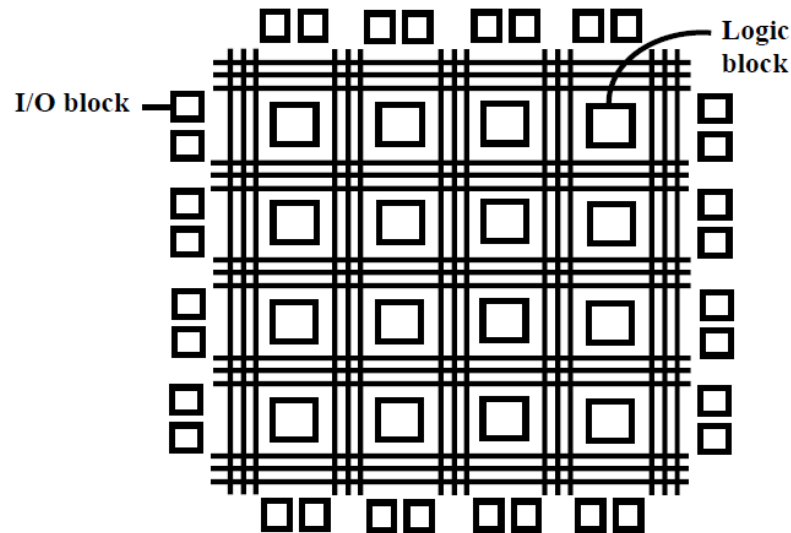


Figure B.2: Simplified Internal Structure of FPGA

By the early 1980's large scale integrated circuits (LSI) formed the backbone of most of the logic circuits in major systems. Microprocessors, bus/IO controllers, system timers etc. were implemented using integrated circuit fabrication technology. Random "glue logic" or interconnects were still required to help connect the large integrated circuits in order to:

1. Generate global control signals (for resets etc.)
2. Data signals from one subsystem to another sub system.

Systems typically consisted of few large scale integrated components and large number of SSI (Small Scale Integrated circuit) and MSI (Medium Scale Integrated circuit) components. Initial attempt to solve this problem led to development of Custom ICs which were to replace the large amount of interconnect. This reduced system complexity and manufacturing cost, and improved performance. However, custom ICs have their own disadvantages. They are relatively very expensive to develop, and delay introduced for product to market (time to market) because of increased design time. There are two kinds of costs involved in development of custom ICs

1. Cost of development and design
2. Cost of manufacture. (A trade-off usually exists between the two costs)

Therefore, the custom IC approach was only viable for products with very high volume, and which were not time to market sensitive. FPGAs were introduced as an alternative to custom ICs for implementing entire system on one chip and to provide flexibility of re-programmability to the user. Introduction of FPGAs resulted in improvement of density relative to discrete SSI/MSI components (within around 10x of custom ICs). Another advantage of FPGAs over Custom ICs is that with the help of computer aided design (CAD) tools circuits could be implemented in a short amount of time (no physical layout process, no mask making, no IC manufacturing).

B.2 Evaluation of FPGA

In the world of digital electronic systems, there are three basic kinds of devices: memory, microprocessors, and logic. Memory devices store random information such as the contents of a spreadsheet or database. Microprocessors execute software instructions to perform a wide variety of tasks such as running a word processing program or video game. Logic devices provide specific functions, including device-to-device interfacing, data communication, signal processing, data display, timing and control operations, and almost every other function a system must perform.

The first type of user-programmable chip that could implement logic circuits was the Programmable Read-Only Memory (PROM), in which address lines can be used as logic circuit inputs and data lines as outputs. Logic functions, however, rarely require more than a few product terms, and a PROM contains a full decoder for its address inputs. PROMS are thus an inefficient architecture for realizing logic circuits, and so are rarely used in practice for that purpose. The device that came as a replacement for the PROM's are programmable logic devices or in short PLA. Logically, a PLA is a circuit that allows implementing Boolean functions in sum-of-product form. The typical implementation consists of input buffers for all inputs, the programmable AND-matrix followed by the programmable OR-matrix, and output buffers. The input buffers provide both the original and the inverted values of each PLA input. The input lines run horizontally into the AND matrix, while the so-called product-term lines run vertically. Therefore, the size of the AND matrix is twice the number of inputs times the number of product-terms.

When PLAs were introduced in the early 1970s, by Philips, their main drawbacks were that they were expensive to manufacture and offered somewhat poor speed-performance. Both disadvantages were due to the two levels of configurable logic, because programmable logic planes were difficult to manufacture and introduced significant propagation delays. To overcome these weaknesses, Programmable Array Logic (PAL) devices were developed. PALs provide only a single level of programmability, consisting of a programmable “wired” AND plane that feeds fixed OR-gates. PALs usually contain flip-flops connected to the OR-gate outputs so that sequential circuits can be realized. These are often referred to as Simple Programmable Logic Devices (SPLDs). Figure B.3 shows a simplified structure of PLA and PAL.

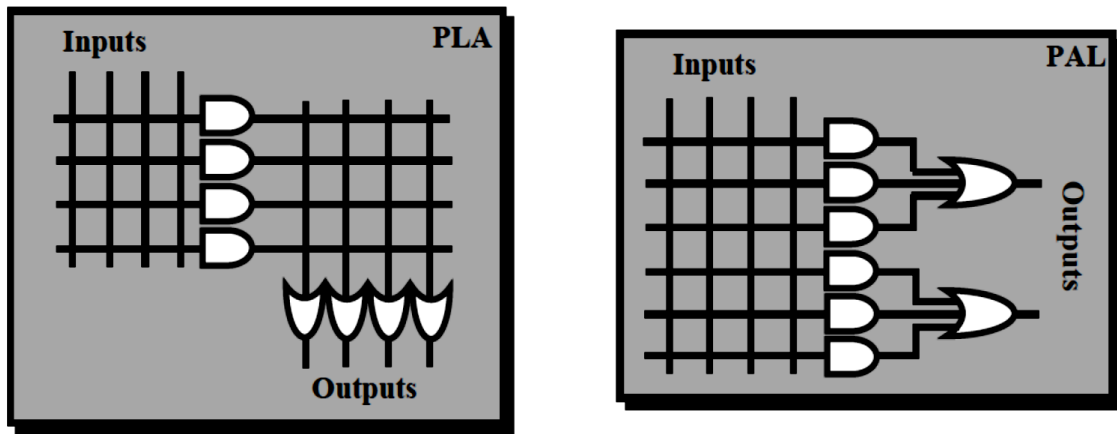


Figure B.3: Simplified Structure of PLA and PAL

With the advancement of technology, it has become possible to produce devices with higher capacities than SPLD's. As chip densities increased, it was natural for the PLD manufacturers to evolve their products into larger (logically, but not necessarily physically) parts called Complex Programmable Logic Devices (CPLDs). For most practical purposes, CPLDs can be thought of as multiple PLDs (plus some programmable interconnect) in a single chip. The larger size of a CPLD allows to implement either more logic equations or a more complicated design.

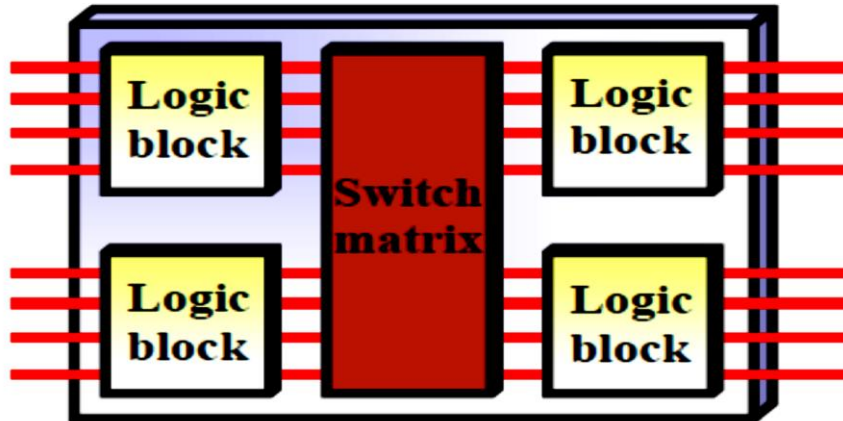


Figure B.4: Internal structure of a CPLD

Figure B.4 contains a block diagram of a hypothetical CPLD. Each of the four logic blocks shown there is the equivalent of one PLD. However, in an actual CPLD there may be more (or less) than four logic blocks. These logic blocks are themselves comprised of macro cells and interconnect wiring, just like an ordinary PLD.

Unlike the programmable interconnect within a PLD, the switch matrix within a CPLD may or may not be fully connected. In other words, some of the theoretically possible connections between logic block outputs and inputs may not actually be supported within a given CPLD. The effect of this is most often to make 100% utilization of the macro cells very difficult to achieve. Some hardware designs simply won't fit within a given CPLD, even though there are sufficient logic gates and flip-flops available. Because CPLDs can hold larger designs than PLDs, their potential uses are more varied. They are still sometimes used for simple applications like address decoding, but more often contain high-performance control-logic or complex finite state machines. At the high-end (in terms of numbers of gates), there is also a lot of overlap in potential applications with FPGAs. Traditionally, CPLDs have been chosen over FPGAs whenever high-performance logic is required. Because of its less flexible internal architecture, the delay through a CPLD (measured in nanoseconds) is more predictable and usually shorter.

The development of the FPGA was distinct from the SPLD/CPLD evolution just described. This is apparent from the architecture of FPGA shown in Figure 8.1. FPGAs offer the highest amount of logic density, the most features, and the highest performance.

The largest FPGA now shipping, part of the Xilinx Virtex™ line of devices, provides eight million "system gates" (the relative density of logic). These advanced devices also offer features such as built-in hardwired processors (such as the IBM Power PC), substantial amounts of memory, clock management systems, and support for many of the latest, very fast device-to-device signaling technologies. FPGAs are used in a wide variety of applications ranging from data processing and storage, to instrumentation, telecommunications, and digital signal processing. The value of programmable logic has always been its ability to shorten development cycles for electronic equipment manufacturers and help them get their product to market faster. As PLD (Programmable Logic Device) suppliers continue to integrate more functions inside their devices, reduce costs, and increase the availability of time-saving IP cores, programmable logic is certain to expand its popularity with digital designers.

B.3 FPGA Structural Classification

Basic structure of an FPGA includes logic elements, programmable interconnects and memory. Arrangement of these blocks is specific to particular manufacturer. On the basis of internal arrangement of blocks FPGAs can be divided into three classes:

B.3.1 Symmetrical arrays

This architecture consists of logic elements (called CLBs) arranged in rows and columns of a matrix and interconnect laid out between them shown in Figure B.2. This symmetrical matrix is surrounded by I/O blocks which connect it to outside world. Each CLB consists of n-input Lookup table and a pair of programmable flip flops. I/O blocks also control functions such as tri-state control, output transition speed. Interconnects provide routing path. Direct interconnects between adjacent logic elements have smaller delay compared to general purpose interconnect.

B.3.2 Row based architecture

Row based architecture shown in Figure B.5 consists of alternating rows of logic modules and programmable interconnect tracks. Input output blocks is located in the periphery of the rows. One row may be connected to adjacent rows via vertical interconnect. Logic modules can be implemented in various combinations. Combinatorial modules contain only combinational elements which Sequential modules contain both combinational elements along with flip flops. This sequential module can implement complex combinatorial-sequential functions. Routing tracks are divided into smaller segments connected by anti-fuse elements between them.

B.3.3 Hierarchical PLDs

This architecture is designed in hierarchical manner with top level containing only logic blocks and interconnects. Each logic block contains number of logic modules. And each logic module has combinatorial as well as sequential functional elements. Each of these functional elements is controlled by the programmed memory. Communication between logic blocks is achieved by programmable interconnect arrays. Input output blocks surround this scheme of logic blocks and interconnects. This type of architecture is shown in Figure B.6.

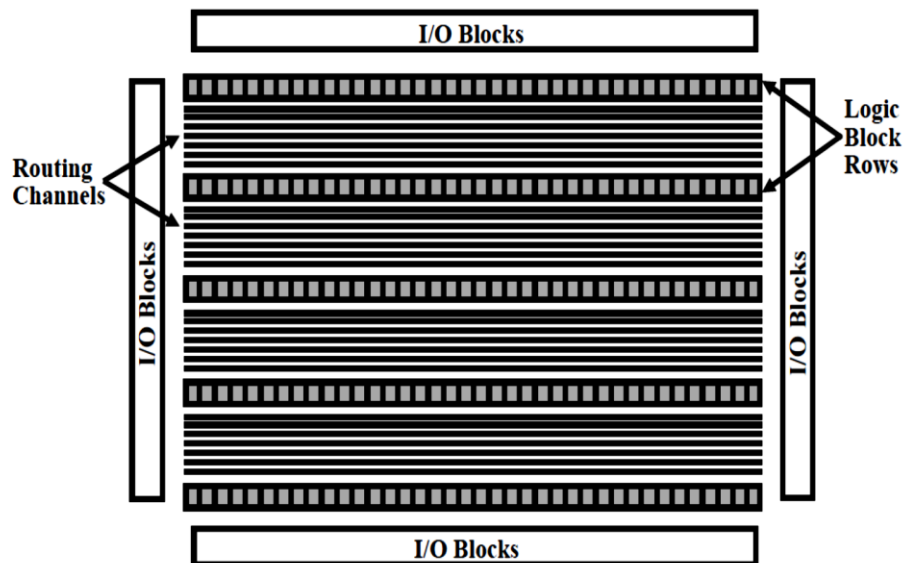


Figure B.5: Row based Architecture

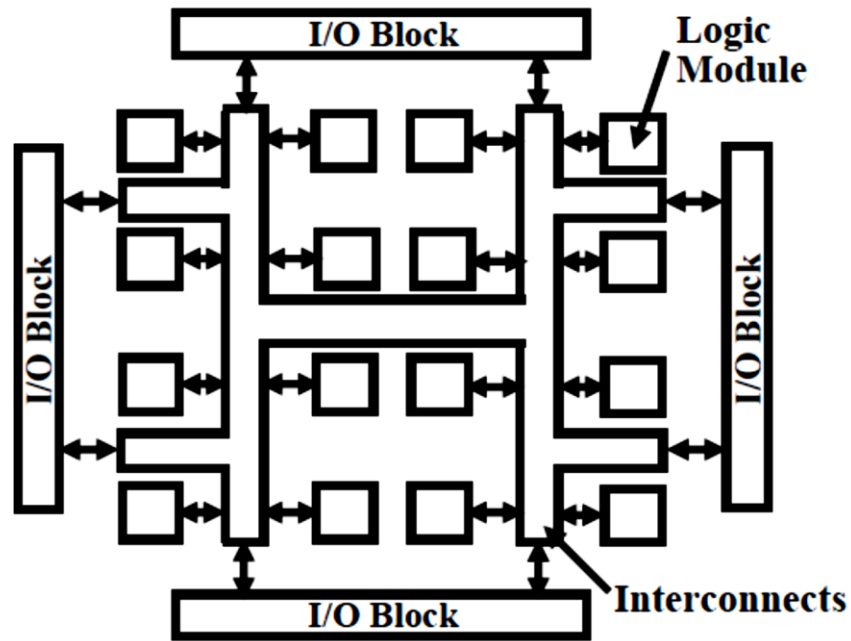


Figure B.6: Hierarchical PLD

B.4 FPGA Classification on User Programmable Switch Technologies

FPGAs are based on an array of logic modules and a supply of uncommitted wires to route signals. In gate arrays these wires are connected by a mask design during manufacture. In FPGAs, however, these wires are connected by the user and therefore must use an electronic device to connect them. Three types of devices have been commonly used to do this, pass transistors controlled by an SRAM cell, a flash or EEPROM cell to pass the signal, or a direct connect using antifuses. Each of these interconnect devices have their own advantages and disadvantages. This has a major effect on the design, architecture, and performance of the FPGA. Classification of FPGAs on user programmable switch technology is given in Figure B.7 shown below.

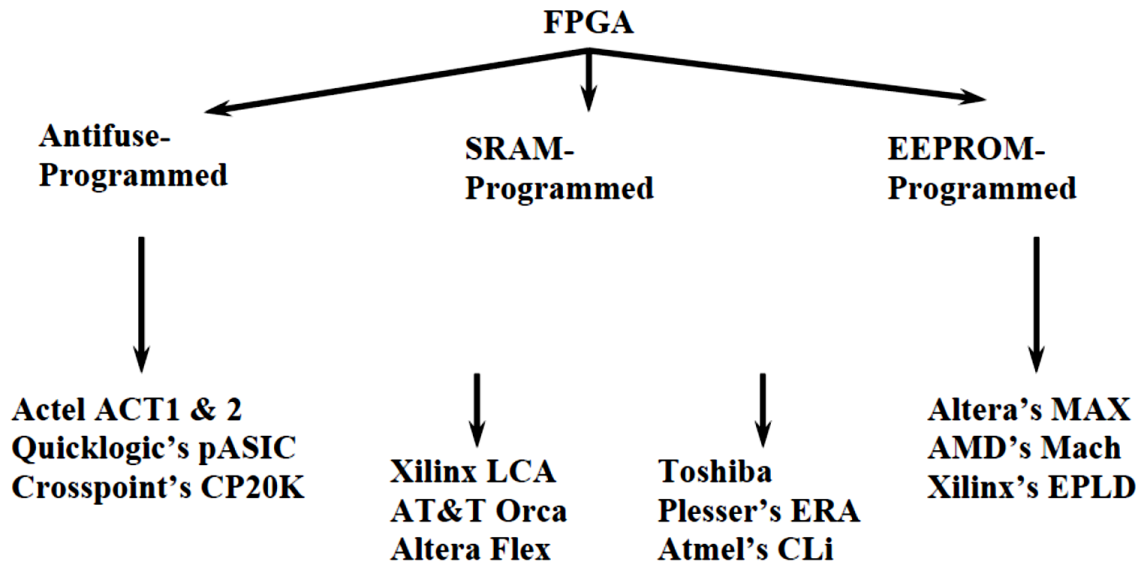


Figure B.7: FPGA Classification on user programmable technology

B.4.1 SRAM Based

The major advantage of SRAM based device is that they are infinitely re-programmable and can be soldered into the system and have their function changed quickly by merely changing the contents of a PROM. They therefore have simple development mechanics. They can also be changed in the field by uploading new application code, a feature attractive to designers. It does however come with a price as the interconnect element has high impedance and capacitance as well as consuming much more area than other technologies. Hence wires are very expensive and slow. The FPGA architect is therefore forced to make large inefficient logic modules (typically a Look Up Table (LUT)). The other disadvantages are: They need to be reprogrammed each time when power is applied, need an external memory to store program and require large area. Figure B.8 shows two applications of SRAM cells: for controlling the gate nodes of pass-transistor switches and to control the select lines of multiplexers that drive logic block inputs. The figures give an example of the connection of one logic block (represented by the AND-gate in the upper left corner) to another through two pass-transistor switches, and then a multiplexer, all controlled by SRAM cells. Whether an FPGA uses pass-transistors or multiplexers, or both depends on the particular product.

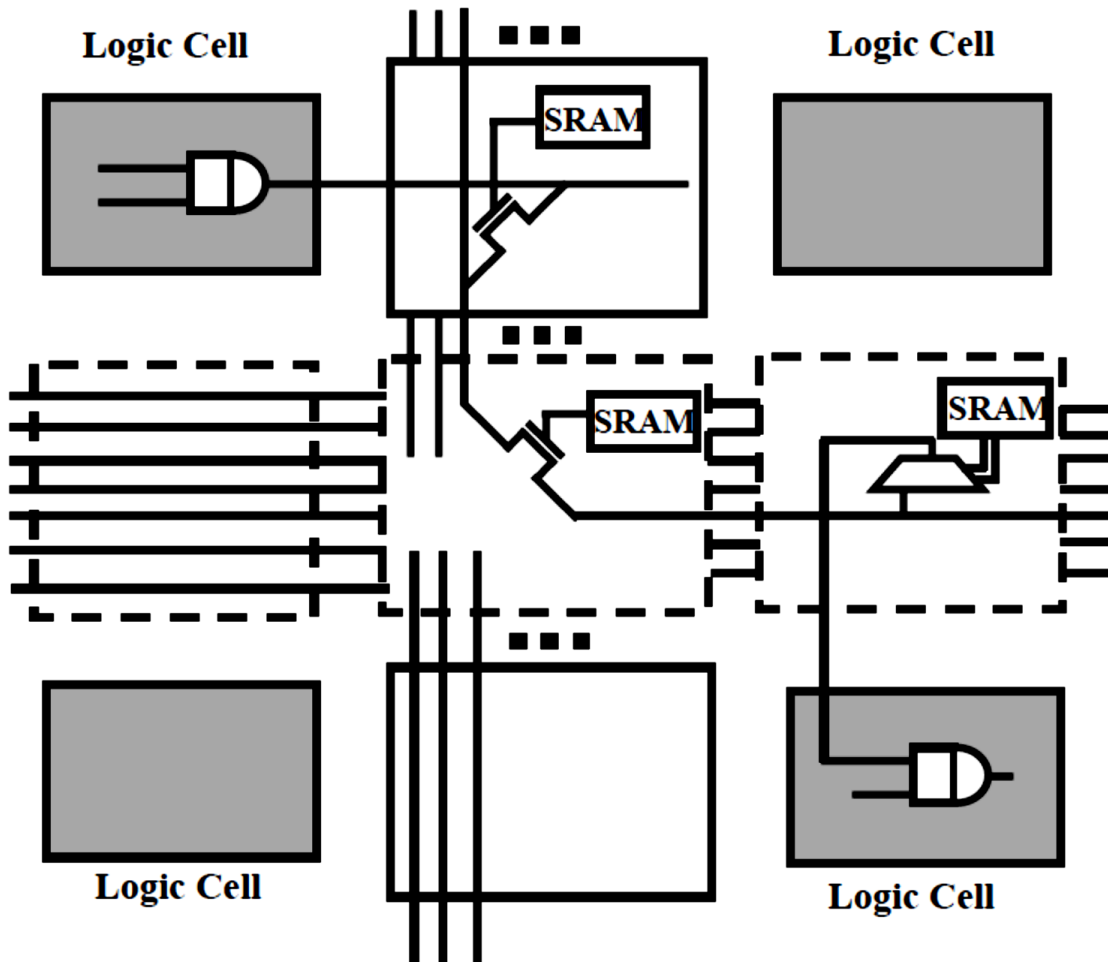


Figure B.8: SRAM-controlled Programmable Switches

B.4.2 Antifuse Based

The antifuse based cell is the highest density interconnect by being a true cross point. Thus, the designer has a much larger number of interconnects so logic modules can be smaller and more efficient. Place and route software also have a much easier time. These devices however are only one-time programmable and therefore must be thrown out every time a change is made in the design. The Antifuse has an inherently low capacitance and resistance such that the fastest parts are all Antifuse based. The disadvantage of the antifuse is the requirement to integrate the fabrication of the antifuses into the IC process, which means the process will always lag the SRAM process in scaling. Antifuses are suitable for FPGAs because they can be built using modified CMOS technology. As an example, Actel's antifuse structure is depicted in Figure B.9. The figure shows that an antifuse is

positioned between two interconnect wires and physically consists of three sandwiched layers: the top and bottom layers are conductors, and the middle layer is an insulator. When unprogrammed, the insulator isolates the top and bottom layers, but when programmed the insulator changes to become a low-resistance link. It uses Poly-Si and n+ diffusion as conductors and ONO as an insulator, but other antifuses rely on metal for conductors, with amorphous silicon as the middle layer.

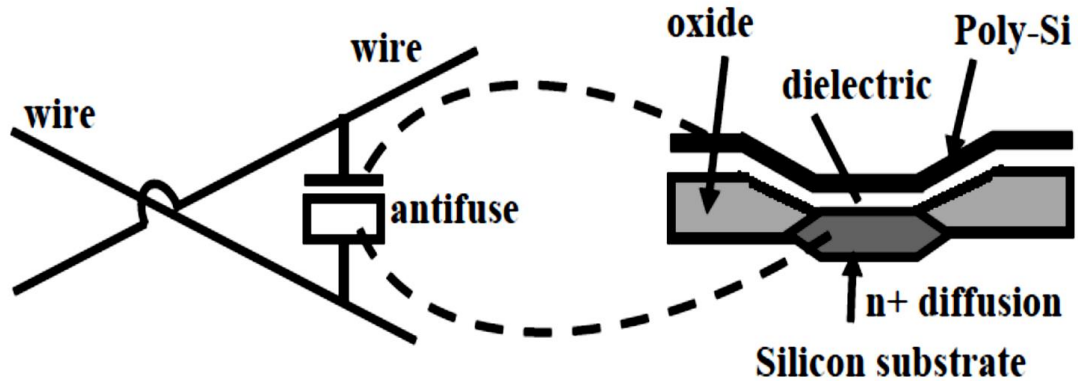


Figure B.9: Actel Antifuse Structure

B.4.3 EEPROM Based

The EEPROM/FLASH cell in FPGAs can be used in two ways, as a control device as in an SRAM cell or as a directly programmable switch. When used as a switch they can be very efficient as interconnect and can be reprogrammable at the same time. They are also non-volatile, so they do not require an extra PROM for loading. They, however, do have their detractions. The EEPROM process is complicated and therefore also lags SRAM technology.

B.5 Logic Block and Routing Techniques

B.5.1 Cross-point FPGA

Consist of two types of logic blocks:

One is transistor pair tiles in which transistor pairs run in parallel lines as shown in figure below.

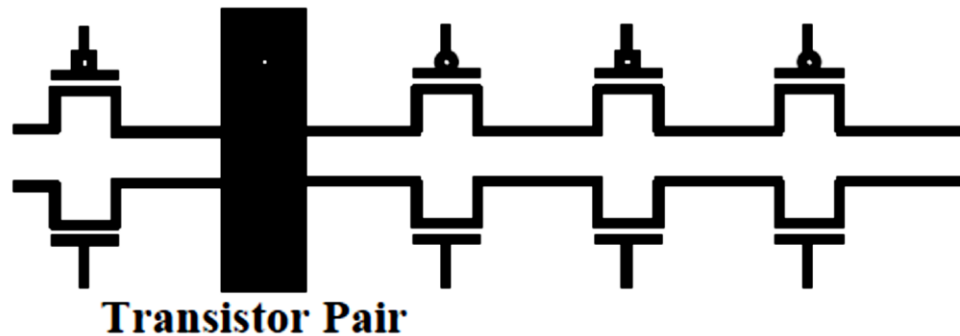


Figure B.10: Transistor pair tiles in cross-point FPGA

Second type of logic blocks are RAM logic which can be used to implement random access memory.

B.5.2 Plessey FPGA

Basic building block here is 2-input NAND gate which is connected to each other to implement desired function.

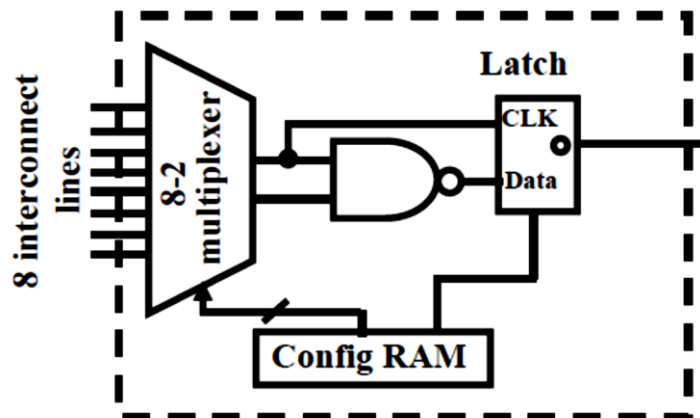


Figure B.11: Plessey Logic Block

Both Cross-point and Plessey are fine grain logic blocks. Fine grain logic blocks have an advantage in high percentage usage of logic blocks, but they require large number of wire segments and programmable switches which occupy lot of area.

B.5.3 Actel Logic Block

If inputs of a multiplexer are connected to a constant or to a signal, it can be used to implement different logic functions. For example, a 2-input multiplexer with inputs a and b, select, will implement function $ac + bc'$. If $b=0$ then it will implement ac , and if $a=0$ it will implement bc' .

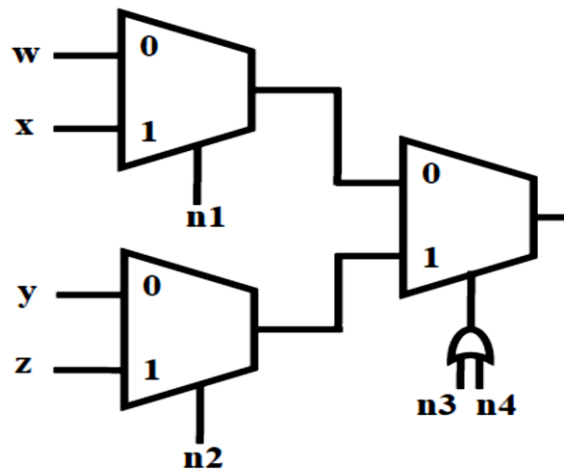


Figure B.12: Actel Logic Block

Typically, an Actel logic block consists of multiple number of multiplexers and logic gates.

B.5.4 Xilinx Logic block

In Xilinx logic block, look up table is used to implement any number of different functionality. The input lines go into the input and enable of look up table. The output of the look up table gives the result of the logic function that it implements. Look up table is implemented using SRAM.

at the expense of delay. Such logic blocks have gates with high threshold as a result they consume less power. Such logic blocks can be used in non-critical paths. Altera, Xilinx are coarse grain architecture.

An intuitive example: Altera's FLEX 8000 series consists of a three-level hierarchy. However, the lowest level of the hierarchy consists of a set of lookup tables, rather than an SPLD like block, and so the FLEX 8000 is categorized here as an FPGA. It should be noted, however, that FLEX 8000 is a combination of FPGA and CPLD technologies. FLEX 8000 is SRAM-based and features a four-input LUT as its basic logic block. Logic capacity ranges from about 4000 gates to more than 15,000 for the 8000 series. The overall architecture of FLEX 8000 is illustrated in Figure B.14.

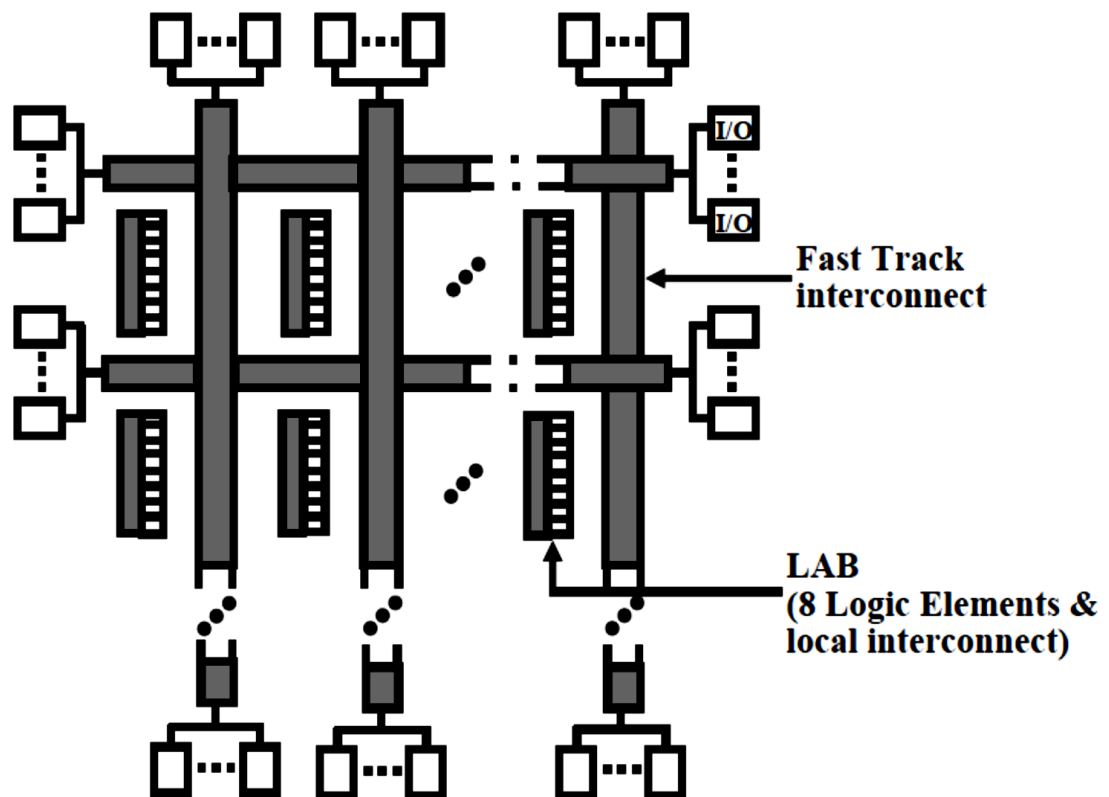


Figure B.14: Architecture of Altera FLEX 8000 FPGAs

The basic logic block, called a Logic Element (LE) contains a four-input LUT, a flip-flop, and special-purpose carry circuitry for arithmetic circuits. The LE also includes cascade circuitry that allows for efficient implementation of wide AND functions. Details of the LE are illustrated in Figure B.15.

In the FLEX 8000, LEs are grouped into sets of 8, called Logic Array Blocks (LABs, a term borrowed from Altera's CPLDs). As shown in Figure B.16, each LAB contains local interconnect and each local wire can connect any LE to any other LE within the same LAB. Local interconnect also connects to the FLEX 8000's global interconnect, called FastTrack. All FastTrack wires horizontal wires are identical, and so interconnect delays in the FLEX 8000 are more predictable than FPGAs that employ many smaller length segments because there are fewer programmable switches in the longer path.

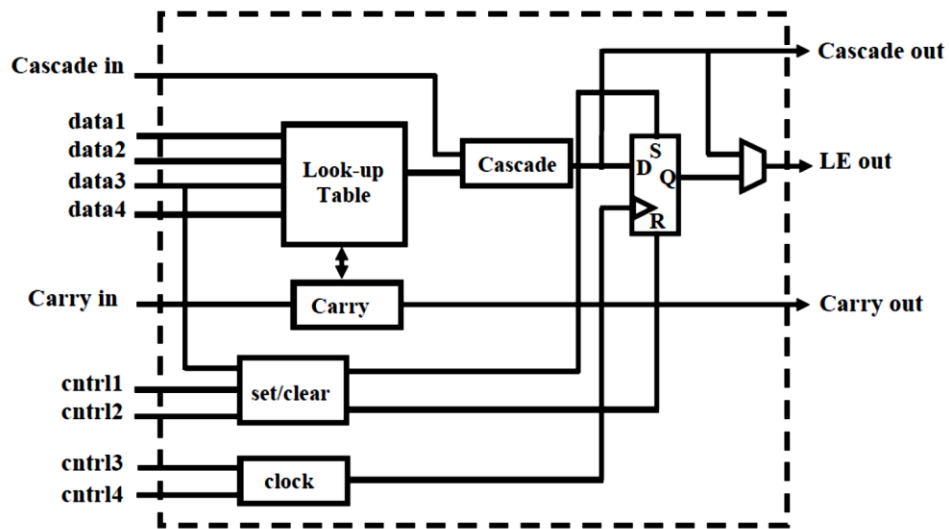


Figure B.15: Altera FLEX 8000 Logic Element (LE)

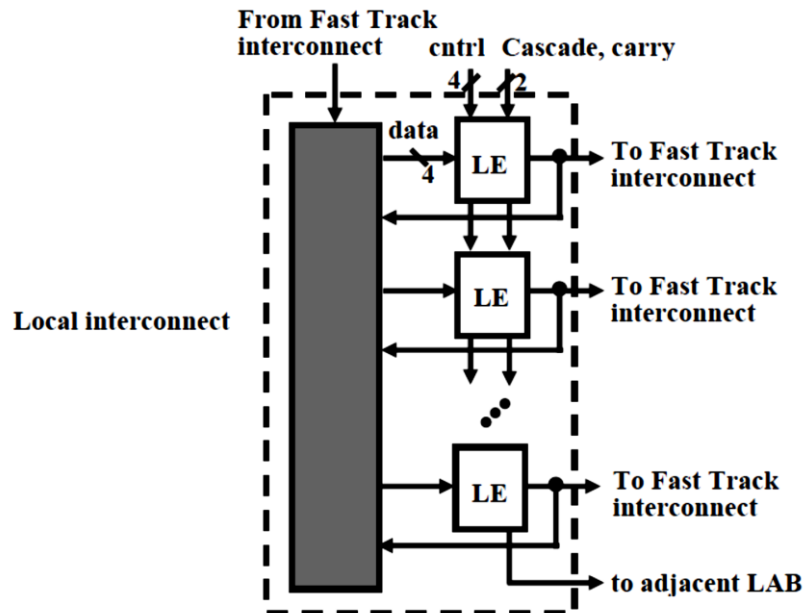


Figure B.16: Altera FLEX 8000 Logic Array Block (LAB)

B.6 FPGA Design Flow

One of the most important advantages of FPGA based design is that users can design it using CAD tools provided by design automation companies. Generic design flow of an FPGA includes the following steps:

System Design

At this stage, the designer has to decide what functions have to be implemented on the FPGA and how to integrate that functionality with the rest of the system.

I/O integration with rest of the system

Input/Output streams of the FPGA are integrated with the rest of the Printed Circuit Board (PCB), which allows the design of the PCB early in the design process. FPGA vendors provide extra automation software solutions for the I/O design process.

Design Description

Designer describes design functionality either by using schematic editors or by using one of the various Hardware Description Languages (HDLs) like Verilog or VHDL.

Synthesis

Once the design is defined, CAD tools are used to implement the design on a given FPGA. Synthesis includes generic optimization, slack optimizations, power optimizations followed by placement and routing. Implementation includes Partition, Place and Route. The output of the design implementation phase is a bit-stream file.

Design Verification

Bit stream file is fed to a simulator which simulates the design functionality and reports errors in the desired behavior of the design. Timing tools are used to determine the maximum clock frequency of the design. Now the design is loaded onto the target FPGA device and testing is done in a real-time environment.

Hardware design and development

The process of creating digital logic is not unlike the embedded software development process. A description of the hardware's structure and behavior is written in a high-level hardware description language (usually VHDL or Verilog) and that code is then compiled and downloaded prior to execution. Of course, schematic capture is also an option for design entry, but it has become less popular as designs have become more complex and the language-based tools have improved. The overall process of hardware development for programmable logic is shown in Figure B.17 and described in the paragraphs that follow.

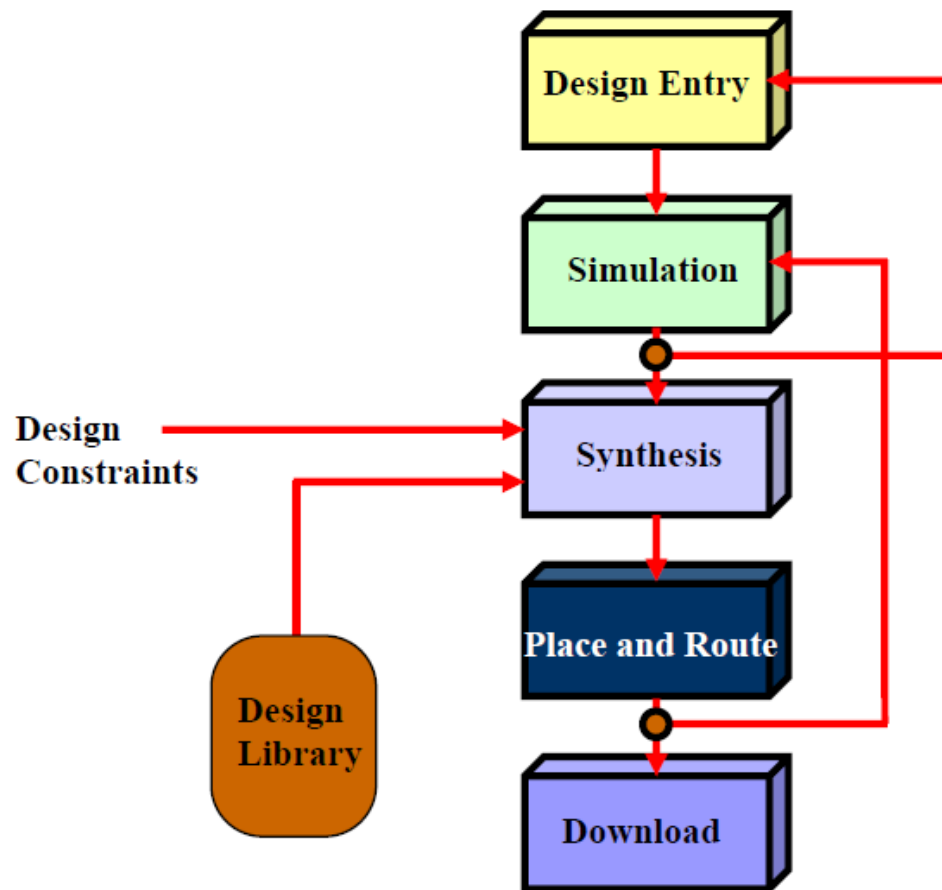


Figure B.17: Programmable Logic Design Process

Typically, the design entry step is followed or interspersed with periods of functional simulation. That's where a simulator is used to execute the design and confirm that the correct outputs are produced for a given set of test inputs. Although problems with the size or timing of the hardware may still crop up later, the designer can at least be sure that the logic is functionally correct before going on to the next stage of development.

Compilation only begins after a functionally correct representation of the hardware exists. This hardware compilation consists of two distinct steps. First, an intermediate representation of the hardware design is produced. This step is called synthesis and the result is a representation called a netlist. The netlist is device independent, so its contents do not depend on the particulars of the FPGA or CPLD; it is usually stored in a standard format called the Electronic Design Interchange Format (EDIF).

The second step in the translation process is called place & route. This step involves mapping the logical structures described in the netlist onto actual macro cells, interconnections, and input and output pins. This process is similar to the equivalent step in the development of a printed circuit board, and it may likewise allow for either automatic or manual layout optimizations. The result of the place & route process is a bitstream. This name is used generically, despite the fact that each CPLD or FPGA (or family) has its own, usually proprietary, bitstream format. Suffice it to say that the bitstream is the binary data that must be loaded into the FPGA or CPLD to cause that chip to execute a particular hardware design.

Increasingly there are also debuggers available that at least allow for single-stepping the hardware design as it executes in the programmable logic device. But those only complement a simulation environment that is able to use some of the information generated during the place & route step to provide gate-level simulation. Obviously, this type of integration of device-specific information into a generic simulator requires a good working relationship between the chip and simulation tool vendors.

Perhaps the most striking difference between hardware and software design is the way a developer must think about the problem. Software developers tend to think sequentially, even when they are developing a multithreaded application. The lines of source code that they write are always executed in that order, at least within a given thread. If there is an operating system it is used to create the appearance of parallelism, but there is still just one execution engine. During design entry, hardware designers must think-and program-in parallel. All of the input signals are processed in parallel, as they travel through a set of execution engines-each one a series of macro cells and interconnections-toward their destination output signals. Therefore, the statements of a hardware description language create structures, all of which are "executed" at the very same time.

Appendix C: Kalman Filter

C.1 Introduction

Statistical estimation is the process of determining the values of certain parameters or signals from empirical (measured or collected) data mixed with noise which is random in nature [380], [381]. Statistical estimation has applications in a multitude of areas. For example, in the area of consumer electronics, estimation techniques are used for mobile wireless communications, intelligent voice and gesture recognition, multimedia enhancement and classification, GPS navigation etc. In defense and security related fields, applications include target tracking, guidance and navigation systems, and threat detection. Statistical estimation methods also play a vital role in health monitoring and medical diagnosis problems.

In the estimation problem, the task is to estimate an unobservable phenomenon of interest (represented by a set of parameters) using observed data. When the parameters vary over time, the estimate may be iteratively updated using continuously obtained data. This type of estimation, termed sequential estimation, involves computing an initial estimate and then iteratively updating the estimate based on the most recent data.

A large number of statistical estimation algorithms exist, ranging from point estimators such as maximum-likelihood (ML) and maximum *a posteriori* (MAP) estimators which compute the single best parameter that maximizes the likelihood of the observed data or *a posteriori* parameter probability, to Bayesian methods which compute the full posterior probability distribution of the parameters. One class of estimation, known as linear estimation, computes the parameter estimate as a simple linear function of the data. Estimation algorithms are designed to satisfy various optimality criteria, such as consistency, efficiency, unbiasedness, minimum variance, and minimum mean square error (MMSE) [381]. Given a model estimation problem, bounds can be calculated on estimation performance. For example, the Cramér-Rao lower bound (CRLB) defines a lower bound on the variance of an estimator [381].

The Kalman Filter (KF) was developed by Rudolph Kalman and Richard Bucy [382], [383] in the 60s and is used for the estimation of the parameters (or states) of a linear

Gaussian dynamical system. Specifically, in a state space setting, the system state must propagate according to a linear evolution model with Gaussian process noise and the data (or measurements) must be linearly related to the state with Gaussian noise. Many systems encountered in real world applications are well characterized by this model. The KF is a popular choice for estimating the parameters of dynamical systems for several reasons, including:

- KF is a Bayesian optimum estimator for sequentially estimating the states of a linear Gaussian dynamical system;
- KF algorithm has low computational complexity and can be easily implemented in DSP hardware for real-time applications;
- Variations and extensions of the KF are readily available for nonlinear, distributed, and non-Gaussian problems, such as the Extended Kalman Filter (EKF), the Unscented Kalman Filter (UKF), the Decentralized Kalman Filter (DKF), and the particle filter [384].

The KF is among the most notable innovations of the 20th century. This algorithm recursively estimates the state variables in a noisy linear dynamical system as new observations are measured and as the system evolves in time. It optimally updates the estimates of the system variables, for example, the position and velocity of an object, by minimizing the mean-squared estimation error of the current state as noisy measurements are received. Each update provides the latest unbiased estimate of the system variables together with a measure on the uncertainty of those estimates in the form of a covariance matrix. Since the updating process is fairly general and relatively easy to compute, the KF can often be implemented in real time.

The KF is used widely in virtually every technical or quantitative field. In engineering, for example, the KF is pervasive in the areas of navigation and global positioning [385], [386], tracking [387], guidance [388], robotics [389], radar [390], fault detection [391], and computer vision [392]. It is also utilized in applications involving signal processing [393], voice recognition [394], video stabilization [395], and automotive control systems [396]. In purely quantitative fields, the KF also plays an important role in time-series analysis [397], econometrics [398], mathematical finance [399], system identification [400], and neural networks [401]. Also KF, as a dynamic estimation technique, has played an

important role in many industrial applications such as sensorless speed estimation in electric drives [402], non-linear mechanical loads [403], power system protection and harmonics estimation [404], [405], robots/particles localization [406], and fault diagnostics [407]. In addition, KF-based techniques are widely used in distributed generation and islanding detection applications [408]. The ability to estimate non-measurable signals, fast convergence, and direct implementation encourages wider utilization of KF-based techniques in various industrial applications.

It has been just over 50 years since Rudolf Kalman's first seminal paper on state estimation [409], which launched a major shift toward state-space dynamic modeling. This big achievement in mathematical systems theory, together with his two other groundbreaking papers [410], [382], helped secure him a number of major awards, including the IEEE Medal of Honor in 1974, the Kyoto Prize in 1985, the Steele Prize in 1986, the Charles Stark Draper Prize in 2008, and the U.S. National Medal of Science in 2009.

As is sometimes the case with revolutionary advances, some were initially slow to accept Kalman's work. According to Grewal and Andrews [411], Kalman's second paper [382] was actually rejected by an electrical engineering journal, since, as one of the referees put it, "it cannot possibly be true." However, with the help of Stanley F. Schmidt at the NASA Ames Research Center, the KF ultimately gained acceptance as it was used successfully in the navigation systems for the Apollo missions, as well as several subsequent NASA projects and a number of military defense systems [411], [412].

Today the Kalman family of state estimation methods, which includes the KF and its many variations, are the factual standard for state estimation. At the time of this writing, there have been over 6000 patents awarded in the U.S. on applications or processes involving the KF. In academia, its influence is no less noteworthy. According to Google Scholar, the phrase "Kalman Filter" is found in over 100,000 academic papers. In addition, Kalman's original paper [383] is reported to have over 7500 academic citations. Indeed, the last 50 years have seen phenomenal growth in the variety of applications of the KF.

The KF is a set of mathematical equations that provides an efficient computational (recursive) means to estimate the state of a process, in a way that minimizes the mean of the squared error. The filter is very powerful in several aspects: it supports estimations of

past, present, and even future states, and it can do so even when the precise nature of the modeled system is unknown.

KF is a popular recursive algorithm for motion prediction [413] as this simple application which has purpose to predict the next position of the object movement walking in straight line. The principle of Kalman Filter is to find the probability of the hypothesis of predicted state is given by hypothesis of prior state and then using the data from measurement sensor to correct the hypothesis to get the best estimation for each time. The KF exploits the dynamics of the target, which govern its time evolution, to remove the effects of the noise and get a good estimate of the location of the target at the present time (filtering), at a future time (prediction), or at a time in the past (interpolation or smoothing). The KF is well suited to use for a digital design because its direct processing ability in time domain is suitable to computer-based calculation.

The Kalman Filter is sometimes also called the Kalman Estimator. As shown in Figure C.1, the Kalman filter generates state and output estimates from input and output with filtering the noises. A literal role of ‘filter’ is reducing the noises contained in the two input signals of the filter, but the Kalman filter is eventually used for estimating the state. Therefore, it has an efficient performance for estimating the state in a dynamic system in a noisy environment.

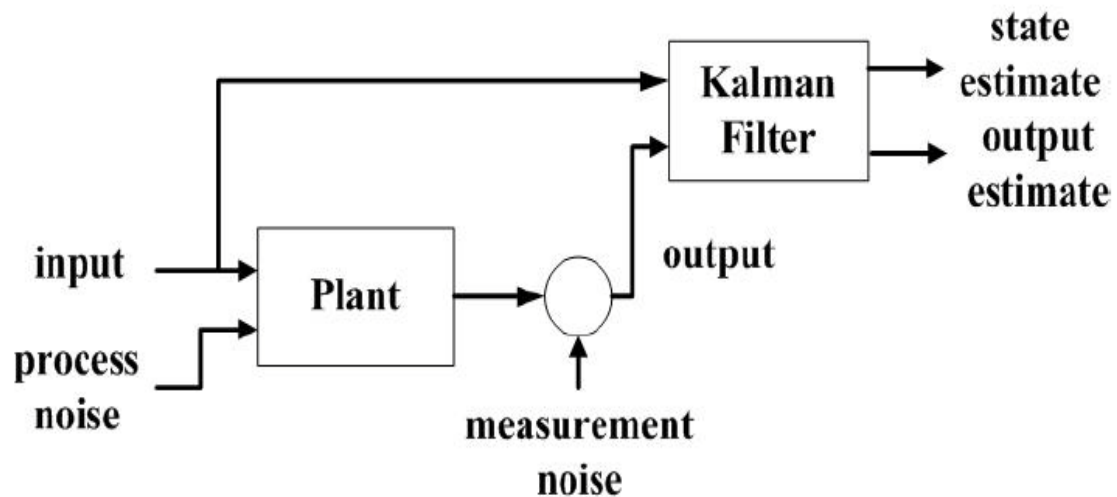


Figure C.1: Kalman Filter (Estimator) diagram [357]

C.2 The Discrete Kalman Filter

This section describes the filter in its original formulation [383] where the measurements occur, and the state is estimated at discrete points in time.

C.2.1 Process to be Estimated

The Kalman filter addresses the general problem of trying to estimate the state $x \in \mathfrak{R}^n$ of a discrete-time controlled process that is governed by the linear stochastic difference equation

$$x_k = Ax_{k-1} + Bu_{k-1} + w_{k-1} \quad (C.1)$$

with a measurement $z \in \mathfrak{R}^m$ that is

$$z_k = Hx_k + v_k \quad (C.2)$$

The random variables w_k and v_k represent the process and measurement noise respectively. They are assumed to be independent (of each other), white, and with normal probability distributions

$$p(w) \sim N(0, Q) \quad (C.3)$$

$$p(v) \sim N(0, R) \quad (C.4)$$

The process noise covariance Q and measurement noise covariance R matrices might change with each time step or measurement.

The $n \times n$ matrix A in the difference equation (C.1) relates the state at the previous time step $k - 1$ to the state at the current step k , in the absence of either a driving function or process noise. The $n \times l$ matrix B relates the optional control input $u \in \mathfrak{R}^l$ to the state x . The $m \times n$ matrix H in the measurement equation (C.2) relates the state to the measurement z_k .

C.2.2 Computational Origins of the Filter

We define $\hat{x}_k^- \in \mathfrak{R}^n$ (note the “super minus”) to be our *a priori* state estimate at step k given knowledge of the process prior to step k , and $\hat{x}_k \in \mathfrak{R}^n$ to be our *a posteriori* state estimate at step k given measurement z_k . Then we can define *a priori* and *a posteriori* estimate errors as

$$e_k^- = x_k - \hat{x}_k^-, \text{ and } e_k = x_k - \hat{x}_k.$$

The *a priori* estimate error covariance is then

$$P_k^- = E[e_k^- e_k^{-T}] = E[(x_k - \hat{x}_k^-)(x_k - \hat{x}_k^-)^T] \quad (\text{C.5})$$

and the *a posteriori* estimate error covariance is

$$P_k = E[e_k e_k^T] = E[(x_k - \hat{x}_k)(x_k - \hat{x}_k)^T] \quad (\text{C.6})$$

In deriving the equations for the Kalman filter, we begin with the goal of finding an equation that computes an *a posteriori* state estimate \hat{x}_k as a linear combination of an *a priori* estimate \hat{x}_k^- and a weighted difference between an actual measurement z_k and a measurement prediction $H\hat{x}_k^-$ as shown below in (C.7).

$$\hat{x}_k = \hat{x}_k^- + K(z_k - H\hat{x}_k^-) \quad (\text{C.7})$$

The difference term $(z_k - H\hat{x}_k^-)$ is known as residual or measurement innovation. The residual reflects the discrepancy between the predicted measurement $H\hat{x}_k^-$ and the actual measurement z_k . A residual of zero means that the two are in complete agreement.

The $n \times m$ matrix K in (C.7) is called the Kalman gain that minimizes the *a posteriori* error covariance (C.6). This minimization can be accomplished by substituting (C.7) into the above definition for e_k (C.6), taking the derivative of the trace of the result with respect to K , setting that result equal to zero, and then solving for K .

$$K_k = P_k^- H^T (H P_k^- H^T + R)^{-1} \quad (C.8)$$

From above equation, we get that as the measurement error covariance R approaches zero, the gain K weights the residual more heavily. Specifically,

$$\lim_{R_k \rightarrow 0} K_k = H^{-1}$$

On the other hand, as the *a priori* estimate error covariance P_k^- approaches zero, the gain K weights the residual less heavily. Specifically,

$$\lim_{P_k^- \rightarrow 0} K_k = 0$$

Another way of thinking about the weighting by K is that as the measurement error covariance R approaches zero, the actual measurement z_k is “trusted” more and more, while the predicted measurement $H\hat{x}_k^-$ is trusted less and less. On the other hand, as the *a priori* estimate error covariance P_k^- approaches zero the actual measurement z_k is trusted less and less, while the predicted measurement $H\hat{x}_k^-$ is trusted more and more.

C.2.3 Discrete Kalman Filter Algorithm

In 1960, R.E. Kalman [383] described a recursive solution to the discrete-data linear filtering problem. Since that time, due in large part to advances in digital computing, the KF has been the subject of extensive research and applications. A common application is in guidance, navigation, and control of vehicles, particularly for aircraft and spacecraft. Furthermore, the KF is a widely applied concept in time series analysis used in fields such as signal processing and econometrics. KF is ideal for systems which are continuously changing. KF has the advantage that it is light on memory (it does not need to keep any history term other than the previous state), and it is fast, making it well suited for real-time problems and embedded systems.

The KF is a recursive filter that estimates the state of a linear dynamic system from a series of noisy measurements [414]. It operates on estimating a process state by using a form of feedback control: the filter estimates the process state at some time and then obtains feedback in the form of noisy measurements. Noise effects in the process are decreased due to recursive cycles which finally lead to the true value of the measurement. Figure C.2 shows the high-level diagram of the KF.

KF equations fall into two groups: The time update equations (also known as predictor equations) which are responsible for projecting ahead (in time) the current state and error covariance estimates to obtain the *a priori* estimates for the next time step. The measurement update equations (also known as corrector equations) are responsible for the feedback—i.e. for incorporating a new measurement into the *a priori* estimate to obtain an improved *a posteriori* estimate. Both equation sets are applied at each k^{th} state. The next figure will show the ongoing discrete Kalman Filter cycle. The time update projects the current state estimate ahead in time. The measurement update adjusts the projected estimate by an actual measurement at that time.

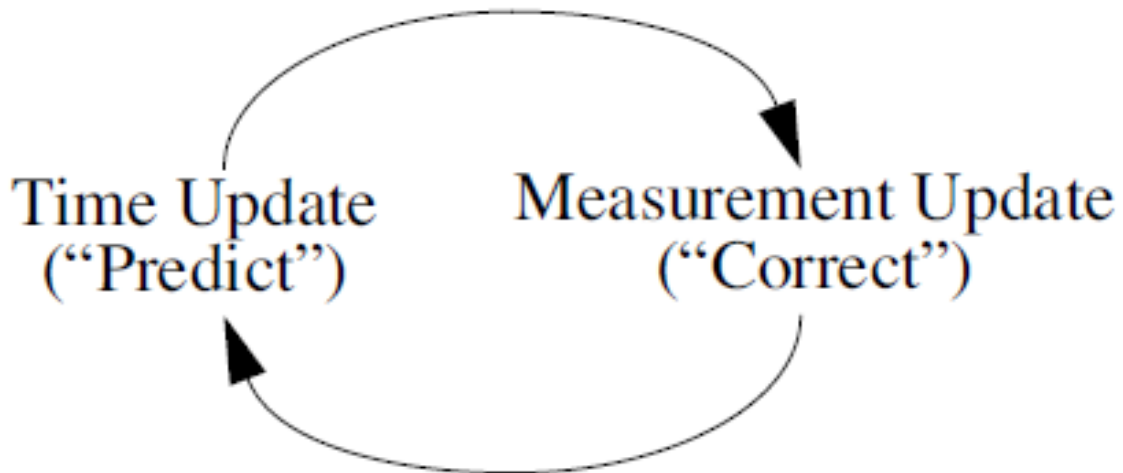


Figure C.2: The high-level diagram of the Kalman Filter

Now, the specific equations for the time and measurement updates will be presented below:

Discrete Kalman Filter time update equations:

$$\hat{x}_k^- = A\hat{x}_{k-1} + Bu_{k-1} \quad (C.9)$$

$$P_k^- = AP_{k-1}A^T + Q \quad (C.10)$$

The time update equations project the state and covariance estimates forward from time step $k - 1$ to step k .

Discrete Kalman Filter measurement update equations:

$$K_k = P_k^- H^T (HP_k^- H^T + R)^{-1} \quad (C.11)$$

$$\hat{x}_k = \hat{x}_k^- + K_k(z_k - H\hat{x}_k^-) \quad (C.12)$$

$$P_k = (I - K_k H)P_k^- \quad (C.13)$$

The next figure will show a complete picture of the operation of the filter, combining the high-level diagram of Figure C.3 with the equations used with KF and also how the iteration happens in each state [415], [416]:

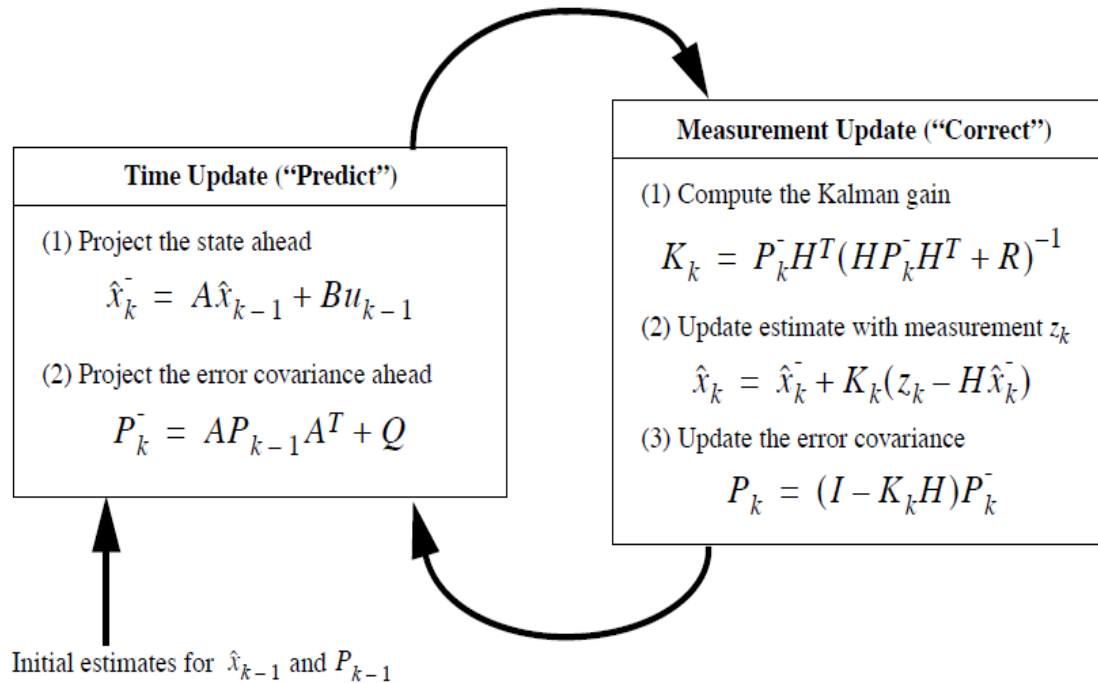


Figure C.3: Kalman Filter equations and iterations

The equations above represent the KF implementation for a generic linear discrete system. The time update stage equations project ahead the state and error covariance estimates from time step $k - 1$ to step k . The estimates from the time update stage are then put into measurement update stage. In this stage, the first step is to compute the Kalman gain K_k , then actually measure the process to obtain the actual measurement z_k to generate an *a posteriori* state estimate. The final step is to obtain an *a posteriori* error covariance estimate.

After each time and measurement update for a particular step, the process is repeated again with the previous *a posteriori* state and error covariance estimates used to predict the new *a priori* state and error covariance estimates. This recursive nature is one of the very appealing features of the Kalman Filter - it makes practical implementations much more feasible than (for example) an implementation of a Wiener filter [417] which is designed to operate on all of the data directly for each estimate. The Kalman filter instead recursively conditions the current estimate on all of the past measurements. As the above cycle takes place multiple times, the noises will be reduced, and the error covariance approaches zero.

C.3 An Intuitive Examples

In order to illustrate the use of the Kalman Filter, a two simple problem examples are explored as shown below.

C.3.1 Simple and Intuitive One-Dimensional Tracking Problem Example

The application of the KF, as a tool for stochastic data fusion, will be illustrated first with the following simple and intuitive one-dimensional tracking problem example, i.e. of an object moving along a line, as shown in Figure C.4. This is a simple one-dimensional Kalman Filter example. The aim of this example was to understand the basics of the Kalman Filter. In the case of a well-defined model, one-dimensional linear system with measurements errors drawn from a zero-mean Gaussian distribution the Kalman Filter has been shown to be the best estimator.

The goal of the filter is to predict the position and velocity of a moving object 2 seconds ahead, having noisy measurements of its positions along the previous 10 seconds (10 samples a second). The object is initially located at the point $x_{old} = 0$ and moves along the X-axis with constant velocity $u = 10$ m/sec, so the motion equation of the object is $x_{new} = x_{old} + time\ difference * velocity$. Easy to see that the position of the object after 12 seconds will be $x_{new} = 120$ m, and this is what we will try to find.

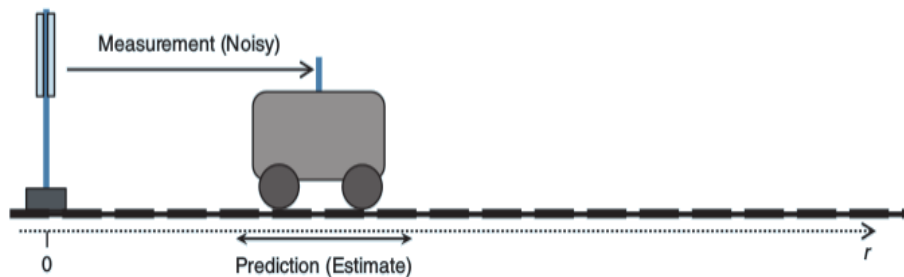


Figure C.4: The one-dimensional linear system under consideration

C.3.1.1 System Model

For a Kalman filter-based state estimator, the system must conform to a certain model. So, if your system model conforms to model mentioned herein, then we can use a Kalman Filter to estimate the state of the system.

I- Motion Model

$$x_{new} = A*x_{old} + B*u + w$$

x_{new} : current state

x_{old} : previous state

A : state transition matrix

B : control input matrix

w : process noise (from a zero mean normal distribution with covariance Q)

II- Sensor Model

$$z = H*x + v$$

z : sensor measurement

H : sensor transformation matrix

x : current state

v : measurement noise (from a zero mean normal distribution with covariance R)

III- Understanding the models

- The state vector 'x' contains the state of the system i.e. the parameters that uniquely describe the current position of the system. In this case, the state vector is a single dimensional vector containing the location of the object. It can also be an N dimensional vector containing position in different axes, velocity in different axes, temperature, state of sensors etc.
- A is the state transition matrix; it applies the effect of each parameter of the previous state on the next state.
- B is the control input matrix that applies the effect of the control signal given to the system onto the next state. So, in this system, the current position is based on the

previous position added to the velocity*time. Mathematically, $x_{new} = I*x_{old} + time\ difference*velocity$.

- In the equation given above, $A = I$ and $B = time\ difference$.
- No system is perfect, given the previous position and the velocity, the new location will not correspond to the equation given above. There will be noise in the system, this noise is modelled as a Gaussian distribution with zero mean (μ) and a certain standard deviation (σ) given by the covariance matrix Q . In simple words, it is the difference between the ideal new location and the actual new location ($x_{new} - (A*x_{old} + B*u) = noise = w$)
- The 'z' vector contains the sensor measurements given by the sensors. The Kalman filter is based on a Hidden Markov Model, meaning that the current 'z' depends ONLY on the current state, and not on any of the previous states, as is evident in the sensor model equation ($z = H*x + v$).
- The 'H' matrix maps the state vector parameters 'x' to the sensor measurements. In simple words, it tells us the sensor measurement that we should get given the current state 'x'.
- Similar to 'w', 'v' is also a parameter representing the noise in sensor measurements. It is also taken from a zero mean Gaussian distribution whose variance is taken from covariance matrix R .

C.3.1.2 Kalman Filter Equations

I. Initialization

We assume that we have a good knowledge of the object's initial position. We can represent this by a Gaussian whose mean is the initial known position and a covariance matrix having small values. This is shown in the Figure C.5 below.



Figure C.5: The state is represented by a Gaussian as shown

II. Prediction Step

The object moves forward with a constant velocity ' u '. We can now have a prediction of the next state from the prediction equations. This prediction is represented by a Gaussian having a mean and a variance. As can see this variance is more than the previous variance, thus showing that we are more uncertain about its position as shown in Figure C.6.

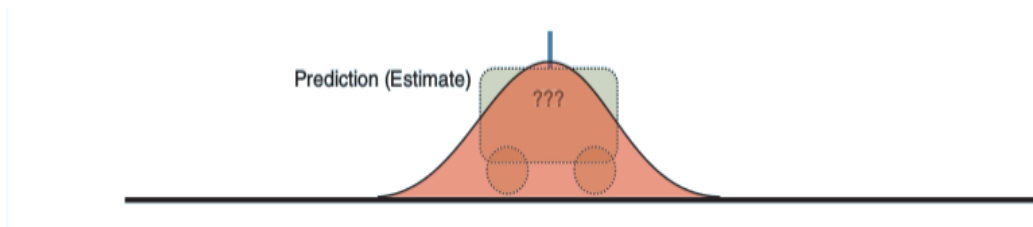


Figure C.6: When the object moves, it becomes more uncertain about its position due to the control being noisy.

Hence, the Gaussian expands

$$x = A*x + B*u$$

$$P = A*P*A^T + Q$$

P : state covariance matrix.

Q : process noise covariance matrix.

- The ' Q ' is the process noise covariance matrix. The diagonal elements contain the variance ($\text{std_dev}(\sigma) * \text{std_dev}(\sigma)$) of each respective variable in the state vector ' x '. So, if the state vector has 2 columns containing the x and y co-ordinates, then Q is a 2x2 matrix whose diagonals contain the variance of each of those variables. The non-diagonal variables are usually set to 0 except in the case of special circumstances. The variances are calculated from the noise variable ' w ', the variance of these values is noted while observing the system.
- The ' P ' is the state covariance matrix, like ' Q ', it models uncertainty in the system. It models uncertainty of the state vector ' x '. Each of the diagonal elements contain the variance (uncertainty in position) of each of those respective state variables in the state vector. For initialization for this matrix, if the state variable's initial location is known to a high degree, the corresponding diagonal element in P is a small. Vice-versa in case the state variable's initial location is not known well.

- In the prediction step, if we look at the second equation we see that the value of P is increasing (due to the addition), this goes to show that in the prediction step, when we do not have any measurement and we only have control command ' u ', the next state will be known with lesser certainty. The opposite happens in the Correction step.

III. Correction Step

In this step, the object makes a measurement of its position using its onboard location sensor i.e. it finds its distance from the pole using a sensor. This measurement is noisy and not exact. This measurement itself is represented by a Gaussian having a mean and covariance. The value of the covariance depends on the accuracy of the sensor; if the sensor is more accurate the covariance value will be small, else it will be large. Figure. C.7 shows the measurement is represented by a blue Gaussian having a covariance smaller than the predicted state

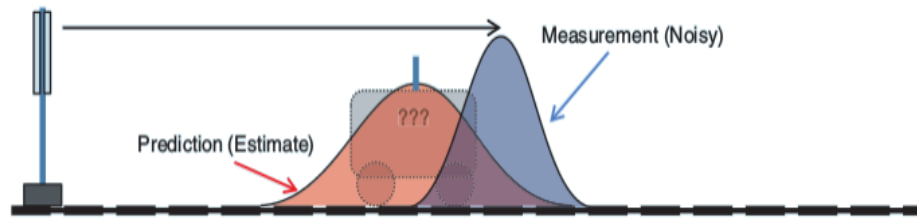


Figure C.7: The measurement is represented by a blue Gaussian having a covariance smaller than the predicted state

$$x = x_{old} + K*(z - H*x_{old})$$

$$P = P_{old} - K*H*P_{old}$$

$$K = P_{old}*H^T * (H*P_{old}*H^T + R)^{-1}$$

K : Kalman Gain

R : Measurement noise covariance matrix

- ' K ' is called the Kalman Gain. It is calculated from state covariance matrix and the measurement covariance matrix. As the measurement covariance matrix R approaches zero, the actual measurement z is “trusted” more and more, while the

predicted measurement $H*x_{old}$ is trusted less and less. On the other hand, as the state covariance matrix P_{old} approaches zero the actual measurement z is trusted less and less, while the predicted measurement $H*x_{old}$ is trusted more and more.

- In the first equation for 'x', we are approximately taking a weighted average of the predicted state vector and the state vector generated from the measurement. This weighting is decided by the Kalman gain.
- In the second equation for 'P', we see that the value of P is decreasing (subtraction), this is because we believe that the sensor is more accurate and our uncertainty about the object's position decreases.
- If we look at it from an analytical perspective, we have two Gaussians. They represent state vector and measured state. If we multiply these 2 Gaussians, we get another Gaussian which is actually the best estimate of the position of the object as shown in Figure C.8.

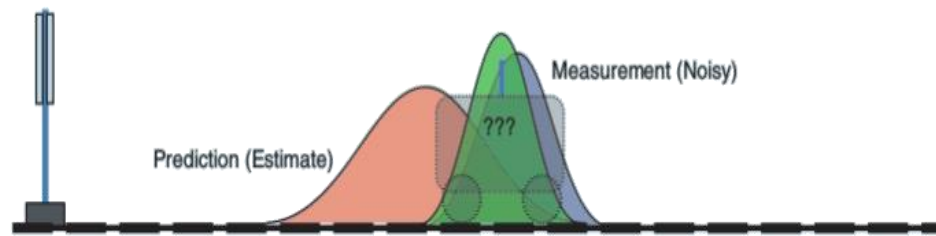


Figure C.8: Multiply the two Gaussians to have the best estimate (green) of the object's position

C.3.1.3 Solution and Simulation Results

We will measure (sample) the position of the object every $dt = 0.1$ seconds. But, because of imperfect conditions, such as weather etc., our measurements will be noisy. So, the instantaneous velocity derived from two consecutive position measurements (remember, we measure only position) will become inaccurate. Hence, we will use KF as we need an accurate and smooth estimate for the velocity in order to predict the object's position in the future. Also, we will assume that the measurement noise is normally distributed, with zero mean (μ) and standard deviation (σ).

At every measurement epoch, we wish to know the best possible estimate of the location of the object. Information is available from two sources: 1) predictions based on the last known position and velocity of the object and 2) measurements from the sensors deployed

at the track side. The information from the predictions and measurements are combined to provide the best possible estimate of the location of the object.

To show the power of the KF algorithm, a comparison between KF algorithm and running average (RA) method was performed by applying these two algorithms to the same task of predicting the position and velocity of a moving object 2 seconds ahead, having noisy measurements of its positions along the previous 10 seconds (10 samples a second).

Matlab is used to simulate the two algorithms. The position estimation results are shown in Figure C.9. As shown the KF algorithm successfully tracks the estimated value very closely to the actual true value even in the presence of high noise.

Figure C.10 shows the velocity estimation results. Again, the results depict the excellent response of the KF algorithm over the running average method even in the presence of high noise from the sensors.

Figure C.11 shows the expected position of the object 2 seconds ahead by using KF algorithm and RA method. Once more, the results indicate the promising predication performance of the KF algorithm over the RA method.

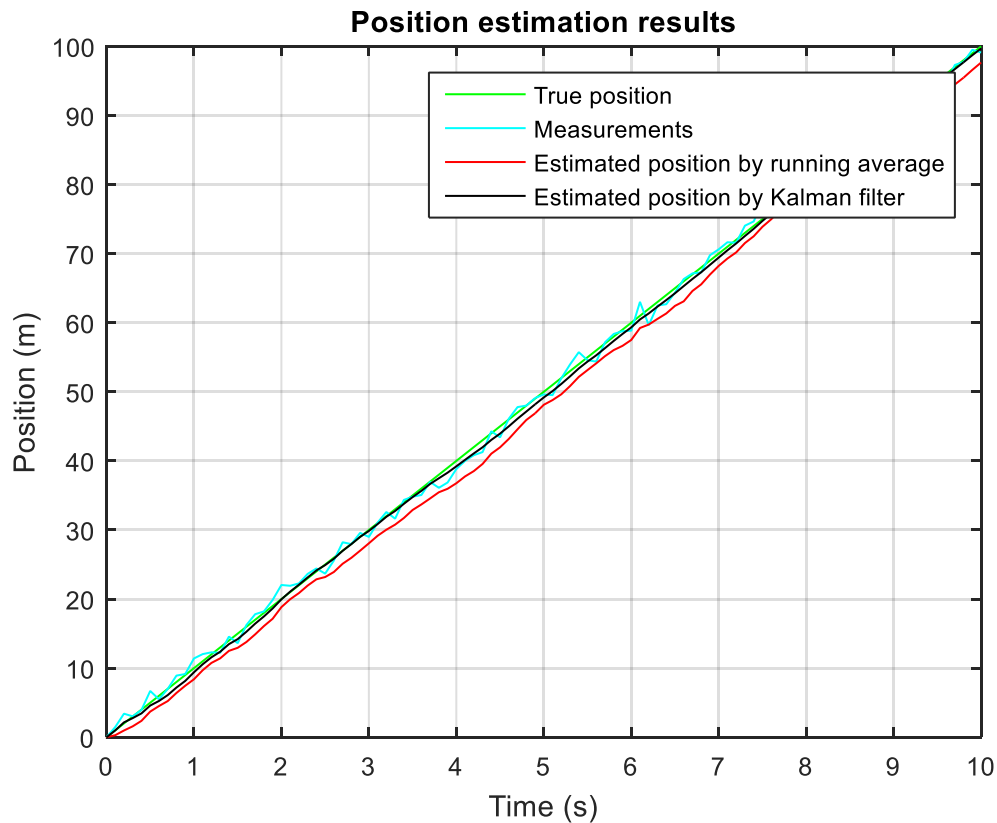


Figure C.9: Position estimation results

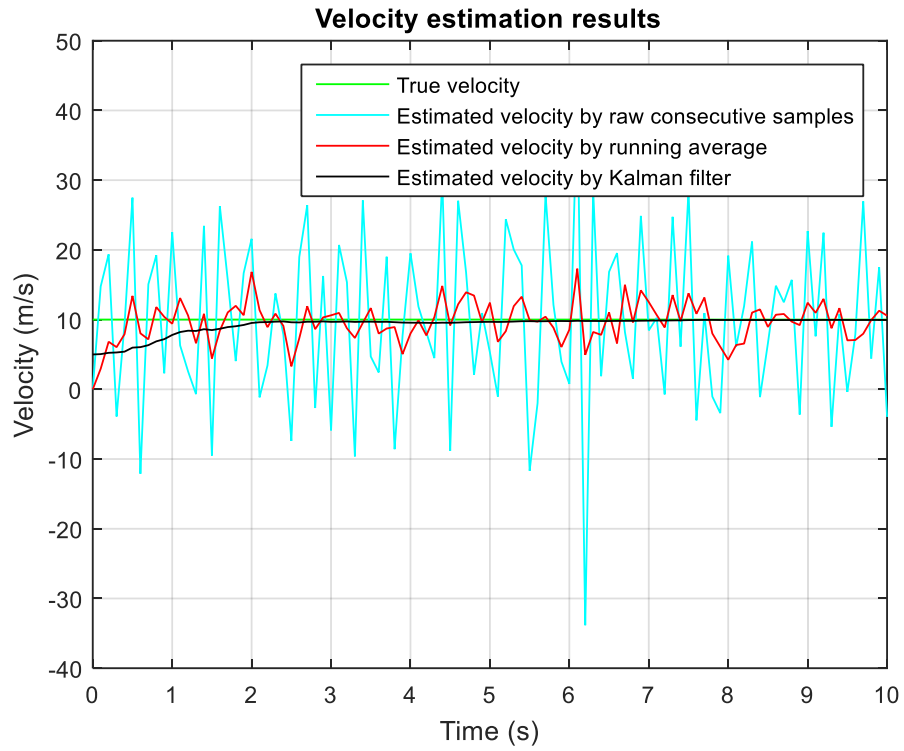


Figure C.10: Velocity estimation results

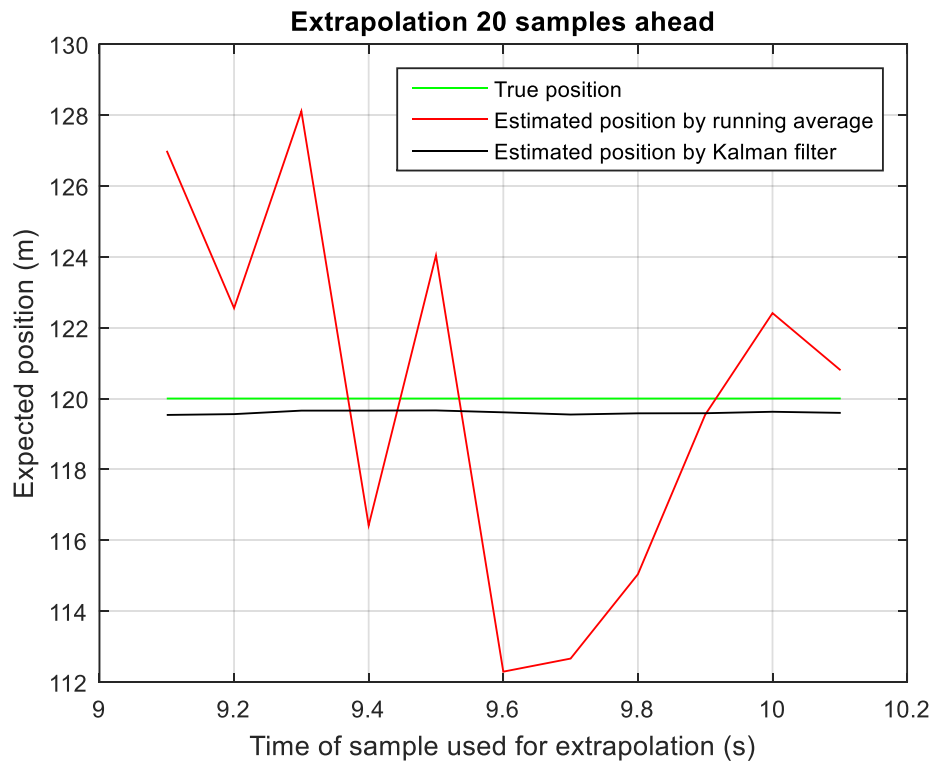


Figure C.11: The expected position of the object 2 seconds ahead

As shown from the previous simple and intuitive one-dimensional tracking problem example that Kalman Filter algorithm is most powerful tool to estimate and predict of any parameters of interest even in the presence of high noise from the sensors.

C.3.2 Kalman Filter in Simulink Example

The Simulink model shown in Figure C.12 is an example explained how the Kalman Filter can be implemented in Simulink. The model itself is configured with a Gaussian process connected with a Kalman Filter. To directly use this model, one only needs to provide model parameters including parameters of the Gaussian process, which are state-space matrices, A , B , C , and D , initial state, x_0 , and covariance matrices, Q and R ; and similar parameters for the Kalman Filter, which can be in different values to mimic the model mismatch, plus the state covariance, P . This Kalman Filter Simulink model can also be used as a standard model block to be connected with any other systems.

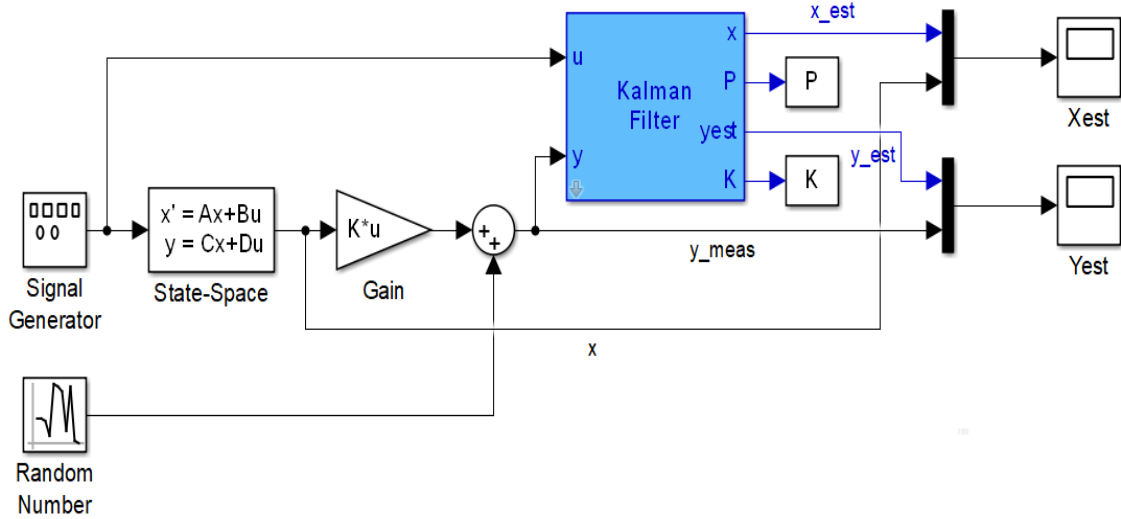


Figure C.12: Kalman Filter Simulink model

The state estimation results are shown in Figure C.13. As shown, the KF algorithm successfully tracks the estimated value very closely to the actual true value even in the presence of high noise.

Figure C.14 shows the output estimation results. Again, the results depict the excellent response of the KF algorithm even in the presence of high noise environment.

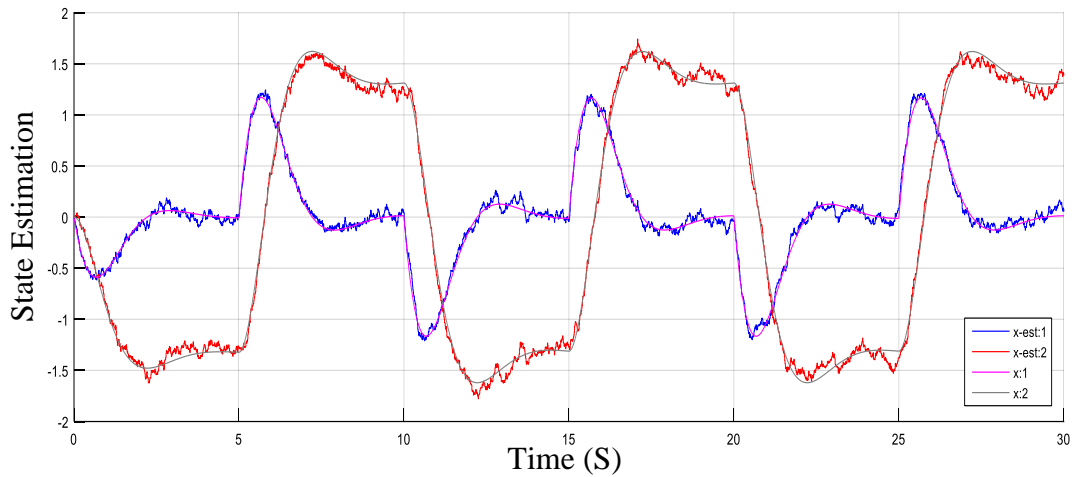


Figure C.13: State estimation results

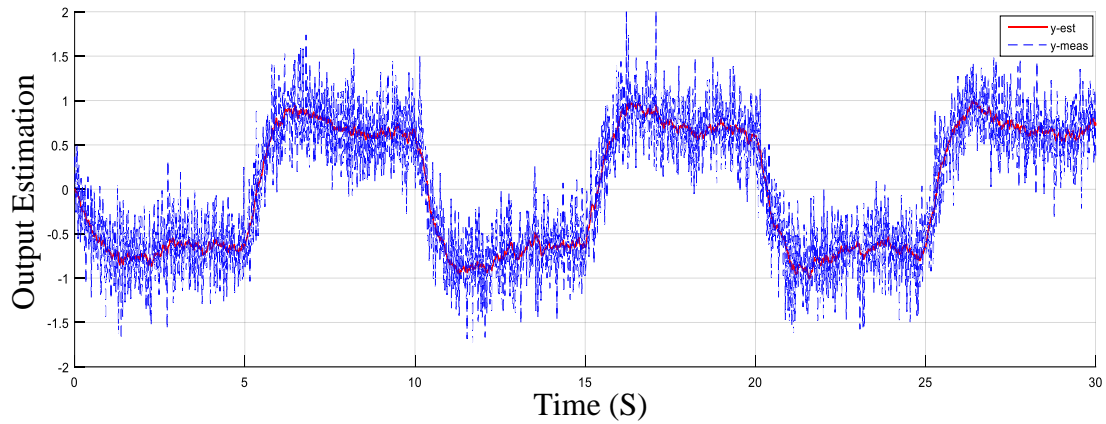


Figure C.14: Output estimation results

As noticed from the previous examples, the superior performance for the KF algorithm as it is able to track the estimated value very closely to the actual true value even in the presence of high noise from the sensors.

C.4 Sensitivity Analysis of the Kalman Filter Parameters

C.4.1 Effect of Noise Covariance Assumptions

The selection of the assumed covariance matrices Q , R and P_{k-1} can have a significant effect on the estimation performance of a Kalman filter. The selection of P_{k-1} is coupled with the assumed initial state and affects the initial convergence of the filter. In many

situations, the effect of P_{k-1} is not significant, and in fact it is often arbitrarily initialized to an identity matrix for simplicity.

The effects of Q and R are much more significant and they affect the overall performance of the filter. A basic way to think of Q and R is that they are weighting factors between the prediction (state) equations and the measurement (output) equations. This ratio is shown within the Kalman gain equation (C.8). Considering a larger Q is equivalent to considering larger uncertainty in the state equations, which is equivalent to trusting the result of these equations less, which effectively means that the filter should correct more with the measurement update. Similarly, considering a larger R is equivalent to considering larger uncertainty in the measurement, which is equivalent to trusting the measurement less, which effectively means that the filter should correct less with the measurement update. A diagram detailing this phenomenon is shown in Figure C.15.

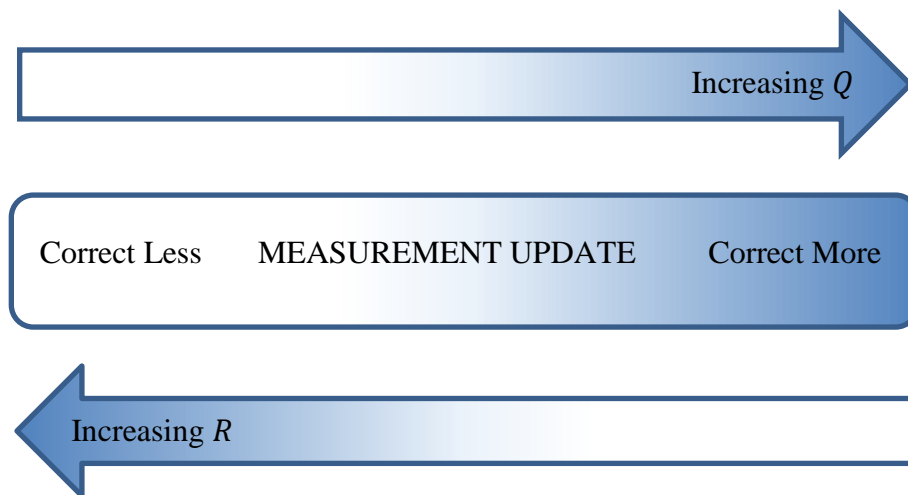


Figure C.15: Diagram of Noise Covariance Assumptions Effect on Filter Operation

C.4.2 H Matrix as a Linear Transformation

The purpose of the H matrix is to essentially convert the states into outputs. For the linear Kalman filter this occurs by considering some linear combination of the states, i.e. H is a linear transformation. In some simple cases, H is just used to select certain states which are measured, when other states are not. For example, if the first, second, and fifth states of a 5-dimensional state vector are measurable, the H matrix would be defined as

$$H = \begin{bmatrix} 1 & 0 & 0 & 0 & 0 \\ 0 & 1 & 0 & 0 & 0 \\ 0 & 0 & 0 & 0 & 1 \end{bmatrix}$$

Since that $z_k = Hx_k$, then

$$z_k = \begin{bmatrix} 1 & 0 & 0 & 0 & 0 \\ 0 & 1 & 0 & 0 & 0 \\ 0 & 0 & 0 & 0 & 1 \end{bmatrix} \begin{bmatrix} x_1 \\ x_2 \\ x_3 \\ x_4 \\ x_5 \end{bmatrix} = \begin{bmatrix} x_1 \\ x_2 \\ x_5 \end{bmatrix}$$

The H matrix can also be used to consider scaling effects. For example, if the radius (r_k) is a state, but the diameter (D_k) can be measured, the output equation could be represented by $z_k = Hx_k$, where $z_k = D_k$, $H = 2$ and $x_k = r_k$.

Other uses of H could be to consider combinations of states. For example, if the lengths of 3 sides of a triangle are states, but the perimeter can be measured, the output equation could be represented by

$$z_k = x_1 + x_2 + x_3, \text{ where } H = [1 \quad 1 \quad 1] \text{ and } x_k = \begin{bmatrix} x_1 \\ x_2 \\ x_3 \end{bmatrix}$$

C.4.3 An Intuitive Example

The effects of the selection of the assumed covariance matrices Q and R and how much significant they can affect the overall estimation performance of a Kalman Filter will be illustrated with the following simple and intuitive one-dimensional tracking problem example, i.e. of an object moving along a specified tracking line that has two (noisy) sensors. One of them is an odometry sensor (otherwise known as control input to the system) that tells you how far your object has moved since the last time step. The other one is an absolute sensor (measurement sensor) that tells you the actual position of the object. Also, this sensor can only be read every 20 time steps. Both of these sensors are noisy and will not give particularly precise readings. Note, however, that the sensors have different characteristics that we would like to take advantage of:

- The odometry sensor can be read very quickly, and so we can use it to update our estimated position on every time step. Unfortunately, because it only tells us the distance it thinks we've traveled since the last time step, relying on this sensor alone will cause us to drift.
- The measurement sensor can only be read slowly, and has larger noise than the odometry, however its noisy readings are always centered on the true position of the object. This means that the readings from the measurement sensor will not drift off too much.

The objective of a Kalman filter is to "optimally" integrate these two kinds of sensors, trying to take advantage of their best characteristics. It does this by keeping track of the current amount of noise in the system, and then mixing in these sensors readings according to how much noise they will introduce.

The aim of this example was to understand and analyze how much the selection of the assumed covariance matrices Q and R can have a significant effect on the estimation performance of a Kalman filter.

To study the effect on the estimation performance of a Kalman filter due to the selection of the assumed covariance matrices Q and R , FOUR scenarios are assumed. In all scenarios, the simulation results will show:

- The object's actual trajectory in blue.
- Green circles showing what our prediction would look like if we just integrated the odometry sensor readings.
- Red stars showing the occasional measurements. Notice how they're usually pretty inaccurate.
- Black dots showing the Kalman filtered prediction.

First scenario will deal with change the values of measurement noise covariance R , being a trustworthy candidate of measurement variable, and analyze its effect whereas the process noise covariance Q keep it at 0.1. The simulation results (Figure C.16, Figure C.17 and Figure C.18) depicts the effect of varying the values of R .

In Figure C.16, R is assigned the value 0.05 that means medium level of trust in the measured value by the sensor, moreover it is suitable for successfully model.

In Figure C.17, R is given the value 0.001 depicting a trust in the measured variables obtained from the sensor because it is approached to 0 so the estimated value is following the measured value more than the actual true value.

In Figure C.18, R is assigned the value 0.1, depicting a minimum level of trust in the measured value by the sensor. Therefore, the estimated value is following the actual true value more than the measured value.

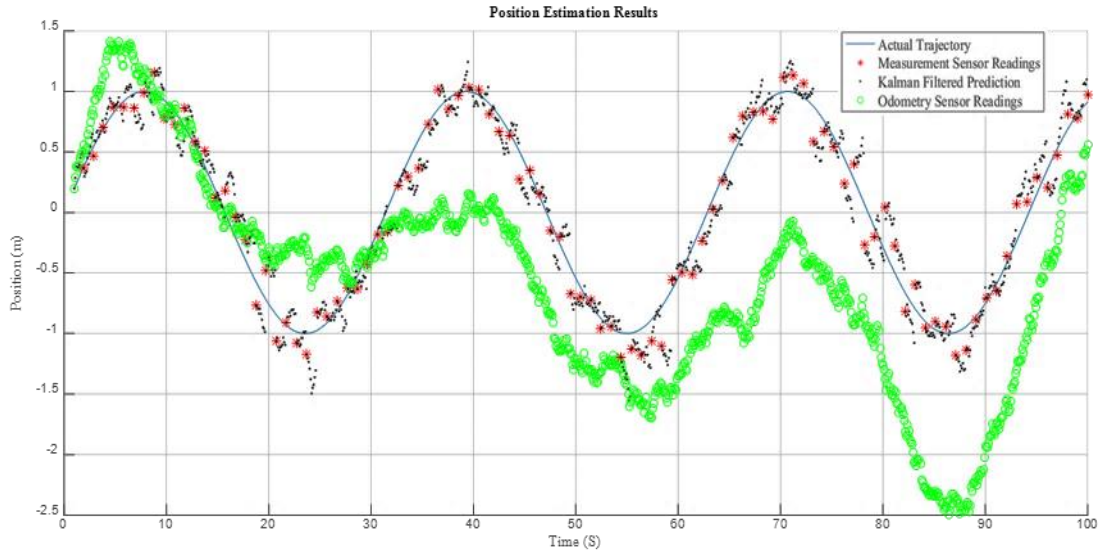


Figure C.16: Position estimation results with $R = 0.05$

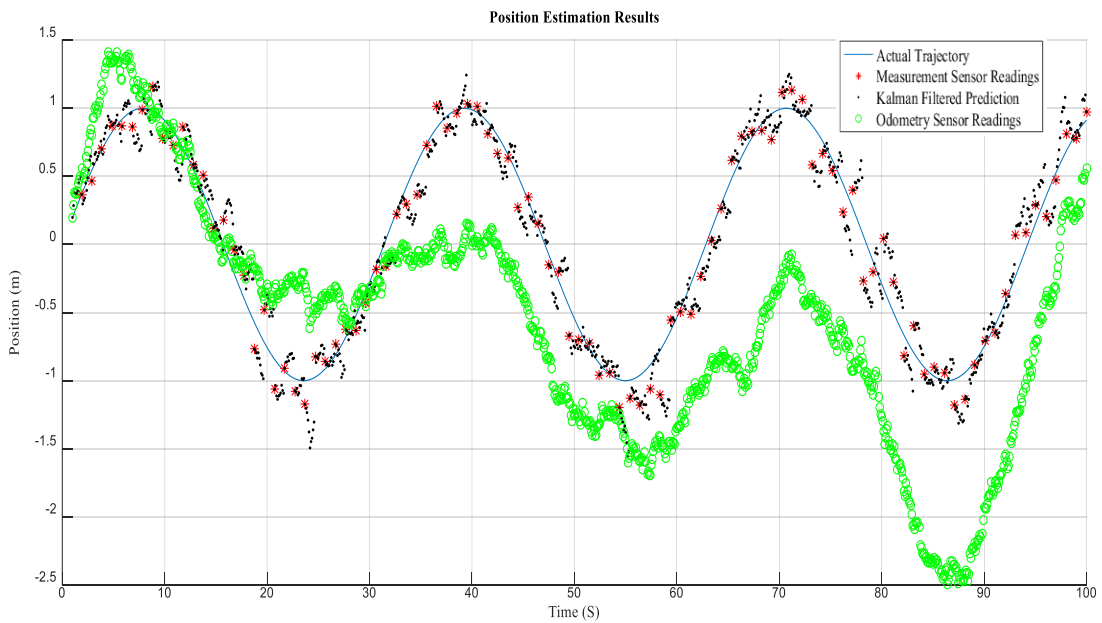


Figure C.17: Position estimation results with $R = 0.001$

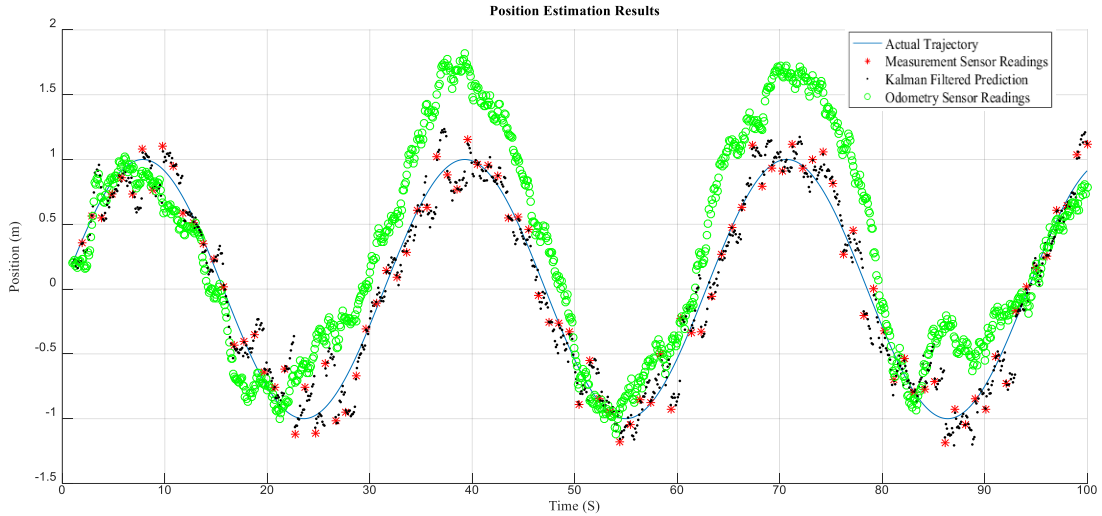


Figure C.18: Position estimation results with $R = 0.1$

Second scenario will deal with depicting a maximum trust in the measured variables obtained from the sensor where in this scenario the measurement noise covariance R will be 0 while the process noise covariance Q will assign the value 10. So, the estimated value is expecting to follow the measured value more and more than the actual true value as shown in Figure C.19.

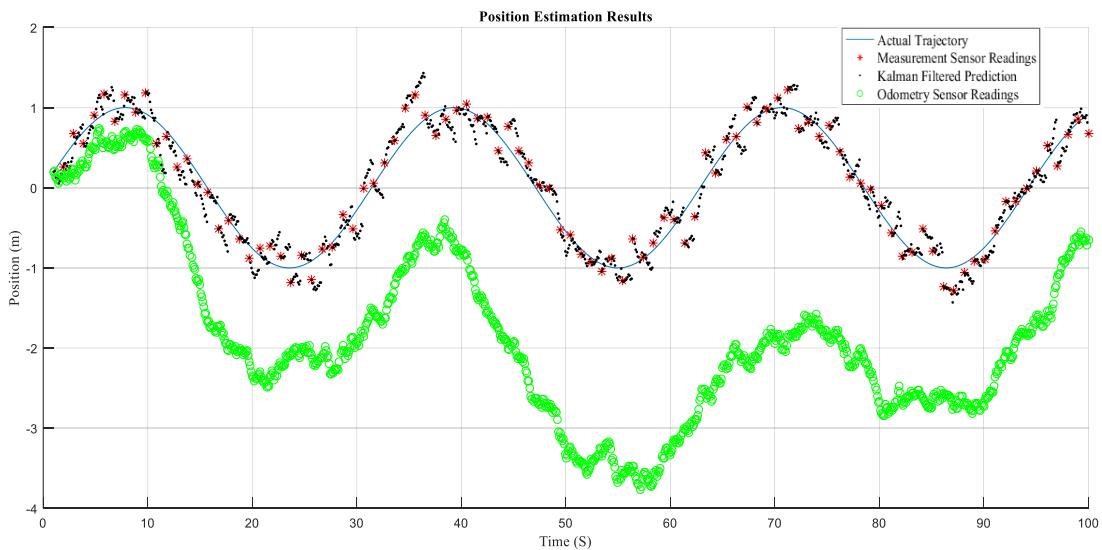


Figure C.19: Position estimation results with $R = 0$

Third scenario will deal with change the values of process noise covariance Q , being a trustworthy candidate of actual true variable, and analyze its effect whereas the

measurement noise covariance R keep it at 0.1. The simulation results (Figure C.20, Figure C.21 and Figure C.22) depicts the effect of varying the values of Q .

In Figure C.20, Q is assigned the value 0.05 that means medium level of trust in the actual true value obtained from the system model, moreover it is suitable for successfully model.

In Figure C.21, Q is given the value 0.001 depicting a trust in the actual true variables obtained from the system model because it is approached to 0 so the estimated value is following the actual true value more than the measured value.

In Figure C.22, Q is assigned the value 0.1, depicting a minimum level of trust in the actual true value obtained from the system model. Therefore, the estimated value is based on the measured value more than the actual true value (same as Figure C.18).

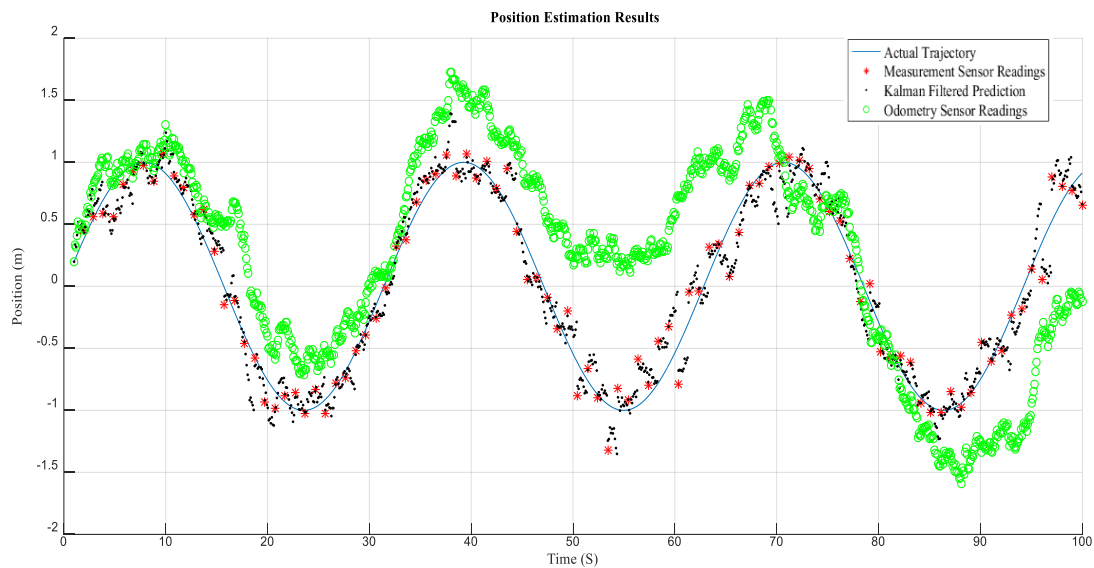


Figure C.20: Position estimation results with $Q = 0.05$

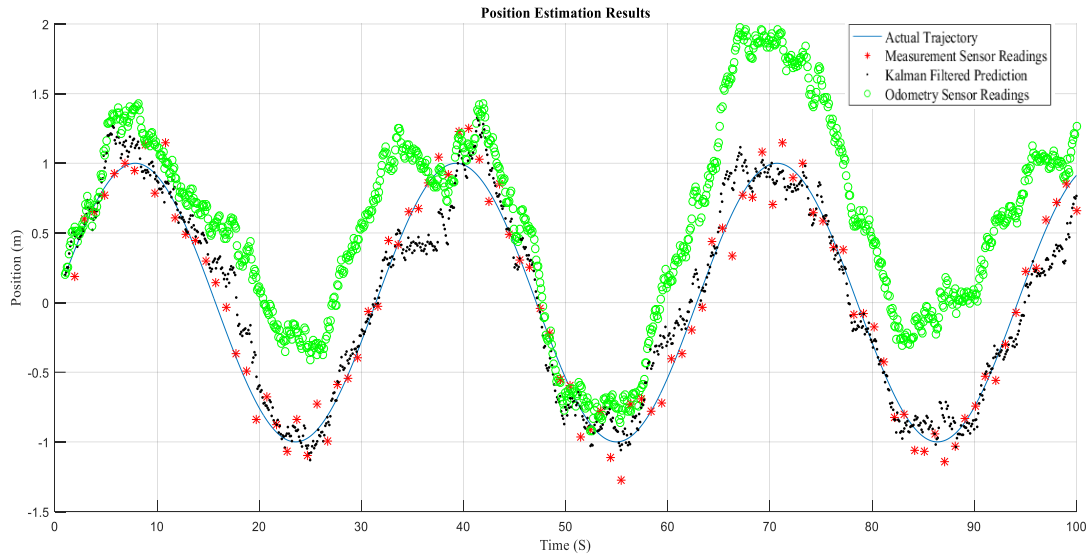


Figure C.21: Position estimation results with $Q = 0.001$

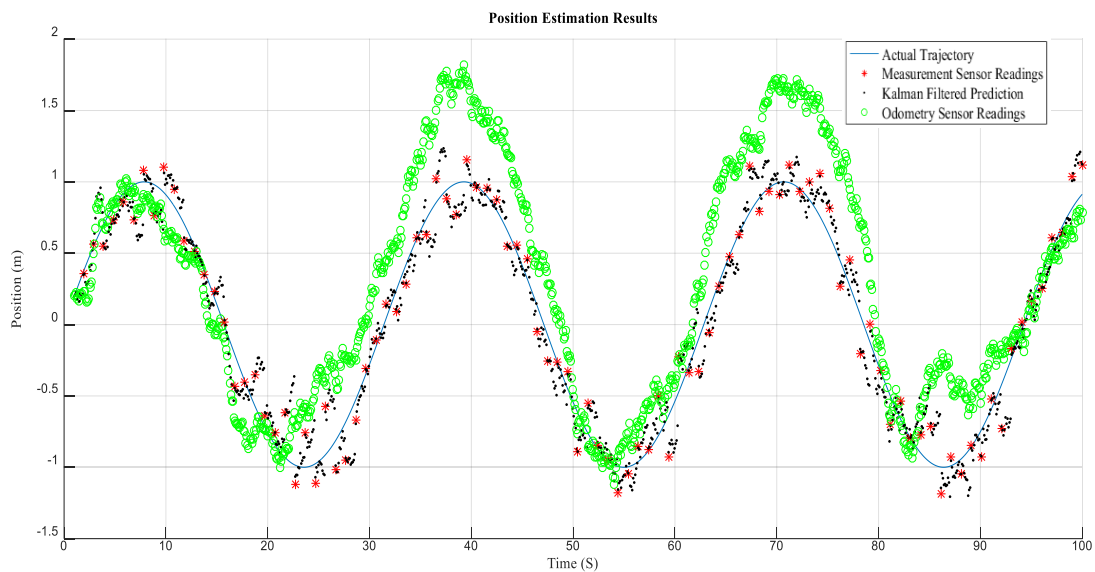


Figure C.22: Position estimation results with $Q = 0.1$

Fourth scenario will deal with depicting a maximum trust in the actual true variables obtained from the system model where in this scenario the process noise covariance Q will be 0 while the measurement noise covariance R will assign the value 10. So, the estimated value is expecting to follow the actual true value more and more than the measured value as shown in Figure C.23.

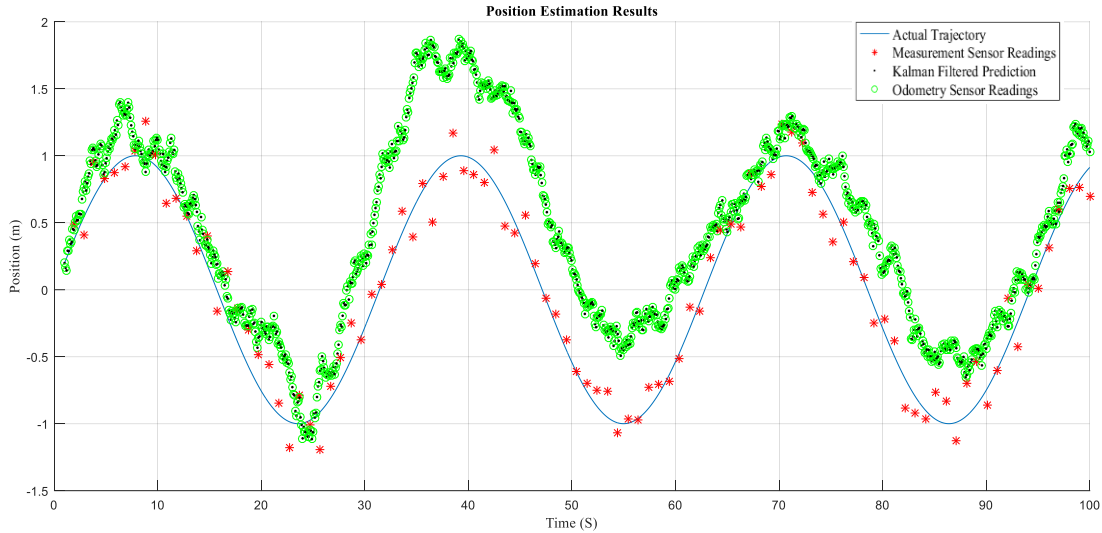


Figure C.23: Position estimation results with $Q = 0$

Through the previous discussion, it is obviously noted that the selection of the noise parameters (i.e. the process noise covariance Q and the measurement noise covariance R) directly have a significant impact on the Kalman filter's performance in estimating dynamic states. So, whether we have a rational basis for choosing the parameters, often times superior filter performance can be obtained by tuning the filter parameters R and Q .

C.5 Conclusion

In this appendix, the Kalman Filter was introduced as a tool for statistical estimation in the context of linear Gaussian dynamical systems. Some simple problems were explored in order to help aid in the basic understanding of this complex topic.

The Matlab simulation results show good performance for the KF algorithm as it is able to track the estimated value very closely to the actual true value even in the presence of high noise from the sensors. Comparison between the KF algorithm and the running average method was performed and showed the superior performance of the KF algorithm.

The effects of the selection of the assumed covariance matrices Q and R and how significantly they can affect the overall estimation performance of a Kalman Filter was investigated with a simple and intuitive one-dimensional tracking problem example.

This appendix serves as an introduction to Kalman filtering and provides a glimpse into some of its features, mathematical and statistical formulations, overview of its history, and applications.